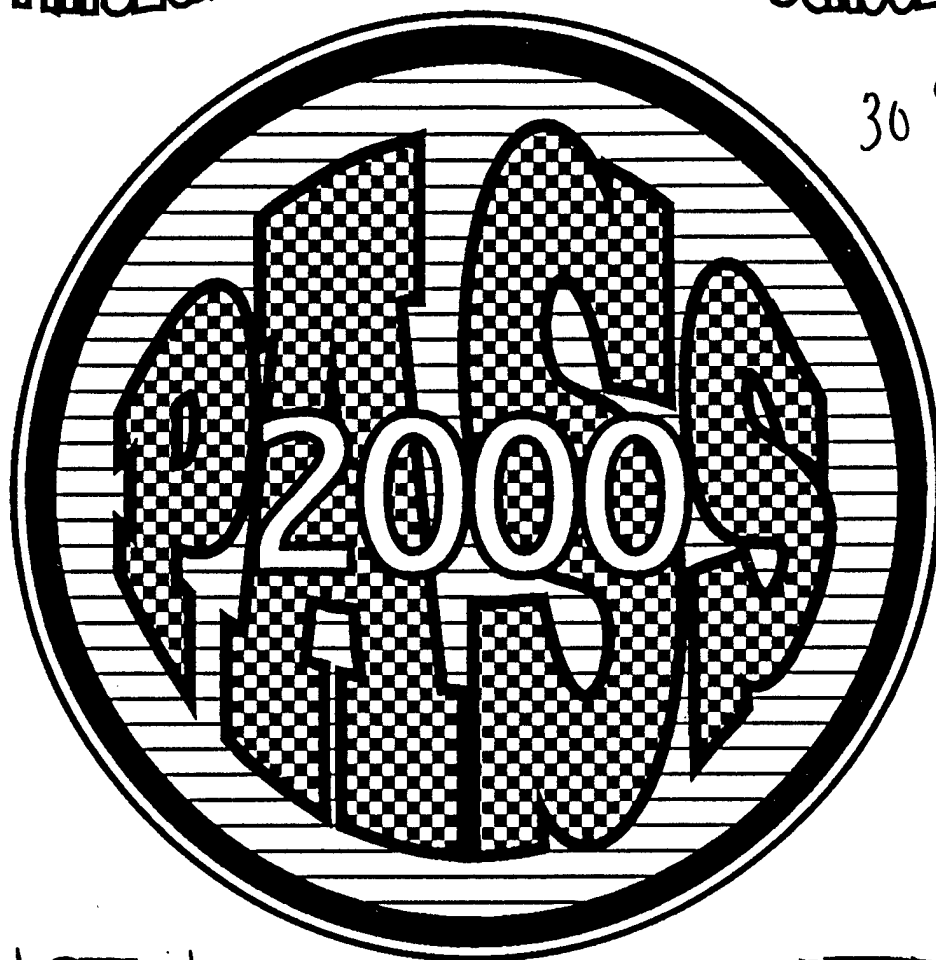


PHYSICAL ACOUSTICS SUMMER SCHOOL

30 Sep 2001



ASTILOMAR CONFERENCE CENTER

VOLUME II

TRANSPARENCIES

DISTRIBUTION STATEMENT A
Approved for Public Release
Distribution Unlimited

20011030 087

2000 PHYSICAL ACOUSTICS SUMMER SCHOOL (PASS 00)

VOLUME II: TRANSPARENCIES

This work relates to Department of Navy Grant 14-98-1-0044 issued by the Office of Naval Research. The United States Government has a royalty-free license throughout the world in all copyrightable material contained herein.

TABLE OF CONTENTS

INTRODUCTION TO PHYSICAL ACOUSTICS, ANTHONY A. ATCHLEY	AA-1
NONLINEAR ACOUSTICS, STEVEN L. GARRETT.....	SLG-1
NOISE AND SENSORS, THOMAS G. GABRIELSON	TGG-1
RESONANT ULTRASOUND SPECTROSCOPY, ALBERT MIGLIORI	AM-1
ATMOSPHERIC AND METEOROLOGICAL ACOUSTICS, KENNETH E. GILBERT	KEG
THERMOACOUSTICS, ROBERT M. KEOLIAN	RMK-1
POROUS MEDIA, JAMES M. SABATIER	JMS-1
MEDICAL APPLICATIONS OF ACOUSTICS, LAWRENCE A. CRUM	LAC-1
SONOLUMINESCENCE, THOMAS J. MATULA	TJM-1
REPORT DOCUMENTATION PAGE	RDP

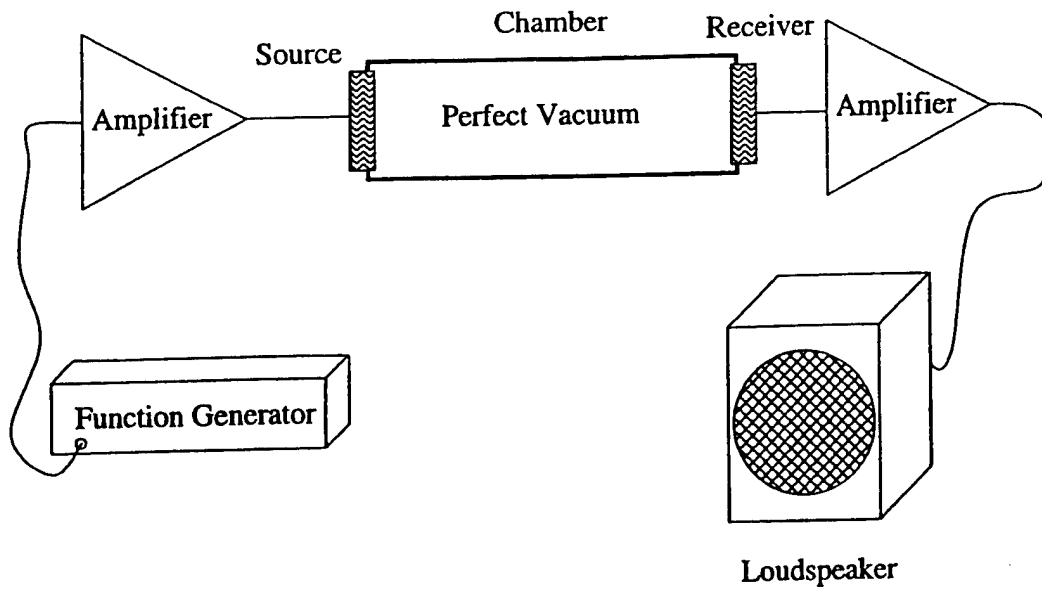
Connections in Physical Acoustics

An Introduction to PASS 2000

Anthony Atchley
Graduate Program in Acoustics
The Pennsylvania State University

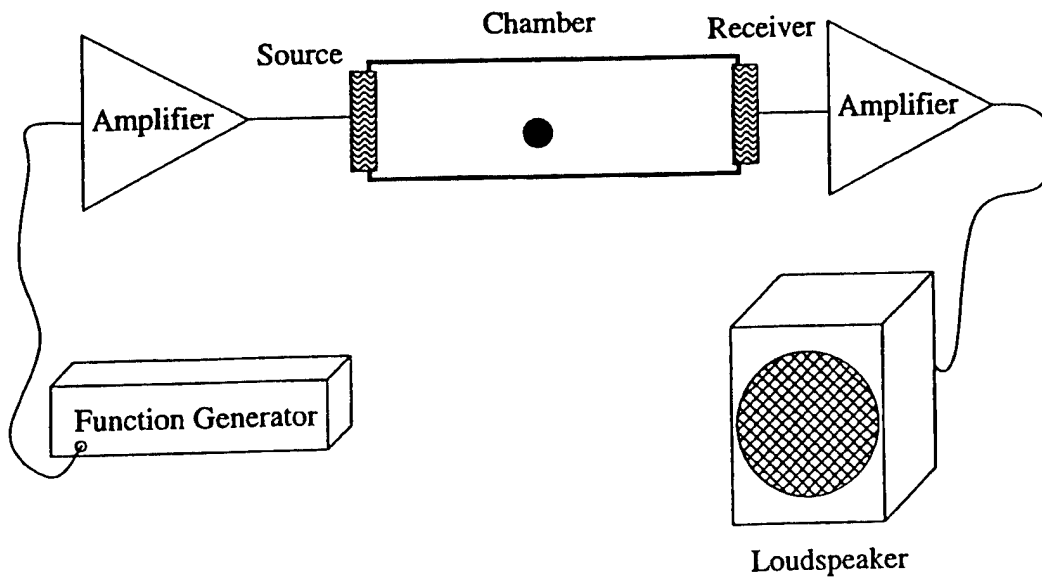
aatchley@psu.edu

Building Up From Nothing(?)

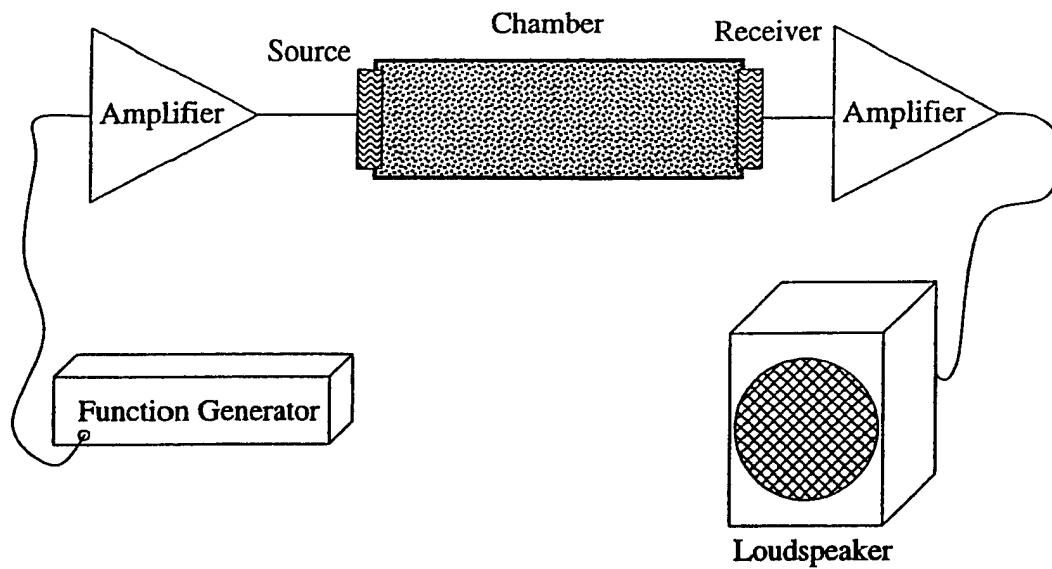


2

Building Up From Next to Nothing



Building Up To Something



4

Fundamental Equations for a Lossless Fluid Continuum

	<u>General Form</u>	<u>Linearized 1-D Form</u>
<u>Momentum</u>	$\rho \frac{d\bar{u}}{dt} = -\nabla P$	$\frac{\partial p}{\partial x} = -\rho_o \frac{\partial u}{\partial t}$
<u>Continuity</u>	$\frac{\partial \rho}{\partial t} + \nabla \cdot \rho \bar{u} = 0$	$\frac{\partial u}{\partial x} = -\frac{1}{\rho_o} \frac{\partial \rho_1}{\partial t}$
<u>Equation of State</u>		$p = \frac{B}{\rho_o} \rho_1$

Simple Finite Difference Forms of the Linearized 1-D Equations

	<u>Linearized 1-D Form</u>	<u>Finite Difference Form</u> *
<u>Momentum</u>	$\frac{\partial p}{\partial x} = -\rho_o \frac{\partial u}{\partial t}$	$p_{n+1} = p_n - j\omega \frac{\rho_o \Delta x}{S} U_n$
<u>Continuity</u>	$\frac{\partial u}{\partial x} = -\frac{1}{\rho_o} \frac{\partial \rho_1}{\partial t}$	$U_{n+1} = U_n - j\omega \frac{S \Delta x}{B} p_n$

* $e^{j\omega t}$ time dependence is assumed.

U is the volume velocity.

S is the cross sectional area.

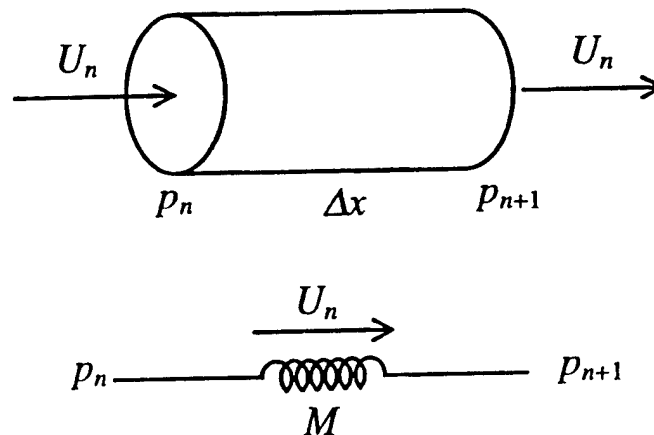
6

Equivalent Circuit Interpretation of F. D. Equations

Momentum

$$p_{n+1} = p_n - j\omega \underbrace{\frac{\rho_o \Delta x}{S}}_M U_n$$

$M = \text{Inertance}$

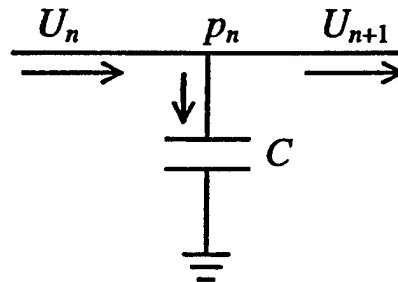
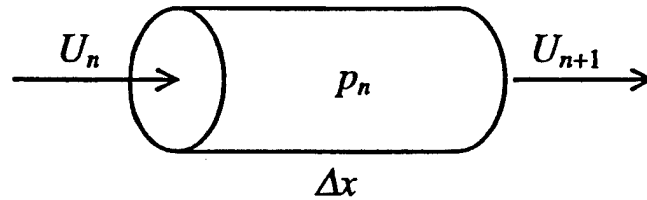


Convention: $p \sim \text{Voltage}$
 $U \sim \text{current}$

Equivalent Circuit Interpretation of F. D. Equations

Continuity

$$U_{n+1} = U_n - j\omega \underbrace{\frac{S\Delta x}{B}}_{C = \text{Compliance}} p_n$$

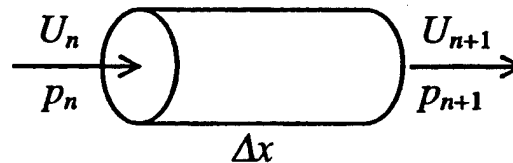


8

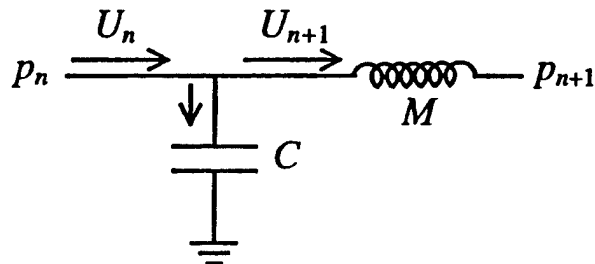
Combined Equivalent Circuit Representation

Coupled Equations

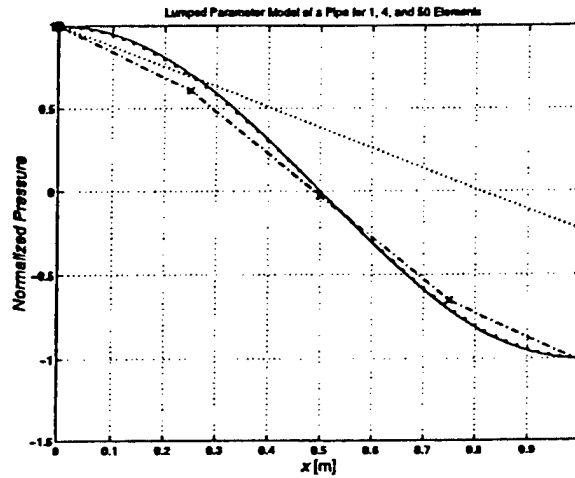
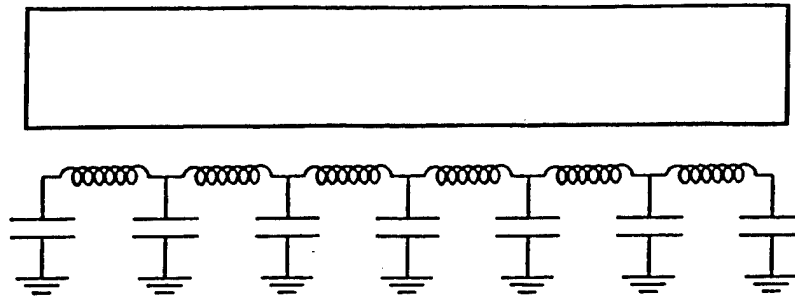
$$U_{n+1} = U_n - j\omega C p_n$$



$$p_{n+1} = p_n - j\omega M U_n$$

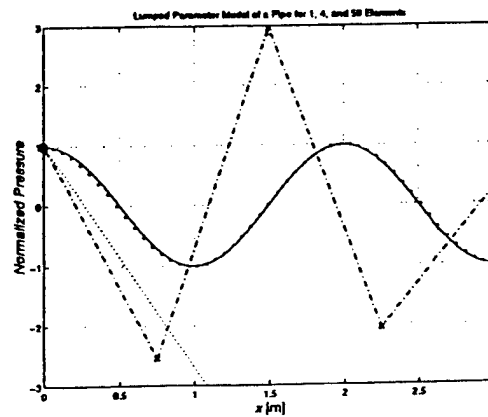
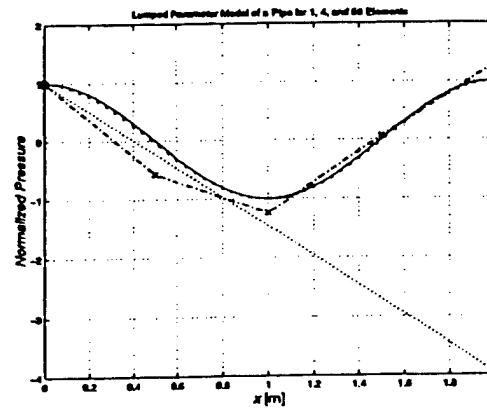
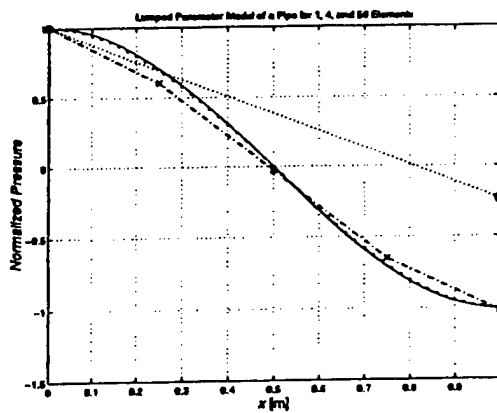


Lumped Parameter Model of a Pipe



10

Effect of Changing Length of Pipe with Fixed N



11

Higher-Order Numerical Schemes

Recast the equations as

$$p_{n+1} = p_n - j\omega \frac{M}{\Delta x} U_n \Delta x \quad U_{n+1} = U_n - j\omega \frac{C}{\Delta x} p_n \Delta x$$

or

$$p_{n+1} = p_n + f(U_n) \Delta x \quad U_{n+1} = U_n + g(p_n) \Delta x$$

Example: 4th Order Runge - Kutta Method

$$p_{n+1} = p_n + \frac{\Delta x}{6} [k_{n1} + 2k_{n2} + 2k_{n3} + k_{n4}] \quad U_{n+1} = U_n + \frac{\Delta x}{6} [\ell_{n1} + 2\ell_{n2} + 2\ell_{n3} + \ell_{n4}]$$

$$\begin{aligned} k_{n1} &= f(U_n) & \ell_{n1} &= g(p_n) \\ k_{n2} &= f\left(U_n + \frac{\Delta x}{2} \ell_{n1}\right) & \ell_{n2} &= g\left(p_n + \frac{\Delta x}{2} k_{n1}\right) \\ k_{n3} &= f\left(U_n + \frac{\Delta x}{2} \ell_{n2}\right) & \ell_{n3} &= g\left(p_n + \frac{\Delta x}{2} k_{n2}\right) \\ k_{n4} &= f(U_n + \Delta x \ell_{n3}) & \ell_{n4} &= g(p_n + \Delta x k_{n3}) \end{aligned}$$

12

The Dispersion Relation

Return to the differential forms of the fundamental equations and seek x -dependence of the form e^{jkx} .

$$\frac{\partial p}{\partial x} = -j\omega M_\ell U \quad \frac{\partial U}{\partial x} = -j\omega C_\ell p,$$

where

$$M_\ell = \frac{M}{dx} = \frac{\rho_o}{S} \quad C_\ell = \frac{C}{dx} = \frac{S}{B}.$$

The coupled equations can be written as

$$\begin{pmatrix} -jk & j\omega M_\ell \\ j\omega C_\ell & -jk \end{pmatrix} \begin{pmatrix} p \\ U \end{pmatrix} = \begin{pmatrix} 0 \\ 0 \end{pmatrix}.$$

Setting

$$\begin{vmatrix} -jk & j\omega M_\ell \\ j\omega C_\ell & -jk \end{vmatrix} = 0$$

yields the dispersion relation

$$k = \pm \frac{\omega}{c} \quad \text{where} \quad c = \frac{1}{\sqrt{M_\ell C_\ell}} = \sqrt{\frac{B}{\rho_o}}.$$

Introducing Viscous and Thermal Boundary Layer Losses

(Swift, et. al.)

Viscous Losses

Conservation of momentum is expressed by the Navier-Stokes Equation:

$$\rho \frac{d\bar{u}}{dt} = -\nabla P + \left(\frac{4}{3}\mu + \mu_B \right) \nabla(\nabla \cdot \bar{u}) - \mu \nabla \times \nabla \times \bar{u}.$$

Assuming propagation in a circular pipe of radius a , and making reasonable approximations the N-S equation reduces to

$$j\omega\rho_o u = -\frac{\partial p}{\partial x} + \mu \frac{1}{r} \frac{\partial}{\partial r} \left(r \frac{\partial u}{\partial r} \right).$$

The solution is

$$u(x, r) = -\frac{1}{j\omega\rho_o} \frac{\partial p}{\partial x} \left[1 - \frac{J_o((j-1)r / \delta_v)}{J_o((j-1)a / \delta_v)} \right],$$

where $\delta_v = \sqrt{\frac{2\mu}{\rho_o\omega}}$ is the viscous penetration depth.

14

The volume velocity is found by integrating $u(x, r)$ over the cross section of the pipe. The result is

$$U = -\frac{S}{j\omega\rho_o} \frac{\partial p}{\partial x} [1 - f_v],$$

where

$$f_v = \frac{2J_1((j-1)a / \delta_v)}{((j-1)a / \delta_v) J_o((j-1)a / \delta_v)}.$$

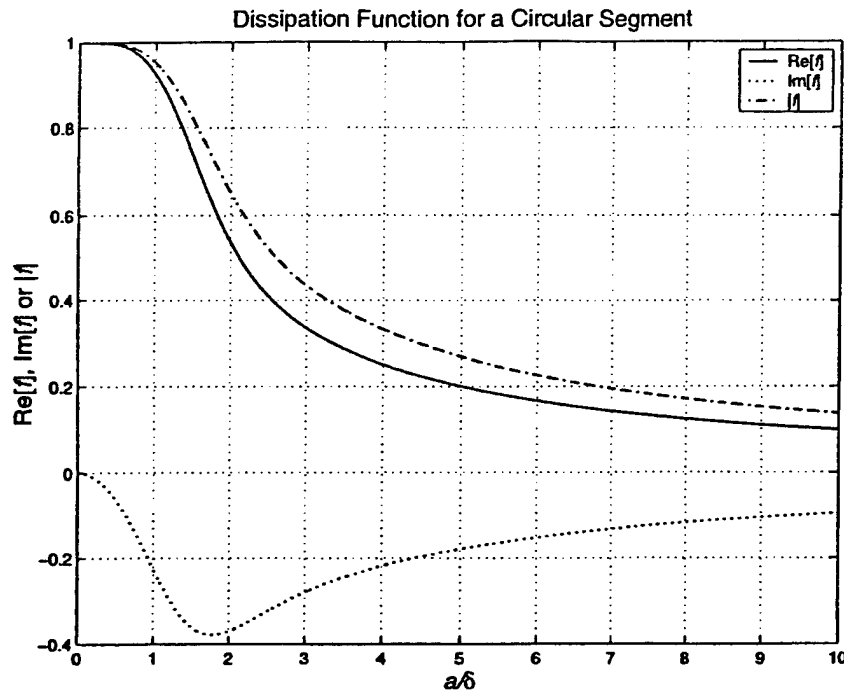
Converting this equation into its finite difference version yields

$$p_{n+1} = p_n - j\omega \frac{\rho_o \Delta x}{S} [1 - f_v]^{-1} U_n.$$

Comparing this result to the lossless version found previously

$$p_{n+1} = p_n - j\omega \frac{\rho_o \Delta x}{S} U_n = p_n - j\omega M U_n$$

shows that including viscosity modifies the inertance. Interpretation of the new inertance is easiest to see in the boundary limit where $a \gg \delta_v$.



16

In the boundary layer limit

$$\frac{J_1((j-1)a / \delta_v)}{J_0((j-1)a / \delta_v)} \cong j,$$

so the effective inertance reduces to

$$M' = M \left[1 - \frac{2j}{(j-1)} \frac{\delta_v}{a} \right]^{-1} \doteq M - j \frac{\delta_v}{a} M$$

The finite difference equation now becomes

$$\begin{aligned} p_{n+1} &= p_n - j\omega M' U_n \\ &= p_n - j\omega M U_n - \omega \frac{\delta_v}{a} M U_n \\ &= p_n - j\omega M U_n - R_v U_n. \end{aligned}$$

Therefore, introducing viscosity adds a resistance term to the momentum equation.

The boundary-layer-limit viscous resistance is given by

$$R_v = \omega \frac{\delta_v}{a} M = \frac{\mu \Sigma}{S^2 \delta_v}.$$

where Σ is the surface area of the segment.

If the boundary layer approximation does not hold, then the momentum equation has the form

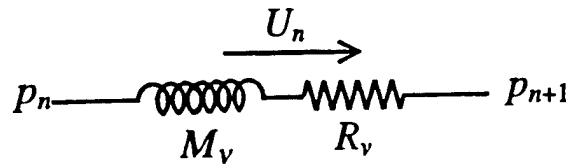
$$\begin{aligned} p_{n+1} &= p_n - j\omega M' U_n \\ &= p_n - j\omega \frac{M}{1-f_v} U_n \\ &= p_n - j\omega M \frac{1-\text{Re}[f_v]}{|1-f_v|^2} U_n - \omega M \frac{\text{Im}[-f_v]}{|1-f_v|^2} U_n \\ &= p_n - j\omega M_v U_n - R_v U_n. \end{aligned}$$

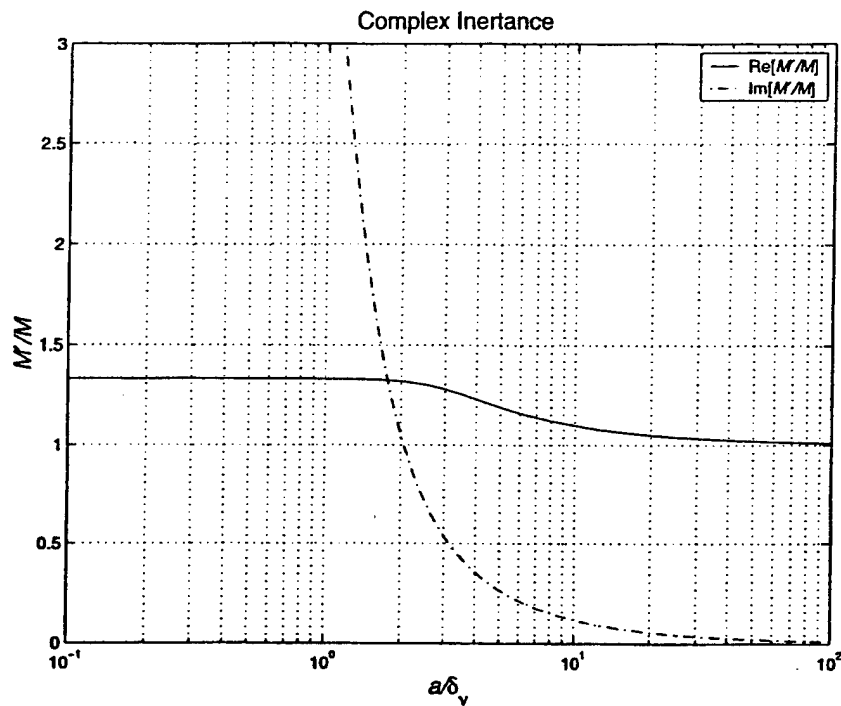
18

The viscosity-modified inertance and resistance are evidently

$$M_v = M \frac{1-\text{Re}[f_v]}{|1-f_v|^2} \quad \text{and} \quad R_v = \omega M \frac{\text{Im}[-f_v]}{|1-f_v|^2}.$$

The modified lumped parameter, equivalent circuit including viscosity is

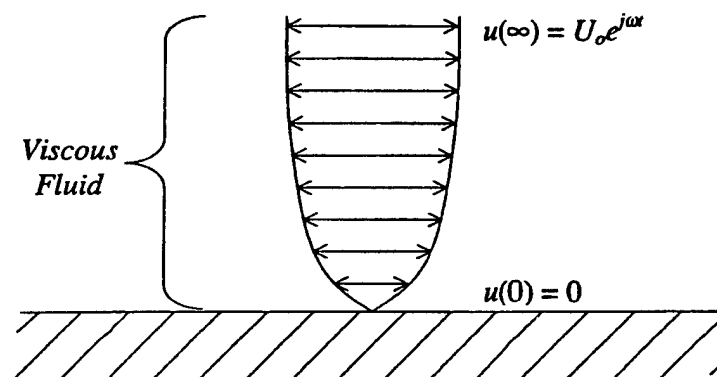




20

A Mini-Tutorial on Viscous Penetration Depth

Consider the problem illustrated in the diagram below. Find $u(y, t)$.



The governing differential equation is

$$\frac{\partial u}{\partial t} = \frac{\mu}{\rho} \frac{\partial^2 u}{\partial y^2}$$

Assume $u(y, t) = A e^{j(\omega t - \kappa y)}$ and substitute to get the dispersion relation

$$\kappa = (1 - j) \sqrt{\frac{\rho \omega}{2\mu}} = \frac{1 - j}{\delta_v}.$$

Substituting back into the assumed solution gives

$$u(y, t) = A \underbrace{e^{-y/\delta_v}}_{\text{decaying part}} \underbrace{e^{j(\omega t - y/\delta_v)}}_{\text{propagating part}} + \text{Constant}$$

Application of the boundary conditions at $y = 0$ and at $y = \infty$ leads to

$$u(y, t) = U_o \left[1 - e^{-(1+j)y/\delta_v} \right] e^{j\omega t}.$$

22

Thermal Losses

The first step is to find the temperature as a function of position within the duct. The starting point is the general equation for heat transfer:

$$\rho T \frac{ds}{dt} = \nabla \cdot (K \nabla T) + \text{quadratic terms in } u,$$

where s is the specific entropy of the fluid. Expressing the s in terms of T and p and making reasonable assumptions leads to a simplified version of this equation.

$$j\omega \rho_o c_P T_1 = j\omega T_o \beta p + K \frac{1}{r} \frac{\partial}{\partial r} \left(r \frac{\partial T_1}{\partial r} \right).$$

The solution is

$$T_1(x, r) = \frac{T_o \beta}{\rho_o c_P} p \left[1 - \frac{J_o((j-1)r/\delta_\kappa)}{J_o((j-1)a/\delta_\kappa)} \right],$$

where $\delta_\kappa = \sqrt{\frac{2K}{\rho_o c_P \omega}}$ is the thermal penetration depth.

Thermodynamics tells us that

$$d\rho = \left(\frac{\partial \rho}{\partial P}\right)_T dP + \left(\frac{\partial \rho}{\partial T}\right)_P dT,$$

which in the linear acoustics limit becomes

$$\rho_1 = \left(\frac{\partial \rho}{\partial P}\right)_T p + \left(\frac{\partial \rho}{\partial T}\right)_P T_1.$$

The partial derivatives can be expressed in terms of the isothermal bulk modulus and isobaric thermal expansion coefficient,

$$B_T = \rho_o \left(\frac{\partial P}{\partial \rho}\right)_T \quad \text{and} \quad \beta = -\frac{1}{\rho_o} \left(\frac{\partial \rho}{\partial T}\right)_P.$$

In terms of these parameters,

$$\rho_1 = \frac{\rho_o}{B_T} p - \rho_o \beta T_1.$$

24

We're almost at the desired result.

Substitute the expression for ρ_1 into the linear 1-D version of the equation of continuity,

$$\frac{\partial u}{\partial x} = -\frac{1}{\rho_o} \frac{\partial \rho_1}{\partial t},$$

to give

$$\frac{\partial u}{\partial x} = -j\omega \left[\frac{p}{B_T} - \beta T_1 \right].$$

Using the expression for T_1 found earlier,

$$\frac{\partial u}{\partial x} = -j\omega \left\{ \frac{1}{B_T} - \frac{T_o \beta^2}{\rho_o c_P} \left[1 - \frac{J_o((j-1)r/\delta_K)}{J_o((j-1)a/\delta_K)} \right] \right\} p.$$

The volume velocity is found by integrating this expression over the cross section of the pipe. The result is

$$\frac{\partial U}{\partial x} = -j\omega S \left\{ \frac{1}{B_T} - \frac{T_o \beta^2}{\rho_o c_P} [1 - f_K] \right\} p,$$

where

$$f_k = \frac{2J_1((j-1)a/\delta_k)}{((j-1)a/\delta_k)J_0((j-1)a/\delta_k)}$$

The finite difference form of this equation is

$$U_{n+1} = U_n - j\omega S\Delta x \left\{ \frac{1}{B_T} - \frac{T_o\beta^2}{\rho_o c_P} [1 - f_k] \right\} p_n.$$

Now is a good time to introduce the following ideal gas relations:

$$B = \gamma B_T = \gamma P_o \quad \beta = \frac{1}{T_o} \quad \frac{\rho_o c_P T_o}{P_o} = \frac{\gamma}{\gamma - 1}.$$

Using these relations U_{n+1} is

$$U_{n+1} = U_n - j\omega \frac{S\Delta x}{B} \{1 + (\gamma - 1)f_k\} p_n.$$

Comparing this expression with the lossless version

26

$$U_{n+1} = U_n - j\omega \frac{S\Delta x}{B} p_n = -j\omega C p_n.$$

shows that including thermal conduction modifies the compliance. The new compliance is

$$C' = C\{1 + (\gamma - 1)f_k\}.$$

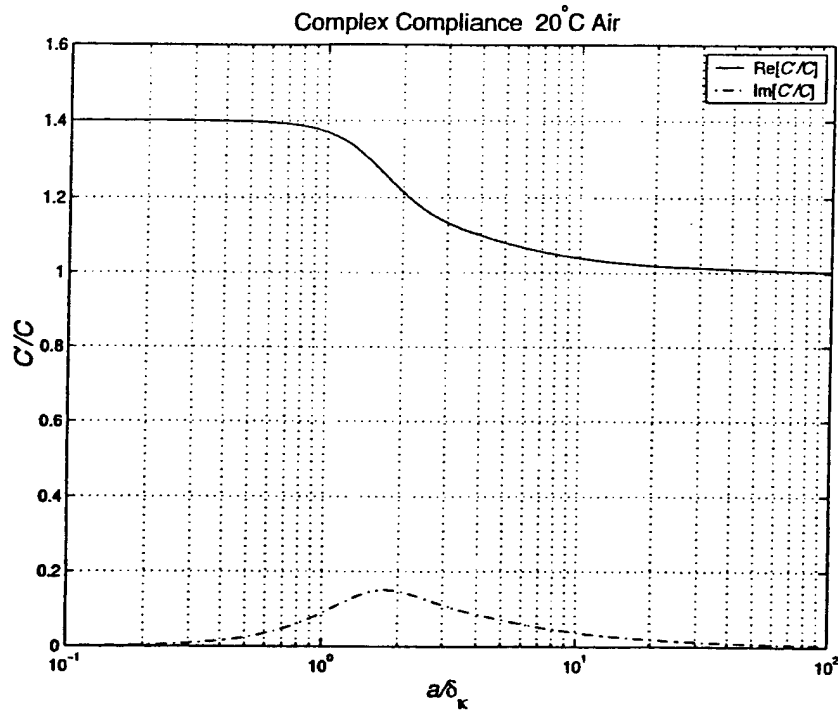
In the boundary layer limit that $(a \gg \delta_k)$,

$$f_k \cong (1 - j) \frac{\delta_k}{a},$$

so the effective compliance reduces to

$$C' = C \left\{ 1 - j(\gamma - 1) \frac{\delta_k}{a} \right\} \doteq C - j(\gamma - 1) \frac{\delta_k}{a} C.$$

The finite difference equation now becomes



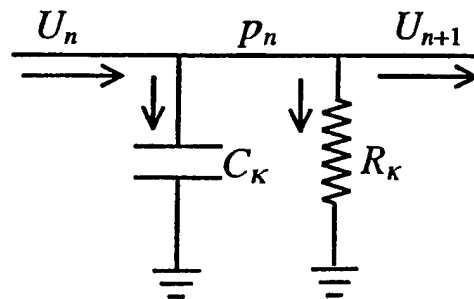
28

$$\begin{aligned}
 U_{n+1} &= U_n - j\omega \left[C - j(\gamma - 1) \frac{\delta_\kappa}{a} C \right] p_n \\
 &= U_n - j\omega C p_n - \frac{p_n}{R_\kappa},
 \end{aligned}$$

where

$$R_\kappa = \left[(\gamma - 1) \frac{\delta_\kappa}{a} \omega C \right]^{-1} = \frac{a\gamma P_o}{\omega(\gamma - 1)\delta_\kappa S \Delta x}$$

is the boundary layer thermal resistance of the segment. Introducing thermal conduction adds a resistance term to the equation of continuity. The modified lumped parameter, equivalent circuit is:



If the boundary layer approximation does not hold, then as shown previously the equation of continuity has the form

$$\begin{aligned}
 U_{n+1} &= U_n - j\omega C' p_n \\
 &= U_n - j\omega C \{1 + (\gamma - 1) f_k\} p_n \\
 &= U_n - j\omega C \{1 + (\gamma - 1) \operatorname{Re}[f_k]\} p_n - \omega C (\gamma - 1) \operatorname{Im}[-f_k] p_n \\
 &= U_n - j\omega C_K p_n - \frac{p_n}{R_K}.
 \end{aligned}$$

The thermal conductivity-modified compliance and resistance are defined as

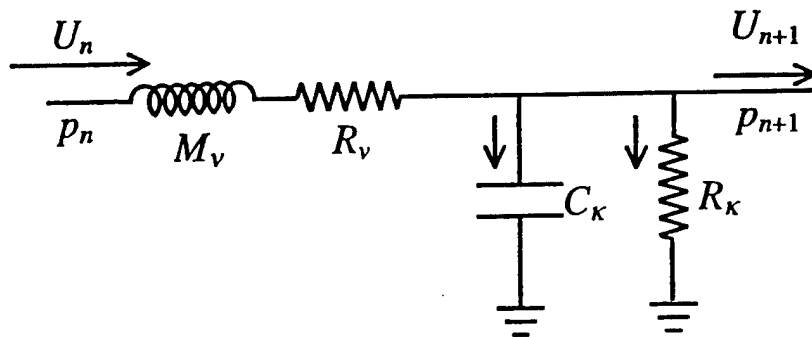
$$C_K = C \{1 + (\gamma - 1) \operatorname{Re}[f_k]\} \quad \text{and} \quad R_K = [\omega C (\gamma - 1) \operatorname{Im}[-f_k]]^{-1}.$$

30

Combined Equivalent Circuit Representation

Coupled Equations

$$U_{n+1} = U_n - j\omega C_K p_n - \frac{p_n}{R_K} \quad p_{n+1} = p_n - j\omega M_v U_n - R_v U_n$$



The Dispersion Relation

Return to the differential forms of the equations and seek x -dependence of the form e^{-jkx} .

$$\frac{\partial p}{\partial x} = -j\omega M'_\ell U \qquad \frac{\partial U}{\partial x} = -j\omega C'_\ell p,$$

where

$$M'_\ell = \frac{M_\ell}{[1 - f_v]} \qquad C'_\ell = C_\ell [1 + (\gamma - 1)f_v].$$

Writing the coupled equations in matrix form

$$\begin{pmatrix} -jk & j\omega M'_\ell \\ j\omega C'_\ell & -jk \end{pmatrix} \begin{pmatrix} p \\ U \end{pmatrix} = \begin{pmatrix} 0 \\ 0 \end{pmatrix}$$

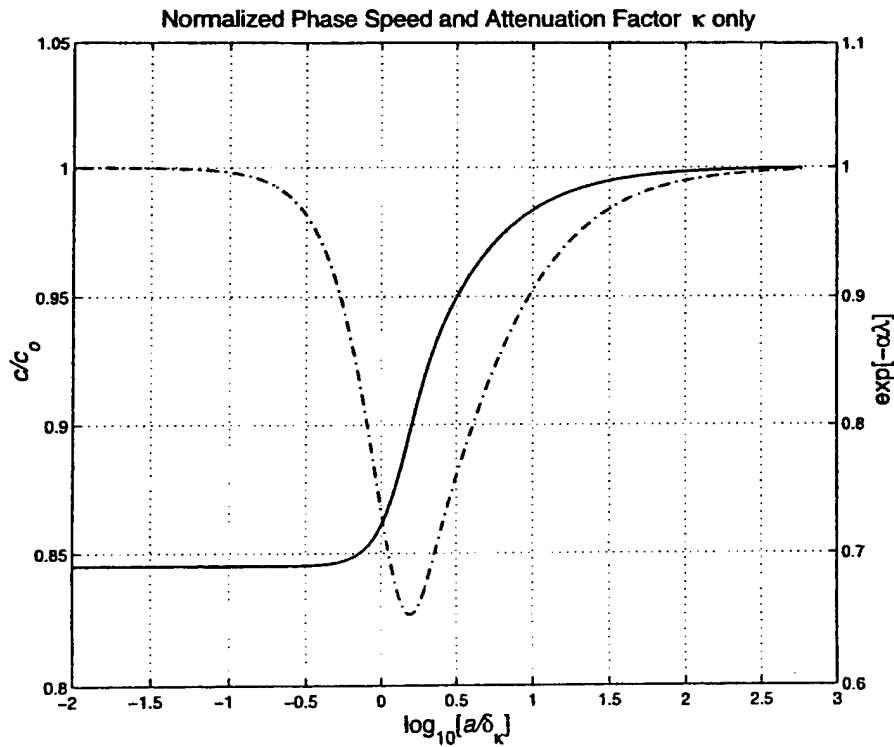
and setting

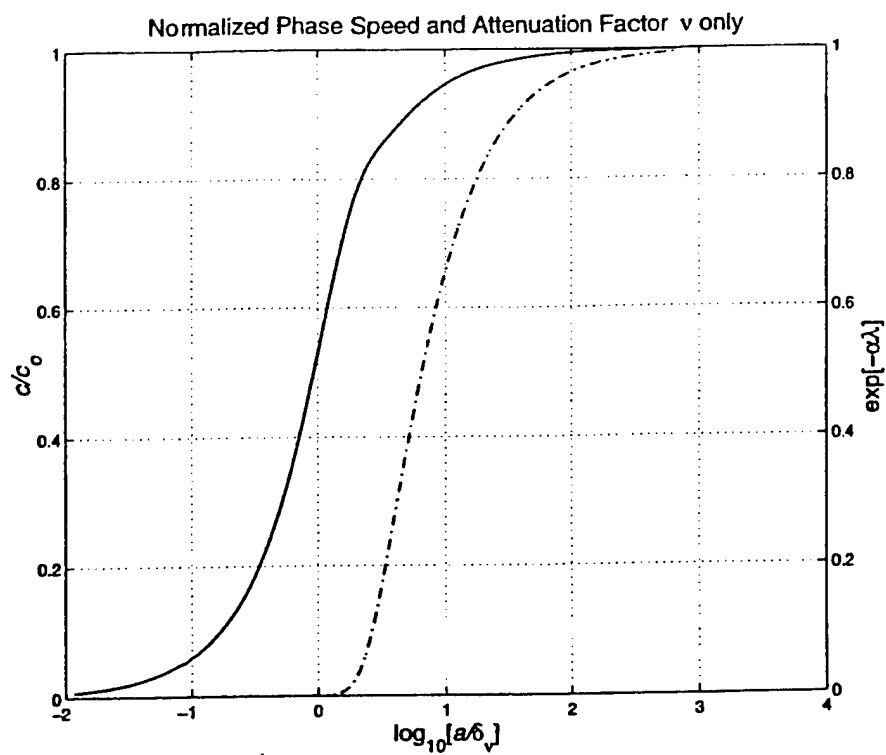
$$\begin{vmatrix} -jk & j\omega M'_\ell \\ j\omega C'_\ell & -jk \end{vmatrix} = 0$$

yields the dispersion relation

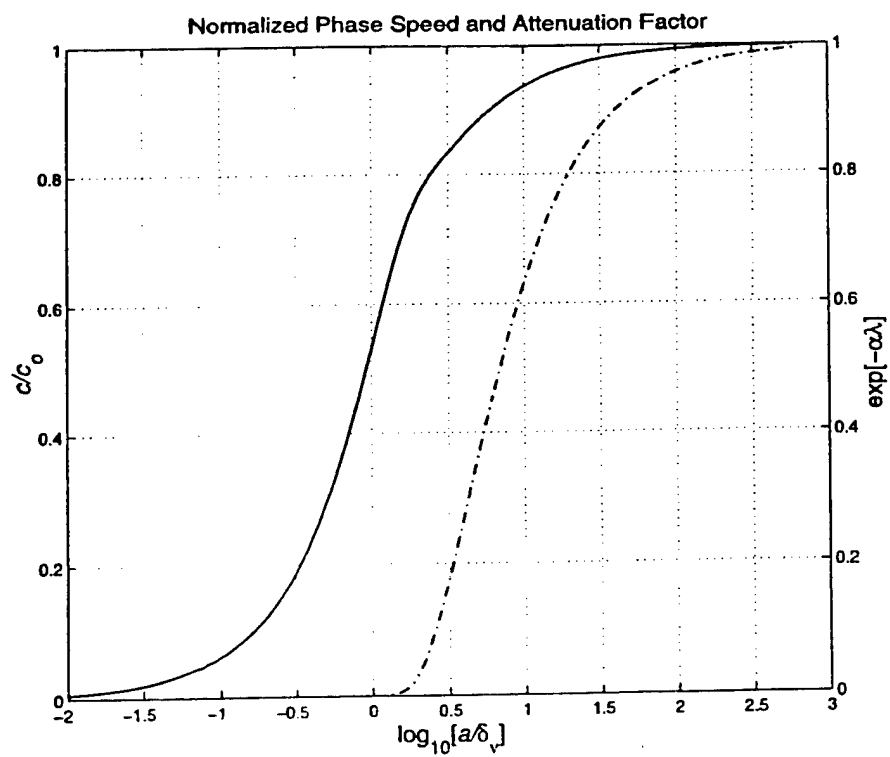
$$k = \pm \frac{\omega}{c_{kv}} \quad \text{where} \quad c_{kv} = \frac{1}{\sqrt{M'_\ell C'_\ell}} = c \sqrt{\frac{1 - f_v}{1 + (\gamma - 1)f_v}}.$$

32





34

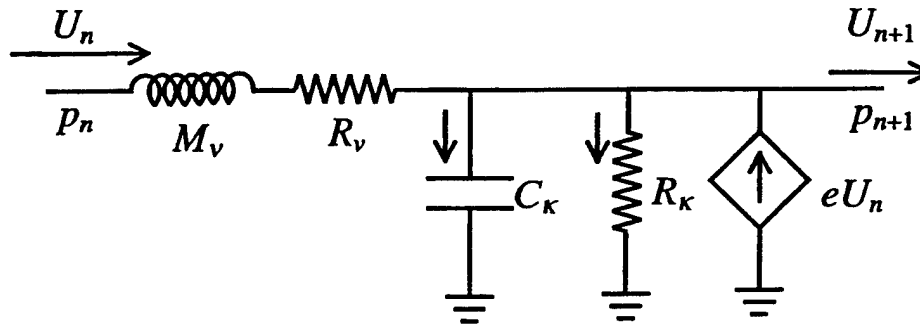


The Essence of Thermoacoustics

Imposing a temperature gradient along the segment leads to a further modification of the equation of continuity. "It can be shown that" the finite-difference version of the new equation of continuity is

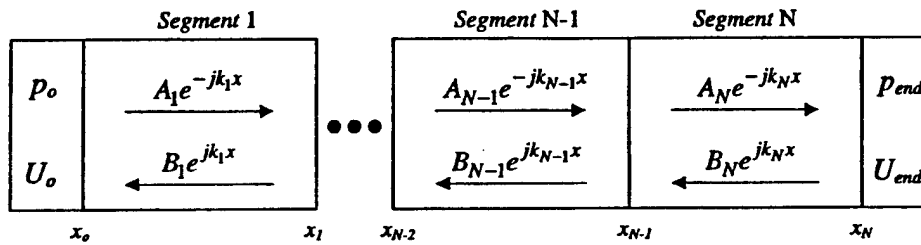
$$U_{n+1} = U_n - j\omega \frac{S\Delta x}{B} \{1 + (\gamma - 1)f_k\} p_n + \frac{(f_k - f_v)}{(1 - f_v)(1 - \text{Pr})} \frac{dT_o}{dx} U_n,$$

where $\text{Pr} = \frac{\mu c_p}{K} = \left(\frac{\delta_v}{\delta_K} \right)^2$ is the Prandtl Number. The modified equivalent circuit is



36

Propagation Matrix Approach



Assume that the pressure and volume velocity in the n^{th} segment are given by

$$p_n = A_n e^{-jk_n x} + B_n e^{jk_n x}$$

and

$$U_n = \frac{1}{Z_n} [A_n e^{-jk_n x} - B_n e^{jk_n x}],$$

where

$$Z_n = \frac{(\rho_o c)_n}{S_n}$$

is the characteristic acoustic impedance of the n^{th} segment.

Boundary Conditions: Pressure and Volume Velocity are continuous at the ends of the segments.

At the end ($x = x_N$)

$$\underbrace{\begin{pmatrix} e^{-jk_N x_N} & e^{jk_N x_N} \\ \frac{1}{Z_N} e^{-jk_N x_N} & -\frac{1}{Z_N} e^{jk_N x_N} \end{pmatrix}}_{\mathbf{M}_N^N} \underbrace{\begin{pmatrix} A_N \\ B_N \end{pmatrix}}_{\mathbf{C}_N} = \underbrace{\begin{pmatrix} P_{end} \\ U_{end} \end{pmatrix}}_{\mathbf{C}_{end}}$$

Boundary Location
 x_j

\mathbf{M}_i^j

Segment #

The coefficients for the N^{th} segment are

$$\mathbf{C}_N = (\mathbf{M}_N^N)^{-1} \mathbf{C}_{end}.$$

38

At $x = x_{N-1}$,

$$\begin{pmatrix} e^{-jk_{N-1} x_{N-1}} & e^{jk_{N-1} x_{N-1}} \\ \frac{1}{Z_{N-1}} e^{-jk_{N-1} x_{N-1}} & -\frac{1}{Z_{N-1}} e^{jk_{N-1} x_{N-1}} \end{pmatrix} \begin{pmatrix} A_{N-1} \\ B_{N-1} \end{pmatrix} = \begin{pmatrix} e^{-jk_N x_{N-1}} & e^{jk_N x_{N-1}} \\ \frac{1}{Z_N} e^{-jk_N x_{N-1}} & -\frac{1}{Z_N} e^{jk_N x_{N-1}} \end{pmatrix} \begin{pmatrix} A_N \\ B_N \end{pmatrix},$$

or

$$\mathbf{M}_{N-1}^{N-1} \mathbf{C}_{N-1} = \mathbf{M}_N^{N-1} \mathbf{C}_N.$$

The coefficients for the $N-1^{\text{th}}$ segment are

$$\mathbf{C}_{N-1} = (\mathbf{M}_{N-1}^{N-1})^{-1} \mathbf{M}_N^{N-1} \mathbf{C}_N,$$

or in terms of the boundary conditions at the end

$$\mathbf{C}_{N-1} = (\mathbf{M}_{N-1}^{N-1})^{-1} \mathbf{M}_N^{N-1} (\mathbf{M}_N^N)^{-1} \mathbf{C}_{end}.$$

Working back to the first segment using the same method gives

$$C_1 = \begin{pmatrix} A_1 \\ B_1 \end{pmatrix} = (M_1^1)^{-1} M_2^1 \dots (M_{N-1}^{N-1})^{-1} M_N^{N-1} (M_N^N)^{-1} C_{end}.$$

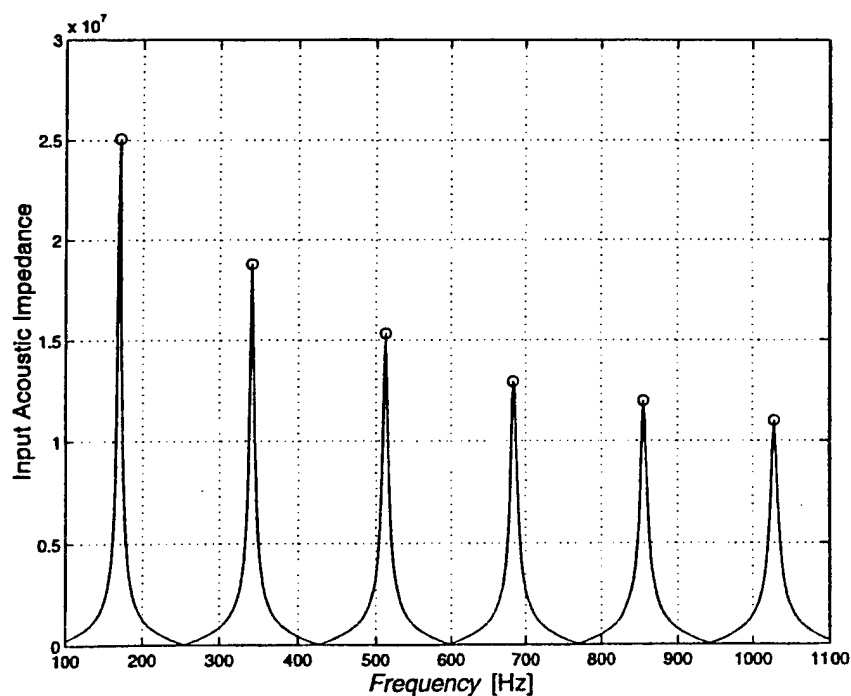
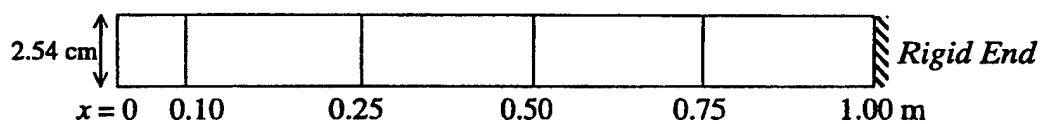
The pressure and volume velocity at $x = x_o$ are then given by

$$p_o = A_1 + B_1$$

and

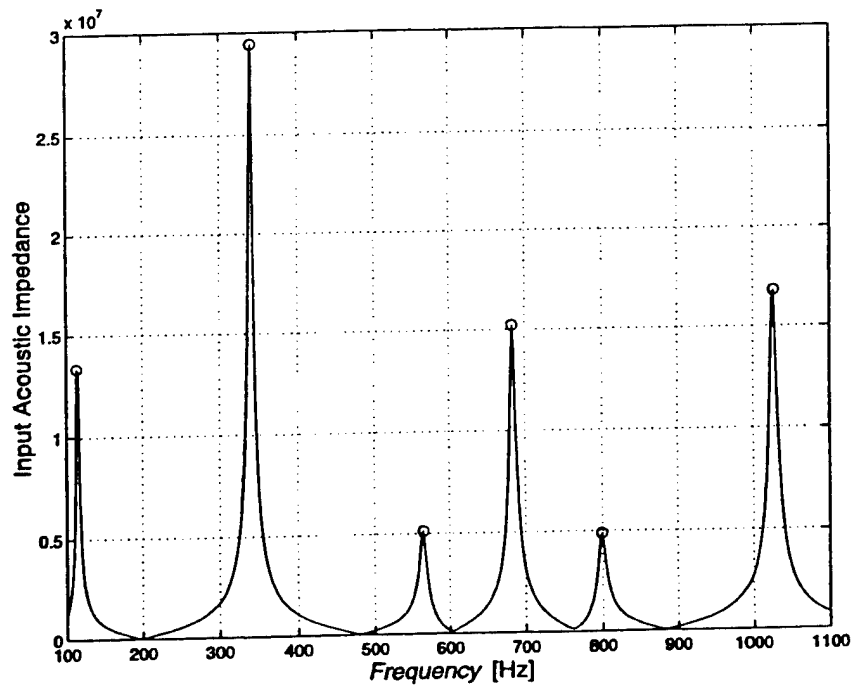
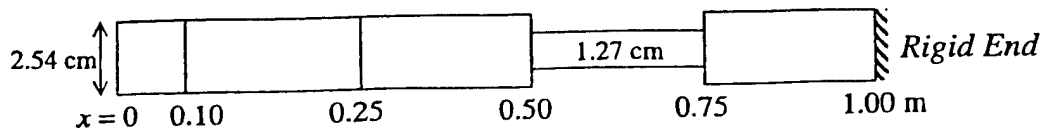
$$U_o = \frac{1}{Z_1} [A_1 - B_1].$$

40



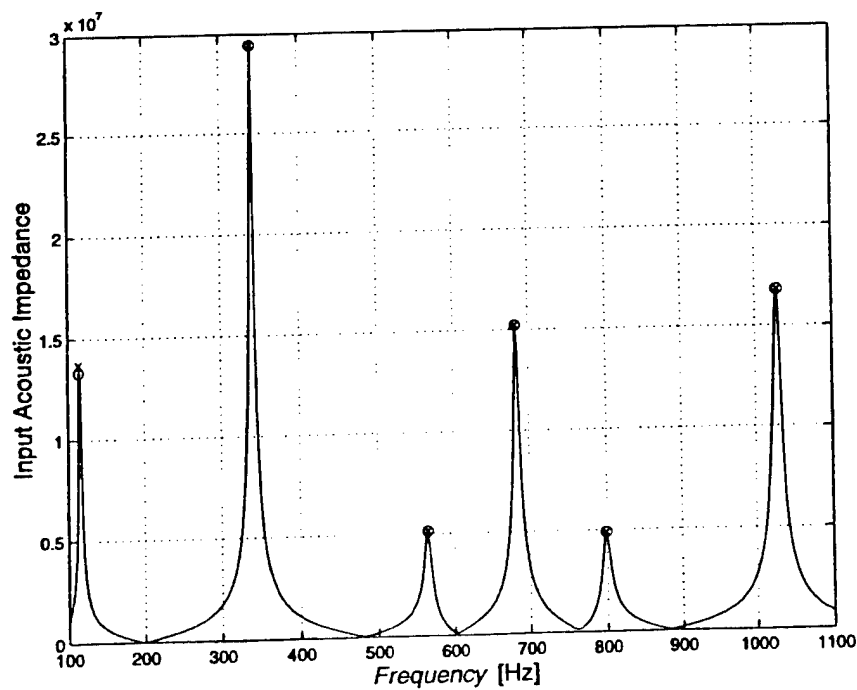
AA-21

41



42

Result of supplying the "measured" peak frequencies and guessing that the radius of segment #4 was somewhere between 0.254 cm and 2.54 cm.
Best fit radius = 1.269 cm.



The Helmholtz Equation

Begin with the linear acoustic wave equation

$$\nabla^2 p(\vec{r}, t) = \frac{1}{c^2} \frac{\partial^2 p(\vec{r}, t)}{\partial t^2}.$$

Taking the temporal Fourier transform of both sides leads to the Helmholtz equation

$$\nabla^2 P(\vec{r}, \omega) + k^2 P(\vec{r}, \omega) = 0,$$

where $k = \omega/c$ is the propagation constant, or the acoustic wave number.

44

Planar Fourier Acoustics

Take the spatial Fourier transform of the Helmholtz equation expressed in rectangular coordinates:

$$\int_{-\infty}^{\infty} \int_{-\infty}^{\infty} \left[\frac{\partial^2}{\partial x^2} + \frac{\partial^2}{\partial y^2} + \frac{\partial^2}{\partial z^2} + k^2 \right] P(x, y, z, \omega) e^{j[k_x x + k_y y]} dx dy = 0,$$

where

$$k^2 = \left(\frac{\omega}{c} \right)^2 = k_x^2 + k_y^2 + k_z^2.$$

$\left[\frac{\partial^2}{\partial z^2} + k^2 \right]$ is independent of x and y and can be brought out of the integral. Recalling

$$\mathcal{F}_x \left[\frac{\partial f(x)}{\partial x} \right] = -jk_x \mathcal{F}_x [f(x)],$$

and similarly for a function of y , the resulting equation is

$$\left[\frac{\partial^2}{\partial z^2} + k^2 - k_x^2 - k_y^2 \right] \tilde{P}(k_x, k_y, \omega, z) = 0,$$

where

$$\tilde{P}(k_x, k_y, \omega) = \int_{-\infty}^{\infty} \int_{-\infty}^{\infty} P(x, y, \omega) e^{j[k_x x + k_y y]} dx dy$$

is the 2-dimensional spatial Fourier transform of $P(x, y, \omega)$.

The transformed Helmholtz equation can be rewritten, by introducing k_z , as

$$\left[\frac{\partial^2}{\partial z^2} + k_z^2 \right] \tilde{P}(k_x, k_y, \omega, z) = 0.$$

The solution of this familiar differential equation is

$$\tilde{P}(k_x, k_y, \omega, z) = A(k_x, k_y, \omega, z) e^{-jk_z z} + B(k_x, k_y, \omega, z) e^{jk_z z}$$

where the coefficients A and B are determined from boundary conditions.

46

Consider a situation in which:

- 1) waves propagate in only one direction, say the +z-direction.
- 2) $\tilde{P}(k_x, k_y, \omega, 0)$ is known.

The solution to the transformed Helmholtz equation at $z = 0$ is

$$\tilde{P}(k_x, k_y, \omega, 0) = A(k_x, k_y, \omega, 0),$$

and the solution for $z > 0$ is

$$\tilde{P}(k_x, k_y, \omega, z) = \tilde{P}(k_x, k_y, \omega, 0) e^{-jk_z z}.$$

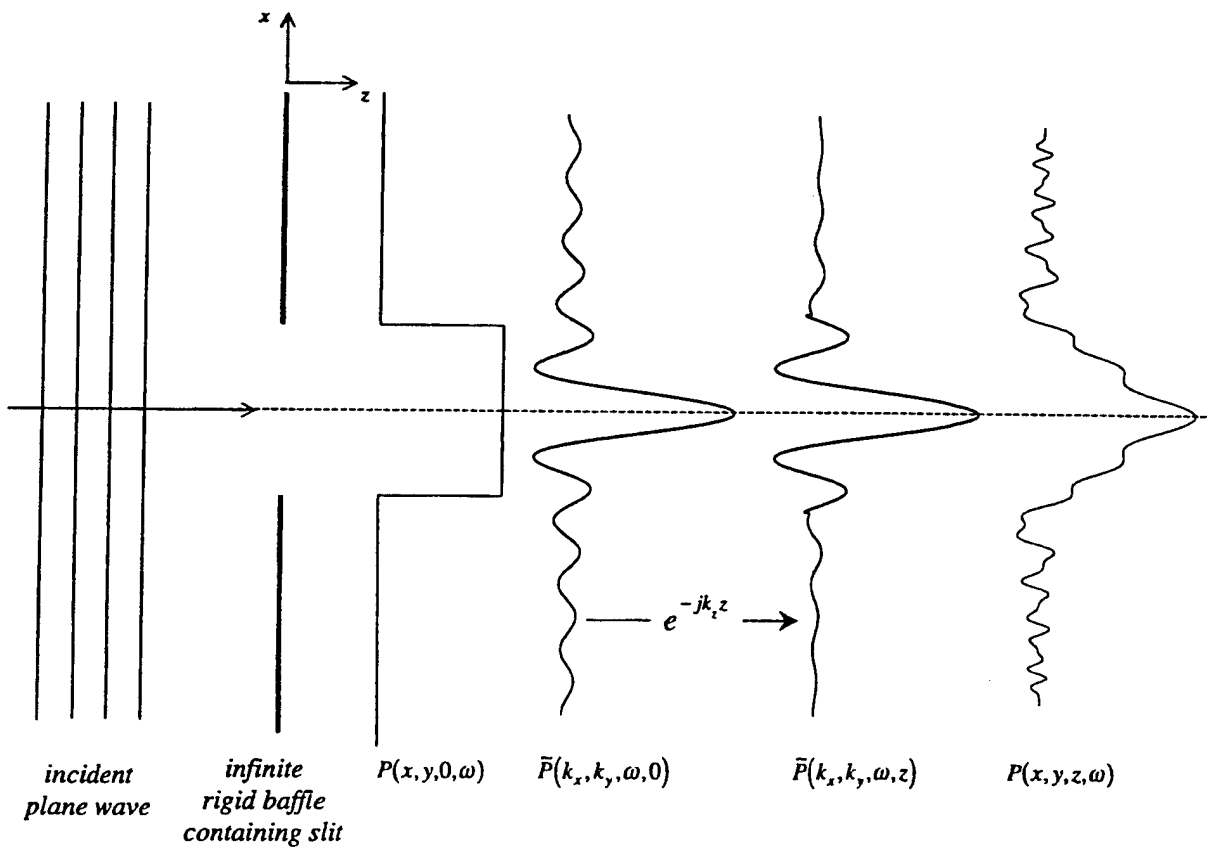
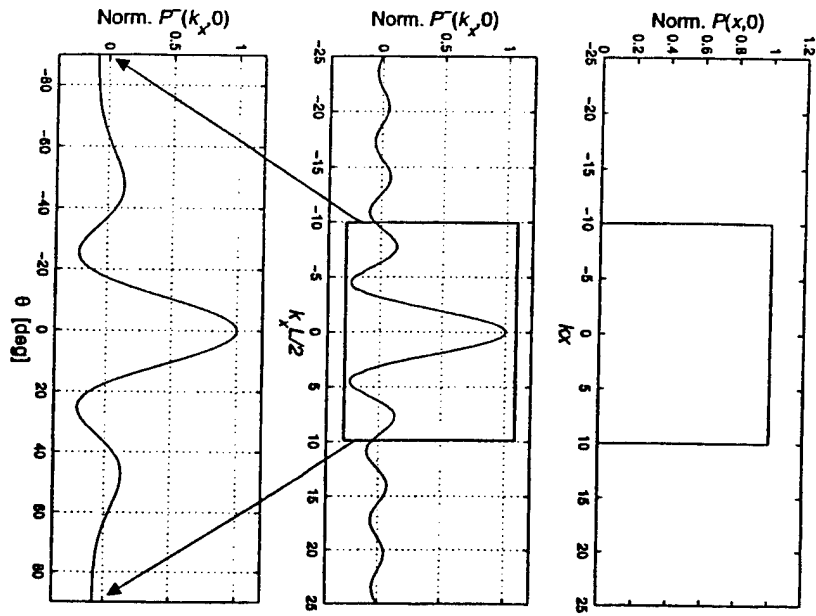
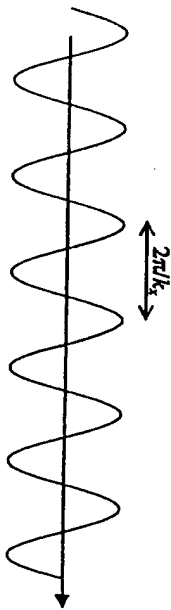
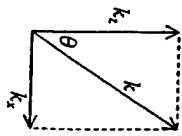
Therefore, if the spatial Fourier transform is known in one plane, it can be found in any other plane simply by multiplying by the phase factor $e^{-jk_z z}$.

k_z is a function of k_x , k_y , and ω .

$e^{-jk_z z}$ can represent either a propagating wave or an evanescent field.

This is the fundamental concept underlying planar Nearfield Acoustic Holography.

47



Fundamental Equations

Continuity

$$\frac{\partial \rho}{\partial t} + \nabla \cdot \rho \bar{u} = 0$$

Momentum

$$\rho \frac{d\bar{u}}{dt} + \nabla P = 0$$

Equation of State

$$p = \frac{B}{\rho_o} \rho_1$$

Alternative Formulation

(Blackstock, Hamilton and Morfey)

Continuity

$$\frac{\partial \rho}{\partial t} + \nabla \cdot \rho \bar{u} = 0$$

Momentum

$$\rho \frac{d\bar{u}}{dt} + \nabla P = 0$$

Equation of State

$$\lambda = \int_{\rho_o}^{\rho} \frac{c}{\rho} d\rho = \int_{P_o}^P \frac{dP}{\rho c}$$

$$\text{where } c^2 = \left(\frac{\partial P}{\partial \rho} \right)_s$$

50

The 1-D versions of conservation of mass and momentum are

$$\frac{\partial \rho}{\partial t} + u \frac{\partial \rho}{\partial x} + \rho \frac{\partial u}{\partial x} = 0 \quad \text{and} \quad \rho \frac{\partial u}{\partial t} + \rho u \frac{\partial u}{\partial x} + \frac{\partial P}{\partial x} = 0.$$

Eliminating P and ρ through the relationships

$$\frac{\partial \rho}{\partial t} = \frac{\rho}{c} \frac{\partial \lambda}{\partial t} \quad \frac{\partial \rho}{\partial x} = \frac{\rho}{c} \frac{\partial \lambda}{\partial x} \quad \frac{\partial P}{\partial x} = \rho c \frac{\partial \lambda}{\partial x}$$

leads to

$$\frac{\partial \lambda}{\partial t} + u \frac{\partial \lambda}{\partial x} + c \frac{\partial u}{\partial x} = 0 \quad \text{and} \quad \frac{\partial u}{\partial t} + u \frac{\partial u}{\partial x} + c \frac{\partial \lambda}{\partial x} = 0.$$

Adding and subtracting these equations and defining $J_+ = \frac{1}{2}(\lambda + u)$ and $J_- = \frac{1}{2}(\lambda - u)$ gives

$$\frac{\partial J_+}{\partial t} + (u + c) \frac{\partial J_+}{\partial x} = 0 \quad \text{and} \quad \frac{\partial J_-}{\partial t} + (u - c) \frac{\partial J_-}{\partial x} = 0.$$

The left sides of the last two equations have the form of a 1-D total derivative, i.e.,

$$\frac{dq}{dt} = \frac{\partial q}{\partial t} + v \frac{\partial q}{\partial x}.$$

The implication of

$$\frac{dq}{dt} = 0$$

is that a particular value of q propagates unchanged with speed

$$\left. \frac{dx}{dt} \right|_q = v.$$

Therefore, the quantities J_+ and J_- (called Riemann invariants) propagate unchanged along characteristics defined by

$$\frac{dx}{dt} = \begin{cases} u + c \\ u - c. \end{cases}$$

This result implies that propagation effects are amplitude dependent, the realm of Nonlinear Acoustics.

(In general, the invariants propagate with speeds $u \pm c$, not $P - P_0$, $\rho - \rho_0$, and u . Progressive waves are an exception.)

Nonlinear Acoustics

Steven L. Garrett <garrett@sabine.acs.psu.edu>
United Technologies Corporation Professor of Acoustics
Graduate Program in Acoustics <www.acs.psu.edu>
The Pennsylvania State University

Motivations

- Provide a general introduction to the simplest concepts and techniques.
- Present a variety of phenomena that can only be understood by extending the acoustic approximation beyond the linearized hydrodynamics.
- Use nonlinear acoustics to improve students' understanding of linear acoustics and its limitations.

Pedagogical Principles

- "One measure of our understanding is the number of different ways by which we can arrive at the same result." R. Feynman
- "A man with one watch knows the time, a man with two is never sure." Japanese proverb

Why Me?

Graduate Students

S. Garrett – The "Geometric Mean" Impedance Matching Layer

The Real "Guys"

Robert Apfel	Robert Keolian
Anthony Atchley	Andrés Larrazá
Robert Beyer	Bart Lipkens
Leif Bjørne	Phil Marston
David Blackstock	Wesley Nyborg
Mack Breazeale	Allan Pierce
Horan Burklay	Seth Putterman
David Crighton	Ron Roy
Larry Crum	Vic Sparrow
Ann Dowling	Greg Swift
Bruce Denardo	Jim TenCate
Carr Everbach	N. & J. Tjøtta
Mark Hamilton	Peter Westervelt
Glynn Holt	Eugenia Zabolotskaya
Michael Howe	
Yuri Il'inski	
Paul Johnson	

← $\lambda/4$ →

Does $\lambda/4$ = "Thick as a brick?"

Lecture Outline

Acknowledgements

Isadore Rudnick (1918-1997)

Seth Putterman

The Danish-American Fulbright Commission

Wave-Wave Interactions

Cumulative effects of convection and material nonlinearity

Shock wave formation and dissipation

Nonlinear wave mixing (e.g., Parametric arrays)

Non-zero Time Averaged Effects

Standing waves and shock suppression

Bernoulli forces and torques

$$\langle p_2 \rangle_t = \frac{1}{2} \rho_0 \langle v_1^2 \rangle_t \neq 0$$

Acoustic levitation and levitation stability

Radiation pressure and the Ehrenfest Adiabatic Principle

$$\frac{E_n}{f_n} = \text{const.}$$

Disclaimers and Cautions

Excluded Topics (Omissions)

Over the years, there have been many topics that have brought excitement and vitality to Physical Acoustics in general, and nonlinear acoustics in particular. I have chosen only a small subset and excluded many other interesting areas, some of which are listed below:

- Bubble dynamics and nonlinear oscillators
- Numerical solutions and 'model' equations
- N-waves and sonic booms
- Wave turbulence
- 2 and 3 dimensions – nonlinear sound beams
- Streaming (mass and thermal)
- Solitons

Draft Status (Errors)

These notes were prepared while I was a guest of the Department of Acoustic Technology at the Danish Technical University (DTU), in Lyngby. Although Bill Gates now rules the World, word processors and equation processors tend to still be 'picky' about available fonts and other 'local' cultural variations.

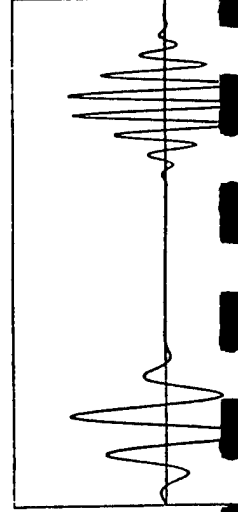
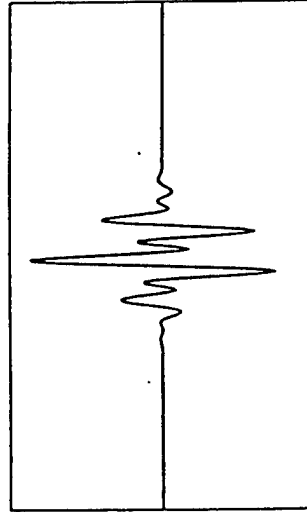
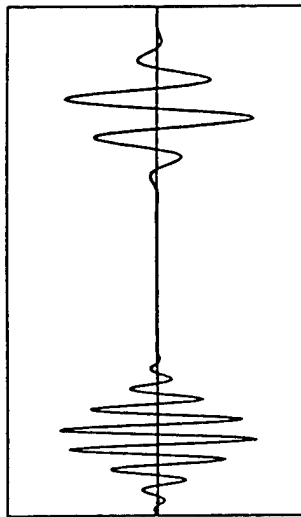
- Square brackets [] and integral signs \int were not available for use in numbered equations presented in this version of the notes. All reasonable effort has been made to work around this limitation (with white-out), but be careful!
- Although DTU has an excellent library, I was not able to access certain personal references and photos which will be added later.

Linear Acoustics

Superposition

Linear acoustics assumes that the presence of the wave does not affect the propagation medium.

Waves only interact in the region of their overlap, after passing through each other they emerge unchanged, and no new disturbance is created which propagates outside the interaction region.

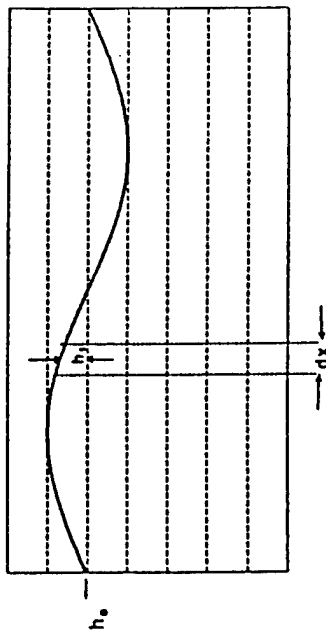


Shallow Water Gravity Waves

Surf

We are so close to the ocean, it was impossible for me to avoid introducing nonlinearity without using water waves. (These waves are also very easy to visualize!)

Simplify the problem by considering uniform "shallow" mean depth, $h_0 < \lambda/2\pi$, an incompressible fluid, and progressive small amplitude ($h_1 \ll h_0$) sinusoidal waves, $h_1(x,t) = h_1 \sin(\omega t - kx)$



Linearized Hydrodynamic Equations

The Continuity Equation

$$\frac{\partial h_1}{\partial t} + h_0 \frac{\partial v_x}{\partial x} = 0$$

[1]

Euler's Equation

$$\frac{\partial v_x}{\partial t} = -\frac{1}{\rho} \frac{\partial}{\partial x} (\rho g h) = -g \frac{\partial h_1}{\partial x}$$

[2]

Note: Subscripts are used to denote the equilibrium state, h_0 , and the "linear" deviation from equilibrium, h_1 :
 $h = h_0 + h_1 + h_2 + \dots$

Wave Propagation Speed

The Wave Equation

Add $\partial/\partial t$ [1] to $-h_0 \partial/\partial x$ [2] to obtain wave equation:

$$\frac{\partial^2 h_1}{\partial t^2} - g h_0 \frac{\partial^2 h_1}{\partial x^2} = 0 \quad [3]$$

Define the equilibrium propagation speed as c_{grav}

$$c_{grav} = \frac{\omega}{k} = \sqrt{g h_0} \quad [4]$$

The exact result for all h_0/λ is given by Landau & Lifshitz

$$c_{grav} = \frac{1}{2} \sqrt{\frac{g}{k \tanh k h_0}} \left[\tanh k h_0 + \frac{k h_0}{\cosh^2 k h_0} \right] \quad [4a]$$

Propagation Speed

Since speed depends upon depth, the presence of the wave will affect the sound speed.

$$\frac{\partial c_{grav}}{\partial h} = \frac{1}{2} \frac{c_{grav}}{h_0} \quad [5]$$

Continuity [1] can be used to relate changes in height, h_1 , to particle velocity in the x-direction, v_x : $[\partial h_1 = h_0] k v_x$

$$\frac{h_1}{h_0} = \frac{v_x}{c_{grav}} \equiv M \Rightarrow \frac{\partial h}{\partial v_x} = \frac{h_0}{c_{grav}} \quad [6]$$

Cumulative Waveform Distortion

"Local" Wave Propagation Speed

We now let the presence of the wave affect its own speed.

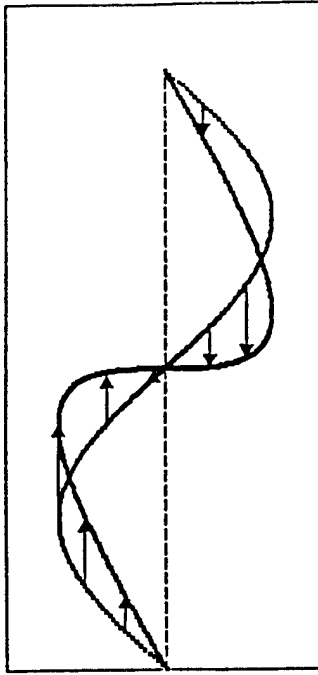
The wave's fluid motion, v_x , adds to the speed.
The wave's change in depth changes c_{grav} .

$$c(v_x) = c_{grav} + v_x + \frac{\partial c_{grav}}{\partial h} \frac{\partial h}{\partial v_x} v_x = c_{grav} + \frac{3v_x}{2} \quad [7]$$

Both convection and the change in speed with depth conspire to modify the "local" speed in the same way.

Shock Formation

Crests move faster than troughs.



Shock Inception Distance (D_s)

Slope is infinite when the peak advances by one radian length, $\lambda/2\pi$.

$$D_s = c_{grav} T_s = c_{grav} \frac{\lambda / 2\pi}{3v_x / 2} = \frac{\lambda}{3\pi M} \quad [8]$$

The Grüneisen Parameter

Other (Acoustical) Media

We can generalize the previous results by defining a distortion parameter that incorporates the convective and the constitutive correction to the equilibrium sound speed,

$$c(v) = c_o + \left[1 + \frac{\partial c_o}{\partial y} \frac{\partial y}{\partial v}\right] v \equiv c_o + \Gamma v \quad [9]$$

where y is some parameter (e.g., temperature or pressure) that affects the equilibrium sound speed.

The choice of Γ as the "distortion parameter" is motivated by its use in studies of the thermal expansion of solids. The designation varies in the acoustics literature and is more commonly given by β or some combination of virial coefficients (B/A) as discussed later.

Density dependent sound speed (for example)

Let $c_o = c_o(\rho)$

$$\Gamma = 1 + \frac{\partial c_o}{\partial \rho} \frac{\partial \rho}{\partial v} = 1 + \frac{\rho_o}{c_o} \frac{\partial c_o}{\partial \rho} \quad [10]$$

where $\partial p / \partial v$ was evaluated from the continuity equation.

$$\frac{\partial \rho}{\partial t} + \nabla \cdot \rho v = 0 \Rightarrow \frac{\rho_1}{\rho_o} = \frac{v_1}{c_o} \quad [11]$$

Ideal Gases

Adiabatic Propagation

The speed of sound in an ideal gas depends on temperature.

$$c_o^2 = \frac{\gamma R T}{M} \Rightarrow \frac{\delta c}{c_o} = \frac{1}{2} \frac{T_1}{T_o} \Rightarrow \frac{\partial c}{\partial T} \Big|_s = \frac{1}{2} \frac{c_o}{T_o} \quad [12]$$

The "local" value of sound speed can be written in terms of convection velocity, v , and a temperature correction:

$$c(v) = c_o + v + \frac{\partial c}{\partial T} \Big|_s \frac{\partial T}{\partial p} \Big|_s \frac{\partial p}{\partial v} \Big|_s \quad [13]$$

Sound propagation in gases is adiabatic, so $p v^\gamma = \text{const.}$

$$p v^\gamma = (n R T)^\gamma p^{1-\gamma} = \text{const.} \quad [14]$$

Logarithmic differentiation of [14] gives,

$$\frac{T_1}{T_o} = \frac{(\gamma - 1)}{\gamma} \frac{p_1}{p_o} \Rightarrow \frac{\partial T}{\partial p} \Big|_s = \frac{(\gamma - 1)}{\gamma} \frac{T_o}{p_o} \quad [15]$$

The last derivative in [13] can be evaluated from the Euler Equation [2] to give $(\partial p / \partial v)_s = \rho_o c_o$ and let $c_o^2 = \gamma p_o / \rho_o$.

$$\frac{\partial v}{\partial t} = - \frac{\nabla p}{\rho} \Rightarrow p_1 = \rho_o c_o v_1 \quad [16]$$

The Grüneisen Constant for an Ideal Gas

$$\Gamma_{\text{gas}} = \left(1 + \frac{\gamma - 1}{2}\right) = \frac{1 + \gamma}{2} \quad [17]$$

For inert gases, $\gamma = 5/3$ so $\Gamma_{\text{inert}} = 4/3 = 1.333$

For diatomic gases (air), $\gamma = 7/5$ so $\Gamma_{\text{air}} = 6/5 = 1.200$

Shocks in Air

Shock Formation Distance

Let's plug in some numbers to get a feel for the magnitude of these effects. 1.0 kHz sound wave in air at the threshold of pain, 120 dB_{SPL} = 20 Pa_{rms} = 28 Pa_{pk} = p₁

$$M_{air} = \frac{v_1}{c_0} = \frac{p_1}{\gamma p_0} = 2 \times 10^{-4} = 200 \text{ ppm} \quad [18]$$

From our result for the shallow water wave shock inception distance [8], where $\Gamma_{sh} = 7/5$, and $\lambda = c_0/f = 0.35 \text{ m}$.

$$D_s = \frac{\lambda}{2\pi \Gamma_{sh} M} = 230 \text{ m} \quad [19]$$

The Goldberg Number

As the frequency increases this shock distance becomes shorter, but attenuation increases roughly as the frequency squared. Eventually attenuation will become important.

At 1 kHz the wave attenuates by e^{-1} (-8.7 dB), in dry air, after travelling a distance, $l = \alpha^{-1} = 4.3 \text{ km}$.

$$G = \frac{l}{D_s} = \frac{1}{\alpha D_s} \quad [20]$$

For our example, $G \approx 19 > 1$. At 10 kHz, and the same amplitude (120 dB_{SPL}), G would only be 2, unless the amplitude increased. At 100 kHz, it would attenuate before it could shock.

For water waves over the deep ocean $G \approx 10^6$

Stable Waveform

Repeated Sawtooth

In an ideal gas, all large amplitude periodic waves ($G \gg 1$) evolve into a sawtooth shape that is stable.

$$v(x-ct) = \frac{v_1}{\pi} \sum_{n=1}^{\infty} \frac{\sin n(x-ct)}{n} \quad [21]$$

This waveform contains all harmonics of the fundamental up to a limit, n_{\max} , set by the shock front thickness.

Rankine-Hugoniot Relations

It is possible to calculate the (non-exponential!) attenuation rate of the sawtooth by going to a frame-of-reference which moves with the shock at velocity c_0 , and applying mass [22], momentum [23], and energy (enthalpy) conservation [24].

$$\rho_- u_- = \rho_+ u_+ \quad [22]$$

$$p_- + \rho_- u_-^2 = p_+ + \rho_+ u_+^2 \quad [23]$$

$$\frac{p_-}{\rho_-} + \frac{u_-^2}{2} + \varepsilon_- = \frac{p_+}{\rho_+} + \frac{u_+^2}{2} + \varepsilon_+ \quad [24]$$

Here we have let u be the relative velocity of the gas, $u = c_0 - v_1$, behind (+ in front) the shock, and ε is the internal energy density.

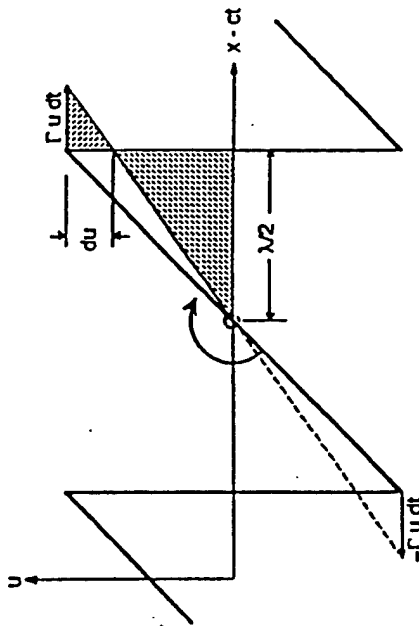
With the ideal gas laws, [22] – [24] can be used to show that the entropy discontinuity across the shock is cubic in the relative pressure discontinuity (L&L, *Fluids*, 2nd ed., Sec. 86).

$$s_+ - s_- = \frac{R}{M} \frac{(\gamma - 1)}{12\gamma^2} \left[\frac{p_+ - p_-}{p_-} \right]^3 \quad [25]$$

Shock Attenuation

Graphical Solution

The entropy discontinuity can be used to calculate the energy loss rate in the shock and hence derive the attenuation, $dE/dt = -T p_0(s_+ - s_-)c_0$, but the same result can be obtained from the graphical construction below:



Since each point on the "unshocked" portion moves ahead in proportion to its amplitude, so the slanted line experiences a "solid body rotation" about the zero crossing. By similar triangles,

$$\frac{du}{\Gamma u dt} = \frac{u}{\lambda/2} \quad [26]$$

If we let $dt = dx/c_0$, then [26] can be integrated.

$$\frac{1}{M} - \frac{1}{M_0} = 2\Gamma \frac{x - x_0}{\lambda} \quad [27]$$

- This result does not depend upon the dissipative transport coefficients such as viscosity or thermal conductivity!
- This decay is not exponential with distance.

Shock Front Thickness

Thermoviscous Attenuation

From linear dissipative hydrodynamics,

$$\alpha = \frac{\omega^2}{2\rho c_0^3} \left\{ \left(\frac{4\mu}{3} + \xi \right) + \kappa \left(\frac{1}{c} + \frac{1}{c_0} \right) \right\} \approx \frac{\tau}{c_0} \omega^2 \approx mfp \frac{\omega^2}{c_0^2} \quad [28]$$

The mean-free-path, mfp , is related to an approximate "collision time," τ , by the sound speed: $c_0 \approx mfp/\tau$.

Shock Thickness

Since attenuation is proportional to ω^2 , only the loss suffered by the highest frequency component of the sawtooth [21] needs to be considered in this approximation.

The energy per unit area in one cycle of the sawtooth is proportional to u^2 .

$$E \approx k u^2 \lambda \quad [29]$$

where k is some constant that includes the fluid density.

The relative energy loss per unit area in one cycle can be calculated from the geometrical model [26].

$$\frac{dE}{E} \bigg|_{Shock} = 2 \frac{du}{u} = 4\Gamma \frac{u}{c_0} \frac{dx}{\lambda} = 4\Gamma M \frac{dx}{\lambda} \quad [30]$$

For thermoviscous attenuation $(dE/E)_{T,V} = -2\alpha dx$. By equating the shock loss [30] over one wavelength to the thermoviscous loss [28] of the highest frequency component [21], $f_{max} = \Gamma_{max} f$, we get a shock thickness, $\delta \approx \lambda_{max}/2$.

$$\delta \approx \frac{\pi^2 (mfp)}{2\Gamma M} \quad [31]$$

For the (weak) 1 kHz example, $\delta \approx 20,000 \text{ mfp} \approx 70 \text{ } \mu\text{m}$, so $\lambda/\delta \approx 5,000$! For a stronger shock, $M = 0.1$, $\delta = 40 \text{ mfp}$!

Distortion in Liquids

Virial Expansion

In the literature on nonlinear effects in liquids, it is common to expand the Equation-of-State in powers of the relative deviation of density from the equilibrium state, $\delta\rho/\rho_o = (\rho - \rho_o)/\rho_o$:

$$p = p_o + A \left(\frac{\delta\rho}{\rho_o} \right) + \frac{B}{2!} \left(\frac{\delta\rho}{\rho_o} \right)^2 + \frac{C}{3!} \left(\frac{\delta\rho}{\rho_o} \right)^3 + \dots \quad [32]$$

The coefficients are related to the thermodynamic derivatives evaluated at equilibrium:

$$A = \rho_o \left. \frac{\partial p}{\partial \rho} \right|_{\rho_o} = \rho_o c_o^2 \quad [32a]$$

$$B = \rho_o \left. \frac{\partial^2 p}{\partial \rho^2} \right|_{\rho_o} = \rho_o \left. \frac{\partial^2 c^2}{\partial \rho^2} \right|_{\rho_o} = 2 \rho_o c_o \left. \frac{\partial c}{\partial \rho} \right|_{\rho_o} \quad [32b]$$

$$C = \rho_o \left. \frac{\partial^3 p}{\partial \rho^3} \right|_{\rho_o} = \frac{3B^2}{2A} + \rho_o c_o \left. \frac{\partial^3 c}{\partial \rho^3} \right|_{\rho_o} \quad [32c]$$

Sound Speed

Sound speed can be expressed in these terms:

$$\frac{c^2}{c_o^2} = 1 + \frac{B}{A} \left(\frac{\delta\rho}{\rho_o} \right) + \frac{C}{2A} \left(\frac{\delta\rho}{\rho_o} \right)^2 + \dots \quad [33]$$

The Grüneisen Constant becomes:

$$\Gamma = 1 + \frac{B}{2A} \quad [34]$$

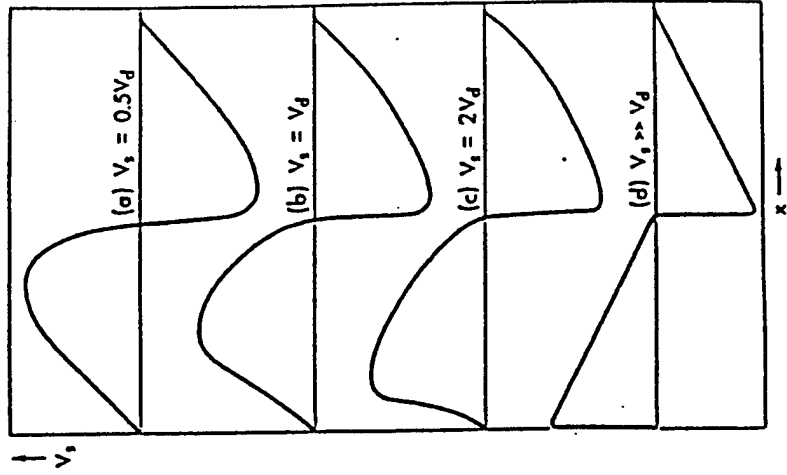
Note: the third term (with coefficient, C) makes a contribution that does not alternate sign!

Double Shock Formation

"Critical" Velocity

We can define a critical Mach Number, $M_d = v_d/c_o$, for which the Grüneisen constant, Γ , and the third term in [32] cancel.

$$M_d = \frac{v_d}{c_o} = \frac{4 + 2(B/A)}{(C/A) + (B/A)[1 - (B/A)]} \quad [35]$$



Double Shock Occurrence

Ideal Gases

The adiabatic gas law can be expanded as a binomial in powers of the density deviation, $p = p_0[1 + (\delta p/p_0)]^\gamma$

$$\frac{p}{p_0} = 1 + \gamma \left(\frac{\delta p}{p_0}\right) + \frac{\gamma(\gamma-1)}{2} \left(\frac{\delta p}{p_0}\right)^2 + \frac{\gamma(\gamma-1)(\gamma-2)}{6} \left(\frac{\delta p}{p_0}\right)^3 + \dots \quad [36]$$

In that case, $B/A = (\gamma-1)$ and $C/A = (\gamma-1)(\gamma-2)$, so the denominator in [35] vanishes. This effect does not occur in ideal gases.

Classical Liquids

For water, $v_d = -1.2 c_0$, corresponding to negative pressures of 26,000 atm. Two orders-of-magnitude greater than maximum observed cavitation threshold!

This effect has been observed in liquids near their critical point [M. S. Cramer, *et al.*].

Quantum Liquids

Double shocks should also occur at relatively small amplitudes in superfluid $^3\text{He-B}$ at temperatures a few millikelvin above absolute zero.

$$v_d(T) = v_d(GL) \sqrt{1 - T/T_c} \quad [37]$$

where $v_d(GL)$ is only a few hundred microns/sec [Garrett, JASA 69(1), 139 (1981)].

Reverse Shocks

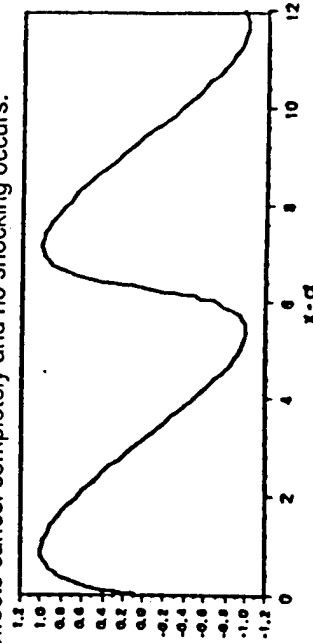
Third Sound Shocks

Van der Waal's force, in analogy to shallow water gravity waves, restores atomically thin films of superfluid ^4He .

$$c_3 = \sqrt{\frac{\langle p_s \rangle}{\rho}} f h = \sqrt{\frac{\langle p_s \rangle}{\rho}} \frac{3\alpha}{h^3} \quad [38]$$

Since $c_3 \approx h^{-3/2}$, the troughs have a higher sound speed than the crests, so the shock forms at the rear, if $h_0 < 10 \text{ \AA} = 10^{-9} \text{ m}$ (about 3 atomic layers of He). Thicker films shock in the normal way.

At only one mean thickness, convective and constitutive effects cancel completely and no shocking occurs.



Second Sound Shocks

The same "backward breaking" behavior occurs for thermal sound waves in $^4\text{He-II}$. Shockless propagation occurs at 1.884 °K. Between 1.884 °K and $T_\lambda = 2.172 \text{ °K}$, the hot 'crests' travel slower than the cold 'troughs.'

Solids

Materials that exhibit this effect are used in shock tubes as 'beam stops' for the shock projectile to 'unshock' the waveform.

1st Review and Summary

Motivation

At this point it is useful to review and summarize the main results obtained before going on to a (slightly) more mathematically self-consistent approach.

Self-Interaction Results

The speed of wave propagation depends upon the amplitude of the wave in two ways:

1. The fluid particle velocity adds a (self-Doppler) convective contribution to the sound speed.
2. The "equilibrium" sound speed, determined by derivatives of the constitutive equation, is affected by the changes in temperature or density or depth, etc., that accompany the wave.

Nonlinear Effects Accumulate with Distance

For sufficiently large Goldberg Number, $G > 1$, the wave will distort before it attenuates by linear (thermoviscous) means.

Fully Developed Shocks have Sawtooth Waveforms

The fate of all (ordinary) nonlinear distortion processes for periodic disturbances is a sawtooth waveform that dissipates its energy through large gradients generated at the shock front that is "thin" on the scale of the mean-free-path in gases.

Deviate Cases

There are some interesting special cases where the convective and constitutive effects can oppose each other or higher-order terms in the constitutive equation (equation-of-state) can produce effects with a sign that does not alternate to co-operate with the convective contribution.

Waveform Instability

The "Weak Shock" Limit

We have demonstrated the sawtooth waveform characteristic of the fully developed shocking of a periodic waveform.

We now revisit the initiation of this distortion process for an initially sinusoidal wave and assume that the distortion amplitudes, e.g., v_2 or p_2 , are small compared to the amplitude of the fundamental component and $v_0 = 0$.

$$v = v_1 + v_2 + v_3 + \dots$$

$$c_0 \gg v_1 \gg v_2 \gg v_3 \gg \dots \quad [38]$$

The Eamshaw Approximation

While the US was fighting its Civil War, Eamshaw published the first solution to the problem of waveform instability [Phil. Trans. Royal Soc. (London) 150, 133 (1860)].

He let a sinusoidal wave of initial amplitude, v' , modify the 'local' sound speed.

$$v_1(x, t) = v' \cos(\omega t - kx) = v' \cos \omega \left[t - \frac{x}{c_0} \right] \quad [39]$$

Substitute $c = c_0 + \Gamma v_1$ to generate the 2nd order contribution,

$$v_1(x, t) + v_2(x, t) = v' \cos \omega \left[t - \frac{x}{c_0 + \Gamma v_1} \right] \quad [40]$$

In the weak shock limit, $M \ll 1$, we expand the argument

$$v_1 + v_2 = v' \cos \omega \left[t - \frac{x}{c_0} \left(1 - \Gamma \frac{v_1}{c_0} \right) \right] \quad [41]$$

Earnshaw Continued

Use identity, $\cos \omega(a+b) = \cos \omega a \cos \omega b - \sin \omega a \sin \omega b$, and assume the weak shock limit, $\Gamma \omega x v_1 / c_0^2 \ll 1$,

$$v_1 + v_2 = v' \cos \omega \left[t - \frac{x}{c_0} \right] - \frac{x \omega \Gamma v_1}{c_0^2} v' \sin \omega \left[t - \frac{x}{c_0} \right] \quad [42]$$

If we substitute the solution for $v_1 = v' \cos \omega(t - x/c_0)$

$$v_2(x, t) = -\frac{x \omega \Gamma v'^2}{c_0^2} \sin \omega \left[t - \frac{x}{c_0} \right] \cos \omega \left[t - \frac{x}{c_0} \right] \quad [43]$$

The identity, $\sin 2a = 2 \sin a \cos a$, produces an explicit result for the amplitude of the second harmonic component,

$$v_2 = -\frac{x \omega \Gamma v'^2}{2 c_0^2} \sin 2\omega \left[t - \frac{x}{c_0} \right] = -\pi \Gamma M \frac{x}{\lambda} v' \sin 2\omega \left[t - \frac{x}{c_0} \right] \quad [44]$$

Second Harmonic Generation

The first-order solution was not changed, since we let $\cos \omega b = 1$. This violates energy conservation, but we will fix that problem soon.

The second-order contribution grows linearly with distance and is 'scaled' by the acoustic Mach number and the wavelength of the fundamental.

The approximation should fail before $v_2 = v_1$. If we set them equal, we can solve for this distance, $x_{1=2}$.

$$x_{1=2} = \frac{\lambda}{\pi \Gamma M}$$

This is just twice the Shock Inception Distance, $x_{1/2} = 2D_s$, as might be expected, so we are safe (self-consistent).

Higher Harmonic Generation

Iterative Approximation

We could repeat the Earnshaw procedure to calculate the growth rate of successively higher harmonics [E. Fubini-Ghiron, Alta Freq. 4, 530 (1935)]. Since calculation of the second harmonic component was no fun, we will take a different approach.

Geometric Construction

The easier approach [Hargrove, JASA 32, 511 (1960)] uses what we have already derived to distort the waveform and then expresses the result in terms of a Fourier series.

The undistorted wave can be parameterized as

$$y = \sin \theta \quad [45]$$

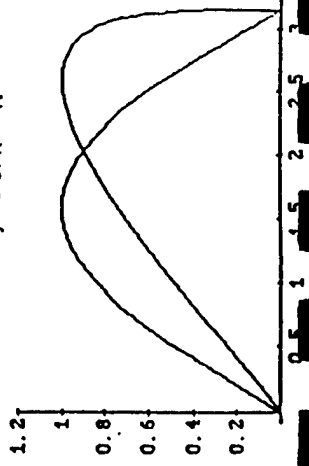
We plot this amplitude at an "advanced" position, scaled by the propagation distance, d , divided by D_s , so

$$k = \frac{d}{D_s} = \frac{2\pi \Gamma d}{\lambda} \quad [46]$$

where $0 \leq k \leq 1$. The x-coordinate in the (distorted) parameterized waveform becomes,

$$x = \theta + k \sin \theta \quad [47]$$

Shown below is one-half cycle of $k = 1$:



Higher Harmonic Generation (Con't.)

Kongensvej

Fourier Analysis

The distorted waveform can be expanded in a sinusoidal basis.

$$b_n = \frac{2}{\pi} \int_0^{\pi} y \sin nx \, dx \quad [48]$$

Using the integral definition of the Bessel Functions of the First Kind and their recurrence relations,

$$b_n = (-1)^{n+1} \frac{2}{nk} J_n(nk) \quad [49]$$

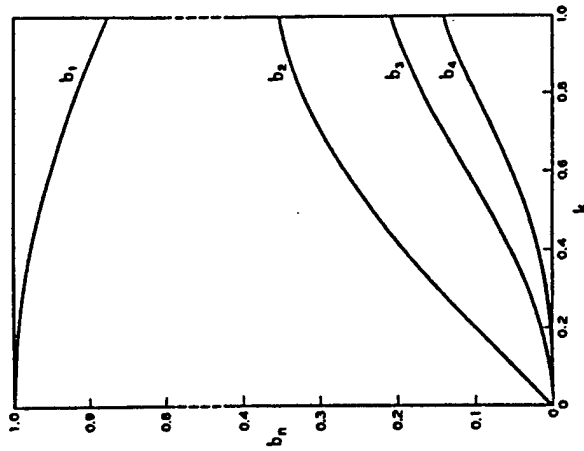


FIG. 2. Calculated Fourier coefficients b_n versus reduced distance k for an initially sinusoidal plane progressive wave of finite amplitude in a dissipationless medium (Hargrove, 1960).

We now see the decrease in the amplitude of the fundamental component (b_1), as well as the linear growth of the second harmonic (b_2), quadratic growth of the third harmonic (b_3), cubic growth of the fourth harmonic (b_4).

The Phenomenological Approach

Hydrodynamics provides a complete description of sound propagation in fluids. All of the phenomena shown thus far should be derivable from that system. As we shall see, that approach will also provide new insights and describe new phenomena.

For a homogeneous, single component fluid, five variables provide a complete description of the dynamics.

Two thermodynamic variables: p and s or p and T

Three components of velocity: v_x, v_y, v_z or vector, \mathbf{v}

The description of the fluid is then "closed" if we can produce five independent equations that govern the dynamics of the variables.

The Hydrodynamic Equations

Conservation of Mass:

$$\frac{\partial \rho}{\partial t} + \nabla \cdot (\rho \mathbf{v}) = 0 \quad [50]$$

Conservation of Entropy:

$$\frac{\partial (\rho s)}{\partial t} + \nabla \cdot (\rho s \mathbf{v}) = \kappa \frac{(\nabla T)^2}{T^2} + \mu \frac{(\nabla \mathbf{v})^2}{2T} \quad [51]$$

Conservation of Momentum (Euler/Navier-Stokes):

$$\frac{\partial \mathbf{v}}{\partial t} + (\mathbf{v} \cdot \nabla) \mathbf{v} = -\frac{\nabla p}{\rho} + \mu \nabla^2 \mathbf{v} \quad [52]$$

Formal Perturbation Expansion

Equation of State

Since Euler/Navier-Stokes [52] contains both p and ρ , we have six variables, so we must add an equation of state:

$$p = p(\rho, s) \quad [53]$$

In the absence of dissipative terms, the chain rule can be used to combine [50] and [51] to show that entropy is constant,

$$\frac{Ds}{Dt} = \frac{\partial s}{\partial t} + v \cdot \nabla s = 0 \quad [54]$$

$$\frac{\partial(\rho s)}{\partial t} + \nabla \cdot (\rho s v) = 0$$

This allows us to expand the Equation of State [54] only in terms of the density excess, $p' = p - p_0$.

$$p(\rho) = p_0 + \frac{\partial p}{\partial \rho} \Big|_s \rho' + \frac{\partial^2 p}{\partial \rho^2} \Big|_s \frac{\rho'^2}{2} + \dots \quad [56]$$

Perturbation Expansion

In the weakly nonlinear approximation, the acoustic variables can be expanded in a perturbation series:

$$\begin{aligned} p &\equiv p_0 + p_1 + p_2 + \dots \\ \rho &\equiv \rho_0 + \rho_1 + \rho_2 + \dots \\ v &\equiv v_0 + v_1 + v_2 + \dots \end{aligned} \quad [57]$$

Subscript:

"0" identifies the equilibrium state

"1" represents the "linear" sound field variables

"2" represents the "second order" corrections

In this expansion, it is assumed that terms of increasing order are successively smaller, e.g., $p_0 \gg p_1 \gg p_2$, etc.

First-Order (Linear) Solution

Linearized Hydrodynamics

Retain only first-order terms in the hydrodynamic equations.

$$\frac{\partial \rho_1}{\partial t} + \rho_0 \nabla \cdot v_1 = 0 \quad [58]$$

$$\frac{\partial v_1}{\partial t} + \frac{\nabla p_1}{\rho_0} = 0 \quad [59]$$

Use the linearized equation of state to eliminate p_1 :

$$p_1 = \frac{\partial p}{\partial \rho} \Big|_s \rho_1 = c_0^2 \rho_1 \quad [60]$$

Add $\partial[59]/\partial t$ to $-\rho_0 \nabla \cdot [60]$ to obtain the wave equation.

$$\frac{\partial^2 \rho_1}{\partial t^2} - c_0^2 \nabla^2 \rho_1 = 0 \quad [61]$$

This is a homogeneous, second-order partial differential equation for the first-order deviations of the fluid density, ρ_1 , from its equilibrium density, ρ_0 .

Traveling Wave Solutions

An expression similar to [61] can be derived for first-order deviations of pressure and particle velocity.

In one dimension, we take the traveling wave solutions to have the form below:

$$\begin{aligned} \rho_1(x, t) &= \rho' e^{j(\omega t \pm kx)} \\ p_1(x, t) &= p' e^{j(\omega t \pm kx)} \\ v_1(x, t) &= v' e^{j(\omega t \pm kx)} \end{aligned} \quad [62]$$

Limits to the Linearized Solution

Implicit Assumptions ($M \ll 1$)

What is the magnitude of terms that were ignored in obtaining the linearized solution?

Assume solutions of the form [62], so $\nabla \rightarrow -jk$ and $\partial/\partial t \rightarrow j\omega$.

From the Mass Conservation equation [50],

$$\left| \frac{v_1 \cdot \nabla \rho_1}{\partial \rho_1 / \partial t} \right| = \frac{k v_1 \rho_1}{\omega \rho_1 c_o} = \frac{v_1}{c_o} \equiv M \ll 1 \quad [63]$$

From the Euler equation [52],

$$\left| \frac{v_1 \cdot \nabla v_1}{\partial v_1 / \partial t} \right| = \frac{k v_1^2}{\omega v_1 c_o} = \frac{v_1}{c_o} \equiv M \ll 1 \quad [64]$$

and using the linearized Continuity equation [58],

$$\left| \frac{(\rho_1 / \rho_o^2) \nabla p_1}{\nabla p_1 / \rho_o} \right| = \frac{\rho_1}{\rho_o} = \frac{v_1}{c_o} \equiv M \ll 1 \quad [65]$$

and with the linearized Euler equation [59], $p_1 = (\rho_o c_o) v_1$,

$$\left| \frac{(\rho_1 / \rho_o^2) \nabla p_1}{\partial v_1 / \partial t} \right| = \frac{\rho_1 k p_1}{\rho_o^2 \omega v_1 \rho_o} = \frac{p_1}{\rho_o} \equiv M \ll 1 \quad [66]$$

Energy Conservation

From $v_1 \cdot \nabla p_1$ [59] and $p_1 \cdot \nabla v_1$ Continuity [58] we get the equation below for Conservation of Energy,

$$\frac{\partial}{\partial t} \left(-\frac{1}{2} \rho_o v_1^2 + \frac{1}{2} \frac{p_1^2}{\rho_o c_o^2} \right) + \nabla \cdot (p_1 v_1) = 0 \quad [67]$$

where the divergence of the acoustic intensity (flux), $I = p_1 v_1$, is the time derivative of the energy density.

Nonlinear Wave Equation

Perturbation Expansion

To remove the restriction that $M \ll 1$, we must include the second-order terms which were previously ignored.

Conservation of Mass from [50]

$$\frac{\partial \rho_1}{\partial t} + \frac{\partial \rho_2}{\partial t} + v_1 \cdot \nabla \rho_1 + \rho_o \nabla \cdot v_1 + \rho_1 \nabla \cdot v_1 + \rho_o \nabla \cdot v_2 = 0 \quad [68]$$

Euler's Equation from [52]

$$\rho_o \frac{\partial v_1}{\partial t} + \rho_o \frac{\partial v_2}{\partial t} + \rho_1 \frac{\partial v_1}{\partial t} + \rho_o (v_1 \cdot \nabla) v_1 = -\nabla p_1 - \nabla p_2 \quad [69]$$

Adiabatic Equation of State from [54]

$$p_2 = \frac{\partial p}{\partial \rho} \bigg|_s \rho_2 + \frac{\partial^2 p}{\partial \rho^2} \bigg|_s \frac{\rho_1^2}{2} \quad [70]$$

Inhomogeneous Second-Order Wave Equation

Combination of [68] – [70] with the linear wave equation [61] produces a wave equation for the second-order components.

$$\frac{\partial^2 \rho_2}{\partial t^2} - c_o^2 \nabla^2 \rho_2 = \nabla^2 (\rho_o v_1^2 + \frac{\partial^2 p}{\partial \rho^2} \bigg|_s \frac{\rho_1^2}{2}) \quad [71]$$

With substitution of the relations for the first-order terms, this can be written in a more familiar form, as done in [10]:

$$\frac{\partial^2 \rho_2}{\partial t^2} - c_o^2 \nabla^2 \rho_2 = \frac{c_o^2}{\rho_o} \left(1 + \frac{\rho_o}{c_o} \frac{\partial c}{\partial \rho} \right) \nabla^2 \rho_1^2 = \Gamma \frac{c_o^2}{\rho_o} \nabla^2 \rho_1^2 \quad [72]$$

The first-order sound field has "formally" become the "source" for the second-order contributions.

Parametric Array

The Quadratic Source Term

The source term on the r.h.s. of [72] can be considered a "virtual array" powered by the first-order ("pump") sound field.

If we let $p_1 = p' \cos(\omega_1 t - k_1 x)$, then the source term becomes,

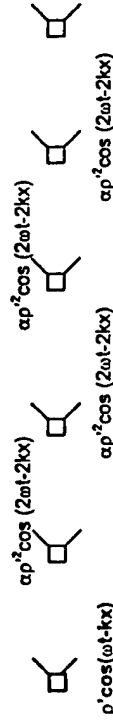
$$\Gamma \frac{c_0^2}{\rho_0} \nabla^2 p_1^2 = \Gamma \frac{\rho'^2 c_0^2}{2 \rho_0} \nabla^2 [1 + \cos(2\omega_1 t - 2k_1 x)] \quad [73]$$

We will postpone consideration of the constant term until our presentation of non-zero time-averaged nonlinear effects.

"Geometrical Resonance"

The phase speed of the source term [73], $c_{\text{phase}} = 2\omega_1/2|k| = c_0$, is the same as the propagation speed of the second-order wave equation [72], so the source is "in resonance" with the propagation of the second-order acoustic field.

We can picture this as a linear end-fire array of virtual sources, properly phased so that their effects add linearly with distance from the real source.



This model reproduces the weak shock result for linear growth of the second-harmonic that is proportional to both Γ and M^2 .

This approach also makes it easy to consider the co-linear interaction of two waves of different frequencies, ω_1 and ω_2 .

Nonlinear (but Co-linear) Wave Mixing

Difference Frequency Array

Consider a real source which emits two pure tones of equal magnitude, p' , at frequencies, ω_1 and ω_2 , that differ from each other by a small amount, $|\omega_2 - \omega_1| \ll \omega_1 \approx \omega_2$.

$$p' = p'' [\cos(\omega_1 t - k_1 x) + \cos(\omega_2 t - k_2 x)] \quad [74]$$

Since the nonlinear source term in [72] is driven by p'^2 , there are now five source terms. For convenience, let $a = (\omega_1 t - k_1 x)$ and $b = (\omega_2 t - k_2 x)$.

$$p'^2 = \frac{\rho'^2}{2} [2 + \cos 2a + \cos 2b + \cos(a+b) + \cos(a-b)] \quad [75]$$

In addition to the self-distortion (shocking) of the two source waves (the $2a$ and $2b$ terms), there is also generation of waves at the sum and difference frequencies.

All of the virtual source components have phase speeds that equal the linear propagation speed (in the absence of dispersion) and are "geometrically resonant."

$$\frac{2\omega_1}{2k_1} = \frac{2\omega_2}{2k_2} = \frac{\omega_1 + \omega_2}{k_1 + k_2} = \frac{|\omega_1 - \omega_2|}{|k_1 - k_2|} = c_0 \quad [76]$$

Directionality of the Parametric End-Fire Array

The effective length of the "virtual array" is determined by the attenuation distance, $l = \alpha^{-1}$, of the pump waves at modestly large amplitudes, where $G \approx 1$. The ratio of the attenuation distance to the wavelength of the difference will determine the "virtual array's" directionality.

The virtual array has the directional characteristics determined by the ratio of the source piston diameter to the wavelength of the pump waves.

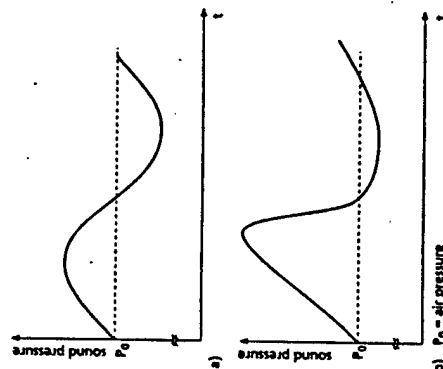
AUDIOBEAM – A WORLD INNOVATION

A New Kind of Sound Reproduction

Imagine sitting in a concert hall... you and everyone else are enjoying some marvelous music when suddenly the artist addresses you. Only you can hear what the artist is saying.

Incredible? Yes, but possible with a completely new sound reproduction technology from Sennheiser. At the 1999 AES Conventions in Munich and New York, Sennheiser introduced a highly directional acoustic radiator, that will open up new areas of application for which conventional loudspeakers are unsuitable: AudioBeam.

In a conventional sound reinforcement environment, a loudspeaker normally covers the whole room uniformly. The AudioBeam radiator, however, has been designed to achieve the exact opposite: sound becomes directional, addressing persons within a defined area.



How does this work?

We know that ultrasound can be easily focused due to its very short wavelength (100 kHz corresponds approx. 3 mm); and radiators with beam angles of 1° are technically well feasible. AudioBeam uses this strongly focused ultrasound as a carrier for the generation and radiation of equally focused audio, making use of two phenomena:

- the non-linearity of air
- intermodulation due to a non-linear characteristic.

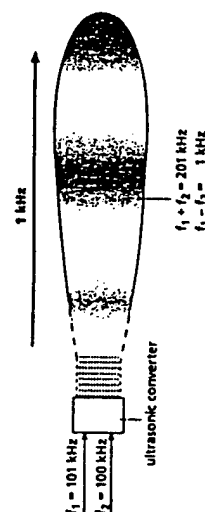


Figure 3: Intermodulation of f_1 and f_2

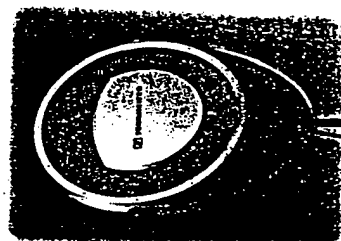


Figure 1: The AudioBeam ultrasonic radiator

compressions and rarefactions of the air caused by the sound travelling through it are no longer equal (Fig. 2). This non-linearity is the prerequisite for utilizing a second effect, that of intermodulation, i.e. the mixing of two frequencies, due to a non-linear characteristic (Fig. 3).

Consider an ultrasonic radiator which simultaneously emits two frequencies, e.g. $f_1 = 101 \text{ kHz}$ and $f_2 = 100 \text{ kHz}$. Similar to the (non-linear) mixing stage of an AM medium waveband receiver, the following intermodulation products will be generated in the air within the ultrasonic beam:

$f_1 + f_2 = 201 \text{ kHz}$
 $f_1 - f_2 = 1 \text{ kHz}$

The summation frequency $f_1 + f_2 = 201 \text{ kHz}$ is inaudible for man, but the desired difference frequency $f_1 - f_2 = 1 \text{ kHz}$ is audible. Now it is easy to imagine that f_1 can be modulated by the audio frequency range $\Delta f = 100 \text{ Hz} \dots 20 \text{ kHz}$ to give $f_1 = 100 \text{ kHz} + \Delta f$.

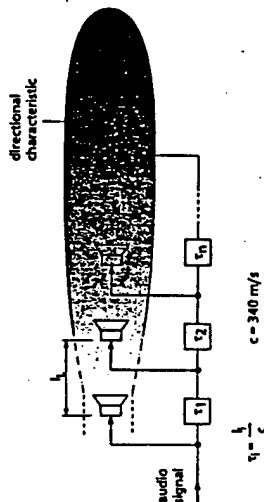
Within the ultrasonic beam, intermodulation due to the non-linearity of air will produce – among other intermodulation products – the original audio frequency signal from 100 Hz to 20 kHz, with the audio

Advantages

- Strongly focused, directional radiation of sound
- No feedback problems from adjacent microphones
- Broadband reproduction with a single transducer
- Compact design

rfe

Figure 4: Virtual loudspeakers



being similarly focused as the ultrasonic beam.

Virtual Loudspeakers

Within the mixing zone of the ultrasonic beam, virtual audio sources are created. They add up in direction of the travelling ultrasonic wave, as ultrasound and audible sound travel at the same speed (340 m/s). This effect can be illustrated by a model: a number of small loudspeakers is mounted closely onto a strip of metal or wood. They all radiate sound in an omni-directional pattern (Fig. 4), and reproduce the same audio signal, but each with a certain time delay. This delay t between two loudspeakers exactly corresponds to the time the sound wave needs to travel to the next loudspeaker. The delay is $t = c/f_1$, with c being the velocity of sound. The sound coming from the first loudspeaker is thus boosted by the second one and so on. Within the ultrasonic beam, an unlimited number of virtual sound sources is generated. The audio wave becomes strongly focused as the multitude of loudspeakers are "switched on" and the sound wave propagates.

The Technical Principle

The audible sound is generated within the ultrasonic beam. Unlike radiation by a conventional loudspeaker, the audible sound becomes louder as the distance increases, until the ultrasonic level has decreased such that the air's non-linear effect no longer works and no portions are added to generate the audio signal (Fig. 5). The length of the active zone, i.e. the zone where the audio signal is

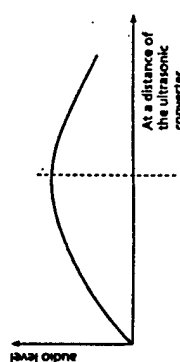


Figure 5: Increasing level because addition of the virtual speakers

generated within the ultrasonic beam, determines the lower limit frequency of the directional AF sound source. Many virtual sound sources are necessary to make the active zone several wavelengths long at the lower limit frequency. Therefore audio frequencies of under 100 Hz would require a great distance as well as higher output power between the ultrasonic radiator and the listener. To circumvent this requirement, psycho-acoustic signal processing can be used.

The high ultrasonic level necessary to generate the audio signal is only required in the active zone of the ultrasonic beam (see Fig. 4). Once the directional audio beam has been generated, the ultrasonic por-

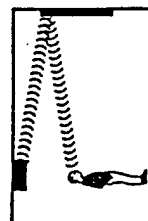


Figure 6: Reflection off an object: Audiobeams do not interfere with one another



Future Prospects

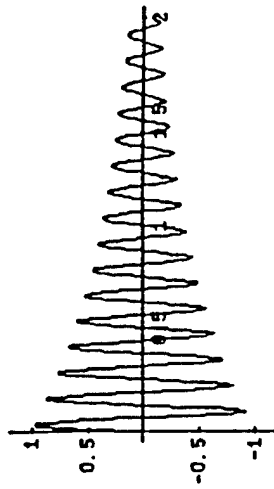
The range of possible applications is wide. Together with various key users, Sennheiser is currently defining the exact requirements for several applications. Simultaneously, the development of ultrasonic transducers and amplifiers with high performance and increased long-term stability is intensified. In close cooperation with the Institute for Acoustics and Speech Communication of Dresden Technical University, the essentials for product development are being mapped out. As a product partner to the EXPO 2000, Sennheiser will present this technology beginning in June at its EXPO booth.

© by HUSS-MEDIEN GmbH
 Am Friedrichshain 22
 10400 Berlin
 Germany

Parametric Array Waveforms

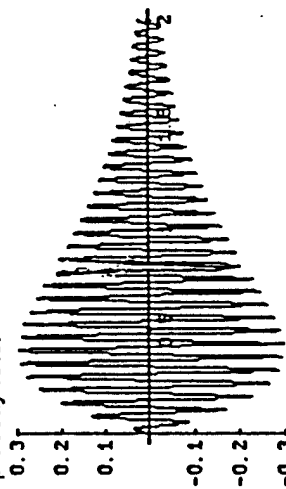
Pump Waves

Two high-frequency directional beams in a lossy medium.



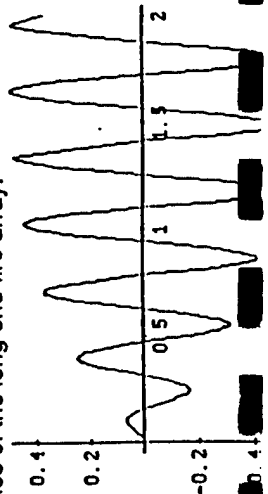
The $2\omega_1$, $2\omega_2$, and Sum Frequency Waves

Initial growth, but attenuation at a rate which is four times the pump decay rate.



The Difference Frequency Wave

Growth in the region of virtual sources, then propagation beyond the interaction region, maintaining the directional properties of the long end-fire array.



Loss of Geometrical Resonance

In order to better understand the concept, it could be useful to look at situations that are not "geometrically resonant."

DISPERSION: In the presence of dispersion, $dc_0/df \neq 0$, the array may "de-phase" after some distance and create cancellation rather than reinforcement. One possible result is "beating" in space, rather than in time.

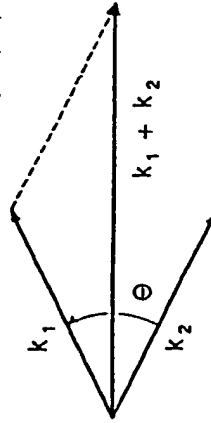
NONLINEAR MODE MIXING: When more than one mode can exist (e.g., longitudinal and transverse modes in solids), co-linear propagation does not "phase match."

The "Scissors" Effect

If we dare venture into a two-dimensional problem, the two "pump" waves do not have to be co-linear!

Assume plane waves at two different frequencies, $\omega_1 \neq \omega_2$, moving in different directions, k_1 and k_2 . The phase speed of the interaction term will be larger than the propagation speed, $c_0 = \omega_1 / |k_1| = \omega_2 / |k_2|$.

To simplify the analysis let $\omega_1 = \omega_2$ and $|k_1| = |k_2|$.



The phase speed, c_{ph} , of the interaction term [73] always exceeds the equilibrium (thermodynamic) sound speed, c_0 .

$$c_{ph} = \frac{\omega_1 + \omega_2}{|k_1 + k_2|} = \frac{2\omega_1}{2|k_1| \cos(\theta/2)} = \frac{c_0}{\cos(\theta/2)} \geq c_0 \quad [76]$$

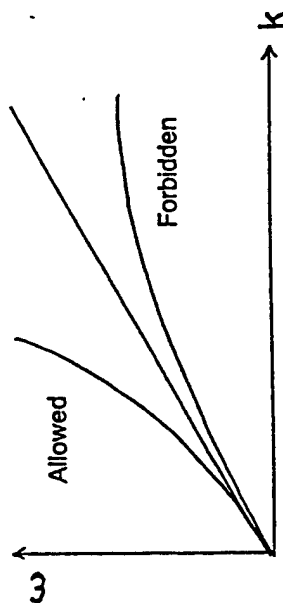
Dispersion

Forbidden Transitions

Although intrinsically acoustical in nature, there are important connections to solid-state physics where nonlinear wave mixing is known as "phonon-phonon" interactions.

- If $dc_0(\omega)/d\omega = d^2\omega/dk^2 > 0$, then "resonant" interaction is possible.
- If $dc_0(\omega)/d\omega < 0$, then "resonant" interaction is forbidden. In this case energy cannot "cascade" to shorter wavelength by nonlinear processes.

Condensed-matter physicists like to plot ω vs. k , instead $c(\omega)$, because it allows them to put Planck's constant, h , in front of all terms and claim that energy, $E = h(\omega/2\pi)$, and momentum, $P = h(k/2\pi)$, are being conserved.



Superfluid Acoustic Microscope

One nice application of the forbidden transition occurs in superfluid helium. The curvature of its dispersion curve can have either sign, depending on static pressure.

In conjunction with the slow sound speed in liquid ^4He , which produces short wavelengths, and low thermoviscous attenuation, Quate's group at Stanford suppressed nonlinear loss mechanisms by working at pressures where $d^2\omega/dk^2 < 0$.

Mode Conversion in Solids

Shear and Longitudinal Waves in Solids

In an isotropic, homogeneous solid, the speed of longitudinal waves, c_L , always exceeds the speed of the shear waves, c_S .

$$c_S^2 = \frac{G}{\rho} = \frac{E}{2\rho(1+\nu)} < c_L^2 = \frac{E}{\rho} \quad [77]$$

E is Young's modulus, G is the shear modulus, and ν is Poisson's ratio. For most materials, $0.25 < \nu < 0.50$.

Resonant Mode Conversion

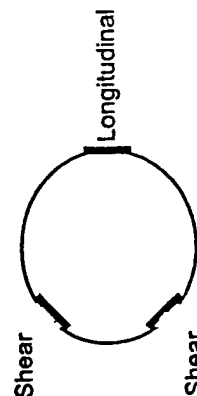
In media where two non-dispersive modes with different sound speed exist, it is possible for nonlinear interactions to convert energy for the slower mode to the faster mode.

It has been observed [Rollins, *et al.*, Phys. Rev. 136A, 597 (1964)], that nonlinear mode conversion can take place in aluminum. Two shear waves will generate a longitudinal wave, if the shear waves interact at the mode conversion angle, θ_{mc} .

$$\cos(\theta_{mc}/2) = \sqrt{\frac{1}{2(1+\nu)}} \quad [78]$$

In aluminum, the angle $\theta_{mc} \approx 52^\circ$.

The experimental apparatus used by Rollins, *et al.*, consisted of a block of aluminum machined so that the surfaces on which the transducers were mounted had the appropriate angles.



Mode Conversion in Superfluid ^4He (Hell)

Second Sound in Hell

In superfluids, heat (temperature/entropy disturbances) propagates as a sound wave called 2nd sound, at the speed, c_2 , which is always less than the speed of ordinary (1st sound) pressure/density disturbances, $c_1 > c_2$.

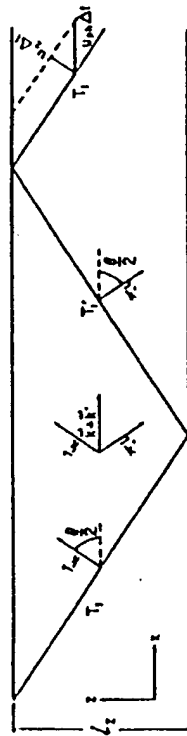
Both speeds depend upon temperature, for $T \leq T_\lambda \approx 2.172^\circ\text{K}$,

$$\cos(\theta_{mc}/2) = \frac{c_2(T)}{c_1(T)} \quad [79]$$

Since $c_1/c_2 > 10$, at all $T \leq T_\lambda$, the resonant interaction angle is nearly anti-parallel, $\theta_{mc}(T) \approx 180^\circ$.

Waveguide Interaction Angle Control

The angle of interaction for the two 2nd sound waves were controlled by use of a waveguide of rectangular cross-section operating near its cut-off frequency, ω_∞ .



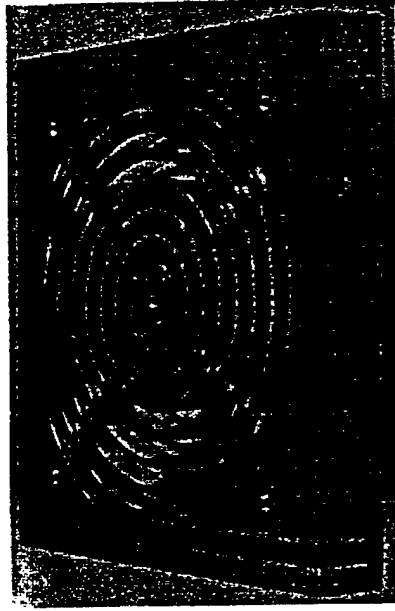
$$\cos(\theta_{mc}/2) = \frac{k}{\sqrt{k^2 + k_z^2}} = \sqrt{1 - \frac{\omega_\infty^2}{\omega^2}} \quad [80]$$

The mode conversion frequency in the waveguide is determined only by the ratio of the two sound speeds.

$$\frac{2\omega_\infty}{\omega_{mc}} = \sqrt{1 - \frac{c_2^2}{c_1^2}} \quad [81]$$

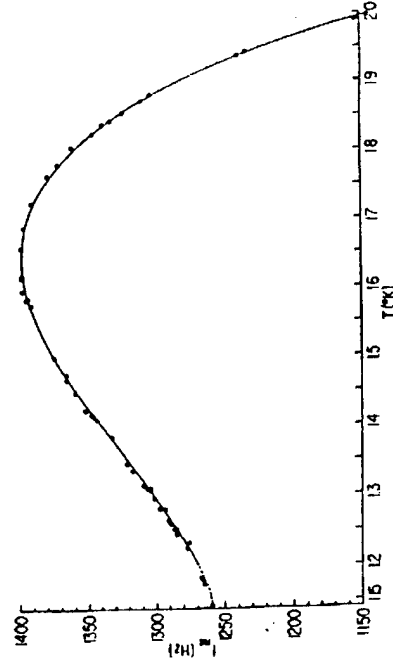
Resonant Conversion in Hell

Waveguide and 2nd Sound Source



Mode Conversion Frequency vs. Temperature

Data from Garrett [Phys. Rev. Lett. **41**(6), 413 (1978)]. Solid line is based on 1st and 2nd sound speed measurements by Heiserman, et al. [Phys. Rev. **B14**, 3862 (1976)] and Maynard [Phys. Rev. **B14**, 3868 (1976)].



2nd Review and Summary

Motivation

At this point it is useful to review the results of the more formal (perturbation expansion) approach. In the final segment we will consider time-averaged nonlinear effects.

Perturbation Expansion Results

LINEARIZATION OF THE HYDRODYNAMICS Assumes $M \ll 1$.

EARNshaw Demonstrated the linear growth of the second harmonic with distance and acoustic Mach number, $M = v/c_0$.

BESSEL SOLUTIONS All harmonics are created and grow initially in proportion to $(x/\lambda)^{n-1}$ and $M^{(n-1)}$, then as Bessel Functions of the 1st Kind.

SOURCE TERM Inclusion of all 2nd order terms produces a wave equation for the 2nd order sound field variables that is "driven" by quadratic combinations of the 1st order field variables.

Parametric End-Fire Array Model

MIXING Quadratic driving terms leads to nonlinear "mixing" of the 1st order field variables.

RESONANCE In the absence of dispersion, the driving term has the same phase speed as the 2nd order field variables.

DIRECTIONALITY The "difference" wave has the directional characteristics determined by the exponential attenuation length of the "pump" waves.

DISPERSION Dispersion will lead to de-phasing of the array.

MODE CONVERSION If the medium supports more than one sound mode, then nonlinear mixing can lead to energy conversion between modes.

Non-Zero Time-Averaged Effects

Introduction

When we "squared" the 1st order sound field variables, for example [73], we produced a "static" term in addition to the terms at frequencies $2\omega_1$, $2\omega_2$, $\omega_1 \pm \omega_2$.

$$v'^2 \cos^2(kx - \omega t) = \frac{v'^2}{2} [1 + \cos 2(kx - \omega t)] \quad [82]$$

The 1st order fields have a sinusoidal time dependence and their time-averaged value must be zero over times long compared to the acoustic period, $T \gg 2\pi/\omega$.

$$\langle p_1 \rangle_t = \frac{1}{T} \int_0^T p_1 dt = 0 \quad [83]$$

The 2nd order term contains a constant which has a time-averaged value $\langle p_2 \rangle_t \neq 0$. This effect can lead to substantial forces and torques. In the early 1940's, Hillary St. Clair [Rev. Sci. Inst. 12, 250 (1941)] used a siren and a reflector to levitate pennies with density, $\rho_{cu} = 8.9$

The Bernoulli Pressure

These effects arise as a consequence of the Bernoulli pressure. In a flow field of velocity, v , the ambient pressure, p_0 , is reduced by the kinetic energy density of the flow.

$$p(v) = p_0 - \frac{1}{2} \rho_0 v^2 \quad [84]$$

This is the effect that provides lift for airplanes and sucks the shower curtain into the shower instead of pushing it out, as you might expect.

The dependence of [84] on v^2 guarantees that the time-averaged effects are non-zero, even for acoustically oscillating flows.

Non-Zero Time-Averaged Effects

Cork Dust in a Kundt's Tube

When cork dust is placed in a standing wave tube, striations of the dust are observed at sufficiently high amplitudes near velocity anti-nodes in the standing wave.

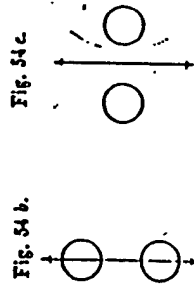
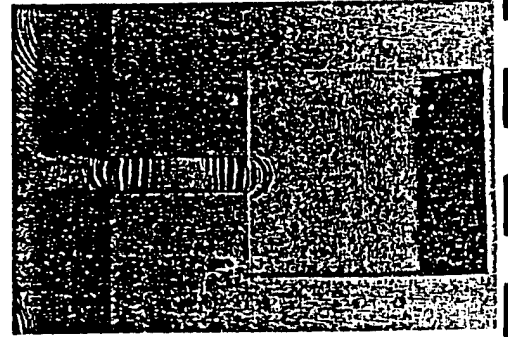
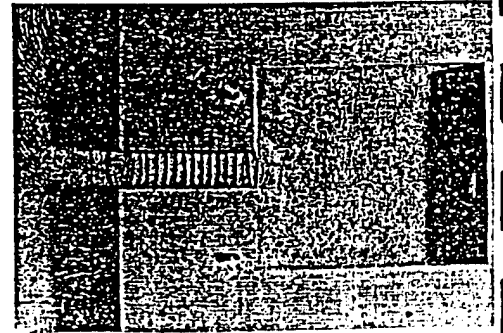


Fig. 54 b.

The above figures are from Rayleigh's *Theory of Sound*, Vol. II, §253b. The double-headed arrows indicate the direction of the oscillating acoustic velocity.

Cork Dust Photos

The images below were from a recent publication [Mukai, et al., "Experimental study on the absorption characteristics of resonance-type brick/block walls," J. Acoust. Soc. Jpn. (E) 20(6), 433-438 (1999)].



The Rayleigh Disk

Extended Flow Obstruction

For an extended (vs. point) object placed within an oscillating flow field, the Bernoulli pressure can be integrated over the surface of the object to produce a non-zero torque.

Pressure is highest at a stagnation point and lowest at the regions of highest velocity. These forces provide a moment that tends to align the disk perpendicular to the flow direction.

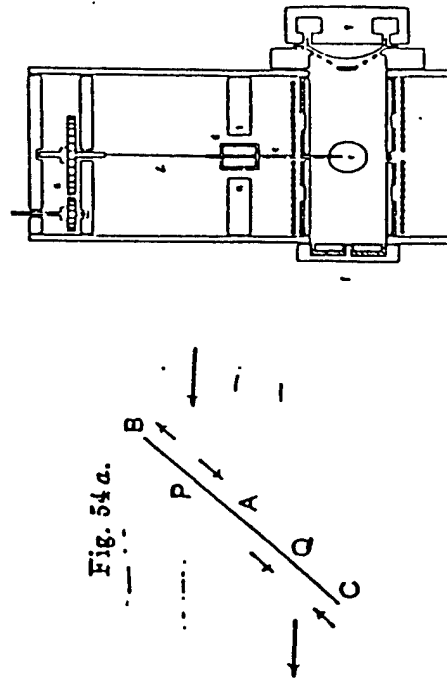


Fig. 54 a.

Torque on a Rayleigh Disk

For a thin circular disk of radius, a , at an angle, θ , between the normal and the flow direction, the net torque, N , is

$$N = \frac{4}{3} \rho a^3 v_1^2 \sin 2\theta \quad [85]$$

The torque vanishes at end-on and perpendicular aspect ($\theta=90^\circ$ or $\theta=0^\circ$), but end-on is unstable.

Prior to the advent of electroacoustics, this torque was used to measure the absolute amplitude of sound waves.

Bernoulli's Equation

Hydrodynamic Derivation

As before, a complete description of the Bernoulli Pressure will be contained within the hydrodynamics.

Starting with the Euler equation [52], and restricting ourselves to one-dimensional flow,

$$\frac{\partial v}{\partial t} + v \frac{\partial v}{\partial x} = - \frac{1}{\rho} \frac{\partial p}{\partial x} \quad [86]$$

Our goal will be to express [86] entirely in terms of the gradient of a scalar, so we introduce the Enthalpy (heat) function, $h = \varepsilon + pV$, that includes the fluid's internal energy per unit volume, ε .

$$dh = d\varepsilon + p dV + V dp \quad [87]$$

From the definition of $d\varepsilon = T dS - p dV$, we have $dh = dp/p$ for an adiabatic flow, $dS = 0$, so substitution into [86] yields,

$$\frac{\partial v}{\partial t} + \frac{1}{2} \frac{\partial v^2}{\partial x} = - \frac{\partial h}{\partial x} \quad [88]$$

By introduction of the velocity potential, ϕ , defined for curl-free flow, $v = \nabla \phi$, then [88] becomes,

$$\frac{\partial}{\partial x} \left[\frac{\partial \phi}{\partial t} + \frac{1}{2} v^2 + h \right] = 0 \quad [89]$$

Bernoulli's Equation

Since the gradient [89] is zero, the function within the gradient must be a constant.

$$\frac{\partial \phi}{\partial t} + \frac{1}{2} v^2 + h = \text{const.} \quad [90]$$

This is the "strong" form of Bernoulli's equation, since it is not restricted only to streamlines.

Time-Averaged Pressure

2nd Order Contribution

The enthalpy function must also be expanded to 2nd order.

$$h = h_0 + \frac{\partial h}{\partial p} (p_1 + p_2) + \frac{1}{2} \frac{\partial^2 h}{\partial p^2} p_1^2 \quad [91]$$

where the derivatives can be evaluated from the adiabatic differential form of enthalpy, $dh = T dS - dp/\rho$.

$$\frac{\partial \phi}{\partial t} + \frac{1}{2} v^2 + h_0 + \frac{p_1 + p_2}{\rho} - \frac{1}{2} \frac{p_1^2}{\rho_0 c_0^2} = \text{const.} \quad [92]$$

We are only interested in the parts of [92] which produce a non-zero time average. Since $\langle \partial \phi / \partial t \rangle_1 = \langle p_1 \rangle_1 = 0$,

$$\langle p_2 \rangle_1 = \frac{1}{2} \frac{p_1^2}{\rho_0 c_0^2} - \frac{1}{2} \rho_0 v_1^2 + \text{const.} \quad [93]$$

This is the difference between the potential and kinetic energy densities.

Traveling Waves

If we assume a plane, progressive wave of the form, $p_1(x,t) = p'_1 e^{j(\omega t - kx)}$, then $p_1 = \rho_0 c_0 v_1$, so substitution into [93] gives,

$$\langle p_2 \rangle_1 = \frac{1}{2} \frac{p_1^2}{\rho_0 c_0^2} - \frac{1}{2} \frac{p_1^2}{\rho_0 c_0^2} = 0 \quad [94]$$

There is no time-averaged 2nd order pressure produced by a pure traveling wave!

Note: The presence of an obstacle in the traveling wave will produce a scattered wave that adds a standing wave component to the original sound field.

Levitation Force

Standing Waves

If we assume a standing wave field:

$$p_1(x, t) = p' \cos(kx) \cos \omega t \quad [95]$$

$$v_1(x, t) = \frac{p'}{\rho_o c_o} \sin(kx) \sin \omega t \quad [96]$$

Then substitution into [93] produces a non-zero time averaged 2nd order pressure,

$$\langle p_2 \rangle_t = \frac{1}{4} \frac{p'^2}{\rho_o c_o^2} (\cos^2 kx - \sin^2 kx) = \frac{1}{4} \frac{p'^2}{\gamma \rho_o} \cos 2kx \quad [97]$$

The static 2nd order pressure variation in the standing wave has a minimum at each 1st order pressure node.

Force on a Thin Disk and Sphere

The static pressure field can be integrated over the surface of a disk of thickness, $t \ll \lambda$, and radius, $a \ll \lambda$.

$$F_{Disk} = \frac{\pi a^2}{2} \frac{p'^2}{\rho_o c_o^2} (kt) \sin 2kx \quad [98]$$

The result for a sphere of radius $a \ll \lambda$ is similar,

$$F_{Sphere} = \frac{4\pi a^2}{3} \frac{p'^2}{\rho_o c_o^2} (ka) \sin 2kx \quad [99]$$

To levitate a sphere of density, ρ_{sphere} , against gravity, the weight can be cancelled by the acoustic levitation force if,

$$p'^2 > \gamma \rho_o \rho_{sphere} \frac{g\lambda}{\pi} \quad [100]$$

When this criterion is met, then the position of the sphere will adjust itself within the (vertical) standing wave field to make the net force zero. The stability of such an equilibrium condition will be discussed shortly.

High Amplitude Standing Waves

Shock Formation

All of the discussion regarding nonlinear distortion, thus far, has assumed that the waves were one-dimensional and progressive (travelling waves).

As shown, levitation (and sonic compressors) requires high-amplitude standing waves. Shocking will dissipate energy that could be useful for levitation or compression.

The "Folding" Model

One way to connect the nonlinear effects in propagating waves with distortion processes already discussed in travelling waves is to consider a standing wave as the superposition of two traveling waves going in opposite directions [Tempkin, JASA 45, 224(1964)].

As the wave distorts by generating harmonics, those harmonics will also "fold over" after reflection from the resonator ends.

One conceptual approach to understanding distortion of a standing wave in a "consonant" resonator is to think of the wave as traveling in a tube with "effective" attenuation length, α^{-1} , that is the physical length, L , times the resonator quality factor, Q . (*Hands wave wildly here, but never leave wrists.*)

Consonant Resonators

An ideal (rigid-walled) plane wave resonator of length, L , with perfectly rigid ends, will have harmonically related (consonant) resonant mode frequencies, $f_n = n f_1 = n (c_o/2L)$.

The nonlinearly generated harmonics at frequencies, f_n , will be resonantly reinforced in the same way as the fundamental at f_1 .

For high enough amplitudes ($G \gg 1$), this leads to shock fronts that "bounce" back and forth through the resonator.

"Accidental" Resonator Dissonance

Thermoviscous Dispersion

Even rigid-walled resonators of constant cross-section exhibit some small amount of dispersion due to thermoviscous boundary layer effects on the resonator walls.

Increased averaged effective density due "infinite mass" at wall.
Isothermal (not adiabatic) sound speed at wall.

Coppens and Atchley [*Encyclopedia of Acoustics*, Vol. 1, Ch. 22 (Wiley, 1997)] define a (detuning) fractional frequency deviation parameter, h_n (not related to enthalpy),

$$h_n = \frac{f_n - n f_1}{n f_1} \quad [101]$$

Resonator Quality Factor

The importance of the detuning will depend upon the half-power bandwidths, Δf_n , of the n^{th} resonant mode. This bandwidth is usually specified by the Quality Factor of the n^{th} resonant mode, $Q_n = f_n / \Delta f_n$.

The parameter, H_n , is used to specify the "overlap" of the resonator response functions in terms of the quality factors of the n^{th} resonance mode, Q_n :

$$H_n = 2h_n \frac{Q_n Q_1}{Q_n + Q_1} \quad [102]$$

It is the ratio of the detuning, $f_n - n f_1$, to the averaged bandwidth of the two response functions.

The more dissimilar the values of H_n are, the more "mistuned" the cavity is and the weaker the nonlinear distortion will tend to be. Interesting waveforms are observed!

Nonlinear Standing Wave Shapes

Cylindrical Resonator

Below is an example [Il'inski, et al., JASA 104(5), 2664 (1998)] of waveforms produced by a cylindrical resonator of uniform cross-section, driven just below ($\Omega < 1$), at ($\Omega = 1$), and just above resonance ($\Omega > 1$).

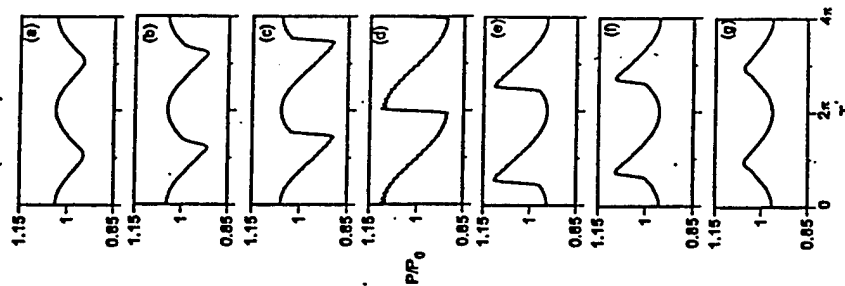


FIG. 2. The wave shapes of the pressure wave near the resonance frequency in the cylindrical resonator: the top three shapes are before resonance: $\Omega = 0.970$ (a), $\Omega = 0.975$ (b), and $\Omega = 0.980$ (c), the fourth waveform corresponds to the resonance frequency $\Omega = 1.0$ (d), and the lower three shapes are after resonance: $\Omega = 1.020$ (e), $\Omega = 1.025$ (f), and $\Omega = 1.030$ (g). Here $\bar{\lambda} = 5 \times 10^{-4}$, $N = 20$, $G_1 = 1 \cdot 10^{-3}$, $\gamma = 1.2$.

Standing Wave Shock Suppression

Intentional (Geometric) Dispersion

As presented earlier for traveling waves, the existence of dispersion destroys the phase coherence between the fundamental (pump) and the harmonics (and/or sum and difference products).

Dispersion, $dc_p/df \neq 0$, has already been used in higher order modes of a waveguide of rectangular cross-section [76] to facilitate resonant mode conversion.

"Geometrical" dispersion can be introduced in a quasi-one-dimensional resonator by changing resonator cross-sectional area, $S(x)$ as a function of position, $dS(x)/dx \neq 0$.

Exponential Horn

The simplest case to analyze is the lossless exponential horn [Morse, *Vibration and Sound*, 2nd ed. (ASA, 1983), pg. 265ff],

$$S_{\text{exp}}(x) = S_0 e^{2x/h} \quad [103]$$

S_0 is the cross-sectional area of the horn at some reference location, x_0 . The flare constant is h .

Energy conservation [67] dictates that the linear acoustic pressure, p_1 , decrease with distance along the horn.

$$p_1(x, t) = p_1 e^{-x/h} e^{j(\omega t - kx)} \quad [104]$$

The resulting wave equation,

$$\frac{1}{S} \frac{\partial}{\partial x} \left[S \frac{\partial p}{\partial x} \right] - \frac{1}{c_0^2} \frac{\partial^2 p}{\partial t^2} = 0 \quad [105]$$

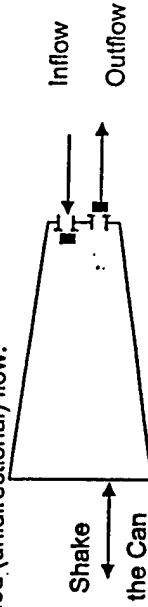
is dispersive, with a cut-off frequency, $f_\infty = c_0/2\pi h$.

$$c_{ph} = \frac{c_0}{\sqrt{1 - (f_{co}/f)^2}} \quad [106]$$

Waveform Shaping

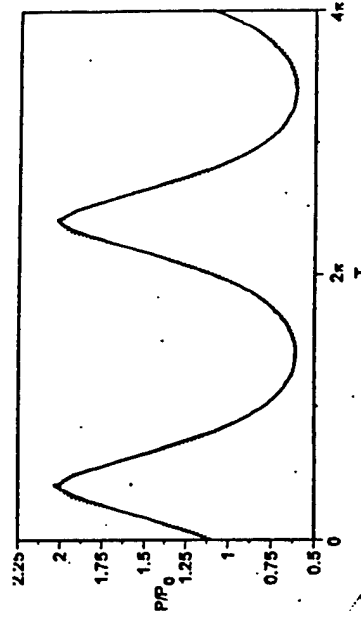
Sonic Compression

A sonic compressor uses high amplitude standing waves and "flapper" (reed) valves (springs not shown) to generate rectified (unidirectional) flow.



"Tailored" Waveforms

Recently, the geometric control of dispersion has been taken to new levels by using dispersion to create specially shaped (asymmetric) waveforms for sonic compression.



The very large peak-to-trough amplitudes shown above,

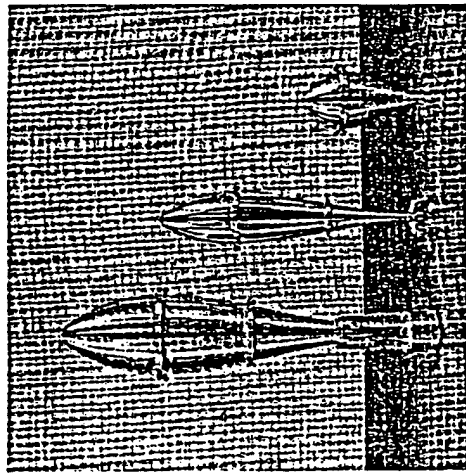
$$\frac{p_+}{p_-} = \frac{2.1}{0.6} = 3.5$$

are well suited to sonic compression applications, since large positive pressures are desirable, but negative pressures are impossible to achieve in a gas.

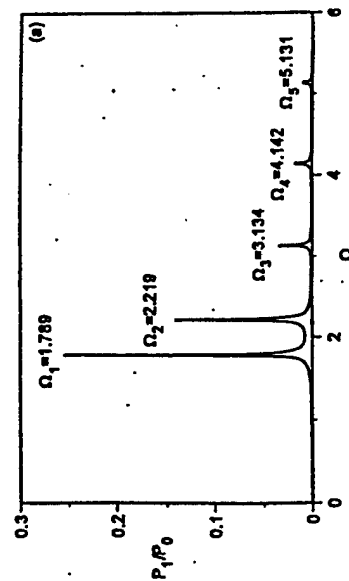
Modal Anharmonicity (Dissonance)

“Bulb” Shaped Resonators

Shown below are three resonator shapes developed for sonic compression. (Courtesy T. Lucas, Macrosonix Corp.)



The anharmonicity of the modes in such a resonator shape are shown below where $\Omega = f/f_0$, and $f_0 \approx c_0/2L$.



A Second Watch

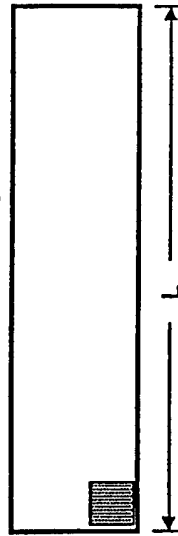
Resonator Obstruction Model

Another way to appreciate the change in modal structure due to a change in resonator cross-sectional area is to consider a resonator of uniform cross-section, S , and length, L , which includes an incompressible obstruction.

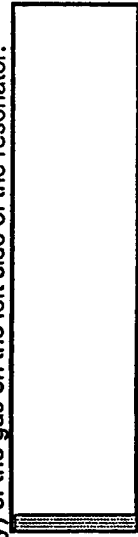
When combined with the Ehrenfest Adiabatic Principle (EAP) [Greenspan, JASA 27, 34 (1955)], this view will also provide a fundamental connection between frequency perturbation and levitation force and will simplify the understanding of levitation instability and super-stability [Putterman, *et al.*, JASA 85(1), 68 (1988)].

Rigid Volume near a Pressure Antinode

Consider a resonator of length L and constant cross-sectional area S , which includes a rigid obstacle of volume, $V \ll L^3 S$, and $V^{1/3} \ll \lambda$, located at the rigid end.



In the absence of the obstacle, the unperturbed fundamental resonance frequency is $f_1 = c_0/2L$. Since the obstacle is incompressible, and much smaller than λ , the volume of the gas it excludes increases the effective stiffness (potential energy) of the gas on the left side of the resonator.

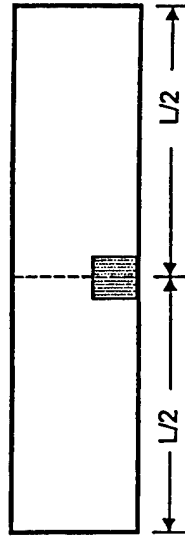


The resonance frequency is increased to $f_1^p = c_0/2L_{\text{eff}} > f_1$, where $L_{\text{eff}} = L - V/S$.

Resonator Obstruction Model

Obstruction at a Velocity Antinode

The same obstruction produces the opposite effect on the resonance frequency if it is placed at the velocity antinode for the fundamental mode.



In this case, the perturbed resonance frequency is reduced due to the increase in gas velocity (kinetic energy) needed to avoid the obstacle, $f_1' < f_1$.

The exact effect of the obstacle at this location is not as easy to calculate, since it also depends upon the shape of the obstacle, not just its volume.

Second Harmonic Effect

The same obstruction, still at the resonator mid-plane, is located at a pressure antinode for the second mode, which occurs at $f_2 = c_0/L = 2f_1$, in the absence of the obstacle.

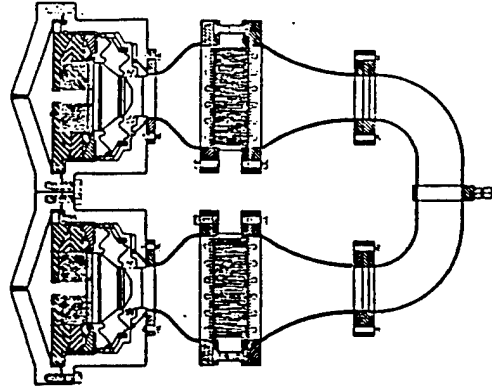
We can use the same excluded volume (potential energy) argument as before by exploiting the symmetry about the mid-plane. Now $L_{eff} = (L/2) - (V/2S)$, so $f_2' = c_0/2L_{eff} > f_2$.

The same object, in the same location, makes the fundamental frequency "flat" while making the second harmonic frequency "sharp," with respect to the unperturbed case.

A double Helmholtz resonator is an extreme case that is used successfully in thermoacoustic refrigerators to suppress shock waves.

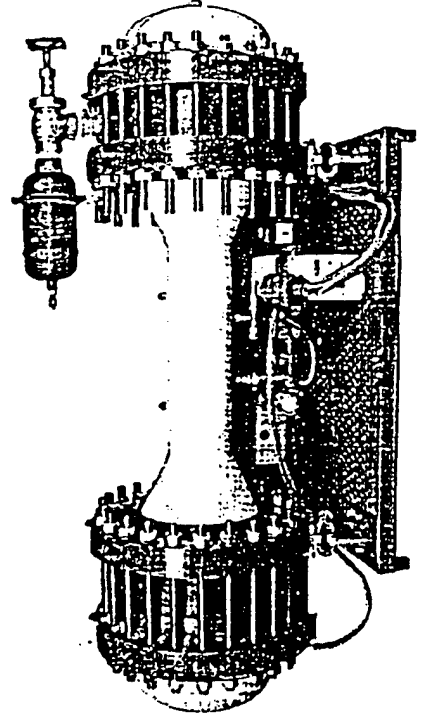
Two Double Helmholtz Resonators

Shipboard Electronics ThermoAcoustic Chiller



3-Ton Shipboard ThermoAcoustic Chiller (TRITON)

One very large double Helmholtz resonator!



Ehrenfest Adiabatic Principle (EAP)

Adiabatic Invariance

If changes are made to a resonator which are on time scales that are "slow" compared to the resonator's period, $T = 1/f$, (so the mode number, n , does not change), then the ratio of the energy in the mode, E_n , to its frequency, f_n , is invariant.

$$\frac{E_n}{f_n} = \text{const.} \quad [107]$$

Oddly enough, the quantum mechanical version of this result for electromagnetic radiative transitions is far more widely known, when the constant belongs to Max Planck!

$$E_n = h f_n \quad [108]$$

Radiation Pressure

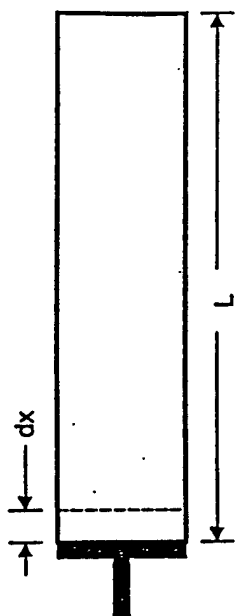
The work done against the time-averaged radiation pressure [97], produced by the Bernoulli effect [84], in a standing wave [95,96] offers a convenient example of the Principal of Adiabatic Invariance [107].

It will also provide an alternative understanding of the acoustic levitation force.

We know that the pressure is lowered at the velocity antinode, but since the mass of the gas contained in the resonator is fixed, the reduced time-averaged pressure (and density) at the antinode must be accompanied by a corresponding increase in the time-averaged pressure (and density) at the rigid ends of the resonator as expressed by the $\cos 2kx$ term in [97].

Work Against Radiation Pressure

Resonator with Frictionless Piston at its End



For the fundamental mode, $f_1 = c_0/2L$, the longitudinal gas velocity is given [96] by, $v(x,t) = v' \sin kx \sin \omega t$.

Energies

The time-averaged energy of the sound field is the spatially averaged maximum kinetic energy.

$$E_1 = \langle KE + PE \rangle_t = KE_{\max} = \frac{A L}{4} \rho_o v'^2 \quad [109]$$

The work done against the time-averaged excess pressure [97], $\langle p_2 \rangle_t = \frac{1}{4} \rho_o v'^2$, by moving the piston of area, S , a distance inward, dx is,

$$W = F \bullet dx = A \langle p_2 \rangle_t dx = \frac{A dx}{4} \rho_o v'^2 \quad [110]$$

Frequency Increase

Using Adiabatic Invariance [107], we expect that $\delta E/E_1 = \delta f/f_1$.

$$\frac{\delta E}{E_1} = \frac{W}{E_1} = \frac{dx}{L} = \frac{\delta f}{f_1} \quad [111]$$

since the resonator is dx shorter after the piston motion.

Levitator Revisited

Frequency/Force Coupling

The "second watch" model of the resonator frequency shifts, due to the position of a solid obstacle and the EAP, lead to an alternative method for determination of the levitation force.

- Resonant frequency depends on position, $f_n(x)$.
- The EAP guarantees $E_n(x)/f_n(x) = \text{const.}$
- Force is the gradient of energy, $F_{\text{levitation}} = -\nabla E_n(x)$

This provides a nice way to predict the levitation force for any given acoustic amplitude, p' , by moving an obstacle and measuring low-amplitude resonance frequency as a function of position.

Levitator De-tuning/De-phasing Instability

Most acoustic levitation systems are driven at a fixed frequency.

De-tuning: Since the position of the levitated object can change, the ratio of the drive frequency and the resonator's resonance frequency will change. This causes the acoustic amplitude in the resonator to change. This changes the levitation force, since it is proportional to the square of the sound pressure level in the resonator.

De-phasing: In a resonator, the sound field approaches its steady-state value with a characteristic exponential time constant $\tau_n = Q_n/\pi f$. The sound field at time, t , corresponds to the position of the object at a (retarded) time, τ , earlier. This produces a phase shift (in radians), $\phi = \tau/T = \tau f$.

Levitator Instability

Harmonic Oscillator Equation

The levitated object has an equilibrium position determined by its weight and the levitation force. Small excursions about equilibrium are governed by the harmonic oscillator equation.

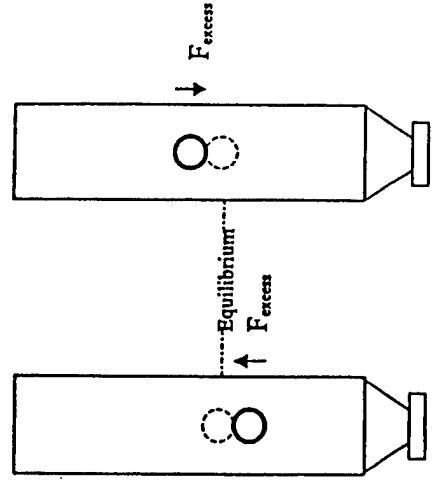
$$m \frac{d^2 x}{dt^2} + R_m \frac{dx}{dt} + kx = 0 \quad [112]$$

Without the "retardation" effect, the force would be in-phase with displacement, x , and would appear as a modification to the stiffness, k .

Retardation produces a component of the excess (detuning) force that is out-of-phase with the velocity, dx/dt , and acts like resistance (exponential damping) or in-phase with velocity to produce exponential growth.

"Sharp" Tuning

If the natural frequency of the resonator is above the drive frequency, motion of the object toward a pressure antinode, as shown below, will increase the levitation force and the oscillation amplitude will increase.

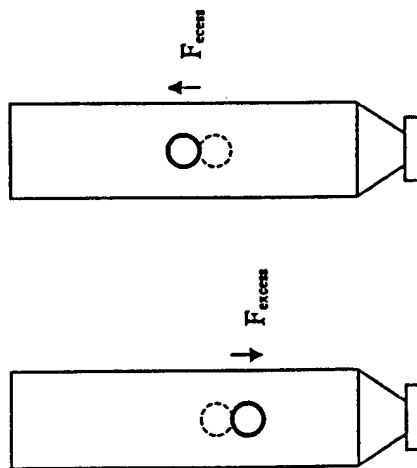


Levitation "Superstability"

"Flat" Tuning

If the natural frequency of the resonator is below the drive frequency, motion of the object toward a pressure antinode will decrease levitation force.

The excess force will be out-of-phase with the object's velocity and will produce damping that is in excess of the viscous (Stokes) drag on the object. This will cause any perturbation in the levitation position to damp out rapidly.



The superstability caused by the "flat" tuning is now used by NASA/JPL [Rudnick & Barnatz, JASA 87(1), 81-92 (1990)] in their "containerless processing" experiments on board the Space Shuttle to prevent samples from slamming against the resonator walls (e.g., STS-41B, January, 1984).

Final Summary and Conclusions

Progressive Plane Wave's Life Cycle

MODULATION Waves affect the propagation medium through convection and changes in the equilibrium sound speed. In most (but not all) cases the two effects add.

$$c(v) = c_0 + \left[1 + \frac{\partial c_0}{\partial y} \frac{\partial y}{\partial v}\right] v \equiv c_0 + \Gamma v$$

WAVEFORM INSTABILITY The initial effect is production of harmonics that grow with distance. The n^{th} harmonic grows at the rate of $(x/\lambda)^{n-1}$. Waveforms are unstable! [9]

SHOCK FORMATION If nonlinear effects dominate the propagation ($G \gg 1$), then the ultimate fate of any progressive periodic disturbance in one-dimension is a sawtooth waveform. A shock front will form from a sinusoidal waveform beyond distances greater than $D_S = \lambda/2\pi\Gamma M$ from their source.

SHOCK DISSIPATION The shock front is thin, on the order of the mean-free-path, and controls the dissipation of the sawtooth's energy in a way that is independent of the transport coefficients.

2nd Order Perturbation Expansion Results

LIMITS OF LINEARIZATION As the acoustic Mach number, $M \equiv v/c_0$, increases, the assumptions used to linearize the hydrodynamic equations are no longer valid.

SOURCE TERMS The inhomogeneous equation for the 2nd order contributions to the sound field has a source term that is driven by quadratic combinations of the 1st order contributions.

PHASE MATCHING The 2nd order terms and the 1st order sources can produce harmonic distortion and sum and difference frequencies which propagate beyond the region of interaction of the 1st order "pump" waves and/or couple different propagation modes.

Final Summary and Conclusions (Con't.)

Non-zero Time Averaged Effects

BERNOULLI The quadratic dependence of the Bernoulli pressure on flow velocity produces forces and torques that have a non-zero time average for standing waves.

Particle agglomeration (the "Maldenform Effect")
Acoustic torque (Rayleigh disk)
Acoustic levitation

STANDING WAVES "Geometrical dispersion" can be used to suppress shock formation by making resonance frequencies anharmonic and can create "custom" waveforms for sonic compressors and other applications.

Horns, cones, bulbs, etc.
Volume exclusions and constrictions

ADIABATIC INVARIANCE The Ehrenfest Adiabatic Principle links changes in resonance frequency with changes in modal energy for "slow" modifications to resonator geometry.

Motion of an obstacle affects stability
Retardation can increase or decrease stability

Nonlinear Acoustics Made Simple

KNOW YOUR LIMITATIONS Linear assumptions may not be valid in some situations (e.g., $M > 10^{-4}$, $G \geq 1$).

SIMPLE TECHNIQUES Detailed mathematics has been avoided (as much as possible) with restriction to 1-D systems, to provide introductory exposure. The "pros" do it differently.

NEW PHENOMENA Extra effort was rewarded by interesting new effects.

Physical Acoustics Summer School - 2000

**Sensor Physics:
Signals and Noise**

*Thomas B. Gabrielson
Applied Research Laboratory
The Pennsylvania State University
P.O. Box 30
State College, PA 16804
(814) 865-1370
tbg3@psu.edu*

Physical Acoustics Summer School -- 2000

(I-2)

Sensor Physics: Signals and Noise

Introduction

Mechanical-Thermal Noise

Relation of fluctuations to dissipation

Total energy; frequency distribution

Radiation

Implications of Causality

Shot Noise

Noise from flow of discrete “particles”

Molecular collisions; independence

Metals and semiconductors

Special Applications

Sensor-electronics interaction

Thermal and shot noise in optical fiber

Domain re-orientation noise in ferroelectrics

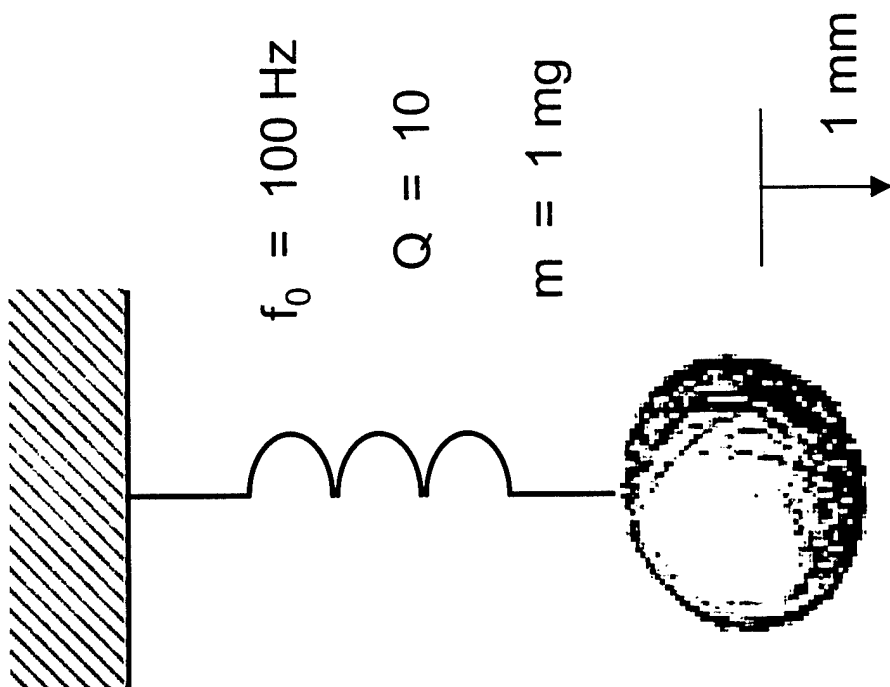
(I-3)

Physical Acoustics Summer School - 2000

**Thermal Fluctuations
and Noise**

QUIZ: Question #1

(I-4)

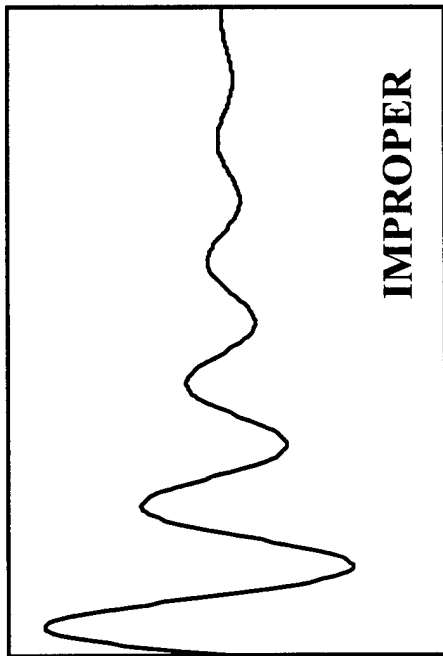


Given an initial displacement of 1mm, how long will it take for the amplitude to decay to 10^{-8} mm?

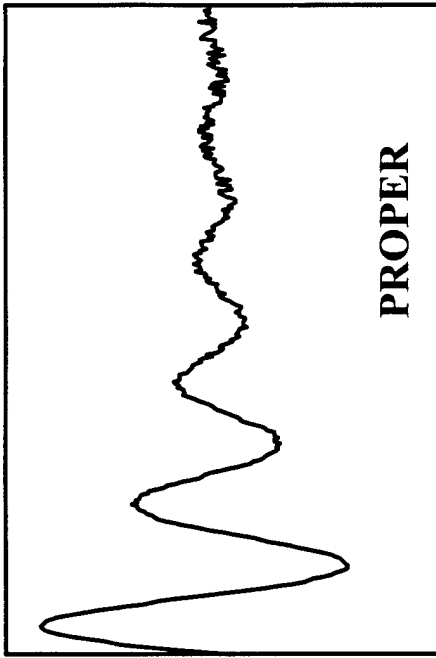
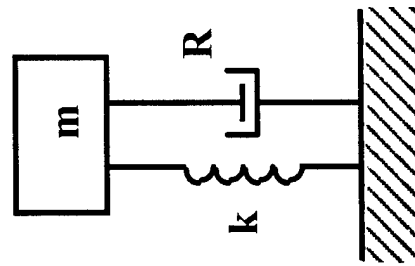
(A 10^{-8} mm amplitude is equivalent to an applied acceleration of 0.5 micro-g's .)

Proper Dynamics for Damped Mass-Spring

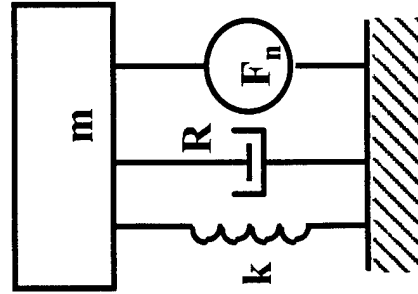
(I-5)



$$m\ddot{x} + R\dot{x} + kx = 0$$



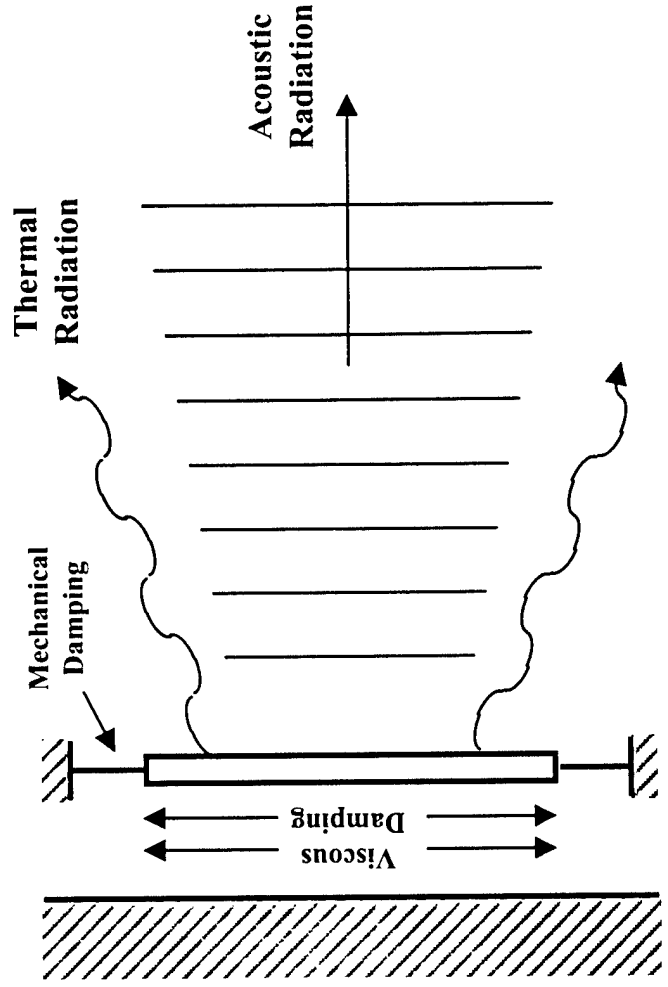
$$m\ddot{x} + R\dot{x} + kx = f_n(R, t)$$



Fluctuation-Dissipation Theorem:

(I-6)

If there is a path along which energy can flow from a system to its environment, *then energy from the environment can flow back into the system*. Dissipation is a measure of the energy that leaves the system (either as ordered energy in the case of radiation or as disordered energy in the case of damping); thermal fluctuations are a measure of the disordered energy that enters the system from the environment. *In thermal equilibrium, the presence of dissipation guarantees the presence of fluctuations.*



Equilibrium Thermal Fluctuations

(1-7)

Total Energy

Each degree-of-freedom of a system has a "thermal" energy of $1/2 k_B T$ where k_B is Boltzmann's constant (1.38×10^{-23} joules/kelvin) and T is the absolute temperature.

This thermal energy associated with each of the components of kinetic energy ($1/2 m v_x^2$, $1/2 m v_y^2$, $1/2 m v_z^2$), spring-potential energy ($1/2 k x^2$), rotational kinetic ($1/2 I \omega^2$), capacitive ($1/2 C V^2$), etc.

$$\begin{array}{ccc} \text{A molecule in a liquid has} & \longrightarrow & \frac{1}{2} m v_x^2 = \frac{1}{2} k_B T \end{array}$$

$$\begin{array}{ccc} \text{A ball-bearing in a liquid has} & \longrightarrow & \frac{1}{2} m v_x^2 = \frac{1}{2} k_B T \end{array}$$

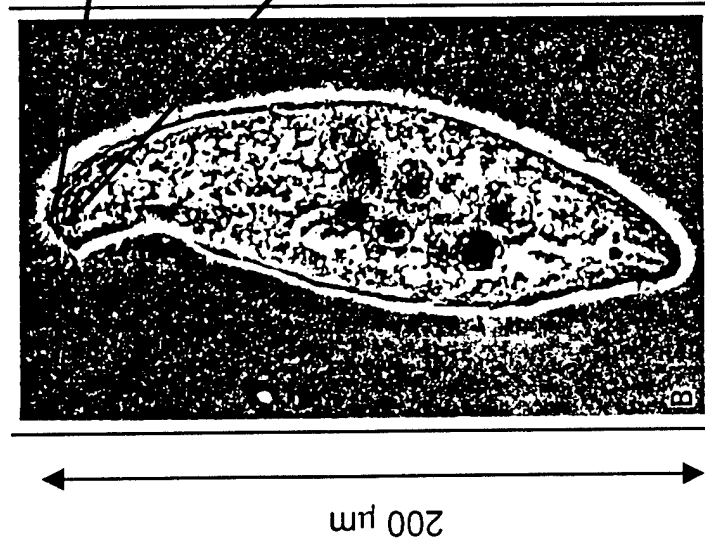
$$\begin{array}{ccc} \text{An atom in a solid OR} & \longrightarrow & \frac{1}{2} k x^2 = \frac{1}{2} k_B T \\ \text{A mass on a spring has} & & \end{array}$$

[The velocities and displacements indicated above are mean-square values; they represent an average of the actual fluctuating velocity or displacement.]

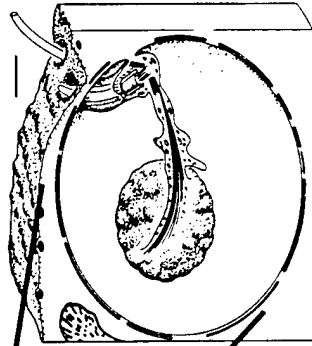
Sensing of Gravity by Protozoa

(I-8)

Loxodes striatus



(reprinted with permission
from Ref. 1)



(reprinted with permission
from Ref. 2)

proof mass, $m = 45$ picograms
range of mass motion, $L = 3 \mu\text{m}$

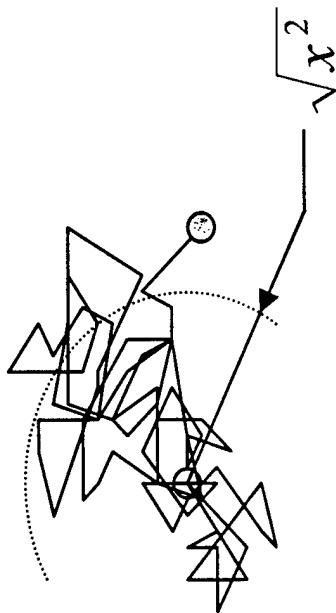
sensor's potential energy = mgL
sensor's thermal energy = kT

$$mgL / kT = 330$$

*If linear dimensions of sense organ were
reduced by a factor of 4, then $mgL/kT = 1$ and
the organism would be unable to distinguish up
from down!*

1. Fenchel and Finlay, "Geotaxis in the ciliated protozoan *Loxodes*," J. Exp. Biol. **110**, 17-33 (1984)
2. Fenchel and Finlay, "The structure and function of Muller vesicles in Loxidid ciliates," J. Protozool. **33**, 69-76 (1986)

Macroswimmer to Nanoswimmer: Molecular Agitation (I-9)



$$\sqrt{x^2} = \sqrt{2Dt}$$

$$D = k_B T / R_{mech}$$

$$R_{mech} = 6 \pi \eta a$$

Drift in 1 Second		
radius a [m]	drift x [m]	body lengths x / a
1	7×10^{-10}	7×10^{-10}
10^{-3}	2×10^{-8}	2×10^{-5}
10^{-6}	7×10^{-7}	0.7
10^{-9}	2×10^{-5}	2×10^4

Equilibrium Thermal Fluctuations

(I-10)

Spectral Distribution of Energy (Nyquist)

$$F_n^2 = 4 k_B T R_{\text{mechanical}} df$$

$$V_n^2 = 4 k_B T R_{\text{electrical}} df$$

Actually --

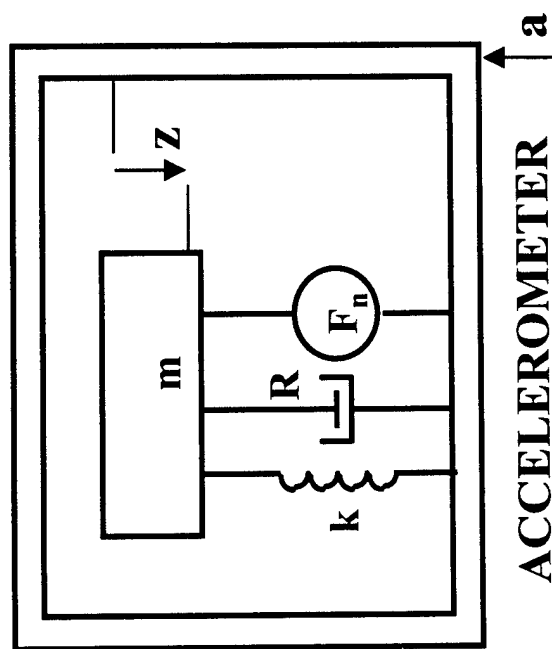
$$F_n^2 = 4 k_B T \frac{e^{hf/k_B T}}{e^{hf/k_B T} - 1} R_{\text{mechanical}} df$$

But, even at 1 kelvin, the factor in the shaded block very nearly one for frequencies below 2 GHz.

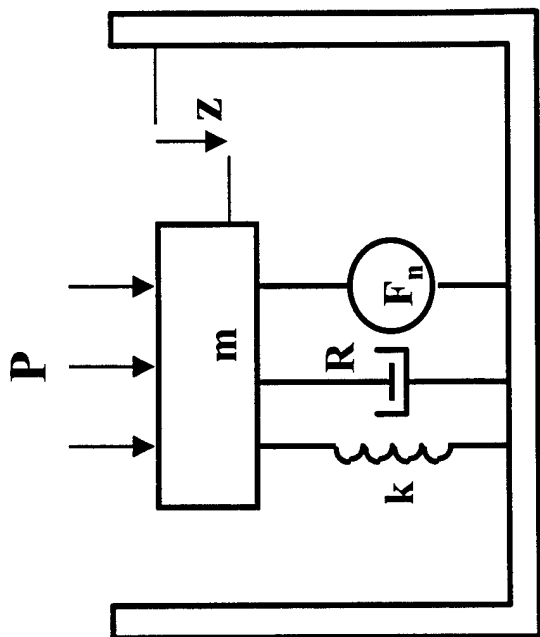
Noise Equivalent Signal

(I-11)

What level of signal does the noise mimic?



ACCELEROMETER



PRESSURE SENSOR

(microphone)

Set noise to zero and solve for signal response: $a = g(z)$

Set signal to zero and solve for output due to noise: $z_n = h(F_n)$

Calculate noise-equivalent signal: $a_n = g(z_n)$

Noise Equivalent Signal

(I-12)

Accelerometer

$$(ma_n)^2 = 4k_B T R df$$

$$a_n^2 / df = 4k_B T \frac{R}{m^2} = 4k_B T \left[\frac{\omega_0}{mQ} \right]$$

Pressure Sensor

$$(p_n A)^2 = 4k_B T R df$$

$$p_n^2 / df = 4k_B T \frac{R}{A^2} = 4k_B T \left[\frac{\omega_0 m}{A^2 Q} \right]$$

Noise Associated with Radiation

(I-13)

Spherical wave (spherical source):
$$p = \frac{A}{r} e^{i(kr - \omega t)}$$

Compute radial particle velocity from Newton's Law in fluid:

$$-\nabla p = \rho \frac{\partial u}{\partial t} \Rightarrow u_r = \left(1 + \frac{i}{kr}\right) \frac{p}{\rho c}$$

Mechanical radiation resistance (ratio of force to velocity):

$$Z = \frac{p A}{u_r} = \rho c A \left\{ \frac{(kr)^2}{1 + (kr)^2} - i \frac{kr}{1 + (kr)^2} \right\}$$

Radiation resistance for a point source ($A = 4\pi r^2$):

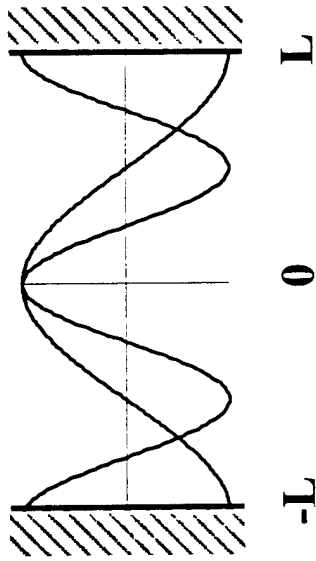
$$\Re \{Z\} \Big|_{r \rightarrow 0} \rightarrow \rho c A (kr)^2 = \pi \frac{\rho f^2}{c} A^2$$

Pressure fluctuations associated with "loss" by radiation:

$$\boxed{p_n^2 = 4 k_B T \frac{\Re \{Z\}}{A^2} = 4 k_B T \pi \frac{\rho f^2}{c} df}$$

Noise Associated with Radiation

(I-14)



Start with a rigid-walled box, side = $2L$,
sensor in the middle.

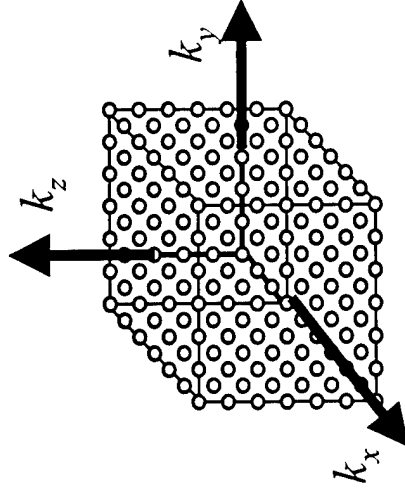
Modes have max pressure at
walls and at center:
 $\cos(l\pi x/L), \cos(m\pi y/L), \cos(n\pi z/L)$

Wavenumbers are then:

$$k_x = l\pi/L, k_y = m\pi/L, k_z = n\pi/L$$

(spacing between k 's = π/L)

$$\text{and } k^2 = k_x^2 + k_y^2 + k_z^2$$



Cell “volume” in k -space is $(\pi/L)^3$ with one k -point per cell.
Each mode gets $k_B T$ (1/2 for kinetic, 1/2 for potential) therefore,

$$\textbf{k-space density of thermal energy} = k_B T (L/\pi)^3$$

Noise Associated with Radiation

(I-15)

Energy in dk is energy in a spherical shell between k and $k+dk$.

$$\begin{aligned} \text{Volume of shell in } k\text{-space} &= (4\pi/3)[(k+dk)^3 - k^3] \\ &= 4\pi k^2 dk \text{ for small } dk. \end{aligned}$$

Therefore, $dE = k_B T (L/\pi)^3 4\pi k^2 dk$, or, since $k = 2\pi f/c$,

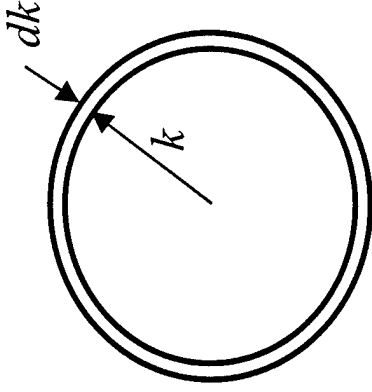
$$dE = 32\pi k_B T L^3 f^2 df / c^3$$

Divide by the spatial volume, $(2L)^3$, to get the true energy density:

$$\mathcal{E} = 4\pi k_B T f^2 df / c^3$$

Another way to write the energy density is $\mathcal{E} = p^2 / \rho c^2$ so the pressure fluctuations associated with the radiation are given by

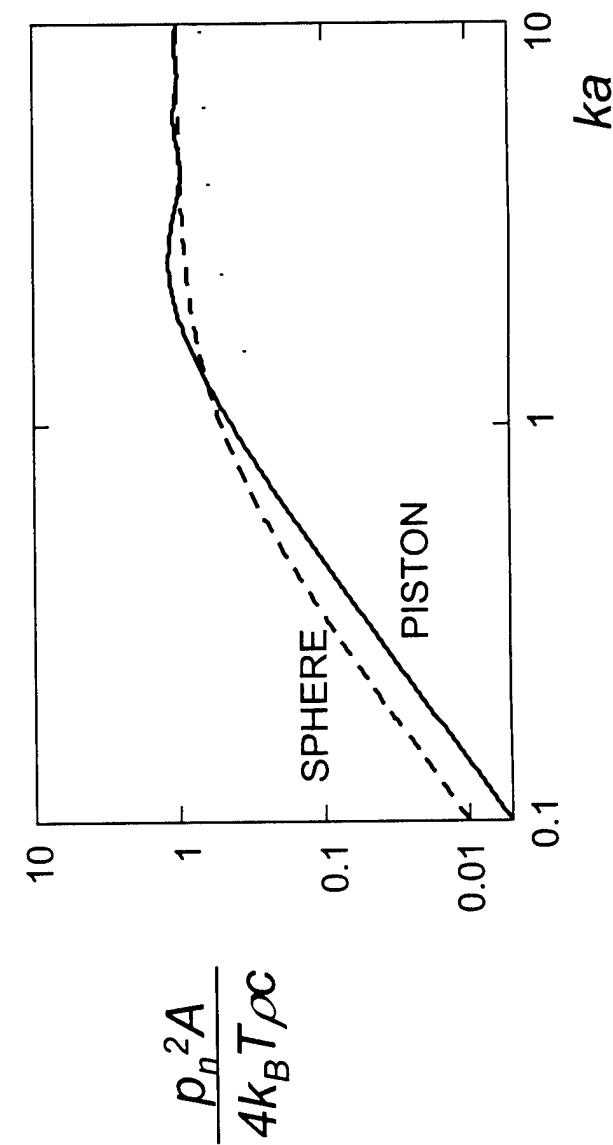
$$p_n^2 = 4k_B T \pi \frac{\rho f^2}{c} df$$



Noise Associated with Radiation

$$\text{Spherical Source:} \quad \Re\{Z_{rad}\} = \rho c A \left[\frac{(ka)^2}{1 + (ka)^2} \right]$$

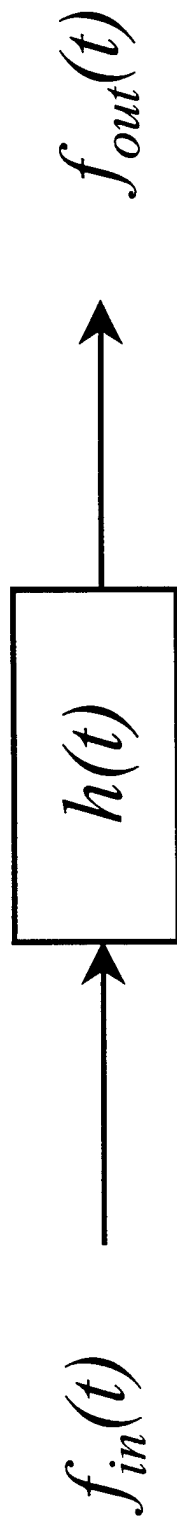
$$\text{Circular Piston in Rigid Baffle:} \quad \Re\{Z_{rad}\} = \rho c A \left[1 - \frac{J_1(2ka)}{ka} \right]$$



Causality in Physical Systems

(I-17)

$$e^{j\omega t}$$



General linear relationship between input and output:

$$f_{out}(t) = a f_{in}(t) + \int_{-\infty}^{\infty} h(t-\tau) f_{in}(\tau) d\tau$$

To prevent the output from anticipating the input:

$$h(x) = 0 \quad \text{for} \quad x < 0$$

Causality in Physical Systems

(I-18)

A. The Fourier transform and complex frequency:

$$H(\omega) = \int_0^{\infty} h(t) e^{-j\omega t} dt \qquad e^{-j\omega t} = e^{-j\omega_r t} e^{\omega_i t}$$

For physical $h(t)$, $H(\omega)$ is analytic if $\omega_i < 0$

B. The inverse-transform integral:

$$h(t) = \frac{1}{2\pi} \int_{-\infty}^{\infty} H(\omega) e^{j\omega t} d\omega$$

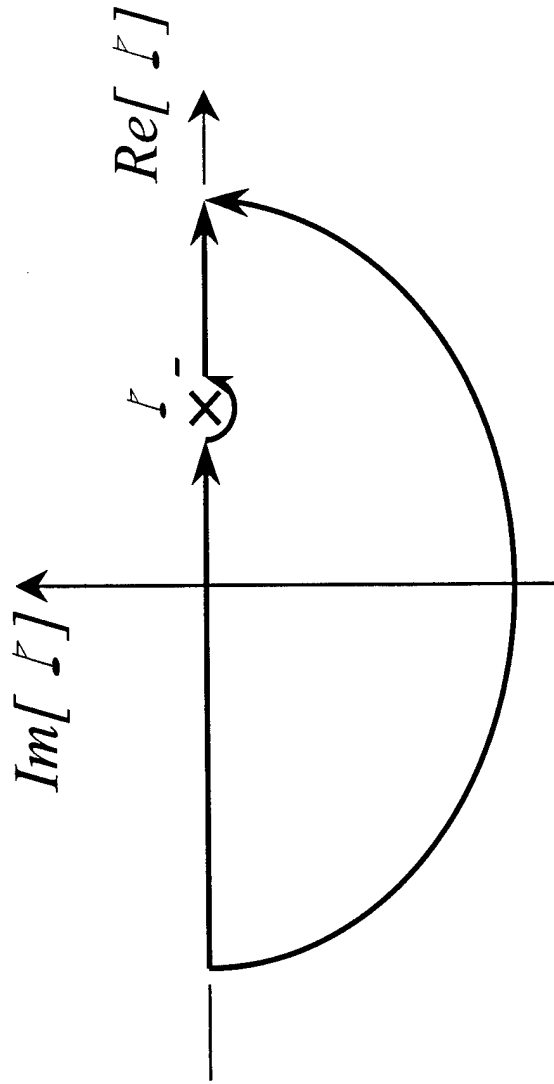
$H(\omega)$ finite along real- ω axis and must go to zero at \pm infinity

The Kramers-Kronig Relationships

(I-19)

$H(\omega)$ is analytic for $\omega_i < 0$ so construct the following integral:

$$I = \int_{-\infty}^{\infty} \frac{H(\omega)}{\omega - \omega_0} d\omega$$



If the large-arc integral is zero, then:

$$\int_{-\infty}^{\infty} \frac{H(\omega)}{\omega - \omega_0} d\omega = \int_{-\infty}^{\infty} \frac{H(\omega) - H(\omega_0)}{\omega - \omega_0} d\omega = -j\pi H(\omega_0)$$

The Kramers-Kronig Relationships

$$H_i(\omega_0) = \frac{1}{\pi} \int_{-\infty}^{\infty} \frac{H_r(\omega) - H_r(\omega_0)}{\omega - \omega_0} d\omega$$

$$H_r(\omega_0) = -\frac{1}{\pi} \int_{-\infty}^{\infty} \frac{H_i(\omega) - H_i(\omega_0)}{\omega - \omega_0} d\omega$$

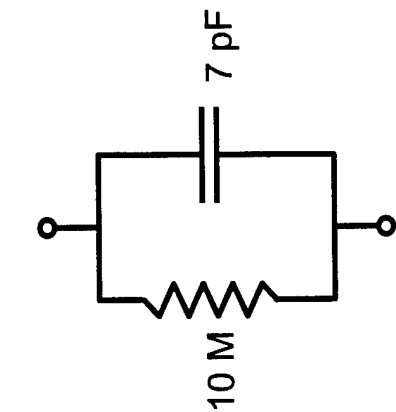
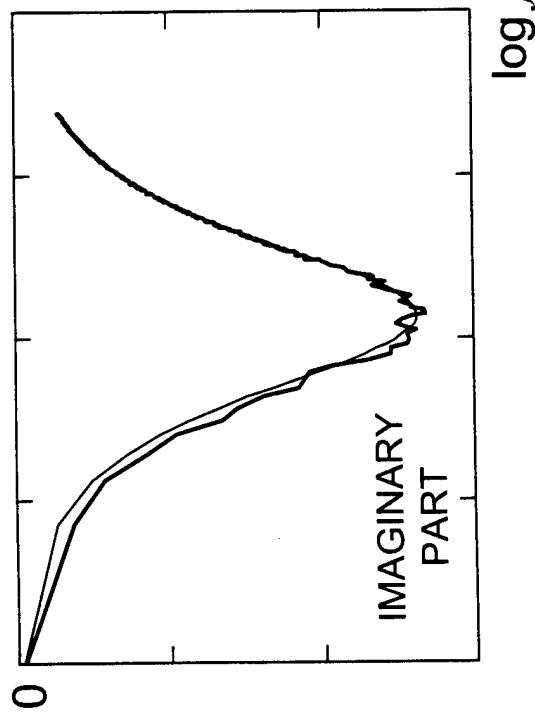
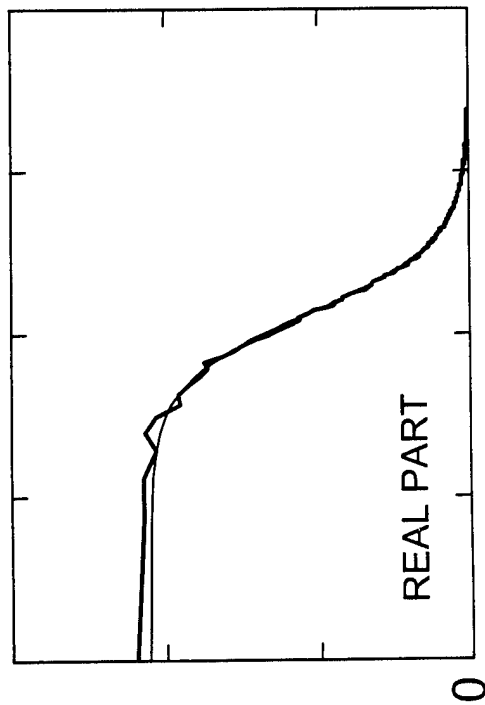
A noise measurement gives the real part of either the impedance, Z , or the admittance, Y . *IN PRINCIPLE*, the imaginary part can be obtained from the Kramers-Kronig relations.

$$e_n^2 = 4k_B T \operatorname{Re}[Z] \qquad i_n^2 = 4k_B T \operatorname{Re}[Y]$$

Usually easier said than done!

Transforming a Noise Measurement

(I-21)



Measure noise and
convert to real part of
impedance:

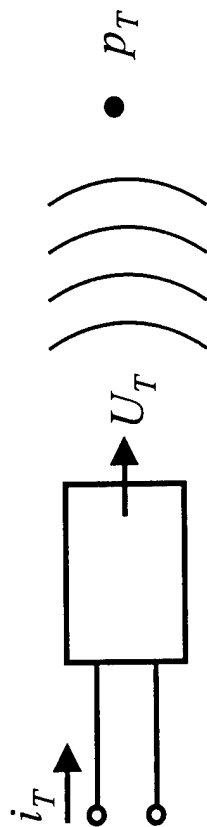
$$Z_r = \frac{e_n^2}{4k_B T}$$

Generate imaginary part of
impedance using discrete form of
Kramers-Kronig relation:

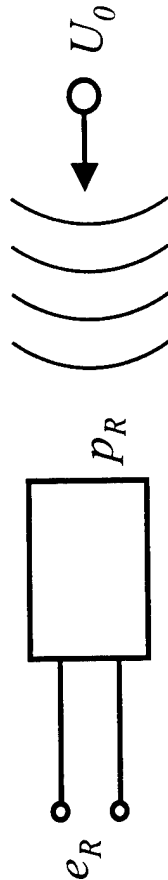
$$Z_i(f_m) = \frac{\Delta f}{\pi} \sum_{n \neq m} \frac{Z_r(f_n)}{f_n - f_m}$$

Self Noise and Efficiency

(1-22)



Pressure, p_T , produced by transmitter with drive current, i_T , and volume velocity, U_T .



Receiver output voltage, e_R , produced by ideal simple source with volume velocity, U_0 , at same point.

Reciprocity for transducer and medium:

$$\frac{p_T}{i_T} = \frac{e_R}{U_0}$$

Reciprocity for medium alone:

$$\frac{p_T}{U_T} = \frac{p_R}{U_0}$$

Eliminate U_0 :

$$\frac{U_T}{i_T} = \frac{e_R}{p_R} \equiv M$$

Self Noise and Efficiency

(I-23)

Pressure noise associated with real part of acoustic radiation impedance:

$$p_{n-rad}^2 = 4k_B T \operatorname{Re}[Z_{rad}]$$

Convert to equivalent electrical noise at receiver terminals:

$$e_{n-rad}^2 = M^2 p_{n-rad}^2 = M^2 4k_B T \operatorname{Re}[Z_{rad}]$$

Total thermal self noise associated with real part of electrical impedance:

$$e_{n-total}^2 = 4k_B T \operatorname{Re}[Z_{in}]$$

Ratio of radiation noise to total noise:

$$\frac{e_{n-rad}^2}{e_{n-total}^2} = M^2 \frac{\operatorname{Re}[Z_{rad}]}{\operatorname{Re}[Z_{in}]}$$

Self Noise and Efficiency

Radiated acoustic power:

$$\mathbf{P}_{out} = U_T^2 \operatorname{Re}[Z_{rad}]$$

Total input electrical power:

$$\mathbf{P}_{in} = i_T^2 \operatorname{Re}[Z_{in}]$$

Transmitting efficiency, η .

$$\eta \equiv \frac{\mathbf{P}_{out}}{\mathbf{P}_{in}} = \left(\frac{U_T}{i_T} \right)^2 \frac{\operatorname{Re}[Z_{rad}]}{\operatorname{Re}[Z_{in}]}$$

$$\eta \equiv \frac{\mathbf{P}_{out}}{\mathbf{P}_{in}} = \frac{e_{n-rad}^2}{e_{n-total}^2}$$

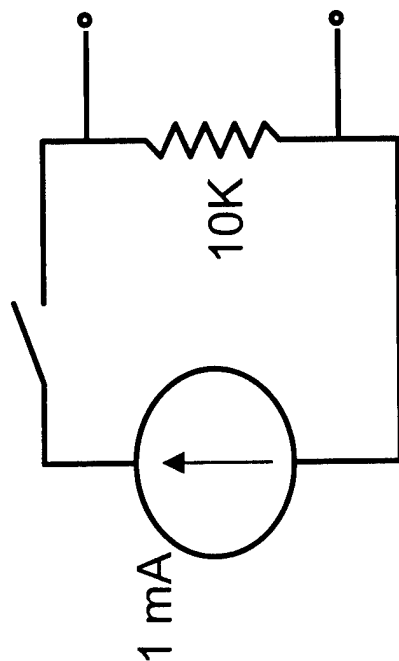
(II-1)

Physical Acoustics Summer School - 2000

Shot Noise

QUIZ: Question #2

(II-2)



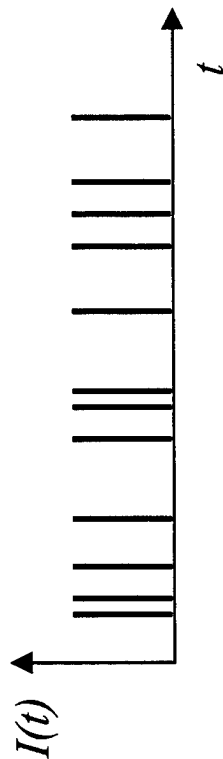
- Measure the spectral density of the voltage noise across a 10 K resistor.
- Put 1 mA DC current through the resistor.
- By what factor does the noise voltage increase? (Ignore $1/f$ noise.)

Shot Noise

(II-3)

Given a current consisting of impulses:

$$I(t) = q \sum_{i=1}^{\infty} \delta(t - t_i)$$



Expand current as a Fourier series:

$$I(t) = \sum_{k=0}^{\infty} [a_k \cos(2\pi f_k t) + b_k \sin(2\pi f_k t)]$$

$$\text{where } a_k = \frac{2}{T} \int_0^T I(t) \cos(2\pi f_k t) dt = \frac{2q}{T} \sum_{i=1}^N \cos(2\pi f_k t_i)$$

(The period, T , is long enough to encompass many (N) events.)

One component of the expansion covers a band of Δf ($= 1/T$). The mean-square value in that band is:

$$\overline{i_k^2} = \overline{a_k^2 \cos^2(2\pi f_k t)} + \overline{b_k^2 \sin^2(2\pi f_k t)} + \overline{a_k b_k \cos(t) \sin(t)} = \frac{1}{2} (a_k^2 + b_k^2)$$

Shot Noise

(II-4)

$$\frac{1}{2} (a_k^2 + b_k^2) = \frac{2q^2}{T^2} \left\{ \sum_{i=1}^N [\cos^2(2\pi f_k t_i) + \sin^2(2\pi f_k t_i)] \right\} + \frac{2q^2}{T^2} \left\{ \sum_{i \neq j} [\cos(2\pi f_k t_i) \cos(2\pi f_k t_j) + \sin(2\pi f_k t_i) \sin(2\pi f_k t_j)] \right\} = \frac{2q^2 N}{T^2}$$

The second summation is zero *only if the impulses are statistically independent*. If the events are not independent, then the cross-terms must be evaluated!

(For independent events, the mean-square value of b_k is identical to that of a_k .)

$$\text{Since} \quad \bar{I} = \frac{qN}{T} \quad \text{and} \quad \Delta f = \frac{1}{T}$$

$$\overline{i_k^2} = 2q \bar{I} \Delta f$$

Applies to processes consisting of events that are:

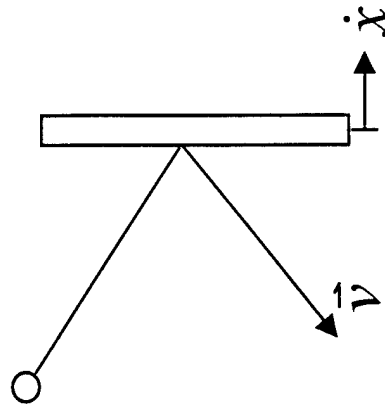
- (1) impulse-like
- (2) independent

Noise from Molecular Collisions FREE-MOLECULAR FLOW (II-5)

Force = $\sum_{\text{molecules}} \left\{ \begin{array}{l} \text{rate of change in momentum of a molecule} \\ \text{initially traveling toward the disk, then} \\ \text{hitting the disk} \end{array} \right\}$

= (molecular flux) (momentum change per collision)

$$\begin{aligned}
 &= \frac{n}{2} A (v_x - \mathfrak{x}) \cdot 2 m (v_x - \mathfrak{x}) \\
 &= n m v_x^2 A - 2 n m v_x A \mathfrak{x} + \cancel{n m (\mathfrak{x})^2 A} \\
 &= P_0 A - R_{mech} \mathfrak{x}
 \end{aligned}$$



$$R_{mech} = 2 n m v_x A$$

Noise from Molecular Collisions

FREE-MOLECULAR FLOW

(II-6)

$$p_n^2 = \frac{F_n^2}{A^2} = \frac{4 k_B T R_{mech} df}{A^2} = 8 n m k_B T \bar{v}_x df / A$$

$$P_0 = n k_B T$$

$$\bar{v} = 2 \bar{v}_x$$

$$p_n^2 = 2 [2 m \bar{v}] \frac{P_0 df}{A}$$

Looks like a shot-noise expression!

Generalized Forms for Shot Noise

(II-7)

$$\left[\begin{array}{c} \text{MEAN-SQUARE} \\ \text{FLUCTUATION IN} \\ \text{FLUX DENSITY} \end{array} \right] = 2 \left[\begin{array}{c} \text{QUANTITY} \\ \text{PER} \\ \text{CARRIER} \end{array} \right] \left[\begin{array}{c} \text{AVERAGE} \\ \text{FLUX} \\ \text{DENSITY} \end{array} \right] \frac{\left[\begin{array}{c} \text{BANDWIDTH} \end{array} \right]}{\left[\begin{array}{c} \text{AREA} \end{array} \right]}$$

electric-charge flux density: $j_n^2 = 2 [q] J_0 \Delta f / A$

photon flux density: $I_n^2 = 2 [hf] I_0 \Delta f / A$

momentum flux density: $p_n^2 = 2 [2mv] P_0 \Delta f / A$

Pressure-fluctuation noise power is
proportional to STATIC PRESSURE

Molecular-Impact Noise

Equilibrium thermal fluctuations in force (Nyquist):

$$F_n^2 = 4 k_B T R_{MECH} \Delta f$$

e.g., Stokes' flow (disk, radius a): $R_{MECH} = 16 \eta a$

$$p_n^2 = 4 k_B T 16 \eta a / A^2$$

Pressure-fluctuation noise power is almost
INDEPENDENT of static pressure

Molecular-Impact Noise

(II-9)

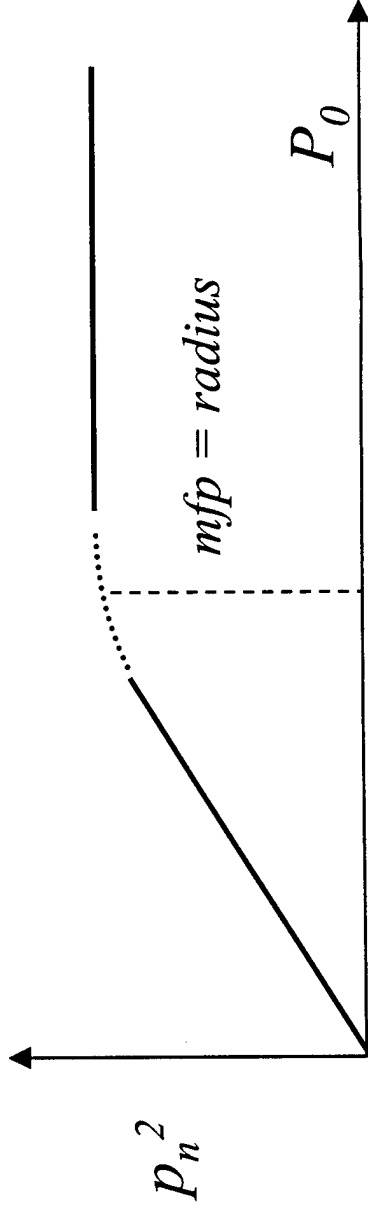
The shot-noise form requires that collisions be INDEPENDENT. As long as the molecular mean-free-path is smaller than the disk radius, the molecular collisions are highly DEPENDENT.

Add some kinetic theory:

$$P_0 = n k_B T$$

$$\eta = n m v (mfp) / 3$$

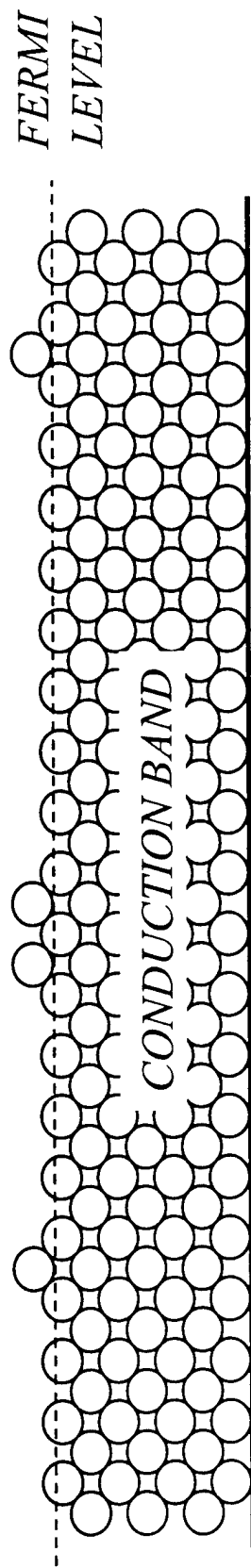
$$(p_{n1}^2) / (p_{n2}^2) = 3 \pi / 8 \text{ (radius)} / (\text{mean-free-path})$$



For a pressure of one atmosphere, there is a ten percent effect for a dimension of 6 μ m.

Noise in Metallic Conductors

(II-10)



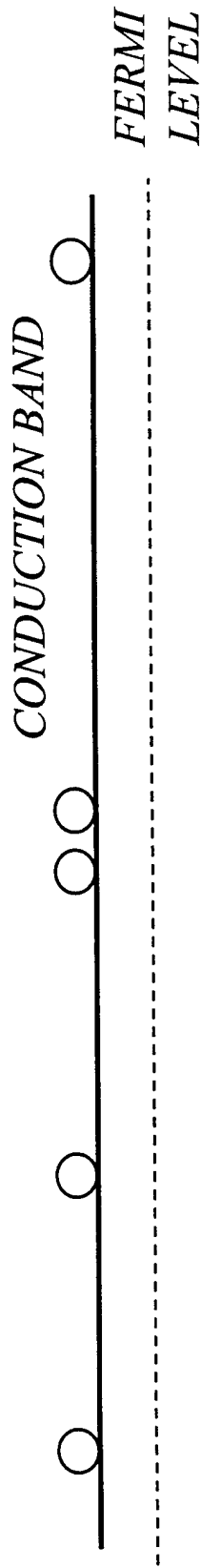
Carriers (electrons) are highly correlated

Noise is independent of flow volume (current)

$$i_n^2 = (4 k_B T / R) \Delta f$$

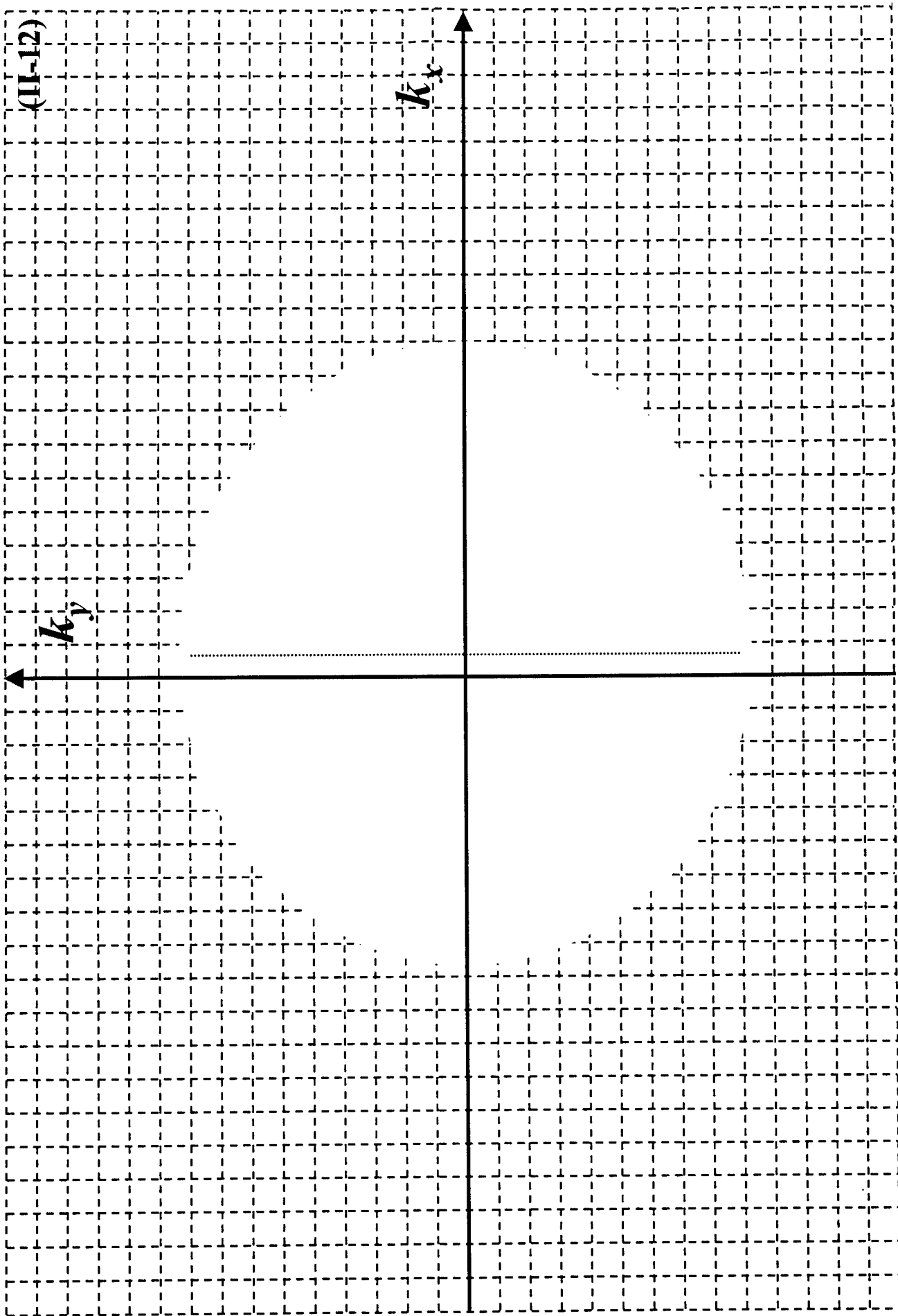
(II-11)

Noise in Semiconductors

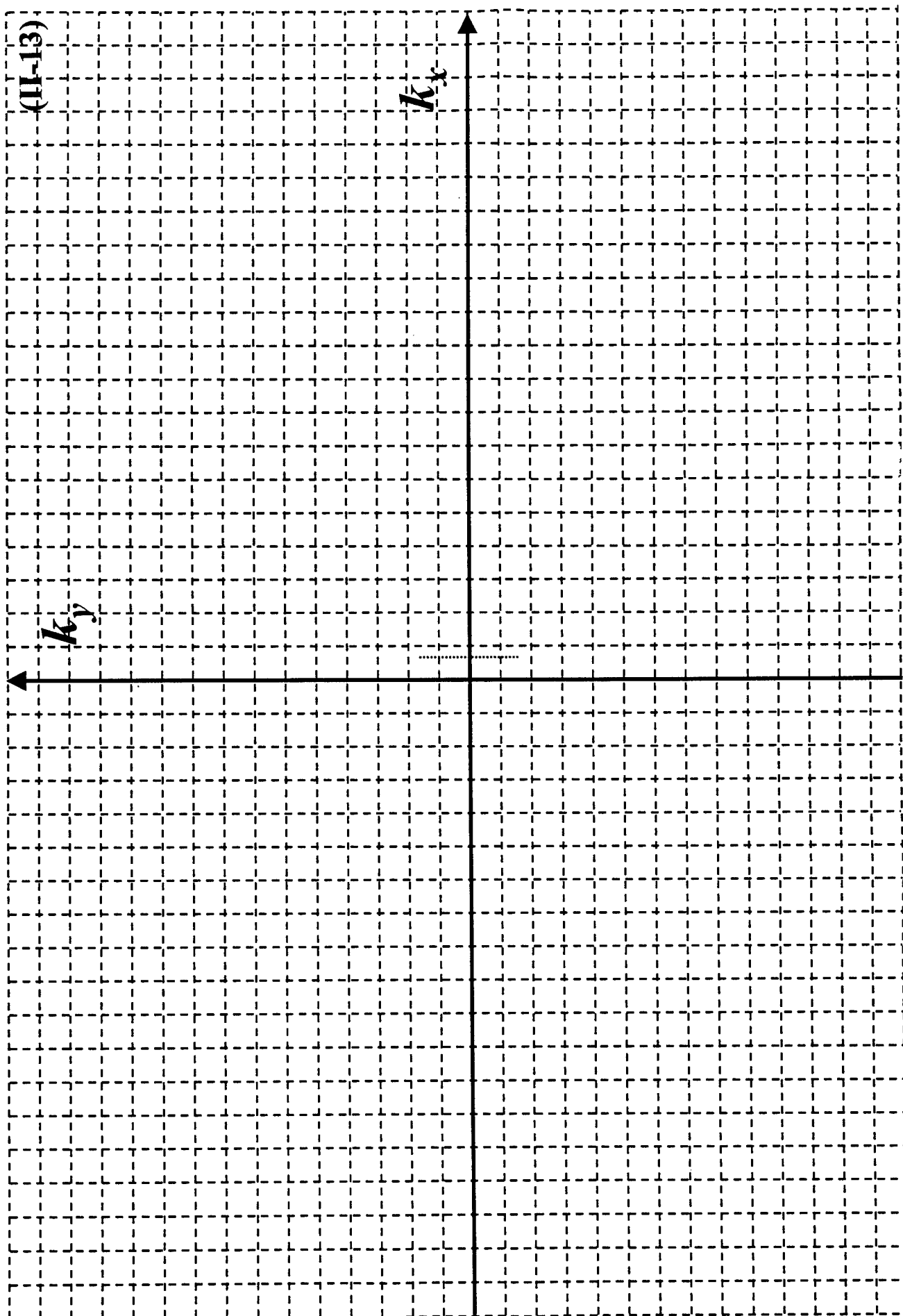


Carriers (holes or electrons) are independent
Noise is dependent on flow volume (current)

$$i_n^2 = 2qI_0 \Delta f$$

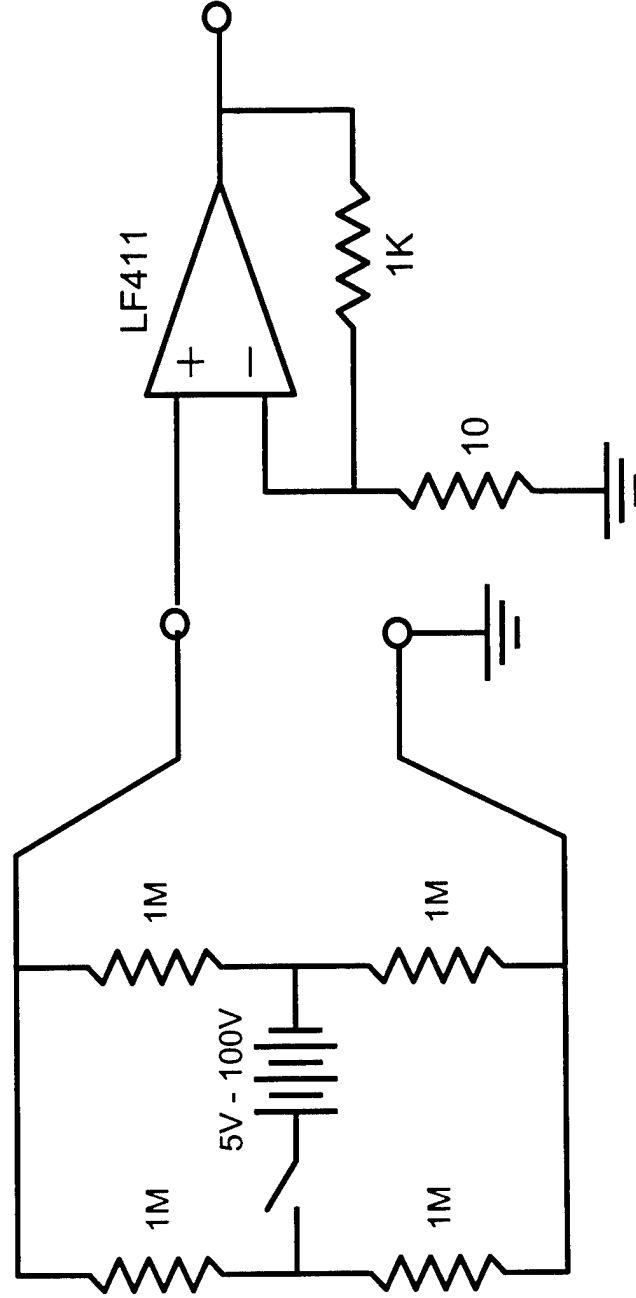


(11-13)

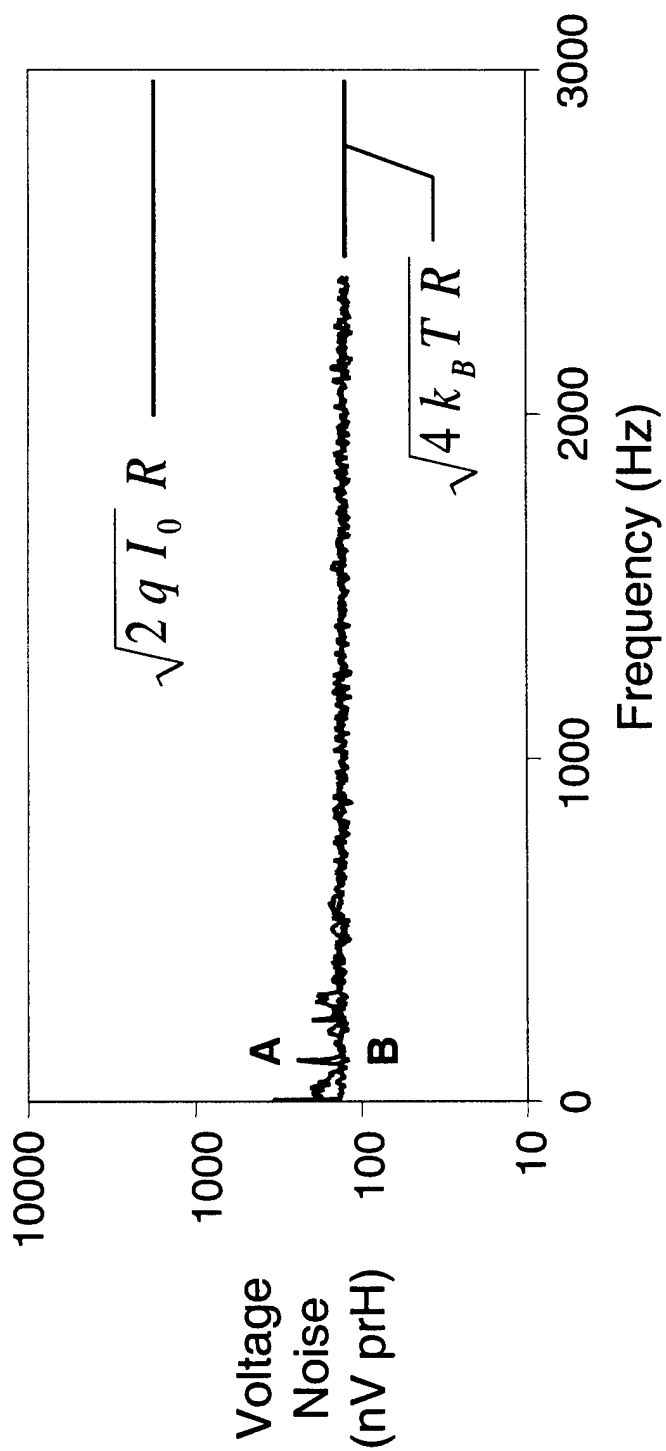


Effect of Current Flow on Noise

Resistance bridge connected to input permits noise measurement of input resistance with and without current. Bridge rejects noise introduced by the battery and prevents introduction of DC bias at input.



Resistor Noise with and without Current Flow

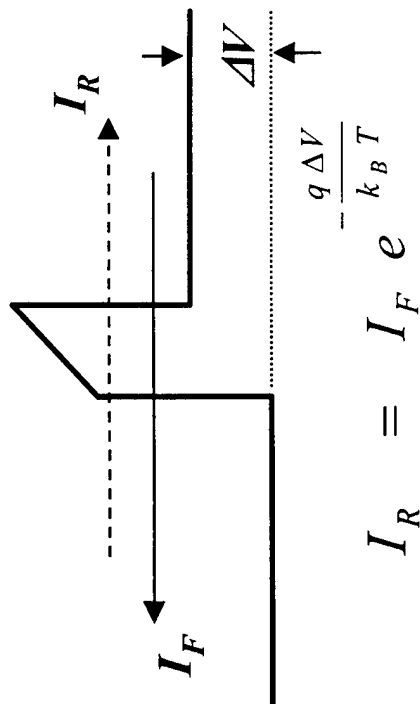
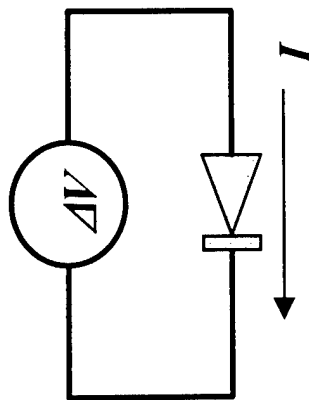


A: Current flow ($V_o = 360 * k_B T/q$)

B: No current flow

Noise as a Function of Applied Voltage

(II-16)



$$I = I_F - I_R = I_F \left[1 - e^{\frac{q \Delta V}{k_B T}} \right] = \frac{\Delta V}{R}$$

$$i_n^2 = 2qI_R df + 2qI_F df = 2qI_F \left[1 + e^{\frac{q \Delta V}{k_B T}} \right] df$$

$$i_n^2 = 2 \frac{q \Delta V}{R} \left(\frac{1 + e^{\frac{q \Delta V}{k_B T}}}{1 - e^{\frac{q \Delta V}{k_B T}}} \right) df$$

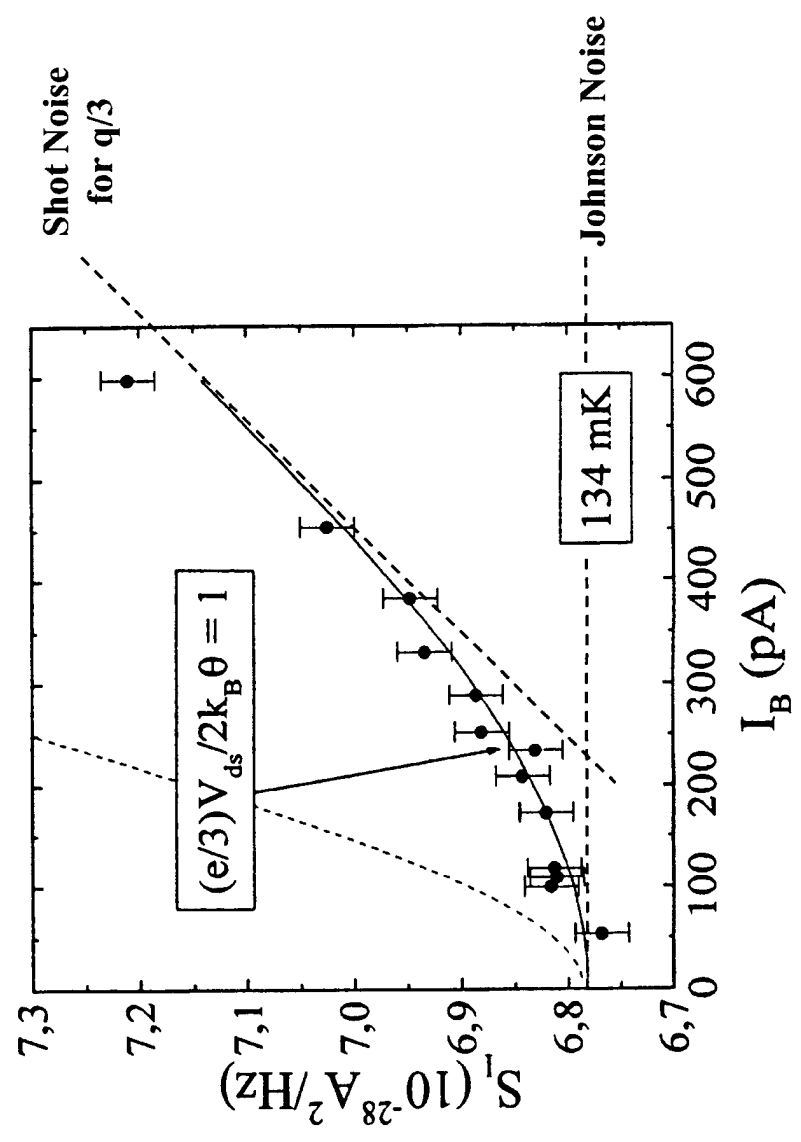
Noise as a Function of Applied Voltage

(II-17)

For $q \Delta V \ll k_B T$ $i_n^2 \rightarrow 2 \frac{q \Delta V}{R} \left(\frac{2}{q \Delta V / k_B T} \right) df = 4 k_B T \frac{df}{R}$

For $q \Delta V \gg k_B T$ $i_n^2 \rightarrow 2 \frac{q \Delta V}{R} (1) df = 2 q I df$

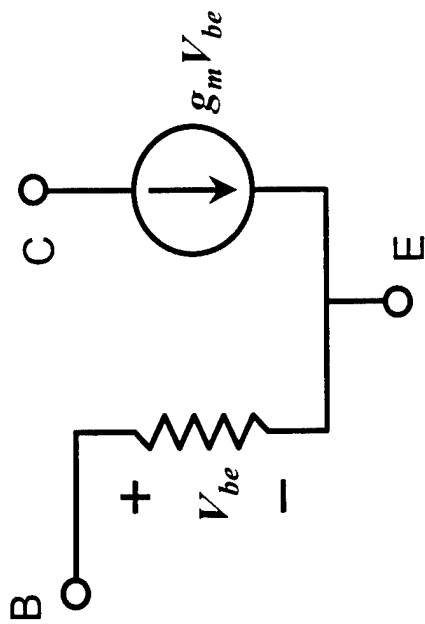
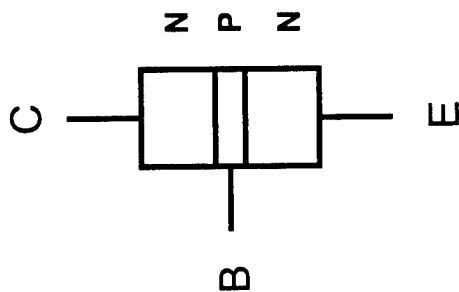
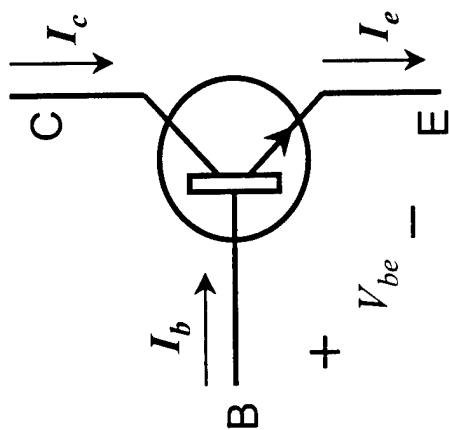
Example from measurements in
search of fractional quantum
Hall effect



Saminadayar, Glatli, Jin, and Etienne,
Phys. Rev. Lett. 79, 2526 (1997)

Basics of Transistor Noise -- Bipolar Transistors

(II-18)



Current gain, β :

$$I_e \approx I_c = \beta I_b$$

$$\beta \gg 1$$

$V_{be} < 0$ so B-E junction is reversed biased diode:

$$I_c = I_0 \left[e^{qV_{be}/k_B T} - 1 \right]$$

$$\frac{dI_c}{dV_{be}} = \frac{qI_c}{k_B T} \equiv \frac{1}{r_e} \equiv g_m$$

Basics of Transistor Noise -- Bipolar Transistors

Input equivalent noise:

$$i_n^2 = 2qI_b = 2q\frac{I_c}{\beta} \quad ; \quad e_n^2 = 4k_B T r_e = \frac{(2k_B T)^2}{qI_c}$$

$$\frac{e_n i_n}{4k_B T} = \frac{1}{\sqrt{2\beta}}$$

Constant (roughly) for a particular device; depends on dimensions and materials

$$\frac{e_n}{i_n} = \sqrt{2\beta} \left(\frac{k_B T}{qI_c} \right)$$

Depends on operating point through I_c

Also, consider the noise associated with physical base resistance; design for $r_b \ll r_e$.

$$e_{bn}^2 = 4k_B T r_b$$

Basics of Transistor Noise -- Bipolar Transistors

Design for $e_n = 1 \text{ nV prH}$

$$I_c = \frac{(2k_B T)^2}{q e_n^2} = 0.4 \text{ mA} \quad ; \quad r_e = 60 \text{ } \blacktriangleright$$

Design for $e_n = 0.1 \text{ nV prH}$

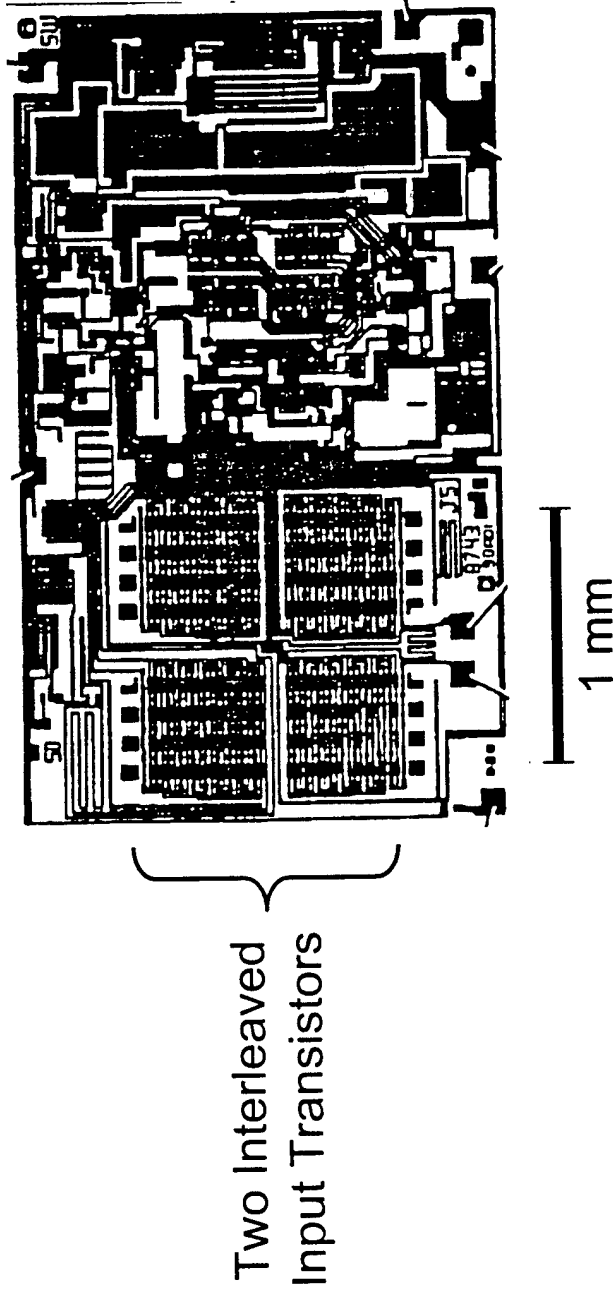
$$I_c = 40 \text{ mA} \quad ; \quad r_e = 0.6 \text{ } \blacktriangleright$$

For low voltage noise:

- high current (heat dissipation)
- small base resistance (massively parallel base structure)
- consequences -- physically large, high power consumption, high input capacitance

Low-Noise Analog Integrated Circuits

AD743



Penalties associated with low-voltage-noise design:

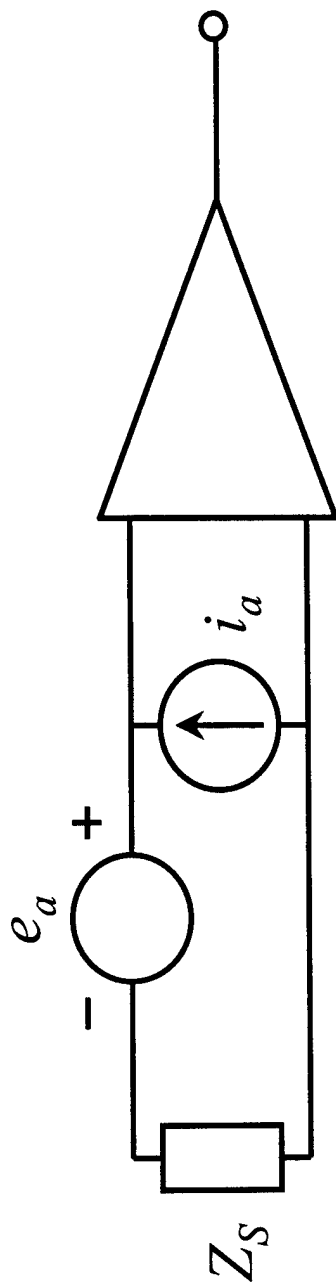
- Large physical size
- High power-supply current
- High input capacitance

Physical Acoustics Summer School - 2000

Special Topics

(III-2)

Sensor-Amplifier Interaction



Three components:

$$e_1^2 = e_a^2$$

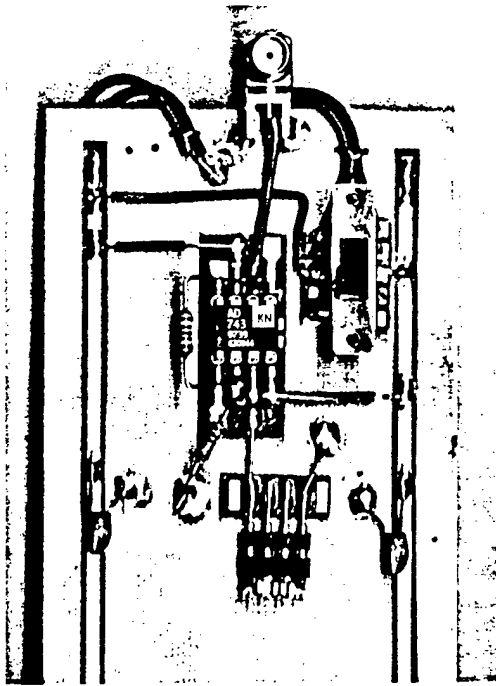
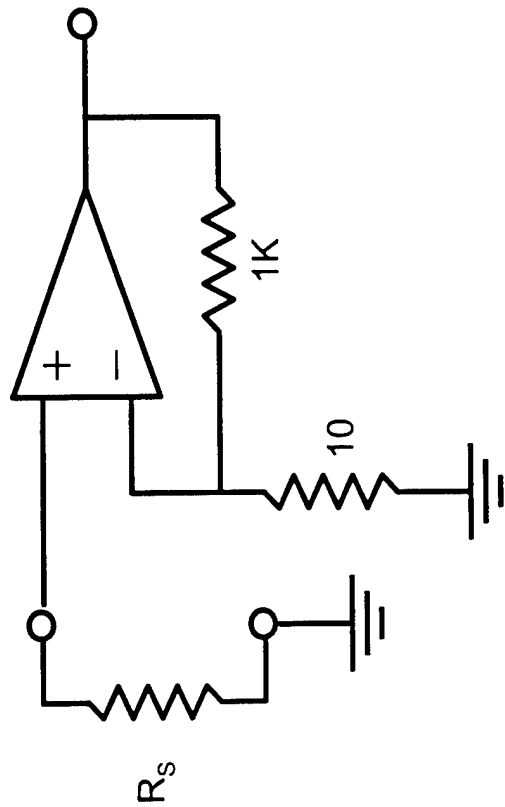
$$e_2^2 = (i_a Z_S)^2$$

$$e_3^2 = 4 k_B T \operatorname{Re}[Z_S]$$

$$e_{TOTAL}^2 = e_1^2 + e_2^2 + e_3^2$$

Measuring Amplifier Noise Performance

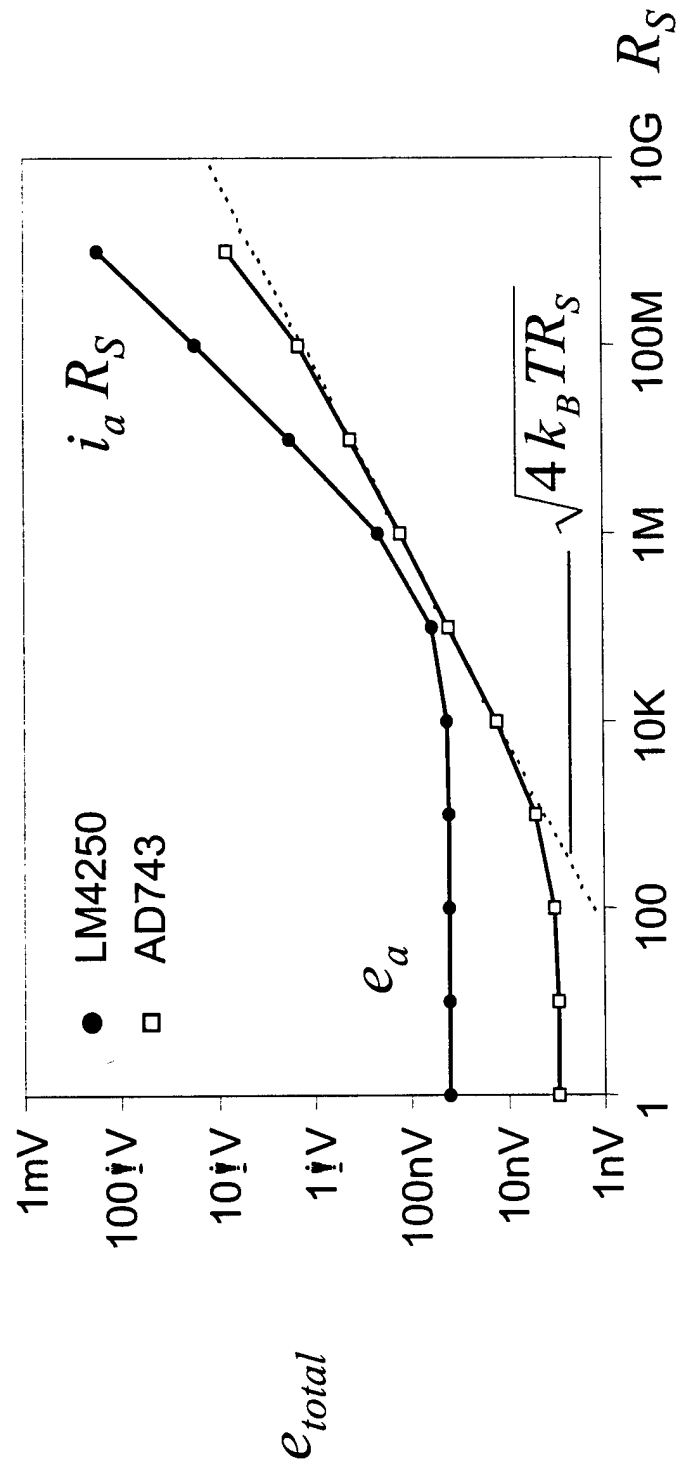
(III-3)



- 1) Bypass power connections
- 2) Use copper ground plane or aluminum box
- 3) Use batteries for power

Sensor-Amplifier Interaction

(III-4)

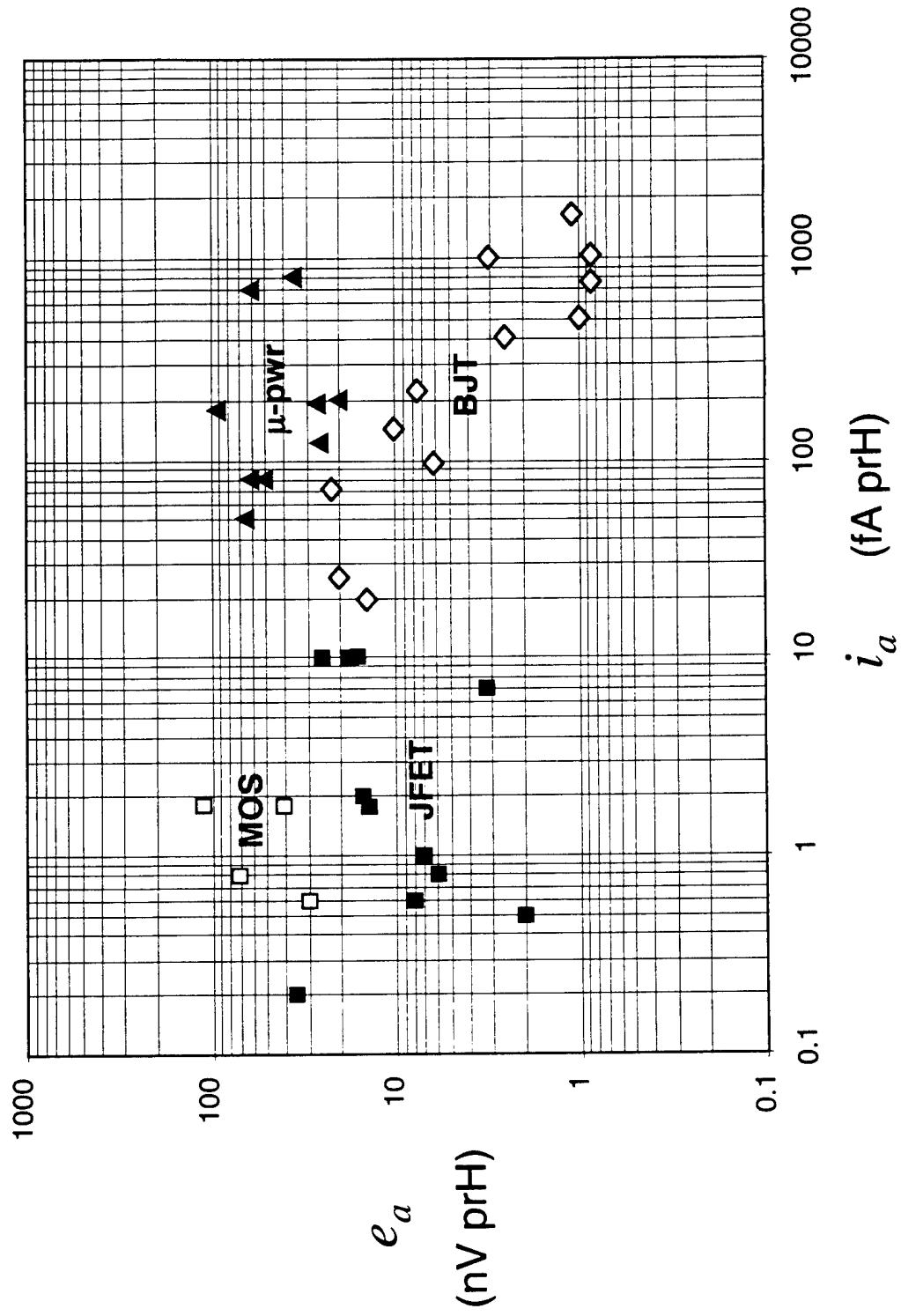


LM4250 AD743

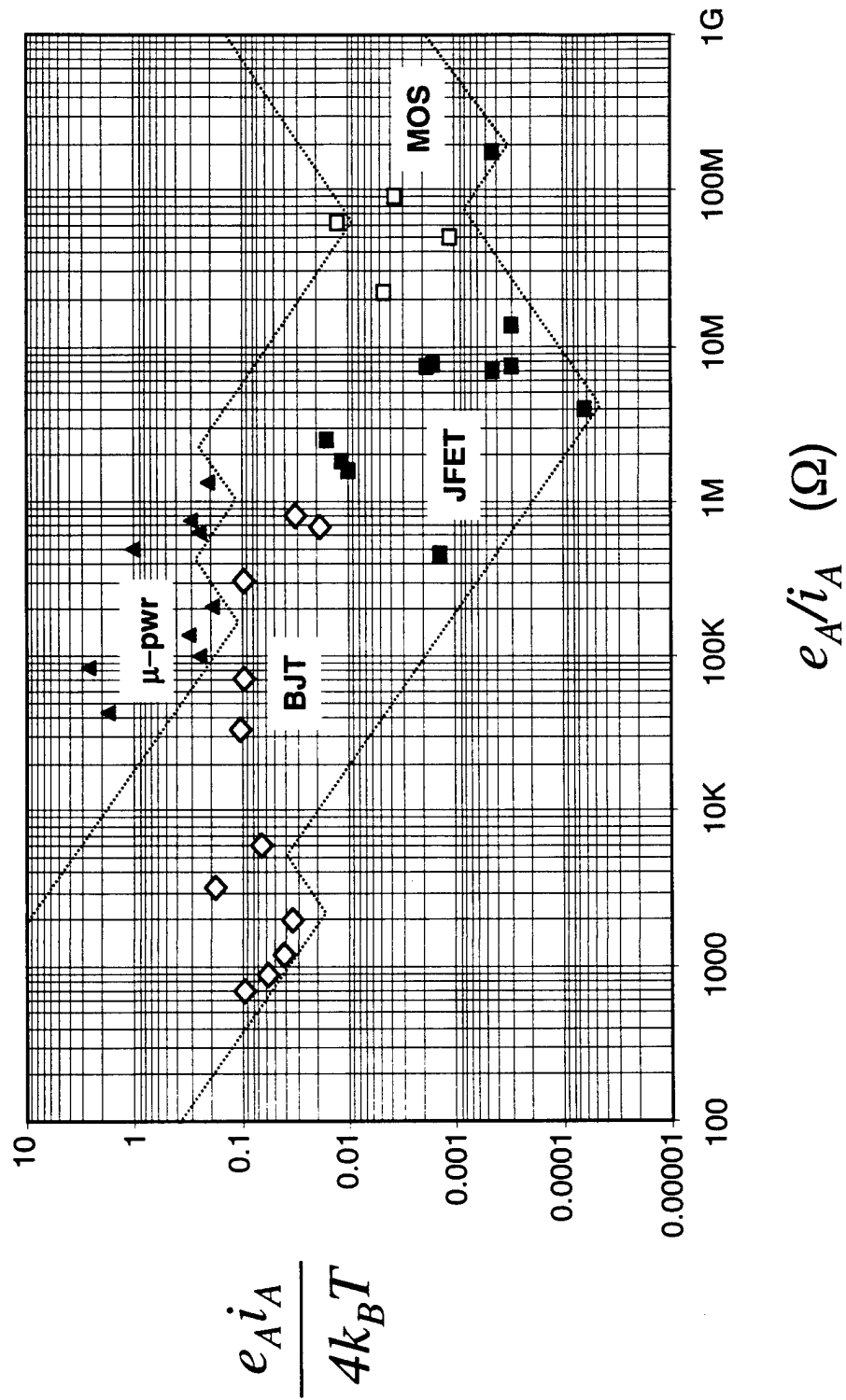
$$e_n i_n / 4 k_B T = 0.42 \quad 0.001$$

$$e_n / i_n = 240K \blacktriangleright 420K \blacktriangleright$$

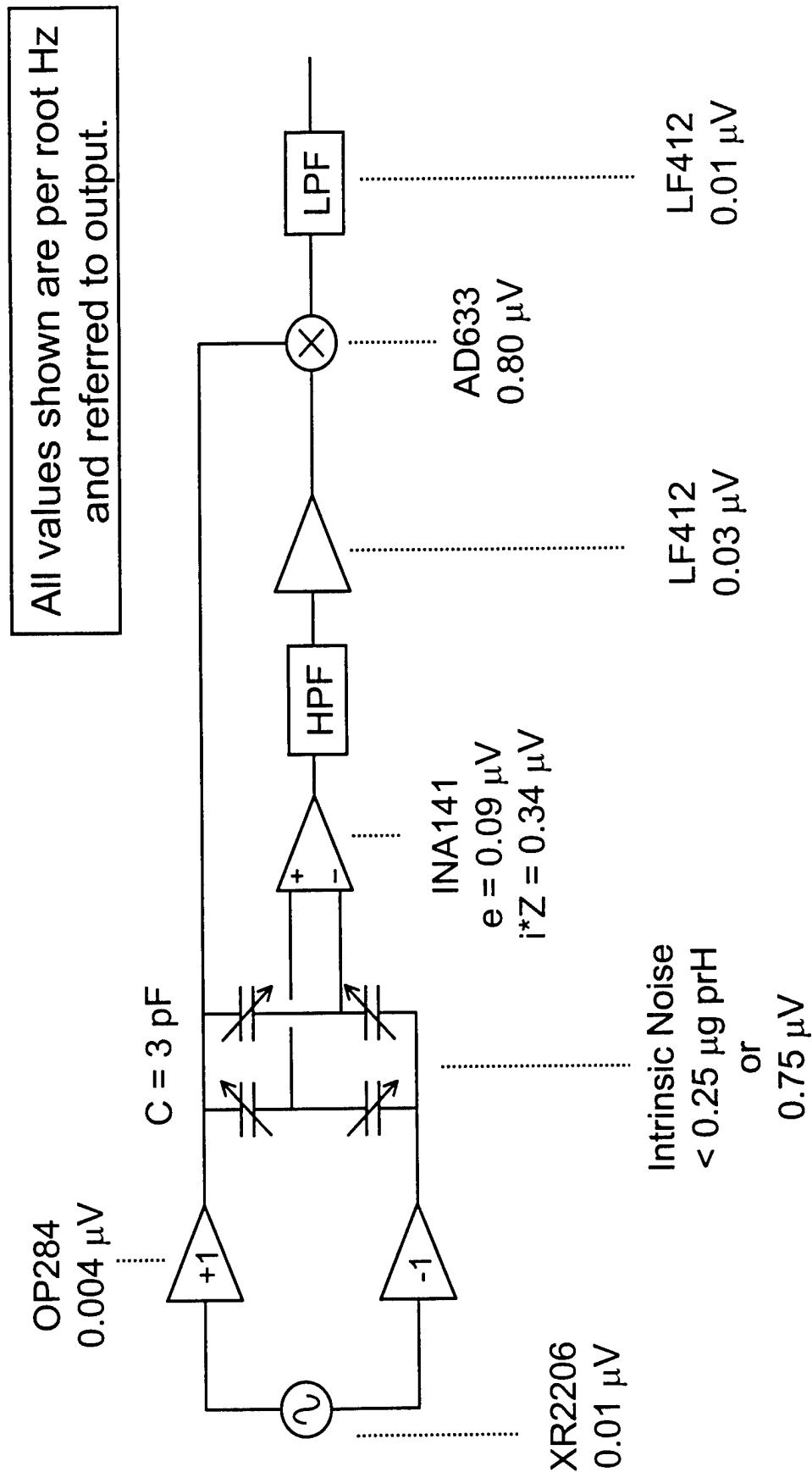
Amplifier Performance



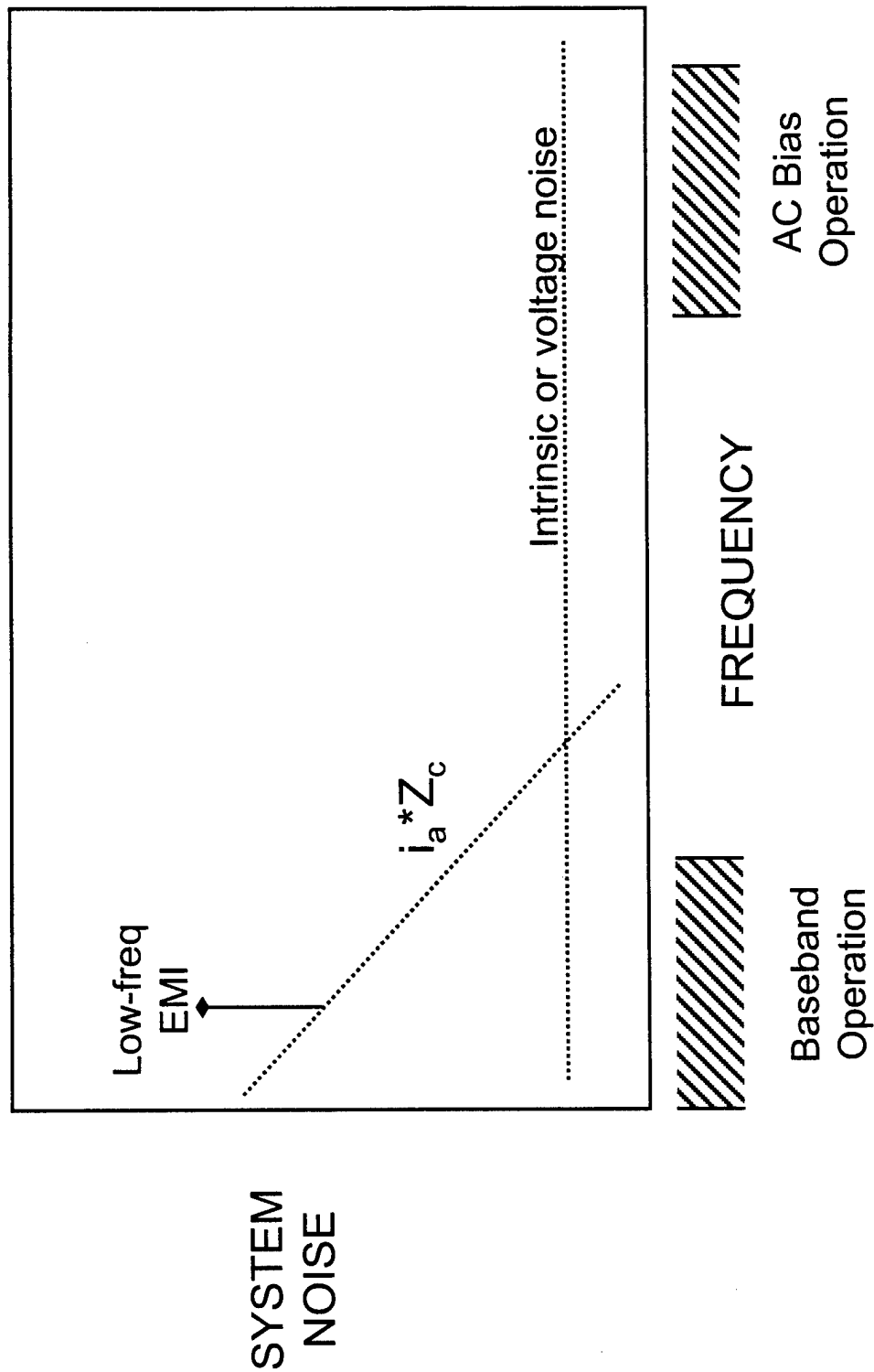
Amplifier Performance



Full-Bridge Configuration: Noise Budget



Advantages of High-Frequency AC Bias

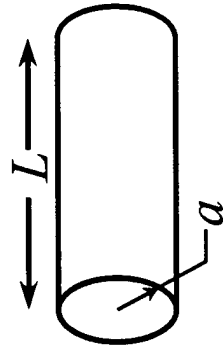
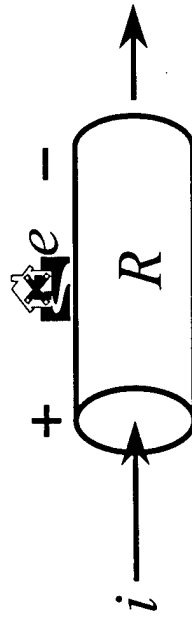


Noise in Fiber-Optic Sensors

- Thermal fluctuations in the sensor structure
- Noise in preamplifier stages
- Shot noise in the photodetection process
- Excess noise in avalanche photodiodes
- Large-signal demodulator limits ($1 \text{ } \mu\text{radian prH}$)
- Laser amplitude noise
- Laser phase noise
- Thermal fluctuations in the fiber
- Coherent Rayleigh Scattering
- Stimulated Brillouin Scattering

Thermal Noise in Optical Fiber Analogy with electrical resistance

$$P = ei \quad \longleftrightarrow \quad \mathcal{Q} = T\mathcal{S}$$



$$\mathcal{Q} = \frac{\kappa \pi a^2 \Delta T}{L}$$

$$i = \frac{1}{R} \Delta e \quad \longleftrightarrow \quad \mathcal{S} = \frac{\mathcal{Q}}{T} = \frac{\kappa \pi a^2 \Delta T}{LT}$$

$$de_n^2 = 4k_B T \Delta f R \quad \longleftrightarrow$$

$$dT_n^2 = 4k_B T \Delta f \frac{LT}{\kappa \pi a^2}$$

Thermal Noise in Optical Fiber

(III-11)

Conversion of temperature fluctuations to phase fluctuations:

$$d\phi = dk_0 \cdot l = dn \cdot k_0 l \quad [l \text{ is coherence length of "patch"}]$$

$$dn = dT \left(\frac{dn}{dT} \right) = dT \left(\frac{\partial n}{\partial T} + \frac{n}{L} \frac{\partial L}{\partial T} \right)$$

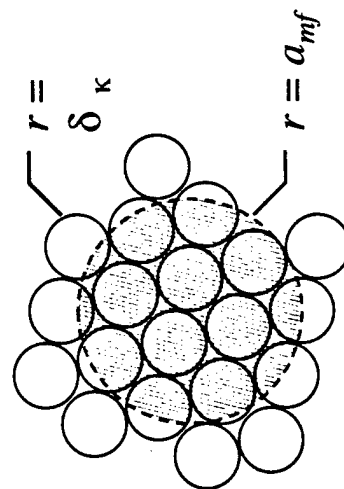
$$\begin{aligned} d\phi_n^2 &= dT_n^2 \left(\frac{\partial n}{\partial T} + \frac{n}{L} \frac{\partial L}{\partial T} \right)^2 (k_0 l)^2 \\ &= 4k_B T \Delta f \frac{LT}{\kappa \pi a^2} \left(\frac{\partial n}{\partial T} + \frac{n}{L} \frac{\partial L}{\partial T} \right)^2 (k_0 l)^2 \end{aligned}$$

Size of coherent patch is, roughly, the thermal penetration depth, δ_κ

$$a \approx l \approx \delta_\kappa = \sqrt{\frac{2\kappa}{\rho c_p \omega}}$$

κ = thermal conductivity
 c_p = specific heat
 ρ = density

$$d\phi_{n-patch}^2 = 4k_B T \Delta f \frac{\delta_\kappa T k_0^2}{\kappa \pi} \left(\frac{\partial n}{\partial T} + \frac{n}{L} \frac{\partial L}{\partial T} \right)^2$$



Optical field averages over cross-section defined by mode-field radius, a_{mf} , until patch size exceeds mode-field size.

And, fluctuations add (mean square) with fiber length, L .

Thermal Noise in Optical Fiber

Case 1: $\bullet_* < a_{mf}$

$$d\phi_n^2 = d\phi_{n-patch}^2 \cdot \frac{\delta_\kappa^2}{a_{mf}^2} \cdot \frac{L}{\delta_\kappa}$$

$$d\phi_n^2 = 4k_B T \Delta f \frac{LTk_0^2}{\kappa\pi} \left(\frac{\partial n}{\partial T} + \frac{n}{L} \frac{\partial L}{\partial T} \right)^2 \left(\frac{\delta_\kappa}{a_{mf}} \right)^2$$

Case 2: $\bullet_* >$

a_{mf}

$$d\phi_n^2 = d\phi_{n-patch}^2 \cdot \frac{L}{\delta_\kappa}$$

$$d\phi_n^2 = 4k_B T \Delta f \frac{LTk_0^2}{\kappa\pi} \left(\frac{\partial n}{\partial T} + \frac{n}{L} \frac{\partial L}{\partial T} \right)^2$$

Thermal Noise in Optical Fiber

(III-14)

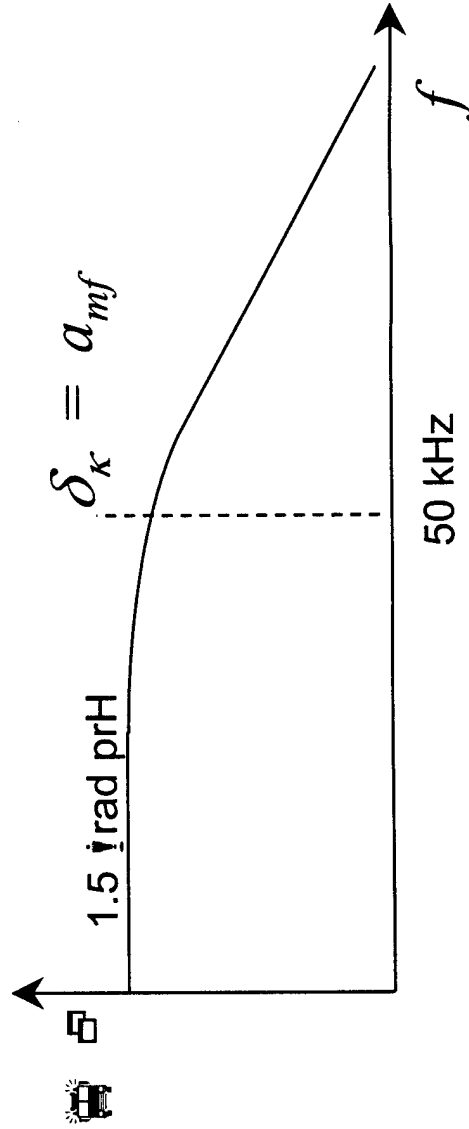
Typical single-mode fiber at 630 nm:

$$\kappa = 1.37 \text{ W / m K} \qquad n = 1.46$$

$$\frac{\partial n}{\partial T} = 1.35 \times 10^{-5} \text{ K}^{-1} \qquad \frac{1}{L} \frac{\partial L}{\partial T} = 0.41 \times 10^{-6} \text{ K}^{-1}$$

$$\rho = 2200 \text{ kg / m}^3 \qquad a_{mf} = 2.28 \text{ } \mu\text{m}$$

For 100 meters of fiber:



Interferometer Shot-Noise Analysis

(III-15)

Basic photodetector response:

$$I_0 = B P_0$$

I_0 = photodetector current

P_0 = incident optical power

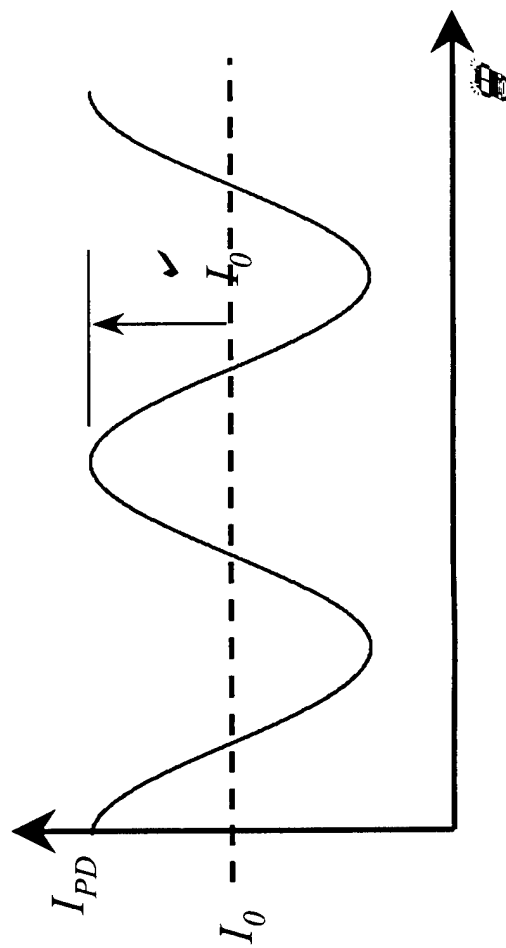
B = response [amps/watt]

Basic interferometer response:

\checkmark = fringe "visibility"

$$I_{PD} = I_0 [1 + \alpha \cos(\phi)]$$

$$\left. \frac{dI_{PD}}{d\phi} \right|_{\max} = \alpha I_0 = \alpha B P_0$$



Interferometer Shot-Noise Analysis

Current noise:

$$\frac{i_n^2}{\Delta f} = 2(q)I_0 = 2(hf_0)P_0 B^2$$

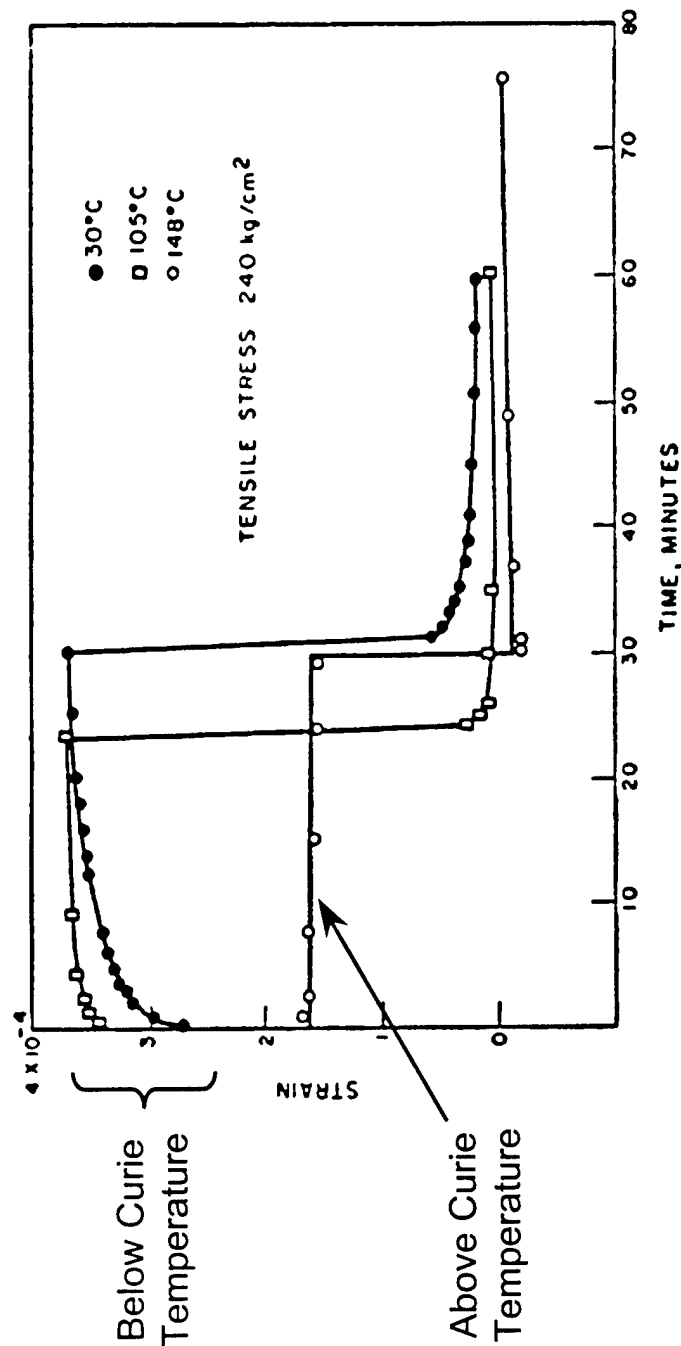
Phase noise:

$$\frac{\phi_n^2}{\Delta f} = \frac{i_n^2}{\Delta f} \div \left(\frac{dI}{d\phi} \right)^2 = \frac{2hf_0}{\alpha^2 P_0} = \frac{2hc}{\alpha^2 \lambda_0 P_0}$$

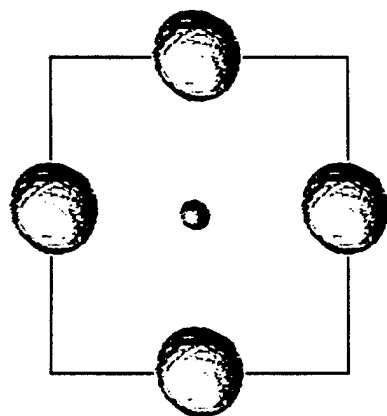
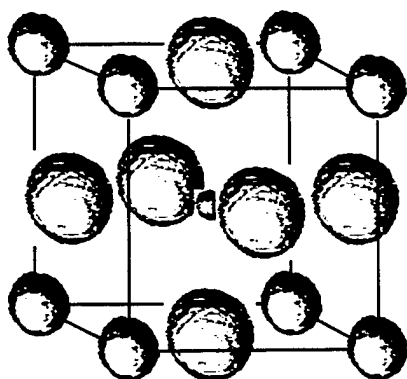
The shot-noise calculation is interesting but frequently misleading. Systems that reach the shot-noise limit are rare. For example, for $\lambda_0 = 630 \text{ nm}$ and 10 μW optical power, the shot noise is only about 0.25 $\mu\text{radians prH}$, well below that obtainable with practical demodulators.

Anelasticity in Ferroelectrics

- Apply a step function stress (24 MPa)
- Measure strain as a function of time

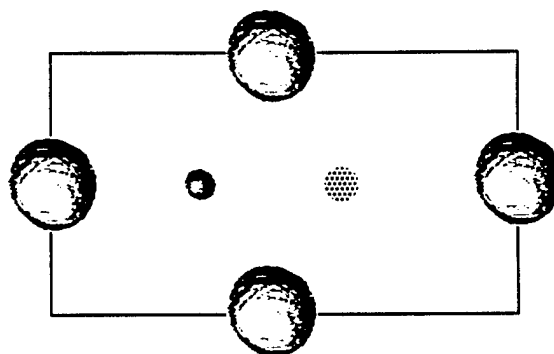
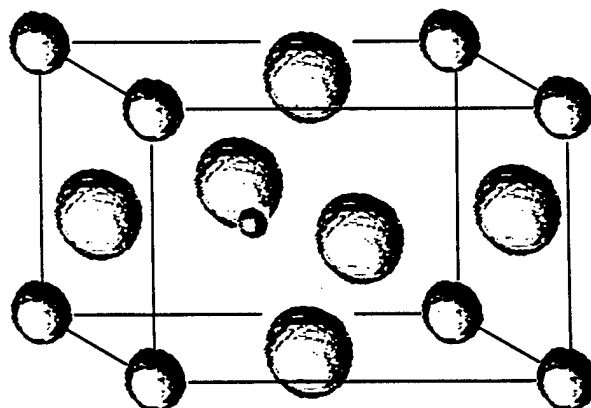


Subbarao, McQuarrie, and Buessem, "Domain effects in polycrystalline barium titanate," J. Appl. Phys. **28**, 1194-1200, 1957.



CUBIC LATTICE:

- One stable configuration
- No net polarization



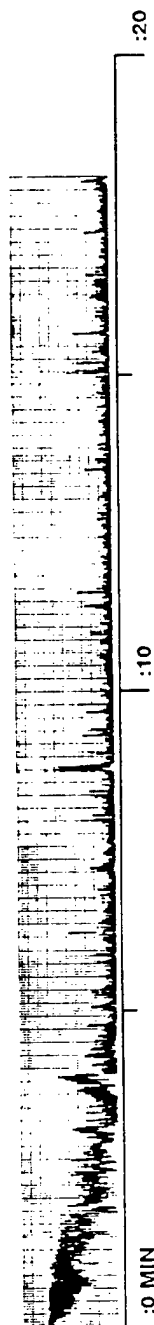
TETRAGONAL LATTICE:

- Two stable configurations
- Net polarization
- Regions of like polarization
- 90- and 180-degree walls

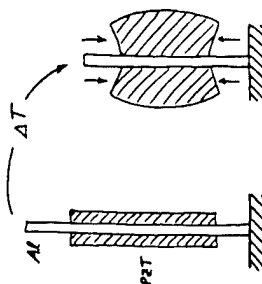
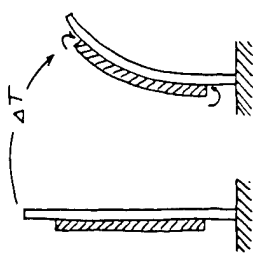
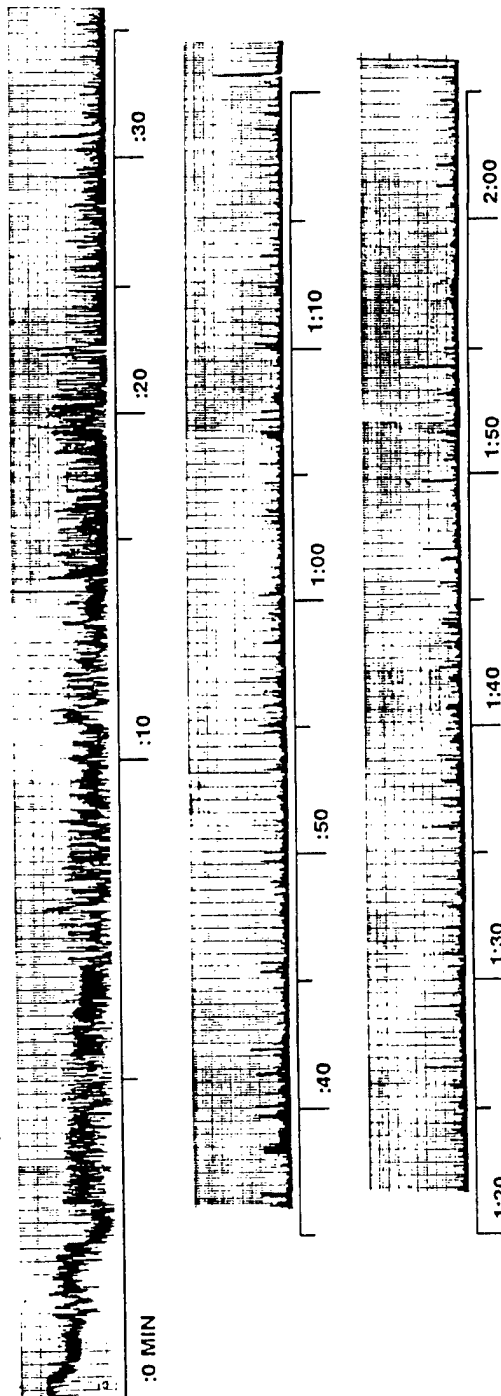
Stress-Induced Noise in Ferroelectrics

Small temperature changes lead to high stress and domain re-orientation in laminated structures.

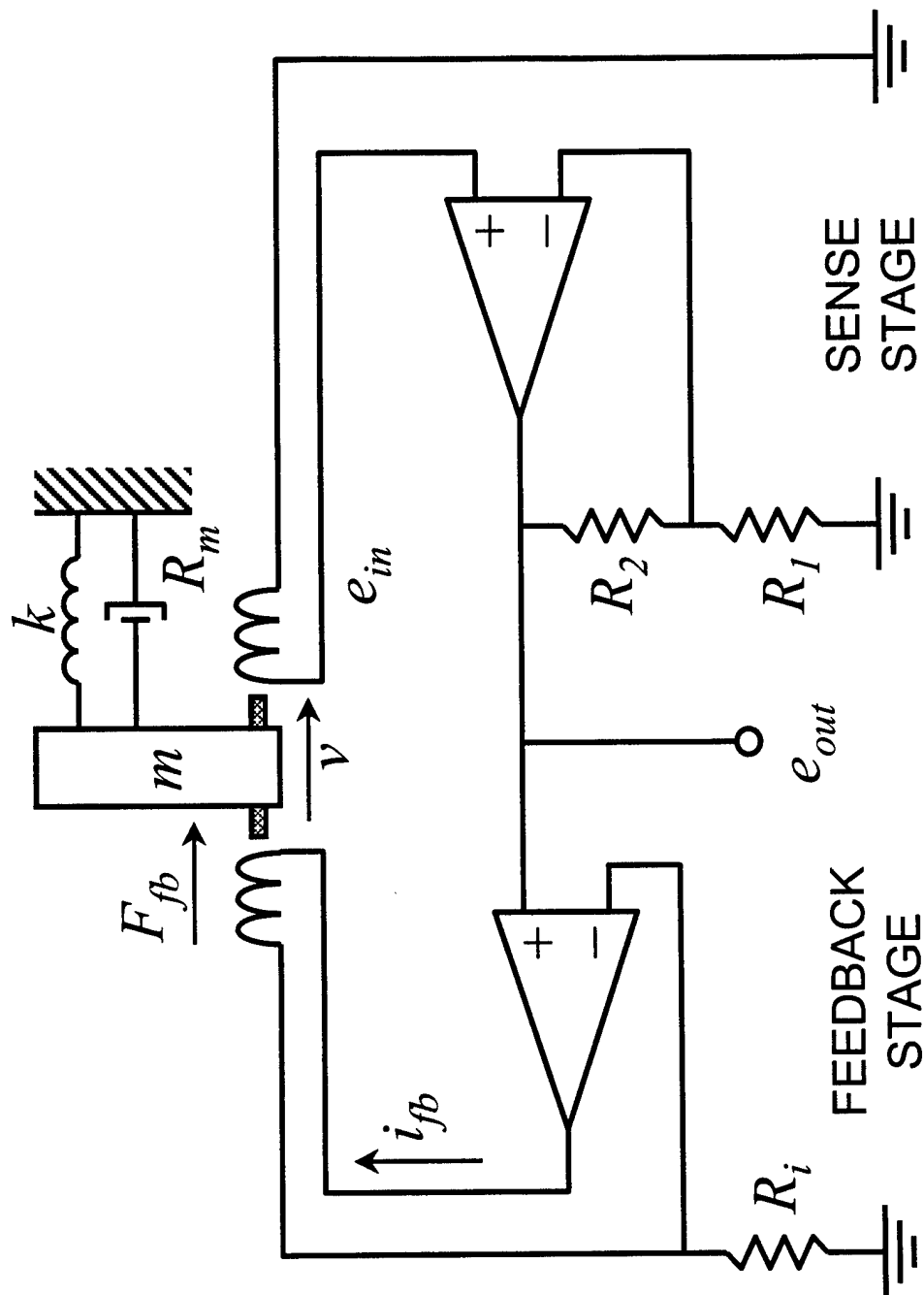
Single-Sided (Ceramic-Metal) Laminate



Double-Sided (Ceramic-Metal-Ceramic) Laminate



Feedback and Sensor Noise

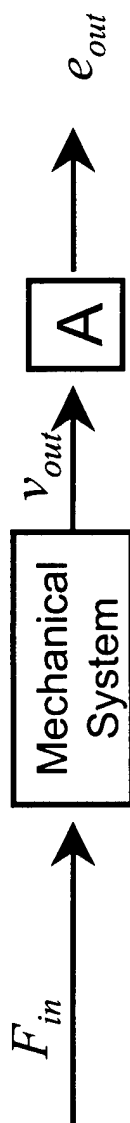


$$F_{fb} = B \cdot e_{out} \qquad e_{out} = A \cdot v$$

Feedback and Sensor Noise

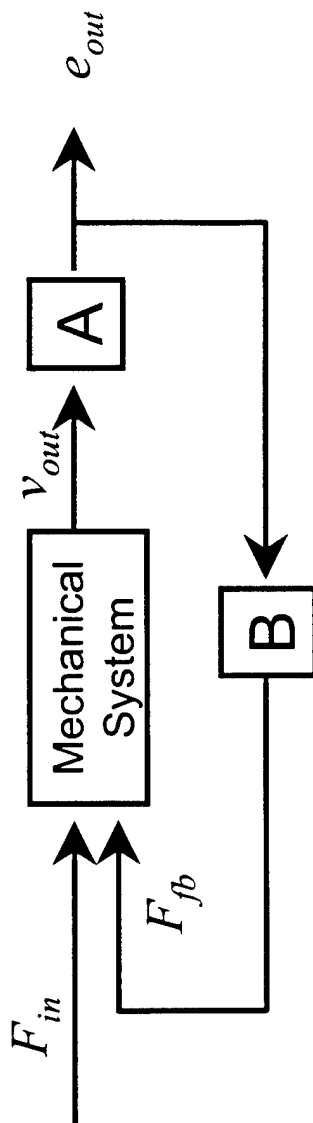
(III-21)

OPEN
LOOP



$$F_{in} = m\ddot{x} + R_m\dot{x} + kx$$

CLOSED
LOOP



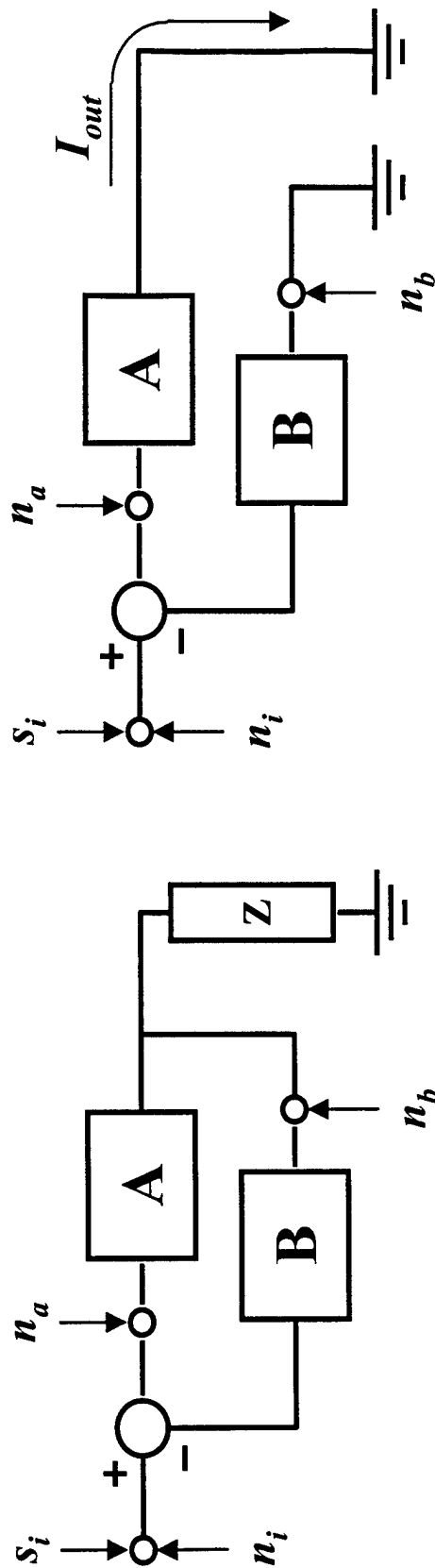
$$F_{in} + F_{fb} = F_{in} + A \cdot B \cdot \dot{x} = m\ddot{x} + R_m\dot{x} + kx$$

$$F_{in} = m\ddot{x} + (R_m - A \cdot B)\dot{x} + kx$$

Signal-to-Noise Ratio: A Useful Theorem

(III-22)

The signal-to-noise ratio at the output of a linear circuit does not depend on the value of the output load.



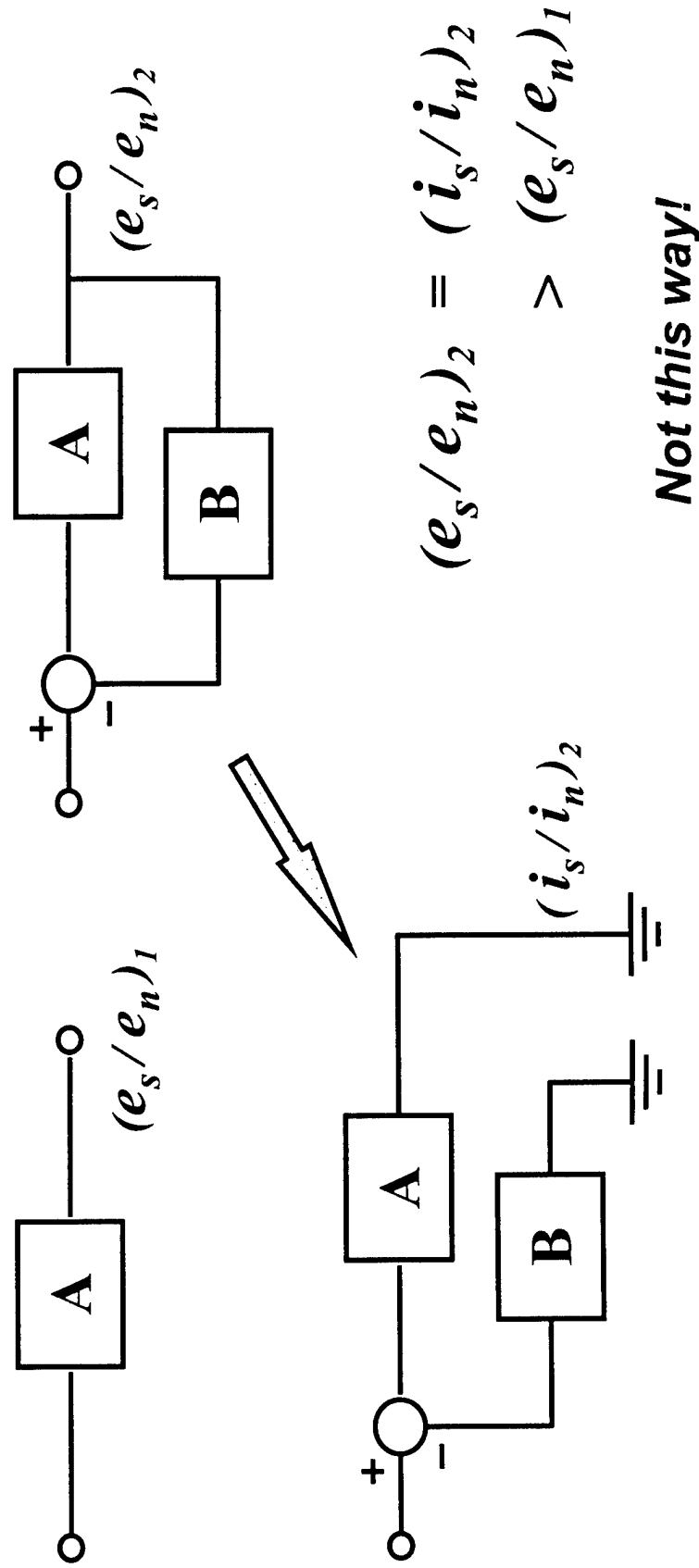
Analysis of complicated circuits can often be simplified by setting the output load to zero and calculating the ratio of signal current to noise current.

Signal-to-Noise Ratio and Feedback

(III-23)

The effective Q of a system can be changed by adding feedback.
Positive feedback increases the Q; negative feedback decreases the Q.

Can the noise of a system be reduced by adding feedback?



Feedback and Sensor Noise

Strategies:

- Design mechanical Q to be low and use positive feedback to raise Q and increase sensor responsivity. Intrinsic noise is still determined by R_m though, so signal-to-noise ratio is not improved.
- Design mechanical Q to be high and use negative feedback to flatten response. Since intrinsic noise is determined by R_m , the result is damped system with lower noise than if the damping were purely mechanical as long as the noise added by the feedback circuitry is small. (“Cold damping”)

Resonant Ultrasound Spectroscopy

Applications to Physics, Materials Measurements,
and Nondestructive Evaluation

Albert Migliori
Los Alamos National Laboratory

Introduction

Basics

How its done

An intro to statistical mechanics and why ultrasound is important

Some results

Electronics details

Seasons Greetings

It brightens the spirits
In times like these,
To know the Moon
Is made of cheese.

Lunar rocks and cheeses	Sound Velocity, Vp (Kilometers/second)
Lunar Rock 10017	1.84
Gjetost (Norway)	1.83
Provolone (Italy)	1.75
Romano (Italy)	1.75
Cheddar (Vermont)	1.72
Emmenthal (Swiss)	1.65
Muenster (Wisconsin)	1.57
Lunar Rock 10046	1.25

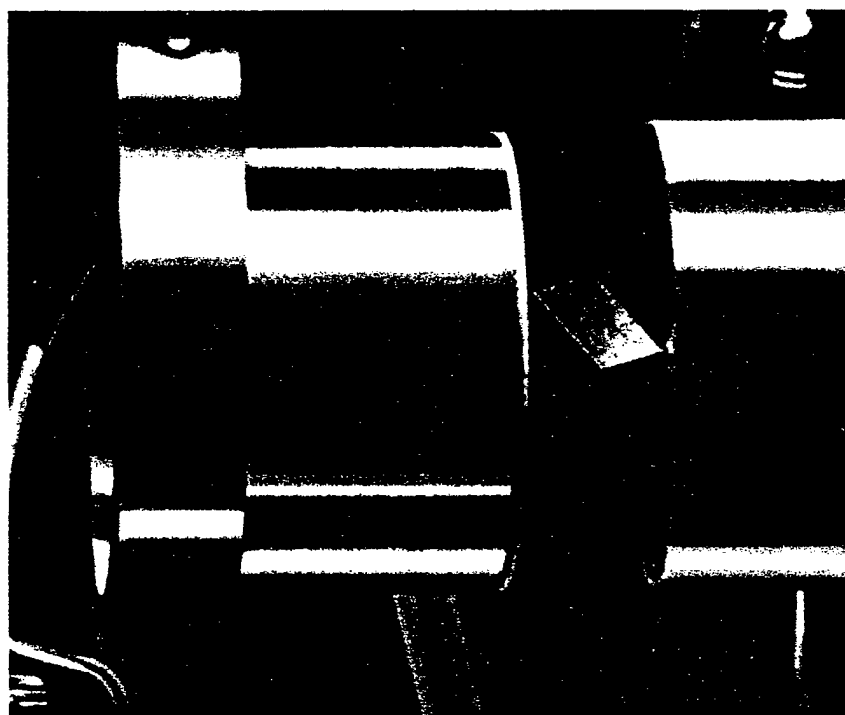
(Science, 168, 1579, 1970)



MINERAL PHYSICS LABORATORY
LAMONT-DOHERTY GEOLOGICAL OBSERVATORY
OF COLUMBIA UNIVERSITY

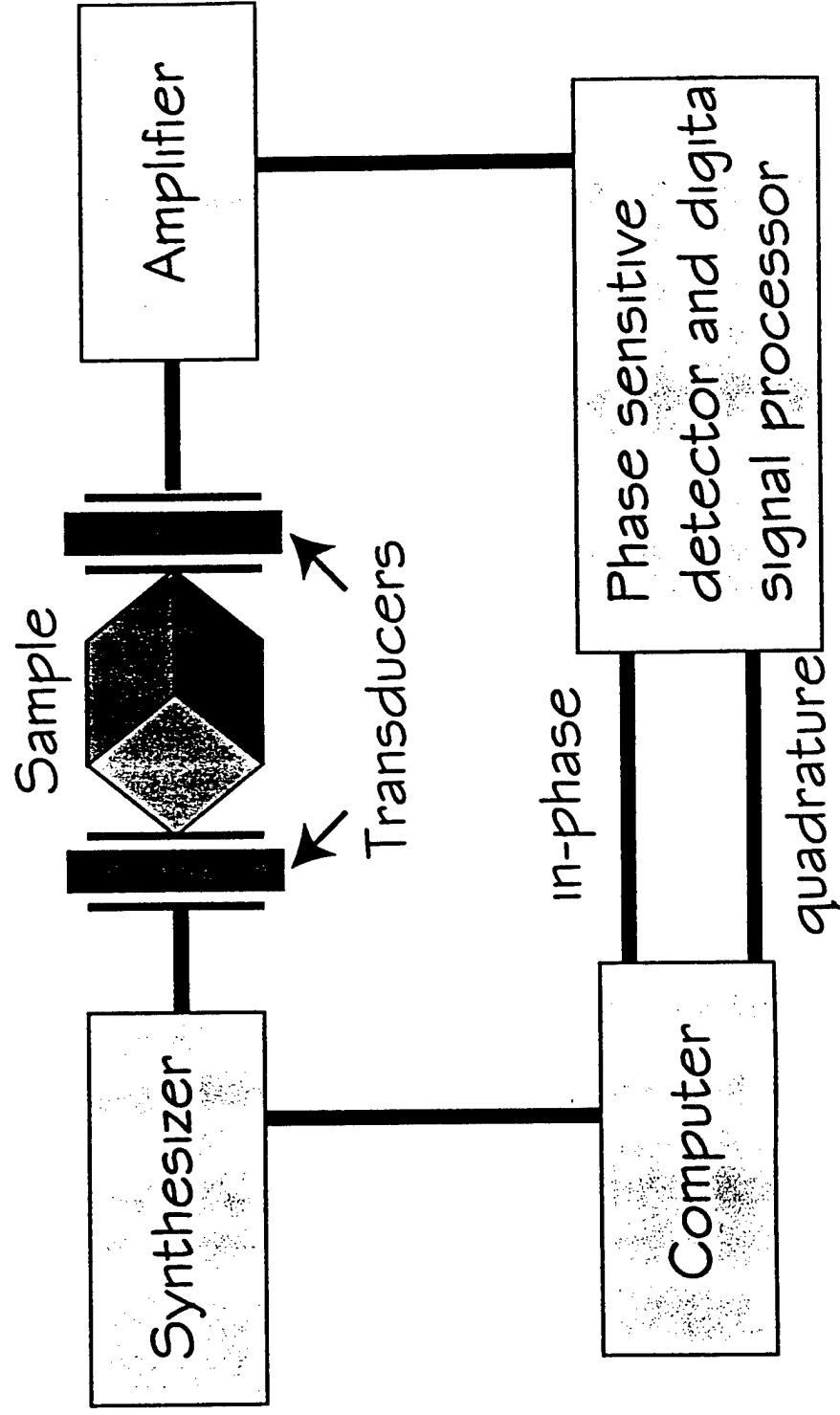
Orson Anderson, famous cartoonist, WWII fighter pilot, physicist and father of RUS, sent this Christmas card out in celebration of the discovery (using RUS and conventional ultrasound) of vacuum microcracking of mineral samples obtained from earth's moon by the U.S. Apollo expeditions.

Measurement of the resonances of small samples having accurate geometry is the key.

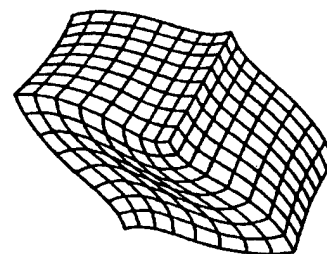
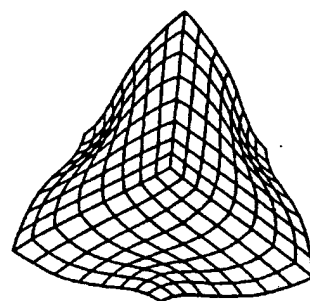
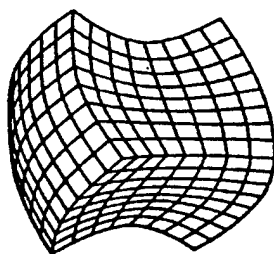
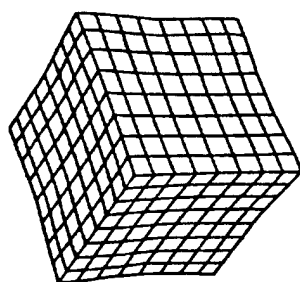
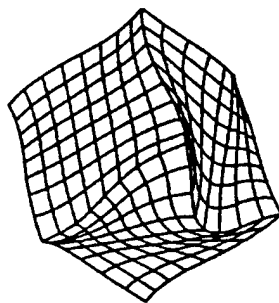
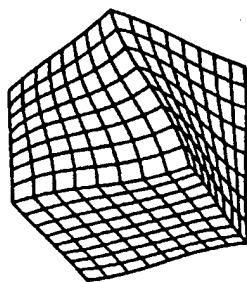
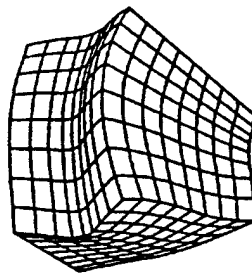
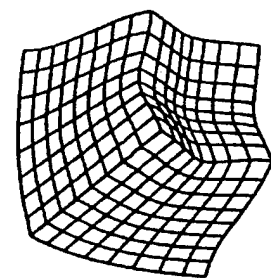


Using carefully designed electronics....

RUS Block Diagram



...to measure normal modes that look like this....

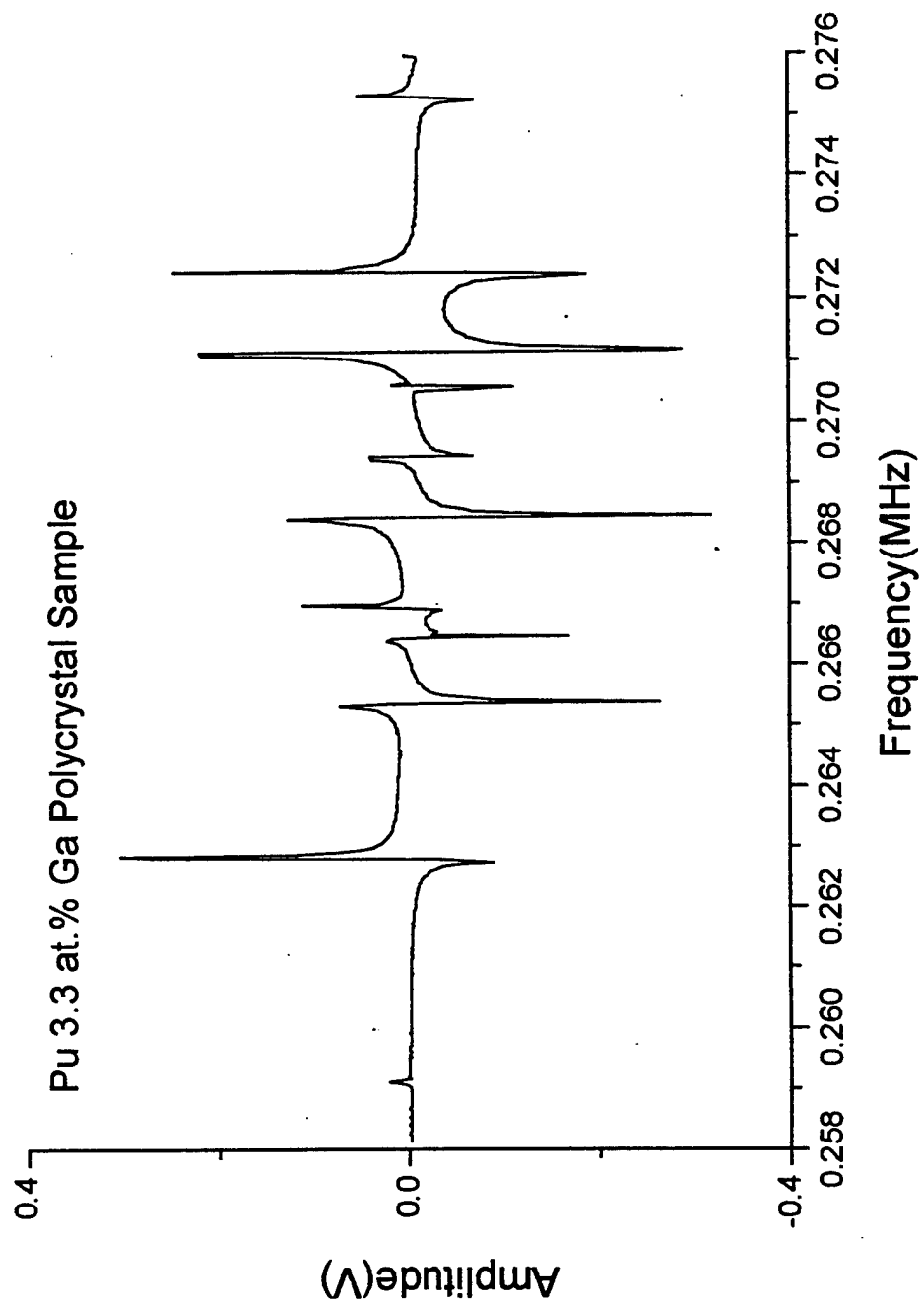


...and using sophisticated,
non-finite-element analysis.....

The "Calvin and Hobbes" model of the vibrations of a rectangular
parallelepiped



...the measured resonances.....



...produce elastic moduli such that

Be s200F Textured Polycrystal

free moduli are c11, c44
using 10 order polynomials mass= 0.4934 gm rho= 1.842 gm/cc

n	fe	fr	%err	wt k l	df/d(moduli)
1	0.633839	0.633252	-0.09	1.00 4 1	0.00 1.00
2	0.635551	0.635684	0.02	1.00 4 2	0.00 1.00
3	0.634344	0.633971	-0.06	1.00 6 2	0.21 0.79
4	0.635120	0.635210	0.01	1.00 1 2	0.22 0.78
5	0.635391	0.636387	0.12	1.00 7 2	0.21 0.79
6	0.661719	0.661065	-0.08	1.00 6 3	1.28 -0.26
7	0.662282	0.662273	0.00	1.00 3 2	0.08 0.92
8	0.662721	0.662542	-0.02	1.00 1 3	1.28 -0.26
9	0.660000	0.663094	0.00	0.00 8 2	0.08 0.92
10	0.664708	0.663590	-0.13	1.00 7 3	1.28 -0.26
11	0.664954	0.663766	-0.14	1.00 2 2	0.08 0.92
12	0.981956	0.982200	0.02	1.00 2 3	0.63 0.37
13	0.982327	0.983148	0.08	1.00 8 3	0.63 0.37
14	0.984162	0.984318	0.02	1.00 3 3	0.63 0.37
15	0.000000	0.986349	0.00	0.00 5 1	0.00 1.00
16	0.000000	0.987323	0.00	0.00 5 2	0.00 1.00
17	0.000000	0.988265	0.00	0.00 5 3	0.00 1.00
18	1.021700	1.022765	0.10	1.00 5 4	1.18 -0.18
19	1.023870	1.023852	0.00	1.00 5 5	1.18 -0.18
20	1.057160	1.057543	0.04	1.00 5 6	2.32 -1.32
21	1.185330	1.185270	-0.01	1.00 6 4	0.49 0.51
22	0.000000	1.185470	0.00	0.00 1 4	0.49 0.51
23	0.000000	1.185631	0.00	1.00 7 4	0.49 0.51
24	1.188630	1.187391	-0.10	1.00 4 3	0.30 0.70
25	1.218560	1.219204	0.05	1.00 2 4	0.04 0.96
26	1.220240	1.220658	0.03	1.00 8 4	0.04 0.96

Bulk Modulus= 116.6 GPa

c11 c66

315.5 149.2

d1 d2 d3
0.64471 0.64572 0.64348

loop# 1 rms error= 0.0704 %

chisquare increased 2% by the following % changes in independent parameters
0.02 0.01
0.00 0.03

Be Single Crystal

free moduli are c33, c23, c12, c44, c66
using 10 order polynomials mass= 0.2264 gm rho= 1.842 gm/cc

n	fe	fr	%err	wt k l	df/d(moduli)
1	0.635039	0.635302	0.04	1.00 4 1	0.00 0.00
2	0.788108	0.788153	0.01	1.00 6 2	0.00 0.00
3	0.635332	0.634795	-0.06	1.00 1 2	0.00 0.00
4	0.659970	0.657946	-0.21	1.00 3 2	0.00 0.00
5	0.999543	1.001015	0.15	1.00 6 3	0.01 0.00
6	1.038990	1.034969	-0.19	1.00 5 1	0.00 0.00
7	1.047030	1.047225	0.02	1.00 4 2	0.00 0.00
8	1.075950	1.076550	0.06	1.00 7 2	0.00 0.00
9	1.121610	1.122433	0.07	1.00 2 2	0.01 0.00
10	1.149920	1.150491	0.05	1.00 5 2	0.00 0.00
11	1.160580	1.161102	0.04	1.00 8 2	0.01 0.00
12	1.195890	1.196787	0.08	1.00 8 3	0.01 0.00
13	1.254030	1.253338	-0.06	1.00 3 3	0.01 0.00
14	1.283260	1.280404	-0.22	1.00 2 4	0.01 0.00
15	1.393150	1.395002	0.13	1.00 2 4	0.01 0.00
16	1.480820	1.485443	0.31	1.00 5 4	0.70 -0.01
17	1.487210	1.486888	-0.02	1.00 1 3	0.47 -0.01
18	1.501830	1.500589	-0.08	1.00 7 3	0.02 0.00
19	1.503350	1.503580	0.02	1.00 1 4	0.30 0.01
20	1.525570	1.524154	-0.09	1.00 7 4	0.72 0.00
21	1.527700	1.530233	0.17	1.00 5 5	0.66 -0.01
22	1.534700	1.531091	-0.24	1.00 6 4	0.00 0.00
23	1.549320	1.547966	-0.09	1.00 4 3	0.01 0.00
24	1.562710	1.560813	-0.13	1.00 3 3	0.78 0.00
25	1.612020	1.615287	0.20	1.00 8 4	0.01 0.00
26	1.641860	1.643048	0.07	1.00 3 4	0.01 0.00

Bulk Modulus= 116.5 GPa

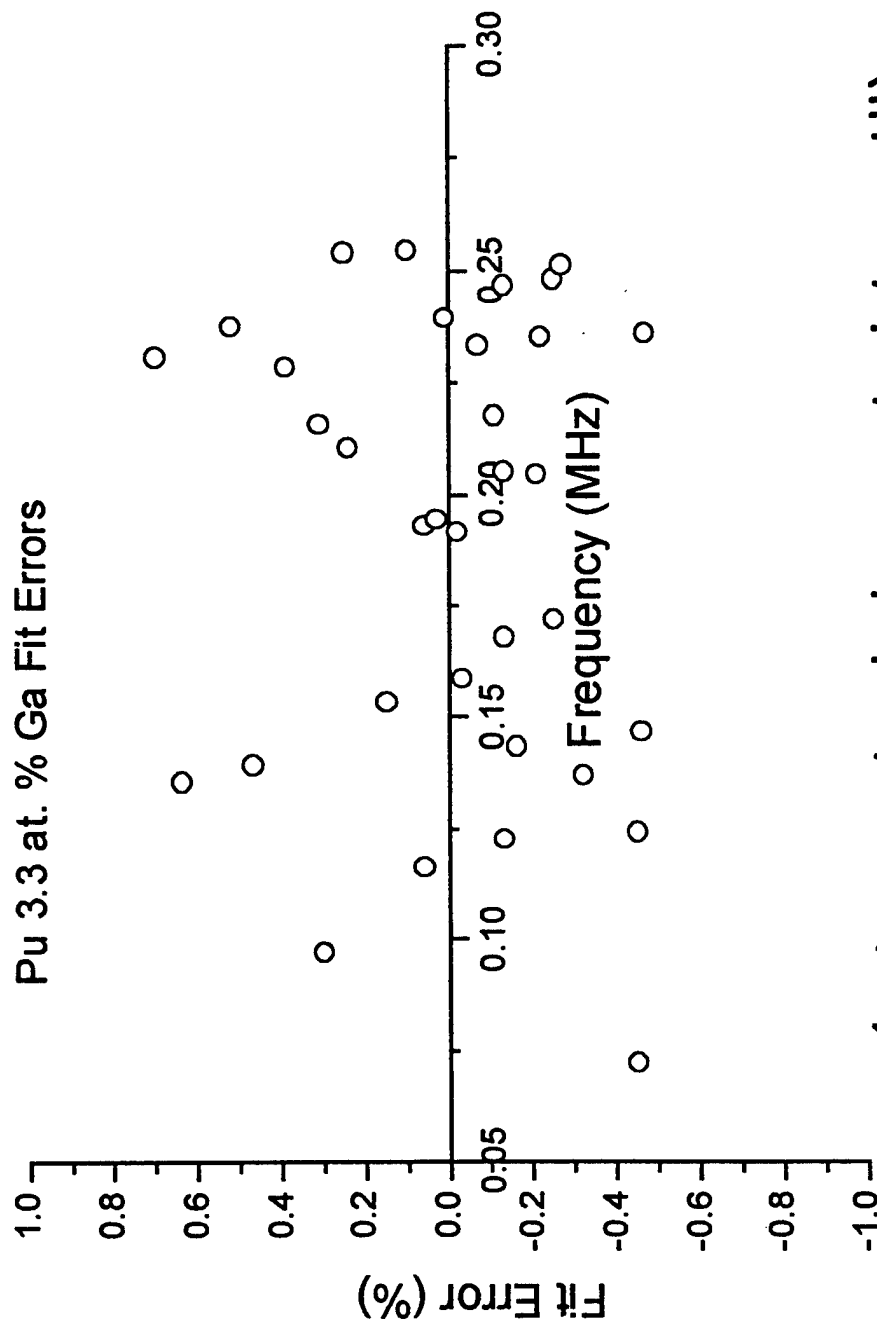
c33 c23 c12 c44 c66

356.7 14.00 26.75 162.2 133.4

d1 d2 d3
0.50540 0.60198 0.40390
loop# 3 rms error= 0.1323 %

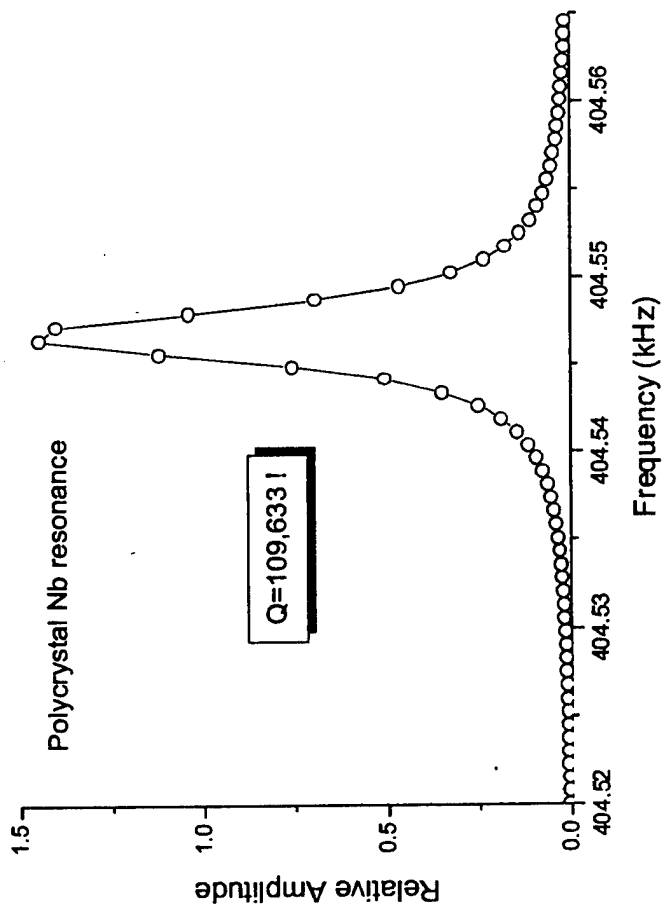
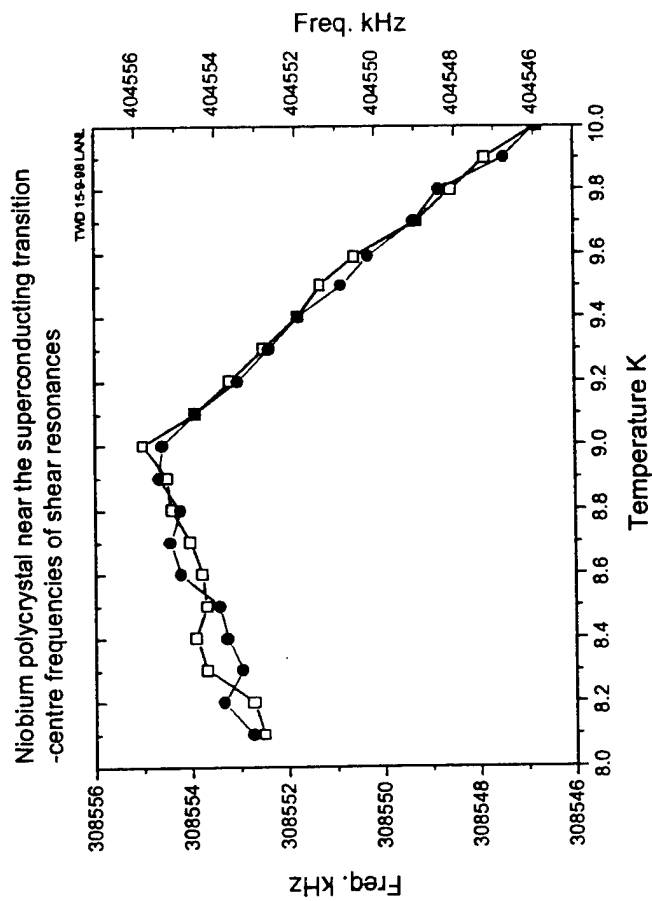
chisquare increased 2% by the following % changes in independent parameters
0.06 7.55 0.72 -0.02 -0.02
0.01 0.62 -1.81 -0.01 0.11
0.10 -0.54 -0.02 -0.01 -0.02

RUS achieves the highest absolute accuracy on the smallest samples in the least time of any routine elastic modulus measurement technique!



(not a particularly great data set!!)

...enabling observation of some marvelous stuff...



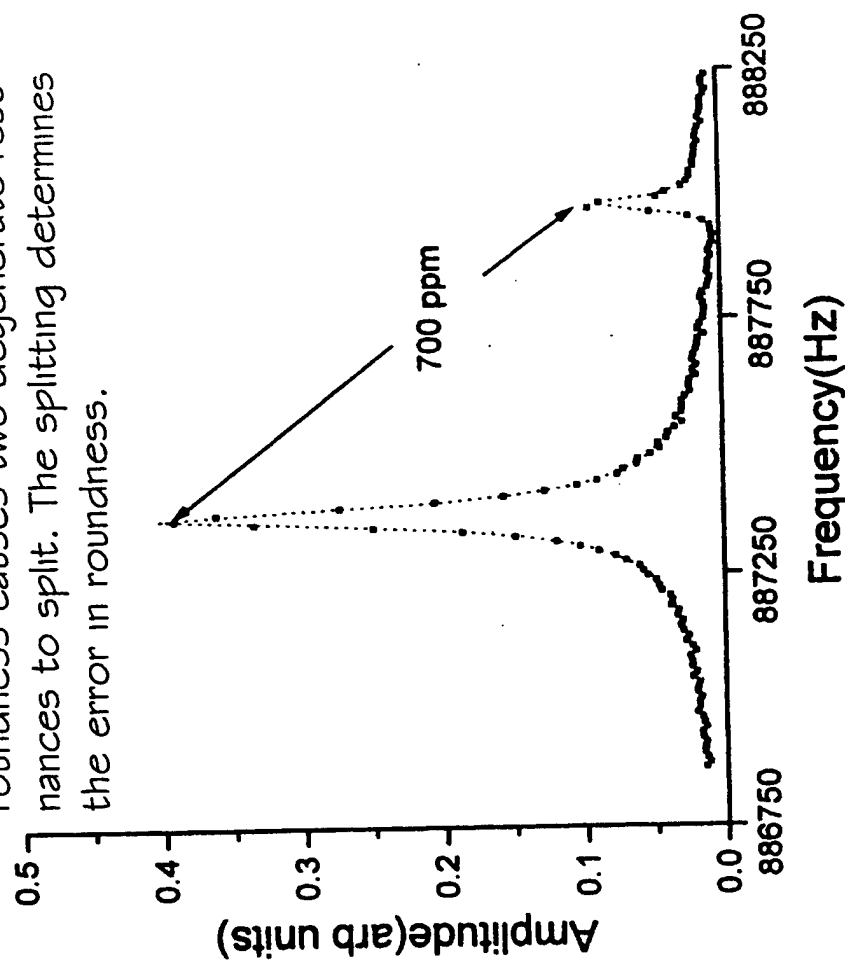
RUS has important applications to nondestructive testing for quality control in industry and government.

First Launch of the Trident II

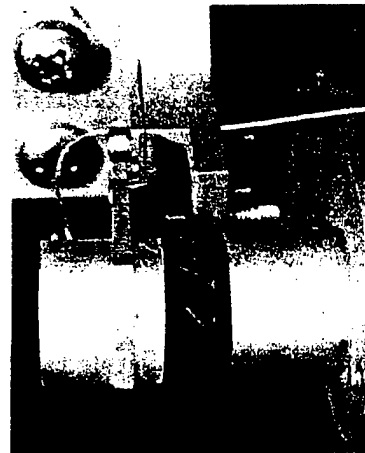
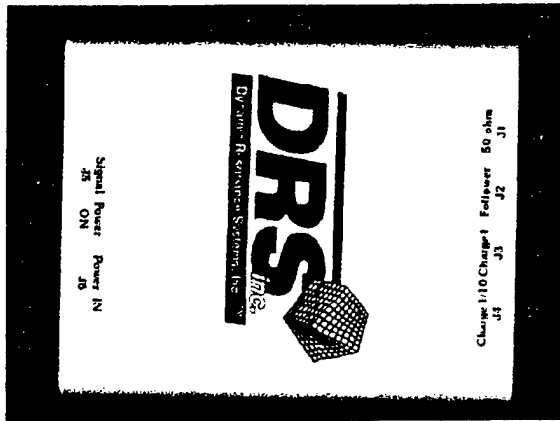
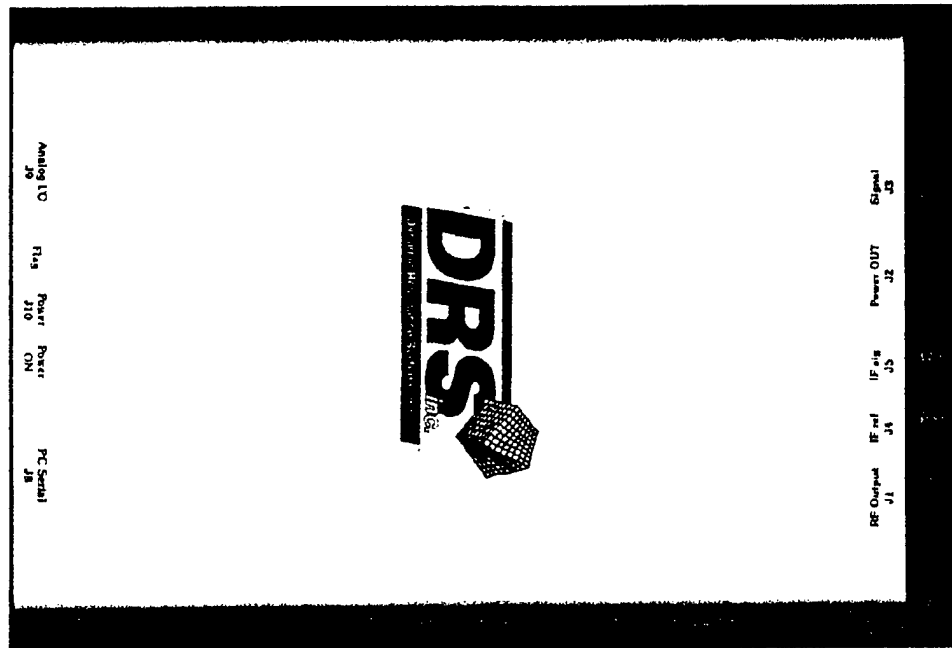
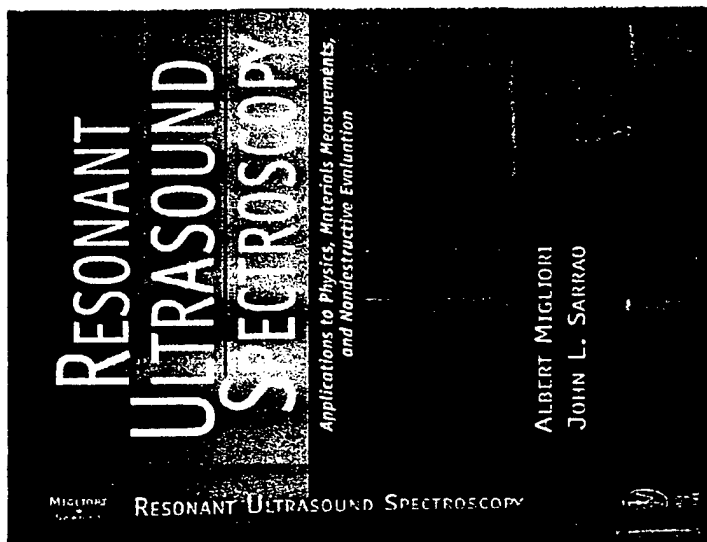


NOT LIKE THIS (from The Economist)

Resonances can be used to determine manufacturing flaws. Below is shown a spectrum taken from a Si_3N_4 ball bearing used in the space shuttle. The error in roundness causes two degenerate resonances to split. The splitting determines the error in roundness.



...and has become important in science and industry.



CHAPTER 1

SIMPLE RESONANCES

1.1 Introduction

The descriptor "resonant ultrasound spectroscopy" (RUS), first used in 1987 [1.1], is a reflection of the richness of information revealed by the natural modes of vibration, or resonances, of solids. RUS, much like other high-precision modulus measurement methods, is sensitive to both microscopic and macroscopic properties of an object. Using it, elastic moduli, ultrasonic attenuation, and geometry can all be probed. To extract this information requires an elegant collection of theoretical, computational, and experimental tools. In attempting to decide whether these are the right tools, it will be important to compare RUS to other acoustic techniques. For the comparison to be useful, it is important to explore the general qualities of resonances. We begin this chapter with a discussion of simple resonances and end it with an exploration of the complications that arise when a resonator is subject to forces that use up the energy stored in oscillatory motion. As expected, the resonator runs down, but what is a little surprising are the intrinsic uncertainties inherent in even the most simple, classic oscillating system.

1.2 Simple resonances

This is a book about the mechanical resonances of solids. More precisely, it is about mechanical resonances of free bodies or bodies not constrained, clamped, or otherwise affected by the outside world. In the overall scheme of things, free resonators are really the only ones that exist. A simple argument for why this is so is to consider a strip of metal clamped in a vise. Pluck the metal with your finger, and it vibrates. Is it not a resonator with one end clamped and one end free? Well, no, it isn't. The free end is pretty clear; however, the clamped end is not clamped by a perfectly rigid object, but by a vise with a

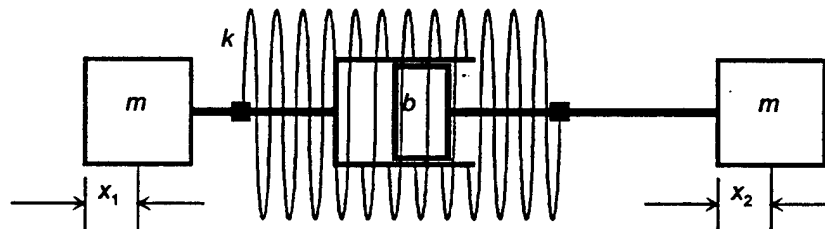


Figure 1.1 A simple mass/spring resonator with free boundary conditions (i.e., it is floating freely in space) and a simple dashpot damping mechanism providing a damping force proportional to velocity.

stiffness not very different from the metal it is clamping. Worse still, only the outer surface of the metal strip is clamped, so the interior of the strip near the vise is only imprecisely constrained. In fact, the resonating system is really the strip, the vise, the table the vise is attached to, etc.

At best, this will be a difficult system to understand exactly, and somewhat unsatisfying (at least to the accuracy that we shall aspire to here—on the order of a part per million) to understand approximately. In contrast, the metal strip unattached to anything and freely suspended in space is, at the very least, a well-posed physical problem, and it is only such problems that we shall address here and later.

So let's begin with a very simple free resonator with all the salient features required for a general discussion of resonances, shown in Figure 1.1. There are two masses in this simplest free resonator because we take the spring and damping piston to be massless; thus the only way to stretch or compress the spring is to accelerate or decelerate the masses in opposite directions. If we had only a single mass and spring, then the spring would need to be attached to the proverbial lab frame of reference in order to get the mass bouncing around, destroying our free boundary condition. Taking x_1 and x_2 to be positive to the right, and t time, we can write down all the forces acting on the joints between masses, spring, and damper, and just for fun, get the signs right. The inertial forces F_{m1} and F_{m2} that the two masses exert on their respective joints are

$$F_{m1} = -m \frac{d^2 x_1}{dt^2}, \quad F_{m2} = -m \frac{d^2 x_2}{dt^2}, \quad (1.1)$$

because when a mass is accelerated to the right, it exerts a force to the left on whatever is accelerating it, the spring and damper in this case. The damping forces act only when the piston is moved in the cylinder. If the piston is compressing the air in it, then $x_1 - x_2$ is decreasing and the dissipative or damping forces F_{d1} and F_{d2} that the dashpot with damping b exerts on the joints are

$$F_{d1} = -b \frac{d(x_1 - x_2)}{dt}, \quad F_{d2} = b \frac{d(x_1 - x_2)}{dt}. \quad (1.2)$$

The spring of constant k also exerts forces F_{s1} and F_{s2} only when $x_1 - x_2$ changes from its equilibrium value. These forces are

$$F_{s1} = -k(x_1 - x_2), \quad F_{s2} = k(x_1 - x_2). \quad (1.3)$$

It is important here that the forces in Equation 1.3 are proportional or linearly dependent on the stretch or displacement. This would not be true if the springs were stretched so far that they bent or broke. In mechanical systems this linear

relationship between force and displacement is called Hooke's law. If the spring is not perfectly elastic in the sense that some of the energy used to compress it is not returned when it expands, being dissipated as heat, for example, then Hooke's law is violated. However, it is usually possible to separate the energy loss mechanisms from the springiness as we have done here by approximating a real spring with an ideal one, and separately adding in losses via a dashpot. We now make a change of variables such that

$$x = x_1 - x_2, \quad y = \frac{x_1 + x_2}{2} \quad (1.4)$$

which makes y the center-of-mass coordinate for the system. Using Equation 1.4 and summing all the forces to zero at each joint, we obtain two equations. They are:

$$-m \frac{d^2 x}{dt^2} - 2b \frac{dx}{dt} - 2kx = 0 \quad (1.5)$$

and

$$-m \frac{d^2 (2y - x)}{dt^2} + 2b \frac{dx}{dt} + 2kx = 0. \quad (1.6)$$

If we add Equations 1.5 and 1.6, we obtain the rather intuitive and somewhat uninteresting equation of motion for a free mass $2m$

$$-2m \frac{d^2 y}{dt^2} = 0, \quad (1.7)$$

which has as a solution $dy/dt = \text{constant}$, i.e., Newton's first law. The more interesting equation is Equation 1.5. This equation is solved by assuming simple harmonic motion at angular frequency $\omega = 2\pi f$, where f is the frequency of oscillation. Then

$$x(t) = x_0 e^{-i\omega t}, \quad \text{and} \quad \frac{d}{dt} \rightarrow -i\omega, \quad (1.8)$$

and we are instructed to take the real part of quantities linear in displacement, force, etc. to obtain measurable quantities.

Using Equation 1.8, Equation 1.5 becomes

$$(\omega^2 m + 2i\omega b - 2k)x_0 e^{-i\omega t} = 0, \quad (1.9)$$

which must be true for any x_0 and t . Thus the quantity in parentheses must always be zero, true only if

$$\omega = \pm \sqrt{\frac{2k}{m} - \left(\frac{b}{m}\right)^2} - \frac{ib}{m}. \quad (1.10a)$$

Defining

$$\omega_0 = \sqrt{\frac{2k}{m}} \quad \text{and} \quad \tau = \frac{m}{b}, \quad (1.10b)$$

we write $x(t)$ explicitly, choosing (arbitrarily maybe) the upper sign in Equation 1.10a to find that

$$x(t) = x_0 e^{-i\omega_0 t (1 - 1/(\omega_0 \tau)^2)^{1/2}} e^{-t/\tau}. \quad (1.11)$$

Note that the dissipative effects that cause decay of the initial amplitude of motion x_0 with time constant τ also shift the frequency to second order in the dimensionless quantity $\omega_0 \tau$. Note also that this equation is valid only if the temperature of the system is at absolute zero. At nonzero temperatures, thermal energy prevents the motion from decaying to zero, a thorn in the side of accelerometer designers among others. The thermal energy partitions itself with $k_b T/2$ (where k_b is Boltzmann's constant) in each degree of freedom. For our oscillator, each mass and the spring acquire this energy for a total of $3k_b T/2$.

1.3 The driven resonator

The simple example presented in Section 1.2 is illustrative of what would happen if a mechanical resonator were, for example, hit (gently!) with a hammer. That is, it rings for a while (of order time τ), completing of order

$$Q = \frac{\omega_0 \tau}{2} \quad (1.12)$$

oscillations during that time. Because the decay is exponential, although we say that Q cycles are completed, this is not a precise statement. It is correct to a factor of order a few in the sense that after several time constants, the amplitude drops below the noise floor of our measuring system. But we could

also drive the resonator with a force iF (where F is real) varying harmonically at angular frequency ω and acting only between the two masses (i.e., the center-of-mass force is zero) so that Equation 1.5 becomes (we shift the phase of the force by $\pi/2$ so that the plot of the amplitude of motion in Figure 1.2 has the real component a maximum on resonance)

$$-m \frac{d^2 x}{dt^2} - 2b \frac{dx}{dt} - 2kx = Fe^{-i(\omega t - \pi/2)}, \quad (1.13)$$

which has as a solution a transient piece from Equation 1.11 at a frequency near ω_0 with amplitude dependent on just how the force is initially applied and that dies away with characteristic time τ plus a steady-state part $x_0(\omega)$ using Equation 1.10b and Equation 1.12 that is

$$x(\omega, t) = x_0(\omega) e^{-i\omega t}, \quad \text{with } x_0(\omega) = \frac{iFm^{-1}}{\omega^2 - \omega_0^2 + i\omega\omega_0 Q^{-1}}. \quad (1.14)$$

As is apparent, the force and displacement are out of phase. The transient piece must not be overlooked in any attempt to measure resonances because before it has decayed away, it beats with the steady-state solution, potentially causing somewhat strange results. This will be discussed in more detail later.

Before we look at some of the properties of Equation 1.14, we shall rewrite it in two other forms below. Noting that the average power P dissipated by the resonator is the time average of the force times the velocity (and is not linear in force, displacement or the like so that we cannot simply multiply the right side of Equation 1.14 by the velocity which is the time derivative of the displacement $-i\omega x(\omega, t)$ because this would produce the instantaneous power dissipation which changes sign over the course of one cycle), it is easy to show that

$$P = \frac{1}{2} \operatorname{Re} \left[\frac{\omega}{2\pi} \int_0^{2\pi/\omega} (iFe^{-i\omega t})^\dagger \frac{dx(\omega, t)}{dt} dt \right] = \frac{\operatorname{Re}((iF)^\dagger (-i\omega x_0))}{2} = -\frac{\omega F x_0}{2}, \quad (1.15)$$

where a \dagger (dagger) denotes the complex conjugate and the overall minus sign indicates that the system is dissipating energy. We will eventually be forced to deal with the real and imaginary parts of Equation 1.14. We might as well get it over with now to obtain

$$x_0 = \frac{iF}{m} \frac{\omega^2 - \omega_0^2 - i\omega\omega_0 Q^{-1}}{(\omega^2 - \omega_0^2)^2 + (\omega\omega_0 Q^{-1})^2}. \quad (1.16)$$

If we define θ as

$$\tan \theta = \frac{Q(\omega^2 - \omega_0^2)}{\omega \omega_0} \quad (1.17)$$

and note that

$$|x_0| = \frac{Fm^{-1}}{\left[(\omega^2 - \omega_0^2)^2 + (\omega \omega_0 Q^{-1})^2 \right]^{1/2}}, \quad (1.18)$$

then θ is the phase between force and velocity ($-i\omega x(\omega, t)$) and the displacement is given by

$$x(\omega, t) = |x_0(\omega)| \left[\cos \theta(\omega) + i \sin \theta(\omega) \right] e^{-i\omega t} \quad (1.19)$$

as illustrated in Figure 1.2.

1.4 Dissipation, frequency, and Q

We will now look in detail at the three not-quite-equivalent representations in Equations 1.11, 1.16, and 1.18. The displacement $|x_0|$ is a maximum when the denominator of Equation 1.18 is a minimum. That occurs at

$$\omega = \omega_0 \left(1 - \frac{1}{2Q^2} \right)^{1/2}, \quad (1.20)$$

not quite the frequency of oscillation

$$\omega = \omega_0 \left(1 - \frac{1}{4Q^2} \right)^{1/2} \quad (1.21)$$

given by Equation 1.11. The displacement is exactly out of phase with the force in Equation 1.16 at $\theta=0$, where

$$\omega = \omega_0, \quad (1.22)$$

at which point the resonator is purely dissipative, i.e., the load produced by the resonator has no inertial or spring-like component; the resonator exhibits a purely frictional response where the velocity of the masses is in phase with the force applied. Because of all this, we can also see that it is not exactly clear

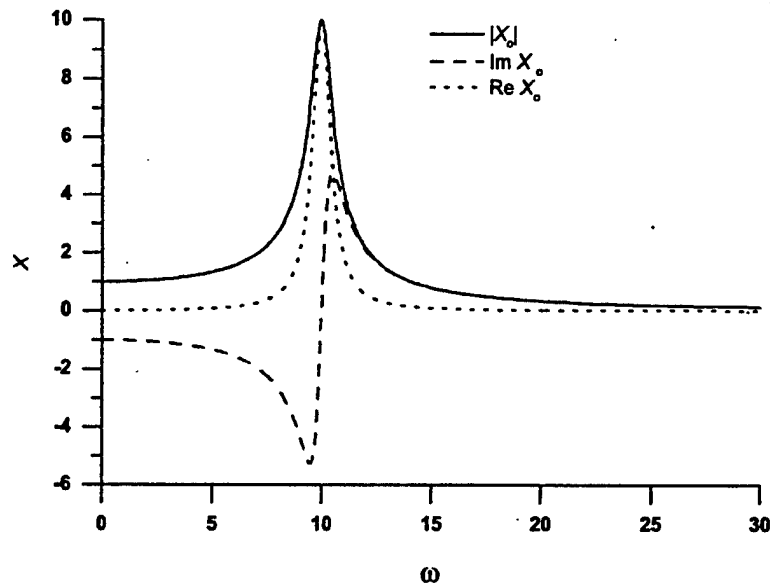


Figure 1.2 The magnitude, and the real and imaginary components of the displacement of the simple driven resonator with $Q=10$ and a resonance frequency $\omega=5\pi$.

what the resonance frequency is. The frequency at which the resonator is purely dissipative (Equation 1.22), the frequency at which the free resonator rings (Equation 1.21), and the frequency at which the displacement is a maximum (Equation 1.20) are all different, with normalized differences of order $1/(2Q^2)$. It might also appear that the best way to determine the frequency is to look for the point where the phase between force and displacement is $\pi/2$, but, unfortunately as we shall see later, this works only if the system has a single resonance. In all of the systems of interest here, there are multiple resonances, so that when attempting to measure the phase shift of some particular mode, the tails of all the other modes affect the phase in a way that is difficult to compute.

The effects of frictional losses not only muddy the meaning of frequency, they also affect the time required to determine the frequency. This is not surprising. Consider what actually happens when an attempt is made to determine the frequency of a sinusoidal wave. In some manner, cycles of mechanical oscillation would be converted to an electrical signal, the cycles of the electrical signal counted, and the time required to make the count measured. Small errors are introduced in the start and stop times. For a simple

digital counter, the error would be one cycle because whatever algorithm is used to determine when a complete cycle ends, it will always have a very difficult time right at the decision point. That is, the stop count trigger might be designed to detect a zero crossing of the waveform, for example. Sometimes the trigger would indicate that zero had not quite been reached when it had, while at other times it would register a crossing just before one occurred. This jitter is the result of real noise. That is, some noise is unavoidable because of the required bandwidth of the trigger circuit. More precisely, the trigger must detect a zero crossing within a time interval very short compared to the period of the wave. If its response time is short, then it must be able to respond to frequencies much higher than that contained in the wave.

Because at best, real noise is white (the noise power present per unit bandwidth, or the noise power spectral density, is independent of frequency), the noise voltage increases with the square root of the bandwidth (power goes like voltage squared), so uniform or white noise power spectral density produces a noise voltage density constant in the square root of the bandwidth. Thus the trigger will always miscount by about one cycle. There is no clever way around this, the limitation is intrinsic to such measurements. Such approaches as digitizing many points on the waveform and then fitting a sine wave to the digitized data might seem to circumvent the count error, but in fact the digitizer bandwidth and the fitting algorithms would all conspire, if correctly analyzed, to generate errors of order one count. Thus the only way to improve the accuracy of a frequency measurement is to measure for a long time, and to improve as much as is practical the signal-to-noise ratio, as will be discussed later—the key point is that the smaller the uncertainties in time and amplitude, the more accurate the measurement of frequency, but the limit is still one count.

Now consider the freely decaying undriven resonator. From Equation 1.11 we see that the resonator completes about Q cycles before it decays away. Thus our accuracy for measurement of frequency is of order $1/Q$. Therefore errors of order $1/Q^2$ are insignificant if Q is reasonably large. However, if $Q=1/2$, the freely decaying oscillator does not complete even one oscillation. If $Q=1/\sqrt{2}$, from Equation 1.18 the maximum amplitude of the driven oscillator occurs at zero frequency. The point here is that, once again, the frequency is really a good number only if the Q is large. For very small (of order unity) Q , the concepts of frequency, Q and, as we shall see later, propagating sound waves in solids are no longer very meaningful, but the response function (Equation 1.18 for example) still tells us everything we need to know.

With what we have covered so far, it is easy to make the transition from a simple discrete mass-spring mechanical resonator to the lumped-constant elastic response of a solid, and then to propagating stress waves. Of course, the main point of this book relates to what happens when we later make the transition back from propagating stress waves to resonances.

Reference

- 1.1 A. Migliori, William M. Visscher, S.E. Brown, Z. Fisk, S.-W. Cheong, B. Allen, E.T. Ahrens, K.A. Kubat-Martin, J.D. Maynard, Y. Huang, D.R. Kirk, K.A. Gillis, H.K. Kim, and M.H.W. Chan, *Phys. Rev. B* **41** (1990) 2098.

CHAPTER 2

PROPAGATING STRESS WAVES

2.1 The wave equation simplified

Propagating stress waves are just elastic waves of various types such as longitudinal, shear, surface and more. Because solids support such a variety of stress waves, and because few of them can produce sound, it is better not to call them sound waves, although such usage is common. There are lots of good references on the theory of propagating stress waves in solids [2.1,2.2]. Let's take advantage of this by developing a really simple, but very intuitive approach to the wave equations in solids, and leave the details for the reader to find elsewhere.

Consider the following simple system where we have a long, thin rod with area A , length L , and density ρ , shown in Figure 2.1. We now consider all the forces acting on the thin plug between x and $x+\Delta x$. Because we are going to study a large chunk of solid, the restoring forces will arise not from little springs, but from the resistance the solid itself presents when any attempt is made to change its shape. We could attempt to change the shape by twisting, stretching, bending, compressing, or some combination of these.

The constants that tell us what the resistance to deformation is are called *elastic moduli*, and there are, in general, lots of them [2.1]. One of the primary applications of RUS is to measure elastic moduli, and so we will, later, discuss

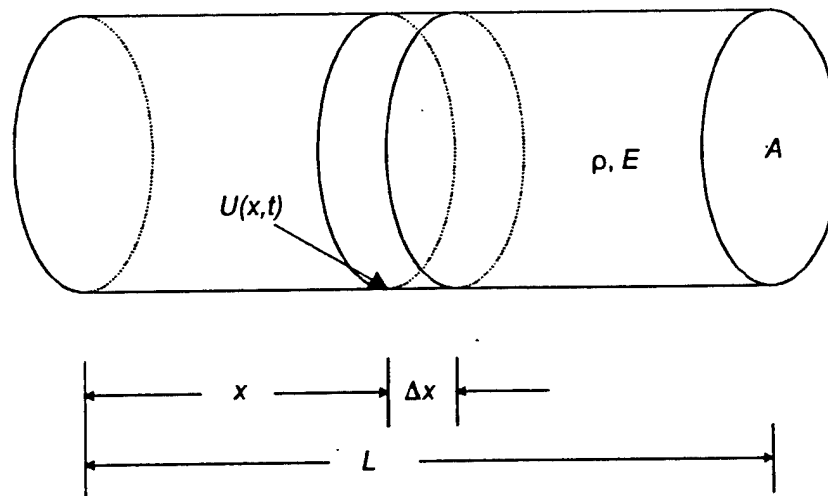


Figure 2.1 A long thin rod of area A , length L , density ρ , and Young's modulus E .

them in detail. For now, let's just consider what happens when we grab the ends of the rod and pull. The rod, of course, gets longer. If we don't stretch it too much, the stretch is elastic. That is, when the force is removed, the rod springs back to its original shape. More importantly, we will treat the restoring force to be such that the response of the rod is linear. This is a very important and precise description that means that the restoring force is exactly proportional to the strain or change in length of the rod. The restoring force is then

$$F_r = -E \frac{\Delta L}{L}, \quad (2.1)$$

where E is Young's modulus and ΔL is the change in length. This is a nice way of defining E because it depends only on the strain $\Delta L/L$ (or dimensionless fractional change in length). For this particular deformation, the bar not only increases in length, but it changes diameter as well. The diameter change is a function of Poisson's ratio σ , where, for a round isotropic solid bar of length L and radius r

$$\sigma = -\frac{L}{r} \frac{dr}{dL}. \quad (2.2)$$

For most materials, a stretched bar decreases in diameter (a classic exception is the cork from a wine bottle—try it yourself—on several samples, of course). It is important for what follows that we can ignore the energy associated with this diameter change. This will work only if the bar is much longer than its diameter. Then the diameter change introduces a negligible contribution to the kinetic and potential energy of the motions we wish to study.

In Figure 2.1, U is a coordinate that measures the displacement of any one particular atom in the bar from its equilibrium position. Each atom in the bar has a coordinate U . As time progresses, the displacement of each atom in the bar from its equilibrium position depends on both time and the position of the atom in the bar. What we are after is a description of that time dependence. To find it, we proceed doggedly along the same lines that we did for the simple free resonator of Chapter 1, concentrating our attention on the motion of the plug. If the plug is very thin, then we can ignore most everything about it except for its mass, and the fact that such quantities as the strain must be continuous across each of its two circular faces. We then write down all the forces acting on it and see what we can do with the resulting equations. The inertial force is

$$F_i = \rho \Delta x A \frac{d^2 U(x, t)}{dt^2}, \quad (2.3)$$

where we note that U for any atom is a function of position x and time t .

If, at the left edge of the plug, the forces present throughout the bar cause

the position of an atom there to change, then the strain at that location is

$$\epsilon_l = \frac{dU(x,t)}{dx}, \quad (2.4)$$

where Equation 2.4 means that the strain at x,t is the variation with respect to x of the equilibrium position $U(x,t)$ of the atoms in the bar. Note that a uniform translation of all the atoms would make $U(x,t)$ constant and hence the strain zero. If the plug is thin then at the right edge of the plug, the strain is

$$\epsilon_r = \frac{dU(x + \Delta x, t)}{dx}. \quad (2.5)$$

Noting that E connects forces and strains as in Equation 2.1, we see that the total of the strain-induced forces p acting on the plug is

$$AE \left(\frac{dU(x + \Delta x, t)}{dx} - \frac{dU(x, t)}{dx} \right) = AE \Delta x \frac{d^2 U(x, t)}{dx^2}. \quad (2.6)$$

When we equate this to the inertial forces in Equation 2.3, we obtain

$$AE \Delta x \frac{d^2 U(x, t)}{dx^2} = A \rho \Delta x \frac{d^2 U(x, t)}{dt^2} \quad (2.7)$$

or

$$\frac{E}{\rho} \frac{d^2 U}{dx^2} = \frac{d^2 U}{dt^2}, \quad (2.8)$$

which is the wave equation for a long, thin rod in which are propagating longitudinal waves (waves that move the atoms parallel to the direction of travel of the wave). This is solved using

$$U(x, t) = U_0 e^{i(kx - \omega t)}, \quad (2.9)$$

where

$$\frac{\omega}{k} = \sqrt{\frac{E}{\rho}} = c_E \quad (2.10)$$

is the Young's modulus sound speed. Note that absent the long, thin rod approximation, the solutions to this problem are not strictly longitudinal plane waves, but waves with complex displacements both parallel and perpendicular

to the direction of propagation. But to the same accuracy required to neglect bulging of the rod in the first place, the wave is a plane, longitudinal one.

2.2 Reflections and resonances

There is another solution to Equation 2.8 obtained by changing the sign of k in Equation 2.9 that corresponds to waves traveling in the opposite direction. Both solutions are linear so that the waves travel undisturbed forever, and linear superpositions of any number of such waves also propagate undisturbed—unless, of course, an obstacle is encountered or some energy loss mechanism introduces attenuation. Let's deal with obstacles first. A very good obstacle is the end of the bar. Obviously the wave heading for it cannot go further, and, with no loss mechanism present just yet, and noting that a whole bunch of things like energy and momentum must be conserved, something very interesting must happen. What happens is that the wave is reflected. Instead, however, of computing what happens for the wave reflecting off the free end of the bar, let's attach another bar of a different material to it as in Figure 2.2. Then later we can make the second material vanish if we like to find out what happens at a free end, and what we need to do mathematically to avoid nonsense when the end vanishes. If we can generate enough equations and waves, we should be able to satisfy the wave equations in both materials as well as a few boundary conditions. Taking $x=0$ at the joint between the two materials, and using a wave of unit amplitude incident on the joint from the left, a wave of amplitude u_r reflected from the joint, and a wave of amplitude u_t transmitted through the joint, we can see that one boundary condition is that the displacements just to the left of the joint must be the same as those just to the right. If this were not so, then the joint would break. Therefore it must be true that (the vertical bar and $x=0$ at its lower right mean that everywhere in the

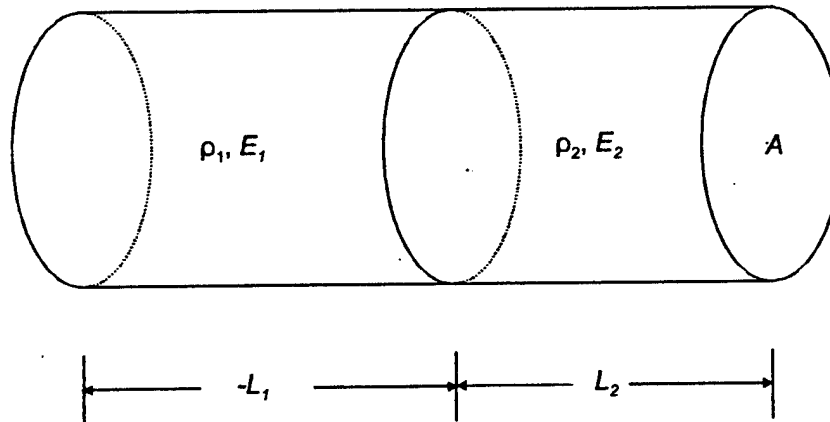


Figure 2.2 A composite oscillator composed of two long, thin rods of different materials and different lengths joined together.

term so marked we substitute $x=0$)

$$e^{i(k_1 x - \omega_1 t)} \Big|_{x=0} + u_r e^{i(-k_1 x - \omega_1 t)} \Big|_{x=0} = u_t e^{i(k_2 x - \omega_2 t)} \Big|_{x=0} \quad (2.11)$$

for all times. Not surprisingly, any possible solution to this equation forces $\omega_1 = \omega_2$, enabling us to factor out all the time dependencies, so that

$$1 + u_r = u_t. \quad (2.12)$$

Another boundary condition must be that the pressure just to the left of the interface equals the pressure just to the right. If not, then we would have a net force acting on an object (the interface) of zero mass, causing infinite accelerations. The pressure is related to the strain via Young's modulus. Therefore

$$E_1 \frac{\partial u_1}{\partial x} \Big|_{x=0} = E_2 \frac{\partial u_2}{\partial x} \Big|_{x=0} \quad (2.13)$$

or, using Equations 2.11 and 2.10

$$\rho_1 c_1 (1 - u_r) = \rho_2 c_2 u_t, \quad (2.14)$$

where $\rho_i c_i$ (remember that we use c_i here as a sound speed) is called the *specific acoustic impedance* of medium i . Using Equations 2.12 and 2.14, we also obtain

$$u_r = \frac{\rho_1 c_1 - \rho_2 c_2}{\rho_2 c_2 + \rho_1 c_1} \quad \text{and} \quad u_t = \frac{2\rho_1 c_1}{\rho_2 c_2 + \rho_1 c_1}, \quad (2.15)$$

a pair of equations that we must be a little careful with for the following reasons. Remember that u_r and u_t are the displacements of the waves, and that we can compute the power density from force and velocity as in Equation 1.15, and noting that the mechanical energy density is positive, we find that the power densities W_i are

$$W_i = \frac{1}{2} \text{Re} \left(E_i \frac{\partial u_i}{\partial x} \frac{\partial u_i}{\partial t} \right) = \frac{1}{2} \omega^2 \rho_i c_i u_i^2, \quad (2.16)$$

so that if $\rho_2 c_2$ is zero, no power is transmitted into medium 2, even though $u_t = 2$, and if $\rho_2 c_2$ is infinite, $u_t = 0$ so no power makes it into medium 2, either. With this caution, we note that for the infinite hard wall ($\rho_2 c_2 = \infty$), all power is reflected but the wave amplitude undergoes a phase reversal ($u_r = -1$), while for a free

surface ($\rho_2 c_2 = 0$) complete reflection occurs with no phase reversal ($u_r = 1$).

Let's now compute the resonances of the composite bar of Figure 2.2. Once again, we can easily make the second medium disappear to obtain the resonances of a uniform bar. Before we begin, let's be a little careful. We are going to do a computation in which there is no dissipation. What we are after are solutions to the equations of motion. The only constraint on these solutions is that they satisfy all the boundary conditions. If we extrapolate from the solutions of the damped mass-and-spring resonator of Chapter 1, we would expect the amplitude of oscillation on resonance to be infinite when driven, but finite at other frequencies. The basic condition for this to occur is as follows. Launch a wave from the left edge of the bar by vibrating that end continuously with constant force at a fixed frequency (and remove medium 2 for the moment, just to make this simpler). Allow the wave to travel to the end of the bar and reflect back. The solutions that we will obtain are characterized by a set of frequencies such that a wave, generated at any one of these special frequencies, arriving back at the left after reflection, is exactly in phase with the wave that started out from there. This means that after the first reflection, the wave leaving the left end is doubled (we are still vibrating the end when the reflection arrives, adding to the vibration). After the second reflection, it triples, etc. We can instantly see that the special frequencies f_n will occur (remember that we have, for the moment, replaced the second medium with vacuum) when

$$f_n = \frac{nc_1}{2L_1}, \quad (2.17)$$

which are just the frequencies at which an integral number of half wavelengths of sound are present in the bar (for $n=1$, this also corresponds to one round trip of a stress wave). If we do not drive the bar then if and only if vibrational energy is already present at one of these special frequencies will the bar continue to ring forever. If we try to drive the bar at some other frequency, and then remove the driving source, does it still ring? The answer is yes, but only at the special (resonant) frequencies, not at the driving frequency. The reason is that the homogeneous (undriven) solutions (just like Equation 1.11 for the simple harmonic oscillator) to the equations of motion take over the instant that the driving force is removed. Because these solutions form a complete set, each described by an f_n , any strain or motion present in the bar at the instant the drive is removed can be described as a sum over this complete set of functions, just like a Fourier transform. The result is that the bar rings with frequency components at all of its resonances. The amplitude of each frequency component is determined by the complete strain and velocity field left in the bar at the instant of drive removal.

To find the resonances of our dissipation-free composite resonator, we proceed in our usual mind-numbingly simple fashion to write down everything we know about the bar. The first thing we know is that in both medium 1 and medium 2 there are waves traveling to the left and waves traveling to the right.

Of these four waves, we are free to pick one amplitude and phase. Thus we have four waves with amplitudes $e^{k_1 x}$, $\alpha_L^1 e^{-k_1 x}$, $\alpha_R^2 e^{k_2 x}$, $\alpha_L^2 e^{-k_2 x}$, where the wave in medium 1 traveling to the right has unit amplitude, R is a wave traveling to the right; L , a wave traveling to the left; k_1 and k_2 , the wave vectors in medium 1 and medium 2; and where we already know that the time dependence of everything is the same so we leave it out.

We also have lots of boundary conditions. At $x=L_1$ and at $x=L_2$ (the ends of the composite bar) the surfaces are free, therefore the strain must be zero there. At the joint ($x=0$), both the displacements and the pressures in the two components must match up. This means that we have four equations for the four unknowns which are α_L^1 , α_R^2 , α_L^2 , and ω .

At the left end we obtain

$$\frac{d}{dx} [e^{k_1 x} + \alpha_L^1 e^{-k_1 x}]_{x=-L_1} = 0 \quad (2.18)$$

or

$$\alpha_L^1 = e^{-2ik_1 L_1}. \quad (2.19)$$

Similarly, at the right end we find that

$$\alpha_L^2 = \alpha_R^2 e^{-2ik_2 L_2}. \quad (2.20)$$

Matching the displacements in the two materials at the joint, and using Equations 2.19 and 2.20 yields

$$\alpha_R^2 = \frac{1 + e^{-2ik_1 L_1}}{1 + e^{-2ik_2 L_2}}, \quad (2.21)$$

while matching the stresses in the materials at the joint and using Equation 2.21 we obtain

$$\frac{\rho_1 c_1}{\rho_2 c_2} = \frac{1 + e^{-2ik_1 L_1}}{1 + e^{-2ik_2 L_2}} \frac{1 - e^{-2ik_2 L_2}}{1 - e^{-2ik_1 L_1}} = \frac{\tan(k_2 L_2)}{\tan(k_1 L_1)}, \quad (2.22)$$

which is an implicit equation for the frequency via Equation 2.10. The two special cases where medium 2 has either zero or infinite specific acoustic impedance force $k_1 L_1$ to be either $n\pi$ or $(n+1/2)\pi$. The resonances occur at

$$\omega_r = n\pi c_1 / L_1 \quad (2.23)$$

for free boundaries, corresponding to an integral number of half wavelengths at resonance (identical to Equation 2.17) or at

$$\omega_r = (n + 1/2)\pi c_1 / L_1, \quad (2.24)$$

corresponding to an odd integral number of quarter-wavelengths at resonance for one fixed (infinite impedance) and one free boundary.

At this point, we have solved enough simple problems to begin to appreciate the difficulties to be encountered when considering a fully three-dimensional mechanical resonator with anisotropic elastic moduli.

References

- 2.1 L.D. Landau and E.M. Lifshitz, *Theory of Elasticity*, 3rd ed. (Pergamon Press, London, 1986).
- 2.2 H.B. Huntington, *The Elastic Constants of Crystals* (Academic Press, London, 1958).

CHAPTER 3

ELASTIC MODULI AND SOLID-BODY RESONANCES

3.1 Elastic moduli of an isotropic solid

An isotropic solid such as ordinary glass needs only two elastic moduli to describe its response to stress. One of the moduli that is customarily quoted to describe such a solid is almost always the shear modulus. The other modulus varies widely and might be Young's modulus, Poisson's ratio, the bulk modulus, or the modulus that determines the longitudinal sound velocity. In what follows, we shall describe these and the more obscure moduli required for single-crystal or other anisotropic solids in a relatively simple way. Common to all the moduli is that any strain introduced in a solid (*strain* is displacement caused by applying a stress) is linearly proportional to the stress (the *stress* is the force per unit area). This obviously requires that whatever stress is applied does not break or permanently bend the object. When this linear relation is valid, the solid obeys Hooke's law just as the spring did in Equation 1.3. However, all real solids dissipate energy when strained so that Hooke's law is not strictly valid. This is an important point, for as relative energy losses increase on application of strain, the elastic moduli commonly used to describe the elastic response of solids become less and less meaningful, just as the frequency of oscillation of the resonator of Figure 1.1 became less well defined as the dissipation increased. Elastic moduli, therefore, are useful only if the dissipation is low. For high-dissipation materials, it is very important to revert to a careful dynamical description of the displacements, forces, and energy. That is, even in high-dissipation materials, if we know the dynamical relationship between stress and strain, we know all we need to know, and we also know that this relationship is not going to be Hooke's law. A related point has to do with the boundary between liquid and solid behavior. This has more to do with patience (the slower things happen, the more liquid-like things are—imagine shear stress applied for 10^9 years to window glass) than with any intrinsic property. For more detail on Hooke's law, moduli in general, and all the messy equations with zillions of subscripts, one can refer to any of several excellent references [3.1,3.2]. What we will do here is develop a useful and simple picture of elastic moduli from an intuitive point of view.

The most important property of the shear modulus is that it describes the stiffness of a solid to forces that do not change its volume. The complication is that there is no unique arrangement of forces that produce a given shear distortion, as depicted in Figure 3.1. The forces on boxes *a* and *c* in Figure 3.1 are called "simple shear," presumably because they are the forces that most readily come to mind, but the forces that generate simple shear also produce a rotation. The forces on *b* produce what is called "pure shear," presumably because they do not introduce a rotation. However, the energy required to

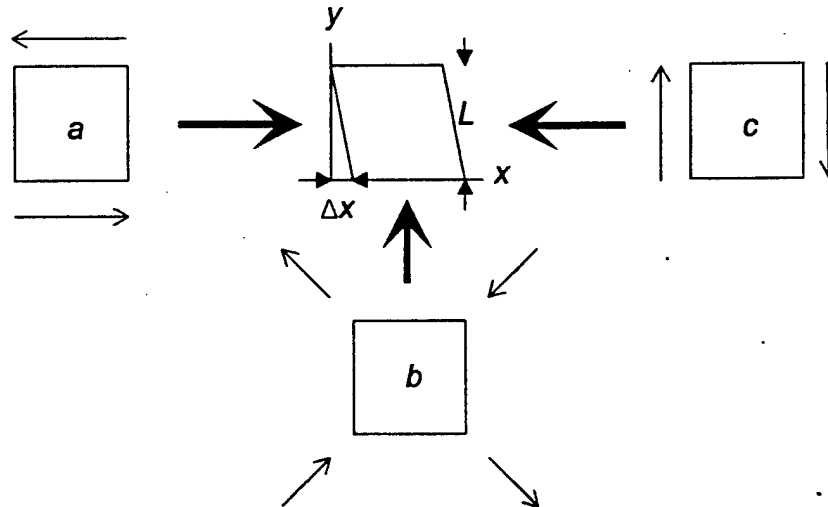


Figure 3.1 Several combinations of forces (light arrows) that lead to the same distortion and that do not change the volume to lowest order in the displacements.

generate each of these distortions must be independent of the arrangement of forces. There is, therefore, a very nice equation lurking here somewhere, if only we can define the shear strain and the stresses that produce it in some invariant manner.

We begin by noting that although the volume of the distorted solid (only the base of the solid is shown) in Figure 3.1 is evidently less than the original solid with a square base of side L , the change in volume ΔA is second-order in Δx and is found from the following:

$$\frac{\Delta A}{A} = \frac{L^2 - L(L^2 - \Delta x^2)^{1/2}}{L^2} \approx \frac{1}{2} \left(\frac{\Delta x}{L} \right)^2. \quad (3.1)$$

To be precise, we compute in Equation 3.1 the change in area of the base of the solid after applying shear forces. As can be seen from Equation 3.1, if the object is sheared a small amount (typically $\Delta x/L = 10^{-4}$ before a solid is permanently changed), then the fractional change in area is dependent on that small amount squared (this is what is meant by second-order), a quantity that can safely be neglected in what follows.

To understand how to express the shear quantitatively and independent of the arrangement of forces, we imagine a sheet of graph paper glued to a table. On it are drawn x and y axes. We place a thick square of clear plastic with side L on the graph paper. With a felt tipped pen, put lots of dots on the

plastic. Each dot i has a coordinate $U_x(i)$, $U_y(i)$. Now apply any of the forces as shown in Figure 3.1 so that shear strain distorts the clear plastic square with the dots on it. The graph paper underneath is still the same shape as it was, but almost all of the dots on the plastic are displaced. They now have new coordinates $U_x^{new}(i)$, $U_y^{new}(i)$.

If we arrange the plastic so that the bottom edge, still of length L , lies exactly where it was before application of the shear stress, then the shear strain is the change in the x displacement from point $i-1$ to point i divided by the difference in y coordinates between the points or

$$\epsilon_{xy} = \frac{\Delta U_x^{new}(i) - \Delta U_x^{new}(i-1)}{y(i) - y(i-1)} = \frac{\partial U_x(i)}{\partial y}, \quad (3.2)$$

where $\Delta U_x^{new}(i) = U_x^{new}(i) - U_x(i)$.

Now align the left edge of the distorted square with the y axis. The shape and the distortions are the same, but there is no x displacement of any point so that Equation 3.2 would yield zero for the strain. But there is another quantity

$$\epsilon_{yx} = \frac{\Delta U_y^{new}(i) - \Delta U_y^{new}(i-1)}{x(i) - x(i-1)} = \frac{\partial U_y(i)}{\partial x} \quad (3.3)$$

that, when evaluated yields the same numerical answer as Equation 3.2. Finally, consider the intermediate case of Figure 3.2. The sheared square is aligned with the graph paper so that the angle between the y axis and the vertical edge is the same as the angle between the x axis and the horizontal edge. If we were to use Equation 3.2 or Equation 3.3 to measure the shear strain, we would get half the correct answer. It should be clear that if the shear distortion is small, rotation of the final shape between alignment of the vertical edge with the y axis through alignment of the horizontal edge with the x axis always leaves unchanged the sum of ϵ_{xy} and ϵ_{yx} . This is a simple description of how the strain tensor transforms under rotation (the strain has two indices, so it is a tensor, and we just rotated the strained object through three positions to see what the general trend is). Averaging Equations 3.2 and 3.3, we obtain what is called the symmetrized strain

$$\epsilon_{12} = \frac{1}{2} \left(\frac{\partial U_1}{\partial x_2} + \frac{\partial U_2}{\partial x_1} \right) \quad (3.4)$$

where we note that the subscripts 1,2,3 refer to x , y , z axes, respectively (so x_2 is the y coordinate), and we arbitrarily use the order for the subscripts as shown. We now have a quantity that is invariant with respect to the force arrangement and final axes of the distorted solid. Because this strain resulted from many different force arrangements or stresses, there also must be a nice

way of defining the stress, with the identical properties under rotation that the strain has. If we define the stress σ_{12} to be half the force per unit area on the 1 (or x) face applied in the 2 (or y) direction plus half the force per unit area on the 2 face applied in the 1 direction, then it too transforms nicely under rotation. The relation between shear stress and shear strain in the linear, dissipation-free limit for an isotropic solid is

$$\sigma_{ij} = \mu \epsilon_{ij}; \quad i \neq j, \quad (3.5)$$

where μ is the shear modulus. Using the same notation, there is also a strain

$$\epsilon_{11} = \frac{1}{2} \left(\frac{\partial U_1}{\partial x_1} + \frac{\partial U_1}{\partial x_1} \right) = \frac{\partial U_1}{\partial x_1}, \quad (3.6)$$

which is the change in the 1 component of the displacement in the 1-direction. This strain does change the volume of the solid to first order in the strain and is a compressive-like change. Consider what happens if compressive-like forces are applied. We hedged the description of these forces by describing them as compressive-like rather than compressive because the strains that result when something is squeezed rather than sheared depend very much on the conditions at the surfaces not being squeezed. This is obvious if we think of compressing the ends of a solid cylinder. We know intuitively that it gets fatter as it decreases in length (except for some very strange "solids" like the cork of a wine bottle, which actually shrinks in diameter—you may have to try

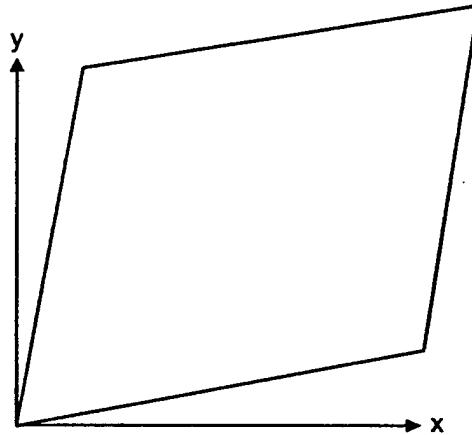


Figure 3.2 A different orientation of the shear-distorted square on the original axes.

several corks before finding one that does this, but it is certainly in the interest of science to do the experiment). If we were to support the walls of our cylindrical solid within a perfectly rigid and perfectly slippery cylindrical bore, then if it were compressed on its ends, it could not grow fatter and it would seem very much stiffer than when its cylindrical surfaces are free.

For an elastically isotropic solid such as unstrained window glass, all the elastic properties can be described with two parameters. One parameter is the already discussed shear modulus μ . To understand what the other parameter is, let's define a quantity λ and attempt to set up the stress-strain equation for window glass. Historically, λ and μ are called Lamé coefficients. Our sample will be a cylinder whose axis lies along the 1 direction. We apply a stress σ_{11} along the 1 direction, producing a shortening or strain ϵ_{11} of the cylinder but also a stress σ_{22} on the walls of our perfectly rigid and slippery supporting cylinder normal to its walls such that

$$\sigma_{22} = \sigma_{33} = \lambda \epsilon_{11}. \quad (3.7)$$

If one thinks of hydraulic fluid, compressing a hydraulic cylinder on its ends transmits pressure to the walls of the cylinder. Solids do this also, but not in exactly the same way: the pressure is less on the wall than the end because the solid supports some shear forces.

What we are after is a constant that we will call c_{11} , such that

$$\sigma_{11} = c_{11} \epsilon_{11} \quad \text{if} \quad \epsilon_{22} = \epsilon_{33} = 0. \quad (3.8)$$

We could have just as well applied the stress along the 2 or the 3 axis, and by symmetry, all the relevant equations and constants must be the same. If we do this we find that

$$\begin{pmatrix} \sigma_{11} \\ \sigma_{22} \\ \sigma_{33} \end{pmatrix} = \begin{pmatrix} c_{11} & \lambda & \lambda \\ \lambda & c_{11} & \lambda \\ \lambda & \lambda & c_{11} \end{pmatrix} \begin{pmatrix} \epsilon_{11} \\ \epsilon_{22} \\ \epsilon_{33} \end{pmatrix}, \quad (3.9)$$

where the usual matrix multiplication rule holds. The rule is that the top row of the 3×3 matrix multiplies, element by corresponding element, the elements of the column of strains to obtain the first equation

$$\sigma_{11} = c_{11} \epsilon_{11} + \lambda \epsilon_{22} + \lambda \epsilon_{33}, \quad (3.10)$$

while the other two equations contained in this shorthand method of Equation 3.9 called matrix notation are obtained by multiplying the second row times the strain column and then the third row times the strain column. These three equations describe the response of our chunk of glass to stresses applied

normal to the three orthogonal axes. But we defined λ first, we threw in c_{11} to get to here, and previously we decided that we needed only two elastic parameters, one of which is μ . Therefore λ and μ must determine c_{11} . The key is Equation 3.9. We will magically set up a situation in which no volume change occurs, undo the shorthand of Equation 3.9, and then note that the ratio between stress and strain with no volume change is μ . For no volume change to lowest order in the strain (you can work this out easily for yourself), we somehow force, using glue and baling wire,

$$\epsilon_{22} = \epsilon_{33} \text{ and } \epsilon_{11} = -(\epsilon_{22} + \epsilon_{33}) \quad (3.11)$$

so that from Equation 3.9 we obtain

$$\sigma_{11} = (c_{11} - \lambda)\epsilon_{11} = 2\mu\epsilon_{11} \text{ or } c_{11} = \lambda + 2\mu, \quad (3.12)$$

where the factor of 2 comes from a careful look at the square labeled b in Figure 3.1. That square undergoes a pure shear distortion in which the strain where it is stretched is exactly opposite to the strain where it is compressed. But this is only one of the two shears that need be applied to get strains of Equation 3.11. If we apply two compressions at right angles to each other along the 2 and 3 directions, then we must have two dilations, one for each compression, linearly added along the 1 direction to achieve pure shear. This is exactly what we did to get to Equation 3.12, and, of course, the modulus that controls this is still just μ , but now it is one μ for each of the two orthogonal shears.

The shear strains are usually separated by using two sets of matrix equations. One is

$$\begin{pmatrix} \sigma_{12} \\ \sigma_{13} \\ \sigma_{23} \end{pmatrix} = \begin{pmatrix} \mu & 0 & 0 \\ 0 & \mu & 0 \\ 0 & 0 & \mu \end{pmatrix} \begin{pmatrix} \epsilon_{12} \\ \epsilon_{13} \\ \epsilon_{23} \end{pmatrix}, \quad (3.13)$$

and the other is exactly the same but with every pair of subscripts reversed. As can be seen from Equation 3.13, each shear strain is related to a single shear stress, nothing mixes as in Equation 3.9.

The combination of Equation 3.9, Equation 3.13, and the symmetry relative of Equation 3.13 produces a matrix equation between 9 stresses and 9 strains. There would appear to be 81 different elastic constants possible. Each elastic constant would have four indices, written as λ_{abcd} . However, the matrix is symmetric (the triangle of moduli above the diagonal is mirror-reflected across the diagonal to obtain the moduli below) for the same reasons that make Figure 3.1 work, so this reduces the possible number to 45. Better still, a strain such as ϵ_{21} is physically identical to ϵ_{12} (but $\sigma_{21} \neq \sigma_{12}$ if external whole-body torques are present such as might be produced by a magnetic field). Once

again, Figure 3.1 shows this to be true because we were able to take the exact same physical distortion and make it either all ϵ_{21} or all ϵ_{12} . This effectively reduces the problem to a relation between 6 stresses and 6 strains. As the matrix relating these must be symmetric, the worst possible case would have 21 different elastic moduli. Solids do indeed exist with this many moduli, and are the most anisotropic it is possible to be without a magnetic field applied. In the next section we examine the elastic properties of anisotropic solids, the most interesting of which are crystals.

Before we do this however, let's briefly examine the propagation of waves in solids. The presence of both longitudinal and shear strains causes some odd complications in the solution of the wave equations for a solid. These equations are

$$\rho \frac{\partial^2 u_i}{\partial t^2} = \sum_{k,j,m} \lambda_{ikjm} \frac{\partial^2 u_m}{\partial x_k \partial x_j}, \quad (3.14)$$

where we find solutions of the form

$$u_i(\bar{x}, t) = u_i^0 e^{i(k_1 x_1 + k_2 x_2 + k_3 x_3 - \omega t)}; \quad \bar{x} = (x_1, x_2, x_3), \quad (3.15)$$

giving

$$\left| \sum_{q,j} \lambda_{iqjm} k_q k_j - \rho \omega^2 \delta_{im} \right| = 0, \quad (3.16)$$

where $\delta_{im}=0$ for $i \neq m$ and $\delta_{im}=1$ for $i=m$ and where the vertical bars indicate the determinant. This set of equations is cubic in ω^2 and is called the dispersion equation. In other than isotropic solids, it has lots of solutions and produces lots of strange waves in which the direction of motion of the atoms is neither parallel nor perpendicular to the direction of propagation. Even in an isotropic solid, a corollary of the possibility of propagating more than one type of wave is that the reflection of a pure longitudinal wave impinging on a plane boundary at other than normal incidence produces both a longitudinal and a shear reflected wave, a consequence of Equation 3.16 and the necessity of keeping both the parallel and perpendicular components of the stress zero at a free surface [3.1].

The combination of these strange waves and the equally strange reflection problem at an interface make it extremely difficult to develop an intuitive set of solutions for solids resonating in three dimensions. Such solids bulge, stretch and shear in non negligible complex ways that turn out to be very important because these resonances, discussed exhaustively in Chapter 4, enable determination of all the moduli in a single measurement of the frequency response of a simply shaped mechanical resonator.

3.2 Elastic moduli of crystalline and anisotropic materials

Things can get very messy, very quickly in studying the elastic properties of crystals. To defend against messiness we can use obscurity in the following way. Everywhere that we see a pair of subscripts, we substitute a single one according to the following magic decoder table

11 \Rightarrow 1 22 \Rightarrow 2 33 \Rightarrow 3

23 \Rightarrow 4 13 \Rightarrow 5 12 \Rightarrow 6

and of course by symmetry

32 \Rightarrow 4 31 \Rightarrow 5 21 \Rightarrow 6.

Using this notation, and the symmetries described earlier, we can write the whole thing as a rather curious 6 x 6 matrix equation that is useful but a little dangerous because it does not really have the proper number of elements to enable the very simple manipulations under a rotation of axes that are possible for its full 9 x 9 parent. With this caution, we write

$$\begin{pmatrix} \sigma_1 \\ \sigma_2 \\ \sigma_3 \\ \sigma_4 \\ \sigma_5 \\ \sigma_6 \end{pmatrix} = \begin{pmatrix} c_{11} & c_{12} & c_{13} & c_{14} & c_{15} & c_{16} \\ c_{12} & c_{22} & c_{23} & c_{24} & c_{25} & c_{26} \\ c_{13} & c_{23} & c_{33} & c_{34} & c_{35} & c_{36} \\ c_{14} & c_{24} & c_{34} & c_{44} & c_{45} & c_{46} \\ c_{15} & c_{25} & c_{35} & c_{45} & c_{55} & c_{56} \\ c_{16} & c_{26} & c_{36} & c_{46} & c_{56} & c_{66} \end{pmatrix} \begin{pmatrix} \epsilon_1 \\ \epsilon_2 \\ \epsilon_3 \\ \epsilon_4 \\ \epsilon_5 \\ \epsilon_6 \end{pmatrix} \quad (3.17)$$

which is Hooke's law for a triclinic crystal, with 21 different elastic moduli. For such a low-symmetry crystal, there are several interesting and difficult to assimilate properties relating to stress waves and elasticity, covered extensively by other authors [3.1,3.2]. These properties relate to what is called *internal strain* in which an external stress produces strains in the unit cell of the crystal different from the macroscopic strain. This can occur if, for example, a lattice has at each lattice point a group of atoms (the basis) with a symmetry different from that of the lattice. A simplified example might consist of a pair of atoms aligned in no particular direction at each point of a cubic lattice. Compressional stress, shown in Figure 3.3, along one of the cubic axes rotates the atom pair, generating a strain in the unit cell not parallel to the strain of the body as a whole.

In high-symmetry crystals, however, there are certain special directions and types of waves in which the polarization (motion of the atoms) is either

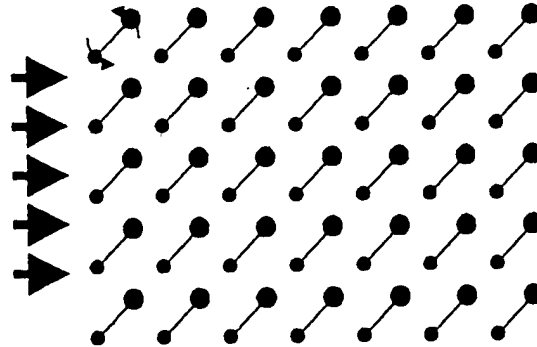


Figure 3.3 A 2-D representation of what happens when a stress is applied to a crystal in which the symmetry of the unit cell (basis) is different from the symmetry of the lattice. In this case the lattice is square and has mirror symmetry about both the vertical and horizontal axes.

parallel (longitudinal) or perpendicular (shear) to the direction of propagation, just like in an isotropic solid. These include cubic, hexagonal, tetragonal, and orthorhombic crystal symmetries. All are characterized by having three mutually perpendicular planes of mirror symmetry, so that any compressive stress applied perpendicular to a mirror symmetry plane cannot produce a lateral (or shear) strain because the crystal doesn't know which way to go.

The matrix of elastic moduli that makes this happen has zeros in all the positions that would mix shear strains applied in different directions. The general form of the elastic modulus matrix for these special higher symmetries is very easy to manipulate and looks like

$$\begin{pmatrix} c_{11} & c_{12} & c_{13} & 0 & 0 & 0 \\ c_{12} & c_{22} & c_{23} & 0 & 0 & 0 \\ c_{13} & c_{23} & c_{33} & 0 & 0 & 0 \\ 0 & 0 & 0 & c_{44} & 0 & 0 \\ 0 & 0 & 0 & 0 & c_{55} & 0 \\ 0 & 0 & 0 & 0 & 0 & c_{66} \end{pmatrix}$$

for an orthorhombic crystal. There are 9 different moduli for an orthorhombic crystal.

If we increase the symmetry to tetragonal, with the 1 axis and 2 axis interchangeable, then only 6 moduli are needed with $c_{44}=c_{55}$, $c_{13}=c_{23}$ and $c_{11}=c_{22}$.

Increasing symmetry further to hexagonal forces the additional constraint that $(c_{11}-c_{12})/2=c_{66}$, requiring now only 5 moduli and with the surprising property

[3.1] that the speed of waves propagating in the 1-2 plane is independent of direction.

Increasing symmetry further to cubic destroys this shear wave isotropy, but leaves only three independent moduli, c_{11} , c_{12} , and c_{44} . For a cubic system, Hooke's law is

$$\begin{pmatrix} \sigma_1 \\ \sigma_2 \\ \sigma_3 \\ \sigma_4 \\ \sigma_5 \\ \sigma_6 \end{pmatrix} = \begin{pmatrix} c_{11} & c_{12} & c_{12} & 0 & 0 & 0 \\ c_{12} & c_{11} & c_{12} & 0 & 0 & 0 \\ c_{12} & c_{12} & c_{11} & 0 & 0 & 0 \\ 0 & 0 & 0 & c_{44} & 0 & 0 \\ 0 & 0 & 0 & 0 & c_{44} & 0 \\ 0 & 0 & 0 & 0 & 0 & c_{44} \end{pmatrix} \begin{pmatrix} \epsilon_1 \\ \epsilon_2 \\ \epsilon_3 \\ \epsilon_4 \\ \epsilon_5 \\ \epsilon_6 \end{pmatrix} \quad (3.18)$$

where we left the independent moduli with the customary subscripts for a cubic system.

Finally, increasing symmetry to isotropic leaves only two independent moduli because the isotropy present only in one plane for a hexagonal system is now present in all directions, making $(c_{11}-c_{12})/2=c_{44}$.

Because this last case is a little too simple to illustrate the uses of Equation 3.17, which itself is too complicated to be transparent, let's use Equation 3.18 to compute Young's modulus, Poisson's ratio, and the bulk modulus for a cubic crystal in order to get a feel for what to do with such matrix equations.

Young's modulus is the measure of stiffness when a long thin bar is stretched. The only stress is applied at the ends. If the long axis of the bar is parallel to the 1 axis, then $\sigma_i=0$ and $\sigma_1 \neq 0$ for $i=2-6$. Then Equation 3.18 becomes

$$\begin{aligned} \sigma_1 &= c_{11}\epsilon_1 + c_{12}(\epsilon_2 + \epsilon_3) \\ 0 &= c_{12}(\epsilon_1 + \epsilon_3) + c_{11}\epsilon_2 \\ 0 &= c_{12}(\epsilon_1 + \epsilon_2) + c_{11}\epsilon_3 \\ 0 &= c_{44}\epsilon_4 = c_{55}\epsilon_5 = c_{66}\epsilon_6, \end{aligned} \quad (3.19)$$

and we see immediately that $\epsilon_2=\epsilon_3$ and

$$E = \frac{\sigma_1}{\epsilon_1} = c_{11} - \frac{2c_{12}^2}{c_{11} + c_{12}}, \quad (3.20)$$

where Young's modulus E is the ratio of stress to strain on the ends of the bar.

Poisson's ratio σ is the negative of the ratio of the strain in the 2 direction to the strain in the 1 direction and is

$$\sigma = \frac{1}{1 + (c_{11}/c_{12})} \quad (3.21)$$

Note that if the shear moduli (c_{44} and $(c_{11}-c_{12})/2$) are zero and the material is isotropic, then from Equations 3.11 and 3.21, $\sigma=1/2$, which is Poisson's ratio for an ordinary liquid.

To compute the bulk modulus, we set $\sigma_1=\sigma_2=\sigma_3$, which is what we would get if we applied hydrostatic pressure to the solid. The shear stresses are of course zero. By symmetry, and inspection, we see immediately that $\epsilon_1=\epsilon_2=\epsilon_3$. We have, then, only one independent equation to solve. It is

$$\frac{\sigma_1}{\epsilon_1} = c_{11} + 2c_{12} \quad (3.22)$$

Noting that the bulk modulus B is the ratio of pressure to the fractional volume change, that the pressure is simply σ_1 and that the fractional volume change is just the sum of the three normal strains such that $\Delta V=3\epsilon_1$ (the volume change is proportional to the product of the three strained dimensions, which, to first order, is just related to the sum of the three strains—higher-order terms in the strain are neglected), we find that

$$B = \frac{\sigma_1}{\Delta V} = \frac{c_{11} + 2c_{12}}{3} \quad (3.23)$$

for a cubic crystal.

3.3 The problem with 3-D resonances in solids

As suggested above, the resonances of three-dimensional solids with small aspect ratios (all the dimensions are comparable) are very difficult to compute. To see why, let's set up a problem that John William Strutt, Baron Rayleigh [3.3, 3.4], worked on during his honeymoon. We will not solve the problem here, nor will we follow through with Rayleigh's approximate solution because, as Rayleigh notes "A more complete solution...has been given by Pochhammer..." [3.3]. Furthermore, in Chapter 4, we will set up all the machinery to solve this and other nasty problems to as high an accuracy as anyone might care about (6 digits is easy on a PC).

The problem here is to redo the computation that resulted in Equation 2.8 but now with a short, fat rod. When such a rod resonates, it alternately bulges and constricts at some places along its length but not at others. The places where it constricts have high strains and act as spring-like regions, while the places where it does not constrict have low strains and are mass-like, in

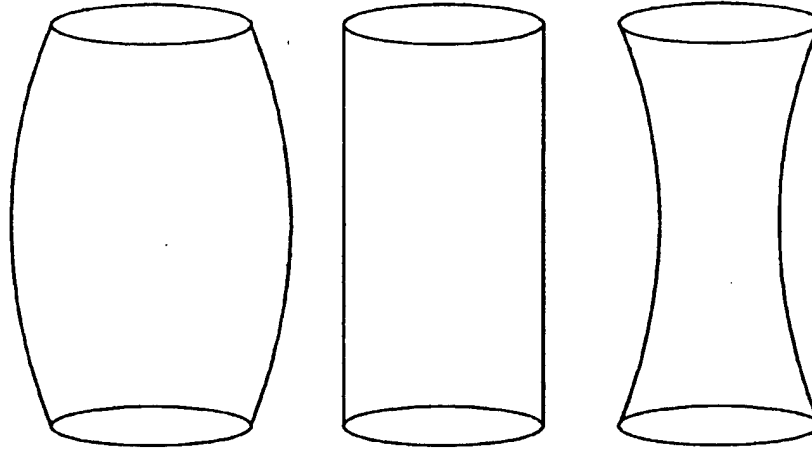


Figure 3.4 A short, fat bar undergoing a longitudinal oscillation. As the bar oscillates between being longer and shorter, it also alternately bulges and constricts near its middle.

analogy with the mass-spring system of Chapter 1. Stresses along the bar associated with longitudinal oscillations, combined with the effect of the Lamé coefficient λ , cause lateral strains as depicted in Figure 3.4. The problem is to understand completely all the strains and velocities of all the material in the bar. This is very difficult to do simply. What we can do is use σ to estimate the lateral motion of the bar, include this lateral motion in the total kinetic energy, and then estimate the frequency shift. This approach relies on an oscillator alternating between brief moments when everything is stopped (think of the top of a pendulum's swing) to brief moments when all that moves is moving at its peak speed and no strains are present. Because we are assuming that no dissipation is present, the total kinetic energy at peak speeds equals the total potential energy when things stop briefly at the end of a swing. If in the case of a short fat bar, more mass moves than in a long thin bar of equal mass, then the increase in effective moving mass reduces the frequency of oscillation. Noting that the lateral strain should be about

$$\varepsilon_2(x) = \sigma \varepsilon_1(x) \quad (3.24)$$

where σ is Poisson's ratio, and that a reasonable approximation is to take

$$\varepsilon_1(x) = \varepsilon_1 \sin \frac{n\pi x}{L}, \quad (3.25)$$

we can see that if T is the kinetic energy, the rod has a length L , radius R and we are looking at the n th resonance, the kinetic energy will increase something

like

$$\frac{\Delta T}{T} = \left(\frac{\pi n \sigma R}{2L} \right)^2 \quad (3.26)$$

and therefore the fractional resonance frequency shift will be half of Equation 3.26 (from a Taylor series expansion of a square root). The n comes in because as the number of modes goes up, each section of the bar between nodes looks like an even shorter, fatter bar, and we must remember that the longitudinal displacement is the integral over the length of the bar, $\sim \epsilon_1 L$. The new contribution to the moving mass arises from the radial displacement, $\epsilon_6 R$. The velocities are just the frequency times these displacements, and the kinetic energy is proportional to the velocities, and therefore the displacements, squared. The actual numerical factor $(\pi/2)^2$ in front of Equation 3.26 comes about when one assumes sinusoidal strain and integrates the strains between nodes. But remember that the lateral strain along the axis of the bar is zero, unlike the outer surface, so that in fact the ends of the bar do not remain flat. Thus the motion is much more complex than Equations 3.24 and 3.25 imply, making the above only an approximate guess. It is an accurate computation of this additional complexity that makes 3-D resonances very difficult to compute.

3.4 Surface waves and resonances

In Chapter 2 we discussed the computation of resonances in simple situations where the problem could be considered one-dimensional. In the previous section, we expanded on this to indicate how the 1-D approximation fails by considering a rod whose length was not much greater than its diameter. We found that lateral motions that accompanied longitudinal ones drastically increased the complexity of the problem. Such motions added substantial shear strains to the longitudinal ones, destroying the plane waves that were crucial to the solution of the 1-D solid resonator. In considering the general problem of solid-body resonances, which are solutions to equations based on Equation 3.16 coupled with appropriate boundary conditions, we note that it is possible for the components of k to be real in all directions or real in one direction and imaginary in others. In the directions in which k is imaginary, the motions are damped because the factor $e^{i(kz)} = e^{-kz}$ that describes the spatial dependence of the amplitude of oscillation decays exponentially. Careful analysis reveals that in many circumstances, no dissipation accompanies such an effect, and such waves are called *evanescent*. An optical analog occurs in prisms. Total internal reflection of a wave at an interior surface of the prism is caused primarily by the fact that the spacing of the electric field antinodes on the glass side of the glass-vacuum interface, reduced by the index of refraction, does not correspond to the projection of the electric field antinodes of a wave propagating at some angle in vacuum at that frequency. This occurs only when the already shortened wavelength (because the index of refraction is greater than unity) of the waves in glass strikes the surface at less than the critical

(Brewster) angle. If the angle is greater than the critical one, light can exit the glass at a smaller angle than the light coming from inside the glass so that the spacing between antinodes coming from inside the glass, projected on the glass surface, equals the spacing of antinodes of the wave exiting the glass at a smaller angle projected on the glass. At incident angles smaller than this, even a wave parallel to the glass surface has too long a wavelength to match the inside wave, no energy escapes and total internal reflection occurs. However, for such a case, within a few wavelengths of the glass surface on the vacuum side, there is a considerable oscillating electric field that decays exponentially away from the glass.

Such effects also occur with stress waves and are responsible for so-called *surface acoustic waves* (SAWs) or *Rayleigh waves*. We end this chapter with a discussion of surface waves and their importance to the completeness of any computation of the normal modes of vibration of a solid body. Because this topic is addressed completely elsewhere [3.1], once again, we shall only set up the problem and discuss the solutions.

Consider a semi-infinite (it extends toward $z=-\infty$) isotropic solid whose surface is perpendicular to the z axis in which a shear oscillating disturbance is generated by touching the surface along a line and shaking it perpendicular to the line. Such a force will produce compressional forces parallel to the surface as well as shear forces. The shear forces will launch shear waves radiating perpendicular to the surface, with the directional dependence of the amplitude such that the intensity decreases from a maximum perpendicular to the surface to zero parallel to the surface. Longitudinal waves will be launched with maximum amplitude parallel to the surface, decaying to zero perpendicular to it. Now add a second line of force, identical and parallel to the first and exactly out of phase with it, but less than a half-wavelength of shear waves (and hence considerably less than a half-wavelength of compressional waves as well) away, and then many more, all equally spaced. The longitudinal wave antinode leaving the first line arrives at the second line not in phase with the second line of force, so partial cancellation occurs. This gets worse and worse as the waves from all the sources add up in what amounts to a random way, eventually killing the wave altogether. The shear waves also cancel because the sources are out of phase and so no net shear of the surface occurs, or, alternately, the shear waves leaving the surface are made up of equal numbers of waves with one phase and equal numbers with exactly opposite phase so they all cancel. The end result is that such an array of sources produces no propagating waves of any sort. Well, not quite. There is a magic frequency such that for any given spacing of out-of-phase force producers, a wave will launch parallel to the surface, composed of complex elliptical motion of the atoms, that is neither shear nor longitudinal and that moves at slightly less than the shear wave speed. This surface wave is of great technological importance, being used for radio-frequency narrow-band filters, surface crack detection and more. The equations that are responsible for this waveguide-like propagating mode begin with the equations for longitudinal and shear waves that are a simplification of the general wave equation for a solid, Equation 3.14, such that

$$\frac{\partial^2 \bar{u}_L}{\partial t^2} = c_L^2 \nabla^2 u_L \text{ and } \frac{\partial^2 \bar{u}_s}{\partial t^2} = c_s^2 \nabla^2 u_s, \quad (3.27)$$

where the general displacement vector u can be composed of components of shear waves (s) or longitudinal waves (L). Noting that we use the appropriate part of Equation 3.27 for the shear component and the appropriate part for the longitudinal component, we can drop subscripts and suppose that a wave exists that looks like

$$u = e^{i(kx - \omega t)} f(z), \quad (3.28)$$

which is a wave propagating along the x direction and damped in the z direction. The function $f(z)$ must be determined using Equation 3.27 and will be a solution of

$$\frac{\partial^2 f(z)}{\partial z^2} = \left(k^2 - \frac{\omega^2}{c^2} \right) f(z), \quad (3.29)$$

which has solutions that are either simple longitudinal or shear waves if the quantity in parentheses in Equation 3.29 is negative or

$$f(z) = A \exp \left(\left(k^2 - \frac{\omega^2}{c^2} \right)^{1/2} z \right) \quad (3.30)$$

if the quantity is positive. In Equation 3.30, the exponent is a positive real number multiplied by $(-1)^{1/4} = (1+i)/\sqrt{2}$. Very carefully applying the free-surface boundary conditions to both solutions of Equation 3.30 (one for shear, one for longitudinal) we would find that the shear and longitudinal components are no longer independently propagating waves, but are coupled. The very odd (SAW) waves that result have displacements that decay to zero away from the surface with a characteristic length slightly less than the shear wavelength, and travel with a speed slightly lower than the shear wave speed (from about 87.4% of the shear speed for $\sigma=0$ to about 95.5% of the shear speed for $\sigma=1/2$).

If instead of a semi-infinite material we studied a thick sheet, we can find even more waves. For example, a symmetric set of surface boundary conditions would produce Lamb waves [3.5], similar to Rayleigh waves but symmetric about the midplane of the sheet. The danger illustrated by the existence of Rayleigh waves, Lamb waves and more is that one's intuition very definitely is not adequate to guess at the various resonances of a solid. To be precise, let's reconsider the short, fat cylinder. In order to compute the resonances, we had to guess what they looked like first. At low frequencies this was sort of okay because the longitudinal resonances were weakly modified as

in Equation 3.26. But at higher frequencies, the simple longitudinal modes disappear completely, replaced by stranger modes in which all the motion is either radial or longitudinal. The higher-order shear and torsional modes are mostly what we imagine, but then a whole set of surface-like waves forms resonances close to the shear resonances where most of the motion is confined, not surprisingly, to the surface. Other modes come in too in which most of the motion occurs in the interior and the unmoving surface sheath acts much like a rigid boundary, rather than the free boundary we are mostly dealing with in this book, recovering longitudinal modes that are governed by the longitudinal wave speed [$c_L = (c_{11}/\rho)^{1/2}$] and behave nearly like what intuition suggests (almost plane waves, but with very little surface motion) if the wavelength is much less than the diameter. Now try thinking about what happens in a cube. The best approach is not to. Just use the procedures in the next chapter in which one does not have to construct a hypothesis of what the resonances look like, thereby eliminating the danger of missing a possible mode. Math and computers simply find them all!

We end this chapter with a thought about phonons. Phonons are quantized vibrations in solids that account for much of their microscopic acoustic and optical properties. In a simple description of the equations of motion for such phonons, the solid is considered as an array of atoms. The equations are solved by introducing Born-von Karman, or periodic, boundary conditions [3.6] that effectively wrap the solid around to form a ring in each of three dimensions (it works if you don't think too hard about it). The phonons are the normal modes of vibration (or resonances) of the solid. For a typical chunk of matter that one might study in the laboratory, this approach gets most of the 10^{23} or so phonon modes correctly. But the first few dozen or so (the very lowest modes, or equivalently the very bottom of the phonon dispersion curve) are wrong. The reasons are described above, and the correct solution is given in Chapter 4.

References

- 3.1 L.D. Landau and E.M. Lifshitz, *Theory of Elasticity*, 3rd ed. (Pergamon Press, London, 1986).
- 3.2 H.B. Huntington, *The Elastic Constants of Crystals* (Academic Press, London, 1958).
- 3.3 John William Strutt, Baron Rayleigh, *The Theory of Sound*, 2nd ed. (Macmillan, London, 1894).
- 3.4 A. E. H. Love, *A Treatise on the Mathematical Theory of Elasticity*, 4th ed. (Dover Publications, New York, 1944).
- 3.5 Horace Lamb, *The Dynamical Theory of Sound*, 2nd ed. (Dover Publications, New York, 1960).
- 3.6 N.W. Ashcroft and N.D. Mermin, *Solid State Physics* (Holt, Rinehart and Winston, Philadelphia, 1976), Chapter 22.

Resonant Ultrasound Spectroscopy

A. Migliori, T.W. Darling, J.P. Baiardo, F. Freibert, Los Alamos National Laboratory, Los Alamos, NM 87545

Introduction

Resonant ultrasound spectroscopy (RUS) uses the mechanical resonances of small cylindrical, rectangular parallelepiped or spherical samples to extract the elastic modulus tensor. Although many resonance techniques employing roughly similar measurement approaches have been used, RUS is qualitatively different in that the measurements and analysis are highly redundant, and when applied to samples of near unity aspect ratio, sensitive to all the components of the elastic tensor. The technique has been applied to samples with the minimum elastic symmetry (triclinic), though it is most often, and most easily, applied to systems of rhombohedral or higher symmetry. Key to the use of this technique is the ability of modern personal computers to perform calculations nearly as rapidly as the supercomputers of recent years. For example, a modern RUS analysis would require approximately 2 hours/iteration on the first IBM PC, 1 second on the first Cray, and 1.2 seconds on a 600 MHz Pentium III. Instrumentation has also benefitted by modern integrated electronics, which enable digital signal processing algorithms to acquire RUS data at rates orders of magnitude higher than in the past, limited only by information theory. In this chapter we describe how RUS works, when to use it, how to make and analyze measurements, and the limitations and accuracy of the technique[1].

I. Motivation for the use of resonances to study elastic moduli.

Why are resonance techniques so valuable for the measurement of elastic moduli? To answer this question, we examine various ultrasonic measuring schemes. Although there are many direct and indirect methods of measuring the elastic modulus tensor[2], consider here for the purposes of comparison, only those methods that use a macroscopic stimulus to launch macroscopic mechanical vibrations into the sample to be studied. We shall call such techniques ultrasonic, even though they may be used at audible or sub-audible frequencies. Our intent is to exclude coherent optical or neutron based techniques, as these are typically special purpose, expensive, and imprecise, though of great power at high frequencies or when the entire acoustic dispersion curve is required. We also exclude static mechanical techniques as well because they require massive hardware normally only found in metallurgy laboratories. This leaves us with a large group of methods in which some sort of ultrasonic transducer drives a sample and another transducer detects the vibrations.

At one extreme of the ultrasonic measurement techniques are pulse-based methods such as pulse-echo, and the like. In a pure pulse-echo system, an acoustic pulse is generated via a single sharp electrical impulse to a non-resonant transducer. The pulse is spatially localized and, absent dispersion, travels without change in shape to a receiving transducer. The time of flight (and distance traveled) determine the sound speed, and hence the elastic moduli. The key measurement is of time, a quantity usually taken to be (with frequency) the most accurately measurable of physical quantities.

The other extreme involves purely resonant schemes such as RUS. A few comparisons can be made immediately between resonance and pulsed techniques. Because resonances are standing waves, there is no propagation involved. Therefore scattering of the ultrasonic beam is not an issue,

and a resonance measurement, via the width of the resonance, measures only the true thermodynamic dissipation, but only for frequencies that correspond to sample resonances. In contrast, pulse methods can see a decrease in the reflected signal from transducer bond material, non-parallelism of the transmit and receive transducers, and scattering of the beam from inhomogeneities of all sorts within the sample, but can measure attenuation at any frequency. Pulse methods can also usually only measure one component of the elastic tensor at a time because only time of flight, a scalar, is measured. Resonances can, in principle measure all components in a single measurement setup. However, pulsed methods require only a pocket calculator to reduce data, while RUS requires a complex algorithm and very large computing capacity(a modern PC is just fine). Accuracy is another factor. In round-robin measurements at LANL, NIST (Boulder), UCLA, and UW Milwaukee,[3] it has been established that RUS has the highest absolute accuracy of any routine elastic modulus measurement technique-an ordinary RUS measurement can achieve 0.05% absolute accuracy, while very carefully set up pulse echo overlap measurements appear to produce errors nearer 0.1%. Finally, we mention that resonance methods can acquire data on very small samples because the frequencies involved are easily accessible (a 1 mm cube might have its first resonance at 1MHz), while pulsed methods must have extreme bandwidth. To get the time of flight to 0.1% on a 1mm sample requires 1GHz receiver bandwidth, causing large increases in system noise. In fact noise and the ability to obtain all moduli simultaneously on small samples are the key reasons for using RUS.

Before we describe measurement techniques and compare signal/noise of pulse and resonance methods, it is important to understand some intrinsic limitations of both techniques. In a resonance measurement, mechanical resonances are measured using any of a variety of techniques. The shape of an ordinary linear mechanical resonance of a solid object is Lorentzian. That is, if e.g. the displacement $x(\omega, t)$ of the system being measured is plotted against frequency, the (complex) result approximates a Lorentzian function if the resonance is narrow and well separated from others, such that

$$x(\omega, t) = x_0(\omega)e^{-i\omega t}, \text{ with } x_0(\omega) = \frac{iA\omega^2 Q^{-1}}{\omega^2 - \omega_0^2 + i\omega\omega_0 Q^{-1}}. \quad (1)$$

A is the peak response and Q is a measure of how narrow the resonance is, or equivalently, how long the resonator would ring after excitation such that

$$Q = \frac{\omega_0 \tau_l}{2} = \frac{f}{\Delta f_l} \quad (2)$$

where τ_l is the characteristic time for exponential decay of displacement (or force, velocity, or any other quantity that is *linearly* related to the forces present). Δf_l is the full width at half maximum of the real part of the displacement. Note that if power (proportional to the square of a linear response such as displacement) is measured, the decay time is half that in Eq. 2, so that

$$Q = \omega_0 \tau_p = \frac{f}{\Delta f_p} \quad (3)$$

where Δf_p is the full width at half maximum of the power driving the resonator. If the *magnitude* (or amplitude) of the displacement is measured as with a meter not sensitive to phase, then the

appropriate Δf , for determination of Q is the full width measured at $1/\sqrt{2}$ of the peak height.

The angular frequency $\omega_r = 2\pi f$ is in fact complex such that

$$\omega_r = \omega_0 \left(1 - \frac{1}{4Q^2} \right)^{1/2} + i\tau \text{ where } \tau = \frac{2Q}{\omega_0}. \quad (4)$$

The effect of Eq. 1 and Eq. 4 is that there is a very real ambiguity in the resonance frequency of a damped oscillator (and, hence, also in the meaning of elastic moduli in dissipative systems). The real part of Eq 4., the frequency where the phase is zero (ω_0), and the frequency of maximum

amplitude $\omega_0 \left(1 - \frac{1}{2Q^2} \right)^{1/2}$ all differ by of order $1/Q^2$. This is a measure of the intrinsic

impreciseness of the frequency (or elastic moduli) of a dissipative system where one cannot measure for an arbitrarily long time because the oscillations disappear as heat. However, in a measurement, it is the ability to measure accurately the width of the resonance that determines how well frequency is determined. This in turn depends on the signal/noise ratio, R_n . The *fractional accuracy* of a resonance frequency measurement is limited to of order $1/(R_n Q)$ up to the point where the error is less than $1/Q^2$, whereupon the intrinsic effects of Eq. 4 take over. It is not uncommon to reach this limit. The exactly equivalent property for a pulse system is the decay time for the pulse. One can only measure the travel time of the pulse for a time τ that is the same as the τ for the resonator (longer, and it disappears). Because the pulse itself must have a finite width (of order $1/f$ where f is the driving frequency, even if only a single cycle pulse is used), the maximum accuracy of a pulse echo measurement is of order $1/(R_n \omega \tau)$, the same as for a resonance measurement.

In any measurement, noise intrudes, and because the noise voltage in most well designed electronic systems is proportional to the square root of the bandwidth, we can estimate the relative R_n of resonant and pulse measurements. Consider a sample with a Q of 10^4 and 10 resonances of average frequency f near MHz required to determine the moduli using RUS. The pulse echo measurement will require a receiver bandwidth of order 10^9 Hz, with peak power levels of 500W to obtain accuracy similar to the RUS measurement at continuous power levels of 5mW. The RUS measurement must be made on all the modes, so the receive bandwidth is the number of modes m times the width of each mode, or about m/fQ . The pulse measurement is over in 1 pass of the pulse through the sample, thus at a pulse repetition rate of 10 KHz (limited by the decay time) the duty cycle is a maximum of 0.01 because the transit time is of order $1/f = 1\mu s$, in contrast to a duty cycle of unity for RUS. Using these figures, RUS measurements have a voltage R_n conservatively estimated at 200 times greater than pulse methods for the same average power into the sample, shown in Table I.

Surprisingly, there is a continuum of methods in between RUS and pulse techniques, with corresponding changes in R_n . For example, a modification of the pulse technique, called pulse-echo overlap, is to drive the system with a tone burst of moderately well defined frequency. That is, a few tens of cycles of sinusoidal excitation are applied to a resonant transmitting transducer, with a similar receiver. The received pulse is overlapped (mixed) with the transmitted pulse in such a way that they are out of phase, and the product of the voltage of the two pulses is averaged over the length of the pulse. When they are exactly out of phase, a null is achieved. With such a system, neither the time of flight nor the frequency are measured precisely, but a combination of both. That is, the system looks for information over a *window* of time (the pulse width) within a *band* of frequencies (if the

pulse has n cycles in it, the band of frequencies is f/n wide centered about f to obtain sound speed. The measurement has an uncertainty of order the pulse period in absolute arrival time (sound speed) but a precision that is determined by the signal/noise (s/n) ratio in a narrow band about the pulse center frequency. That is, the time precision is $1/(R_n f)$, and R_n is improved because the receiver bandwidth is reduced to f/n . Absolute accuracy, however is limited to of order the pulse width divided by the transit time.

A resonance method can also be modified toward behaving partly like a pulse method by driving the system with an impulse with frequency components that span all the resonances desired. A Fourier transform of the received signal provides the resonances. Because the receiver bandwidth must now span all the resonances, R_n is degraded over the swept frequency pure resonant measurement, but acquisition time is reduced, and signal averaging can recover some of the degraded R_n . There are very good reasons to use impulse RUS and pulse-echo-overlap, especially if R_n is already excellent in the former, or if absolute accuracy is not so important, only precisely determined relative changes (for example, with temperature), as in the latter.

II Measurements.

Although impulse RUS measurements are used, swept frequency methods are the technique of choice at low temperatures in small samples where power dissipation matters, where absolute accuracy is important, and where small changes must be detected. Analysis is the same for both techniques, so our discussion will mainly center around swept-frequency RUS. A complete swept-frequency RUS measurement system block diagram is shown in Fig. 1. We describe below desirable features of each of the blocks[4].

A. Samples.

Although any shaped sample resonator can, in principle, be used, there are very substantial savings in computation time if rectangular parallelepiped resonators(RPR)[5], spherical, or cylindrical ones are used, (the time savings is less with cylinders). An RPR sample is generally prepared with the edges parallel to crystallographic symmetry directions for rhombohedral, orthorhombic, tetragonal, hexagonal, or cubic samples. For cylinders, only the axis can be matched to sample symmetry. RUS is rarely used for samples of lower symmetry, and for isotropic samples, alignment is irrelevant. For the higher symmetries, it is also desirable to make the RP sample have different-length edges to prevent resonances from being degenerate, and therefore hard to detect.

The accuracy with which the sample is prepared determines the overall accuracy of the measurement because sample geometry is the most difficult quantity in the measurement to control, and all the analysis codes assume accurate sample geometry. A 0.1% error in parallelism, perpendicularity, or measured length translates to a similar-sized error in elastic moduli, and, worse still, makes the codes unable to compute accurately frequencies that match the measured ones because the mathematical model does not correspond to the sample shape. Many methods are appropriate for preparation of RPR samples, including the use of a conventional surface grinder, precision saws and manual polishing systems. A typical arrangement for polishing is illustrated in Fig.2. This arrangement is very inexpensive, while easily producing samples with geometry accurate to 0.1%.

Measurements on single crystals of rhombohedral or higher symmetry usually requires orientation of the sample crystallographic axes with the edges of the RPR, primarily because greater

accuracy can be achieved if one needs only to compute elastic moduli, not orientation as well. Although computations of orientation from resonance data have been successful, more resonances are required for an accurate modulus determination if more parameters must be fit. X-ray diffraction, etching to reveal facets, or simply planes appearing during crystal growth have all been used successfully to orient samples.

B. Transducers.

The transducers used for RUS measurements are generally somewhat unusual. The reason relates to the requirement for free-surface boundary conditions required for the computation of elastic moduli from frequencies, discussed below. Typically, and unlike all other ultrasonic techniques, RUS transducers are most frequently designed to make dry point contact with the sample. For rectangular parallelepiped samples, this means the corners touch, very lightly (0.01N is a typical force). Because of the weak, bond-free contact, there are no transducer corrections required under most circumstances (long buffer rods are an exception). A typical commercially available arrangement is shown in Fig. 3. The sample shown is about 3mm on the longest edge, and is mounted to PZT-5A transducers 0.1mm thick by 1.5 mm diam. The transducers are, in turn, fixed with epoxy to a DuPont Kapton film 12 mm diam by 25 μ m thick, coated with Au to create a ground plane and one electrical contact, shown in Fig. 4. There is a 1mm diam hole through the Kapton film that enables the sample to make direct contact with the transducer element. The drive or receive electrical contact is made from a 1mm wide, 20mm long strip of the same Au coated Kapton used to support the transducer. Although this transducer arrangement is only a typical example, it exhibits several important features. In order to ensure that the resonances of the transducers are not mistaken for sample resonances, the backload, often single crystal diamond, is chosen to push the first transducer resonance above 4 Mhz. The epoxy bonds and Kapton film provide some damping so that the transducer resonance Q is low, of order 10, thereby making it so broad that it usually appears only as a background behind the sample resonances which are usually much sharper. The large metallized ground plane disk and the shell to which this assembly is epoxied to provide extremely good shielding so that the drive electrical signal that leaks to the receiver electrical contact is much less than the noise floor, even in extremely low noise systems.

C. Electronics

The necessity to preserve a good approximation to free-surface boundary conditions requires weak coupling between transducers and sample. The weak coupling also tends to preserve the Q so that when attenuation studies are performed, the measured Q corresponds to that of the sample, not the equipment for samples with a Q less than 10^5 and a mass less than 0.5 g or so. Larger samples are heavier, couple better, and so their Q is degraded because excessive energy leaks into the transducer assemblies.

To capture the weakest signals produced requires considerable care in electronics design. Modern operational amplifiers with very low noise should be used in the preamplifiers. For frequencies above 2MHz or so, bipolar designs work best, yielding noise values of $2\text{nV}/\sqrt{\text{Hz}}$ and $1\text{Pa}/\sqrt{\text{Hz}}$. For lower frequencies, JFET devices can attain values of $6\text{nV}/\sqrt{\text{Hz}}$ and $0.005\text{Pa}/\sqrt{\text{Hz}}$ down to about 30kHz. Below this frequency, typical charge-sensitive preamp designs become more difficult to stabilize, degrading noise, but samples are larger and produce stronger signals, so that in practice there is no real difficulty in making RUS measurements from 20 MHz to nearly DC. Int

the more typical frequency range around 1 MHz, the capacitance of the cable connecting the receive transducer to the preamplifier, especially in a cryogenic or elevated temperature system, requires that charge sensitive preamps be used. For example, typical transducer capacitance may be of order 5 pF, while 2 m of coaxial cable may have a capacitance of 100 pF. Thus the voltage developed at the end of the cable is reduced by a factor of 20 if no care is taken to eliminate this. A conventional approach is to use a "guard" actively driven, but at 1 MHz, this is nearly impossible. A more viable approach is to use a charge amplifier, shown in Fig. 5. Operation, described in the figure caption, is dependent upon the impedance of R being much higher than that of C at the frequencies of interest. R is necessary to prevent the Op-Amp from integrating offset currents until it saturates, thus the charge amplifier only works at frequencies above $1/RC$. Below this frequency, the gain of the preamplifier drops. More importantly, the low frequency noise voltage is determined by the thermal noise of R. For a typical RUS system, C may be about 10 pF and R 1 M Ω . Thus the low frequency limit begins near 100 kHz. Much below this, the noise output goes from of order $2 \text{ nV}/\sqrt{\text{Hz}}$ derived from the Op-amp to $(4Rk_bT)^{1/2}$ or about $127 \text{ nV}/\sqrt{\text{Hz}}$. The total noise from the resistor is confined to frequencies below a few hundred kHz, but is about 80 μV RMS. This is to be compared with the total noise above this of about 8 μV RMS. The net result is that unless the remainder of the electronics is not sensitive to noise below a few hundred kHz, serious degradation of the system performance occurs. The way around this at low frequencies for conventional laboratory instrumentation is to use a lock-in amplifier. A lock-in amplifier is sensitive to frequencies within about $1/RC$ of the excitation frequency, and so only sees a narrow slice of the noise, near the signal frequency. Lock-ins have been successfully used for RUS measurements, but there are several drawbacks. One is that a lock-in uses homodyne detection. That is, the signal is mixed (or multiplied with) a reference signal of the same frequency. The result is a DC component with its attendant sensitivity to drift of the electronics with temperature, and with the requirement that one must wait several RC time constants for the signal to stabilize. A better approach, used in a commercial RUS system[6], is to use a heterodyne system. In a heterodyne system, a reference signal is generated at a fixed difference frequency above or below the frequency used to drive the transducer. When mixed and low-pass filtered with the signal from the receive transducer preamp, the desired resonance information appears at the fixed difference frequency (the intermediate frequency or IF), typically 1 kHz. Digital synthesizers can easily generate the required frequencies rapidly, and, by using a clever bit of digital signal processing, shown in Fig. 6, the waiting time for RC filters is reduced. This is not a minor point of convenience. Because the accurate measurement of a resonance may require sweeping through 1000 frequencies around the center frequency, and there may be dozens of frequencies to be measured, an RUS measurement, especially in a cryogenic system where liquid He costs are important, can take a long time. Anything to reduce this time will minimize temperature drifts during a scan and minimize cryogen costs. Remembering that in almost any measurement performed today, the final result needs to be inside a computer, somewhere along the line an A/D converter is needed. By driving that A/D at an integer multiple of four times the IF frequency and digitizing for an integral number of IF cycles, shown in Fig. 6, we can obtain the amplitude of the IF signal. This amplitude, obtained by summing the product of the digitized values multiplied by a similarly digitized reference signal at the IF frequency, is independent of exactly when the digitizer starts, and so the system "settles" instantly, instead of having to wait many RC time constants for stabilization, as in a lock-in. By choosing the number of cycles, we also limit the noise bandwidth. For example, using 10 cycles of a 1 kHz IF takes 10 ms, and produces a noise bandwidth of $1/10\text{ms}=100 \text{ Hz}$. Thus such a system picks up noise within only 100 Hz of the actual transducer

drive signal, just what is needed. In addition, because the IF reference signal has been digitized, at a rate of four times an integer multiple of its frequency, it is easy to digitally phase shift this signal and redo the detection process, thereby producing both in-phase and quadrature signals, important for data analysis, especially for obtaining Q . All of these operations can be performed before the result ever gets to the data acquisition computer. The net result is that a modern RUS system with only 10V drive to the transducer, such as that produced by DRS, is thermal noise limited, at least an order of magnitude faster than a lock-in based system, and can achieve a dynamic range of 117dB (the difference in amplitude between the smallest and largest resonance that can be detected is about 1000).

D. Apparatus

RUS systems are compact and easy to build, lending themselves to temperature controlled environments. There are too many strategies for constructing such systems to describe them here, but suffice it to say that RUS measurements have been performed from 1825K to 0.25K[7], and at pressures up to 150 Bar[8]. It is important, however, to note that the gas surrounding the sample has some effect[5]. At atmospheric pressure, and with strong signals that might be obtained from a 3mm sample, there is usually little to worry about. At elevated pressures, the gas shifts the resonances in ways not fully explored, but which affect accuracy. That is, the gas couples to the sample, reducing the perfection of free surface boundary conditions.

At lower temperatures and with sub-millimeter samples, resonances in the gas can intrude. This is mitigated by reducing the experimental pressure to of order 100 Pa. Much further reduction will reduce thermal coupling of the sample to the temperature controlled environment, thereby making accurate determination of sample temperature impossible. Such effects are particularly troublesome if radioactive heating is involved, as it is with U, Pu and other radioisotopes.

E. Data

The frequencies of a set of resonances are used to determine elastic moduli, while the widths of those resonances determine ultrasonic attenuation. With in-phase and quadrature data available, one can perform accurate least-squares fits to each resonance to determine these quantities. If this is done, the frequency of a resonance with a Q of 10^4 can be determined to better than a part in 10^6 . Such precision can be of great value in studies at very low temperature, or to determine the temperature variation of moduli over very small temperature ranges (the temperature derivative of the elastic moduli of a metal at ambient temperature can usually be determined to an accuracy of 0.3% by measuring over only a 10K range). However, the absolute determination of moduli is limited by sample geometry, so that determining resonance frequencies to about 0.05% is often entirely adequate. This is most easily done by adjusting the phase of a resonance to zero and simply selecting the peak position. The reason for adjusting the phase is that the in-phase component is visually about 1/3 the width of the amplitude or the quadrature component.

Having acquired data this way, in preparation for the computer-intensive determination of moduli, some important considerations remain. One is that if the sample has, for example, six independent elastic moduli, then it is nearly certain that many more than six resonances are required for a determination of the moduli. The reason, illustrated in Table II below, is that many of the lower lying resonances are determined by the same shear modulus. Thus, for example, the first two

resonances may depend only on c_{44} , hence measurement of these two resonances gives information about only one modulus. Typically about three times as many resonances as moduli are required. With present RUS instrumentation, data on modes up to about 10MHz is reliable, but limitations of the fitting procedures mean that only the first 40-50 lines are useful for determining quantitative elastic constants.

Another consideration is that occasionally a resonance will be missed. The causes are: 1) the geometry and exact mounting position of the sample are such that the resonance displacement is zero or along a direction that the transducer is not sensitive to. Note that this will occur much more frequently if the sample makes contact with the transducers at a high symmetry point such as the center of a face instead of the low-symmetry points at the corners. The cure is often as easy as simply remounting or rotating the sample. 2) The shape of the sample produces degeneracies. For example, a perfect cube or cylinder of an isotropic material will have many pairs of resonances that have the same frequencies. Even in anisotropic materials, accidental degeneracies can occur for samples not cut as cubes. If a degeneracy occurs, then a mode will be missed and the data fed to the computation program will have a critical flaw. Re-cutting the sample may help, but one can often guess at a degeneracy or missing mode by using the analysis program to "predict". We illustrate this in Table II. It is difficult to give recipes for finding missing modes, but the better the initial guesses for the moduli, the easier this is to do. Unfortunately, some experience is required.

F. Results

RUS has been used to great effect in physics, materials science and metallurgy. It has also been used successfully for non-destructive testing [9,10] by matching the characteristics of the resonances of a manufactured component with those of a known good one, an extensive area beyond the scope of this chapter. What is important here are modulus measurements. In Fig. 7 we present a typical (neither best nor worst) example of a set of RUS measurements on Be. The data are for a polycrystal and a single crystal sample. Be is hexagonal, with five independent elastic moduli. The polycrystal sample, will however, exhibit only two. Directly comparable between the two samples is the bulk modulus, which is expected to be identical. These data confirm this experimentally with very high accuracy. The computations were done with the Los Alamos code, with output discussed at length elsewhere. Of particular note here is a discussion of error bars. At the bottom of Fig. 7 is a matrix that describes degradation of the fit for a 2% change in chi-square, the conventionally defined goodness-of-fit parameter. The 2% is the result of much experience by us [11] as to how well we can actually determine fit degradation, and is, therefore, somewhat arbitrary, but it does reflect many direct comparisons of RUS measurements on the same material using differently sized and shaped samples. This matrix has columns that correspond to the free elastic moduli in the order they appear at the top of the fits. The entries in the columns are determined by the principle radii of curvature of the error function used in the fit. These radii are not in the directions of elastic moduli. That is, the n -dimensional bowl formed by the error function (where n is the number of free moduli) has principle curvatures directed along vectors determined by the sample shape and moduli, and these are not along elastic modulus axes. Thus the fit may be degraded much less if several moduli are varied in such a way as to track along a principle curvature direction than if a single modulus is varied. The entries in the matrix describe how much degradation occurs in the moduli as combinations of moduli are varied along the principle curvature vectors. Only the few shallowest directions (rows) are computed. The effect is as follows. Looking at the hexagonal fit on the right

of Fig.7, we see that the largest entry in the first column is 0.1%, and this is our estimated error in c_{33} . Similarly, in the second column, the largest entry is 7.55%, and this is our estimated error for c_{23} . Note that although this error appears large, c_{23} is small, so the effect on the sound speeds and bulk modulus, all of which use c_{23} in combination with c_{33} , is small. Finally, the errors for the shear moduli are always small, such as the 0.02% estimated error for c_{44} . None of these errors are closely related to the 0.132% RMS error for the fit, and it is very wrong to use this RMS error as an error bar for moduli. The principle curvatures of the error function *must* be accounted for!

III. Computation of resonances and data analysis.

The aim of any spectroscopic technique is to extract information about the sample from the experimentally determined spectrum. In the case of RUS, the information we seek is the linear, second order elastic tensor. As described above, RUS is used to measure the normal frequencies of vibration of the object under study. These normal frequencies of vibration depend on the physical symmetry of the object (i.e., its shape), the symmetry of its elastic tensor (which is determined by the crystal symmetry of the object -cubic, orthorhombic, isotropic, etc.), its density, and dimensions. Although RUS has proved quite successful in extracting the elastic moduli of many new materials, including single crystal as well as polycrystalline samples, successful implementation depends on a number of key factors, one of which is the ability to perform very complex computations of resonances.

From a computational perspective, the most important requirement is the availability of a rapid and robust algorithm to compute the normal frequencies of the object given its dimensions, density and elastic moduli. One can then employ this 'forward' computation as part of another algorithm to find a "best fit" (in a least-squares sense) between the observed and calculated spectrum with the elastic moduli as the variable parameters. A variety of such minimization algorithms using different methods to search the parameter space are available. Energy minimization for the forward computation and the Levenberg-Marquardt process [11] for the fitting algorithm were chosen for application to RUS by us and have been incorporated into the Los Alamos code, application of which was briefly described in the previous section.

In this section we summarize the essential features of Lagrangian energy minimization techniques for the computation of resonances, and highlight the features necessary for the effective implementation of the 'inverse' problem-namely, extraction of the elastic moduli from experimentally measured resonance frequencies.

A. Formulation of the problem: Lagrangian minimization

Because a complete analytical solution for the computation of the free vibrations of solids does not exist, one must rely on available approximate methods. Of these, the most frequently invoked computational approaches have been finite-element methods and energy minimization techniques. Finite-element methods rely on balancing the forces on a differential volume element and calculating its response. This requires complete knowledge of the relevant forces acting on a particular volume element and the forms of solutions that are possible in order to prevent the accidental exclusion of one or more modes. Energy minimization methods on the other hand, determine the minimum energy, and thus the equilibrium, configuration for the object. They are therefore independent of specific solutions, and produce energy minima that automatically determine all vibrational modes.

Of the energy minimization techniques, that of Lagrangian minimization is the one most used in the analysis of RUS data, having the further advantage of speed because, unlike finite element methods, Lagrangian minimization computational time goes roughly as the area of an object, not the volume. Using modern PC's, for example, the lowest 40 (approximately) modes may be determined in several seconds; equivalent solutions by finite-element methods would require at least several minutes.

The stationary solutions of the mechanical Lagrangian for an elastic solid are precisely the free vibrations of the body – this amounts to finding the solutions to the elastic wave equation with free surface boundary conditions; Migliori and Sarrao [1] give a complete treatment of this. The essential procedure begins with an arbitrarily shaped object whose volume, V , is bounded by its free surface, S – a critical point that needs to be remembered when making a measurement. The Lagrangian is given by

$$L = \int_V (KE - PE) dV \quad (3.1)$$

where KE is the kinetic energy density

$$KE = \frac{1}{2} \sum_i \rho \omega^2 u_i^2 \quad (3.2)$$

and PE is the potential energy density

$$PE = \frac{1}{2} \sum_{i,j,k,l} c_{ijkl} \frac{\partial u_i}{\partial x_j} \frac{\partial u_k}{\partial x_l} \quad (3.3)$$

Here, u_i is the i th component of the displacement vector, ω , the angular frequency, derives from the assumption of harmonic time dependence (i.e., $u(t) = u_0 e^{i\omega t}$), c_{ijkl} is a component of the elastic tensor, and ρ is the density. Except where noted, subscripts i, j , etc., refer to Cartesian coordinates and run from 1 to 3.

To find the minimum of the Lagrangian (and hence the desired equilibrium configuration of the system) we calculate the differential of L as a function of δu , the arbitrary variation of u in V and on S . Substituting Eqs. 3.2 - 3.3 in Eq. 3.1, calculating the differentials, keeping only first order terms, and finally integrating by parts yields

$$\delta L = \int_V \left\{ \sum_i \left[\rho \omega^2 u_i - \sum_{j,k,l} c_{ijkl} \frac{\partial^2 u_k}{\partial x_j \partial x_l} \right] \delta u_i \right\} dV - \int_S \left\{ \sum_i \left[\sum_{j,k,l} \bar{n}_j c_{ijkl} \frac{\partial u_k}{\partial x_l} \right] \delta u_i \right\} dS. \quad (3.4)$$

Because δu_i is arbitrary in V and on S , the values of u_i that correspond to stationary points of L , that is $\delta L = 0$, must satisfy the condition that both terms in square brackets in Eq. 3.4 are zero. Setting the first such term equal to zero yields the elastic wave equation. The second square bracketed term is

an expression of free-surface boundary conditions (and it also describes the surface traction); \bar{n}_j is

the unit vector normal to S . For a free body, the latter term sums to zero and need not be considered further. Thus, the set of u_i that satisfies the above conditions are precisely those displacements that correspond to ω being one of a discrete set of normal mode frequencies of (free) vibration of the system. This simple result suggests that the normal vibrations of an object may be calculated by applying a variational method to determine both the normal mode frequencies and the description of the physical oscillations. The Rayleigh-Ritz method provides the means to do this.

B. Application of the Rayleigh-Ritz (R-R) variational method.

The implementation of such an approach involves expansion of the u_i in a complete set of basis functions, substituting that expression into Eq. 3.1 and carrying out the process outlined above to find the stationary points of the Lagrangian. One arrives at an equation similar to Eq. 3.4 in which the u_i are replaced by expansions in basis functions. This procedure yields an eigenvalue problem easily solved by common techniques.

Let $\{\phi_\lambda\}$ be a complete set of (R) functions suitable for expansion of the displacement vector u_i , thus,

$$u_i = \sum_{\lambda} a_{i\lambda} \phi_{\lambda} = (\cdots a_{i\lambda} \cdots)_i (\cdots \phi_{\lambda} \cdots)^T = \mathbf{a}_i \boldsymbol{\phi}^T. \quad (3.5)$$

Eq. 3.5 expresses the expansion in matrix notation, where the $()$ term is a product of a row vector with a column vector; and as usual, $()^T$ denotes the transpose, and $()_i$ denotes the i th row of the \mathbf{a} matrix. Substituting this expression for u_i in Eq. 3.1 (via Eqs. 3.2 - 3.3) eventually gives

$$L = \frac{1}{2} (\omega^2 \mathbf{a}^T \mathbf{E} \mathbf{a} - \mathbf{a}^T \boldsymbol{\Gamma} \mathbf{a}). \quad (3.6)$$

Here, \mathbf{E} and $\boldsymbol{\Gamma}$ are matrices whose order is determined by R , the number of basis functions, and whose elements are given by

$$E_{\lambda\lambda'} = \delta_{\lambda\lambda'} \int_V \phi_{\lambda} \rho \phi_{\lambda'} dV \quad (3.7a)$$

and

$$\Gamma_{\lambda\lambda'} = \sum_{j,j'} c_{jj'} \int_V \frac{\partial \phi_{\lambda}}{\partial x_j} \frac{\partial \phi_{\lambda'}}{\partial x_{j'}} dV. \quad (3.7b)$$

We will return to briefly describe some relevant properties of \mathbf{E} and $\boldsymbol{\Gamma}$ later. Following the earlier prescription to find the stationary points of the Lagrangian, we note that now we should obtain an equation analogous to Eq. 3.4, but with δL in terms of δa , instead of δu . To obtain δL from Eq. 3.6, we first note that \mathbf{E} and $\boldsymbol{\Gamma}$ are not operators, but are functions of the basis functions ϕ only (and of course the density and elastic tensor, respectively), but not of displacement variables; second, we see that the displacement is now in terms of the expansion coefficients a , and third, we note that

$\mathbf{a}^T \mathbf{M} \mathbf{a} \sim a^2 \langle m \rangle$ and $\partial(a^2 \langle m \rangle) / \partial a = 2a \langle m \rangle$ for any matrix \mathbf{M} , given the above constraints. Thus, the differential of the Lagrangian (Eq. 3.6) in matrix notation becomes

$$\delta L = \omega^2 \mathbf{E} \mathbf{a} - \Gamma \mathbf{a} = 0. \quad (3.8)$$

In this form, the stationary points of the Lagrangian are found simply by solving the eigenvalue problem that results from Eq. 3.8, namely,

$$\omega^2 \mathbf{E} \mathbf{a} = \Gamma \mathbf{a} \quad (3.9)$$

C. Choice of basis functions.

Most samples encountered are homogeneous so that both the density and the elastic moduli are independent of position within the sample. Thus, with ρ and c constant in Eq. 3.7 the computation of matrix elements for \mathbf{E} and Γ is greatly simplified. The choice of basis functions is quite arbitrary. However, since Eq. 3.9 is a formulation of the problem defined by Eq. 3.4, which is a function of both the displacement functions and their derivatives, it is important that, not only will a series of basis functions converge to any reasonable displacement functions, but also that the series consisting of derivatives of the displacement functions will also be convergent. This was first recognized by Demarest [12]. Thus, any complete set capable of representing the displacement functions and their derivatives will work. Then as the number of functions approaches infinity, all the eigenvalues in Eq. 3.9 approach the exact values. Practically, however, one must truncate the basis set to some finite number. The effect of this truncation is that the eigenvalues approach the true value from above as the number of basis functions increases (Cauchy's inequality). The following examples confirm that the choice of functional form for the basis functions is important.

Holland [13] used products of trigonometric functions and the R-R method to compute the resonant properties of a piezoelectric ceramic RP. These functions were of the form

$$\phi_{mnp} \sim \cos\left(\frac{m\pi x}{l_x}\right) \sin\left(\frac{n\pi y}{l_y}\right) \sin\left(\frac{p\pi z}{l_z}\right); \text{ and } \phi'_{mnp} \sim \sin\left(\frac{m\pi x}{l_x}\right) \cos\left(\frac{n\pi y}{l_y}\right) \sin\left(\frac{p\pi z}{l_z}\right); \text{ etc.}$$

where l_s ($s=x, y, \text{ or } z$) are the dimensions of the RP. The basis set is then built up by generating various combinations of (m,n,p) triplets; Holland used selected triplets with values of 0 to 15 (not continuous).

Because the first three modes of a cube are triply degenerate and are known exactly, (Lame' modes), Holland computed these for comparison with results obtained using his trial functions. He found that his computation led to a splitting of the lowest Lame' mode (as well as the next higher Lame' mode) into a doublet and a singlet. He used 9, 30, and 99 basis functions and found that even for 99 functions, the doublet converged to an accuracy limited to ~1-2% in both cases, but the singlet exhibited much slower convergence-10% for the lower Lame' mode and 4% for the higher one. Demarest [12] used a basis set consisting of products of Legendre polynomials

$$\phi_{ijk} = P_i\left(\frac{2x}{l_x}\right) P_j\left(\frac{2y}{l_y}\right) P_k\left(\frac{2z}{l_z}\right) \quad (3.10)$$

to compute the resonance frequencies of a solid cube. Here, i, j , and k are the order of the Legendre polynomial. Demarest found that the maximum order of (i, j, k) triplets depends on the symmetry of the mode represented. For example, he could use any combination up to $i=j=k=9$ for antisymmetric torsion and dilation modes, while for symmetric flexure modes the total order could not exceed 10 (i.e., $i+j+k \leq 10$). Demarest used a basis set of 60 functions and found that the accuracy with which the 4 lowest Lamé modes were computed was 0.05% or better. Both Holland and Demarest used similar symmetry considerations in selecting and grouping basis functions, determined the mode shapes of some of the lowest frequency vibrations and also worked out techniques for extraction of the elastic moduli from their measured resonance spectra. Although the work of Demarest was pivotal in the application of the resonance method to obtain accurate elastic moduli of solids, it was limited to cubic specimens with cubic crystal symmetry.

Ohno[14] then extended the work of Demarest by working out the free vibrations of a crystal of general symmetry and RP geometry. He also used Legendre polynomials as basis functions but worked out the Γ matrix elements including the symmetry properties imposed by all seven crystal classes. This occurs in Eq. 3.7b because of the symmetry of the c tensor. For example, for a triclinic crystal (lowest symmetry) there are 21 elastic moduli represented in the two-index notation by a 6×6 matrix whose elements $c_{ij} = c_{ji}$ and where c_{ij} are all unique and non-zero. For crystals with higher symmetry, $c_{ij} = 0$ for various i and j depending on the symmetry: for cubic crystals for example, only 3 independent moduli are needed, c_{11} , c_{12} , and c_{44} . The c_{ij} matrix then has $c_{11} = c_{22} = c_{33}$, $c_{44} = c_{55} = c_{66}$, and $c_{12} = c_{13} = c_{23}$ with $c_{ij} = 0$ for all other i and j . A more detailed discussion of the representation of the c matrix for various crystal classes and the conversion of the four-index tensor notation to the two-index matrix notation for c may be found in Migliori and Sarrao[1].

Introduction of the symmetry properties of c in Eq. 3.7b reduces the number of elastic constants to be determined. In addition to crystal symmetry the physical geometry of the RP sample introduces 3 mirror planes of symmetry (xy , yz , etc.). The displacement functions must then be invariant to $x \rightarrow -x$, $y \rightarrow -y$, and $z \rightarrow -z$. This reduces the Γ matrix to block diagonal form (eight blocks, corresponding to all combinations of symmetric and antisymmetric with respect to reflection in the 3 mirror planes) thus significantly lowering the computation time in the diagonalization of Eq. 3.9. The above considerations require the crystal axes to be parallel with the axes of the RP. For the case where this is not possible, the solution is much more complicated but tractable[1], [15], [16]. For readers interested in a more in-depth treatment of group theoretical applications to mechanical vibrations in RP, Mochizuki [17] also provides a good starting point.

Ohno also reported a scheme for the determination of the elastic moduli from the RU spectrum which, although superior to that of Demarest, was not completely amenable to automatic computation. Such a method was later developed at Los Alamos [4] and will be briefly described in the next section.

As mentioned in a previous section, the resonant ultrasound method has been applied to samples of other geometries with associated advantages and disadvantages. The use of RUS to determine elastic constants for a spherical solid has been called the resonant sphere technique- RST. The basis functions used to treat such spherical samples take advantage of the spherical symmetry and are products of radial functions and spherical harmonics [18], [19], [20], [21].

The choice of an orthonormal basis set simplifies Eq. 3.9 because in this case E becomes the unit matrix and the resulting eigenvalue problem becomes easier to solve. This is so because for the more general problem Eq. 3.9, the matrix E is required to be positive definite.

Visscher[5] was able to show that using basis functions of simpler form one can easily compute the vibrations of all sample shapes examined for use in RUS measurements (cube, RP, and sphere) including anisotropic materials, as well as several additional shapes. It is thus the most general method proposed to date. Further, using this general basis, resonances for shapes in transition from one symmetry to another (i.e., sphere to spheroid or ellipsoid) were computed to show the behavior of vibrational modes as a function of symmetry; and, for several shapes, families of spectra were shown as a function of aspect ratio. The basis functions are simple algebraic polynomials in Cartesian coordinates, where ϕ of Eq. 3.5 is of the form

$$\phi_{\lambda} = x^l y^m z^n \quad (3.11)$$

where $\lambda=(l,m,n)$ serves as a basis function index and has the same meaning as in Eqs. 3.5-3.7. Because of the form of Eq. 3.11, this computational approach has been called the XYZ method, and has been used in applications of RUS. The XYZ method has also been used by others in conjunction with the RST[16],[20],[22]. Once again, use of the physical symmetry of the object whose normal vibrations are sought reduces the problem as was mentioned above. Visscher also gives an algorithm coded in Fortran to compute the vibrations for the most general case to date, that which occurs for the case where c_{ijk} has the lowest possible symmetry.

The most unique aspect of the XYZ algorithm is that Eq. 3.11 reduces the matrix elements of both E and Γ to the following form

$$f(p,q,r) = \int_V x^p y^q z^r dV. \quad (3.12)$$

Here, p , q , and r are positive integers which arise, for example, in the computation of matrix elements of E in Eq. 3.7a with $\lambda=(l,m,n)$ and $\lambda'=(l',m',n')$ so that $p=l+l'$, $q=m+m'$, and $r=n+n'$.

Similar expressions then occur for Γ in Eq. 3.7b, because the derivatives of ϕ_{λ} will be of the same form. Reduction of all necessary integrals to this simple form allows their analytical evaluation for a variety of shapes, V , as mentioned above. For the case of the RP Eq. 3.12 becomes

$$f(p,q,r) = \frac{8d_1^{p+1}d_2^{q+1}d_3^{r+1}}{(p+1)(q+1)(r+1)}, \quad (3.13)$$

while for the case of the solid sphere, as well as less symmetric objects, one obtains a slightly more complicated expression which is nevertheless only a function of p , q , r , and the dimensions d .

For comparison with discussions of basis set size earlier in this section, the XYZ method

selects all basis functions specified by the condition $l+m+n \leq N$, which generates E and Γ matrices of order $R=3(N+1)(N+2)(N+3)/6$. The accuracy of the method was checked by direct measurement of a large computer machined isotropic aluminum sample with no particular symmetry shaped as an ellipsoid with all semi-major axes different [5]. The results indicate that for the lowest 30 modes and a basis set size where $N=9$ the difference between measured and computed resonances was $< 0.3\%$, consistent with the machining accuracy. The XYZ method thus allows the analytical evaluation of all necessary integrals by means of simple algebraic expressions of the form of Eq.

3.13; and is able to calculate both the resonance frequencies and mode shapes (determined by the eigenvectors in Eq. 3.9) applicable to a variety of shapes and to materials with any crystal symmetry.

Our experience with numerical computations involving Eq. 3.9 is that as one increases the number of basis functions E may no longer be positive definite. This phenomenon is usually mode dependent and may be caused by insufficient numerical precision, even when double precision is used. Similar numerical instabilities were reported by Young and Dickinson[23], for example, who also used the R-R method to compute resonance frequencies of solids of various shapes. The basis set chosen consisted of simple algebraic polynomial series in x , y , and z (as for the XYZ method – of which, apparently, these authors were not aware). An excellent review of the historical developments leading to RUS as an established technique for elastic moduli determination may be found in Migliori and Sarrao [1].

D. Determination of the elastic moduli from RU spectra- the inverse problem.

Several authors have reported work on the problem of extracting elastic moduli from experimental RUS data[4],[12],[14],[18],[24]. However, of these, only Migliori and coworkers [4] have advanced the solution of the so-called inverse problem significantly enough to enable an automatic algorithm that includes proper error analysis and goodness-of-fit parameters. The algorithm is based on the Levenberg-Marquardt functional minimization scheme [11] and is part of the Los Alamos code for use in RUS applications. This computational package has successfully determined elastic moduli, crystal dimensions, and Euler angles relating crystallographic axes to sample surfaces in the case of a misaligned sample. Simply stated, the algorithm carries out a non-linear least-squares fit by minimizing the functional defined by the sum of weighted residuals

$$F = \sum_{i=1}^N w_i (f_i - g_i)^2, \quad (3.14)$$

where g and f are the vectors of measured and calculated frequencies, respectively, and w_i is a weighting factor (as usual in such fitting methods, this may be taken as $1/g^2$). N has to be chosen large enough to insure some amount of overdetermination (i.e., where there are more data than the number of parameters one wishes to fit). The minimization of the above functional begins by expansion of F into a Taylor series about x_0 – the vector (of length M) containing the initial guesses of the parameters to be determined. The expansion will contain derivatives (first order only are retained) of f with respect to each of the variable parameters. Recall that $f = \omega/2\pi$, with ω obtained from the diagonalization of Eq. 3.9. These derivatives are then used in an iterative scheme to compute the next approximation to the parameters. An in-depth discussion of the fitting procedure as well as detailed analysis of errors and goodness-of-fit may be found in [1]. Unfortunately, both experience and good initial guesses of elastic moduli are still important for consistent success in using even these well-tested and frequently used codes to analyze RUS data. The rewards, are, however, substantial, as shown by the examples in the next section.

IV Examples of Applications of RUS

The data from a RUS experiment is of the form $A(f)$, where f is a set of discrete frequencies in the region of interest. Near a resonance, the sample will take of order Q cycles to reach a stable

amplitude of oscillation. Each discrete data point must therefore be measured for at least $t=Q/f$ seconds. For a material with a Q of 10,000, and a resonance near 200kHz, $t=50\text{ms}$. For a scan containing 500 data points this gives 25s per scan. The measurement system needs to have good temperature stability over this time interval. Materials with low Q (<100) can be measured more quickly, but rarely produce enough amplitude for accurate measurement. For measurement times less than Q/f per point, peaks will still appear in $A(f)$, but the line shape may be distorted. The center frequencies and widths of the peaks are the most useful data – the amplitude is generally such a critical function of the point-contact support that it is not a reliable measurement. A peak finder program is useful to extract peak information from a large number of scans, but in noisy data, or where peaks interfere, accurate results are best obtained by fitting to a Lorentzian model. The center frequencies are the input to the RPR codes discussed elsewhere in this article which can provide quantitative results for the elastic moduli. The widths represent the internal friction of the specific mode at f . This represents the actual mechanical dissipation (and losses via nonlinear effects), compared to a pulse-echo experiment where scattering may attenuate a pulse without dissipation. An accurate determination of peak widths clearly requires a sufficient number of data points within each peak.

Even without determining the elastic tensor from the measured resonance frequencies, the experimental setup that RUS uses is so amenable to varying environmental parameters (temperature, magnetic field) that a large amount of information can be resolved from the variation of the frequencies and widths with some parameter. This enables us to obtain useful data from any piece of material – often a randomly shaped fragment – which displays measurable resonances.

The expected behavior of the elastic moduli of a “stable” solid with varying temperature, and thus of the resonance frequencies, is well parameterized within some simple models [26], [27], [28], [29]. This general behavior is linear with a negative slope at high temperatures, curving at lower temperatures to approach $T=0$ with zero gradient. Deviations from this behavior show interesting properties of the material, in particular, since the moduli are derivatives of the free energy with respect to strain, phase transitions of all thermodynamic orders will affect the variation of the resonance frequencies with temperature. The expected deviations may be predicted within various theories (e.g. Landau theory, [30] enabling model parameters, temperature gradients, and thermodynamic orders to be determined.

Fig. 8 shows the variation of the frequency of the first four resonances of a single crystal sample of the Colossal Magnetoresistance (CMR) material $\text{La}_{0.83}\text{Sr}_{0.17}\text{MnO}_3$. This composition lies near both a structural and a magnetic phase boundary. The first order nature of the structural transition is shown by the hysteresis observed, even though the transition does not show a very sharp step. The magnetic transition shows a break in slope without hysteresis, and like the structural transition, is more apparent in some lines.

This material is only slightly distorted from cubic throughout this temperature range, and cubic fits to this sample show the lowest line to be dominantly (cubic) c_{44} and the fourth line to be (cubic) $c^* = (c_{11}-c_{12})/2$ and the middle lines to be mixed modes. By observing just the first and fourth lines the effects of an applied magnetic field on the shear moduli may be observed, Fig. 9, without the need to fit the moduli at each field and temperature. The mounting of the sample within the vertical superconducting magnet constrains the field to be only along a body diagonal. If the atomic structure of the material is known, the actual atomic displacements associated with the strains for the particular mode can be determined and connected to details of the transition [31].

Other anomalous behavior is shown in the B2-structure martensites. The plot for a single crystal of AuZn, Fig. 10, shows that many of the modes have a positive temperature coefficient, even at temperatures 150K above the martensitic transition. The same is true for another B2 system, $\text{Ni}_{0.62}\text{Al}_{0.38}$, Fig. 11, for which only the center frequency and width for the first mode is shown. The hysteresis (not shown) is about 20K for this transition, but the transition itself is enormously wide taking nearly 100K from start to finish. The dissipation, as indicated by the width of the peak, jumps at the first transformation "snap" and then becomes so large at the main bulk transformation that the peak cannot be detected. The low temperature behavior of the dissipation is presently under more detailed study.

Although qualitative data like this on dissipation is straightforward to extract from RUS data, quantitative results are more difficult and need certain model assumptions to be made. Dissipation can be included as a complex contribution to the elastic modulus and fitted along with the real part, but care must be taken, as relaxation processes may have a large frequency dependence, which may cause variations over the range of a RUS scan [32], [1].

The process of fitting the elastic moduli at each temperature can be very time-consuming, but if there are resonances that are dominated by one modulus, the variation of that line will reflect the variation of the c_{ij} . In general this will require a good fit at one temperature, and will only be useful for the diagonal moduli c_{ii} . A test of this was made using a sample of polycrystalline (isotropic) heat-treatable steel, Fig. 12, and good agreement between "extrapolated" values and those fitted at each point was found.

Electronic, as well as structural effects, appear in the free energy and will show up in both the frequency and width data. Fig. 13 shows the frequency dependence of two resonances of a sample of polycrystal Nb. RUS measurements are intrinsically very precise, but this measurement is only possible because the Q of the sample was $\sim 100,000$. The superconducting transition is clearly visible as a break in the slope of the temperature dependence of these low frequency resonances. The elastic constants have been found to exhibit the same temperature dependence as the free energy in both states [33].

The narrow band-gap semiconductor FeSi, because its small activation energy corresponds to near room temperature, shows an electronic contribution to the free energy which is apparent at low temperatures. This causes a deviation from the expected elastic behavior, shown in Fig. 14 by a function of the form used by Varshni. The agreement is good at low temperatures but deviates at higher temperatures. Inset is a plot of the width (dissipation) of a shear resonance. The maximum in the dissipation corresponds to the activation energy ($\Delta/2$) [34]. This data suggests unusual properties of the electronic density of states near the Fermi level, later confirmed by thermodynamic and photoemission experiments. ([35], [36]).

In summary, RUS has many strengths and a few weaknesses. For a reasonably homogeneous sample of almost any shape, and sizes down to a fraction of a millimeter, the temperature and magnetic field dependence of the resonance frequencies and widths can be measured, and useful data extracted. The mounting configuration we used makes it difficult for us to apply a magnetic field in an arbitrary direction, but transducers using piezoelectric films [37] can be made to overcome this.

To extract quantitative results we need the sample to conform reasonably to a theoretical model – for moduli, it must be an homogeneous solid of measured size and density, with a well defined symmetry; for dissipation, we must apply a model of the dissipation mechanism with some idea of the apparent symmetry of the internal friction and its frequency dependence. Without this

correspondence, one cannot obtain quantitative results, and for samples with cracks or inclusions, there may even be no useful qualitative results.

RUS does provide a measure of assurance over the results of pulse echo measurements, where a series of wave velocities will be measured, but whether the results of pulse echo measurements are consistent with the overall elastic symmetry of the sample may not be certain. However, in both RUS and pulse-echo measurements, it is crucial to prepare samples specifically oriented to enhance measurements sensitive to the moduli required.

References:

- [1] Migliori, A. and Sarrao, J.L. (1997) "Resonant Ultrasound Spectroscopy" John Wiley & Sons, Inc., New York.
- [2] Schreiber, E., Anderson, O. L., and Soga, N. (1973) "Elastic Constants and Their Measurement" McGraw-Hill
- [3] Renken, M.C., Kim, S., Hollman, K.W., Fortunko, C.M., Schneider, S.C., Levy, M. and McAvoy, B.R. (1997) Accuracy of resonant ultrasound spectroscopy: an experimental study. IEEE Ultrasonics Symposium Proceedings, 5-8 Oct., Toronto, Canada
- [4] Migliori, A., Sarrao, J.L., Visscher, W.M., Bell, T., Lei, M., Fisk, Z., and Leisure, R. G. (1993) Resonant ultrasound spectroscopic technique for measurement of the elastic moduli of solids. *Physica B* 183, 1-24.
- [5] Visscher, W.M., Migliori, A., Bell, T. and Reinert, R. (1991) On the normal modes of free vibration of inhomogeneous and anisotropic elastic objects. *Journal of the Acoustical Society of America* 90, 2154-2162.
- [6] DRS, Inc., 225 Lane 13, Powell, Wy, www.ndtest.com
- [7] Goto, T., and Anderson, O.L. (1988) Apparatus for measuring elastic constants of single crystals by a resonance technique up to 1825 K. *Rev. Sci. Instr.* 59, 1405-1408
- [8] Isaak, D. G., Carnes, J. D., Anderson, O. L., and Oda, H. (1998) Elasticity of fused silica spheres under pressure using resonant ultrasound spectroscopy. *J. Acoust. Soc. Am.* 104, 2200-2206
- [9] Migliori, A., and Darling, T.W. (1996) Resonant ultrasound spectroscopy for materials studies and non-destructive testing. *Ultrasonics* 34, 473-476
- [10] Heyliger, P., and Ledbetter, H (1998) Detection of surface and subsurface flaws in homogeneous and composite solids by resonant ultrasound. *Journal of Nondestructive Evaluation* 17, 79-87
- [11] Press, W. H., Flannery, B. P., Teukolsky, S. A., Vetterling, W. T., (1986) "Numerical Recipes" Cambridge University Press, Section 14.5
- [12] Demarest, H.H.Jr. (1971) Cube-Resonance Method to Determine the Elastic Constants of Solids. *Journal of the Acoustical Society of America* 49(3), 768-775.
- [13] Holland, R. (1968) Resonant Properties of Piezoelectric Ceramic Rectangular Parallelepipeds. *Journal of the Acoustical Society of America* 43(5), 988-997

- [14] Ohno, I. (1976) Free vibration of a rectangular parallelepiped crystal and its application to determination of elastic constants of orthorhombic crystals. *Journal of Physics of the Earth* **24**, 355-379.
- [15] Sarrao, J.L., Chen, S.R., Visscher, W.M., Lei, M., Kocks, U.F., and Migliori, A. (1994) Determination of the crystallographic orientation of a single crystal using resonant ultrasound spectroscopy. *Rev. Sci. Instr.* **65**, 2139-2140.
- [16] Oda, H. (1994) Free Oscillation of an Elastically Anisotropic Ellipsoid with Arbitrary Crystal Orientation. *Journal of Physics of the Earth* **42**, 97-101.
- [17] Mochizuki, E. (1988) Sphere-resonance method to determine the elastic constants of crystal. *Journal of Applied Physics* **63**(12), 5668-5673.
- [18] Oda, H., Isoda, S., Inouye, Y. and Suzuki, I. (1994) Elastic constants and anelastic properties of an anisotropic periclase sphere as determined by the resonant sphere technique. *Journal of Geophysical Research* **99**(B8), 15517-15527.
- [19] Suzuki, I., Oda, H., Isoda, S., Saito, T. and Seya, K. (1992) Free Oscillation of an Elastically Anisotropic Sphere and Its Application to Determining the Elastic Constants of Rutile. *Journal of Physics of the Earth* **40**, 601-616.
- [20] Oda, H., Hirao, J., Suzuki, I., Visscher, W.M. and Anderson, O.L. (1994) Free oscillations of elastically anisotropic spheres and ellipsoids. *Geophysics, J. Int.* **118**, 555-565.
- [21] Mochizuki, E. Application of Group Theory to Free Oscillations of an Anisotropic Rectangular Parallelepiped. *Journal of Physics of the Earth* **35**, 159-170 (1987).
- [22] Oda, H. (1996) Aspherical Correction for Free Vibration of Elastically Anisotropic Solid by Means of the XYZ Algorithm. *PAGEOPH* **147**(4), 719-727.
- [23] Young, P. G., and Dickinson, S. M. (1994) Free vibration of a class of solids with cavities. *Int. J. Mech. Sci.* **36**(12), 1099-1107.
- [24] Ohno, I., Yamamoto, S. and Anderson, O.L. (1986) Determination of elastic constants of trigonal crystals by the rectangular parallelepiped resonance method. *Journal of Physical Chemistry of Solids* **47**(12), 1103-1108.
- [25] Oda, H., Suzuki, I. and Ohno, I. (1993) Partial Derivatives of Eigenfrequencies of a Rectangular Parallelepiped and a Sphere of Elastically Anisotropic Solid. *Journal of Physics of the Earth* **41**, 271-289.
- [26] Born, M. and Huang, K. (1954) "Dynamical Theory of Crystal Lattices" Oxford University Press

- [27] Varshni, Y.P. (1970) Temperature dependence of the elastic constants. *Phys. Rev.* **B2**, 3952-3958
- [28] Garber, J.A. and Granato, A.V. (1975) Theory of the temperature dependence of second-order elastic constants in cubic materials. *Phys. Rev.* **B11**, 3990-4007
- [29] Sorokin, B.P., Glushkov, D.A., and Aleksandrov, K.S. (1999) Temperature dependence of second-order elastic constants of cubic crystals. *Physics of the Solid State* **41**, 208-212
- [30] Carpenter, Michael A. and Salje, Ekhard K.H. (1998) Elastic anomalies in minerals due to structural phase transitions. *Eur. J Mineral.* **10**, 693-812
- [31] Darling, T.W., Migliori, A., Moshopoulou, E.G., Trugman, S.A., Neumeier, J.J., Sarrao, J.L., Bishop, A.R., and Thompson, J.D. (1998) Measurement of the elastic tensor of a single crystal of $\text{La}_{0.83}\text{Sr}_{0.17}\text{MnO}_3$ and its response to magnetic fields. *Phys. Rev.* **B57**, 5093-5097
- [32] Ledbetter, H., Fortunko, C., and Heyliger, P. (1995) Elastic constants and internal friction of polycrystalline copper. *Journal of Materials Research*; **10**, 1352-1353
- [33] Trivisonno, S., Vatanayon, M., Wilt, J., Washick, J., and Reifenberger, R. (1973) Temperature dependence of the elastic constants of Niobium and Lead in the normal and superconducting states. *J. Low Temp. Phys.* **12**, 153-169
- [34] Sarrao, J.L.; Mandrus, D.; Migliori, A.; Fisk, Z.; Bucher, E. (1994) Elastic properties of FeSi. *Physica* **B199-200**, 478-479
- [35] Mandrus, D., Sarrao, J.L., Migliori, A., Thompson, J.D., and Fisk, Z. (1995) Thermodynamics of FeSi. *Phys. Rev.* **B51**, 4763-4767
- [36] Park, C.-H., Shen, Z.-X., Loeser, A.G., Dessau, D.S., Mandrus, D.G., Migliori, A., Sarrao, J., and Fisk, Z. (1995) Direct observation of a narrow band near the gap edge of FeSi. *Phys. Rev.* **B52**, R16981-16984
- [37] Maynard, J.D. (1992) The use of piezoelectric film and ultrasound resonance to determine the complete elastic tensor in one measurement. *J. Acoust. Soc. Am.* **91**, 1754-1762

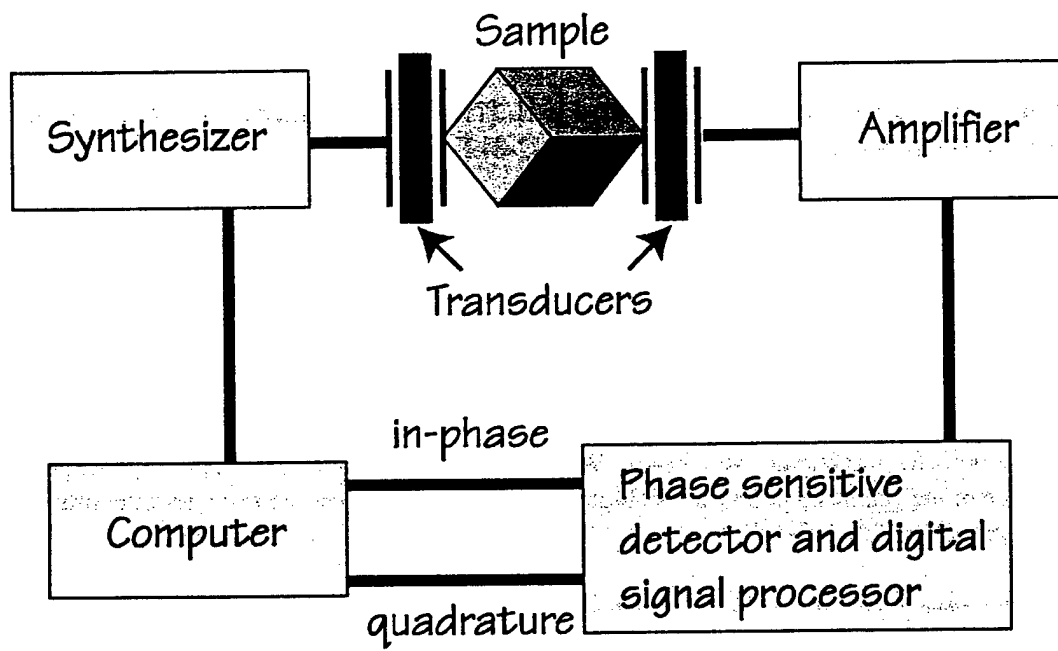


Figure 1. Swept-frequency RUS block diagram

Parameter	Pulse	Resonance
Transducer drive voltage	160V into 50 Ω , 1 ns pulse, 10kHz rep rate=5 mW average	5V into 5000 Ω =5mW average
Measurement bandwidth	10 ⁹ Hz	10 ³ Hz
Electronic noise	10 ⁻⁹ V/(Hz) ^{1/2}	10 ⁻⁹ V/(Hz) ^{1/2}
Detect duty cycle	0.01	1
Voltage signal/noise ratio R_v	2 x 10 ⁵	5x10 ⁷

Table I. A signal/noise comparison between pulsed and RUS measurements.

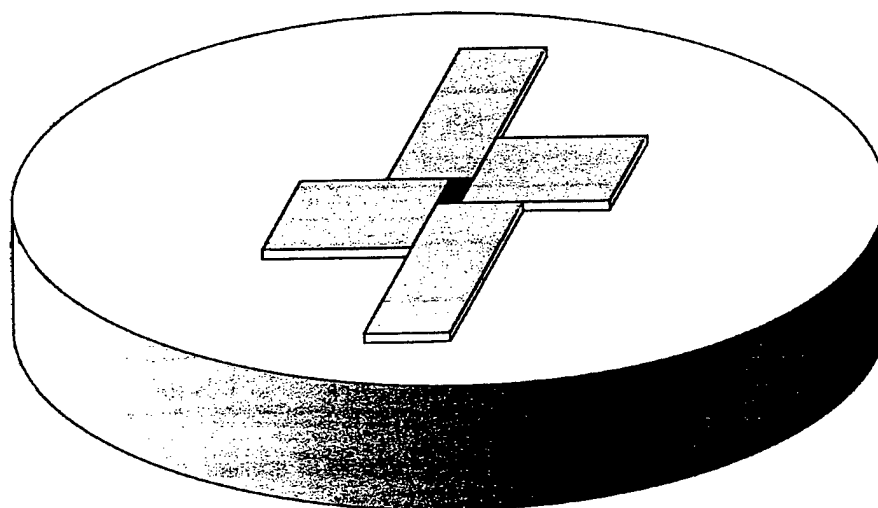


Figure 2. Shown is a plate glass disk with steel shims used to hand-polish RPR samples to produce accurately parallel and perpendicular edges. Wax or other adhesives locate the shims. The sample is the dark area in the center. Lateral finger pressure on the shims ensures perpendicularity if the shims are surface-ground square.

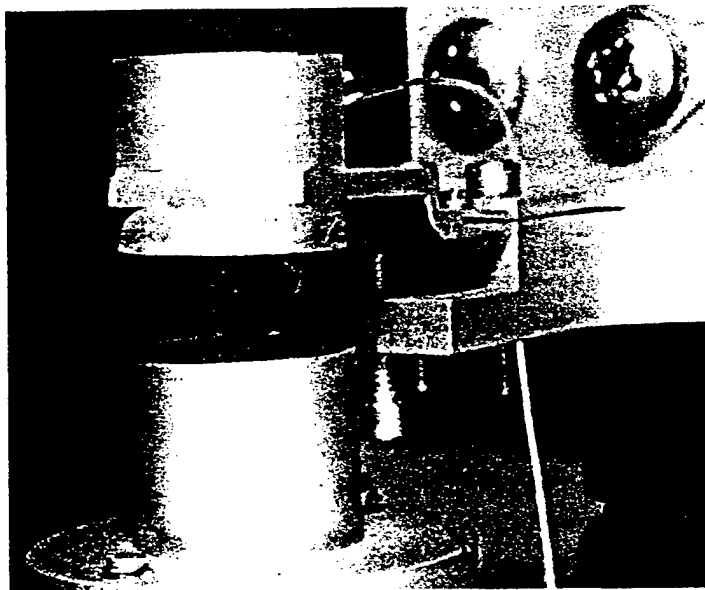


Figure 3. A typical room temperature RUS stage showing transducers and sample. The stage is commercially available from Dynamic Resonance Systems[6].

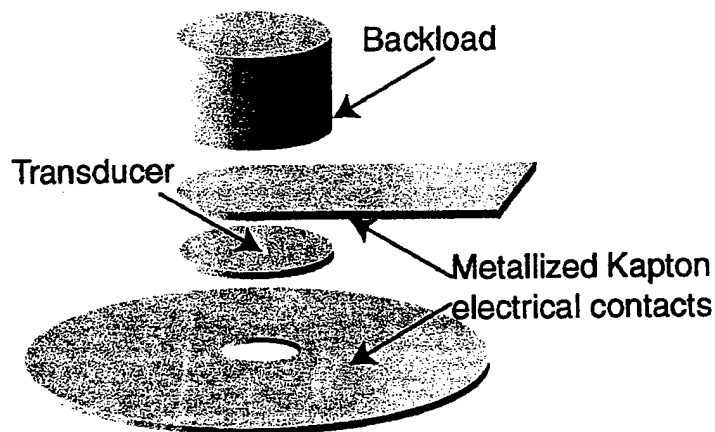


Figure 4. A typical transducer assembly for RUS that has high resonant frequency, high damping and extremely good electrical shielding. The Kapton components are metallized on the surfaces that contact the transducer. The transducer is 0.1 mm thick LiNbO₃, or PZT-5A, and the backload is single crystal diamond about 1.5 mm diam by 1 mm long. An alternate scheme, adequate for room temperature, uses a PZT-5A transducer the same size as the diamond, and no backload. The assembly is held together with non-conducting epoxy, which always seems to allow electrical contact between components when compressed during curing.

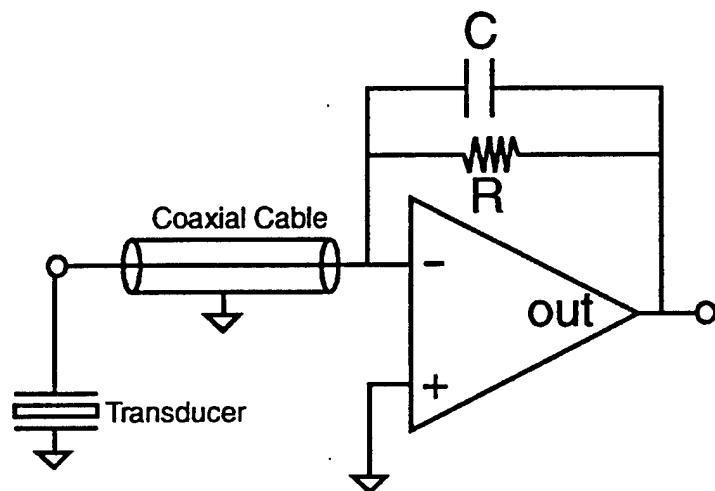


Figure 5. A charge amplifier based on an operational amplifier (Op-Amp). The Op-Amp maintains its inverting terminal (-) at ground so that no voltage is developed between center conductor and shield of the coaxial cable. This ensures that all the charge developed by the transducer appears on the capacitor C as well. If C is set to equal the transducer capacitance, unity gain is achieved, independent of frequency and cable capacitance at frequencies where the impedance of C is much less than that of the DC stabilizing resistor R.

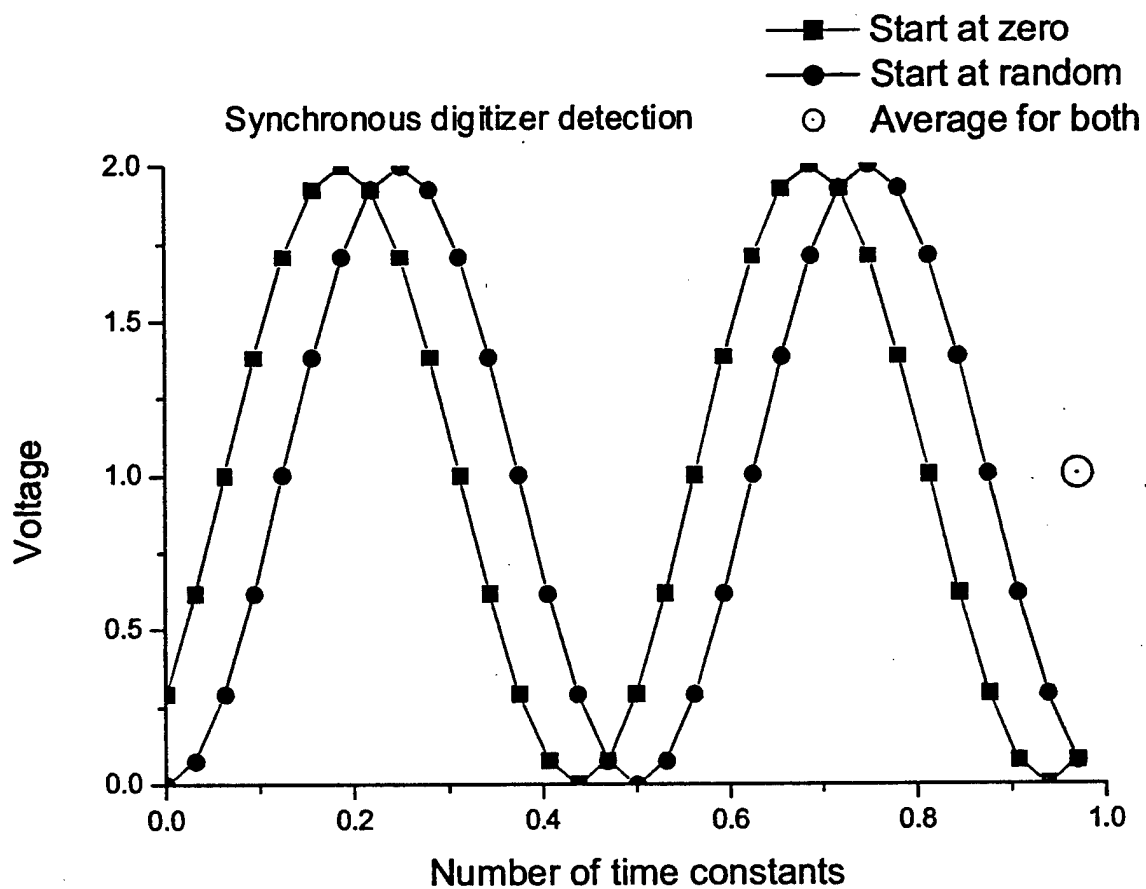


Figure 6. Shown is the synchronous digitization scheme used to acquire stable, low noise RUS data at as high a rate as possible. No matter where one starts digitizing, as long as the digitizer rate is an integer multiple of the frequency, and the digitizer runs for an integer number of cycles, the sum of all the digitized values is the same, with full settling in exactly one cycle, unlike a lock-in.

n	fex	fr	%err	wt	k	i	df/d(moduli)	n	fex	fr	%err	wt	k	i	df/d(moduli)
1	0.488260	0.489423	0.24	1.	4	1	0.00 1.00	1	0.488260	0.486970	-0.26	1.	4	1	0.00 1.00
2	0.578550	0.581709	0.55	1.	4	2	0.00 1.00	2	0.578550	0.577454	-0.19	1.	4	2	0.00 1.00
3	0.662500	0.665424	0.44	1.	6	1	0.10 0.90	3	0.662500	0.662692	0.03	1.	6	1	0.09 0.91
4	0.664360	0.667556	0.48	1.	7	1	0.10 0.90	4	0.664360	0.664805	0.07	1.	7	1	0.09 0.91
5	0.711500	0.715707	0.59	1.	3	1	0.02 0.98	5	0.711500	0.711540	0.01	1.	3	1	0.01 0.99
6	0.714380	0.718480	0.57	1.	2	1	0.01 0.99	6	0.714380	0.714246	-0.02	1.	2	1	0.01 0.99
7	0.758640	0.763605	0.65	1.	8	1	0.01 0.99	7	0.758640	0.758487	-0.02	1.	8	1	0.01 0.99
8	0.766650	0.773214	0.86	1.	1	1	0.04 0.96	8	0.766650	0.767904	0.16	1.	1	1	0.04 0.96
9	0.785160	0.790428	0.67	1.	5	1	0.02 0.98	9	0.785160	0.786240	0.14	1.	5	1	0.02 0.98
10	0.825220	0.831537	0.77	1.	5	2	0.01 0.99	10	0.825220	0.826347	0.14	1.	5	2	0.01 0.99
11	0.836490	0.839861	0.40	1.	6	2	0.32 0.68	11	0.836490	0.836457	0.00	1.	6	2	0.31 0.69
12	0.844280	0.847863	0.42	1.	7	2	0.32 0.68	12	0.844280	0.844243	0.00	1.	7	2	0.31 0.69
13	0.845020	0.848405	0.40	1.	8	2	0.17 0.83	13	0.845020	0.844656	-0.04	1.	8	2	0.17 0.83
14	0.906710	0.870343	-4.01	1.	5	3	0.00 1.00	14	0.000000	0.864396	0.00	0.	5	3	0.00 1.00
15	0.908130	0.910573	0.27	1.	1	2	0.36 0.64	15	0.906710	0.906418	-0.03	1.	1	2	0.34 0.66
16	0.913660	0.912945	-0.08	1.	2	2	0.17 0.83	16	0.908130	0.908173	0.00	1.	2	2	0.16 0.84
17	0.952560	0.918683	-3.56	1.	3	2	0.17 0.83	17	0.913660	0.913771	0.01	1.	3	2	0.16 0.84
18	0.952560	0.952736	0.02	1.	8	3	0.01 0.99	18	0.952560	0.952736	0.02	1.	8	3	0.01 0.99

rms error= 1.3927 %

rms error= 0.1028 %

Table II. 18 resonances of a small sample. The number of resonances is n, fex are the measured frequencies, fr are the best fits to a set of computer determined moduli. %err is the difference in percent between fitted and measured frequencies, wt is the weight given each mode in the fit, k and i are symmetry and harmonic values, and df/d(moduli) are the fractional dependence of each mode on c_{11} and c_{44} for this isotropic sample. Rms error is the rms sum of the errors between fitted and measured resonances. Note that the measurement missed the 14th resonance, so that the fit on the left was poor. Informing the code that a missed resonance exists there immediately produced an adequate fit. Careful examination of the fit on the left reveals how we "guessed" that a resonance was missing. The code used for this is available from Los Alamos National Laboratory.

Be S200F Textured Polycrystal Be Single Crystal

free moduli are c11, c44
using 10 order polynomials
rho= 1.842 gm/cc

mass= 0.4934 gm

free moduli are c33, c23, c12, c44, c66
using 10 order polynomials mass= 0.2264 gm
rho= 1.842 gm/cc

n	fex	fr	%err	wt	k	i	df/d(moduli)	n	fex	fr	%err	wt	k	i	df/d(moduli)
1	0.633839	0.633252	-0.09	1.00	4	1	0.00 1.00	1	0.635039	0.635302	0.04	1.00	4	1	0.00 0.00 0.00 0.29 0.71
2	0.635551	0.635684	0.02	1.00	4	2	0.00 1.00	2	0.788106	0.788153	0.01	1.00	6	2	0.00 0.00 0.05 0.15 0.79
3	0.833434	0.833971	0.06	1.00	6	2	0.21 0.79	3	0.835332	0.834795	-0.06	1.00	1	2	0.00 0.00 0.07 0.00 0.93
4	0.835120	0.835210	0.01	1.00	1	2	0.22 0.78	4	0.959970	0.957946	-0.21	1.00	3	2	0.00 0.00 0.01 0.00 0.99
5	0.835391	0.836387	0.12	1.00	7	2	0.21 0.79	5	0.999543	1.001015	0.15	1.00	6	3	0.01 0.00 0.08 0.16 0.76
6	0.861719	0.861065	-0.08	1.00	6	3	1.26-0.26	6	1.036990	1.034969	-0.19	1.00	5	1	0.00 0.00 0.05 0.00 0.95
7	0.862282	0.862273	0.00	1.00	3	2	0.08 0.92	7	1.047030	1.047225	0.02	1.00	4	2	0.00 0.00 0.00 0.81 0.09
8	0.862721	0.862542	-0.02	1.00	1	3	1.26-0.26	8	1.075950	1.076550	0.06	1.00	7	2	0.00 0.00 0.07 0.00 0.93
9	0.000000	0.863094	0.00	0.00	8	2	0.08 0.92	9	1.121610	1.122433	0.07	1.00	2	2	0.01 0.00 0.03 0.35 0.61
10	0.864708	0.863590	-0.13	1.00	7	3	1.26-0.26	10	1.149920	1.150491	0.05	1.00	5	2	0.00 0.00 0.07 0.00 0.93
11	0.864954	0.863766	-0.14	1.00	2	2	0.08 0.92	11	1.160580	1.161102	0.04	1.00	8	2	0.01 0.00 0.01 0.69 0.30
12	0.981956	0.982200	0.02	1.00	2	3	0.63 0.37	12	1.195890	1.196787	0.08	1.00	8	3	0.01 0.00 0.06 0.41 0.53
13	0.982327	0.983148	0.08	1.00	8	3	0.63 0.37	13	1.254030	1.253338	-0.06	1.00	5	3	0.01-0.01 0.11 0.00 0.89
14	0.984162	0.984318	0.02	1.00	3	3	0.63 0.37	14	1.283260	1.280404	-0.22	1.00	2	3	0.01 0.00 0.01 0.89 0.09
15	0.000000	0.986349	0.00	0.00	5	1	0.00 1.00	15	1.393150	1.395002	0.13	1.00	2	4	0.01 0.00 0.01 0.55 0.43
16	0.000000	0.987323	0.00	0.00	5	2	0.00 1.00	16	1.480820	1.485443	0.31	1.00	5	4	0.70-0.01 0.01 0.06 0.24
17	0.000000	0.988265	0.00	0.00	5	3	0.00 1.00	17	1.487210	1.486888	-0.02	1.00	1	3	0.47-0.01 0.01 0.11 0.42
18	1.021700	1.022765	0.10	1.00	5	4	1.18-0.18	18	1.501830	1.500589	-0.08	1.00	7	3	0.02 0.00 0.03 0.00 0.95
19	1.023870	1.023852	0.00	1.00	5	5	1.18-0.18	19	1.503350	1.503580	0.02	1.00	1	4	0.30 0.01 0.01 0.08 0.60
20	1.057160	1.057543	0.04	1.00	5	6	2.32-1.32	20	1.525570	1.524154	-0.09	1.00	7	4	0.72 0.00 0.00 0.18 0.10
21	1.185330	1.185270	-0.01	1.00	6	4	0.49 0.51	21	1.527700	1.530233	0.17	1.00	5	5	0.66-0.01 0.04 0.03 0.28
22	0.000000	1.185470	0.00	0.00	1	4	0.49 0.51	22	1.534700	1.531091	-0.24	1.00	6	4	0.00 0.00 0.04 0.43 0.53
23	0.000000	1.185631	0.00	1.00	7	4	0.49 0.51	23	1.549320	1.547966	-0.09	1.00	4	3	0.01 0.00 0.03 0.62 0.33
24	1.188630	1.187391	-0.10	1.00	4	3	0.30 0.70	24	1.562710	1.560613	-0.13	1.00	3	3	0.76 0.00 0.00 0.08 0.15
25	1.218560	1.219204	0.05	1.00	2	4	0.04 0.96	25	1.612020	1.615287	0.20	1.00	8	4	0.01 0.00 0.02 0.45 0.52
26	1.220240	1.220856	0.03	1.00	8	4	0.04 0.96	26	1.641860	1.643048	0.07	1.00	3	4	0.01 0.00 0.05 0.00 0.95

Bulk Modulus= 116.6 GPa Bulk Modulus= 116.5 GPa

C₁₁ C₆₆ C₃₃ C₂₃ C₁₂ C₄₄ C₆₆
315.5 149.2 356.7 14.00 26.75 162.2 133.4

d1 d2 d3 d1 d2 d3
0.64471 0.64572 0.64348 0.50540 0.60198 0.40390
loop# 1 rms error= 0.0704 % loop# 3 rms error= 0.1323 %

chisquare increased 2% by the following
% changes in independent parameters
0.02 0.01
0.00 0.03

chisquare increased 2% by the following
% changes in independent parameters
0.06 7.55 0.72 -0.02 -0.02
0.01 0.62 -1.81 -0.01 0.11
0.10 -0.54 -0.02 -0.01 -0.02

Figure 7. Results for polycrystal and single crystal Be at 295K. Note the correspondence between the bulk moduli, which are expected to be the same. d1, d2, d3 are dimensions in cm.

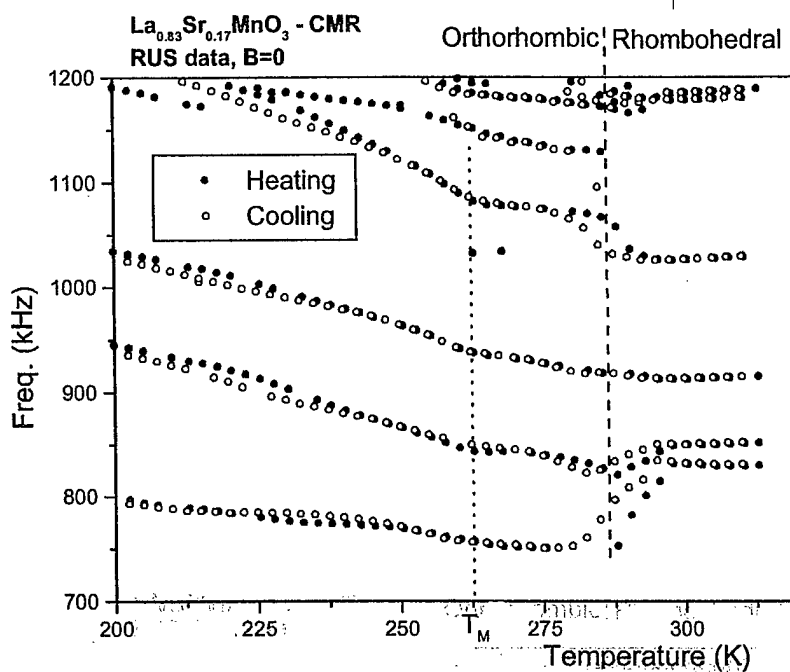


Figure 8. Temperature variation of the center frequencies of the four lowest modes of a single crystal CMR material.

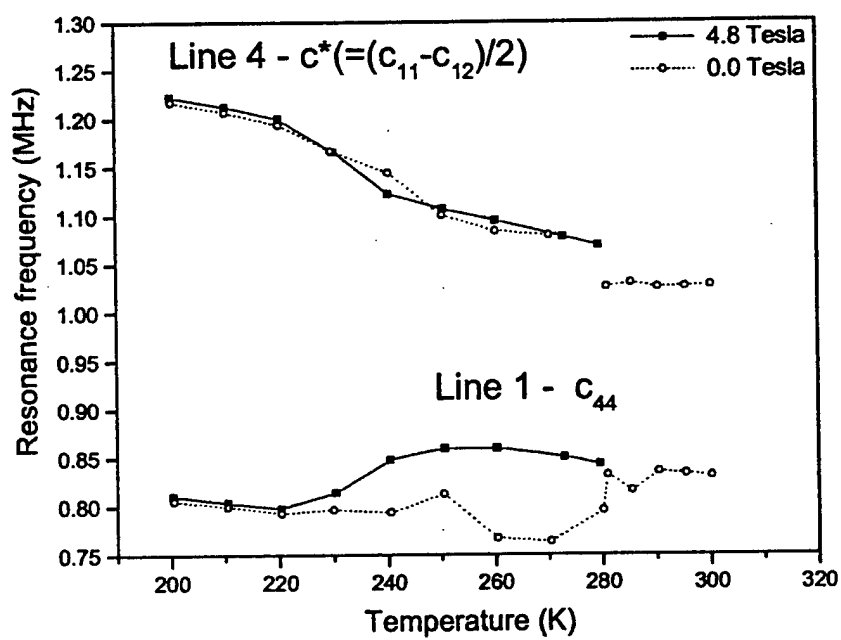


Figure 9. Temperature variation of the (cubic) shear moduli of a single-crystal CMR sample at different magnetic fields.

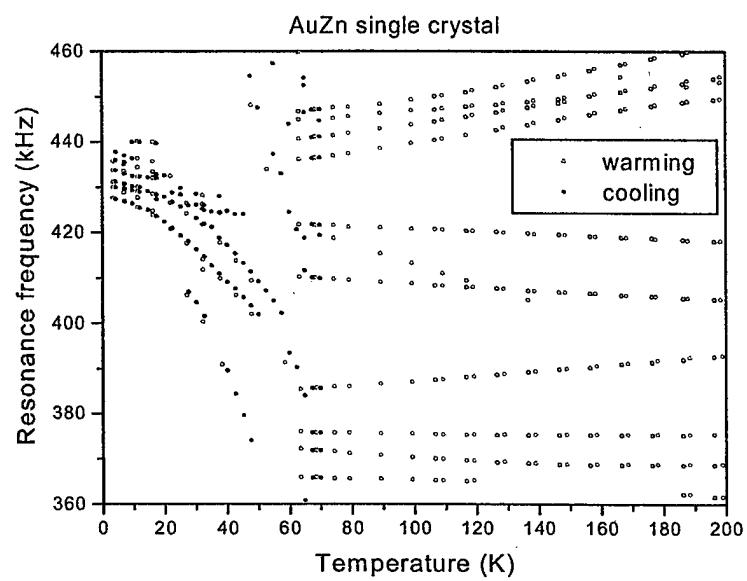


Figure 10. Temperature variation of the mode frequencies for AuZn, $M_s = 64\text{K}$.

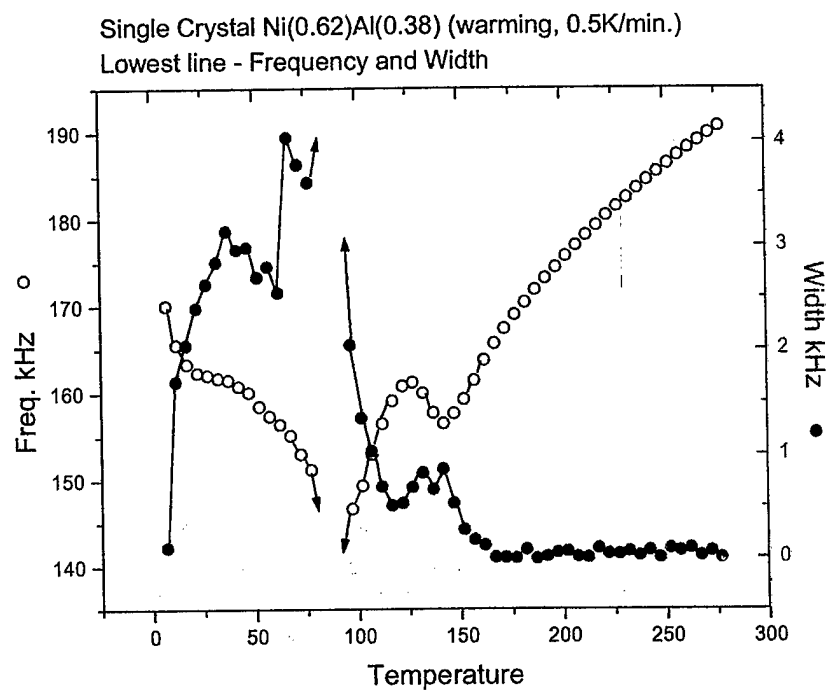


Figure 11. Frequency and width (dissipation) of a C* shear mode at the martensitic transformation of $\text{Ni}_{0.62}\text{Al}_{0.38}$, $M_s = 78\text{K}$.

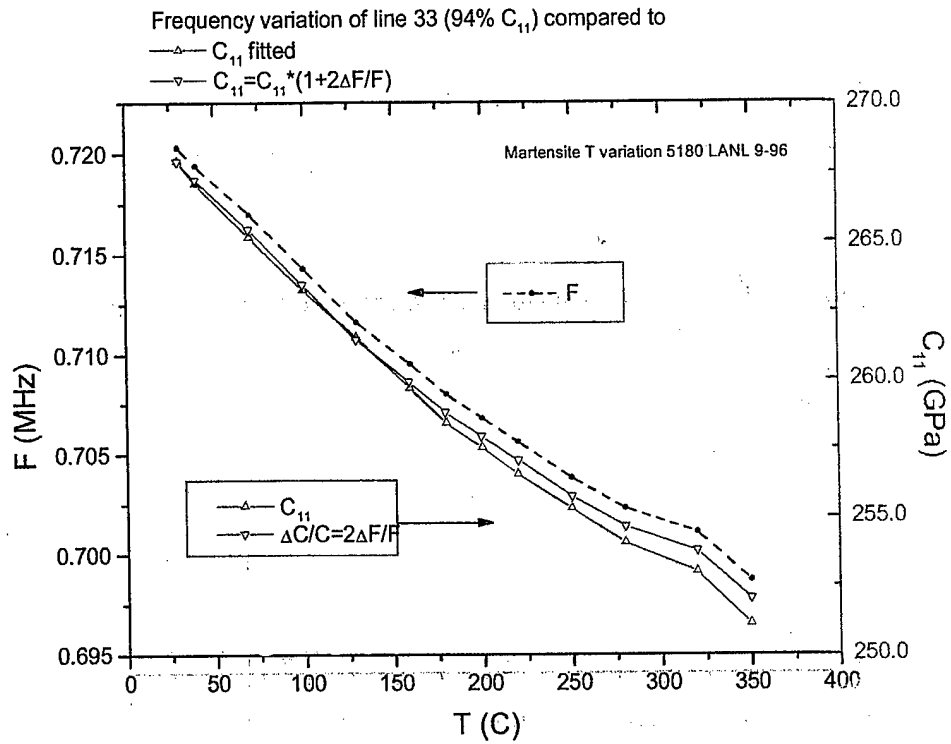


Figure 12. Compares the variation of the frequency, fitted C_{11} modulus and the value of C_{11} extrapolated from the room temperature fit by assuming $\Delta C/C = 2\Delta f/f$.

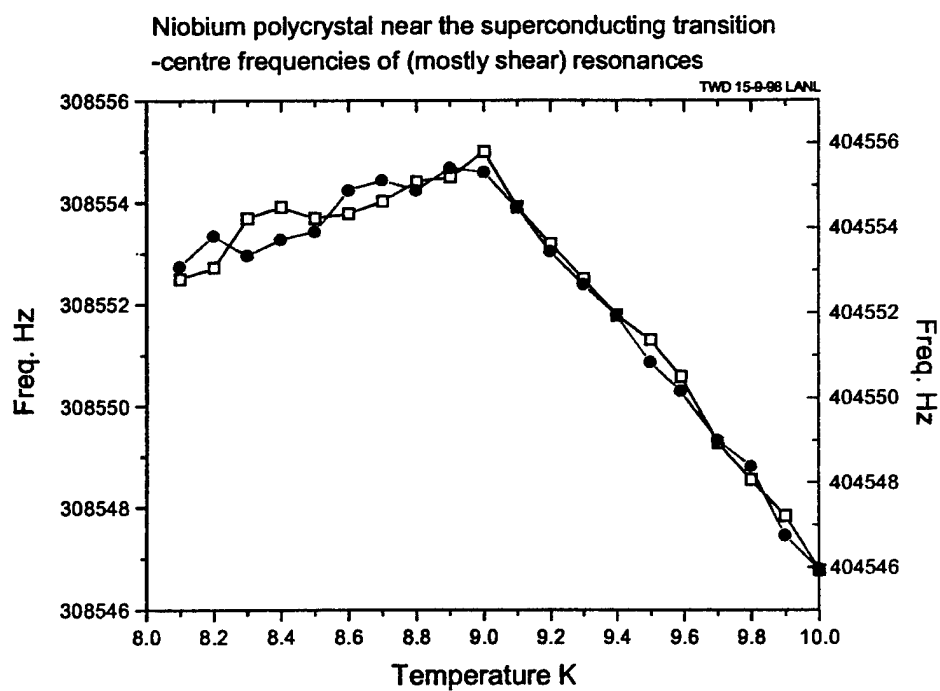


Figure 13. The superconducting transition in polycrystalline Nb.

Elasticity, Entropy and Pu Albert Migliori, Joseph P. Baiardo, Timothy W. Darling

Elastic moduli are the material constants that connect stress with strain. They also play a leading role in determining how thermal energy is distributed among internal vibrations, which, for the most part, control the entropy at ambient temperatures and above. Because elastic moduli are crucial to engineering as well as helping us compute much of the energy and entropy, they are very fundamental physical properties. The purpose of what follows is to see how this works in detail, how we are measuring moduli, and what we expect to learn. The plan will be to review statistical mechanics just enough so that the concepts of temperature, entropy, and free energy are revealed at a basic level and related to the stability of different crystal structures (or phases). Applying this to Pu, we will find that the very soft elastic behavior of Pu, combined with a relatively high melting point for such a soft solid leads to some very odd behavior without needing to invoke unusually temperature dependent electronic structure.

Statistics and large numbers

Our goal in these introductory sections on statistical mechanics is to understand how a phase with a higher, and therefore less likely, energy can become stable because there are so many more configurations with the higher energy that it becomes more probable than other phases with lower energies but fewer configurations. To get to this point, we discuss first systems with large numbers in order to see how very accurate statistical representations can become. We then use simple properties of probabilities to define temperature and entropy. Finally, we discuss the probabilities of observing specific classes of configurations, relying on the properties of systems with large numbers of identical components, and where each class might be labeled by some measurable parameter such as crystal structure.

The configuration of a large group of atoms is called its phase, and the study of what happens to large groups of atoms, and what phases they exhibit as temperature or pressure are varied has fascinated scientists for many years. It is, of course, a subject strongly pursued today. Pu exhibits so many different phases as temperature or pressure is varied that it appears to be complicated and mysterious. What controls the phase of Pu, or anything else for that matter, and how can we understand factors affecting the stability of the various Pu phases? One key to such an understanding relates to the properties of systems composed of very large numbers of identical objects. When the numbers are really large, there is no hope of computing anything exactly—but one can make approximations, and the accuracy of the approximations becomes phenomenally good! In fact, so good that very precise behavior arises strictly out of the large numbers.

Statistics

Lets take a collection of 8 coins, each with a different date. We put the coins in a sack and then remove them, one by one, and place them in a row. The first coin in the row can be any one of eight. The second, any one of seven, and so on. Thus the total number of possible arrangements, or states, is $8 \times 7 \times 6 \times 5 \times 4 \times 3 \times 2 \times 1$ which is called 8! (eight factorial)

and is 40,320. But we were careless in placing the coins in a row, and so some are heads and some are tails. Of the 40,320 ways of placing the coins on the table, there are also 40,320 ways of placing the coins all heads up, because each coin has a distinct date. However, if we could not read the date (the coins become indistinguishable from each other), things change.

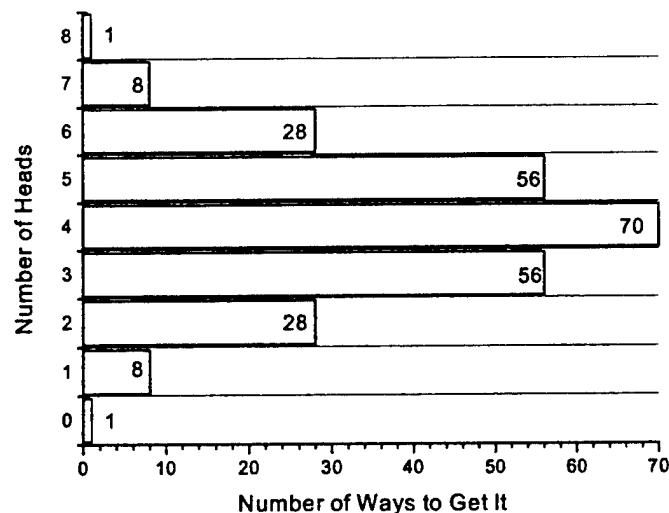


Table I. The number of states of a system of eight coins where the only quantity of interest is the number of heads.

There are far fewer distinguishable states if the objects are indistinguishable (256 to be exact, heads or tails for each of 8 objects $= 2^8$). Of those 256 states, only one is all heads, only one all tails. There is also only one with the first coin heads and the others tails. There is only one with the first, second and fifth coins heads and the rest tails, etc. Each distinguishable state has the same probability of appearing, $1/256$. But how many states have 1 head and 7 tails? The answer is eight. That is, the head can be in any one of eight different positions. How about 3 heads and 5 tails? We have eight choices for the first head, seven for the second and six for the third. But if we put the first head in position one, and the second in position two, this is the same result as putting the first in position two and the second in position one. In fact, there are $3!$ Ways of arranging the order of placing three coins heads up. Thus the total number of states with 3 heads is $8 \times 7 \times 6 / (3 \times 2 \times 1) = 56$. From the above reasoning we construct Table I. The most likely occurrence is equal numbers of heads and tails, and the probability of other outcomes slowly drops as we move to either side of the peak probability of $70/256$. In general, we see that the number of states $\Omega(n)$ of a system of N objects, n of which are of one equally probable type, and $N-n$ of which are of the other equally probable type, but where we don't care about the exact arrangement of the n objects is

$$\Omega(n) = \frac{N!}{n!(N-n)!}. \quad (1)$$

We can also see, recalling the binomial expansion, that

$$(a+b)^N = a^N + Na^{N-1}b + \frac{N(N-1)a^{N-2}b^2}{2!} + \dots = \sum_{m=0}^N \frac{a^{(N-m)}b^m N!}{m!(N-m)!}, \quad (2)$$

if $a=b=1$ then

$$(1+1)^N = 2^N = \sum_{m=0}^N \frac{N!}{m!(N-m)!}, \quad (3)$$

which is just the sum of all the states. For our example in the table, we knew the sum was 256, something we reasoned out by knowing that each object had two possible states, and there were 8 objects.

The effect of large numbers

If instead of eight random flips, we took $N=10^{22}$ flips, about the number of atoms in a small chunk of matter, then there are $2^{10^{22}}$ distinguishable states. The most probable result is equal numbers of heads and tails. If we compute the probability to obtain equal numbers of heads and tails and call it P , then what outcome has a probability of $P/2$? Using Equation 3 we find that with probability $P/2$ we get about 10^{11} more heads than tails (or vice versa). In other words, in 10^{22} flips, it would be reasonably likely to get 10^{11} more heads than tails, or a *hundred billionth* the total number of flips (i.e. about $1/\sqrt{N}$ of the total). We also know there is only one state, far from the maximum probability, where we get 10^{22} heads.

Thus the width of the peak in the probability distribution is \sqrt{N} and there is not much left outside the peak. What we learn from this is that as the numbers become large, the peak becomes very very narrow, and that all practically useful information is in the peak. It will be very accurate, later on, to approximate the real peak with a very tall rectangular distribution with constant probability over the width of the peak and zero probability elsewhere. From this we can state some important rules for systems (visible pieces of matter) with of order Avogadro's number of particles in them (6.02×10^{23}).

The first rule is that **we can count on all the numbers to be very large**. This will make what may seem to be wildly inaccurate approximations be nearly exact. The errors will be of order either the square root of a large number (which we have seen to be a very small percentage error) or of order the logarithm of a large number (51, the \ln of 10^{22} is pretty small compared to 10^{22}).

The next rule is that **any accessible state of the system is equally likely but we only see the group of very probable ones**. Accessible states are those that do not violate any constraints (fixed volume might be one) or physical laws such as conservation of energy, momentum or charge. A system composed of a large number of objects with a reasonably large (lets beg off on the definition of reasonably for now) total energy, as time progresses,

explores all the possible states with that energy (there are, however, some systems that violate this ergodicity hypothesis). That is, if we were to take suitably fast snapshots of the system, each picture would be of an accessible state. In more concrete terms, we take our sack of coins, empty it on the floor, count the number of heads, and then repeat the process. But our sack has 10^{22} coins, and we perform the experiment, say, 10^{11} times per second (that's about the number of times per second that a gas molecule undergoes a collision with another gas molecule). Because each state is equally likely, we only see a very few of the total of about $2^{10^{22}}$ possible states. Let's say the universe will last 10^{10} seconds. Then in the life of the universe, we will perform the experiment $10^{11} \times 10^{10} = 10^{21}$ times. If the experiment is really done on a gas instead of coins, then one possible observable that we might use instead of the number of heads is the fraction of gas molecules in, say, the left half of the container they reside in. The probability of any one atom of gas to be in the left half is $\frac{1}{2}$. The probability that all of them are in the left half is $2^{-10^{22}}$. The number of times that we observe this to happen in the entire life of the universe is $2^{-10^{22}} \times 10^{21} \approx 2^{-10^{22}}$. We won't see it happen! What we do see in the time we have to observe it is that the gas mostly accesses the states near the most probable one. That is, we expect the total mass in the left half of the box to vary from half the total mass by $1/\sqrt{10^{22}}$, or about 1 part in 10^{11} on a regular basis. In more practical terms, we would expect the pressure, or the energy or other macroscopic physical quantity to be observed within about 1 part in 10^{11} of its most likely value. The statistical properties of systems of very large numbers come round again to behaving like a systems of only one or two particles—that is, even though we can only take a probabilistic view of a system way too complicated to compute exactly, the results are, for all practical purposes exact!

The last rule is that the **total number of states of a system is a very strongly increasing function of the total energy**. Let's illustrate this with a simple quantum harmonic oscillator. Unlike most other physics problems, the quantum version of statistical mechanics is easier to deal with because the quantum numbers of such systems make it very easy to count states, while various obscure crutches must be used for classical systems. A quantum system might be composed of a mass and spring, or an atom and a chemical bond. In either case, the energy of the oscillator increases proportional to the square of the amplitude of vibration and no matter what the amplitude, the frequency is $f = \omega/2\pi$, just like a tuning fork or pendulum. When the vibrational energy of this oscillator is very small, quantum effects become noticeable in a simple way. The oscillator can only have a total energy $E = (n + \frac{1}{2})\hbar\omega$ where n is any positive integer, and \hbar is Planck's constant. Now consider a set of three harmonic oscillators, shown in Figure 1. If the total energy of the three is $E = (2 + 3/2)\hbar\omega$, then the system can be in one of the following states (110 means the first oscillator has one quantum, the second, one and the third, zero):

200 020 002 110 101 011 for a total of 6 states.

If the total energy is $E = (3 + 3/2)\hbar\omega$, then the available states are

300 030 003 210 201 120 102 012 021 111 for a total of 10 states.

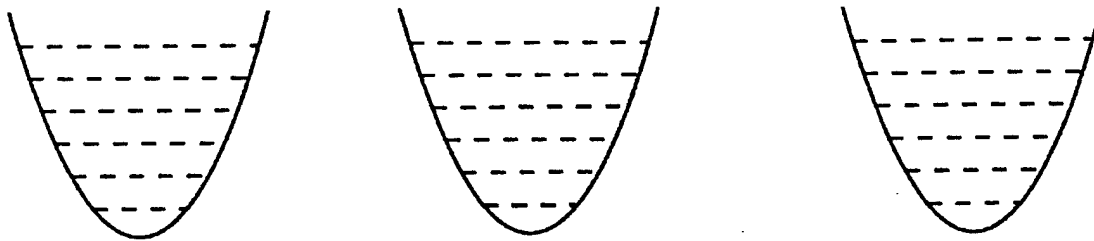


Figure 1. Three harmonic oscillators. Each has equally spaced energy levels shown as dashed lines.

If we increase the energy of the system, the number of available states increases, as does the average energy of each object in the system, and the increase *per object* is roughly proportional to the fractional energy increase. Therefore, if we have 10^{22} objects, and the total energy of the system is increased by 10%, then so is the average energy of each

object and therefore the total number of states increases by a factor of $(1.1)^{10^{22}} \approx 2^{1.4 \times 10^{20}}$, which is an enormous increase. We now also realize that "a reasonably large amount of energy" is enough energy so that roughly every element of the system has more than its ground-state energy.

Entropy and Temperature

Let's use simple properties of probabilities to generate a universal definition of temperature. Consider a very small chunk of matter that is touching (or part of) a very much larger chunk. The total energy is fixed at E ; the smaller piece is taken to have an energy E_1 , the larger, $E - E_1$. What is the probability that we observe this? If the number of states of the smaller system is $\Omega_1(E_1)$, and of the larger system, $\Omega_2(E - E_1)$, then the probability of observing this configuration is the product of the probabilities of observing each system separately and is proportional to

$$P(E_1) \propto \Omega_1(E_1) \Omega_2(E - E_1). \quad (4)$$

Note that we have also used the property that the probability of a particular set of states of energy E_1 is proportional to the total number of states with energy E_1 . To convert Equation 4 to an equality, we must divide by the total number of states Ω_1 . This constant is found by computing the total number of states for each value of E_1 where E_1 ranges from zero to E , and adding them up. Equation 4 is a very important result. Let's review what it means. Things in each system are whizzing and banging around all the time. The systems individually do not have fixed energy, and therefore the number of states of each system will vary as energy is exchanged between them. Every time we look at the whole system, we will see it in one of its equally likely configurations. We have shown that as energy increases, the number of states increases very rapidly, conversely if energy decreases, the number of states drops very rapidly. The large subsystem and the small subsystem, when in contact, trade probabilities. Equation 4 is a very sharply peaked function that is the product of a rapidly increasing function of E_1 and a rapidly decreasing. For large numbers,

the maximum is extremely sharp—so sharp that it is unlikely that anything but the most probable configurations will ever be observed. Thus after a while, no matter what the initial states were, the system is observed near its most likely configurations. Those configurations divide the energy between the two subsystems in a very special way so that the **fractional increase** in the number of configurations of the smaller system as energy is added to it is exactly matched by the **fractional decrease** in the number of configurations of the large system as energy is removed from it. That is, for small fluctuations in the energy of either part of the system, the overall probability stays about the same, or

$$\frac{dP(E_1)}{dE_1} = 0 = \Omega_2 \frac{d\Omega_1}{dE_1} + \Omega_1 \frac{d\Omega_2}{dE_1} \text{ or } \frac{d \ln \Omega_1}{dE_1} = - \frac{d \ln \Omega_2}{d(E - E_1)}. \quad (5)$$

Equation 5 expresses one property common to both systems once things have settled down (reached thermal equilibrium), something we already know about. What we know is that after a while, the temperature of both systems is the same. The definition of the temperature is

$$T = 1 / \left(k_b \frac{d \ln \Omega}{dE} \right) \quad (6)$$

where k_b is Boltzmann's constant. We also define entropy to be

$$S = k_b \ln \Omega. \quad (7)$$

The choice of the definition for entropy is particularly important because it is a general way of constructing an additive quantity from things multiplied together (the probabilities). The consequences of Equations 4, 5, 6, 7 are as follows:

Thermal equilibrium occurs when the temperatures of the subsystems are the same, which is equivalent to saying that the system is very near a maximum probable configuration.

Because the logarithms of products add, entropy is a good extrinsic quantity (i.e. 2lbs. of butter have twice the entropy of 1lb.).

There is also a strange property of the system relating to entropy. We already mentioned the intuitively attractive property that no matter what state we start the system in, after a while it will be observed in one of its very probable accessible configurations (mathematically equivalent to maximum entropy). Noting that all the laws of classical mechanics are time reversal invariant, then if only such rules applied, such a system must have come from one of higher entropy in the past. Therefore, if we go either forward or backward in time, entropy should increase. Whenever we observe this system, its entropy must be a minimum—something the universe does not, in fact, provide for. If we observe a very probable configuration in the past, we continue to observe a very probable

configuration! But if we arrange the system in a very improbable configuration in the past, it rapidly adjusts itself to a probable one. The behavior of entropy is not time-reversal invariant (we cannot tell the state of the system in the past by observing it in the present). To quote the English translation of "Statistical Physics" by L.D. Landau and E.M. Lifshitz,

"The question of the physical foundations of the law of monotonic increase in entropy thus remains open: it may be of cosmological origin and related to the general problem of initial conditions in cosmology; the violation of symmetry under time reversal in some weak interactions between elementary particles may play some part. The answers to such questions may be achieved only in the course of further synthesis of physical theories".

Free Energy

To make the connection between statistics and quantities we could measure, we need to study how to calculate the values of measurables if we know the probabilities of possible states. Consider a small system in exactly one definite state i of energy E_i (there are many states with energy E_i) connected to a much larger system. Then a simple Taylor expansion yields

$$\ln \Omega(E - E_i) \cong \ln \Omega(E) - \frac{d \ln \Omega}{dE} E_i \text{ or} \quad (8)$$

$$\frac{\Omega(E - E_i)}{\Omega(E)} = e^{-\frac{E_i}{k_b T}}$$

where we used the definition of temperature and relied on E_i to be small. We can easily compute probabilities from this by remembering that the sum of all the probabilities is 1. The correct normalized probability, where the sum is over each distinct state i , is

$$P_i = \frac{e^{-\frac{E_i}{k_b T}}}{\sum_i e^{-\frac{E_i}{k_b T}}} \quad (9)$$

which describes the probability of observing a state i with energy E_i . The numerator of Equation 9 is the famous Boltzmann factor. The equally famous partition function is just the normalization factor in Equation 9 and is

$$Z = \sum_i e^{-\frac{E_i}{k_b T}}. \quad (10)$$

But there are many states $\Omega(E_i)$ with energy near E_i . Equation 10 can be rewritten as a sum over each distinct energy E_i to find that

$$Z = \sum_{E_i} \Omega(E_i) e^{-\frac{E_i}{k_b T}}. \quad (11)$$

Because numbers are large and probability distributions sharply peaked, we can accurately approximate the real shape of $\Omega(E_i)$ by a rectangular distribution that is constant over the approximate width of the real distribution, and zero everywhere else. The width and height are adjusted so that the area of the rectangle is the correct total number of states near energy \bar{E} . "Near" in this case can be very crude, and errors in it and this process will only affect the answers to of order $\ln \Omega$, a very very small error. With these approximations, we perform the sum in Equation 11 to obtain

$$Z \cong \Omega(\bar{E}) e^{-\frac{\bar{E}}{k_b T}} = e^{-\frac{F}{k_b T}} \text{ where } \ln Z = \ln \Omega(\bar{E}) - \frac{\bar{E}}{k_b T} \text{ and } -k_b T \ln Z = \bar{E} - TS = F \quad (12)$$

where $\Omega(\bar{E})$ is the total number of states near the most probable energy \bar{E} , we used the definition of entropy, and we have defined a quantity F , the (Helmholtz) free energy. The significance of this is as follows. If the system can be in two phases at once (ice in water) then somehow, the fantastically large numbers and wildly swinging probabilities must conspire to make both phases equally likely, even though their energies are obviously different. In addition, the partition function Z must now have two pieces, one for ice and one for water. For the two phases to be observable simultaneously, keeping in mind the monstrous numbers, the two pieces of the partition function must be equal. Therefore we see that when the free energy of ice per molecule equals the free energy of water per molecule, it is equivalent to saying that the partition functions for equal numbers of molecules are equal, or

$$Z_{\text{water}} = \Omega_{\text{water}}(\bar{E}_{\text{water}}) e^{-\frac{\bar{E}_{\text{water}}}{k_b T}} = Z_{\text{ice}} = \Omega_{\text{ice}}(\bar{E}_{\text{ice}}) e^{-\frac{\bar{E}_{\text{ice}}}{k_b T}}. \quad (13)$$

If the free energies differ, the numbers are so large that only the phase with the lowest free energy is sufficiently probable to be observed. This is the primary concept that determines the observed phase.

Because it is the product of the number of states that have a particular energy times the probability of observing any one state with that energy that determines how likely such a state is to be observed, both energy, which determines the probability of any one state with that energy and entropy which determines how many states have that energy, control phase stability in equivalent ways. In this example, it can be seen that the increase in energy per molecule associated with stretching and breaking the bonds that lock water into a frozen state makes water less probable by itself because of the Boltzmann factor. But because there are many more ways to arrange the molecules in the liquid than in the solid, this reduction in probability is offset by the increase in the number of states of water. When

the energy is just right, the overall probabilities are equal, the free energy is a minimum, and ice begins to melt.

Phase Stability and Pu

We have seen how the energy and the number of configurations (entropy) both contribute to determining the most probable states (phase) of a system. What controls the most probable, and therefore the only observable, phases of Pu? We will, of course, fail to answer this question fully, but we can get large parts of the answer at temperatures above ambient, and we will be able to catalog what parts are missing.

The largest contribution to the phase stability of Pu will depend on the temperatures of existence of the phase in question. At low temperatures and low pressure, the monoclinic α -phase of Pu is stable, where it is primarily the electronic structure and its energy that are important. Entropy, or the number of states available, can be neglected without affecting the validity of an electronic structure calculation because the entropy is zero at zero temperature, and, up to about 400K, Pu retains the zero-temperature phase. In fact, modern calculations by John Wills and co-workers appear to describe completely and astonishingly accurately the behavior of the low-temperature phase of Pu, essentially from first principles.

As temperature rises, the theorist must decide how to include the effects of temperature. The central problem focuses on the various contributions to the free energy. One contribution is the electronic internal energy already accurately understood for the α -phase of Pu at zero temperature. Other contributions relate to entropy and include a harmonic phonon piece, a conduction electron piece and as Duane C. Wallace writes, an aggregate piece associated with anharmonic phonons and electron-phonon coupling. Everything but the harmonic phonon contribution is less than 6%-12% of the total, so these effects are not huge, but still, they are three times as large as in the average metal. The problem is, however, exacerbated by thermally activated anharmonic effects such as thermal expansion, and the temperature dependence of the phonon frequencies (and therefore the entropy and specific heat) that arise directly from the electronic structure combined with thermal energy, but the root of all the entropy contributions is the fundamental electronic structure, and the vibrational modes that it determines.

It is attractive, therefore, to use all the available data to attempt to understand the root causes of the unusual set of structures that Pu exhibits. Remembering that isolated atoms in a vacuum have completely localized, unmovable electrons with no overlap, it is clear that the interaction via electrons, of the atoms is what must be understood. As atoms are moved closer, electronic wave functions at first weakly overlap to produce so-called localized electrons that are effectively heavy and hard to move. As the overlap increases, the electrons become more and more mobile, limited finally to behaving as a gas of nearly free electrons as in Na. In metals with localized electrons, such as Pu, it is not surprising that the structure is very open-else more overlap would occur, and second, that the overlap, and hence localization, is extremely sensitive to interatomic spacing and, therefore, pressure. Such a system is expected to be very compressible. It is also reasonable to expect that in a very compressible system, as vibrational motion increases with increasing temperature, the average atomic separation will increase more than usual, producing a greater variety of phases than in a system where overlap is already strong.

To put this in perspective, the thermal expansion coefficient of Fe is about 13 ppm/K while that for α -Pu is near 42 ppm/K. The bulk modulus of α -Pu that we have measured on high quality research samples is about 55 Gpa. In contrast, the bulk modulus of ordinary steel is about 170 Gpa. The stiffest phase of Pu is three times easier to compress than steel!

Another effect of temperature is to increase entropy directly. Associated with this increase is the selection of high-entropy/high energy phases that become more and more favorable as temperature rises. Wallace provides a very careful computation of the total entropy of Pu as a function of temperature (and phase) by using measured specific heat data. He finds that by far the largest contribution to the entropy of Pu at temperatures above ambient is that from the harmonic vibrations.

To understand the vibrational entropy of Pu, a simple approach is to approximate Pu as a collection of masses and springs. A mass/spring picture connects directly to such mechanical properties as the Young's and shear moduli, the compressibility, and the speed of sound, all critical quantities for the only known practical application of Pu²³⁹. The normal modes or vibrational frequencies of the masses and springs, though entirely determined by the electronic structure, are measurable as separate independent quantities via ultrasound and neutron scattering experiments. These quantities can also be computed directly from theoretical models of Pu. It is for this reason that measurements of the elastic modulus tensor, dependent on the type of strain and its direction, provide so much stronger feedback to the theorist than simple scalar thermodynamic measurements such as heat capacity and bulk modulus.

To make the connection between the elastic modulus tensor and microscopic models, we compute some properties based on a simple elastic model. Consider a long, thin bar of Pu (we'll keep it under a kilogram or so, just to be safe). If we set the bar to vibrating, we quickly see that the lowest tone it makes is one where a half-wavelength of sound just fits in the bar (and the wavelength is very much longer than the springs we connect the atoms with, so the system behaves as if it were continuous). The next tone up is two half

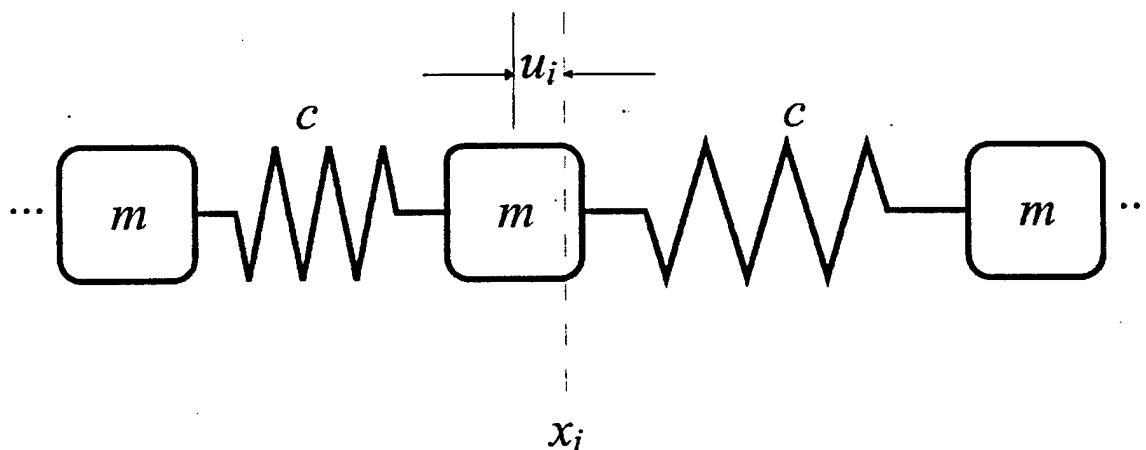


Figure 3. A small portion of a very long string of masses connected by springs. u_i is the displacement of each mass from its rest position x_i .

wavelengths and so on. These are the allowed vibrations for a given type of mode in a perfect crystal. Each tone has a fixed frequency, but any amplitude (careful there, with Pu, anyway). This is just like the simple harmonic oscillator discussed above. There are $3N$ tones, or normal modes, where N is the number of atoms in the sample. For the lower frequency normal modes, the frequency is just $f = mv/(2l)$ where v is a sound speed (there are several—compressional and different types of shear), m is an integer less than about $N^{1/3}$, about the number of atoms in a row along the length of the bar l . We see from this that the sound speeds control the frequencies of the vibrations in Pu.

We need however, to find all the frequencies even when the wavelength becomes comparable to the atomic spacing in order to compute their effect on entropy at temperatures above 300K. Neutron scattering measurements can, in principle, measure them all (rather imprecisely and with great difficulty), but it is also possible to make excellent guesses if we know the sound speeds to high accuracy. Of course, the usual ultrasonic techniques, including the ones we employ, can only determine the sound speeds at very long wavelengths, essentially within only a few parts in 10^6 away from zero in Figure 4. But the variation with frequency is usually understood as we suggest below, and we are going to take a logarithm of the result to compute entropy. Surprisingly, only a few sound speeds are known, mostly averages of polycrystal samples and one measurement at ambient temperature on a Ga stabilized δ -Pu single crystal.

To compute guesses for the higher-frequency modes, we must include the discrete effects of the masses and springs as the wavelength of sound approaches the interatomic spacing. Take a very long string of masses (atoms) a distance a apart and springs (bonds) as shown in Figure 3. This model is one for which only nearest neighbors interact. When longer range interactions occur, things change, as we shall discuss below. Looking at one of the masses, we find that the stretching of springs to the left and right of that mass produce an acceleration (Newton's famous $F=ma$) such that

$$m \frac{d^2 u_i}{dt^2} = -c(u_i - u_{i-1}) + c(u_{i+1} - u_i). \quad (13)$$

We can solve Equation 13 to find that there are many different vibrational frequencies with different wavelengths. For each angular frequency $\omega = 2\pi f$, where λ is the wavelength,

$$\text{if } u_i(t) = u_{i0} e^{i(kx_i - \omega t)} \text{ and } k = \frac{2\pi}{\lambda} \text{ then } \omega = \sqrt{\frac{2c}{m}} \sin ka. \quad (14)$$

For all the allowed vibrations (corresponding to an integral number of half-wavelengths fitting on the string) the frequencies are given by Equation 14, and these correspond to the (discrete) vibrational modes. In Figure 4 we show a plot of this, which, because of the number of modes, looks like a continuous line. The slope of the dashed line, which is the slope of the curve at the origin, is what is normally taken to be the sound velocity. The largest value of the wavevector k occurs when the wavelength of the vibration on the string equals twice the distance between masses (any shorter, and we could describe the wave

as if it had a longer wavelength and get exactly the same motions). The flattening of the curve at short wavelengths is the effect of the discrete system over the continuous one. For the real solid, the plot is four-dimensional, three for directions of the wavevector, one for frequency. The endpoint of the plot in any direction depends on details of the crystal symmetry. There are, in addition, two shear-like waves and one compressional-like wave in any direction, so that there are three branches. The shear wave speeds are usually of order 2/3 the compressional wave speed (but not for Pu, and not for BCC metals, where some shear frequencies are much lower). Therefore the shear modes have lower frequencies of vibration and contribute more to the entropy as we shall see below.

Note: Elastic moduli are the stiffness constants for solids. In general, there are 21 of them, but for an isotropic polycrystalline sample, only 2. They are usually written with two subscripts (they really need 4 because they are a fourth-rank tensor). Each elastic constant is a ratio of a particular type of stress to a particular strain. For example, c_{44} is a shear modulus that controls the shear stiffness in a particular high-symmetry direction in a crystal. Associated with it is a shear wave

whose speed is $v_s = \sqrt{\frac{c_{44}}{\rho}}$ where ρ is density.

Also in Fig. 4 is shown as a dotted line the effect of second nearest neighbor forces. Even with these included, there are very few free parameters required to construct the full plot.. If we have the full plot, it is straightforward to compute an "average" vibrational frequency, and hence, the entropy.

For any individual vibrational mode, we can use the partition function (Equation 10) to compute its entropy. Remembering that the energies of each harmonic oscillator or normal mode i are equally spaced such that $E_i = (n + 1/2)\hbar\omega_i$, we find that the average number of quanta \bar{n}_i thermally populating each normal mode (or allowed vibration) can be written as

$$\bar{n}_i = \frac{1}{Z} \sum_{n=0}^{\infty} n e^{-(n+1/2)\frac{\hbar\omega_i}{k_b T}} = \frac{1}{e^{\frac{\hbar\omega_i}{k_b T}} - 1}. \quad \text{If } k_b T \gg \hbar\omega_i \text{ then } \bar{n}_i \approx \frac{k_b T}{\hbar\omega_i}. \quad (15)$$

where we have used the partition function to compute the expectation value of the quantum number.

Similarly, we can obtain expressions for energy \bar{E}_i , free energy F_i , and entropy S_i , where

$$\bar{E}_i = \hbar\omega_i (\bar{n}_i + 1/2) = k_b T \quad (16)$$

$$F_i = -k_b T \ln Z \text{ where } Z = \frac{1}{e^{\frac{\hbar\omega_i}{2k_b T}} - e^{-\frac{\hbar\omega_i}{2k_b T}}} \quad (17)$$

$$TS_i = \overline{E_i} - F. \quad \text{If } k_b T \gg \hbar\omega \text{ then } TS_i \approx k_b T (1 + \ln \bar{n}_i). \quad (18)$$

To compute the entropy of the entire system, an average of the \ln of the frequencies is needed. The Debye temperature, Θ_D is the average most familiar, but for our purposes it is not accurate because of the particular approximations it embodies, and because it is not the average of the \ln of frequencies. Instead we define a characteristic temperature in the high temperature limit that is found by taking an average over Equation 18 for all modes along all the dispersion curves exemplified in Fig.4. We define this temperature in the high temperature limit to be Θ_0 where

$$TS \approx 3Nk_b (1 + \ln(T/\Theta_0)). \quad (19)$$

Equation 19 describes the total vibrational entropy of a solid of N atoms, and can be calculated from a measurement of the speed of sound at all wavelengths and in all

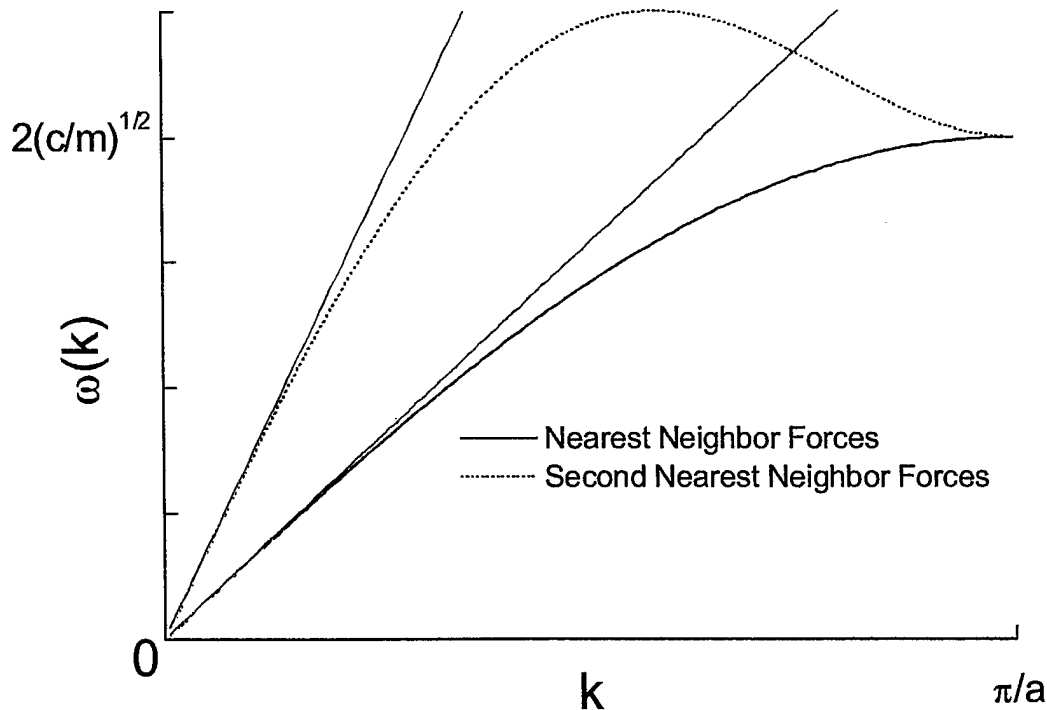


Figure 4. A plot of the vibrational modes versus frequency. The slope of the dashed line is the sound velocity.

directions. It would be nice if it could be computed from first principles. The catch is that

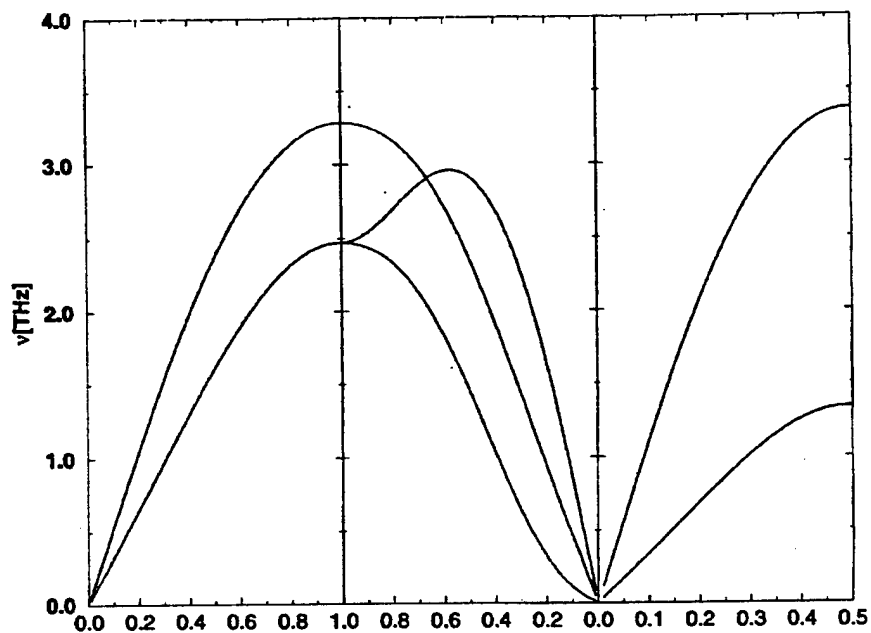


Figure 4. Estimate of the dispersion curves for fcc Pu from careful analysis of diffuse neutron scattering data. Constraints on the initial slope are obtained from elasticity measurements, greatly improving the confidence in such a calculation. Note the obvious presence of second-nearest-neighbor forces. The horizontal axis is the fraction of the Brillouin zone in each symmetry direction.

it is extremely difficult to compute the energy with the atoms vibrating. Ideally, there would be a way to use the accurate zero-temperature electronic structure parameters for monoclinic α -Pu to calculate the elastic moduli for a forced fcc δ -Pu model with the atoms vibrating. The amplitude of vibration is, in turn determined by the elastic moduli, so the procedure would be iterated until convergence occurred. This sort of self-consistent phonon molecular dynamics calculation is beyond reach at present. But if it could be done, the end result would be a good theory of Pu with the electronic structure parameters fixed at their zero-temperature value. The difference between this free energy the actual one would instruct us about the missing energy/entropy that needed to be made up by changes in the electronic structure. This is a crucial datum. Let's try to estimate it.

To estimate the importance of vibrational entropy for phase stability of Pu, we need also to get a handle on the energy changes with volume so that we can sort out the importance of volume changes from other effects. We can make some very crude guesses by noting that the bulk modulus B of Pu (measured, of course, by the sound speeds as well as x-ray diffraction) is known, as are the volume changes and latent heats at all the phase boundaries. If we consider, for definiteness the δ - ϵ phase transition at 753K, and we isothermally pre-compress Pu just below this phase boundary by 3.58%, the measured volume decrease across the boundary (Pu shrinks in volume on warming throughout the existence of the δ phase, and also upon transition to the ϵ phase), then we wind up with the correct volume for the ϵ phase but at a temperature infinitesimally too low for it to be stable, and with the wrong structure. We can now compare the energy required to compress to this state with the latent heat. The compressional energy is

$$\Delta \bar{E} = \frac{1}{2} B \left(\frac{\Delta V}{V} \right)^2. \quad (20)$$

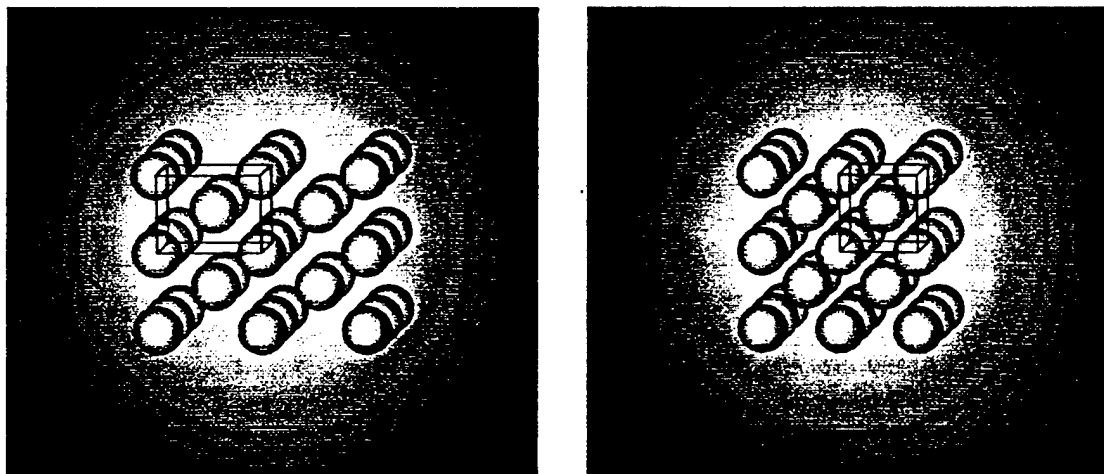


Figure 5. On the left is fcc (face-centered cubic) δ -Pu, on the right, bcc ϵ -Pu. The fcc phase is shown as an exactly equivalent bct (body centered tetragonal) phase. It is clear how the system can shrink continuously from fcc to bcc (called a Bain path).

Using the unit cell size (4 atoms in $(4.64 \text{ \AA})^3$ of δ -Pu and $B=29\text{GPa}$ for the only single crystal data (on Ga stabilized δ -Pu), also in agreement with our recent RUS measurements, we find the energy required to compress is 3 meV/atom. The latent heat is about 20 meV/atom. It is clear, therefore, that simply changing the volume of Pu cannot account for much of the energy changes across the phase boundary, and furthermore, Pu can essentially ignore volume changes in its search for a minimum free energy. This is a direct result of the unusual ease with which Pu can be compressed. It also implies that other moduli beside the bulk modulus are the most important at this transition, and that more than the specific heat (a scalar like volume) is required to sort things out.

If it isn't volume, what is it? This is the key question. To get the 20meV/atom needed would require drastic changes in electronic structure. Or, we could look for other, entropy-based mechanisms that do not require changes in electronic configuration, or we could look to both, which is probably closer to the truth. Our task, then would be to attempt to separate the entropy effects from the electronic configuration changes (such as changing the number of f-electrons), and in fact, this is one of the goals of our current research. If we note that at 753K, $3k_bT=192 \text{ meV/atom}$, an enormous energy, it is very attractive to see if the actual structure changes that do occur could, without much help from electronics, capture a small fraction of this via entropy differences. The small fraction is, of course, the latent heat because across a phase boundary the free energy change is zero, therefore the latent heat is

$$\Delta E = T \Delta S. \quad (21)$$

If we can get most of this with vibrational entropy alone via sound speed changes across the phase boundary, then the electronic structure calculations might have little or no work left to do. That is, except for the inclusion of thermal effects, the present electronic structure parameters that describe the zero-temperature properties of Pu so well might also be correct at all temperatures!

There is, in fact, a very suggestive way to understand at least what type of strain or distortion is primarily responsible for the 20 meV/atom needed. Consider Figure 5. On the left is the fcc δ -Pu structure, shown as a bct structure with the long edge $\sqrt{2}$ times the short edges. If we are just below the δ - ϵ phase boundary and we uniaxially and isothermally stress δ -Pu so that it shrinks from fcc to bcc (it shrinks along the stress direction and expands perpendicular to it), we produce exactly the right structure at just below the temperature at which it is stable. This is a Bain path. On raising temperature a tiny amount, absolutely nothing happens except that the bcc structure becomes stable. There is no latent heat for this process. Therefore the measured latent heat without a Bain strain must be equal to the energy required to strain the fcc phase into a bcc shape along the Bain path. A small volume adjustment might be needed, but we have shown this to be small. What strains are involved in this process?

Measured elastic properties of δ -Pu show an unusually large shear anisotropy. What this means in Pu is that the shear stiffness in one direction (the 110, or an angle $\pi/4$ from an

edge) is very low compared to the shear stiffness parallel to an edge. This has two effects. One is that Young's modulus, exactly the modulus encountered along the Bain path, is also very low. The other is that Poisson's ratio (which describes how much a material bulges when uniaxially compressed) is very large (0.424), hence the Bain path is traversed with little volume change, and with the energy required coming mostly from shear. We have now connected a shear strain energy to the measured entropy change, and we learn that shear-like rearrangement of the Pu atoms must be the important process at this phase transition! Can we get a handle on this via sound speeds as well?

Note: the starting structure and ending structures along the δ - ϵ Bain path are cubic. If the stress is applied uniaxially, then surprisingly the ending stress is zero. That is, we start with a cubic material with zero stress. We end with a cubic material with zero stress perpendicular to the distortion. Therefore the stress is also zero in the distorted direction because the system must have cubic symmetry in all its properties.

In general bcc materials also have a very large shear anisotropy, typically even larger than for δ -Pu. As we have seen, if the stiffness is low, the vibrational modes using that stiffness have low frequencies, and, therefore, lots of entropy. We expect, then, that the generally low shear stiffness in one direction of bcc structures should provide them with lots of entropy, thereby making them favorable as temperature rises. Even though we don't know the vibrational spectrum of ϵ -Pu, we do know ultrasonically-derived average phonon frequencies (or, equivalently, temperatures) for both δ - and ϵ -Pu from Ledbetter and from Kmetko and Hill. Though they did not use exactly the right average for our purposes, both phases likely have similarly large shear anisotropy so that perhaps the errors in using this less-than-ideal but available number might not be too bad. Using the ultrasonic characteristic temperature at 750K for δ -Pu of 106K and for ϵ -Pu of 89K, we find, using Equation 19 and the measured latent heat Q , that

$$3k_b \left(1 + \ln \left(\frac{T}{\Theta_\delta} \right) \right) + Q = 3k_b \left(1 + \ln \left(\frac{T}{\Theta_\epsilon} \right) \right) \quad (22)$$

to within a few percent. Thus based on a few arguments relating elastic effects and measured latent heat, we can account for essentially all the energy and entropy changes. There is, therefore, probably not a lot wrong with using the zero-temperature electronic structure parameters to understand the δ - ϵ phase transition. More work must be done to establish the importance of these arguments for the lower temperature phases, where entropy is less. This is another of our goals.

The Bain path may account for the negative volume thermal expansion coefficient of δ Pu. The very very large strains that accompany the Bain route ensure that, using the latent heat and the starting and ending moduli, we can only roughly construct the elastic moduli along the route. There is also no constraint that the end-point volume be larger or smaller

than the starting volume. For Pu, the end-point bcc volume just happens to be smaller, and the route itself is very soft. An attractive argument for the negative thermal expansion, then, is that below the δ - ϵ boundary, Pu thermally "samples" the bcc volume along the very soft Bain path. Thus part of the time, it has a volume closer to bcc, which is smaller than the fcc volume. The negative thermal expansion may be a direct consequence of the lower bcc volume, and the existence of a Bain path. The low value of Young's modulus in this direction assists this process.

The size of these entropy-driven effects is very large in Pu. For example, in Ni with a melting point less than twice that of Pu, the bulk modulus is about five times higher, and the Debye temperature, (related to the sound speeds and therefore the Bulk modulus) four times higher than in Pu. Therefore in Ni compressional energies are larger than in Pu, and entropy effects are smaller. Ni has far fewer options in its search for stable high-temperature phases, and in fact, Ni exhibits far fewer structures than Pu over the range of existence of the solid, and always has a positive thermal expansion coefficient. The root of all the odd behavior of Pu, then, may be the localized electrons with weak overlap that force Pu to have an easily compressed open structure.

Measurements of the Elastic Moduli

Knowledge of the elastic modulus tensor as a function of temperature and pressure for each of the phases of Pu would provide an almost complete experimental understanding of its thermodynamics. Although such data exists for many elements, it requires single crystals of each phase. The phase diagram of Pu makes this extremely difficult for ultrasonic techniques because as Pu cools from the melt, the phase changes it undergoes destroy the ability to grow single crystals of α -Pu except under extreme pressure, while all the other phases only exist at high temperature. Thus a single crystal of pure δ -Pu would have to be kept above 700K for the entire measurement process. Things are also difficult for neutron scattering studies because Pu^{239} absorbs neutrons, so isotopically pure Pu^{242} , a very rare item, must be used. Worse still, measuring the moduli in such a dangerous system entails extreme environmental and safety overhead, so that, notwithstanding their importance, there is little in the way of accurate and reliable elasticity information on Pu.

The little data we have is decidedly unusual. For example, the only measurement on a Pu single crystal was made in 1975 by Moment¹ at ambient temperature on a 7mm-long heavily Ga stabilized (1 weight % Ga) δ -Pu grain. It took them over a year to grow the crystal, even in the then much-less-regulated environment, and the results, summarized in Table 2 are, to say the least, amazingly anisotropic. Note that c^* is the shear modulus at $\pi/4$ to the cubic axis, c_{11} controls the compressional sound speed and c^* and c_{44} control shear speeds.

c_{11}	36.28 ± 0.36 GPa
c_{44}	33.59 ± 0.11 GPa
$1/2(c_{11}-c_{12})=c^*$	4.78 ± 0.38 GPa

Table 2. The elastic moduli of Pu-1 weight % Ga δ -phase at ambient temperature as measured by Moment and Ledbetter.

There are several points to be made about this measurement. First, at a radioactive heating rate of 50 mW/cm^3 , a larger crystal is not accurately measurable because it heats internally. Second, Ga stabilized δ -Pu is not the same as δ -Pu. That is, in Pu 3 at.% Ga, along any of the principal crystallographic directions, there are only about two Pu atoms between Ga atoms. Thus the structure is quite thoroughly distorted by the Ga, as are the phase transitions, the temperature at which they occur, and even the sign of the thermal expansion coefficient. Although it is known that the atomic volume of Pu-Ga varies very smoothly, with a zero-Ga intercept at the atomic volume of pure δ -Pu, elastic properties are often more than an order of magnitude more sensitive to atomic volume than other physical quantities. Thus it is possible that the elastic moduli of pure δ -Pu are different from those of Ga stabilized δ -Pu. Third, the elastic anisotropy, c_{44}/c^* is the largest for any fcc metal (to put this in perspective, an isotropic system like glass has $c^*=c_{44}$). Thus the strong variation of

moduli with direction requires more care when computing averages, especially because the soft directions contribute more strongly to entropy. Fourth, c_{44} nearly equals c_{11} , thus the material, when compressed along a cubic axis, doesn't change volume much, a lot like a liquid. Fifth, radiation damage changes the properties of Pu. Taken together, this suggests that we must be very careful with modulus data on δ -Pu derived from Ga-Pu alloys, and that elasticity measurements must be made to determine the effect of Ga. Nevertheless, the Ga stabilized phases are possible to work with and crucial are for engineering, so that is where our initial measurements focus.

Finally, we note that the very large shear anisotropy in Pu means that elastic measurements on polycrystalline samples will produce averages of strongly varying quantities, masking the underlying physics. To get at these details, it is important to make as many measurements as possible on single crystals. This will provide much more information for use in a fundamental understanding of Pu, and, as shown in Figure 6, Pu with six phases (δ' Pu is

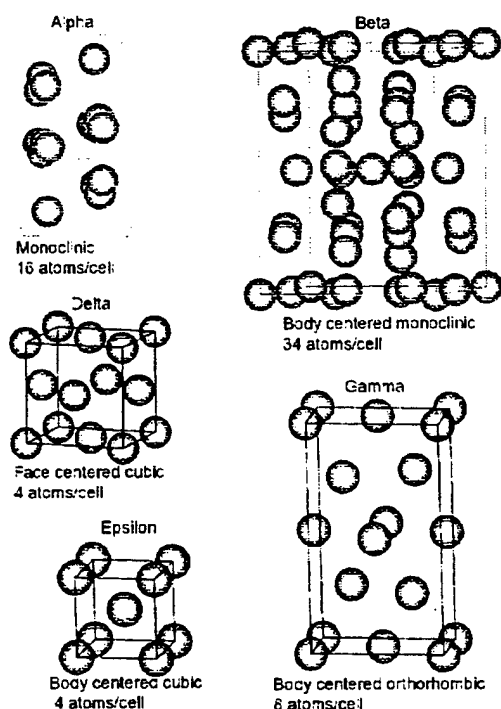


Figure 6. The six crystal structures of Pu. Only five are shown because δ' and δ look about the same.

hard to identify, and looks like a slightly stretched δ structure), can have as few as three moduli (cubic phases) to as many as 13 (monoclinic phases).

To perform elasticity measurements on Pu, there are powerful regulatory and safety issues that come to bear, ensuring that only Ga stabilized δ -Pu crystals of a few mm are likely to appear in the next several years. Such small samples are difficult to study using

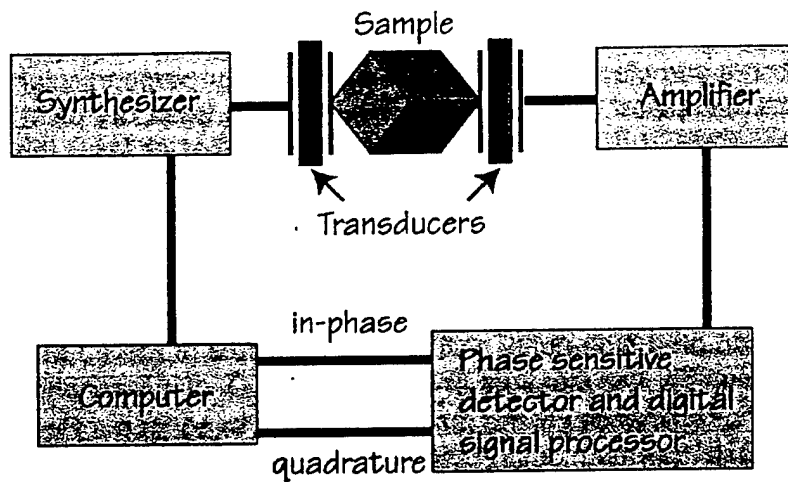
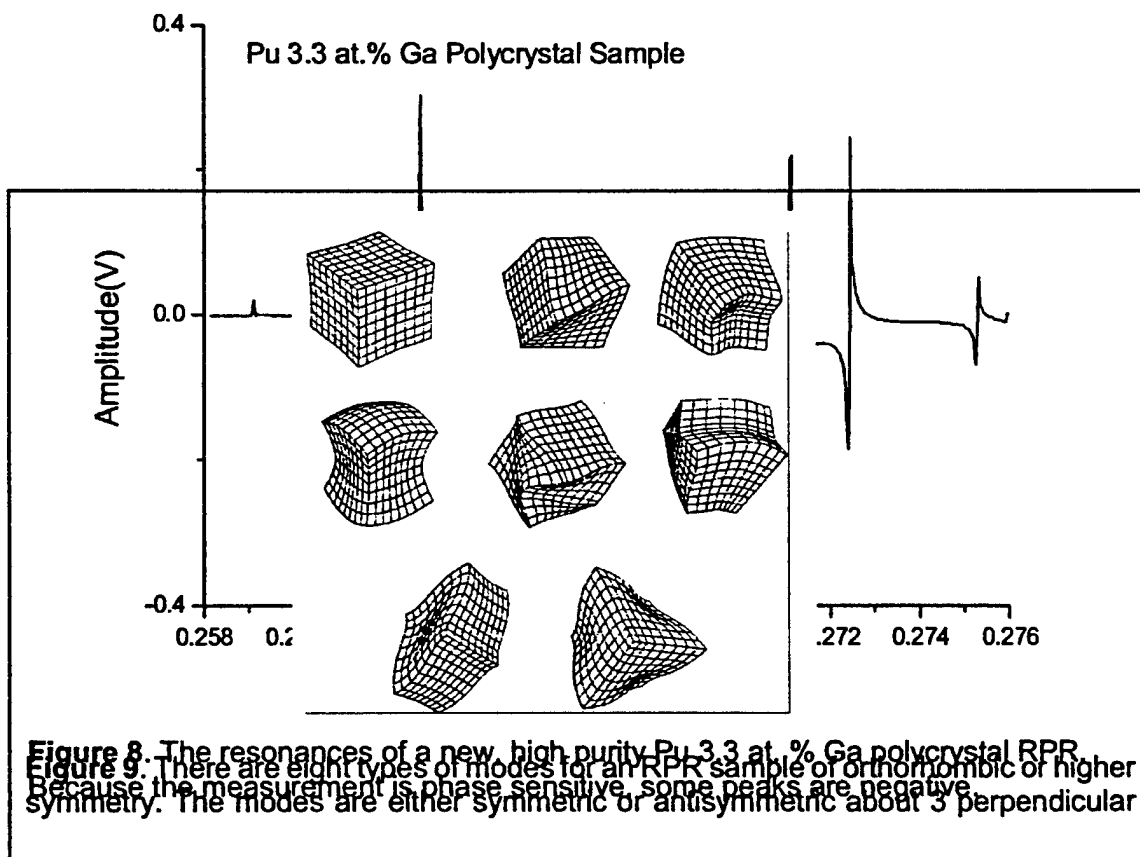


Figure 7. Block diagram of a Resonant ultrasound spectrometer.

conventional pulsed ultrasound because of both size and attenuation effects. Fortunately, RUS (Resonant Ultrasound Spectroscopy), heavily developed at LANL over the last several years, is perfectly suited for a re-measure of Pu, both single- and polycrystal material.

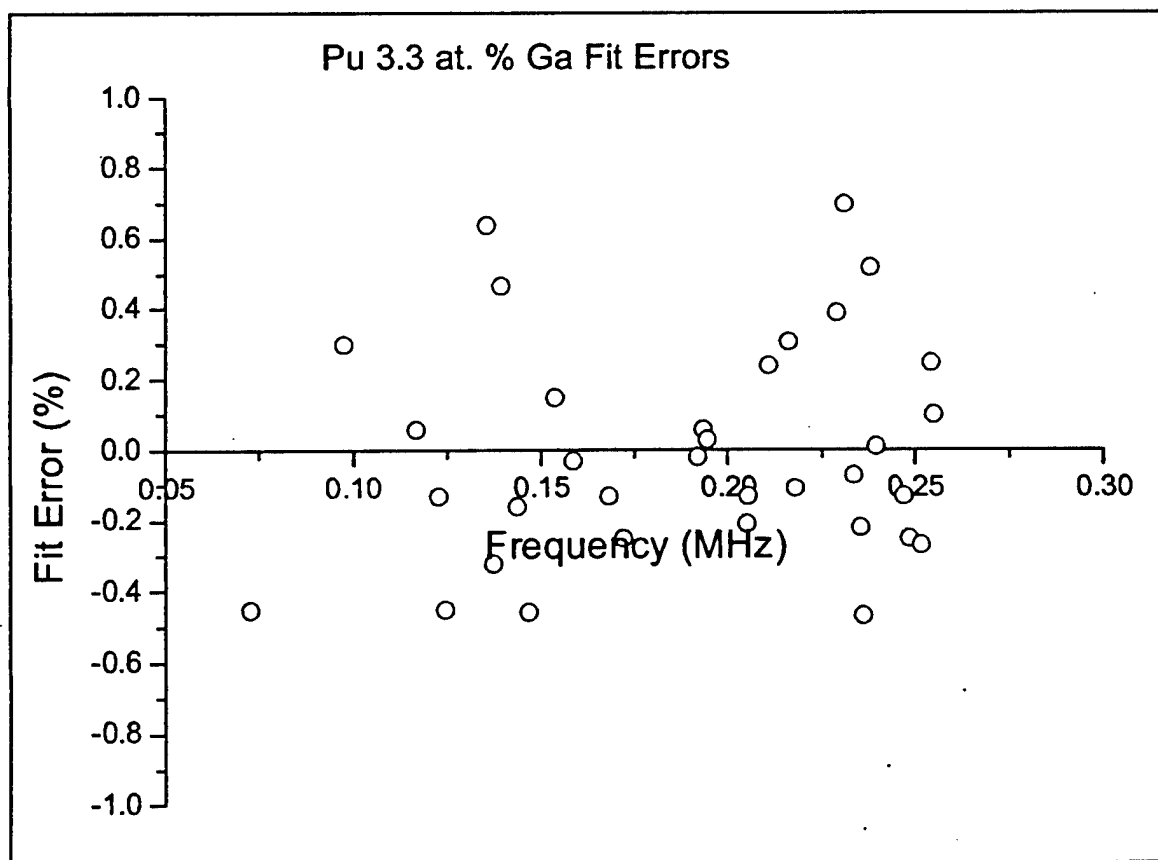
RUS is a very simple technique whereby the mechanical resonances of a solid object of known shape are analyzed to provide the complete elastic tensor. The system is usually implemented on a sample with all faces either parallel or perpendicular to each other (a rectangular parallelepiped resonator or RPR). Because weak dry point contact is made between transducers and very small samples (a few mm or less) this system is both extremely accurate and well suited for glove-box operations. The weak contact requires that extreme care must be taken with the electronics. The current state-of-the-art system was designed by one of us and is now in production by Dynamic Resonance Systems. A block diagram is shown in Figure 7. The resonances that we have observed for Pu with this system are ideal for this technique, being very sharp, as shown in Figure 8 where we display data taken on a high-purity chill cast new sample of Pu-3.3 at. % Ga polycrystal supplied by J. Lashley. The measure of sharpness, or Q, of a resonance is $f/\Delta f$ where f is the frequency of a resonance (in the range of 0.2 MHz or so for our Pu samples) and Δf is the full width at half maximum of the resonance. The Q is a direct measure of the intrinsic dissipation. If the Q is greater than 1000, then we expect very high accuracy for modulus measurements.

Although it is quite straightforward to acquire extremely accurate resonances on carefully prepared Pu samples, the analysis of those resonances is computational intensive. To put this in perspective, a computation took 10 seconds of CPU time on the first Cray, 12 hours on a PC-AT and 13 seconds on a 600MHz PIII. The reason for this is illustrated in Figure



9 where we show the deformations occurring with several different mode types. The RUS algorithm adjusts elastic moduli of the model RPR to match the measured ones. A typical result is illustrated in Figure 10 where we show the deviation between fitted and measured resonances. The actual accuracy of the measurement is not quite the RMS error in the fit because the best fit has different curvatures in the different directions in elastic modulus space. The typical result is that we obtain shear moduli on Pu to about 0.1% and compressional moduli to about 0.7%. There are no corrections to such results, which is why RUS typically provides the highest absolute accuracy for any routine modulus measurement technique. For the measurement of Figure 10, we used a sample weighing 1.33 g, with a geometrically determined density of 15.968 g/cc. The sample was rather large for RUS, 0.30814 x 0.49280 x 0.56032 cm. The errors for this measurement were about 0.9% for c_{11} , which determines the compressional wave speed and 0.1% for c_{44} which determines the shear wave speed.

In Table 4, we provide a summary of our recent measurements, as well as older studies by others. Of particular interest is the almost exact correspondence between the very carefully done studies of Moment and Ledbetter on a single crystal of new Pu 3.3 at. % Ga and our measurement on a nominally identical polycrystal sample. This is one of the few examples of agreement between modulus measurements on Pu that, because of age and



composition, should agree. In contrast, there are disagreements in other measurements that don't appear reasonable. For example, the data for the 3.2 at% Ga sample are so different from ours and Moment's that there is either an uncontrolled variable, or they are wrong. We also point out the agreement between our modern measurement of pure polycrystal Pu (α phase) at room temperature with one older measurement, but not another.

Finally, the variation in the results of pure Pu in the δ phase at higher temperatures are so extreme that they beg for corroboration. We hope to address all these points and others in

Sample	C_{11} (GPa)	Bulk(GPa)	Shear (GPa)
polycrystal pure δ -Pu 703K	41.3	33.9	5.59
polycrystal pure δ -Pu 655K	63.6	55.9	5.79
polycrystal δ -Pu 5.9 at. % Al	54.9	30.9	18.0
polycrystal δ -Pu 2.1 at. % Al	40.3	19.1	15.9
polycrystal δ -Pu 5.8 at.% Ga	65.1	37.1	21.0
polycrystal δ -Pu 3.2 at.% Ga	64.4	37.7	20.0
single crystal δ -Pu 3.2 at.% Ga new	51.4	29.9	16.1
polycrystal δ-Pu 1.73 at. % Ga 15y	47.5	26.7	16.3
polycrystal δ-Pu 2.36 at. % Ga new	52.3	30.6	16.3
polycrystal δ-Pu 3.3 at. % Ga new	51.8	29.6	16.7
polycrystal δ-Pu 4.64 at. % Ga new first polish (not square)	53.3 53.9	30.7 31.3	16.98 16.98
polycrystal δ-Pu 3.902 at. % Ga 15y	58.4	34.3	18.1
polycrystal δ-Pu 5.4 at. % Ga 44y	50.0	27.0	17.2
cast α -Pu (Laquer)	104.6	46.6	43.5
cast α-Pu*	109.1	55.8	40.0
cast α -Pu (DeCadenet)	109.0	54.5	40.9

Table 4. A summary of ours and other measurements of the elastic moduli of Pu. Our results, supported by the LANL Enhanced Surveillance Program, are in bold. All measurements were at ambient temperature except where noted.

the next few years.

For all the measurements we have made on Pu, the Qs were greater than 3000, and as much as 12000 for the sample used for the data of Figure 10. With a Q of 10000, and signal/noise ratios typified by Figure 8, we are able to track frequency changes smaller than 1 part in 10^6 . This extraordinary sensitivity to changes makes possible two unique measurements. The first is real-time studies of the effect of radioactive decay on the elastic properties of Pu. For example, a Q of 10000 would enable us to see a change of about 1ppm in stiffness, something we might expect to see in a few days if the temperature can be held stable to 0.005K, a perfectly feasible task. It is also possible to study the effects of aging on phase stability in real time as well. For example, if Ga stabilized δ -Pu is cooled, it may become increasingly and measurably (for RUS) unstable, exhibited by a very slow change in elastic moduli versus time. Such metastability is observed in many systems including steel and precipitation hardened (so-called aircraft Al) Al. To observe both radioactivity induced changes and metastability will require a precision temperature controlled environment for the measurement. Such a system will leverage another critical set of measurements-the variation of moduli with temperature.

One source of the variation of the elastic properties of Pu with temperature comes from changes in the phonon frequencies with vibrational amplitude, an important non-linear effect, as is thermal expansion. Noting that Pu has a very large thermal expansion coefficient, it is expected that other non-linear effects will also be unusually large, so that their study will be particularly revealing. There have been few temperature dependent modulus measurements so far, and there are no single-crystal data. The polycrystal work has been done on large samples that self-heat and only one set of data appears on the Ga stabilized alloy. For those measurements, the elastic moduli are substantially different from our recent results (the value for the 3.2 at. % Ga sample in Table 4 was taken from the temperature-dependence study). To understand why will be difficult and time-consuming, however it badly needs to be done. Our approach, especially considering the safety concerns, is to begin with measurements of the temperature variation of elastic moduli around ambient by using thermoelectrically cooled stages to vary temperature by 30K or so. Such a variation will enable us to determine the slope of the temperature dependence at ambient temperature to about 0.3%. This work is well under way while we attack the much more difficult problem of introducing furnaces and cryogens into the RUS experimental area so that other phases can be studied. But for all the reasons discussed in this article, the results will be well worth the effort.

High-speed low noise measurements

Albert Migliori, Fedor Balakirev, Jon Betts, Greg Boebinger



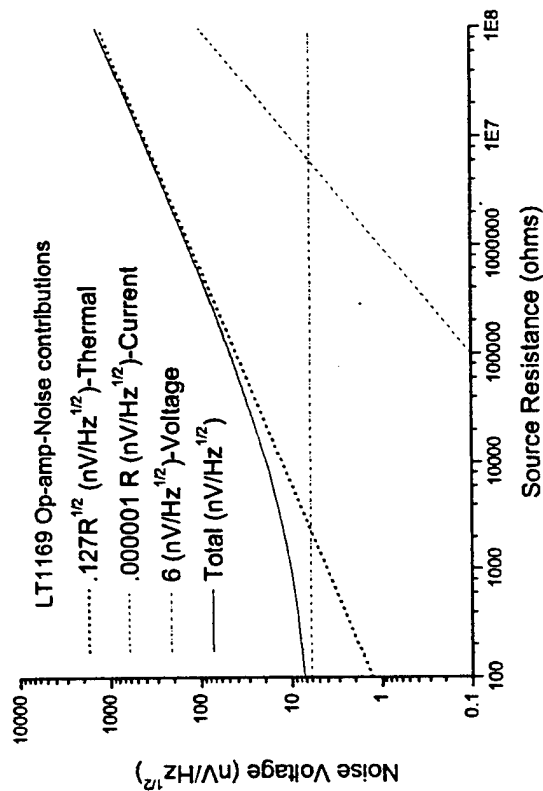
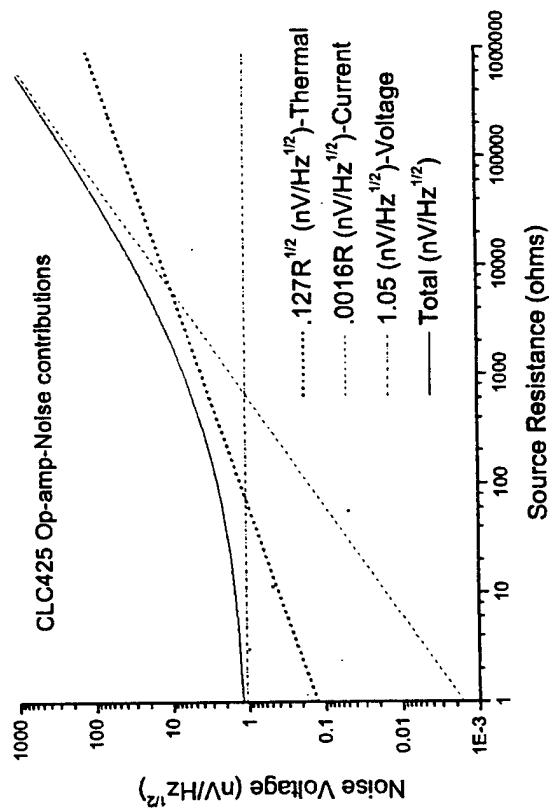
The problem:
No general-purpose instrument is optimized for high magnetic field measurements.

Solution:
Build custom instruments optimized for NHMFL measurements in pulsed and DC magnets.

Goals:
Make transport measurements better, faster, more reliable. Thermal conductivity and specific heat measurements can be made using 3ω techniques.

Op-amp noise comparison-the best of each

Bipolar -150 MHz max

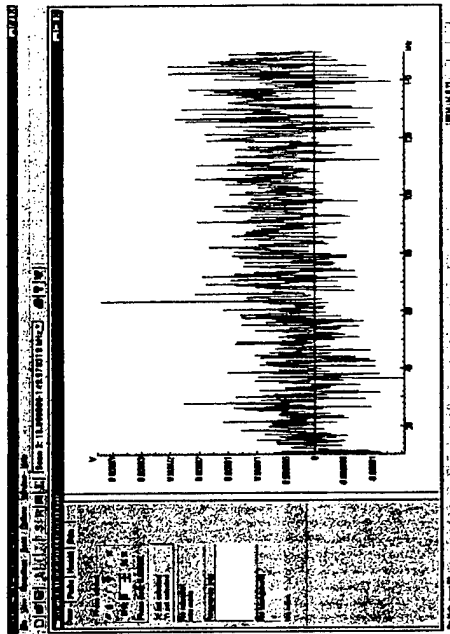


J-FET 1 Mhz max

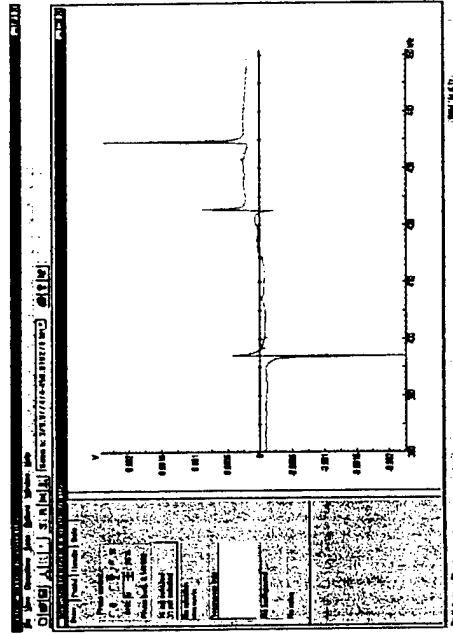
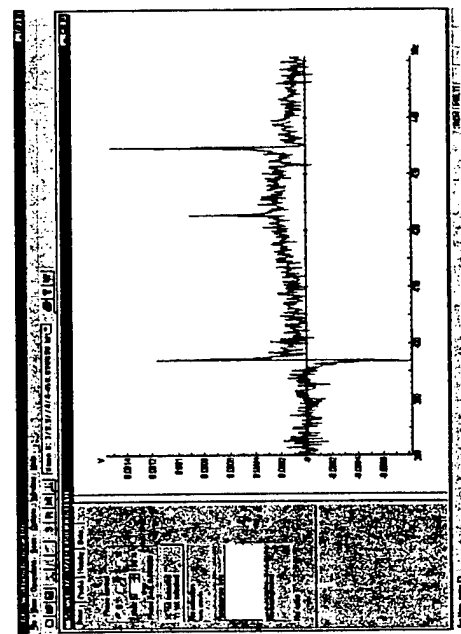
White noise is good! (Less noise is better)

If you get this, with no sample, then all is right with the world. The system here is a swept-sine, phase sensitive resonant ultrasound spectrometer, equivalent to a high frequency lock-in with swept reference frequency (designed by Migliori).

A bipolar op-amp with very low voltage noise was chosen for a high impedance measurement. Its high current noise ruins the signal/noise ratio.



A J-FET preamp with 3 times higher voltage noise but 2 orders of magnitude lower current noise fixes things right up.



You can only make things worse!

The very strongest thermodynamic arguments relate fluctuations (noise) to dissipation (resistance) such that "Johnson noise" is

$$E_n = \sqrt{4Rk_b T \Delta f} = 0.127 nV R^{1/2} \Delta f^{1/2}$$

= Noise voltage density at room temperature

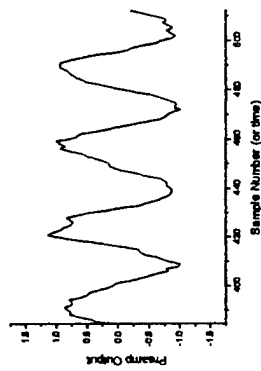
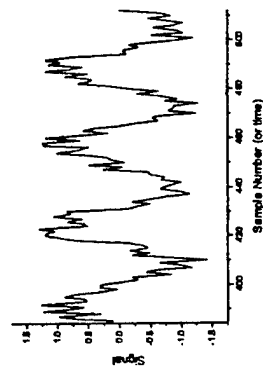
(Δf is bandwidth in Hz, R is resistance in Ω , T is temperature in K.)

Johnson noise is "white". The current noise is just E_n / R .

A 100Ω resistor has a noise voltage density of $1.27 nV/Hz$ at room temperature

Lock-Ins

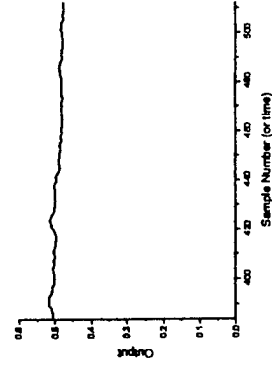
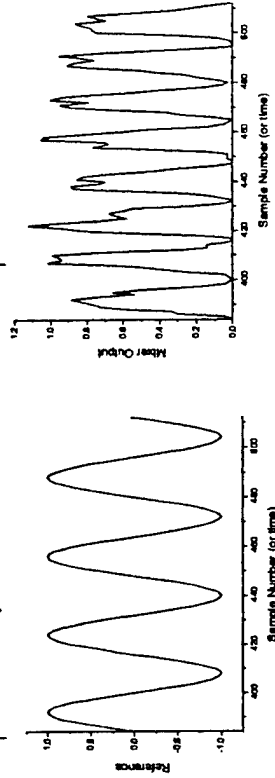
The input noise is often band-limited with a preamp. This is **ONLY** to prevent overloading of the lock-in and to prevent problems with slow digitizers that lock-ins usually contain. It does not reduce output noise.



The filtered signal is analog or digitally multiplied by the reference sine wave, here set at 0° phase.

The result is at 0 and $2f$, and **ALL** the post-preamp noise, as well as the component of the signal in-phase with the reference.

The final operation of $\tau=RC$ filtering (analog or digital) now removes noise by bandwidth limiting the mixer output to $1/(2\pi\tau)$ -this is the only place noise reduction occurs. Often a D/A conversion is then made.



Why bother?? There are excellent alternatives.

Digitizers:

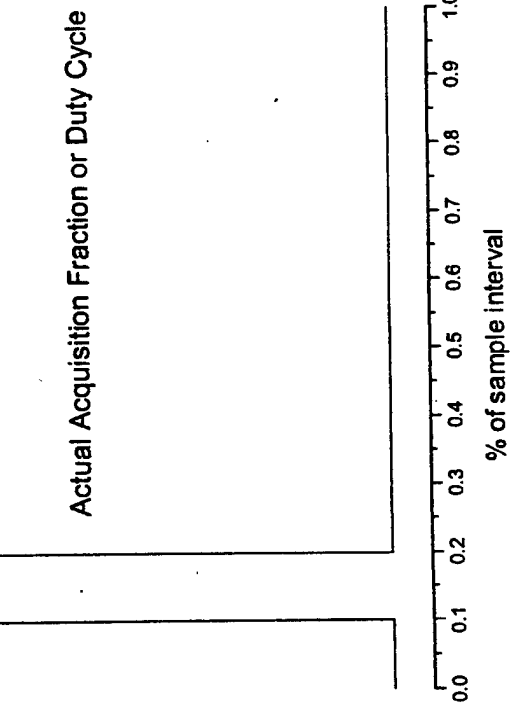
Digitizers are a way of life. There are several points to consider:

Duty cycle: the ratio of the time that a digitizer spends acquiring data to the total measurement time. This is not the same as speed, and is very important!

S/N decreases with /duty cycle. Thus it can be very costly to use a 10MS/s digitizer at 100kHz. The best approach is to run digitizers near maximum speed.

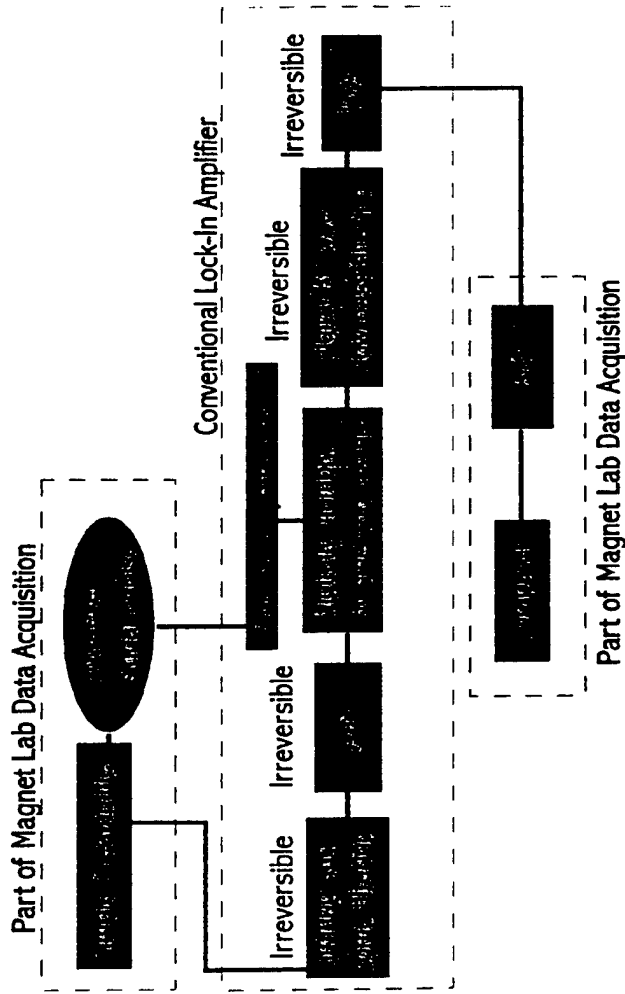
All 10MS/s digitizers are not alike. The sampling time (aperture) can vary an order of magnitude-affecting S/N. It is also useful to use a low-pass filter in front of a digitizer to increase the effective duty cycle, and thereby reduce the number of points required for best S/N.

Bits of resolution:



Make CERTAIN that the digitizer LSB is greater than the RMS noise voltage. This is the maximum and minimum usable gain, no further increase helps. If so then if you use an 8MS/s / 8-bit digitizer at full speed, but need only 500kHz bandwidth, the key strategy is to average each set of 16 samples. You get 4 free bits(the 8-bit digitizer properly resolves 12 bits!)

Conventional Instrumentation:



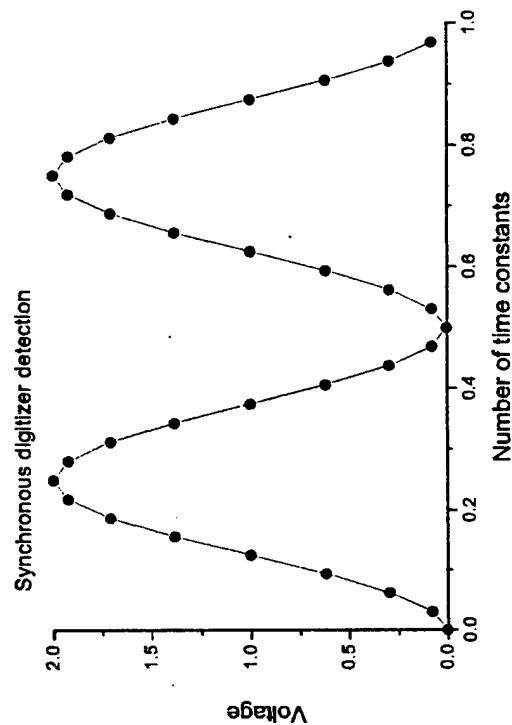
Unnecessary irreversible loss of information.

Three separate digital conversions.

Only frequency-domain filtering...algorithms restricted to what is available in the commercial lock-in.

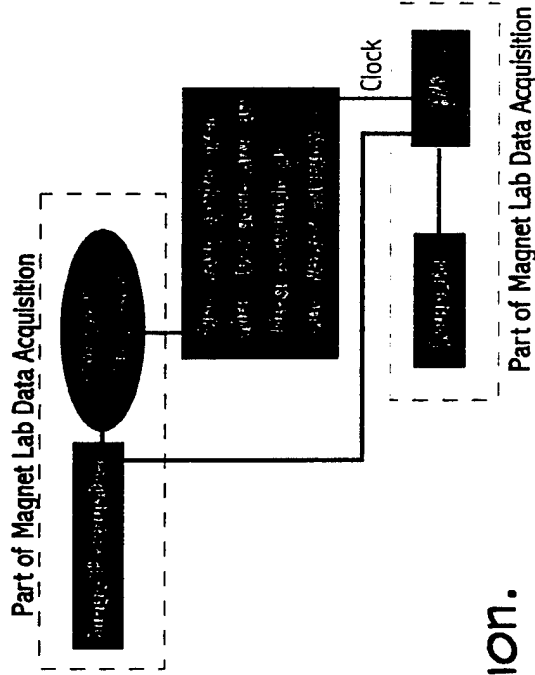
If a sine wave is digitized at a frequency nf where f is the sine wave frequency and n is the number of digitizations per cycle then upon averaging:

1. an m -bit digitizer produces $m+n$ bits of precision
2. the noise bandwidth of the digitizer drops by $1/n$
3. the signal/noise ratio improves by $n^{1/2}$
4. all information about the signal is retained so that AFTER the acquisition
 - a) the time-constant or noise bandwidth can be tweaked
 - b) the in-phase and quadrature signals, relative to the synchronous driving signal can be fully recovered and manipulated.



5. this does everything that a lock-in does, but better and more completely-knobs can be tweaked AFTER data is acquired!!!

NHMFLL Custom Instrumentation:



Much simpler, cheaper.

No irreversible loss of information.

All normal lock-in functions (gain, phase, time constant) implemented reversibly after data is recorded.

Time-domain filtering to remove spikes.

One-cycle-settling-time frequency-domain filtering.

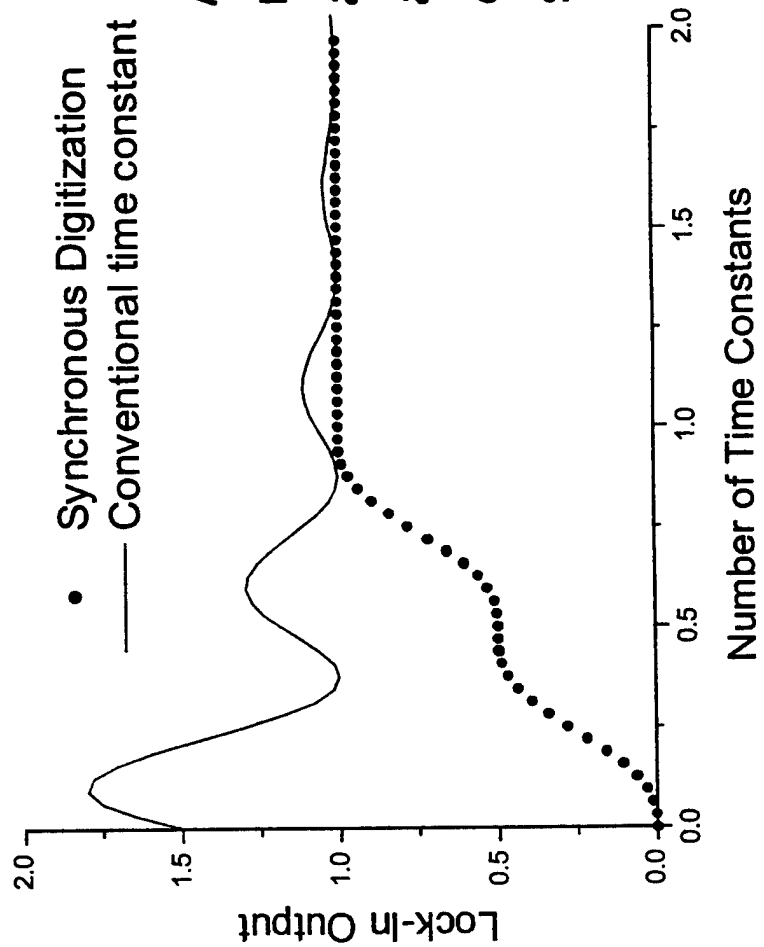
Zero-delay time constants.

none of which are possible with conventional lock-ins.

Digital Lock-ins:

If a sine wave of frequency f is digitized at a rate nf , then upon averaging n points:

- | an m -bit digitizer produces $m+n$ bits of precision.
- | the noise bandwidth of the digitizer drops by $1/n$.
- | the signal/noise ratio improves by $n^{1/2}$.



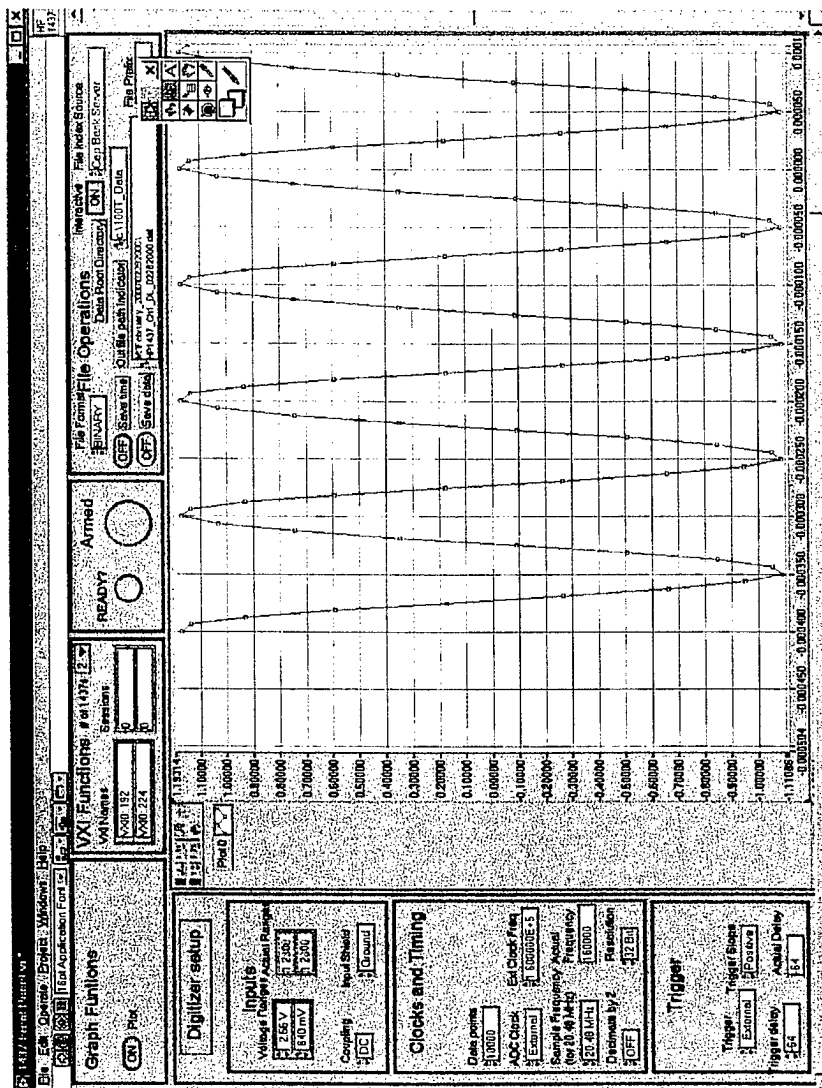
A lock-in function implemented in software produces an exactly settled value in exactly one cycle if the reference sine-wave excitation is synchronously digitized.



The NHMFL digital lock-in: how it works

First step:

Acquire ALL the data with a synchronous digitizer fast enough to capture all that the preamp can put out.

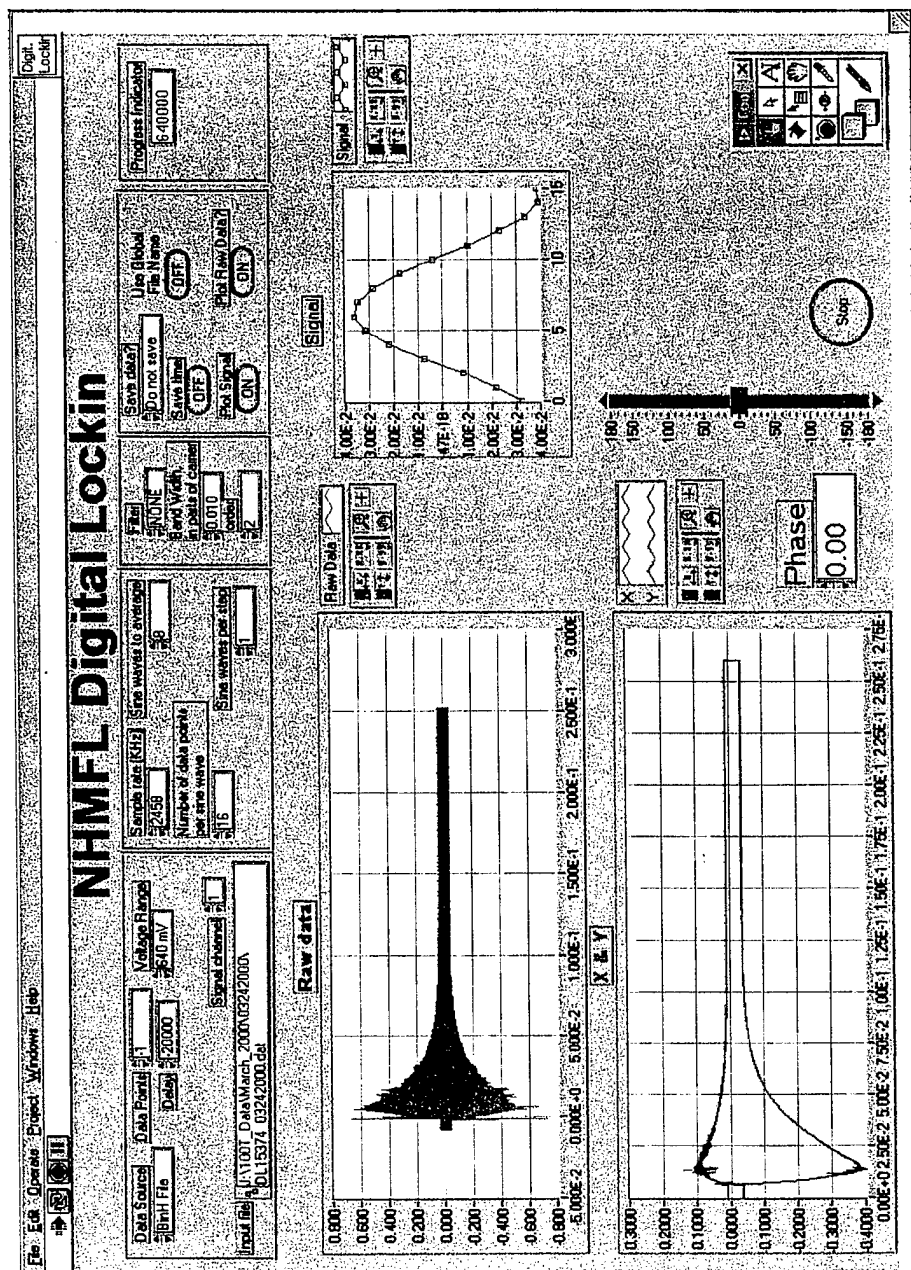


Second step:

Read data into computer.

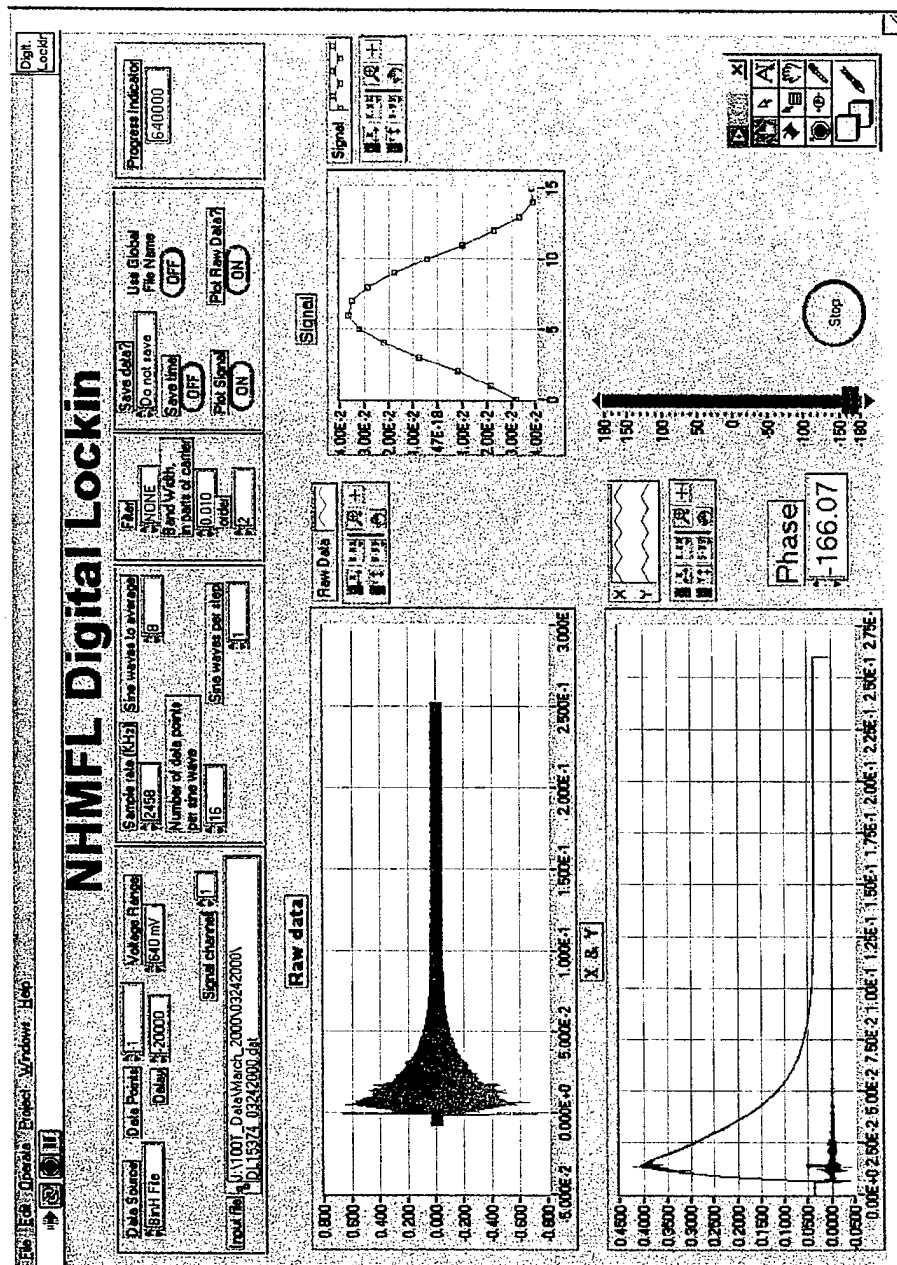
Clip noise spikes in time domain.

Detect by multiplying by sine and cosine (in software) and plot detected signal.



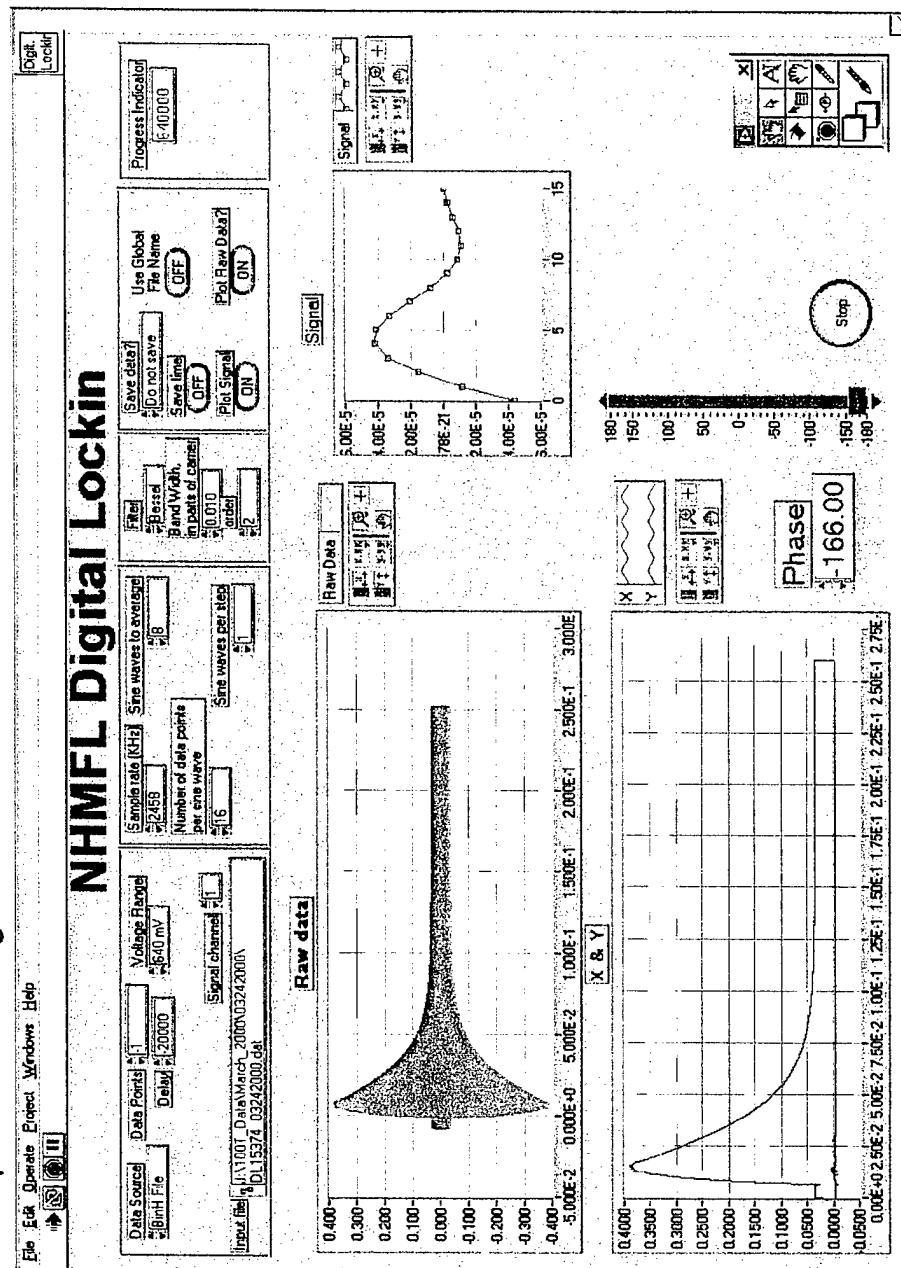
Third step:

Optimize phase, limit spikes in time domain.



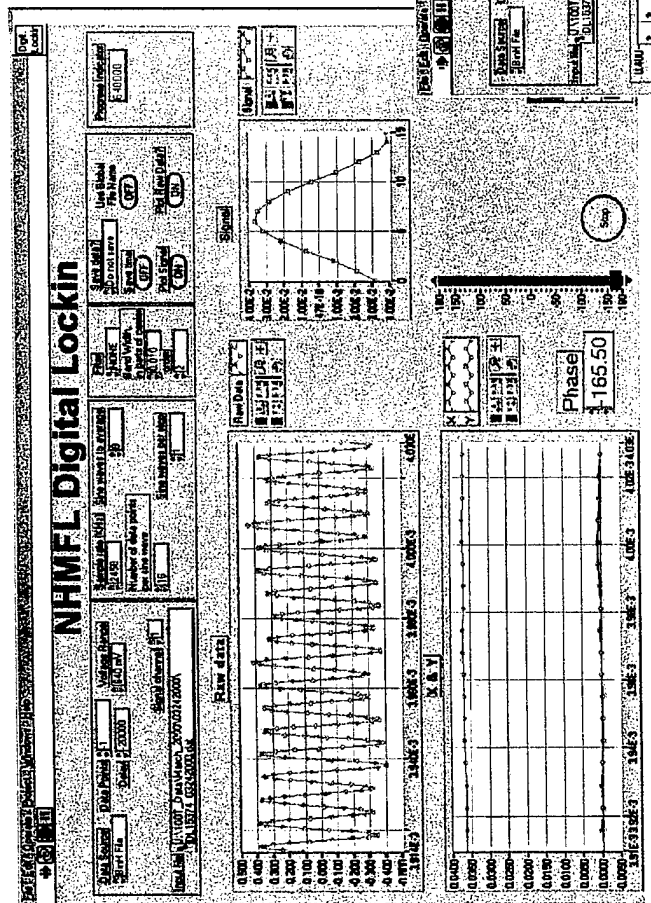
Fourth step:

Adjust filtering, time constant for desired response. Note that once data is acquired, all the processes performed afterward can be changed, undone, redone, and mistakes in initial setup can be corrected! This includes changing the phase, spike-limiting, and time constant.



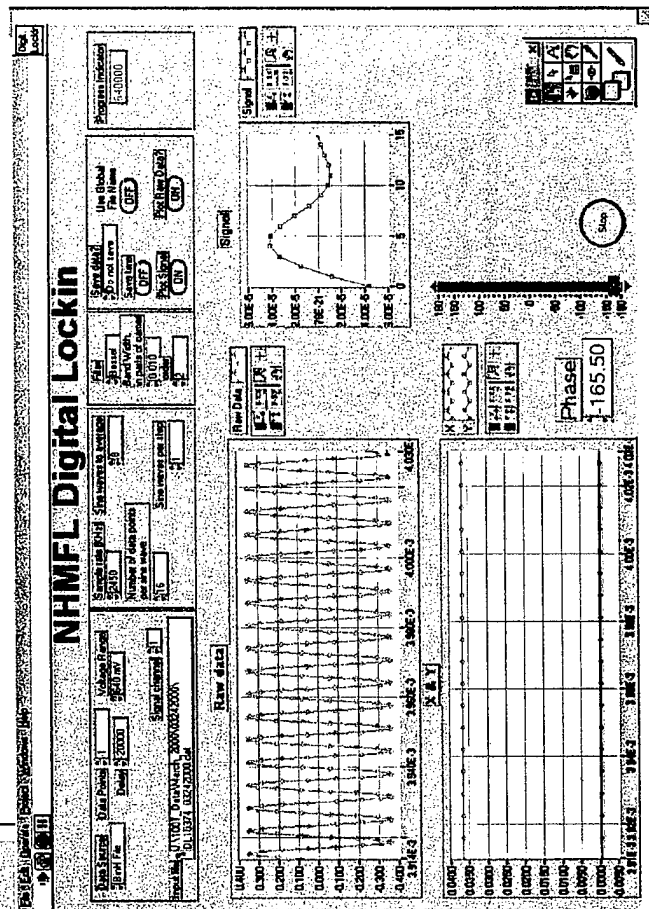
Details:

Effect of post-shot filter



6-pole Bessel filter
centered at carrier
frequency

no filter

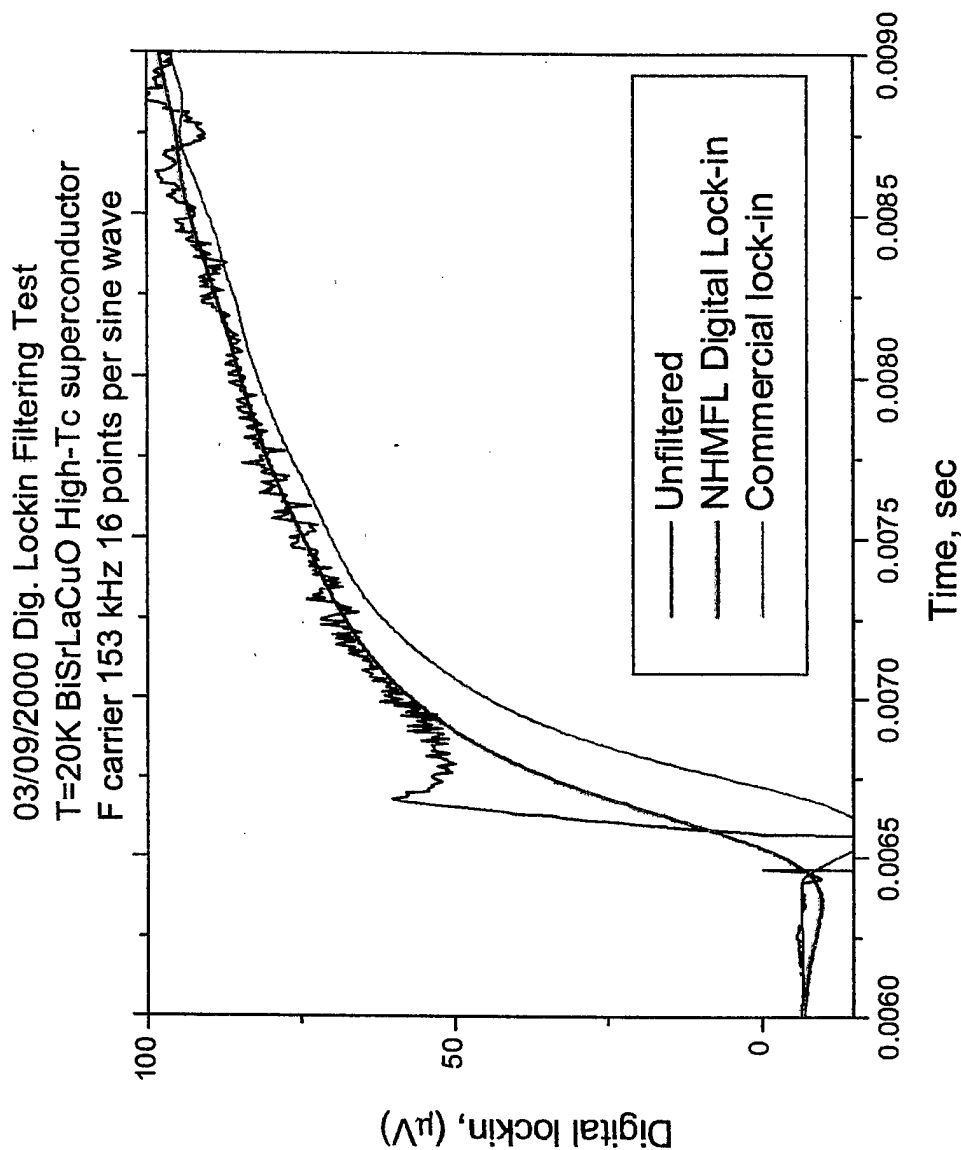


Details:

An ordinary lock-in applies the time constant and other filters in real time.

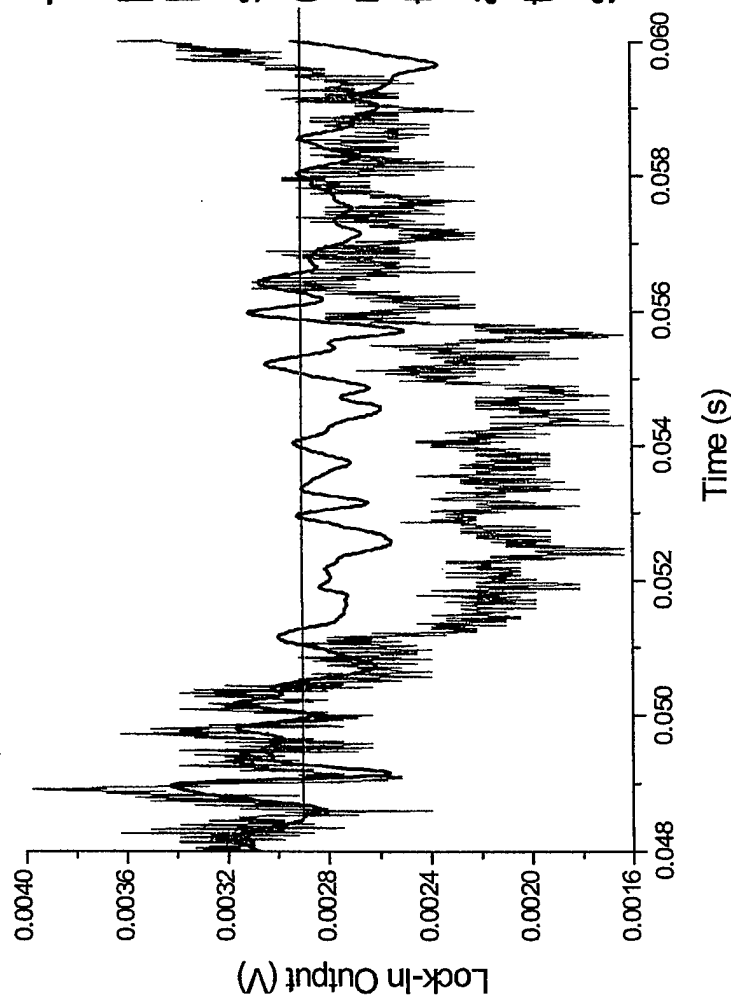
This causes an unavoidable time delay in the output.

This is illustrated with the superconducting transition of BSLCO at $T=20\text{K}$ during a magnet pulse of 60T. Note the effect of the delay in the red trace, easily eliminated for the synchronous lock-in (blue).



Details: Noise and drift

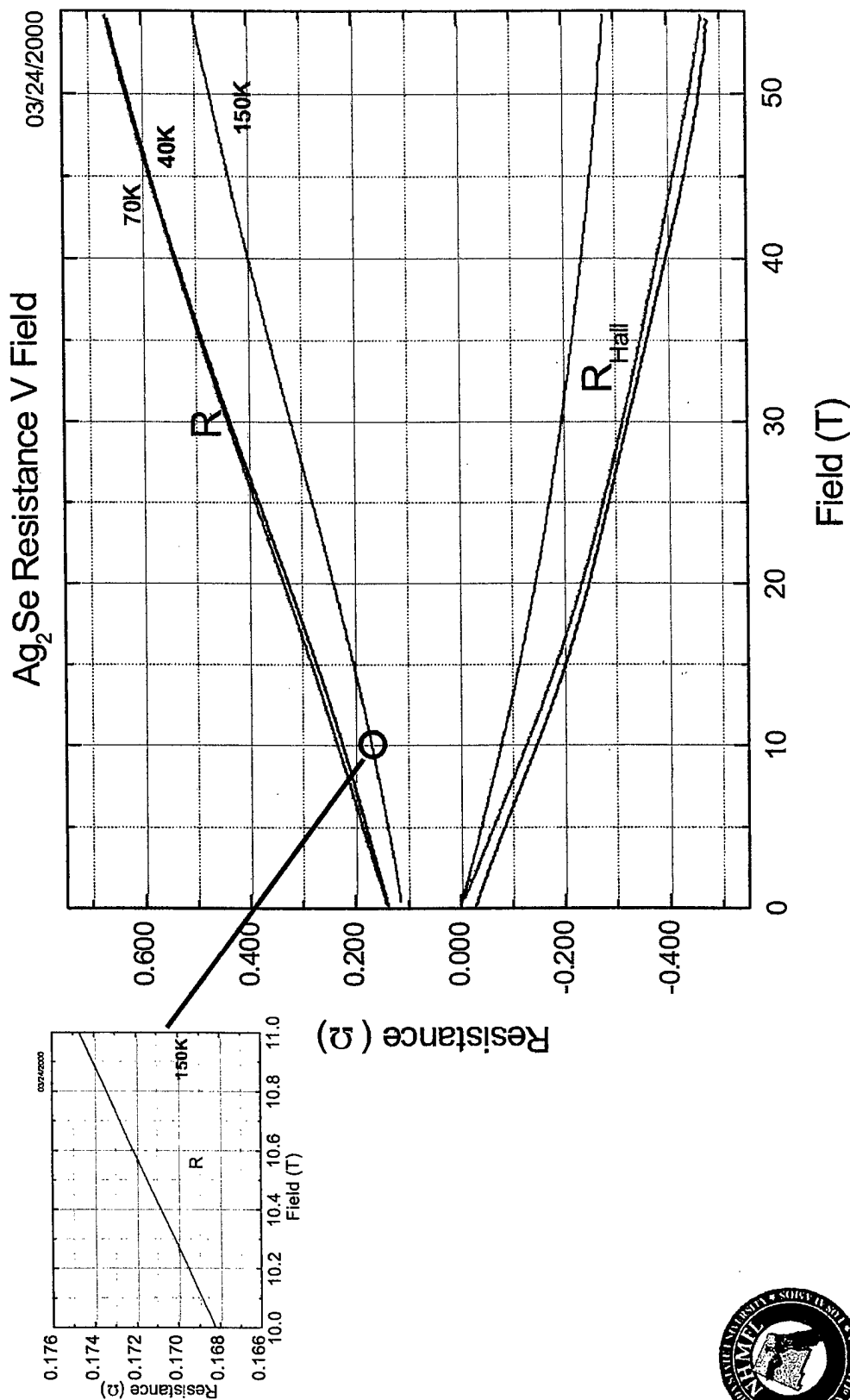
A properly designed commercial lock-in amplifier should have the same noise and drift as the NHMFL synchronous digital lock-in. However....



The NHMFL system (black) compared to a popular commercial lock-in (red). The commercial system exhibits excessive drift (large swings) and digitization noise (rapid excursions) on its fast-time-constant output that are properly handled in our system, even though the time response is set to be identical.

Details:

Typical result-resistance and Hall resistance of Ag_2Se , a nearly compensated semimetal measured with the NHMFL synchronous digitization system.



The NHMFL Synchronous digitization phase sensitive detector

Provides full dynamic range of the final digitizer

Enables after-the-shot adjustments of phase, time constant

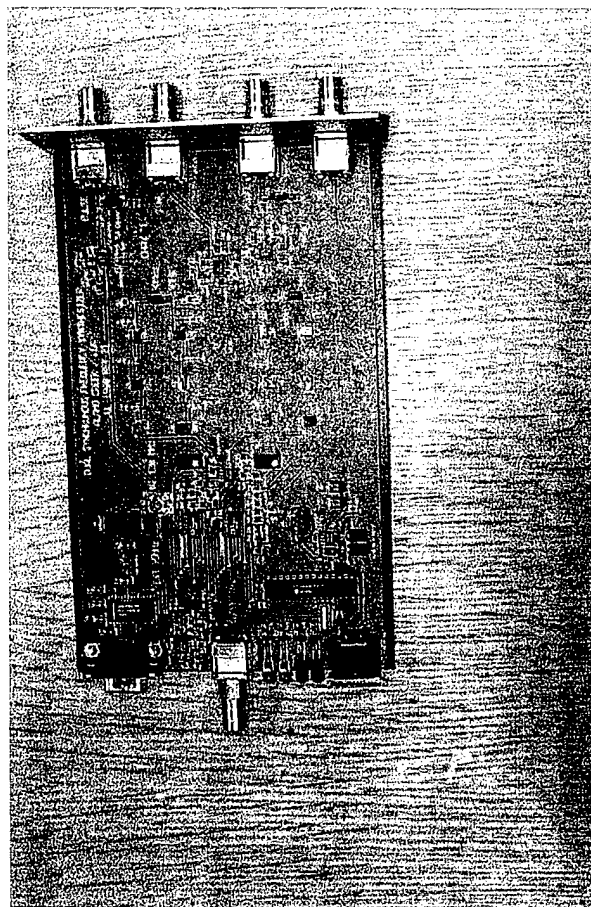
Enables after-the-shot limiting, and *variation* of filter bandwidth over the data set

Provides better acquisition of unexpected transients

Eliminates the lock-in, replaces it with an inexpensive (\$1K) dual digital synchronous clock/reference generator

Components will be commercially available fall 1999 (from LGK Corp., Albuquerque, NM 505 856-1412)

The first of a line of building blocks (the sine-wave and clock generator) is now commercially available from:
 LGK Corp.
 Albuquerque, NM
 (505) 856-1412



Atmospheric and Meteorological Acoustics

Kenneth E. Gilbert
National Center for Physical Acoustics
University of Mississippi

WELL, SON, I STARTED
OUT IN QUANTUM MECHANICS,
BUT I MADE A WRONG
TURN SOMEWHERE

GEE, POPS HOW DID
YOU END UP AS AN
AUTO MECHANIC?



**OUTDOOR SOUND PROPAGATION
AND METEOROLOGY:
PROGRESS IN UNDERSTANDING
DAYTIME SOUND LEVELS**

OUTLINE

- WHAT IS THE QUESTION?
- ATMOSPHERIC BOUNDARY LAYER
- PROPAGATION BASICS
- PARABOLIC EQUATION APPROXIMATION TO
THE WAVE EQUATION
- A RESEARCH STORY

QUESTION: WHAT ARE THE MECHANISMS THAT

CONTROL SOUND LEVELS IN THE DAYTIME

ACOUSTIC SHADOW REGION?

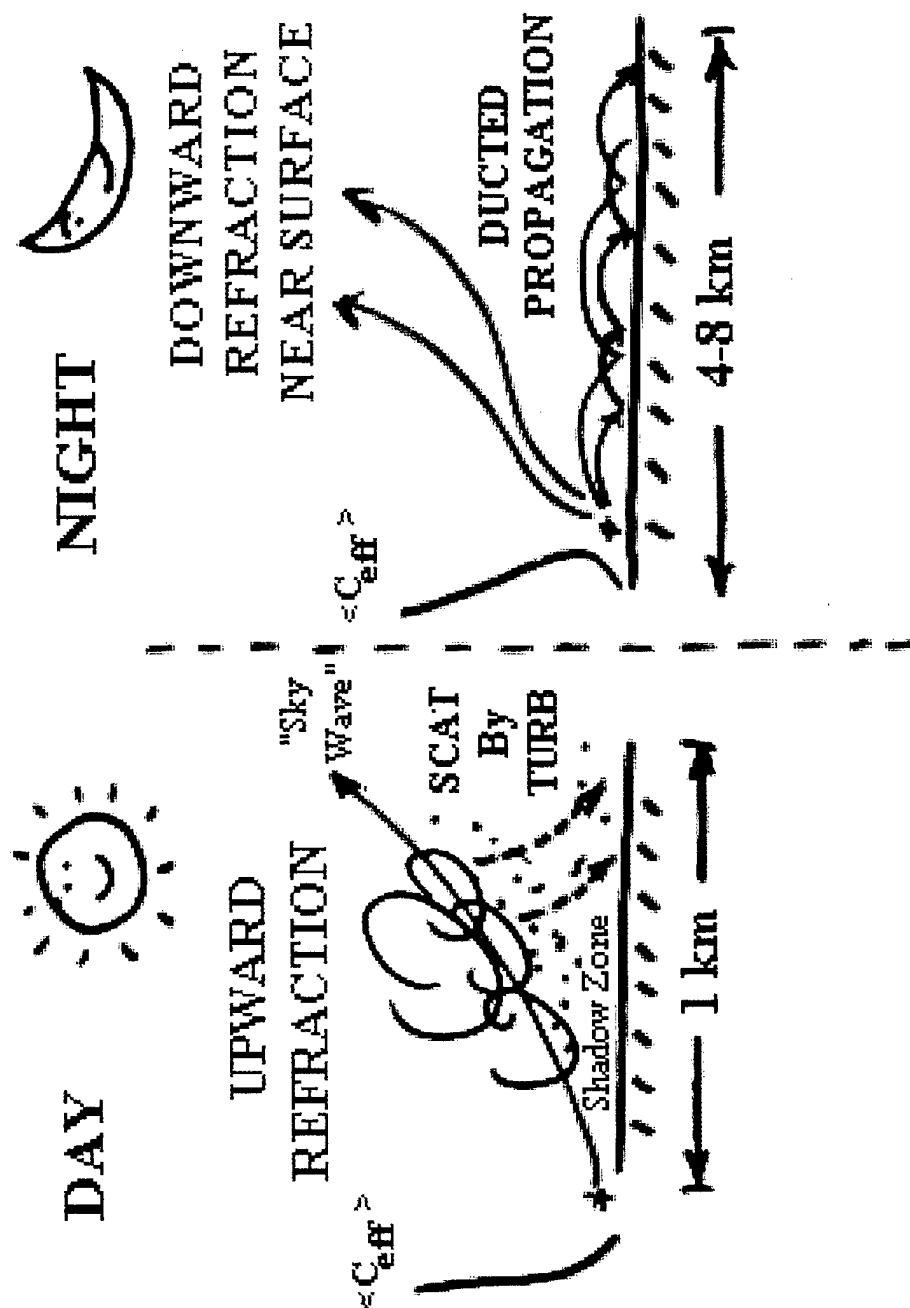
APPROACH: GOVERNING EQUATION IS THE

ACOUSTIC WAVE EQUATION:

$$\nabla^2 p = \frac{1}{c_e^2} \frac{\partial^2 p}{\partial t^2}$$

c_e = EFFECTIVE SOUND SPEED

DAY/NIGHT PROPAGATION



EFFECTIVE SOUND SPEED

ADIABATIC SOUND SPEED:

$$C_A = \sqrt{\gamma R T} \quad \gamma = .4 \quad R = 287 \text{ (J/kg } ^\circ\text{K)}$$

$$= C_0 \sqrt{\frac{T}{T_0}}$$

T_0, C_0 ARE REFERENCE
TEMPERATURE AND
SOUND SPEED

$$\text{EX: } T_0 = 293^\circ\text{K}$$

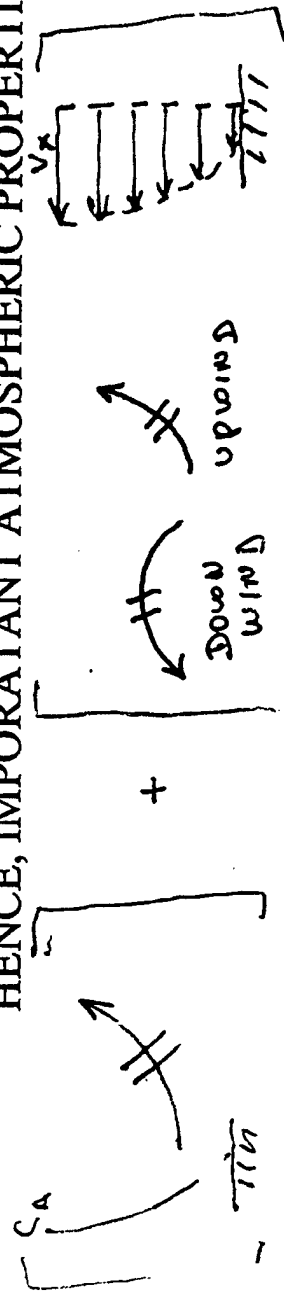
$$C_0 = 331 \text{ m/s}$$

EFFECTIVE SOUND SPEED:

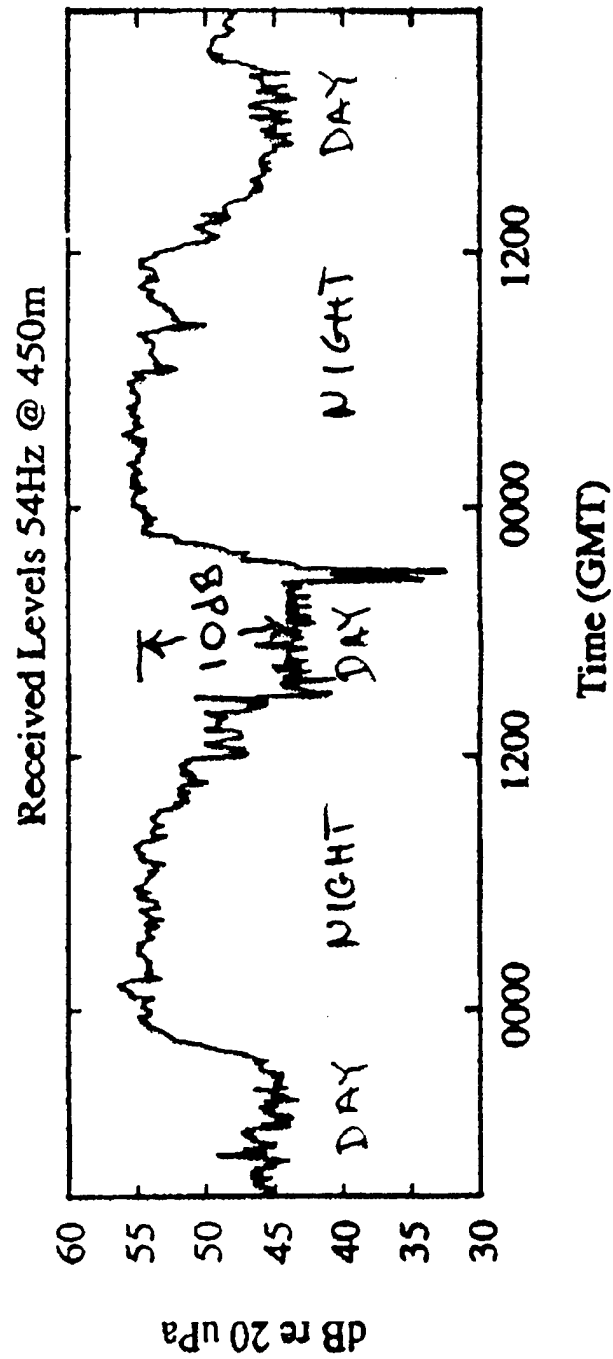
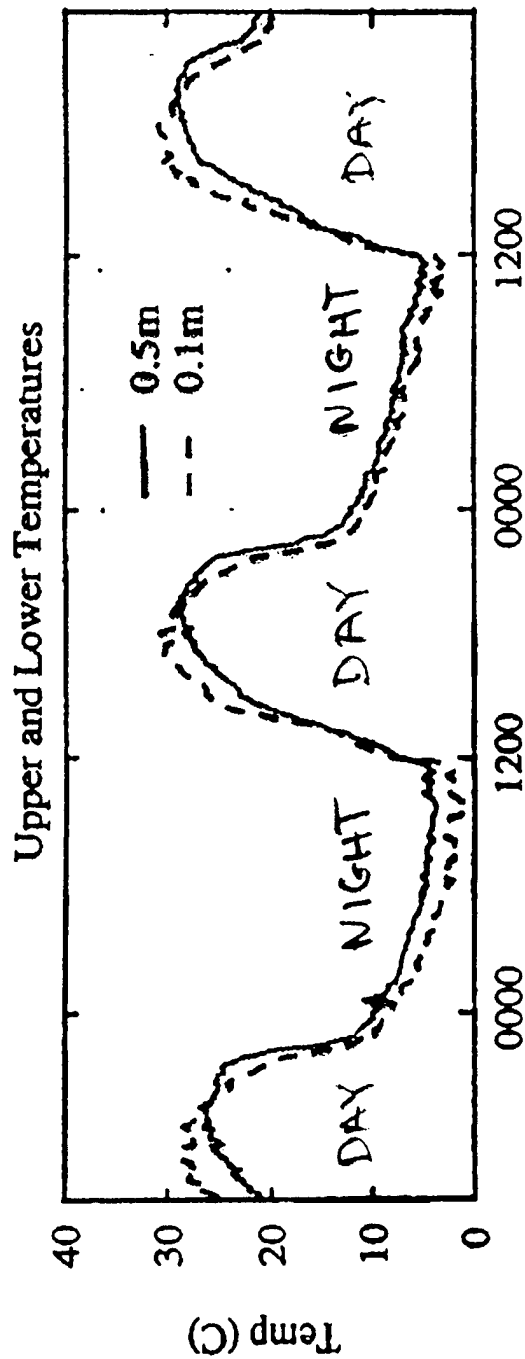
$$C_e = C_A + V_x \quad V_x = \hat{n}_p \cdot \vec{V}$$

$$C_0 \sqrt{\frac{T}{T_0}} + V_x$$

HENCE, IMPORATANT ATMOSPHERIC PROPERTIES ARE T AND V_x

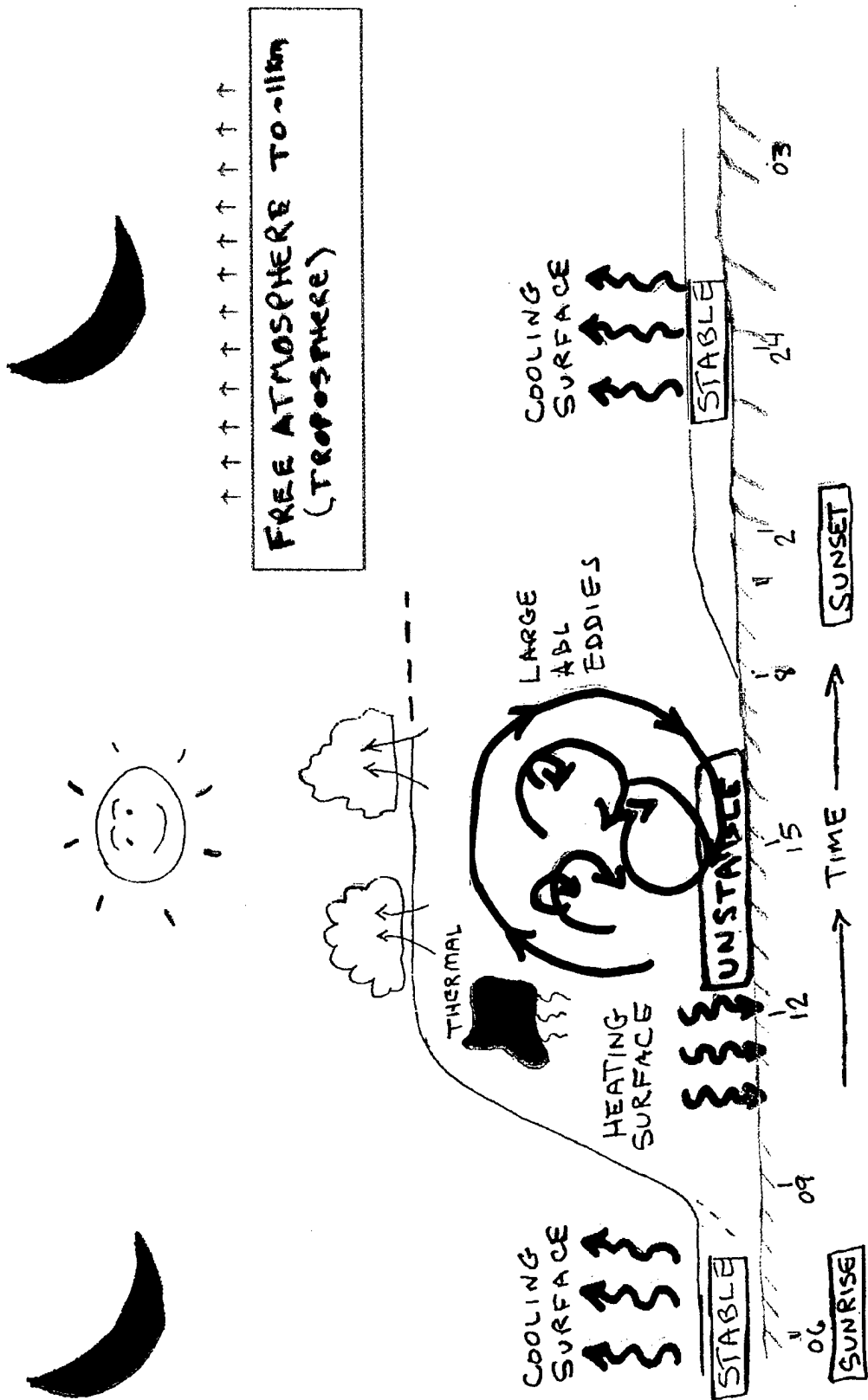


DIURNAL VARIATION IN TEMPERATURE AND SOUND LEVEL

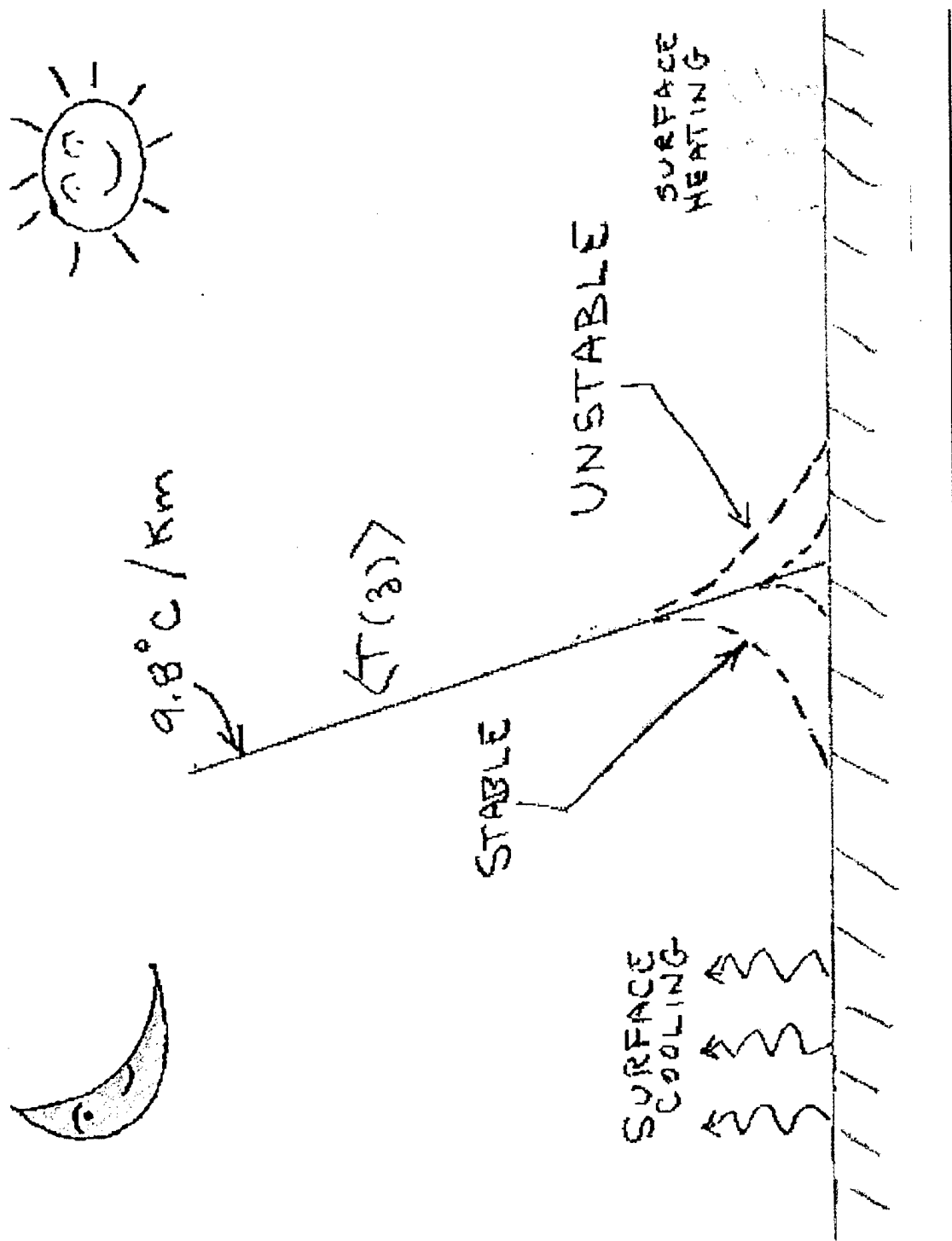


ATMOSPHERIC BOUNDARY LAYER (ABL)

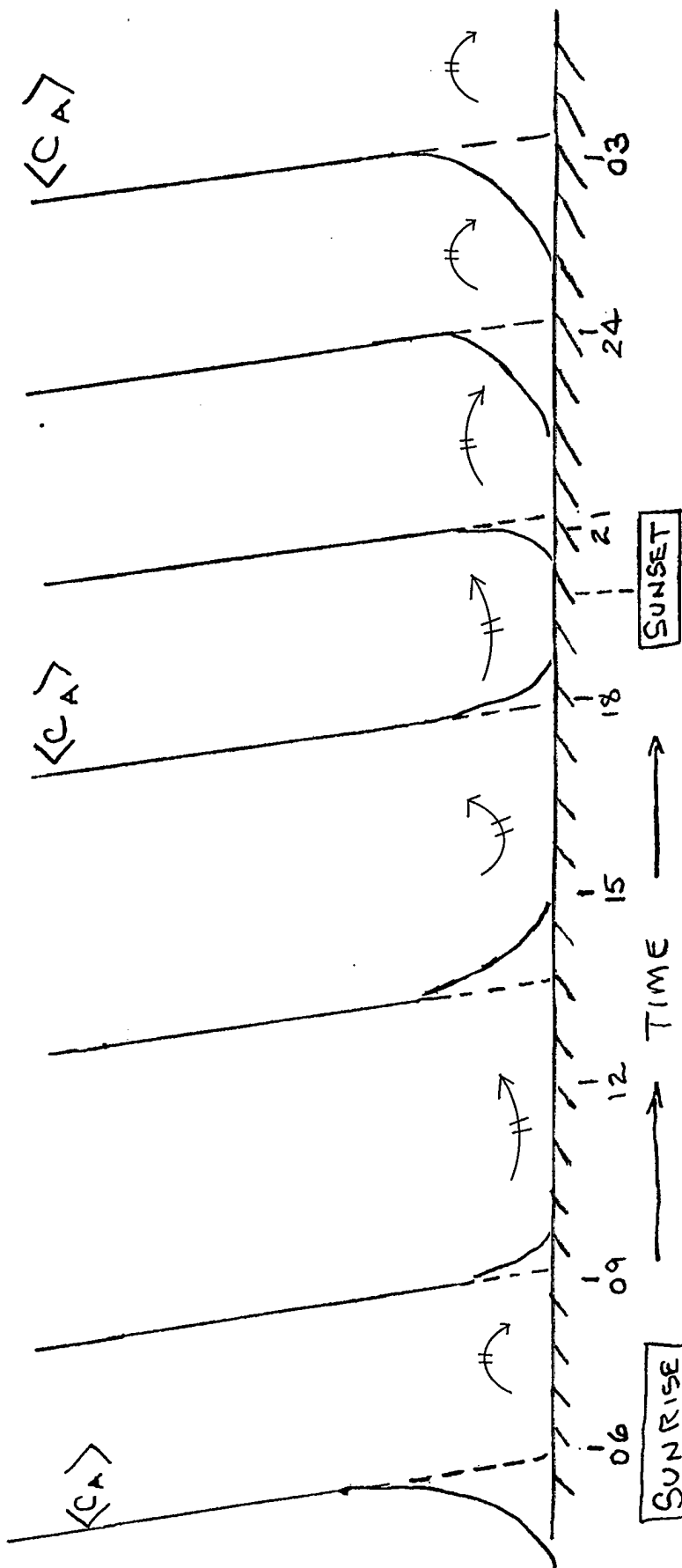
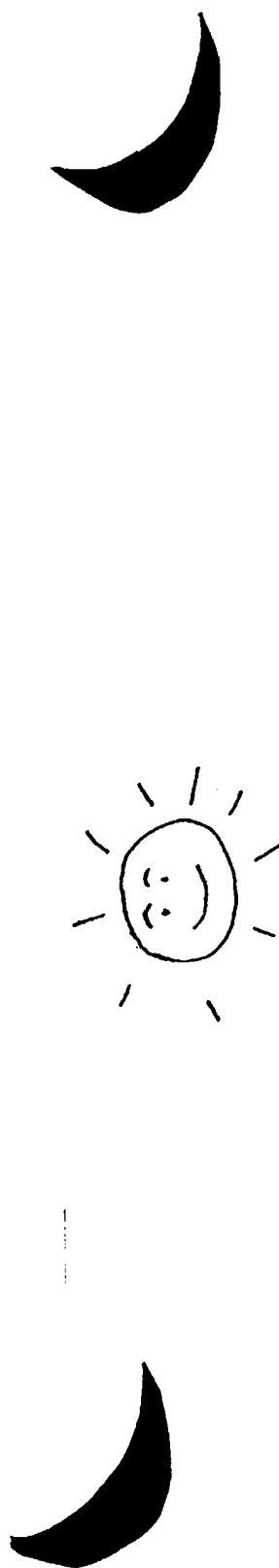
THE DIURNAL CYCLE OF THE ATMOSPHERIC BOUNDARY LAYER (ABL)



EVOLVING ABL: MEAN ADIABATIC LAPSE RATE

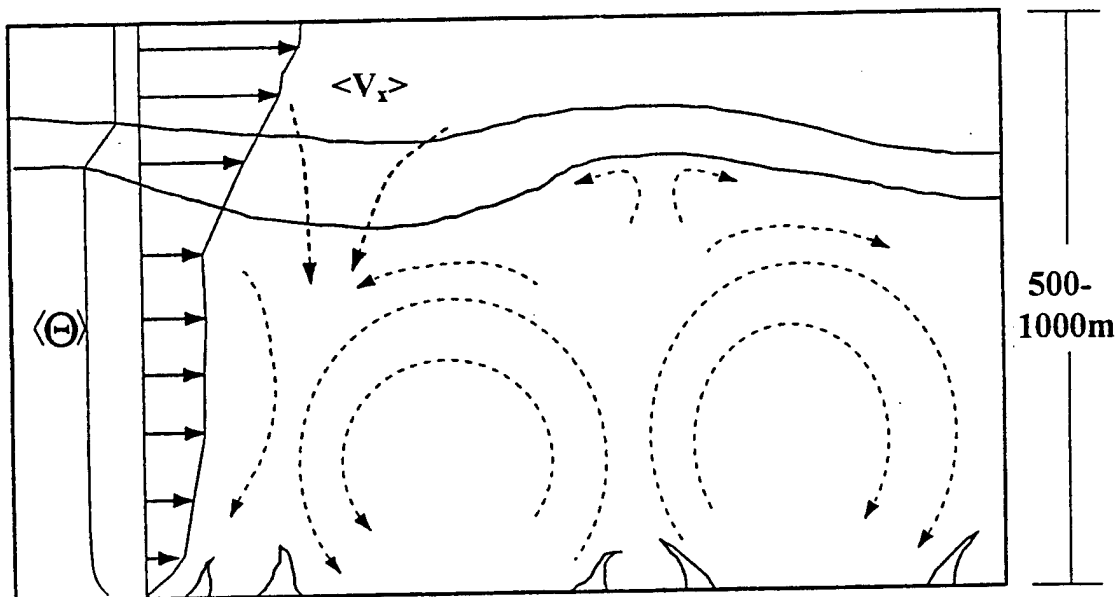


MEAN ADIABATIC SOUND SPEED

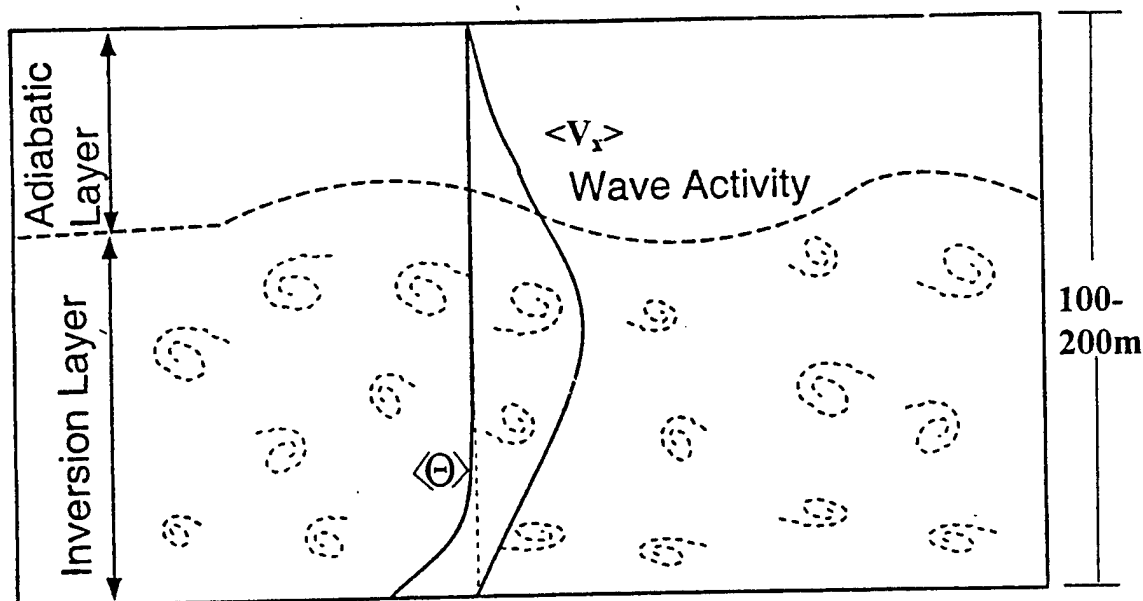


MEAN POTENTIAL TEMPERATURE AND MEAN HORIZONTAL WIND

DAYTIME ABL



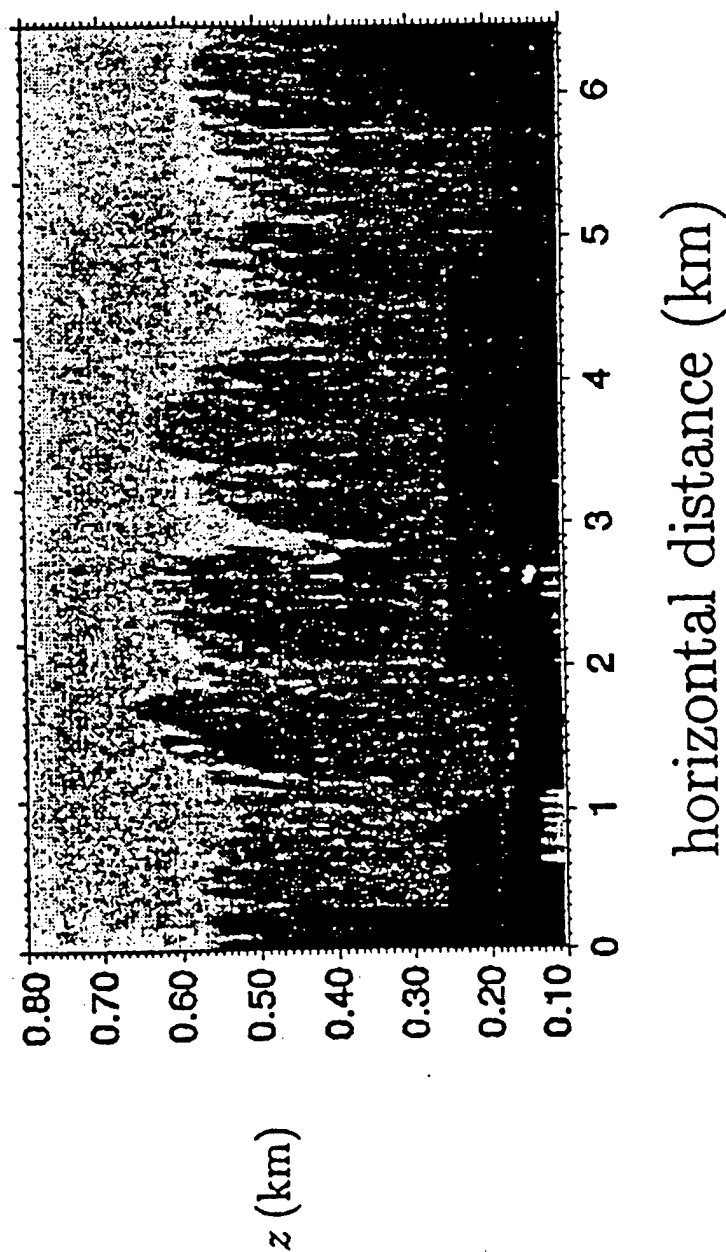
NOCTURNAL ABL



$\langle V_x \rangle$ = Mean Horizontal Wind is a Logarithmic Function of Height

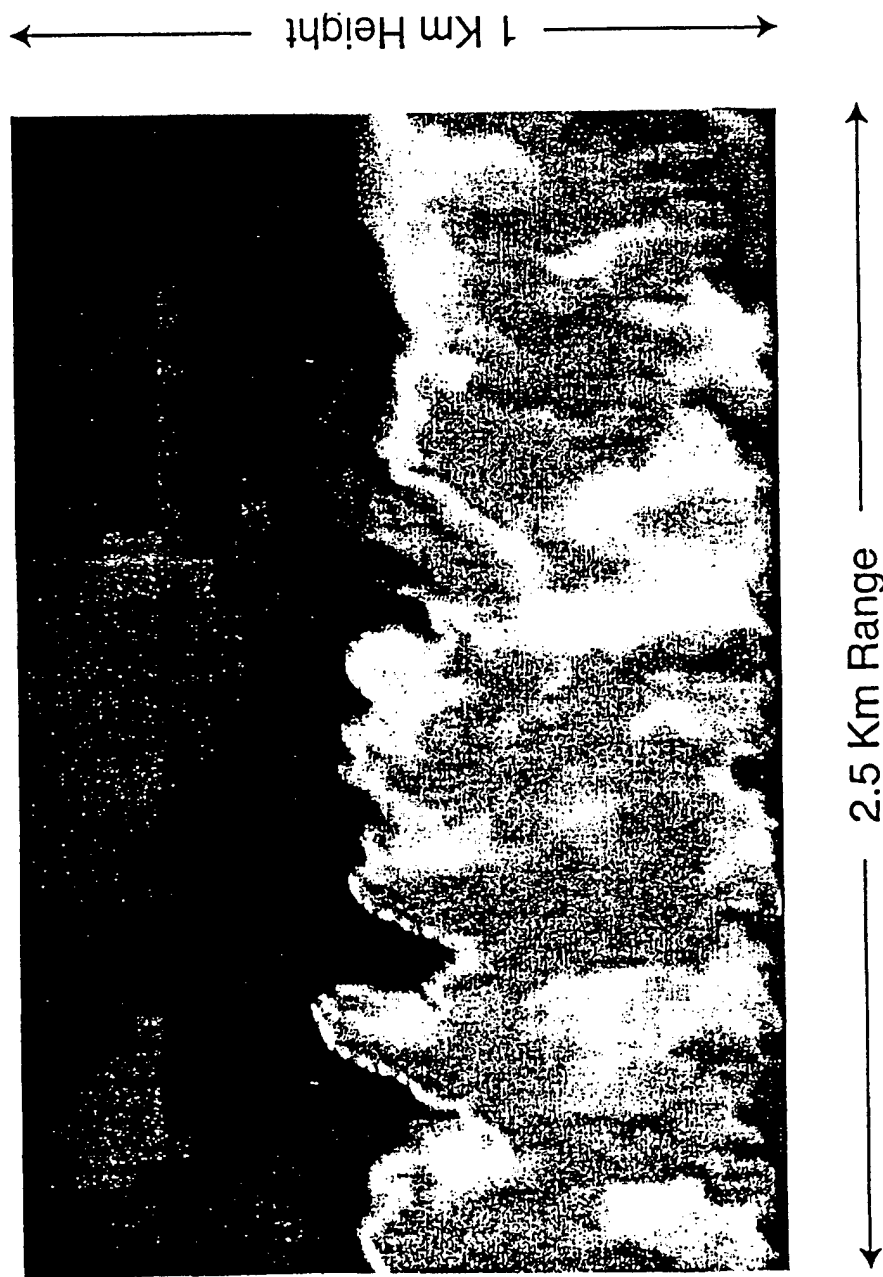
$$\langle \Theta \rangle = \text{The Mean "Potential Temperature"} \\ = \langle T \rangle + (9.8^\circ \text{K/km}) \cdot z$$

LIDAR MEASUREMENTS OF AEROSOL CONCENTRATION



Airborne-Lidar measurements of aerosol-concentration in a vertical plane of a convective boundary layer with substantial mean and wind shear [Kiemle *et al.*, 1998]. The instantaneous top is quite irregular and appears that only a portion of the overall jump in aerosol concentration occurs across it.

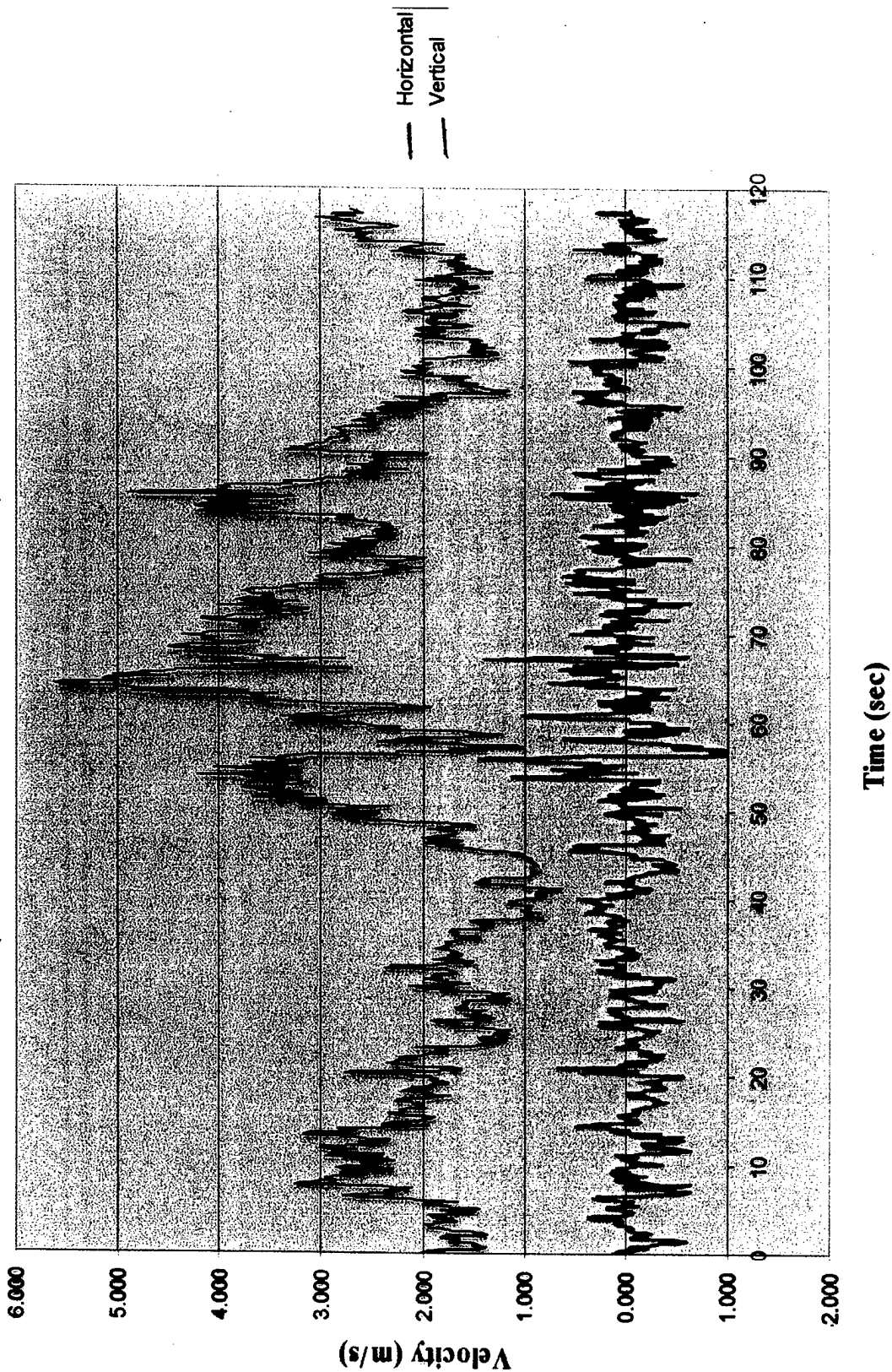
WATER VAPOR FIELDS CALCULATED FROM LARGE-EDDY SIMULATION (LES)



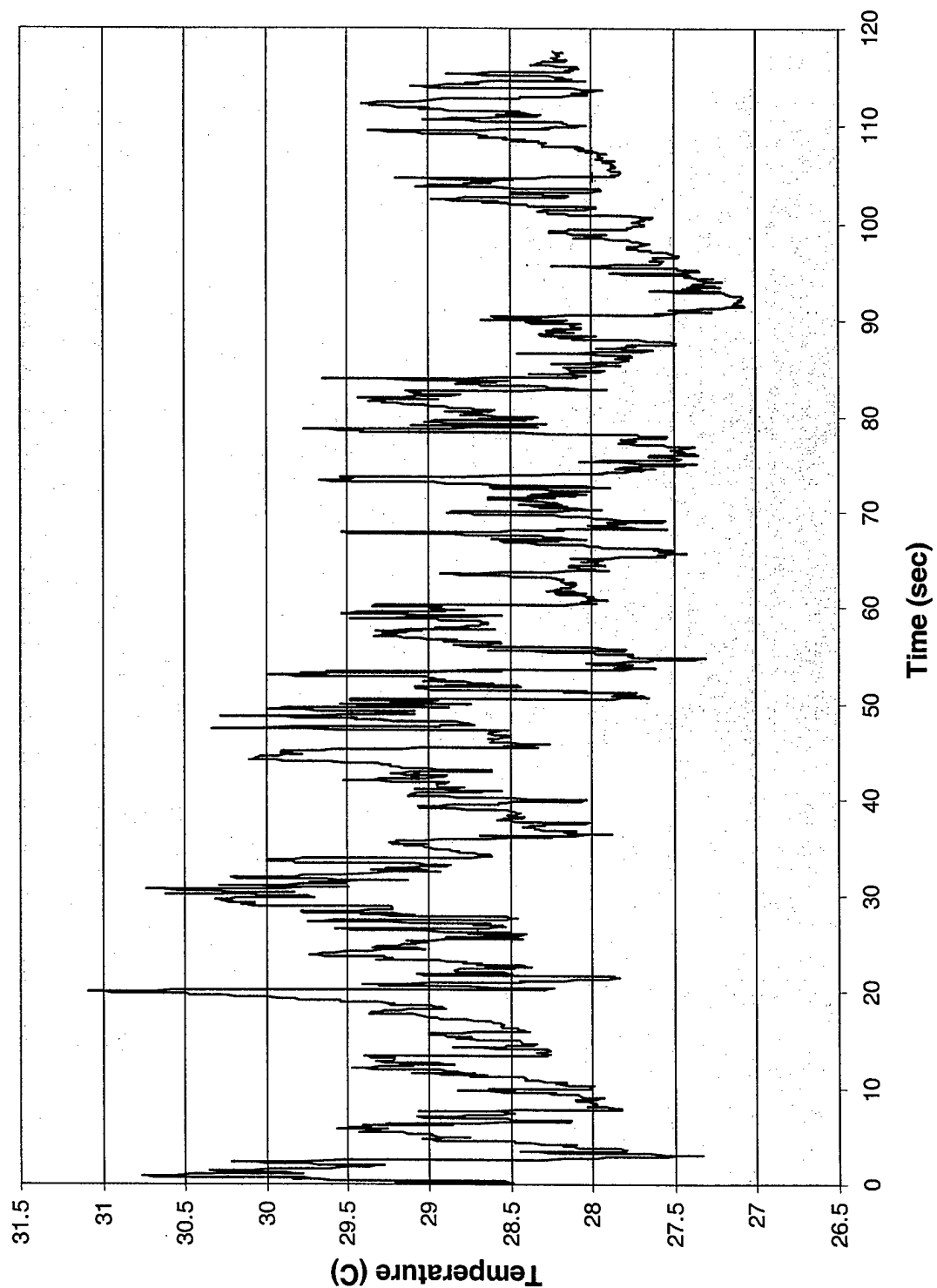
Detailed water-vapor fields calculated from LES for a 2.5 km domain and resolution of 20 m. Graphics courtesy of Martin Otte.

HORIZONTAL AND VERTICAL WIND SPEED

(Sonic Anemometer at 1 m)



Temperature



MEAN AND FLUCTUATING COMPONENTS OF TEMPERATURE AND WIND

$\langle T \rangle$ (DAYTIME) CAN BE FAIRLY WELL
REPRESENTED BY MONIN-OBUKOV SIMILARITY
THEORY.

$\langle \vec{V} \rangle$ (DAYTIME) IS LOGARITHMIC

$$\langle \vec{V} \rangle = \begin{cases} \langle \vec{V}_0 \rangle \ln(z/z_0) & z \gg z_0 \\ \langle \vec{V}_0 \rangle & z < z_0 \end{cases}$$

WHERE z_0 IS THE "ROUGHNESS LENGTH." EX: .1m
WITH FLUCTUATING COMPONENTS
 δT , $\delta \vec{V}$ THE TEMPERATURE AND
HORIZONTAL WIND ARE:

$$T = \langle T \rangle + \delta T \quad \vec{V} \cdot \hat{n}_p = V_x = \langle V_x \rangle + \delta V_x$$

ORDERS OF MAGNITUDE (PREVIEW)

$$\Delta \langle T \rangle \cong 5-10^\circ \text{K} \quad \Delta \langle V_x \rangle \cong 5-10 \text{ m/s}$$

$$\sqrt{\langle \delta T^2 \rangle} \cong 4^\circ \text{K} \quad \sqrt{\langle \delta V_x^2 \rangle} \cong \frac{.5}{\cancel{1}} \text{ m/s}$$

CAN APPROXIMATE C_e AS $C_e = 331 \text{ m/s} + .6 T_{oc} + V_x$

$$\Delta C_e = 331 + \underbrace{.6 \Delta \langle T \rangle}_{3-6 \text{ m/s}} + \underbrace{\Delta \langle V_x \rangle}_{5-10 \text{ m/s}}$$

$$\sqrt{\langle \delta C_e^2 \rangle}$$

$$= \left[\underbrace{.36 \langle \delta T^2 \rangle}_{.058} + \underbrace{\langle \delta V_x^2 \rangle}_{.25} \right]^{1/2}$$

MEAN AND FLUCUATING COMPONENTS OF THE EFFECTIVE SOUND SPEED

ADIABATIC SOUND SPEED:

$$C_A = \sqrt{\gamma R T}$$

$$\gamma = 1.4, R = 287 \text{ (J/kg} \cdot \text{°K)}$$

$$= C_0 \sqrt{T/T_0}$$

T_0, C_0 ARE REFERENCE TEMPERATURE AND SOUND SPEED.

$$\text{EX: } T_0 = 273 \text{ °K } C_0 = 331 \text{ m/s}$$

EFFECTIVE SOUND SPEED:

$$\begin{aligned} C_e &= C_A + V_x \\ &= C_0 \sqrt{\frac{T}{T_0}} + V_x \end{aligned}$$

$$\begin{aligned} C_e &= \langle C_e \rangle + \delta C_e \\ &= C_0 \sqrt{\frac{\langle T \rangle + \delta T}{T_0}} + \langle V_x \rangle + \delta V_x \end{aligned}$$

$$\begin{aligned} &= \underbrace{\left[\langle C_A \rangle + \langle V_x \rangle \right]}_{\langle C_e(z) \rangle} + \underbrace{\frac{1}{2} \langle C_A \rangle \frac{\delta T}{\langle T \rangle} + \delta V_x}_{\delta C_e(x, y, z, t)} \end{aligned}$$

MEAN AND FLUCTUATING COMPONENTS OF THE EFFECTIVE INDEX OF REFRACTION

$$k_e = \frac{\omega}{c_e} = \frac{\omega}{c_0} \frac{c_0}{c_e} = k_0 n_e = \text{EFFECTIVE WAVELENGTH}$$

$$\begin{aligned} n_e &= \frac{c_0}{c_e} = \frac{c_0}{\langle c_e \rangle + \delta c_e} \approx \frac{c_0}{\langle c_e \rangle} \left(1 - \frac{\delta c_e}{\langle c_e \rangle} \right) \\ &= \underbrace{\frac{c_0}{\langle c_e \rangle}}_{\langle n \rangle} - \underbrace{\frac{c_0}{\langle c_e \rangle} \frac{\delta c_e}{\langle c_e \rangle}}_{\delta n} = \text{EFFECTIVE INDEX OF REFRACTION} \end{aligned}$$

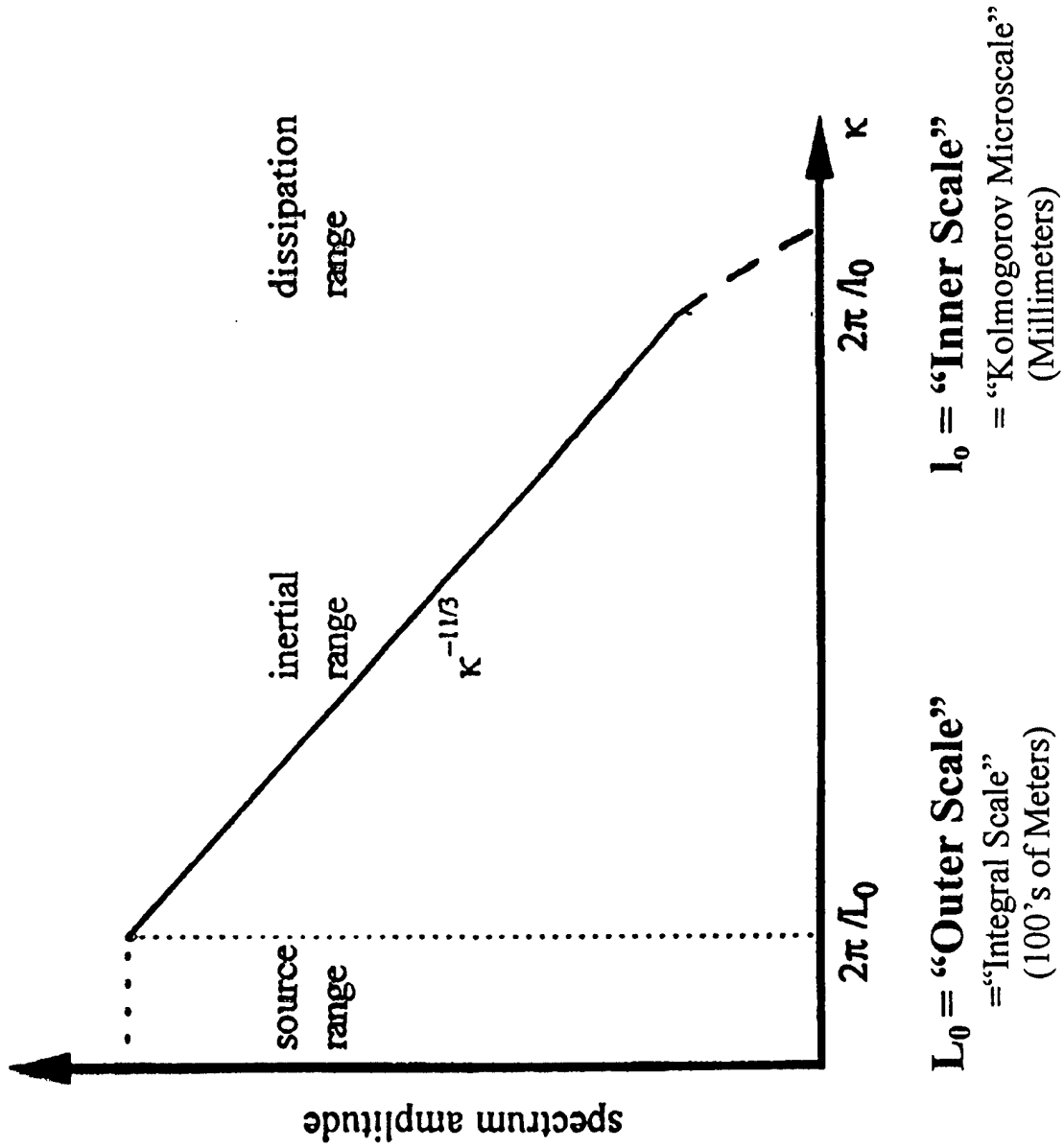
$$\langle n \rangle \equiv \frac{c_0}{\langle c_A \rangle + \langle v_x \rangle} = \text{MEAN INDEX OF REFRACTION}$$

$$\begin{aligned} \delta n &\equiv - \frac{c_0}{\langle c_e \rangle^2} \left[\frac{1}{2} \langle c_A \rangle \frac{\delta T}{\langle T \rangle} + \delta v_x \right] \\ &= \text{FLUCTUATING COMPONENT OF THE INDEX OF REFRACTION} \end{aligned}$$

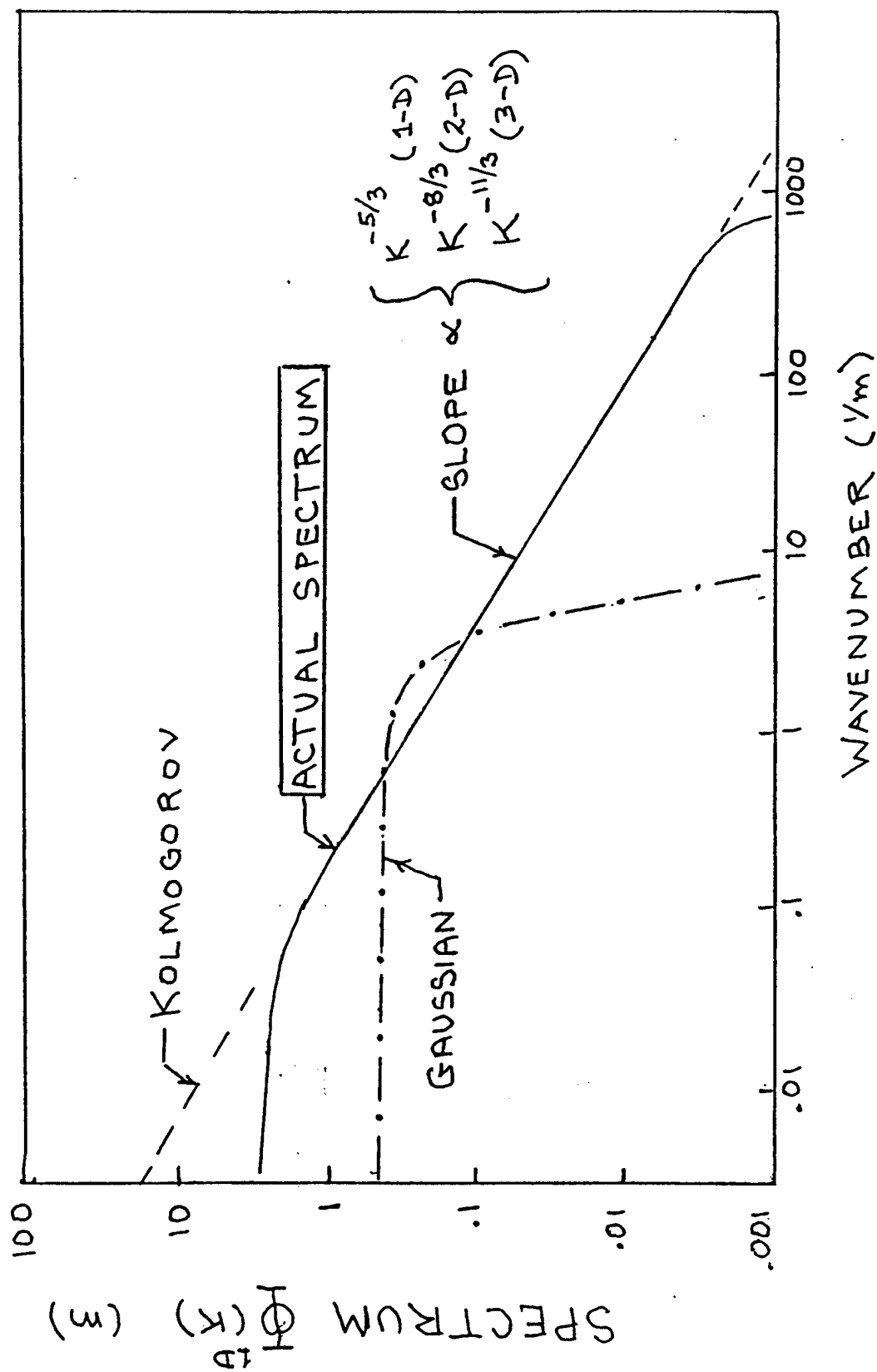
FINALLY,

$$k_e = k_0 (\langle n \rangle + \delta n)$$

TURBULENCE SPECTRUM FOR TEMPERATURE AND HORIZONTAL WIND FLUCTUATIONS



NORMALIZED TURBULENCE SPECTRUM (1-D) FOR INDEX OF REFRACTION FLUCTUATIONS



PROPAGATION BASICS

Outdoor sound propagation is governed by the linear wave equation (plus boundary conditions)

$$\nabla^2 p = \frac{1}{c_e^2} \frac{\partial^2 p}{\partial t^2}$$

Where $C_e(x,y,z,t)$ is the effective sound speed and contains the effects of temperature and wind:

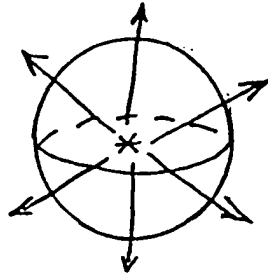
$$C_e = C_0 \sqrt{\frac{T}{T_0}} \pm \vec{V} \cdot \hat{n}_p$$

Mechanisms contained in the linear wave equation:

- Geometric Spreading
- Refraction
- Diffraction/Scattering
- Attenuation/Absorption

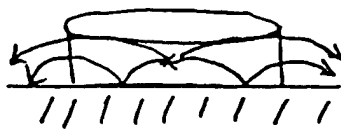
GEOMETRIC SPREADING

SPHERICAL
SPREADING



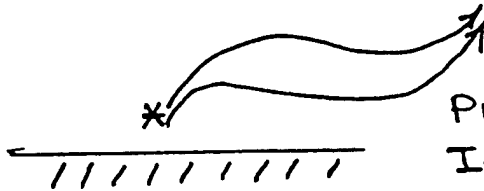
$$\text{PRESSURE} \propto \frac{1}{r}$$
$$\text{INTENSITY} \propto \frac{1}{r^2}$$

CYLINDRICAL
SPREADING



$$\text{PRESSURE} \propto \frac{1}{\sqrt{r}}$$
$$\text{INTENSITY} \propto \frac{1}{r}$$

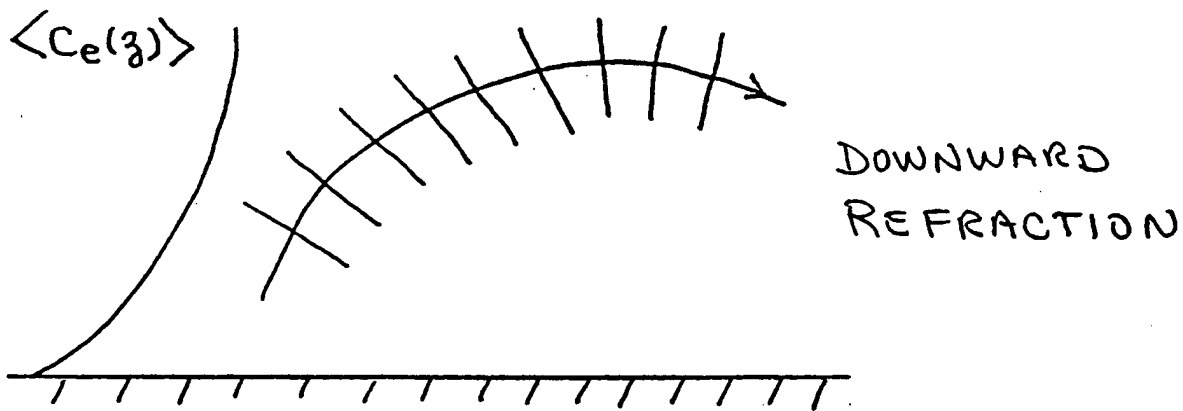
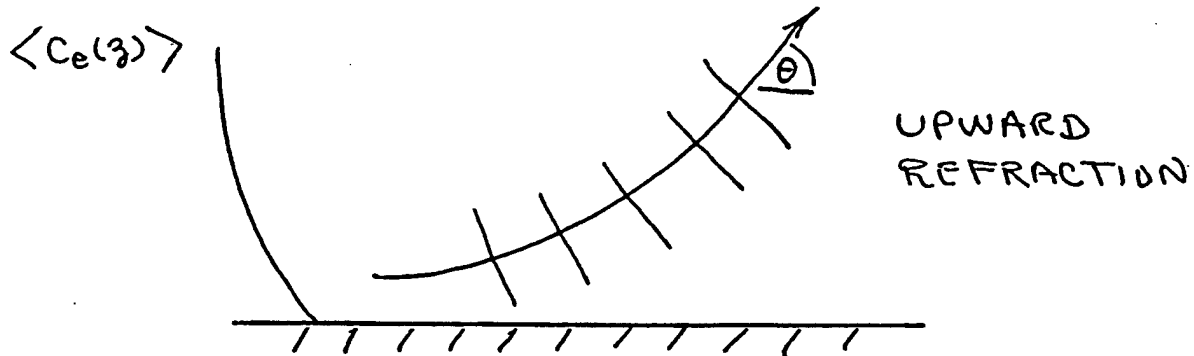
OTHER



$$\text{PRESSURE?}$$
$$\text{INTENSITY?}$$

Unfortunately, no simple geometrical
spreading law applies in general.

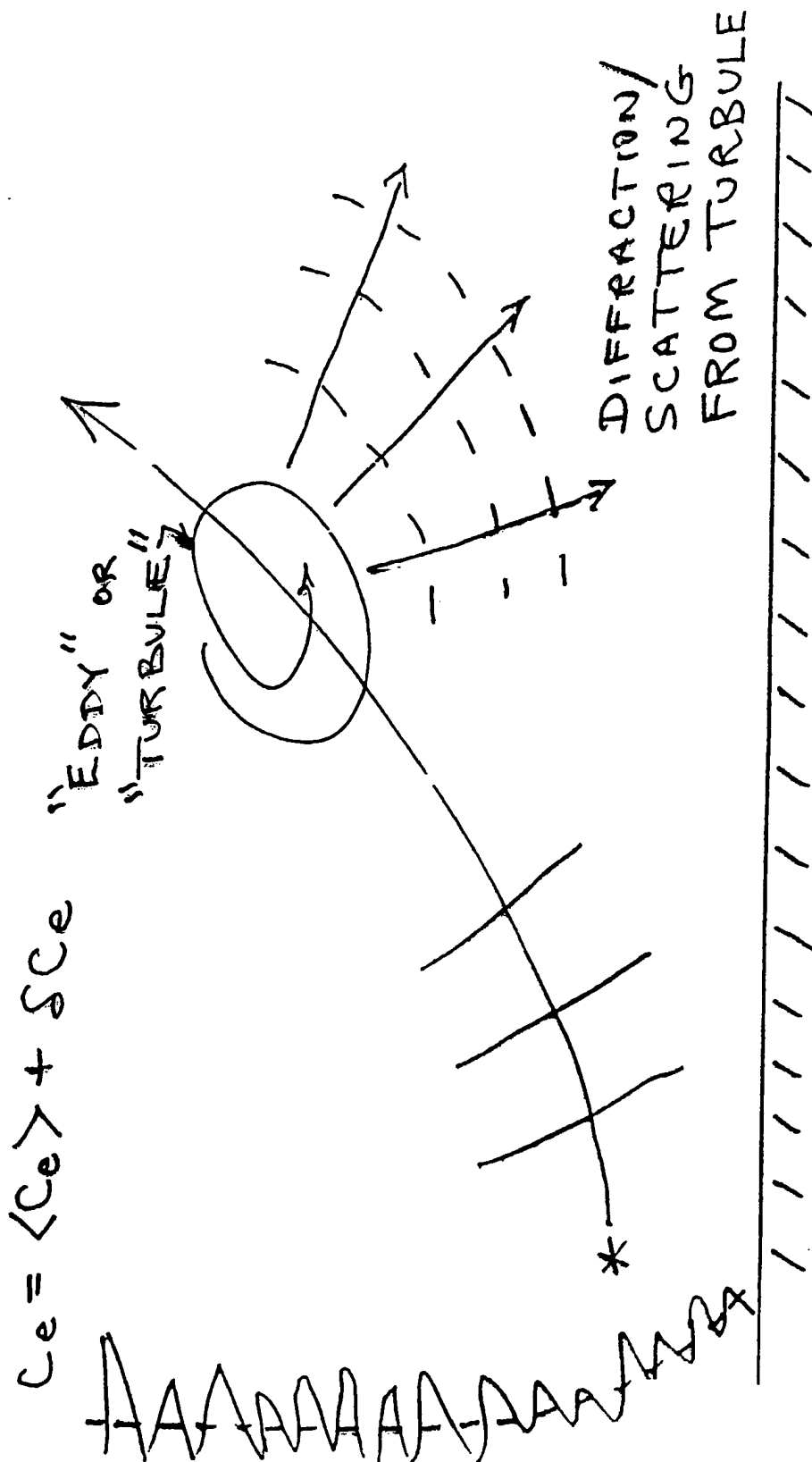
REFRACTION DUE TO THE MEAN SOUND-SPEED PROFILE



SNELL'S LAW: $\frac{\cos \theta(z)}{\langle C_e(z) \rangle} = \text{CONSTANT}$

$$\frac{\cos \theta(z_1)}{\langle C_e(z_1) \rangle} = \frac{\cos \theta(z_2)}{\langle C_e(z_2) \rangle} = \dots = \frac{\cos \theta(z_N)}{\langle C_e(z_N) \rangle}$$

DIFFRACTION AND SCATTERING DUE TO TURBULENCE

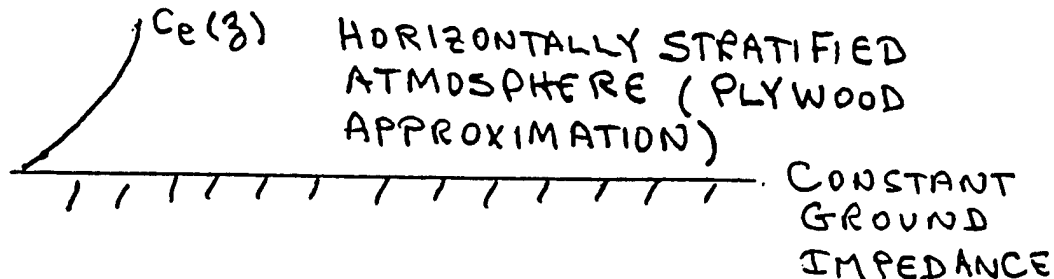


INTRODUCTION TO THE PARABOLIC EQUATION APPROXIMATION

QUESTION: What is so special about the parabolic equation method for outdoor sound propagation?

ANSWER: At present, it is the only practical method for "range dependent" environments.

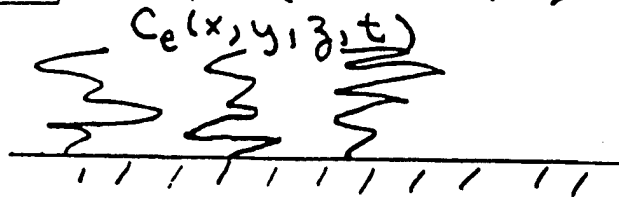
RANGE INDEPENDENT ENVIRONMENT:



CAN APPLY SEPARATION OF VARIABLES
AND REDUCE TO O.D.E. SOLVABLE
BY STANDARD METHODS

RANGE DEPENDENT ENVIRONMENTS:

TURBULENCE:



IRREGULAR
TERRAIN:

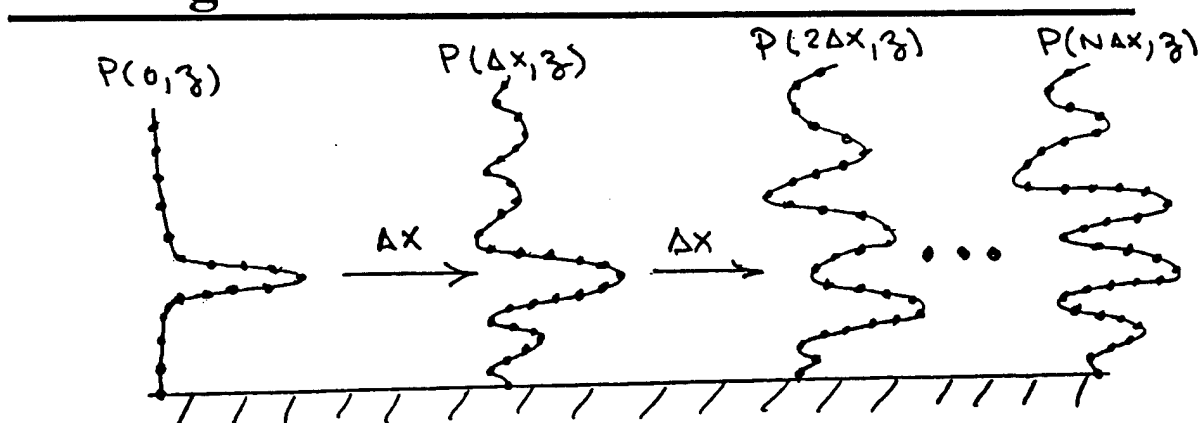


For range dependent environments, we need to consider a new approach:

- Parabolic Equation (PE)
- (AKA) One-Wave Wave Equation
- (AKA) Wave Extrapolation

Important points to remember for range-dependent environments:

- Conventional separation of variables does not apply globally (but can be applied in vertical “slices”).
- Direct discretization of the acoustic wave equation is not practical (yet) Ex. In 2D, number of grid points $\cong 10^7$ - 10^8 . In 3D, number of grid points $\cong 10^{10}$ - 10^{11} .
- PE method is practical and sufficiently accurate. The method “marches out” (extrapolates) the acoustic field in range.



With the PE method, only the vertical field at a given range needs to be “gridded”:

In 2D, number of points $\cong 10^3$

In 3D, number of points $\cong 10^5$ - 10^6

TIME HARMONIC SOLUTIONS OF THE ACOUSTIC WAVE EQUATION

Acoustic wave equation:

$$\nabla^2 P = \frac{1}{c^2} \frac{\partial^2 P}{\partial t^2}$$

Harmonic Solutions are of the form:

$$\begin{aligned} P(\vec{r}, t) &= A(\vec{r}) \cos(\phi(\vec{r}) - \omega t), \quad \vec{r} = (x, y, z) \\ &= \text{Re} \left[\underbrace{A(\vec{r}) e^{i\phi(\vec{r})}}_{\hat{P}(\vec{r})} e^{-i\omega t} \right] \\ &= \text{Re} \left[\hat{P}(\vec{r}) e^{-i\omega t} \right] \end{aligned}$$

SUBSTITUTE $\hat{P}(\vec{r}) e^{-i\omega t}$ INTO THE ACOUSTIC WAVE EQUATION:

$$\frac{\partial^2}{\partial t^2} \rightarrow -\omega^2, \text{ SO WE HAVE}$$

$$\begin{aligned} \nabla^2 \hat{P}(\vec{r}) + \underbrace{\left(\frac{\omega}{c}\right)^2}_{k^2 = (\text{WAVENUMBER})^2} \hat{P}(\vec{r}) &= 0 \\ k^2 &= \left(\frac{2\pi}{\lambda}\right)^2 \end{aligned}$$

DROP \wedge FROM HERE ON. WE HAVE THEN:

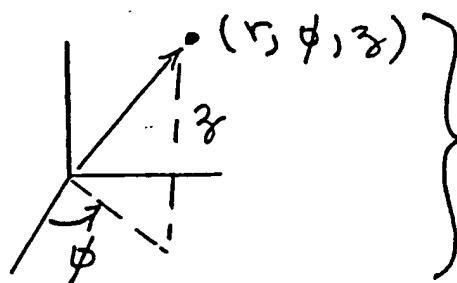
$$\nabla^2 P(\vec{r}) + k^2(\vec{r}) P(\vec{r}) = 0$$

HELMHOLTZ EQUATION

For time-harmonic sources and a "frozen" (in time) atmosphere, the Helmholtz equation can describe all the acoustic phenomena discussed earlier.

HELMHOLTZ EQUATION SOLUTIONS WITH AZIMUTHAL SYMMETRY

FOR SIMPLICITY, WE ASSUME AZIMUTHAL SYMMETRY (NO ϕ DEPENDENCE)



$$\left. \begin{array}{c} \text{Diagram of point } (r, \phi, z) \end{array} \right\} \nabla^2 = \frac{\partial^2}{\partial r^2} + \frac{1}{r} \frac{\partial}{\partial r} + \frac{\partial^2}{\partial z^2} + \frac{1}{r^2} \frac{\partial^2}{\partial \phi^2}$$

DEFINE $P = \left(\frac{r}{r_0}\right)^{\frac{1}{2}} p$ WHERE $r_0 = 1\text{m}$
AND SUBSTITUTE IN THE HELMHOLTZ EQUATION.

$$\frac{\partial^2}{\partial r^2} p + \frac{\partial^2 p}{\partial z^2} + k^2 \left(1 + \frac{1}{4k^2 r^2}\right) p = 0$$

AT SUFFICIENT DISTANCES $k r = \frac{2\pi}{\lambda} r \gg 1$
FOR EXAMPLE FOR $r = \lambda$ WE HAVE

$$(4k^2 r^2) = 16\pi^2 \approx 160, \text{ SO } (4k^2 r^2)^{-1} = \frac{1}{160}$$

THEREFORE FOR $r/\lambda \gg 1$, WE HAVE SIMPLY

$$\left. \begin{array}{c} \frac{\partial^2 p}{\partial r^2} + \frac{\partial^2 p}{\partial z^2} + k^2 p = 0 \end{array} \right\} \text{ FAR-FIELD HELMHOLTZ EQN.}$$

AT THIS POINT WE LET $r \rightarrow x$ AND CONSIDER A 2-D HELMHOLTZ EQUATION:

$$\frac{\partial^2 p}{\partial x^2} + \frac{\partial^2 p}{\partial z^2} + k^2 p = 0$$

TWO-WAY AND ONE-WAY WAVE EQUATIONS

The Helmholtz equation is a two-way wave equation. Consider a 1-D Helmholtz equation.

TWO-WAY
WAVE EQUATION

$$\frac{d^2 \psi}{dx^2} + k^2 \psi = 0 \quad k = \text{CONSTANT}$$

WITH $e^{-i\omega t}$ TIME DEPENDENCE, THE TWO SOLUTIONS ARE

$$\begin{aligned}
 e^{ikx} &\rightarrow \text{RIGHT-GOING} \\
 e^{-ikx} &\rightarrow \text{LEFT-GOING}
 \end{aligned}$$

To obtain a one-way equation, we write the Helmholtz as

$$\left(\frac{d}{dx} + ik\right)\left(\frac{d}{dx} - ik\right)\psi = 0$$

solutions to

ONE-WAY
WAVE EQUATION

$$\frac{d\psi}{dx} = \pm ik\psi \quad \left. \begin{array}{l} + \text{ RIGHT-GOING} \\ - \text{ LEFT-GOING} \end{array} \right\}$$

satisfy the Helmholtz equation but are one-way solutions. That is, the solutions are either right-going or left-going, but not both.

ONE-WAY WAVE EQUATION IN TWO DIMENSIONS

HELMHOLTZ EQUATION (TWO-WAY): $\left[\frac{\partial^2}{\partial x^2} + \underbrace{\frac{\partial^2}{\partial z^2} + k^2}_Q \right] p = 0$
 $Q = \text{OPERATOR}$

$$\left(\frac{\partial^2}{\partial x^2} + Q \right) p = 0$$

Split into right and left-going equations as before:

$$\left(\frac{\partial}{\partial x} + i\sqrt{Q} \right) \left(\frac{\partial}{\partial x} - i\sqrt{Q} \right) p = 0$$

ONE-WAY WAVE EQUATION

$$\left. \frac{\partial p}{\partial x} = \pm i\sqrt{Q} p \right\} \begin{array}{l} + \rightarrow \text{RIGHT-GOING} \\ - \rightarrow \text{LEFT-GOING} \end{array}$$

WHAT DOES $\sqrt{Q} = \sqrt{\frac{\partial^2}{\partial z^2} + k^2}$ MEAN?
 CONSIDER $k^2 = k_0^2 = \text{CONSTANT}$, SO $\frac{\partial^2}{\partial z^2} = -k_z^2$.
 SINCE $k_0^2 = k_x^2 + k_z^2$, WE HAVE $k_x^2 = k_0^2 - k_z^2$
 $= (\text{HORIZONTAL WAVELENGTH})^2$ HENCE
 $\sqrt{Q} \Rightarrow \sqrt{k_0^2 - k_z^2} = \pm (\text{HORIZONTAL WAVELENGTH})$

When $k^2 = \omega^2/c^2 \neq \text{constant}$, Q is a true operator and the Eigenvalues of \sqrt{Q} are \pm (horizontal wavenumber). Then accurate approximations for \sqrt{Q} become a mathematical issue.

A LINEAR APPROXIMATION FOR \sqrt{Q}

OUT-GOING } $\frac{\partial r}{\partial x} = i \sqrt{Q} r$
WAVE EQN.

WHERE $Q = \frac{\partial^2}{\partial z^2} + k^2$, $k^2 = \omega^2/c_e^2$

CONSIDER $k = k_0 = \text{CONSTANT}$ SO $k_x^2 + k_z^2 = k_0^2$



$$k_x = \sqrt{k_0^2 - k_z^2}$$

IN GENERAL, k_x ARE THE EIGENVALUES OF \sqrt{Q} . FOR SMALL-ANGLE PROPAGATION

$k_x \approx k_0$ AND WE CAN EXPAND \sqrt{Q} LINEARLY ABOUT k_0 :

$$\begin{aligned} \sqrt{Q} &\approx k_0 + \frac{1}{2k_0} (Q - k_0^2) \\ &= k_0 + \frac{1}{2k_0} \left(\frac{\partial^2}{\partial z^2} + k^2 - k_0^2 \right) \end{aligned}$$

WITH $(k^2 - k_0^2)/2k_0 \approx k - k_0$, WE HAVE

$$\frac{\partial r}{\partial x} = i \left(\frac{1}{2k_0} \frac{\partial^2}{\partial z^2} + k \right) r$$

The Linear Expansion of \sqrt{Q} is equivalent to the original approach of Tappert. There are many, much more accurate representations of \sqrt{Q} .

ORIGINAL TAPPERT APPROACH

$$\psi = \underbrace{e^{ik_0 x}}_{\text{CARRIER}} \underbrace{\psi(x, z)}_{\text{MODULATOR}}$$



SUBSTITUTE INTO HELMHOLTZ EQN.

$$\cancel{\frac{\partial^2 \psi}{\partial x^2}} + 2ik_0 \frac{\partial \psi}{\partial x} + \frac{\partial^2 \psi}{\partial z^2} + (k^2 - k_0^2)\psi = 0$$

SINCE $\frac{\partial^2 \psi}{\partial x^2} \ll 2ik_0 \frac{\partial \psi}{\partial x}$, WE CAN DROP $\frac{\partial^2 \psi}{\partial x^2}$

$$\begin{aligned} \frac{\partial \psi}{\partial x} &\approx \frac{i}{2k_0} \frac{\partial^2 \psi}{\partial z^2} + \frac{i}{2k_0} (k^2 - k_0^2) \psi \\ &\approx \frac{i}{2k_0} \frac{\partial^2 \psi}{\partial z^2} + i(k - k_0) \psi \end{aligned}$$

IN TERMS OF ψ

$$\frac{\partial \psi}{\partial x} = \frac{i}{2k_0} \frac{\partial^2 \psi}{\partial z^2} + i(k - k_0) \psi$$

PHYSICAL INTERPRETATION OF THE TAPPERT PARABOLIC EQUATION

THE LINEAR EXPANSION OF $\sqrt{k_0^2 - k_z^2} - k_0$

IS $-k_z^2/2k_0$. SO WE CAN REPLACE

$\frac{1}{2k_0} \frac{\partial^2}{\partial z^2}$ WITH $\sqrt{k_0^2 + \frac{\partial^2}{\partial z^2}} - k_0$ AND

THE TAPPERT PE BECOMES

$$\frac{\partial p}{\partial x} = i \left(\underbrace{\sqrt{k_0^2 + \frac{\partial^2}{\partial z^2}}}_{\text{HORIZONTAL WAVENUMBER FOR } k=k_0} + \underbrace{k - k_0}_{\text{DEPARTURE OF } k \text{ FROM } k_0} \right) p$$

THE TERM $(k - k_0)$ REPRESENTS
REFRACTION AND THE TERM

$\sqrt{k_0^2 + \frac{\partial^2}{\partial z^2}}$ REPRESENTS DIFFRACTION

The gist of the so-called split-step Fourier solution is that, for “small enough” range steps, we can do diffraction and refraction sequentially instead of simultaneously.

FORMAL SOLUTION FOR THE SPLIT-STEP FOURIER METHOD DUE TO HARDIN AND TAPPERT

$$\text{PE EQN: } \frac{\partial p}{\partial x} = i \left[\sqrt{k_0^2 + \frac{\partial^2}{\partial z^2}} + (k - k_0) \right] p$$

DEFINE OPERATORS

$$A \equiv i(k - k_0), B \equiv i \sqrt{k_0^2 + \frac{\partial^2}{\partial z^2}}, \quad U \equiv A + B$$

PE EQN. BECOMES $\frac{\partial p}{\partial x} = U p$

FORMAL SOLUTION IS $p(x, z) = \exp \left[\int_{x_0}^x U dx' \right] p(x_0, z)$

WHERE $\int U dx' \equiv \bar{U} \Delta x = (\bar{A} + \bar{B}) \Delta x$. THE QUANTITY $\bar{A} \Delta x$ IS CALLED A "PHASE SCREEN."

$$\bar{A} = (k - k_0) = k_0(\bar{n} - 1), \quad \bar{n} = \frac{1}{\Delta x} \int_{x_0}^{x_0 + \Delta x} n(x', z) dx', \quad \bar{B} = B = i \sqrt{k_0^2 + \frac{\partial^2}{\partial z^2}}$$

HENCE $p(x, z) = e^{\Delta x (\bar{A} + \bar{B})} p(x_0, z)$

IF WE ASSUME $\bar{A}\bar{B} = \bar{B}\bar{A}$, THEN WE CAN WRITE THE SOLUTION AS

$$p(x + \Delta x, z) = e^{\Delta x \bar{A}} e^{\Delta x \bar{B}} p(x, z)$$

THIS IS THE SPLIT-STEP APPROXIMATION.

SUMMARY OF THE SPLIT-STEP FOURIER SOLUTION FOR THE PARABOLIC EQUATION

DEFINE $F^{\pm 1} \equiv e^{i\sqrt{k_0^2 - k_y^2} \Delta x} \mathcal{F}^{\pm 1}$

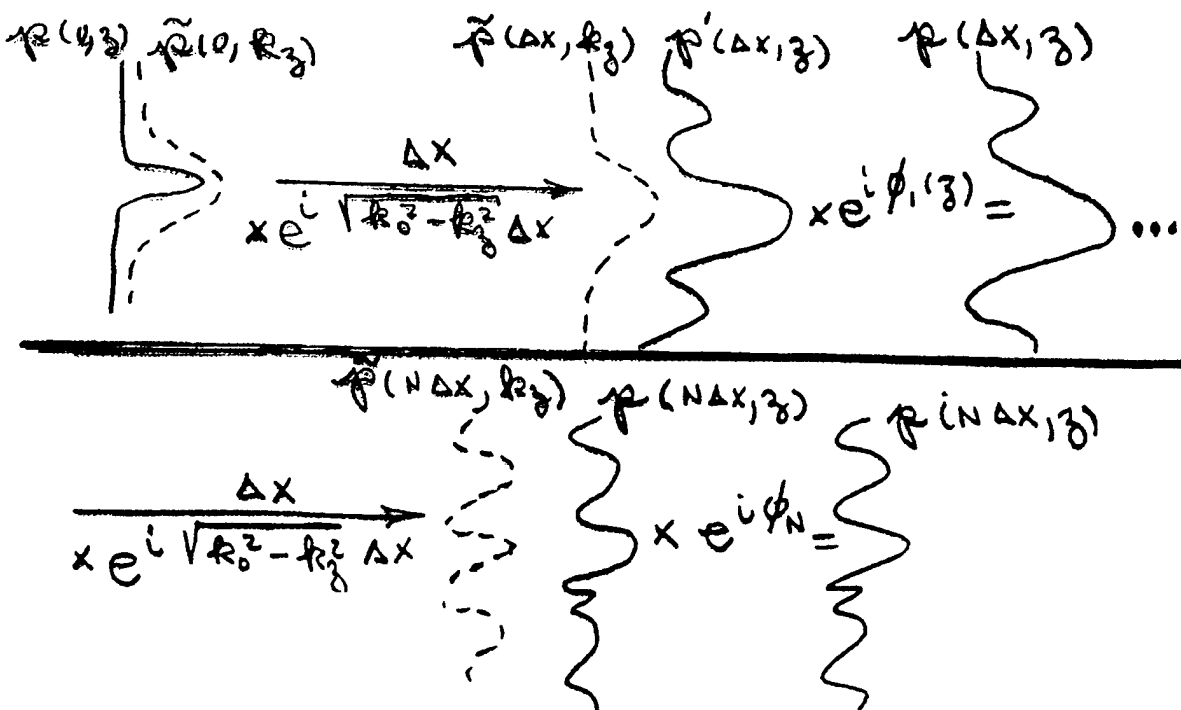
WHERE $\mathcal{F}^{\pm 1}$ ARE FORWARD
INVERSE FOURIER TRANSFORMS, ALSO
DEFINE WHERE $\phi_j = k_0 (K(z) - 1) \Delta x + k_0 \bar{n}(z) \Delta x$
IS THE j^{th} PHASE SCREEN

THEN,

$$p(N\Delta x, z) = e^{i\phi_N} \mathcal{F}^{-1} \{ \dots [e^{i\phi_2} \mathcal{F}^{-1} (e^{i\phi_1} \mathcal{F}^{-1} p(0, z))] \}$$

WHERE $p(0, z)$ IS THE "STARTING FIELD,"

EX: A GAUSSIAN; $p(0, z) = \sqrt{\frac{k_0}{2}} e^{-(z-z_0)^2 k_0^2 / 4}$



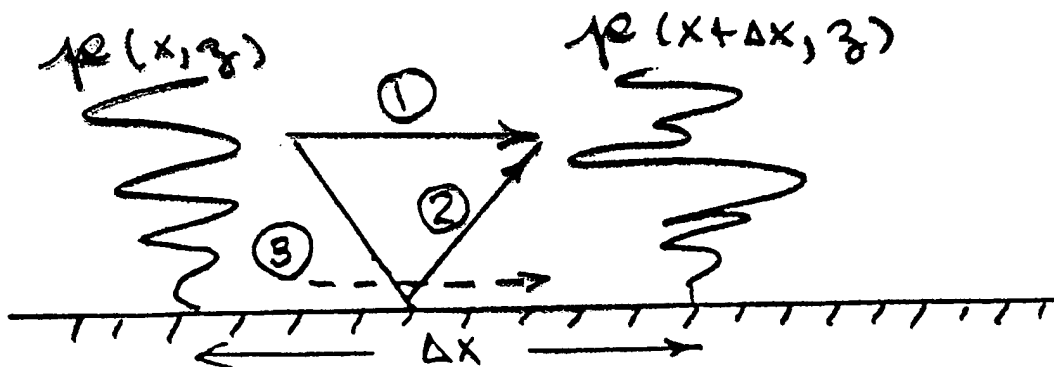
IMPEDANCE CONDITION ON GROUND

It can be shown (Gilbert and Di) that a finite ground impedance can be accounted for with the following form of the split-step FFT solution.

$$p(x+\Delta x, z) = e^{i k_0 (\bar{R}-1) \Delta x} \int_{-\infty}^{+\infty} e^{i \Delta x \sqrt{k_0^2 - k_z^2}} \underbrace{\tilde{p}(x, -k_z)}_{\substack{\text{---} \tilde{p}(x, -k_z) = \int_{-\infty}^{+\infty} e^{i k_z z} p(x, z) dz}} \\ \times \left[\tilde{p}^{(1)}(x, k_z) + R i k_z \right. \\ \left. + 2 i \beta \tilde{p}^{(3)}(x, \beta) e^{-} \right] e$$

WHERE $\beta = \frac{1}{2} \frac{Z_g}{Z_0}$, $\hat{Z}_g = Z_g / \rho_0 c_0 = [a(\omega) + i b(\omega)]$
 = (NORMALIZED GROUND IMPEDANCE)

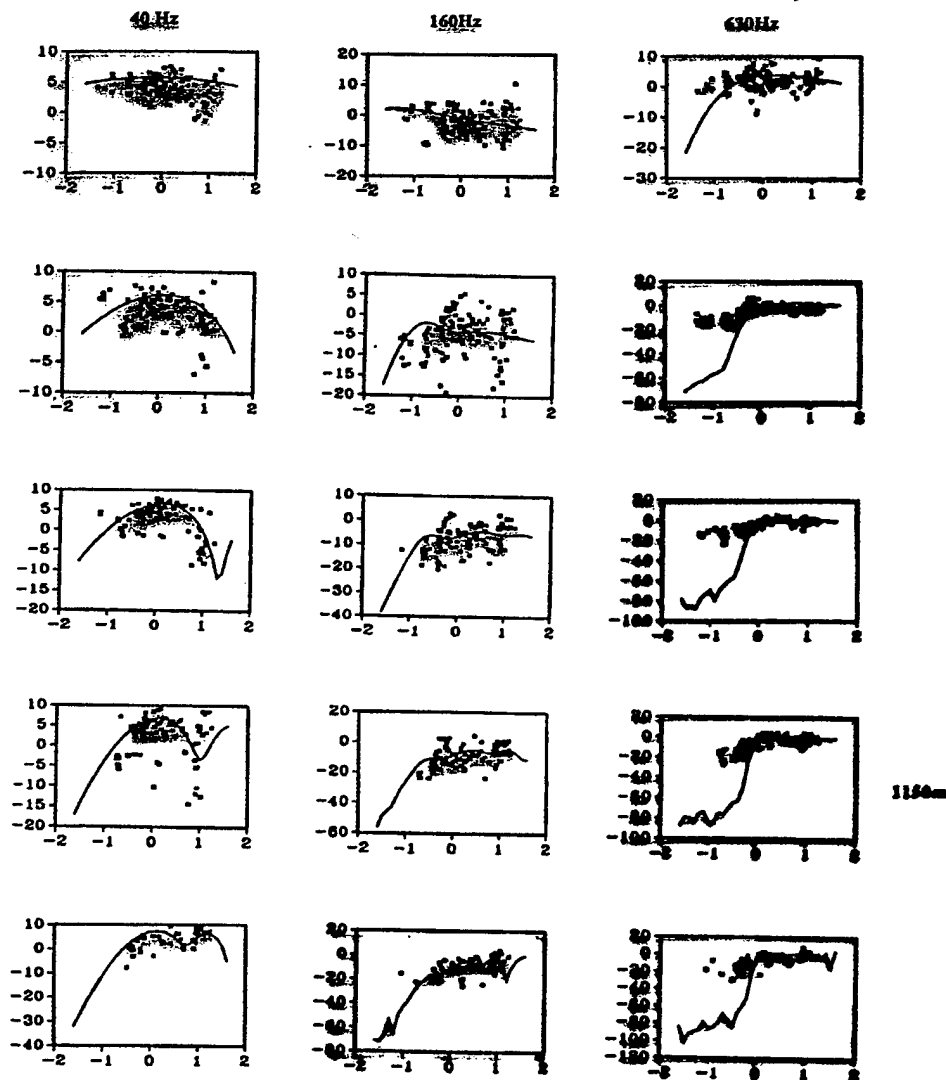
- 1) = Direct Wave (not new)
- 2) = Reflected Wave (new)
- 3) = Surface Wave (new)
- 4) = Phase Correction (not new)



A RESEARCH STORY

COMPARISON OF MEASURED LEVELS AND PARABOLIC EQUATION CALCULATIONS (WITHOUT TURBULENCE)

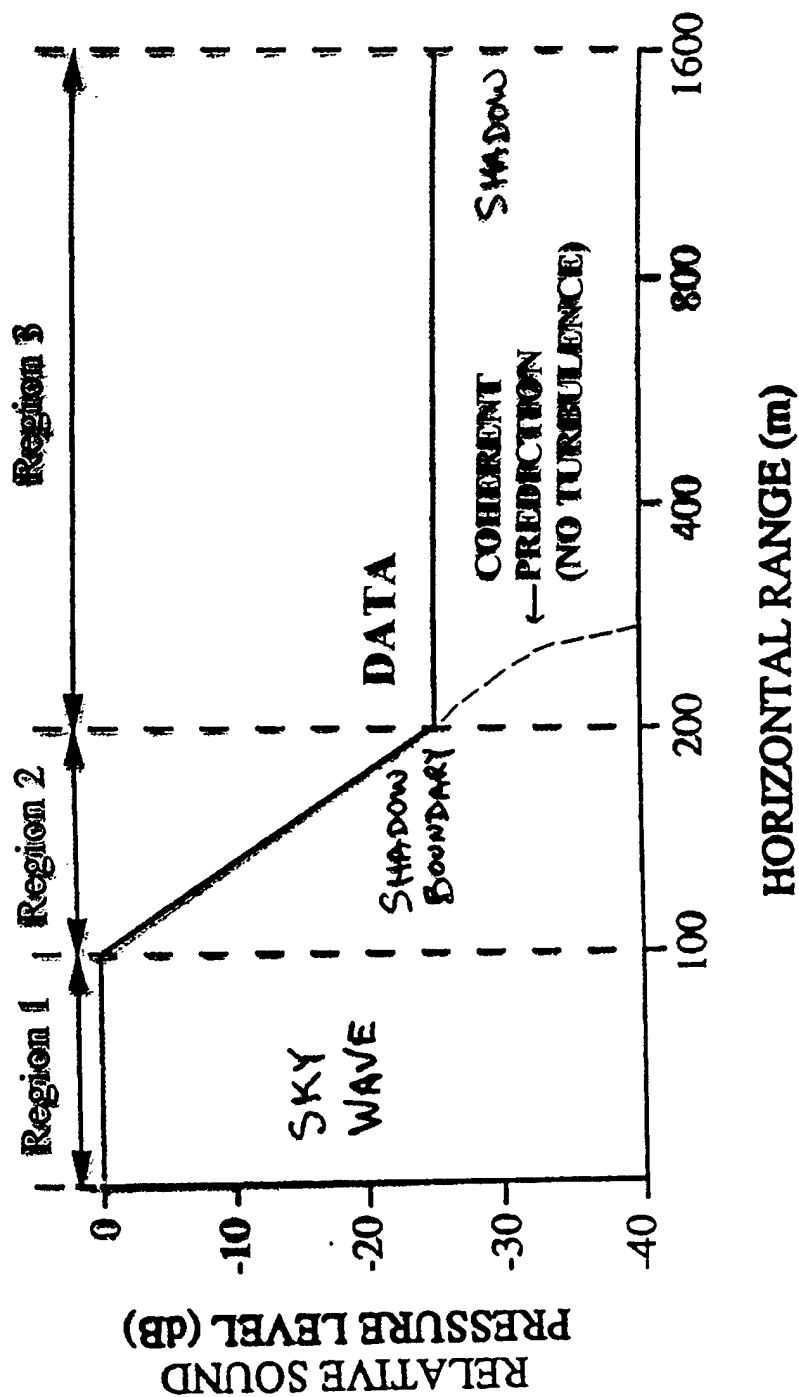
RELATIVE SOUND PRESSURE LEVEL



REFRACTION PARAMETER, a

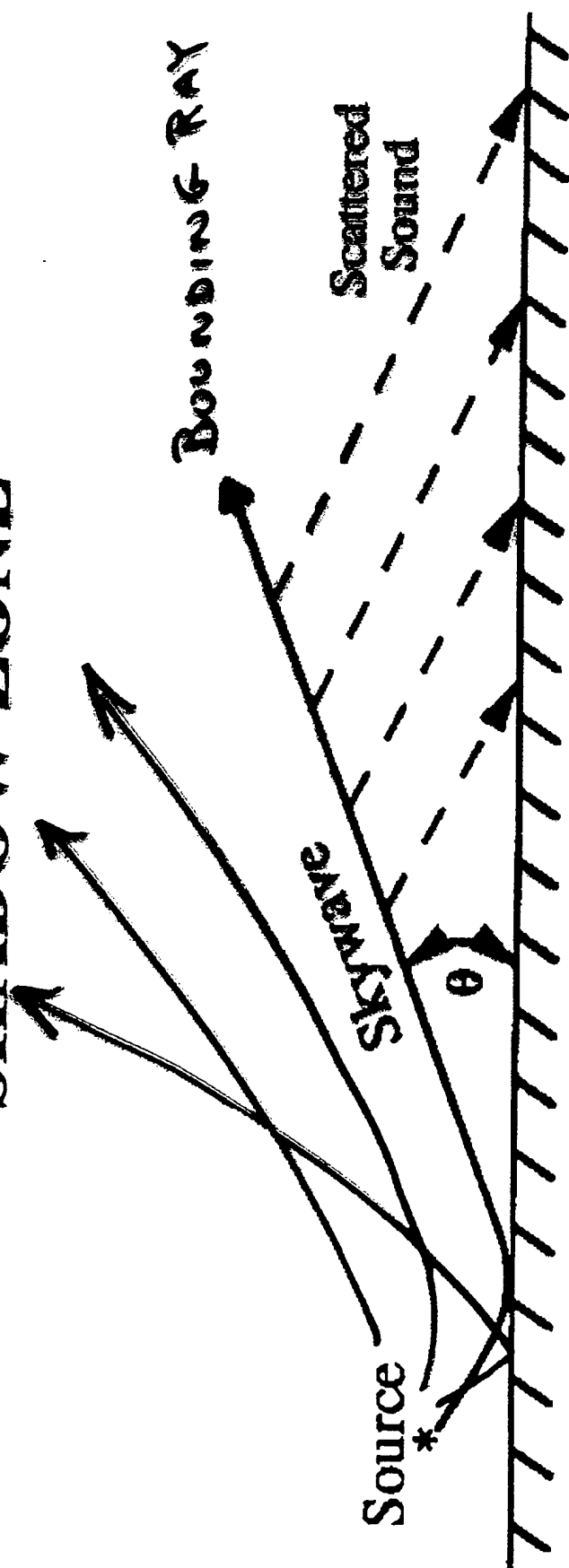
$$\langle C_e(z) \rangle = \begin{cases} 340 \text{ m/s} + a \ln(z/z_0) & z \geq z_0 \\ 340 \text{ m/s} & z < z_0 \end{cases} \quad (z_0 = .1 \text{ m})$$

CHARACTERISTIC STEP FUNCTION



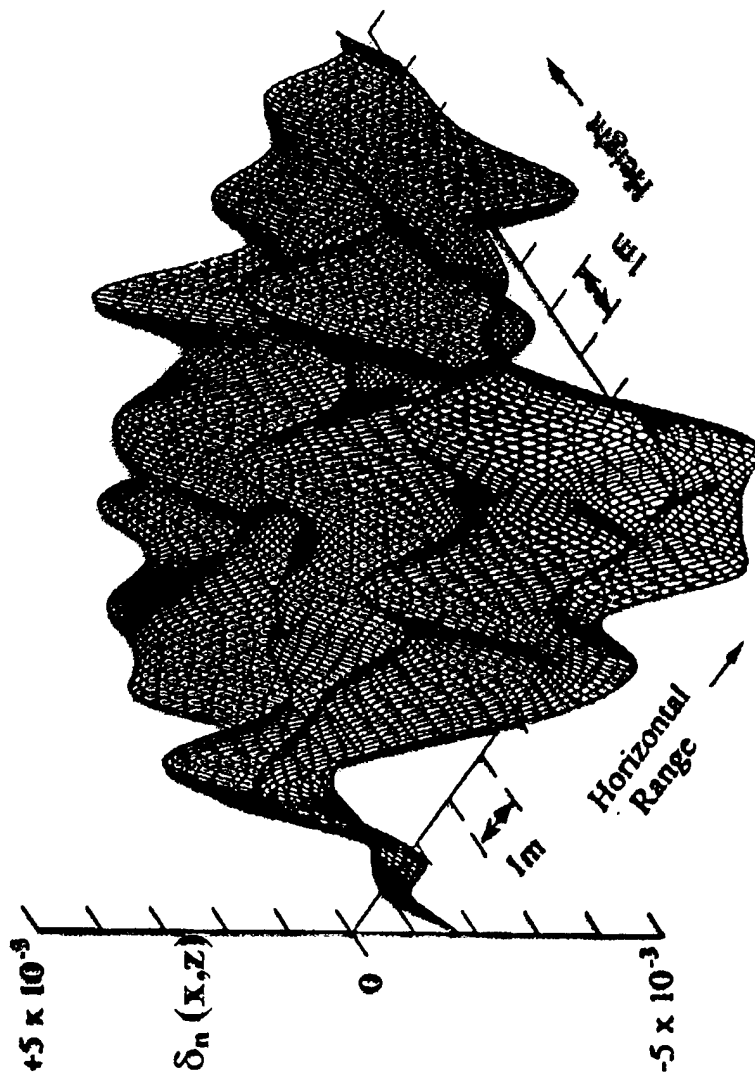
Characteristic step function for the relative sound pressure level versus range for sound propagation in an upward-refracting atmosphere.

SCATTERING OF SOUND INTO A SHADOW ZONE



Schematic representation of the scattering of sound into a shadow zone. The angle of the skywave is small, usually less than 10 degrees.

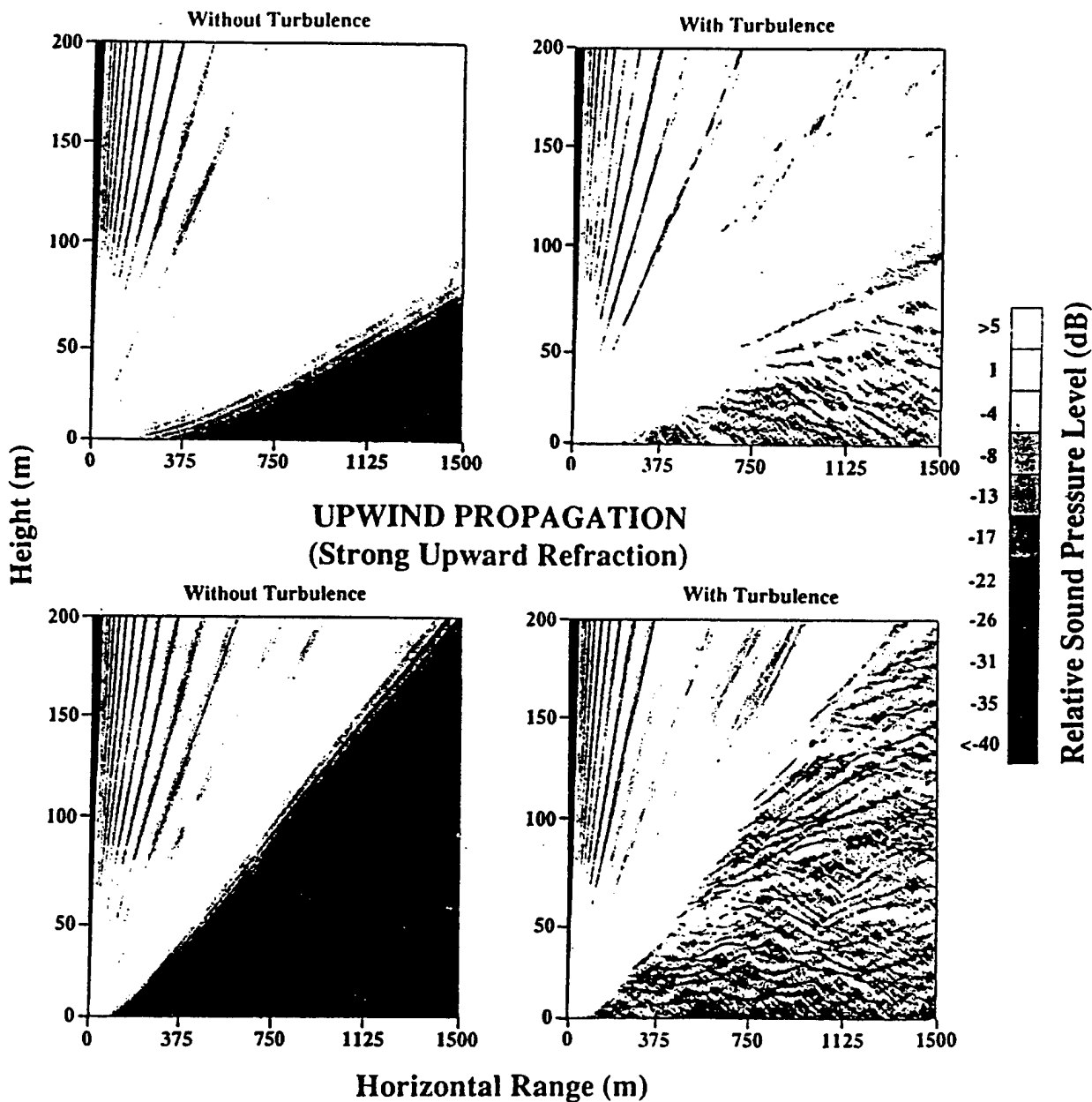
A REALIZATION OF INDEX OF REFRACTION FLUCTUATIONS



A 10x10-m sample of the stochastic part of the index of refraction $\delta n(r,z)$ for a given realization. On each trial, the index of refraction fluctuations were different in detail but had the same correlation length and root mean square amplitude.

RELATIVE SOUND PRESSURE LEVEL VERSUS HORIZONTAL RANGE AND HEIGHT

CROSSWIND PROPAGATION (Weak Upward Refraction)



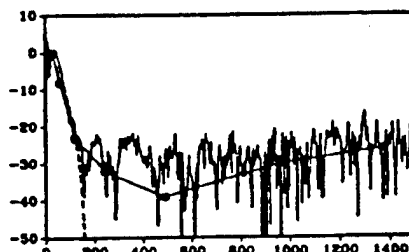
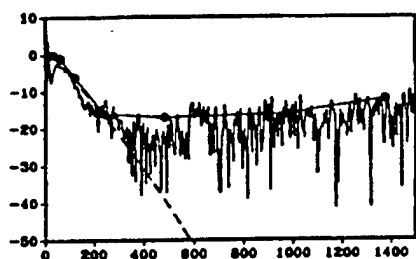
Gray-scale plots of relative sound pressure level versus height and horizontal range for a non-turbulent atmosphere. The frequency is 424 Hz., and the source height is 3.7m. (12ft.).

COMPARISON OF MEASURED AND PREDICT RELATIVE SOUND PRESSURE LEVELS

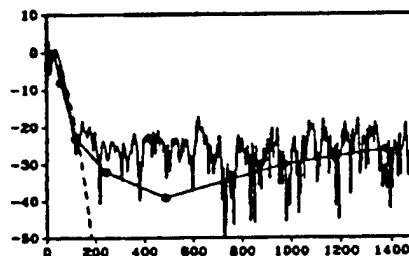
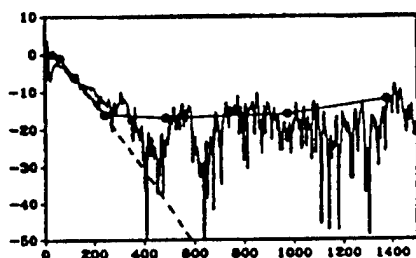
CROSSWIND PROPAGATION
(WEAK UPWARD REFRACTION)

UPWIND PROPAGATION
(STRONG UPWARD REFRACTION)

FREQUENCY = 424 Hz



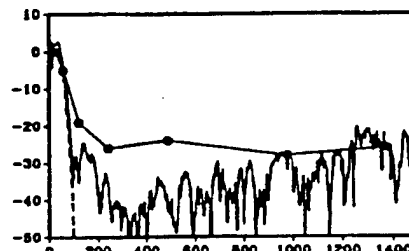
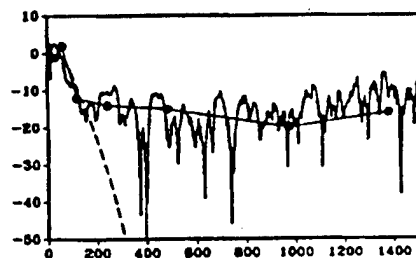
TRIAL 1



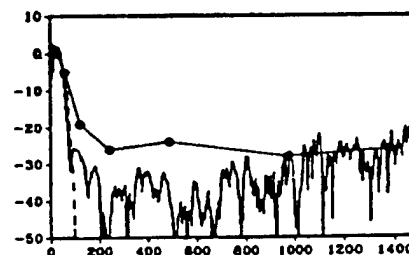
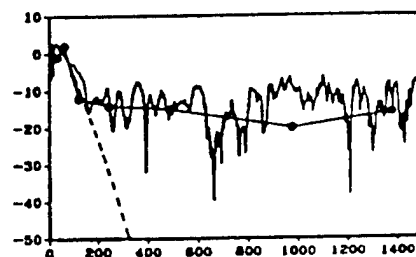
TRIAL 2

RELATIVE SOUND PRESSURE LEVEL (dB)

FREQUENCY = 848 Hz



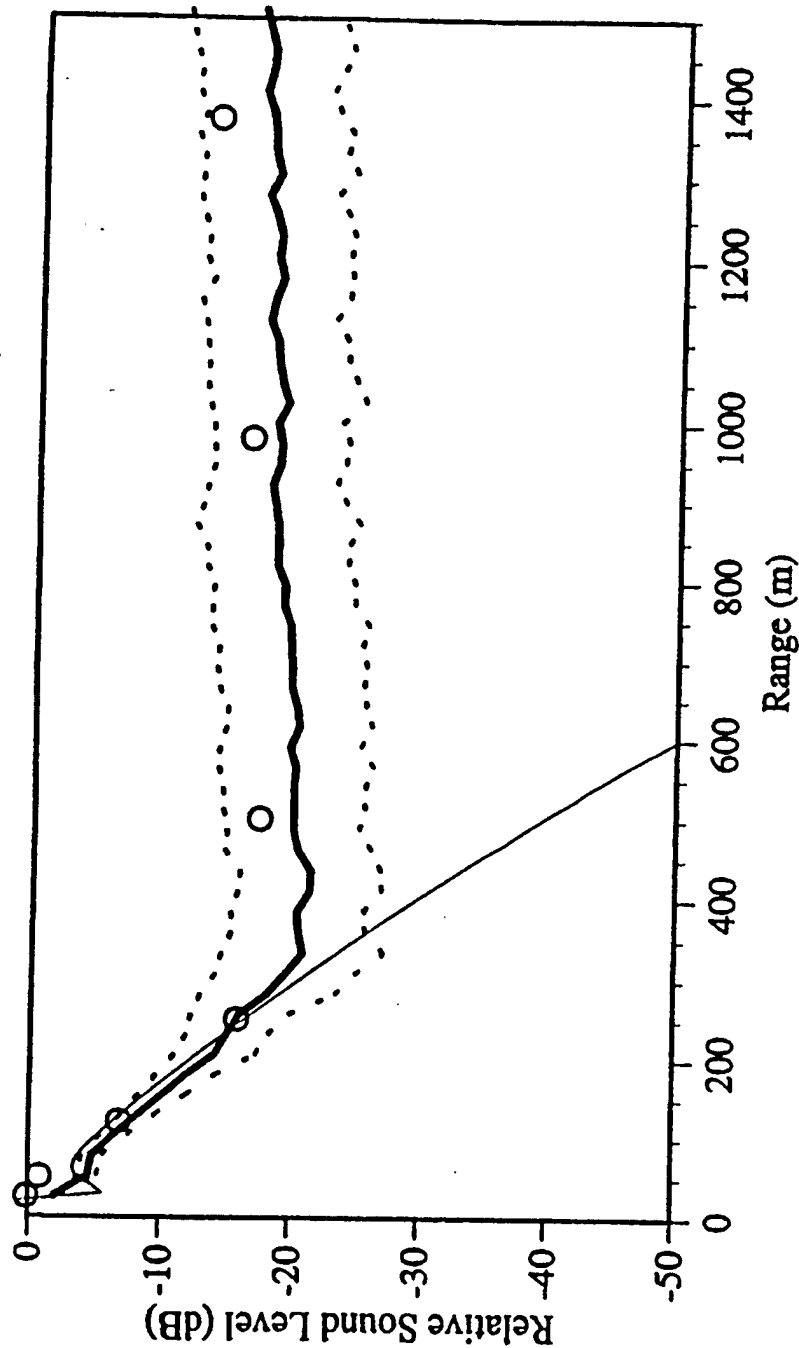
TRIAL 1



TRIAL 2

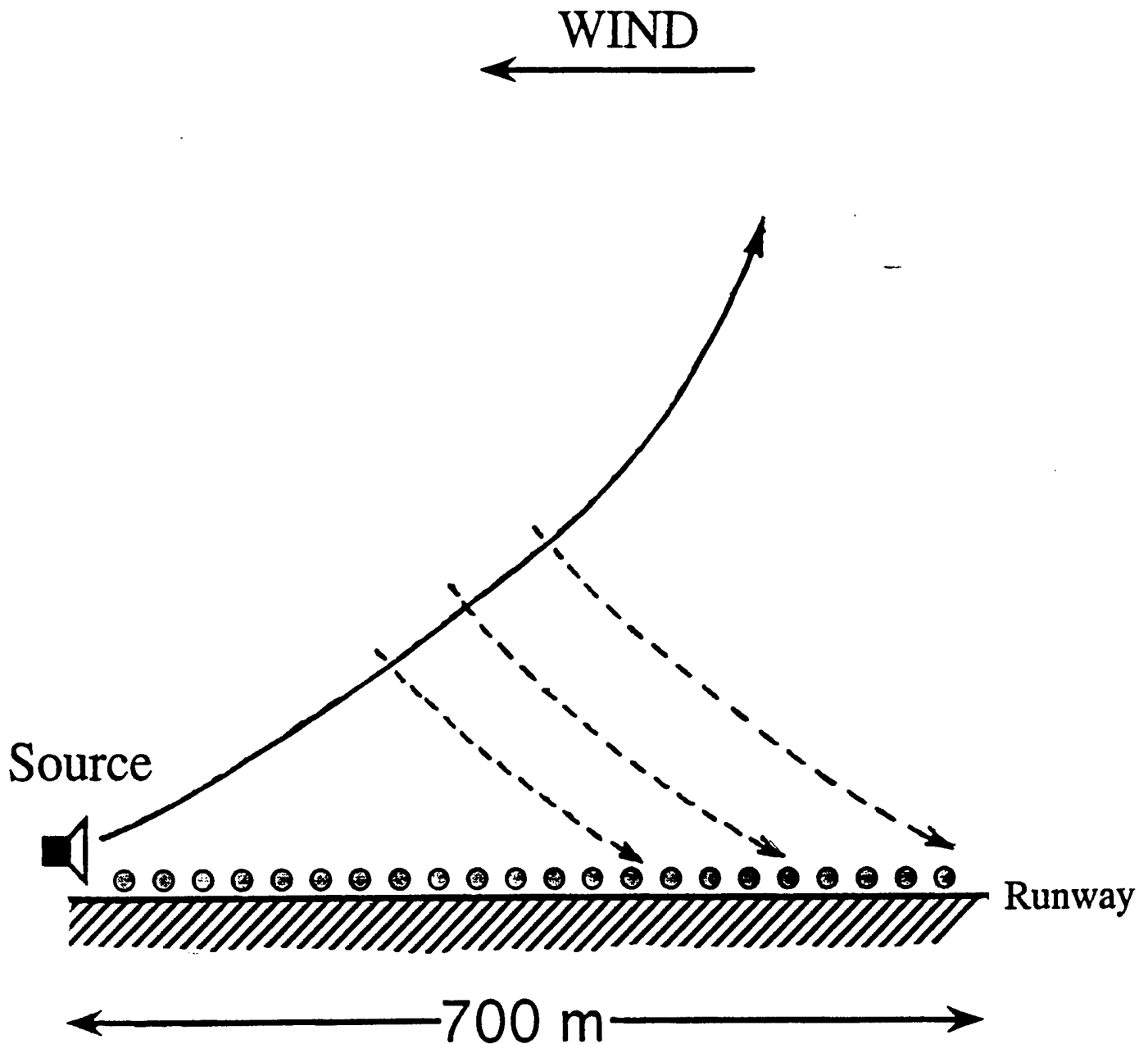
HORIZONTAL RANGE (m)

MEAN SOUND LEVEL AND STANDARD DEVIATION (424 Hz, CROSSWIND)



GF-PE calculation (300 realizations) of mean sound level (solid thick line) and standard deviation (dotted lines) for a turbulent atmosphere with an average sound speed that decreases with height (upward refracting). The circles are the experimental data of Weiner and Keast and the thin line is the GF-PE calculation without turbulence.

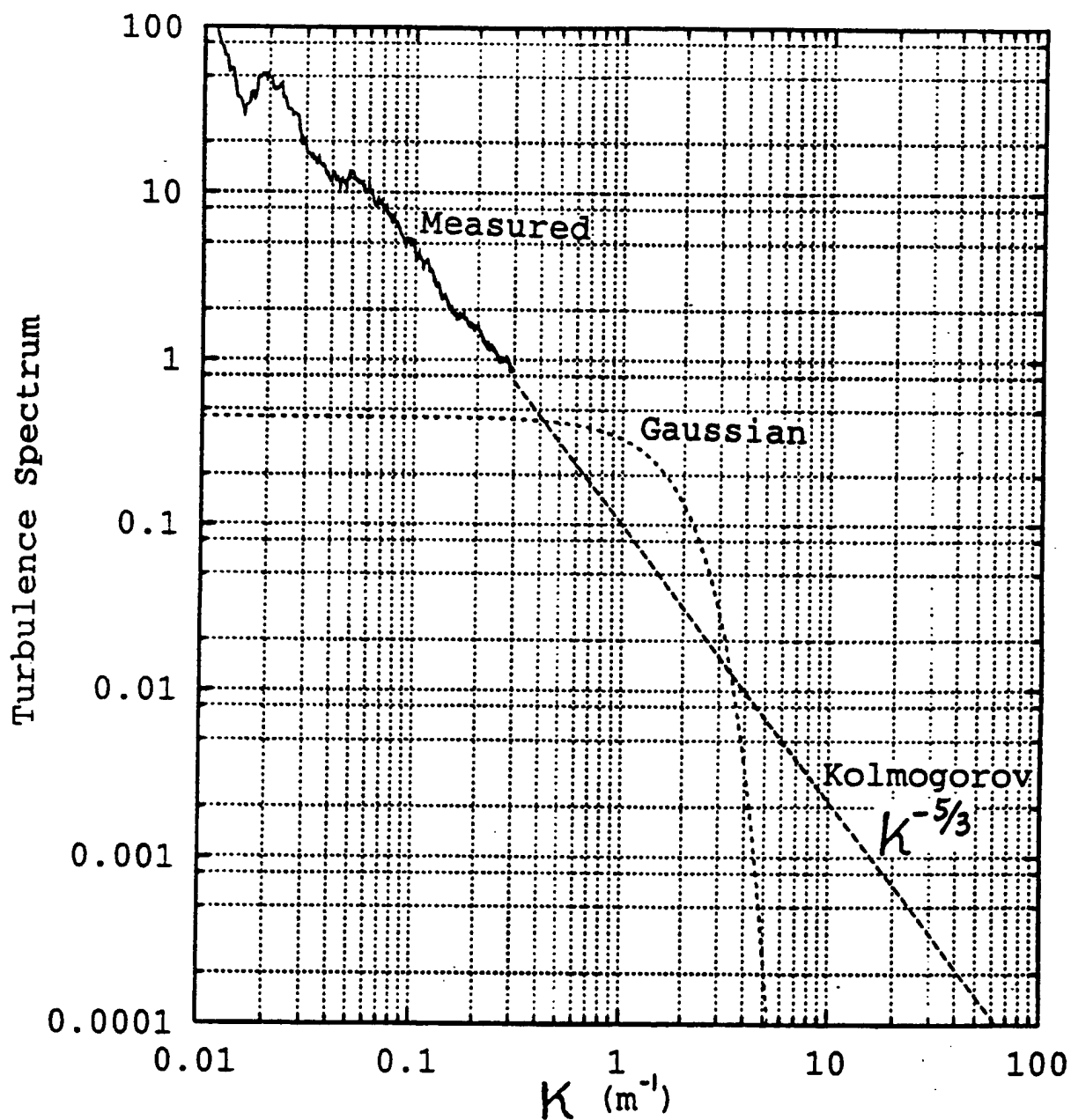
NRC (OTTAWA) EXPERIMENT



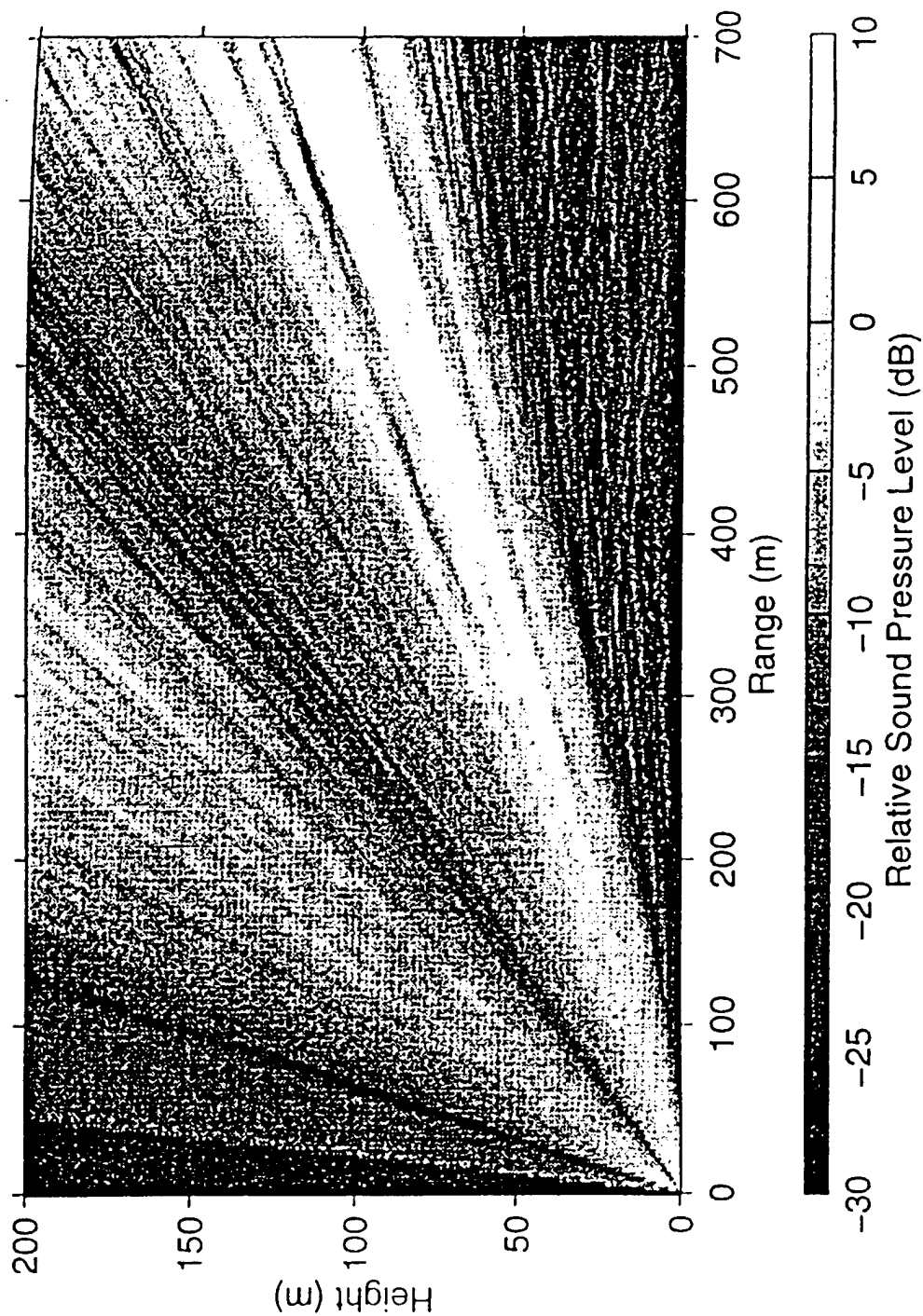
Freq = 40, 90, 210 Hz

Freq = 380, 500, 600, 700, 820, 940 Hz

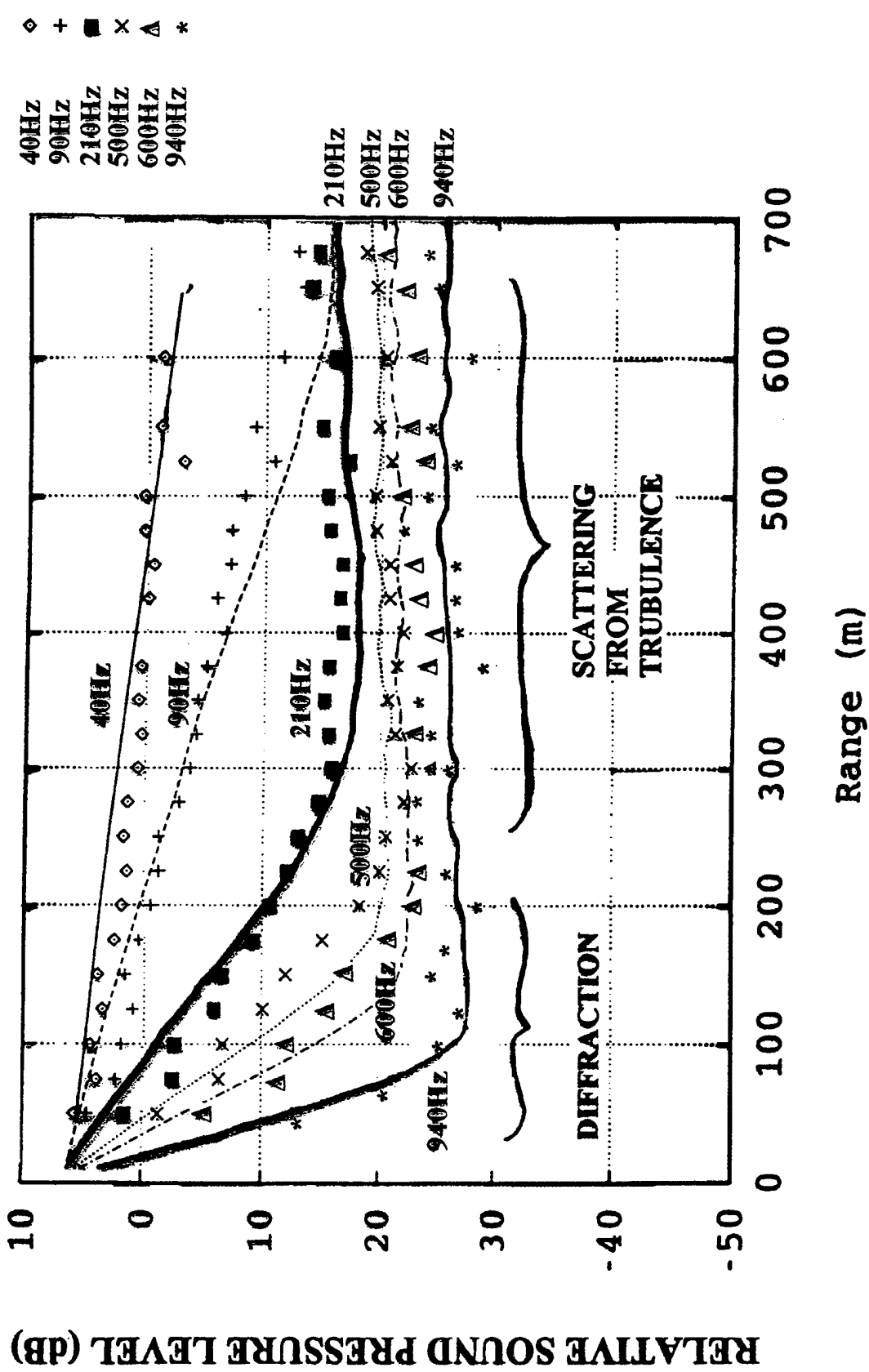
Horizontal Wind Turbulence Spectrum



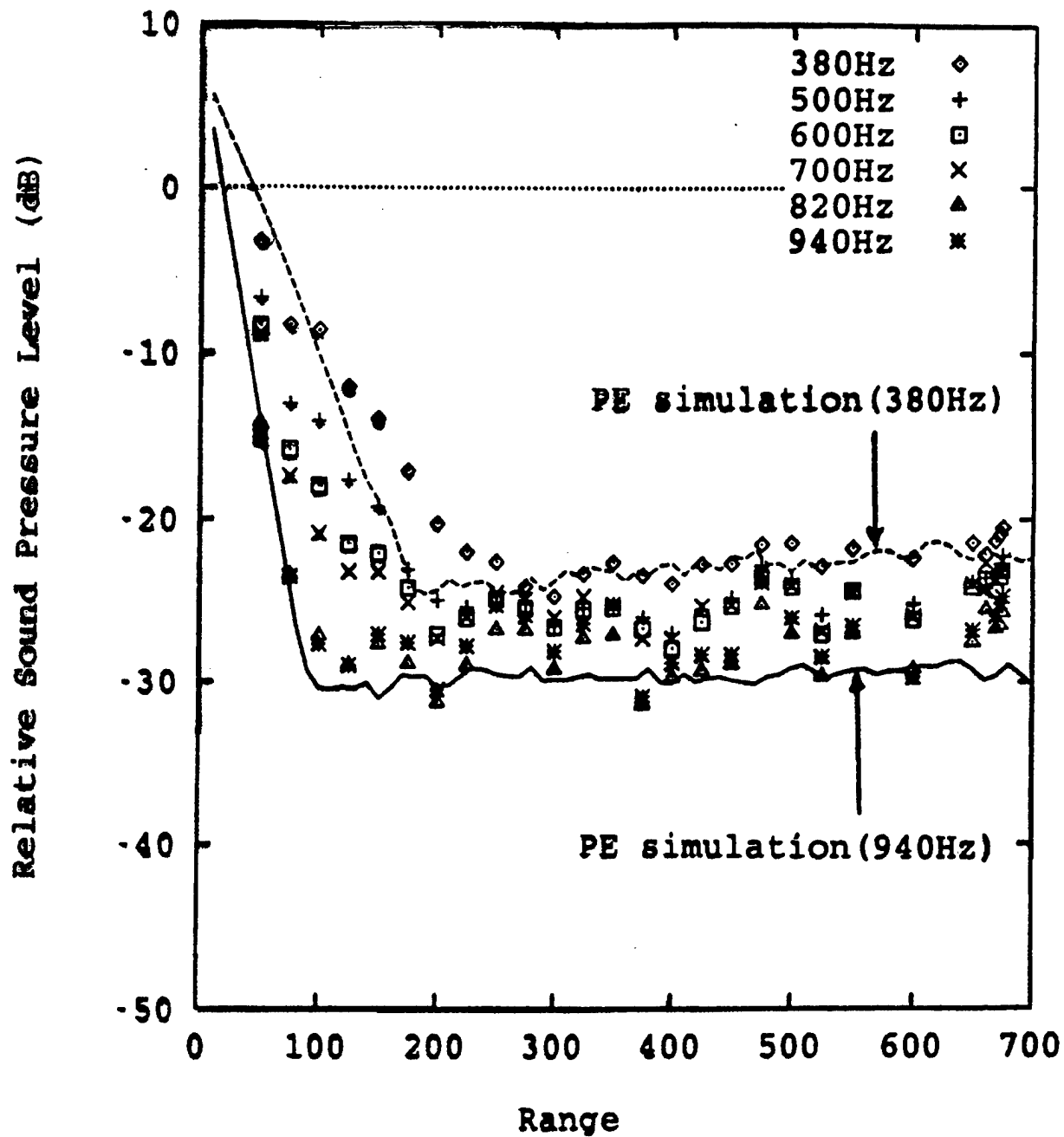
NRC (OTTAWA) EXPERIMENT FREQUENCY = 940Hz



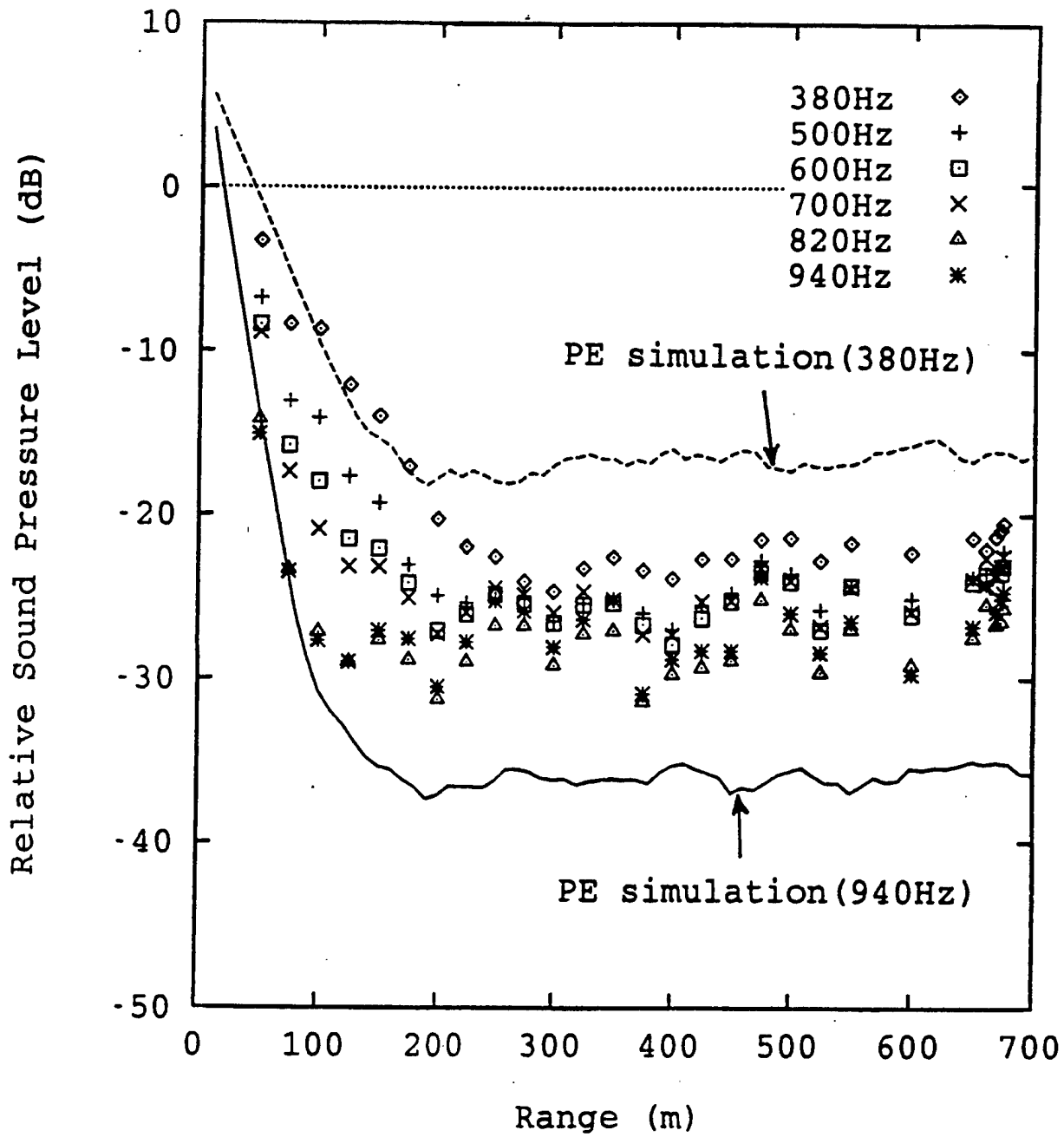
NRC (OTTAWA) DATA AND PE CALCULATION



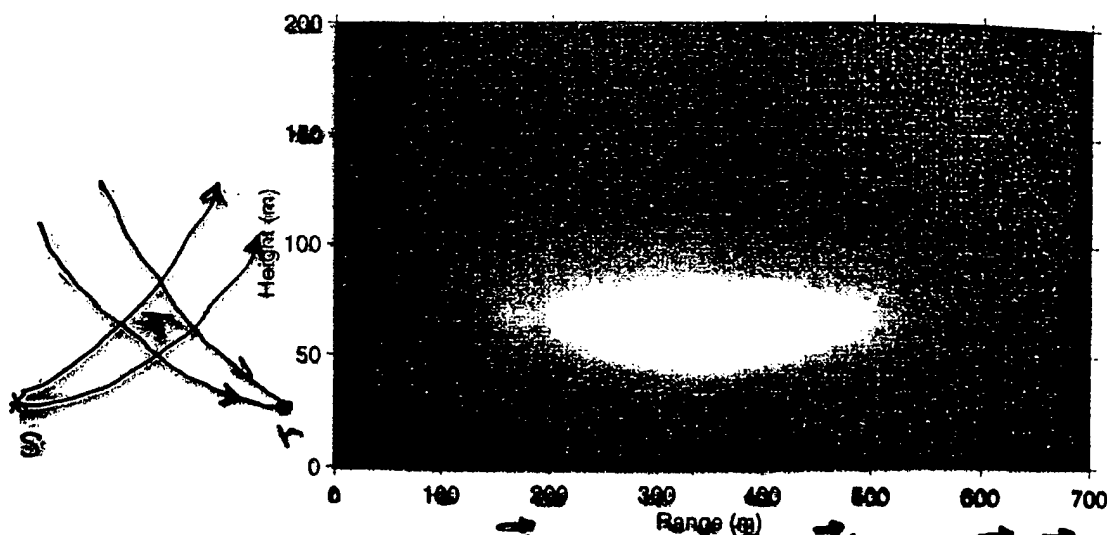
RELATIVE SOUND LEVEL VS. RANGE WITH MEASURED TURBULENCE SPECTRUM



RELATIVE SOUND LEVEL VS. RANGE WITH GAUSSIAN TURBULENCE SPECTRUM

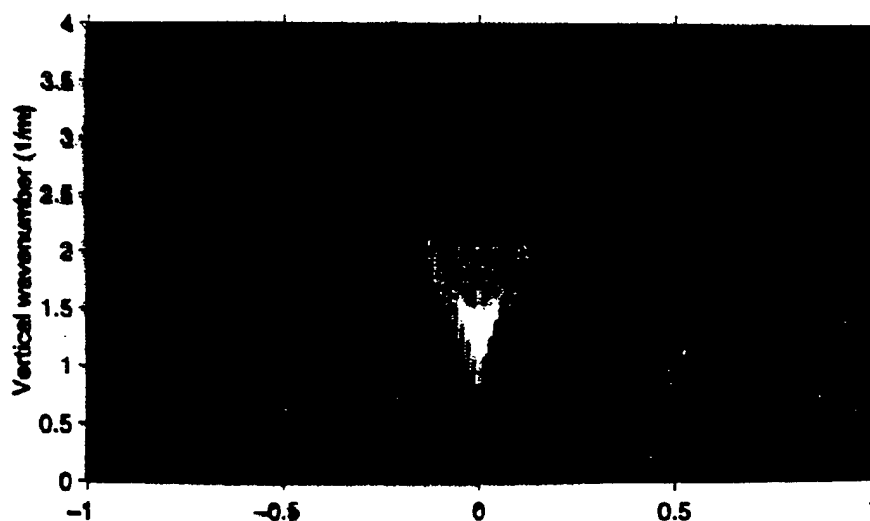


FREQUENCY = 210 Hz



$$W_{rs}(\vec{R}')^2$$

$$W_{rs}(\vec{R}') \equiv G_o(\vec{R}_r, \vec{R}') G_o(\vec{R}', \vec{R}_s)$$

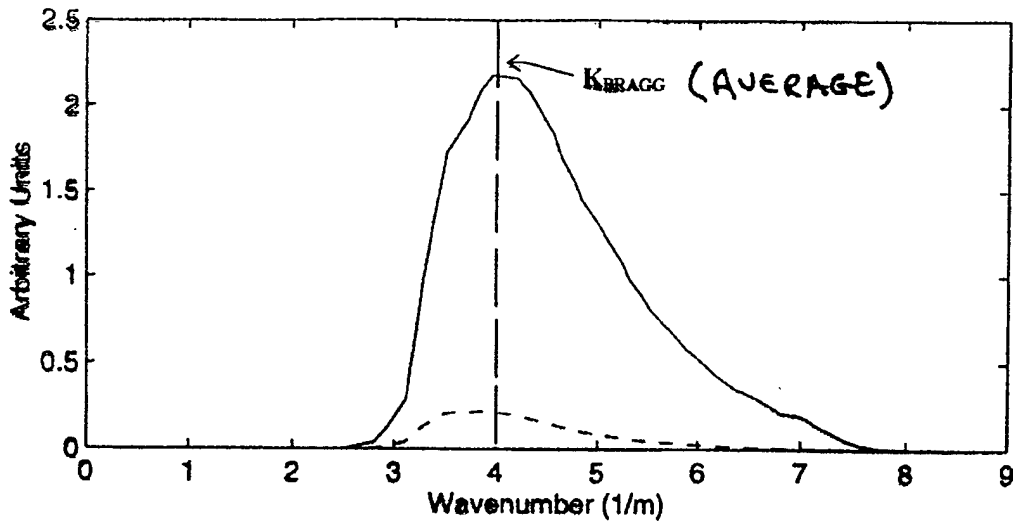


$$\tilde{W}_{rs}(\vec{k})^2$$

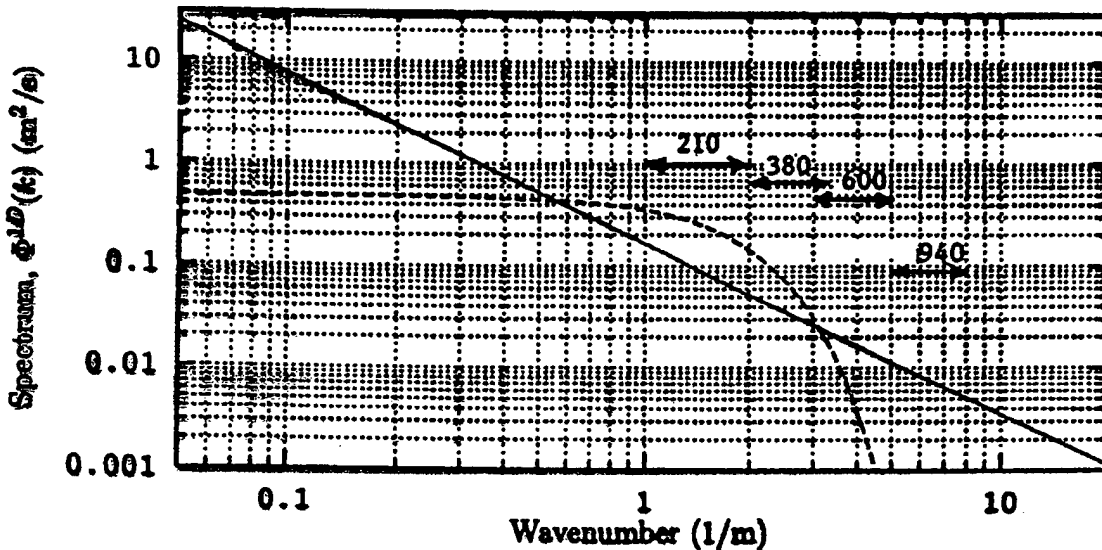
$$\tilde{W}_{rs}(\vec{k}) \equiv \int e^{-i\vec{k} \cdot \vec{R}'} W_{rs}(\vec{R}') d^3\vec{R}'$$

Magnitude squared of the two-dimensional R -space sampling function $[W_{rs}(r,z)]^2$ (top). Magnitude squared of the two-dimensional k -space sampling function $[W_{rs}(k_x, k_z)]^2$ (bottom). In both figures, a shading change from white to solid black indicates a decrease of a factor of ten.

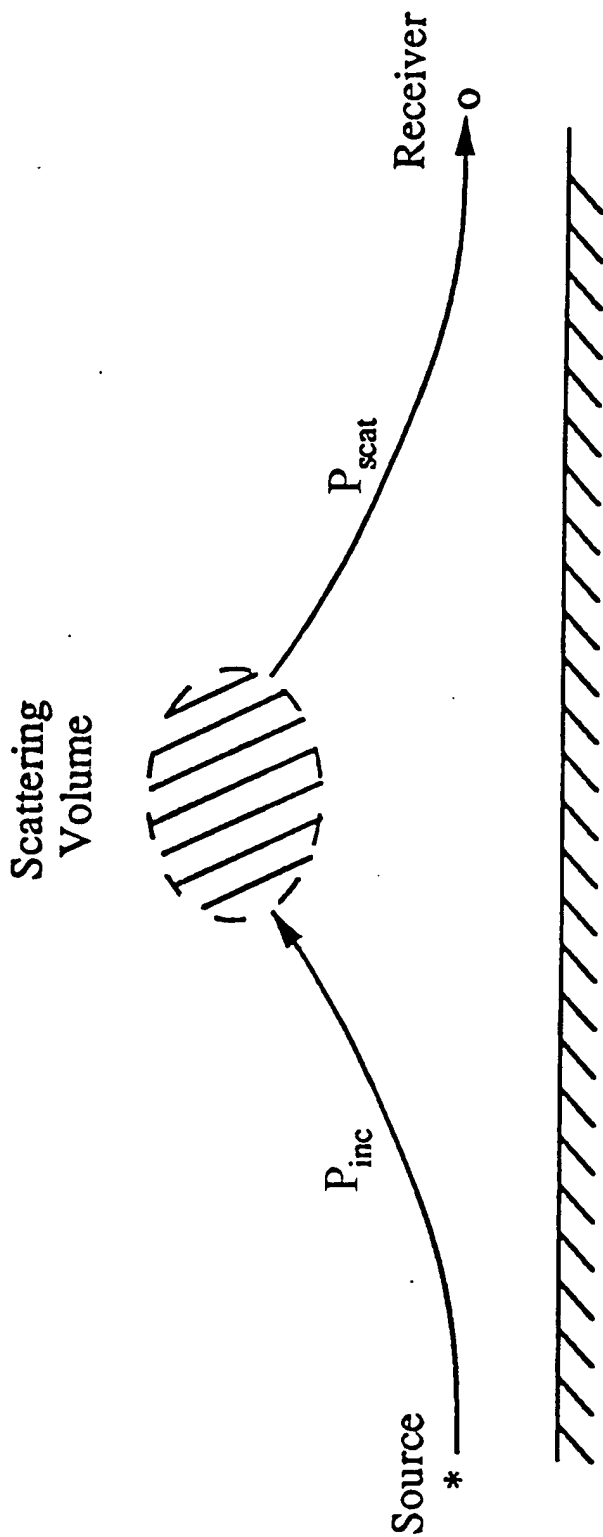
FREQUENCY = 600 Hz



The one-dimensional sampling function $\Omega_{r_0}^{1D}(k)$ (solid line) and $\Phi^{1D}(k)\Omega_{r_0}^{1D}(k)$ (dashed line), where $\Phi^{1D}(k)$ is the spectrum for index of refraction fluctuations due to turbulence. The sound level in a refractive shadow zone is proportional to the integral over $\Phi^{1D}(k)\Omega_{r_0}^{1D}(k)$. Note that a relatively narrow band of wavenumbers contributes to the integral for the shadow zone sound level.

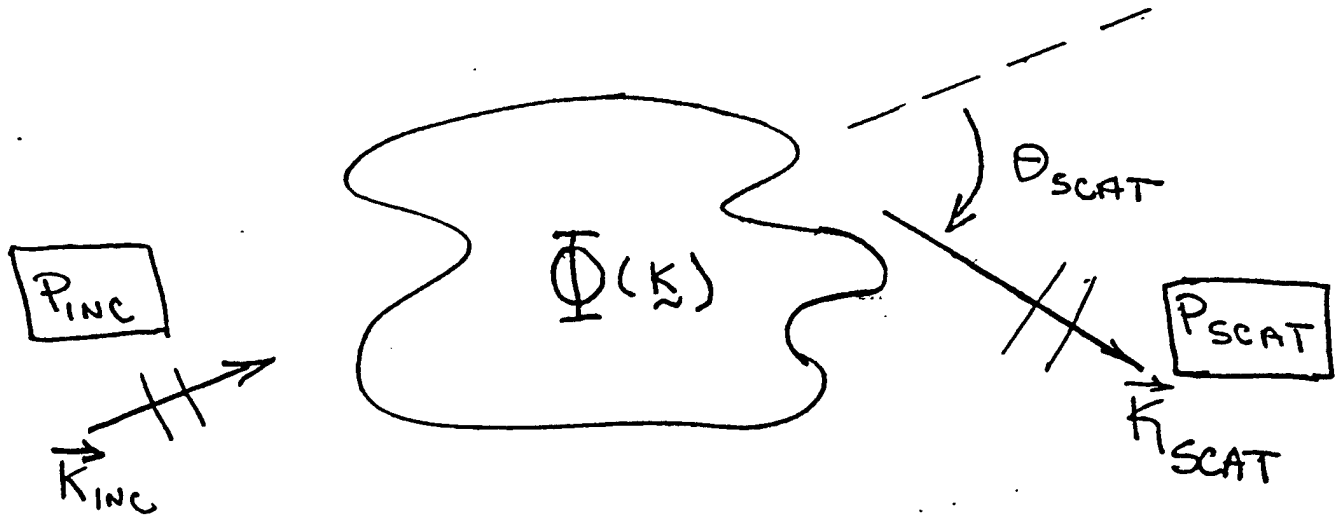


Regions of k -space that contribute to the shadow zone level at various frequencies (shown by arrows). The solid and dashed curves are for Kolmogorov and Gaussian spectra, respectively. Because the region sampled at a given frequency is relatively narrow, the two spectra predict significantly different shadow zone levels, especially at higher frequencies.



Schematic representation of scattering from turbulence. The quantity P_{inc} is the acoustic field incident on a particular scattering volume, and P_{scat} is the scattering acoustic field. The total scattered acoustic field is obtained by integrating over the volume between the source and receiver.

BRAGG SCATTERING



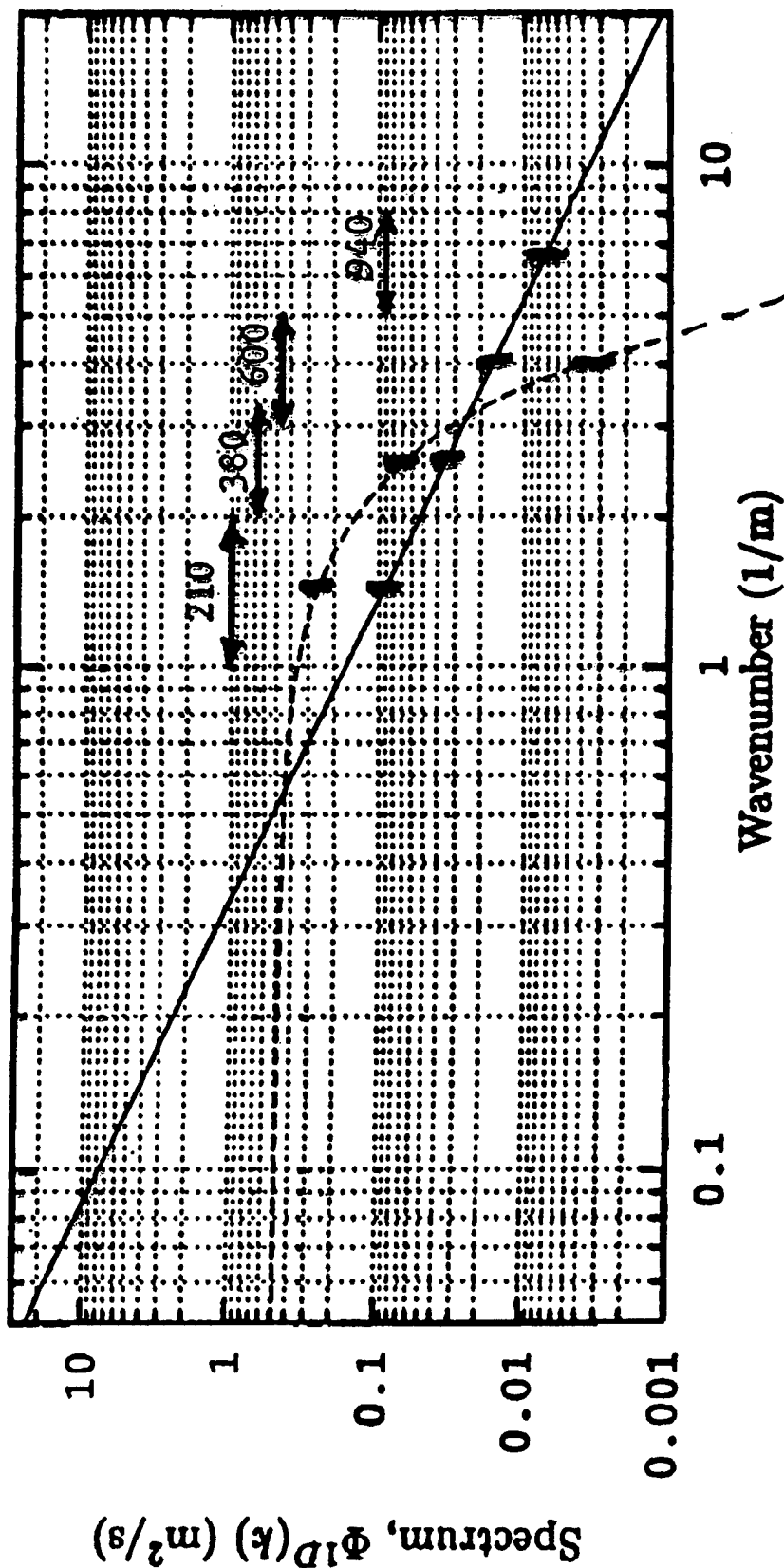
$$\langle |P_{SCAT}|^2 \rangle = \text{CONSTANT} \times K_0^4 \Phi(\vec{k}_B) V_{SCAT}$$

$$K_0 = |\vec{k}_{INC}| = |\vec{k}_{SCAT}|$$

$$\vec{k}_B = \vec{k}_{SCAT} - \vec{k}_{INC} = \text{BRAGG WAVENUMBER}$$

$$|\vec{k}_B| = 2K_0 \sin(\theta_{SCAT}/2)$$

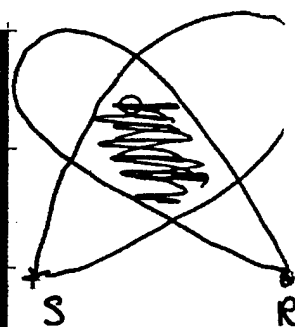
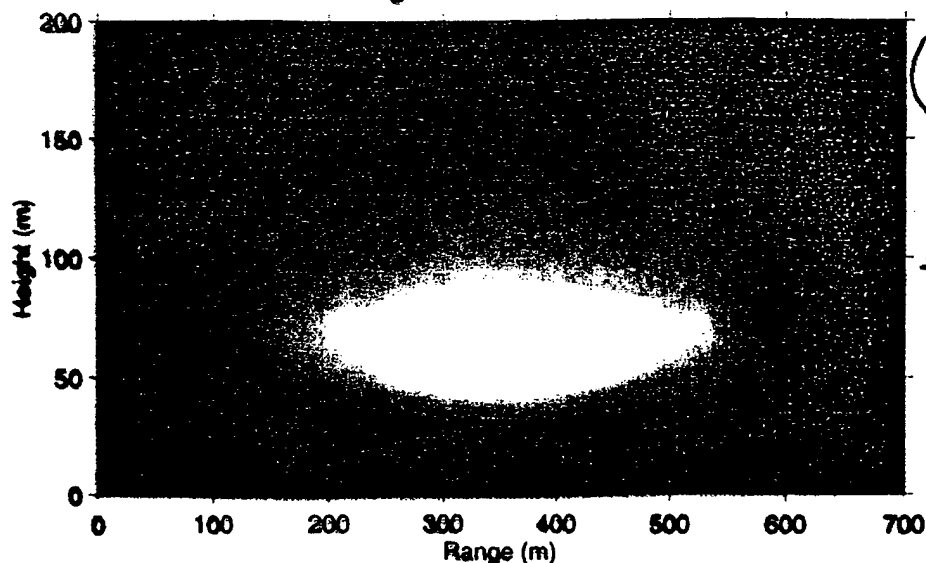
$$V_{SCAT} = \text{SCATTERING VOLUME}$$



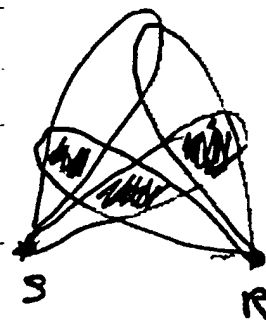
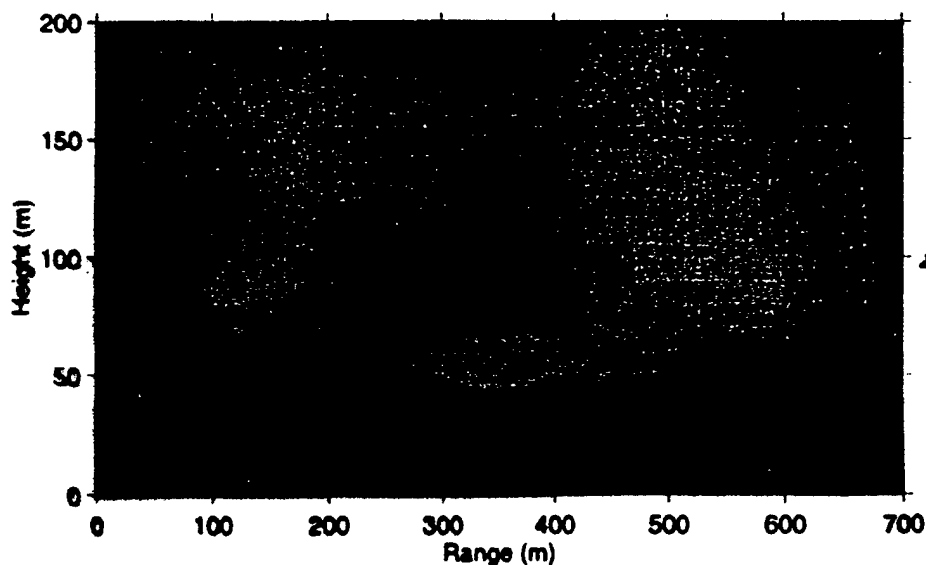
Regions of k -space that contribute to the shadow zone level at various frequencies (shown by arrows). The solid and dashed curves are for Kolmogorov and Gaussian spectra, respectively. Because the region sampled at a given frequency is relatively narrow, the two spectra predict significantly different shadow zone levels, especially at higher frequencies.

R-SPACE SAMPLING FUNCTION

FREQUENCY = 210 Hz



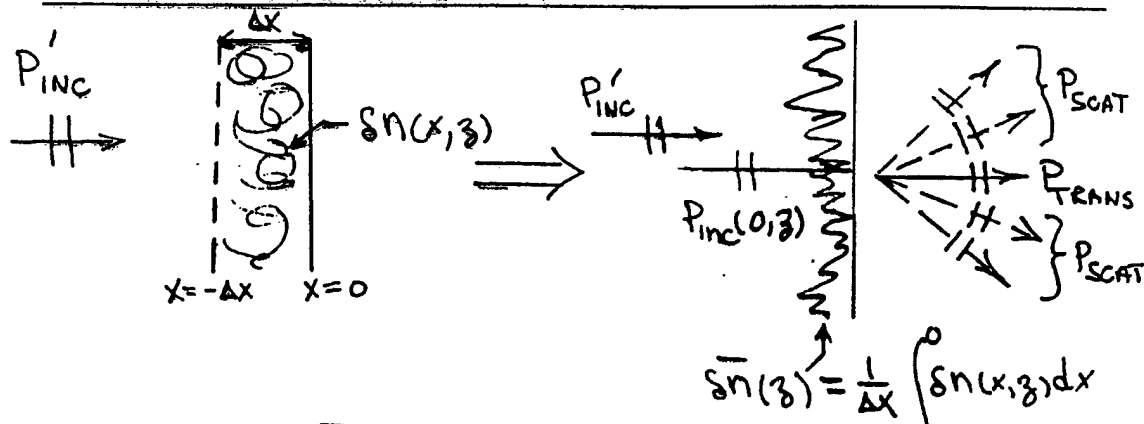
FREQUENCY = 940 Hz



Magnitude squared of the two-dimensional R -space sampling function $[W_{rs}(r,z)]^2$ at 210 Hz (top) and 940 Hz (bottom), respectively. Due to interference between the source and its ground reflection, the sampling volume depends strongly on frequency. At 210 Hz, the interference is constructive, while at 940 Hz, regions of destructive interference are present, and consequently, the effective scattering volume is greatly reduced.

PHASE SCREEN EXPLANATION OF SCATTERING BY TURBULENCE

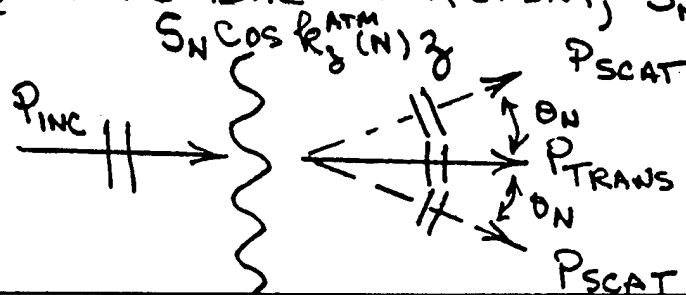
TURBULENCE AS A SUPERPOSITION OF SINUSOIDAL DIFFRACTION GRATINGS



CONSIDER $\bar{n}(z) = \sum_j S_j [\cos(k_z^{ATM}(j)z + p_j)]$

WHERE $S_j \propto \sqrt{\Phi(k_z^{ATM}(j))}$ (P_j = RANDOM PHASE)

FOR ONE SINUSOIDAL COMPONENT, S_N :



CONSTRUCTIVE INTERFERENCE OCCURS FOR

$$(k_z^{SCAT} - k_z^{INC}) = k_z^{ATM} \equiv k_{BRAGG} = 2k_0 \sin(\theta/2)$$

N TERMS OF WAVELENGTHS:

$$\lambda_z^{ATM} = \lambda_z^{BRAGG} = \frac{\lambda_0}{2 \sin(\theta/2)} \quad \lambda_0 = \text{ACOUSTIC WAVELENGTH}$$

$$\text{EX: } \sin(\theta/2) = \frac{\lambda_0}{2\lambda_z^{ATM}(N)} \text{ FOR } \lambda_0 = 5 \text{ m } \lambda_z^{ATM} = 5 \text{ m} \rightarrow \theta = 11.5^\circ$$

↑
SCATTERING
ANGLE DUE
TO Nth FOURIER
COMPONENT

PARABOLIC EQUATION ANALYSIS OF SCATTERING

$$\text{GENERAL, } P(\Delta x, z) = \int_{-\infty}^{+\infty} e^{i \Delta x \sqrt{k_0^2 - k_z^2}} e^{i k_z z} \frac{dk_z}{2\pi} \int_{-\infty}^{+\infty} P(0, z') e^{-i k_z z'} dz'$$

$$\text{TAKE } P(0, z') = A e^{i k_z^{\text{INC}} z'} e^{i k_0 \delta n(z) \Delta x}$$

($\phi(z)$ = PHASE SCREEN)

$$\approx A e^{i k_z^{\text{INC}} z'} (1 + i k_0 \Delta x B_N \cos k_z^{\text{ATM}}(N))$$

$$\tilde{P}(0, k_z) = \int_{-\infty}^{+\infty} P(0, z') e^{-i k_z z'} dz'$$

$$A \int_{-\infty}^{+\infty} (1) e^{-i k_z z'} e^{i k_z^{\text{INC}} z'} dz'$$

$$+ i k_0 \Delta x A S_N \int_{-\infty}^{+\infty} e^{i (k_z^{\text{INC}} - k_z) z'} \left[\frac{e^{i k_z^{\text{ATM}}(N) z'} + e^{-i k_z^{\text{ATM}}(N) z'}}{2} \right] dz'$$

$$\text{SINCE } \int_{-\infty}^{+\infty} e^{i(\alpha - \beta)z} dz = 2\pi \delta(\alpha - \beta) = 2\pi \delta(\beta - \alpha)$$

$$\tilde{P}(0, k_z) = 2\pi A \delta(k_z - k_z^{\text{INC}}) \rightarrow \text{Diagram: A horizontal axis labeled } k_z \text{ with a vertical line at } k_z^{\text{INC}}.$$

$P_{\text{TRANS}}(0, k_z) \quad P_{\text{SCAT}}(0, k_z)$

$$+ i\pi k_0 \Delta x A S_N \left[\delta(k_z - k_z^{\text{INC}} - k_z^{\text{ATM}}(N)) + \delta(k_z - k_z^{\text{INC}} + k_z^{\text{ATM}}(N)) \right]$$

Diagram: A horizontal axis with three vertical lines. The first line is labeled $k_z^{\text{INC}} - k_z^{\text{ATM}}$, the second k_z^{INC} , and the third $k_z^{\text{INC}} + k_z^{\text{ATM}}$.

$$\left[(k_z - k_z^{\text{INC}}) = k_z^{\text{BRAGG}} = k_z^{\text{ATM}}(N) \right] \quad \left[(k_z - k_z^{\text{INC}}) = k_z^{\text{BRAGG}} = -k_z^{\text{ATM}} \right]$$

MULTIPLY $\tilde{P}(0, k_z)$ BY $e^{i\Delta x \sqrt{k_0^2 - k_z^2}}$ AND
FOURIER TRANSFORM TO GET $P(\Delta x, z)$

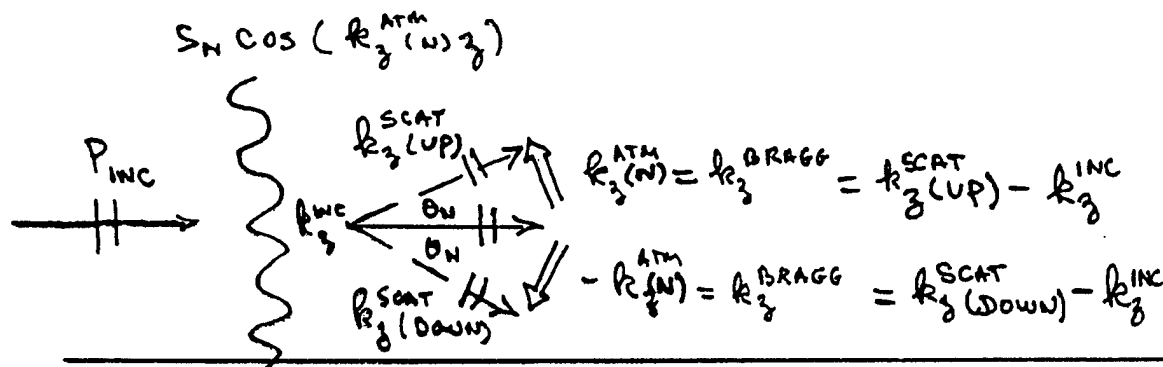
$$P(\Delta x, z) = \int_{-\infty}^{\infty} e^{i\Delta x \sqrt{k_0^2 - k_z^2}} e^{ik_z z} \tilde{P}(0, k_z) \frac{dk_z}{2\pi}$$

$$= A e^{i\Delta x \sqrt{k_0^2 - k_z^{INC2}}} e^{ik_z^{INC} z}$$

$$+ i\Gamma k_0 \Delta x A S_n \left[e^{i\Delta x k'_x} e^{ik_z^{SCAT}(UP) z} + e^{i\Delta x k_x} e^{ik_z^{SCAT}(DOWN) z} \right]$$

WHERE $k_z^{SCAT}(UP) = k_z^{INC} + k_z^{ATM}(N)$, $k_z^{SCAT}(DOWN) = k_z^{INC} - k_z^{ATM}(N)$

$$k'_x = \sqrt{k_0^2 - k_z^{SCAT2}(UP)} \quad k_x = \sqrt{k_0^2 - k_z^{SCAT2}(DOWN)}$$



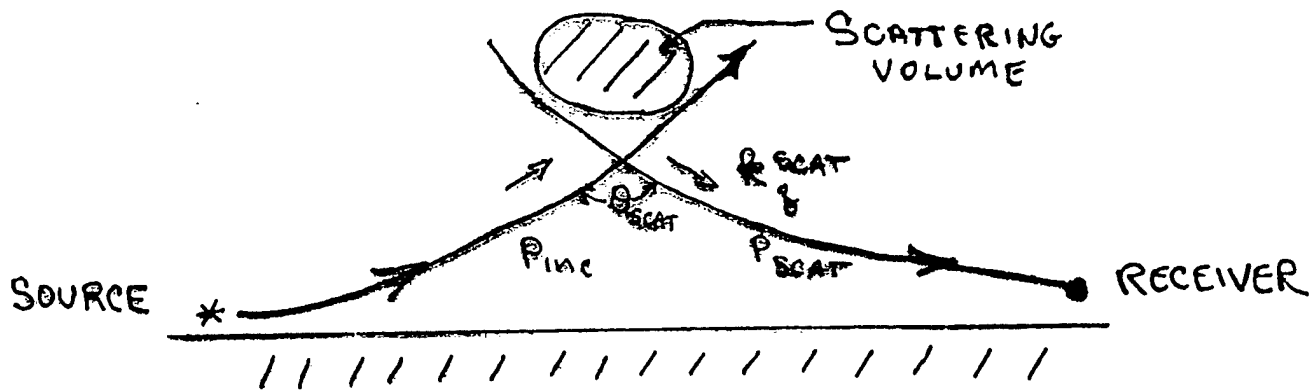
The above PE analysis shows that constructive interference occurs for the n th sinusoidal component of turbulence when we have:

$$k_z^{SCAT}(UP/DOWN) - k_z^{INC} = k_z^{BRAGG} = (+/-) k_z^{ATM}(N)$$

OR-

$$k_z^{SCAT}(UP/DOWN) = k_z^{INC} +/- k_z^{ATM}(N)$$

QUESTION: At a given range, what do the sound levels in a shadow zone tell us?



$$\langle |P_{scat}|^2 \rangle \propto |A|^2 |S_N|^2$$

$$\propto |A|^2 \Phi_{TURB}(|k_z^{BRAGG}|)$$

$$\text{WHERE } |k_z^{BRAGG}| = |k_z^{ATM}(N)|$$

$$= |k_z^{scat} - k_z^{inc}|$$

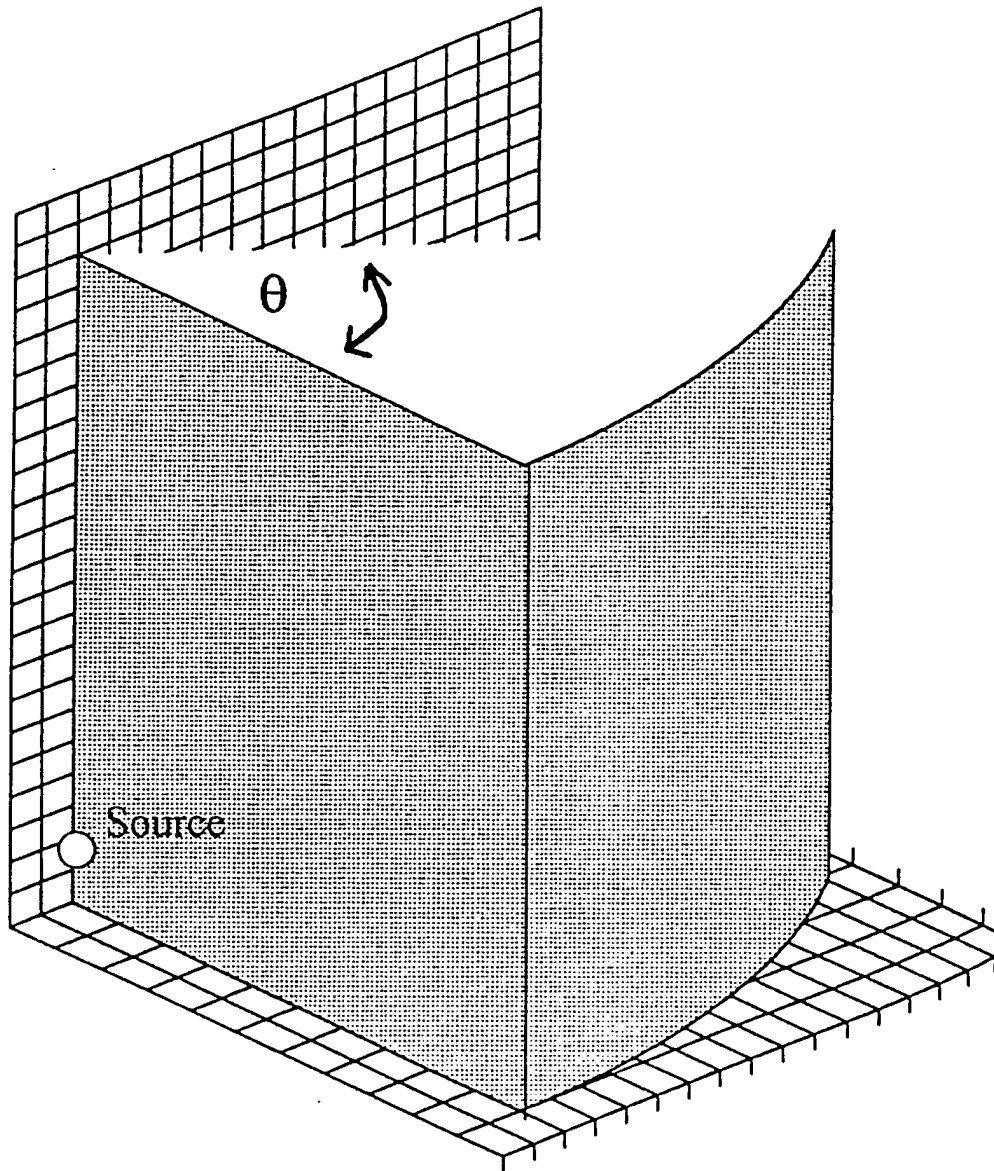
$$= 2k_0 \sin(\theta_{scat}/2)$$

ANSWER: The mean strength of the wave scattered at an angle $\theta_{scat} = \theta_N$ tells us the mean strength of the n th Fourier component of the index of refraction.

THAT IS, WE COULD HAVE INFERRED THE KOLMOGOROV SPECTRUM FROM THE SOUND LEVELS IN THE SHADOW ZONE

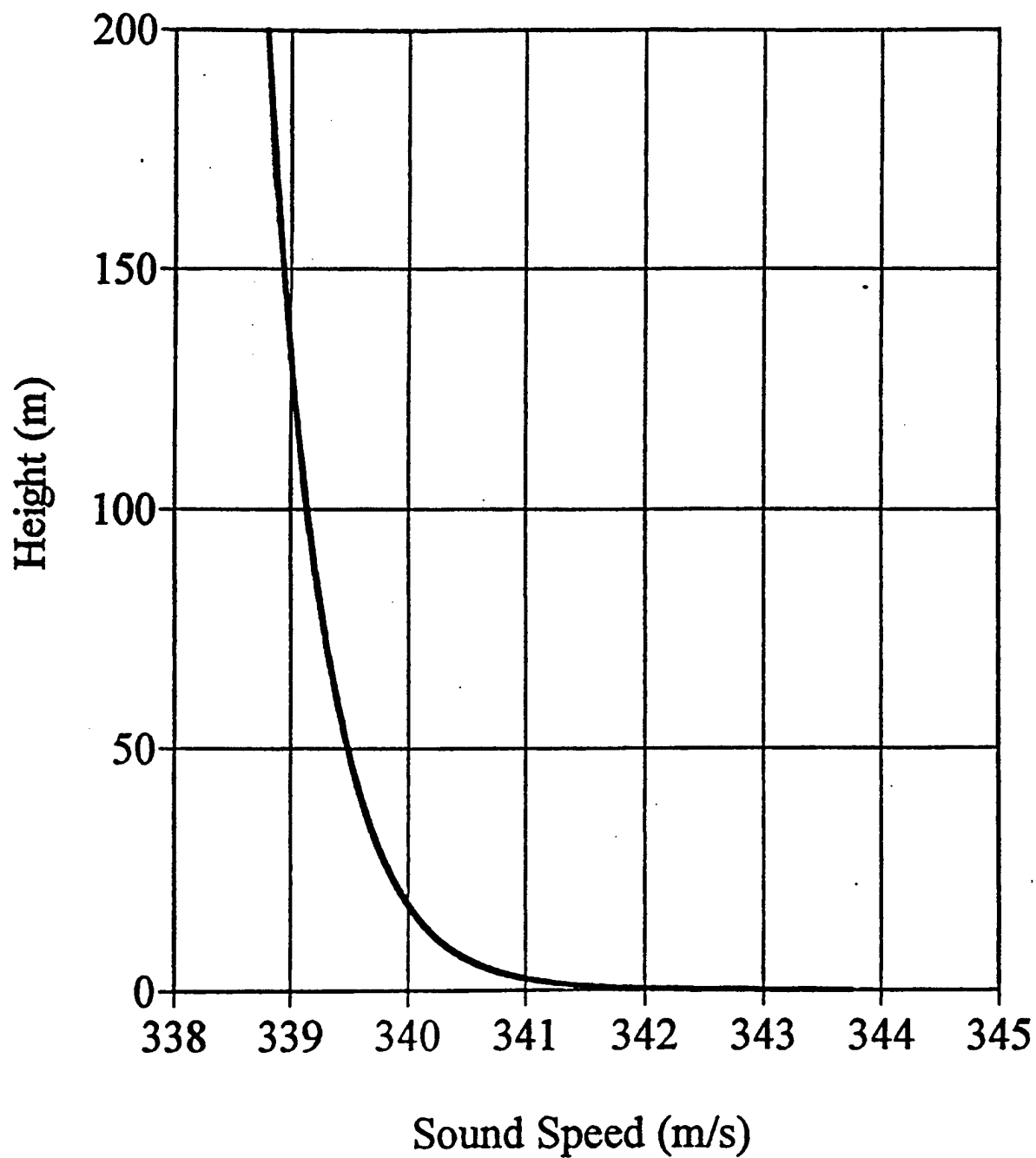
THREE-DIMENSIONAL PARABOLIC EQUATION CALCULATIONS

THREE-DIMENSIONAL COMPUTATIONAL DOMAIN

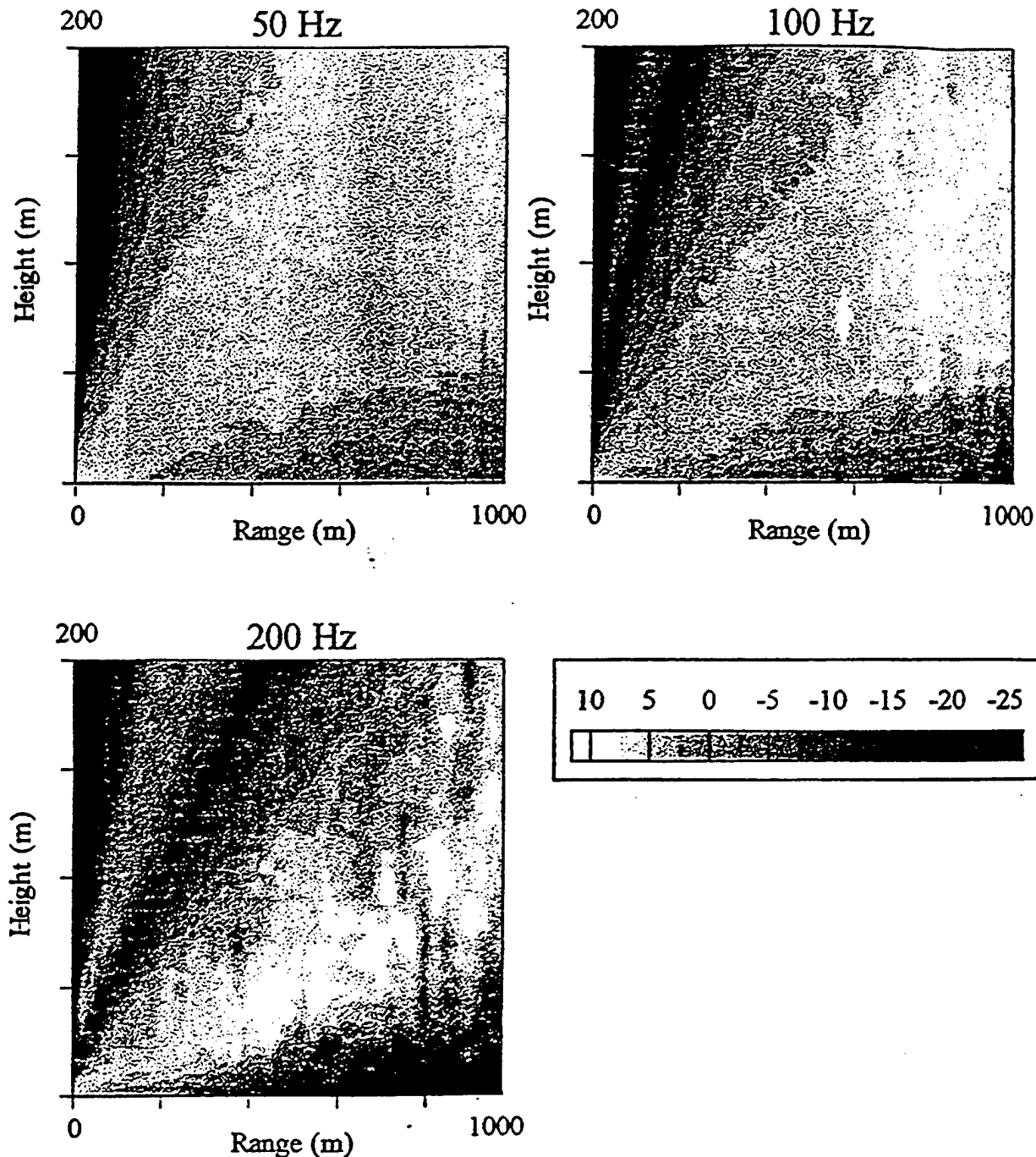


Geometry of the three-dimensional computational domain of GF-PE calculations (pie slice). The lower boundary is a finite impedance surface. The upper portion of the pie slice is an absorptive sponge. Periodic boundary conditions are enforced on the two straight sidewalls of the pie slice.

UPWARD-REFRACTING SOUND-SPEED PROFILE

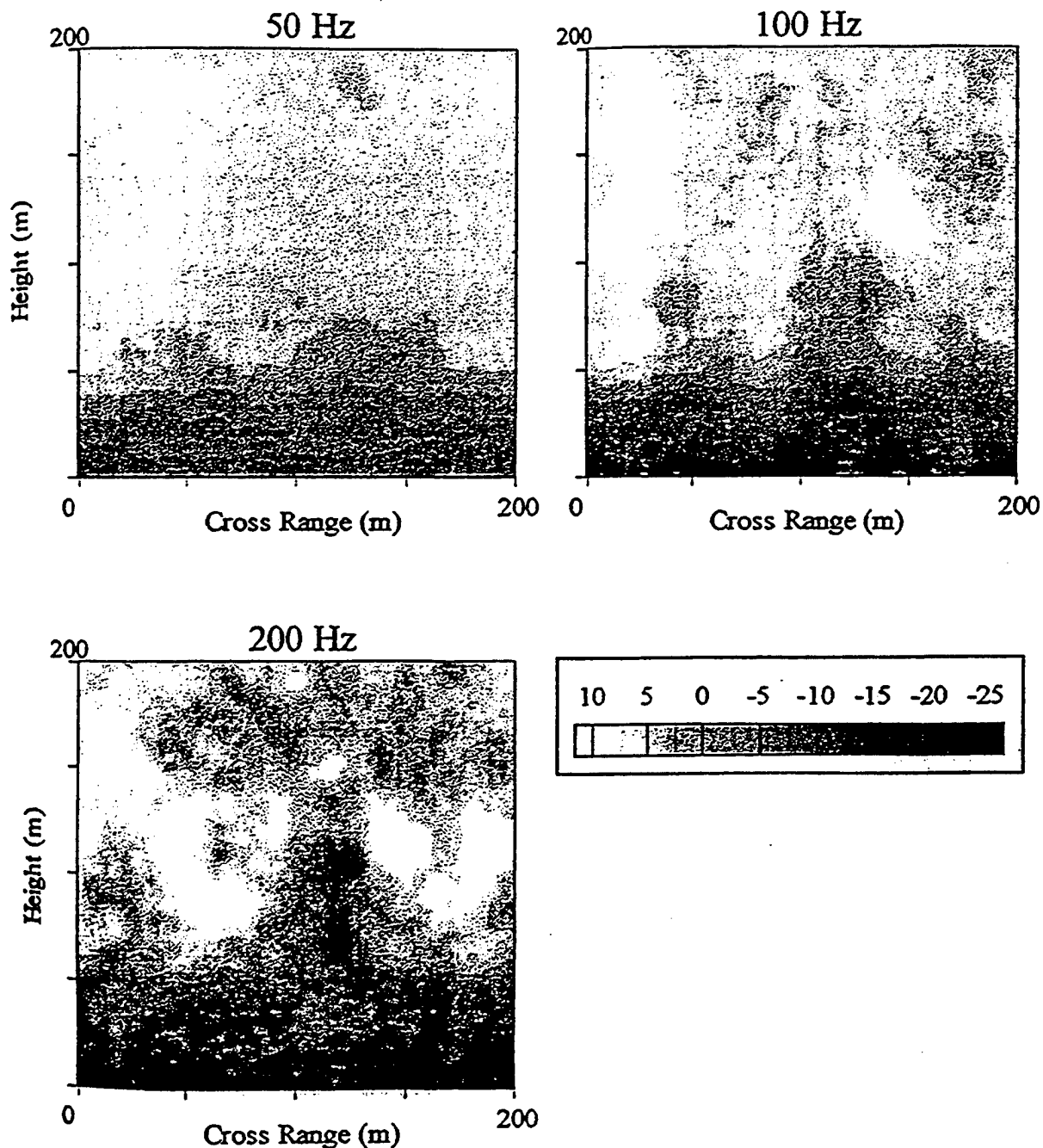


RELATIVE SOUND PRESSURE LEVEL VERSUS RANGE AND HEIGHT



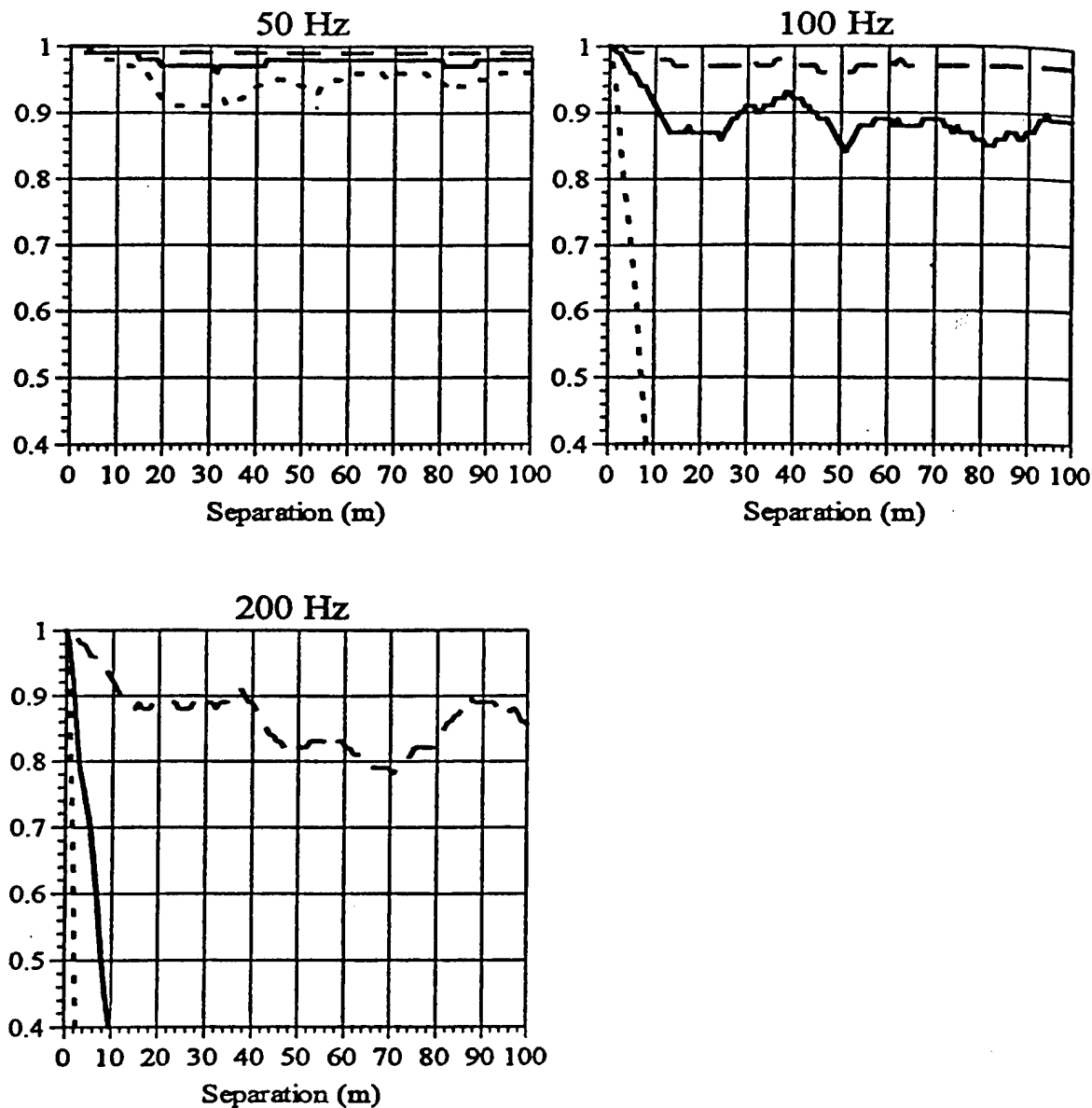
Single realization of the relative sound pressure level (dB) versus range and height at 50 Hz (top left), 100 Hz (top right), and 200 Hz (bottom left). The aspect angle is zero degrees.

RELATIVE SOUND PRESSURE LEVEL VERSUS CROSS-RANGE AND HEIGHT



A single realization of relative sound pressure level (dB) versus corss range and height for 50 Hz (top left), 100 Hz (top right), and 200 Hz (bottom left). The horizontal range is 1 km.

TWO-POINT CROSS-RANGE CORRELATION VERSUS SEPERATION DISTANCE



Two-point cross-range correlation function versus separation distance for 50 Hz (top left), 100 Hz (top right), and 200 Hz (bottom left). The short-dashed, solid, and long-dashed lines are for receivers at heights of 0 m, 25 m, and 100 m, respectively. The horizontal range is 1km.

SUMMARY

Important understandings for research in outdoor sound propagation.

- **Basics of the atmospheric boundary layer**
- **Basics of sound propagation**
- **Basics of the parabolic equation method (an important tool)**
- **Understanding of existing measurements and theoretical analyses**
- **Other?**

Thermoacoustic Devices

- Refrigerators
- Heat pumps
- Prime movers (engines)

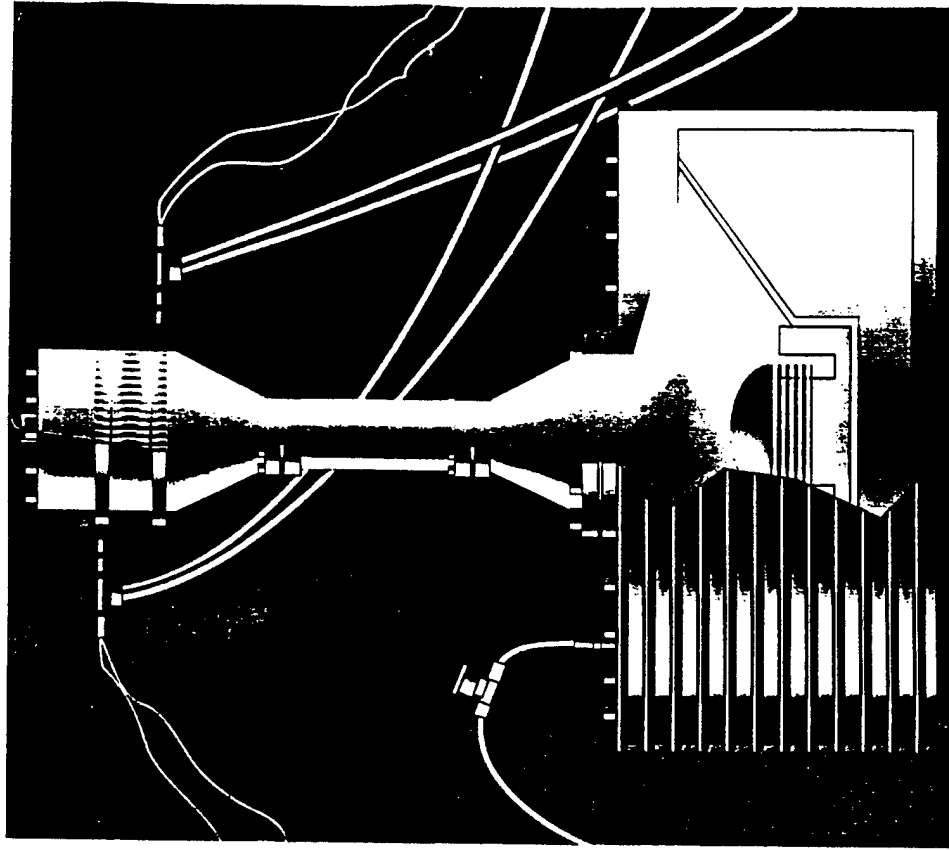
Robert Keolian
The Pennsylvania State University
Applied Research Laboratory
Graduate Program in Acoustics

- Part I: Introduction
Part II: Standing wave devices
Part III: Traveling wave devices
Part IV: Conclusion

RK-1

PHYSICS TODAY

JULY 1995



THERMOACOUSTICS

③

Why?:

- No environmentally nasty refrigerants
 - uses He, He/Ar, He/Xe, air
 - not many alternatives to vapor compression
- Can be simply constructed
 - potentially cheap
 - potentially reliable
- (low maintenance)
- Can be driven off of waste heat
 - no need for electricity
 - free cooling

RK-2

Why not?:

- So so efficiency

Some Thermodynamics

④

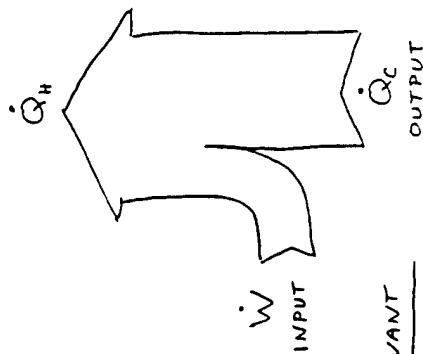
Refrigerator:

1st law: $\dot{Q}_H = \dot{W} + \dot{Q}_C$

2nd law: $\frac{\dot{Q}_H}{T_H} \geq \frac{\dot{Q}_C}{T_C}$

first law efficiency (COP)

$$\eta_I = \frac{\dot{Q}_C}{\dot{W}} = \frac{\text{WHAT YOU WANT}}{\text{WHAT YOU PAY FOR}}$$



ideal Carnot efficiency (COPC)

$$(\eta_I \text{ for } \frac{\dot{Q}_H}{T_H} = \frac{\dot{Q}_C}{T_C})$$

$$\eta_C = \frac{T_C}{T_H - T_C} \quad \text{CAN BE } \gg 1$$

second law efficiency (COPR)

$$\eta_{II} \equiv \frac{\eta_I}{\eta_C} \leq 1$$

⑤

Heat pump:

1st law: $\dot{Q}_H = \dot{W} + \dot{Q}_c$

2nd law: $\frac{\dot{Q}_H}{T_H} \geq \frac{\dot{Q}_c}{T_c}$

first law efficiency (COP)

$$\eta_I = \frac{\dot{Q}_H}{\dot{W}}$$

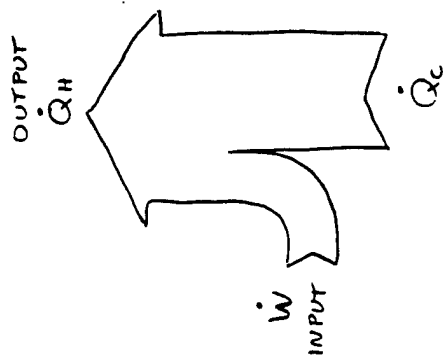
ideal Carnot efficiency (COPC)

(η_I for $\frac{\dot{Q}_H}{T_H} = \frac{\dot{Q}_c}{T_c}$)

$$\eta_c = \frac{T_H}{T_H - T_c} > 1$$

second law efficiency (COPR)

$$\eta_{II} = \frac{\eta_I}{\eta_c} \leq 1$$



⑥

Prime mover (engine):

1st law: $\dot{Q}_H = \dot{W} + \dot{Q}_c$

2nd law: $\frac{\dot{Q}_c}{T_c} \geq \frac{\dot{Q}_H}{T_H}$

first law efficiency

$$\eta_I = \frac{\dot{W}}{\dot{Q}_H}$$

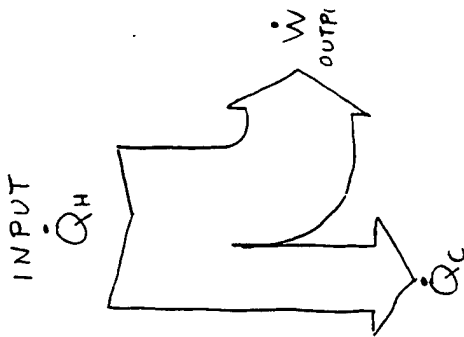
ideal Carnot efficiency

(η_I for $\frac{\dot{Q}_c}{T_c} = \frac{\dot{Q}_H}{T_H}$)

$$\eta_c = \frac{T_H - T_c}{T_H} < 1$$

second law efficiency

$$\eta_{II} = \frac{\eta_I}{\eta_c} \leq 1$$



REVIEW: SOUND WAVES

⑧

Notation: pressure = $p_m + \text{Re}[p_1(x)e^{i\omega t}]$ etc

Momentum:
$$i\omega\rho_m u_1 = -\frac{dp_1}{dx}$$

Continuity:
$$i\omega\rho_1 + \rho_m \frac{du_1}{dx} = 0$$

Equation of state:
$$\frac{p_1}{\rho_1} = \left(\frac{\partial p}{\partial \rho}\right)_s = a^2$$

Combine to get
$$p_1 + \frac{a^2}{\omega^2} \frac{d^2 p_1}{dx^2} = 0$$

Rott's more elaborate result:

$$[1 + (\gamma - 1)f_\kappa]p_1 + \frac{a^2}{\omega^2} \rho_m \frac{d}{dx} \left(\frac{1 - f_\nu}{\rho_m} \frac{dp_1}{dx} \right) - \frac{a^2}{\omega^2} \frac{f_\kappa - f_\nu}{1 - \sigma} \frac{1}{T_m} \frac{dT_m}{dx} \frac{dp_1}{dx} = 0$$

⑦

LENGTH SCALES

Along propagation direction x:

Wavelength $\lambda = a/f$

Gas displacement amplitude $|x_1| = |u_1|/\omega$

Perpendicular to x:

Thermal penetration depth $\delta_\kappa = \sqrt{2K/\omega\rho c_p}$

Viscous penetration depth $\delta_\nu = \sqrt{2\mu/\omega\rho}$

Relative sizes:

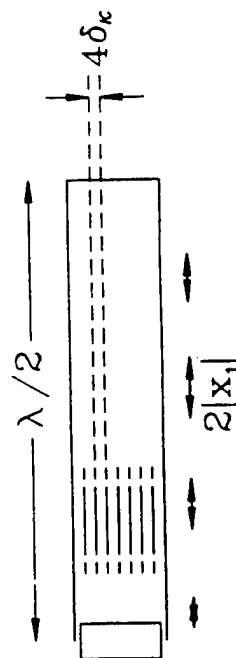
$$\frac{\delta_\nu}{\delta_\kappa} = \sqrt{\frac{\mu c_p}{K}} \lesssim 1$$

"Audio" acoustics:

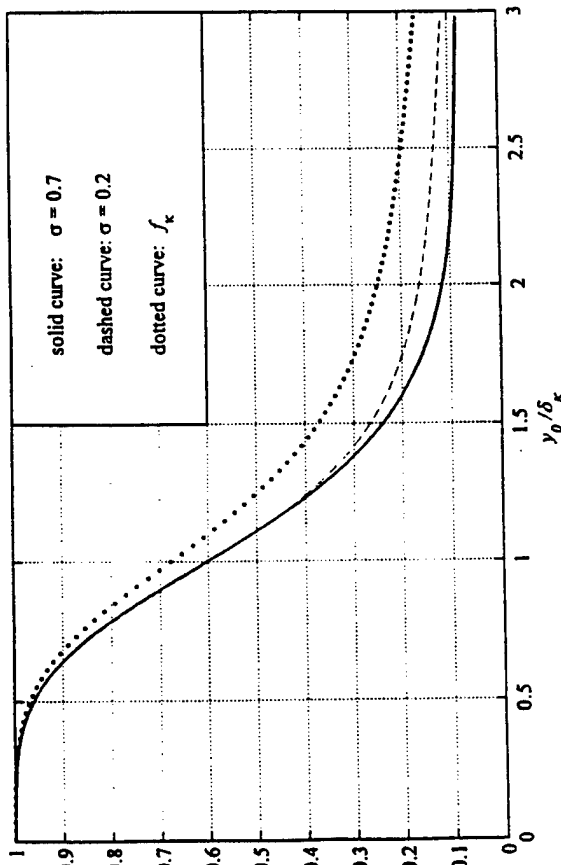
$$|x_1| \ll \delta_\kappa \ll \lambda$$

Thermoacoustic engines and refrigerators:

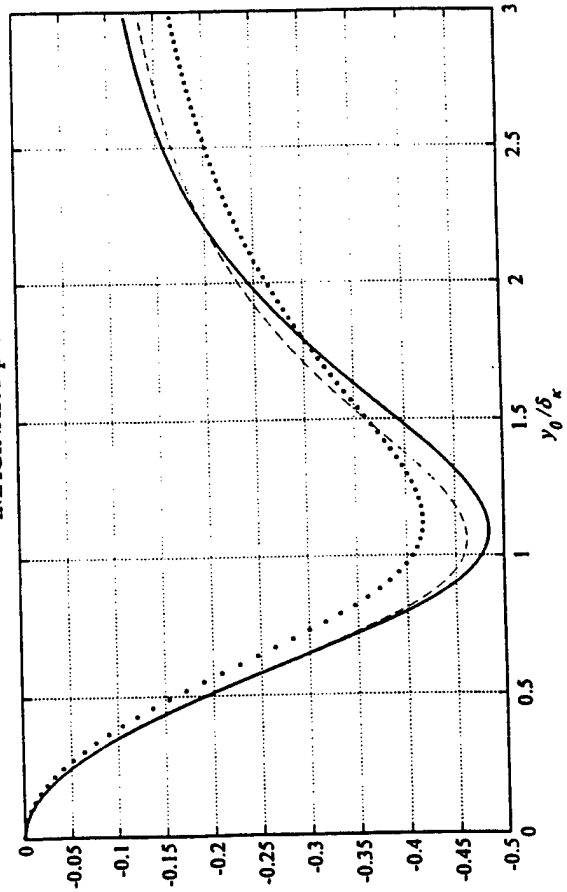
$$\delta_\kappa \ll |x_1| \ll \lambda$$



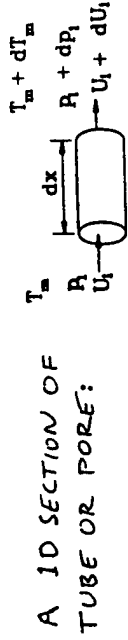
REAL part of $(f_\kappa - f_\nu) / [(1 - f_\nu)(1 - \sigma)]$ for Parallel Plates



IMAGINARY part



UNIFIED THERMODYNAMIC THEORY SUMMARY



MOMENTUM EQUATION:

$$dp_1 = -\frac{i\omega\rho_m dx/A}{1-f_\nu} U_1,$$

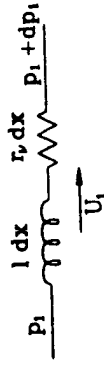
OR

$$dp_1 = -(i\omega l dx + r_\nu dx) U_1,$$

WHERE

$$l = \frac{\rho_m}{A} \frac{1 - \text{Re}[f_\nu]}{|1 - f_\nu|^2},$$

$$r_\nu = \frac{\omega\rho_m}{A} \frac{\text{Im}[-f_\nu]}{|1 - f_\nu|^2}.$$



CONTINUITY + HEAT TRANSFER EQUATIONS:

$$dU_1 = -\frac{i\omega A dx}{\gamma p_m} [1 + (\gamma - 1)f_\kappa] p_1 + \frac{(f_\kappa - f_\nu)}{(1 - f_\nu)(1 - \sigma)} \frac{dT_m}{T_m} U_1$$

OR

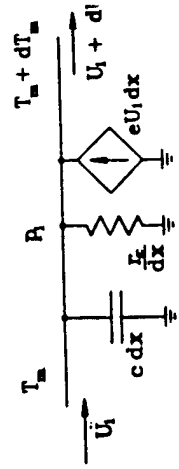
$$dU_1 = -\left(i\omega c dx + \frac{1}{r_\kappa} dx\right) p_1 + c dx U_1,$$

WHERE:

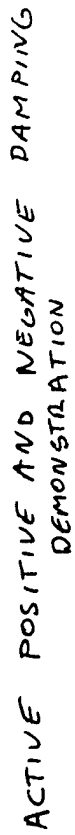
$$c = \frac{A}{\gamma p_m} (1 + [\gamma - 1] \text{Re}[f_\kappa])$$

$$\frac{1}{r_\kappa} = \frac{\gamma - 1}{\gamma} \frac{\omega A}{p_m} \frac{\text{Im}[-f_\kappa]}{dx}.$$

$$e = \frac{(f_\kappa - f_\nu)}{(1 - f_\nu)(1 - \sigma)} \frac{1}{T_m} \frac{dT_m}{dx}$$

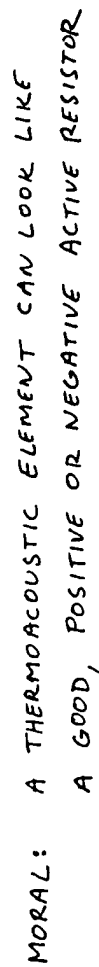


80



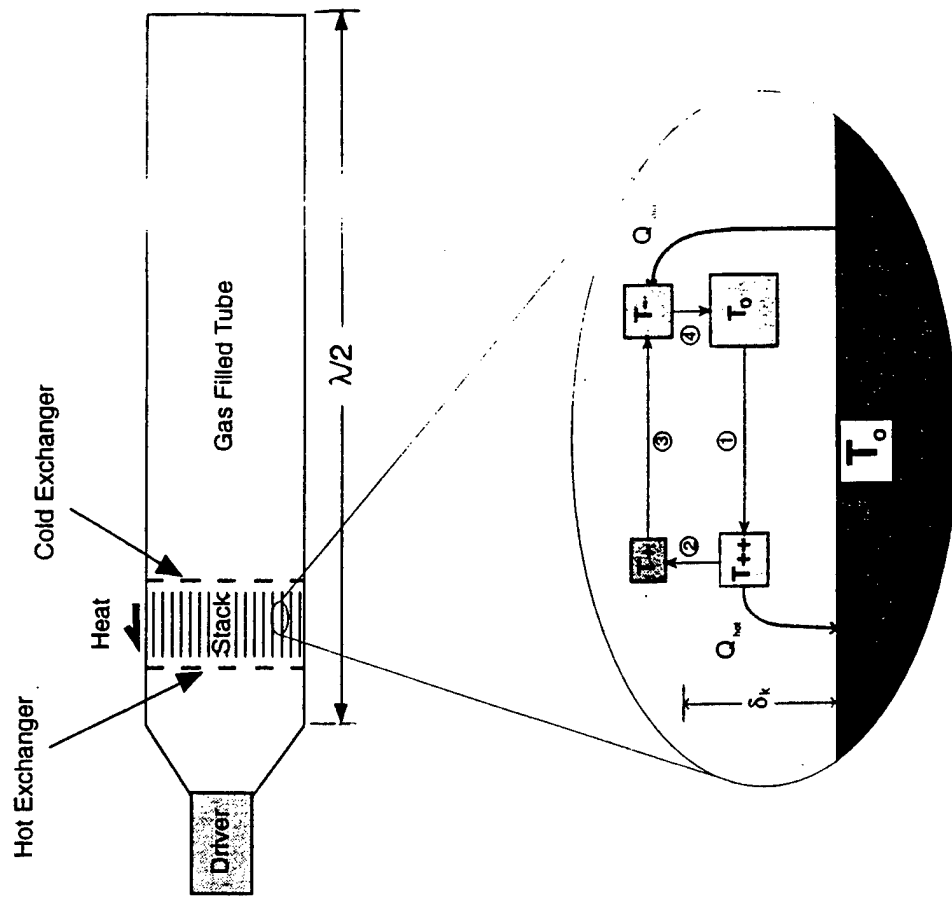
89

RK-6



JASA 99(2), 1260-1261, FEB. 1996

ThermoAcoustic Refrigeration



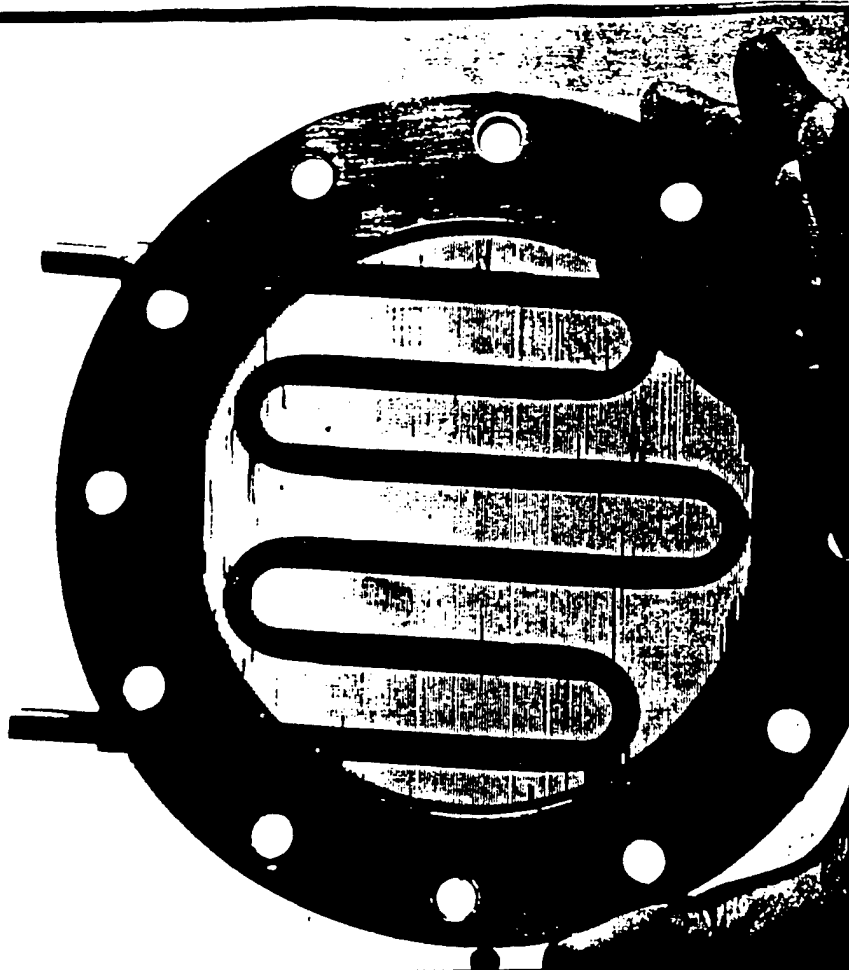
Part II

Intrinsically Irreversible

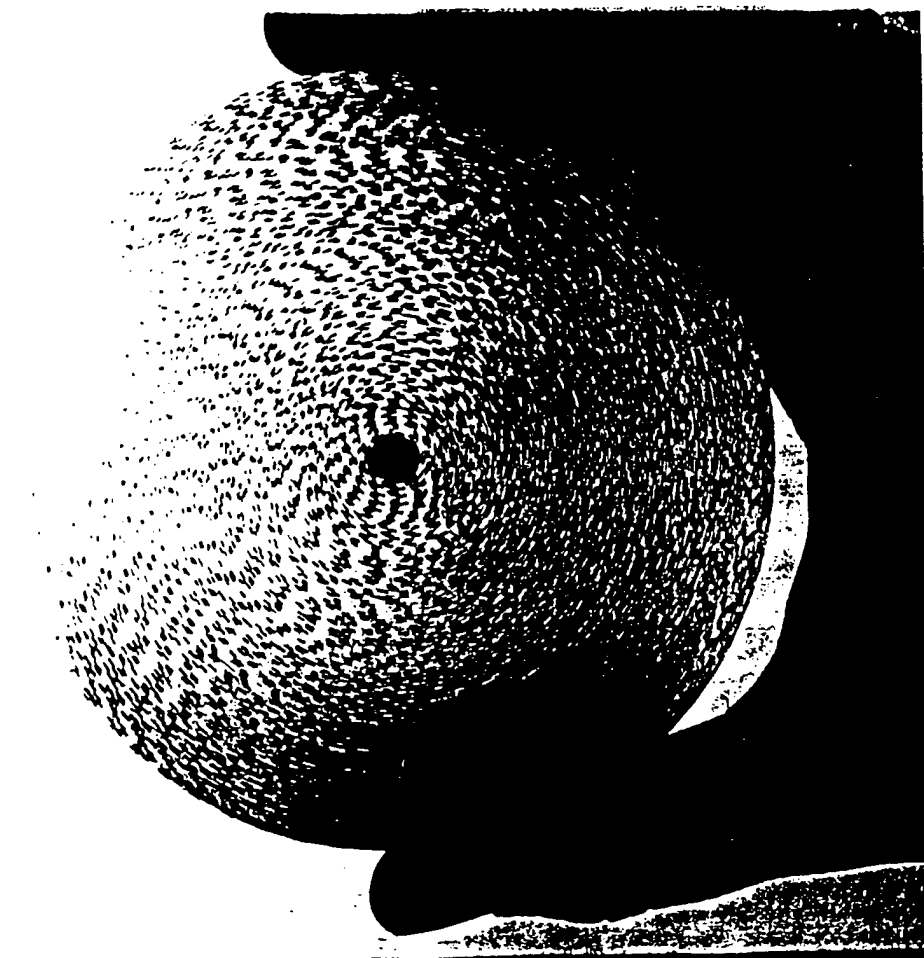
Standing Wave

Thermoacoustic Devices

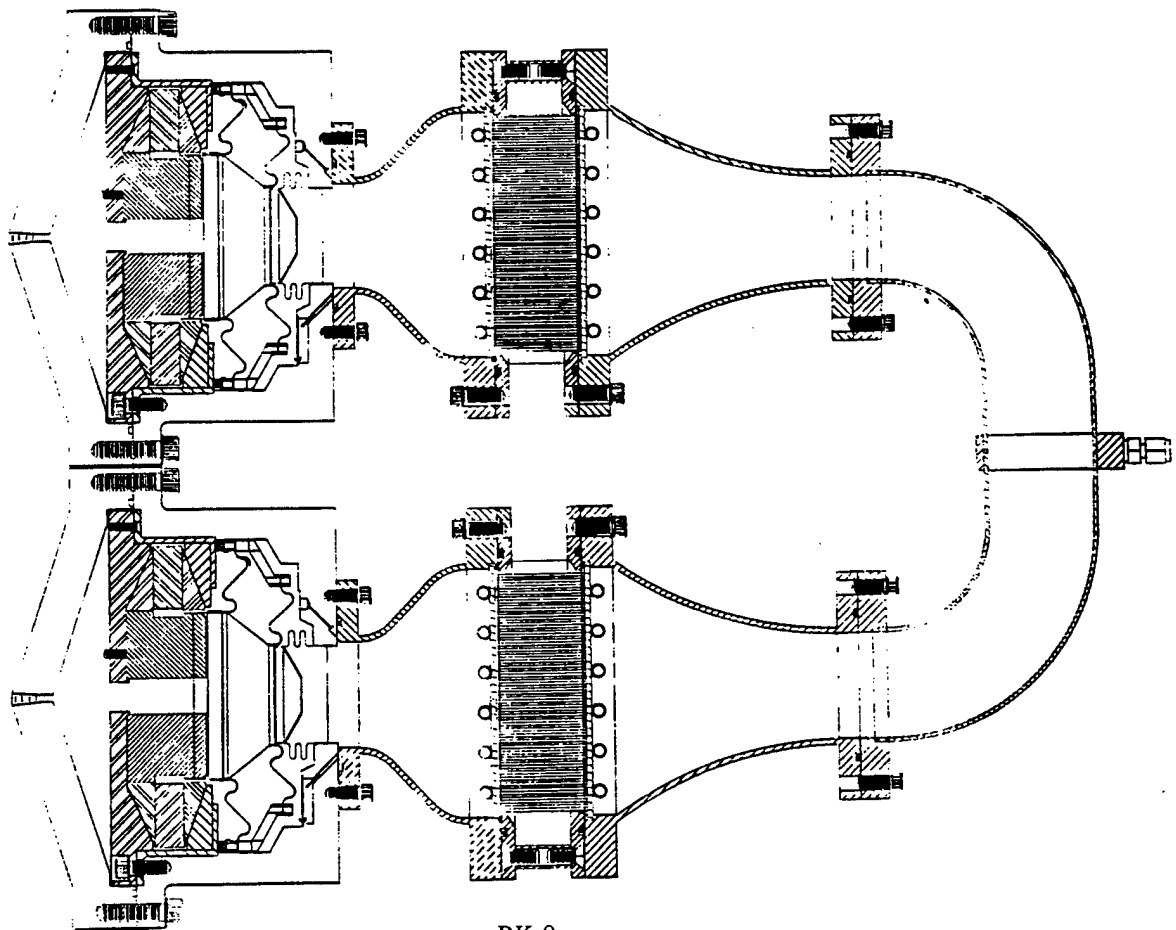
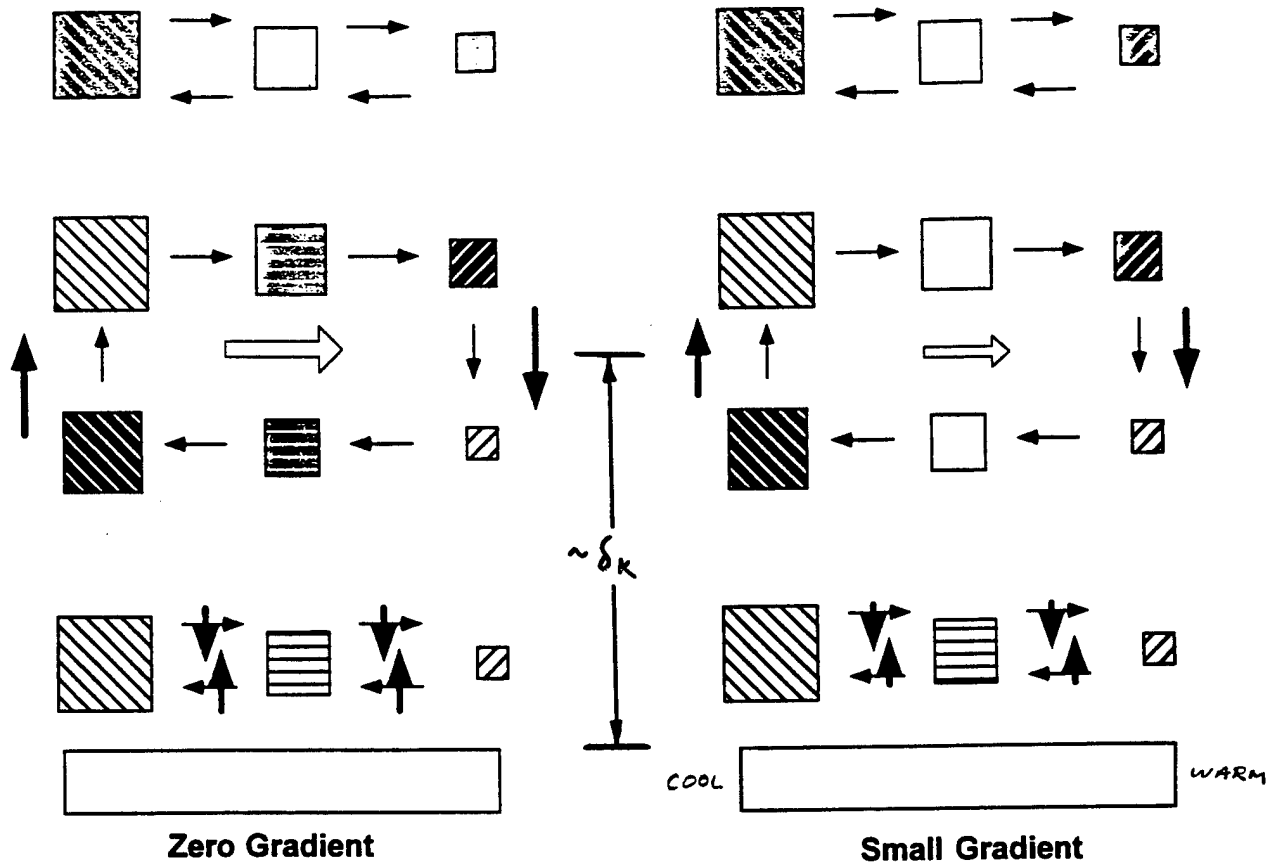
(12)



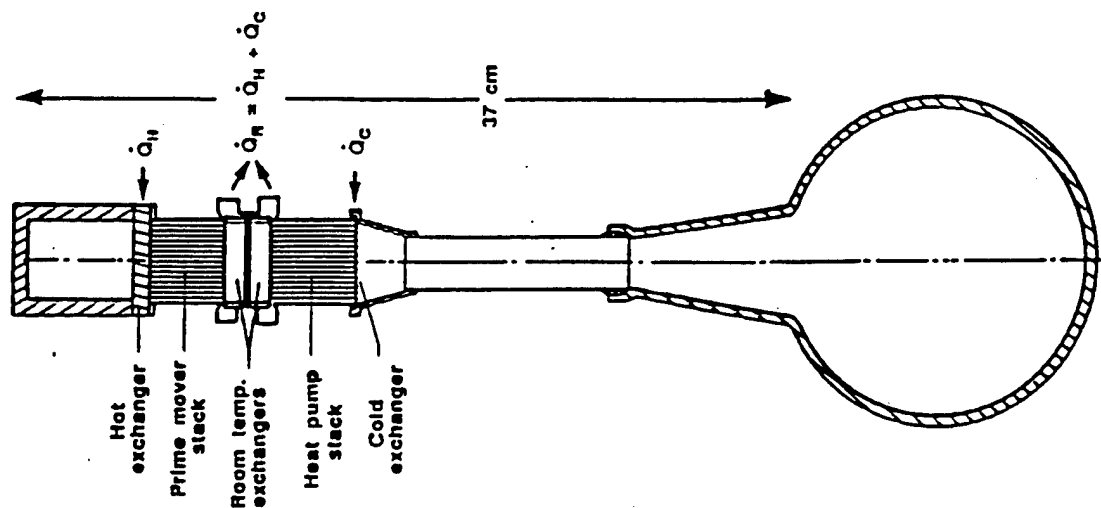
(11)



Standing Wave

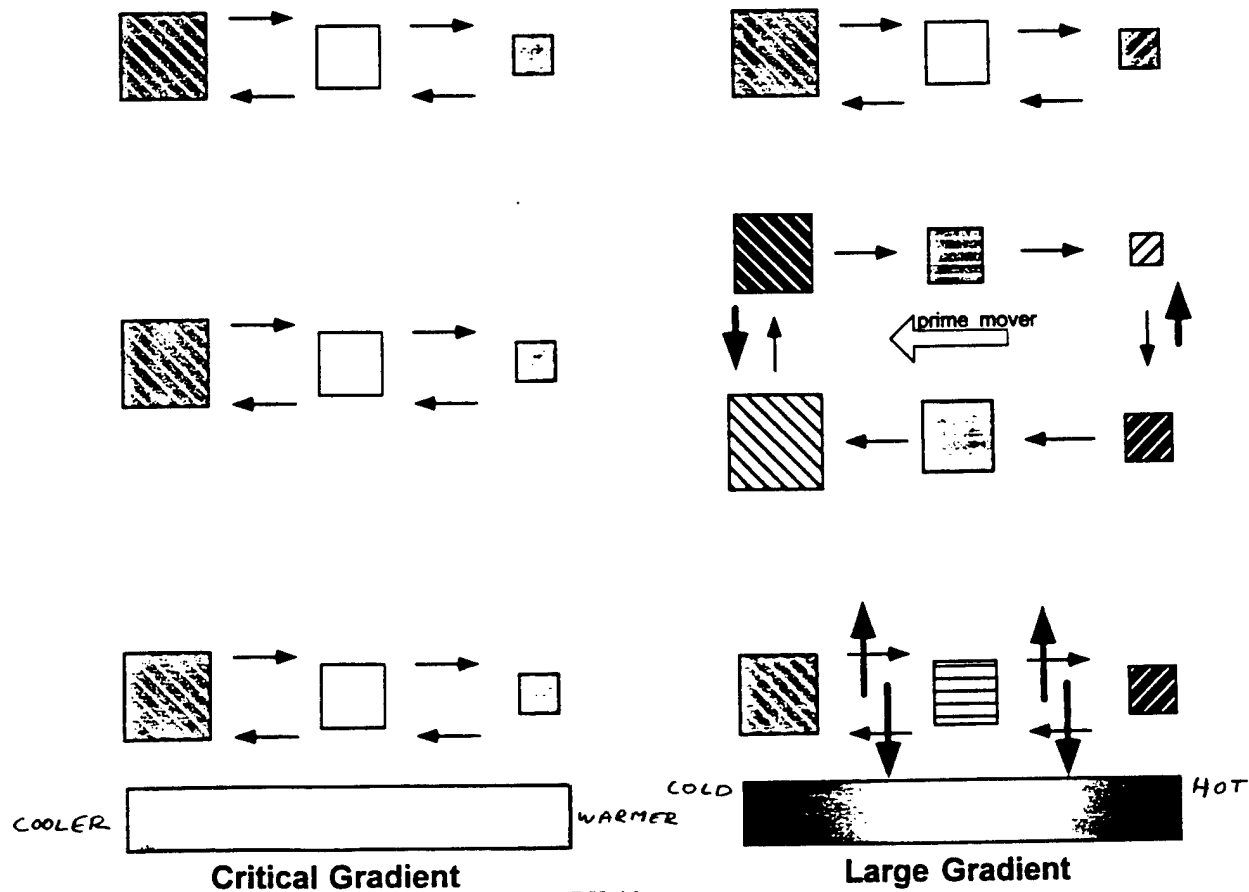


(16)

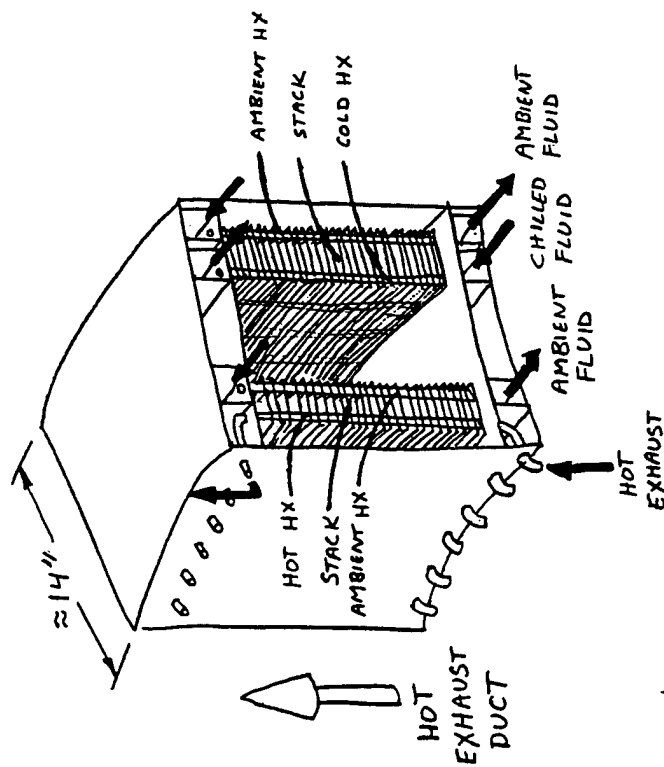


(15)

Standing Wave



(17)

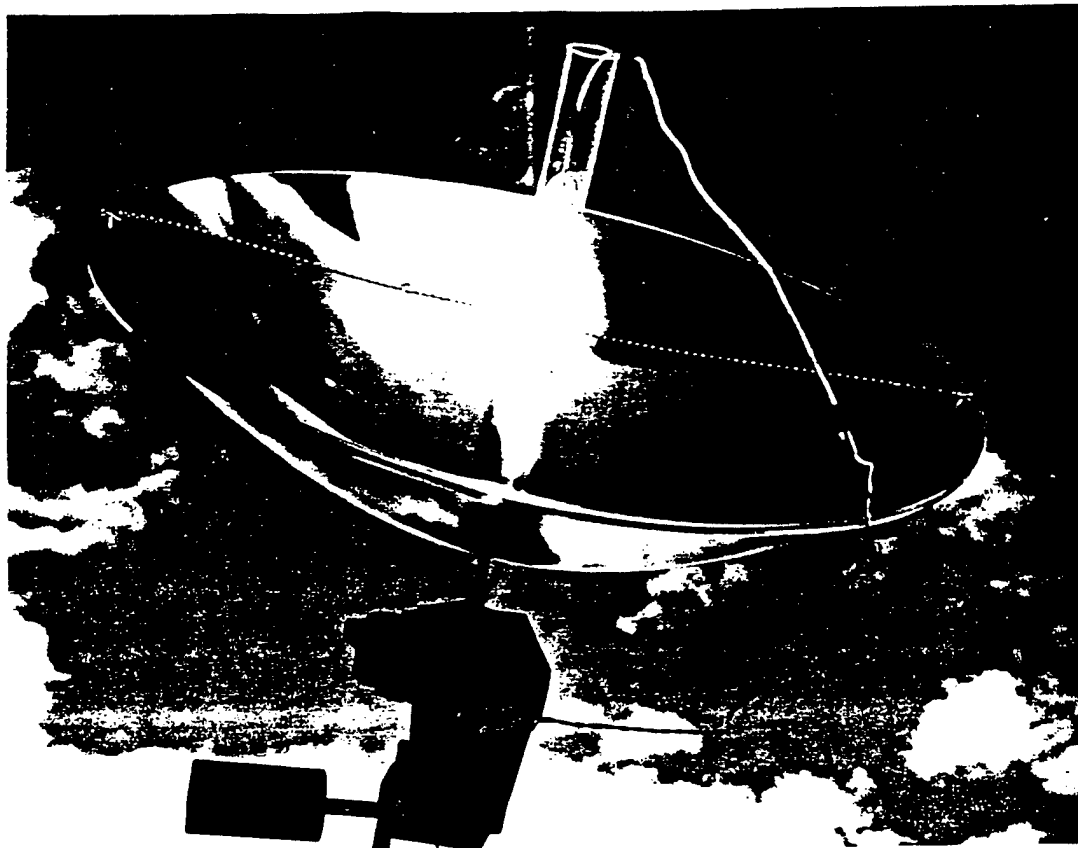


$$\text{Power} = A p_m a \left(\frac{p_1}{p_m} \right)^2 \frac{1}{30 \pm A \text{ or}}$$

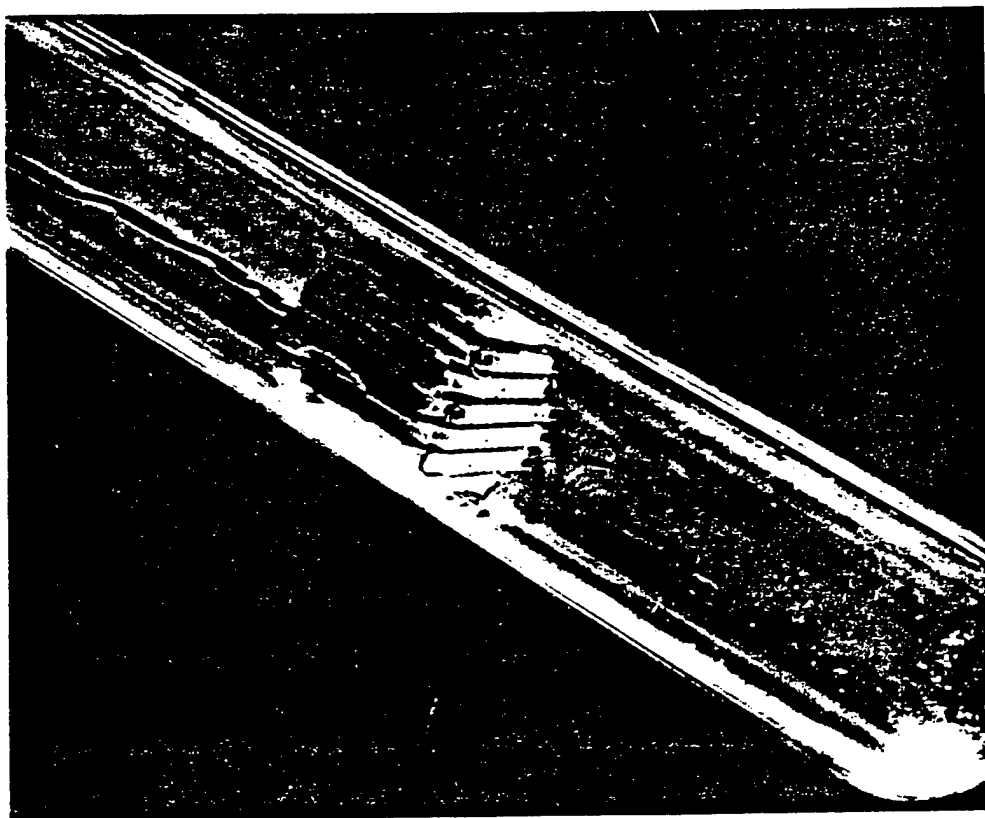
$$\text{Length} \propto \frac{1}{f}$$

(18)

(20)



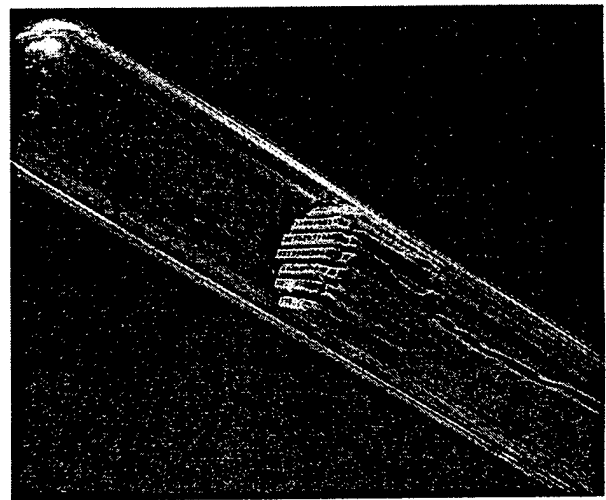
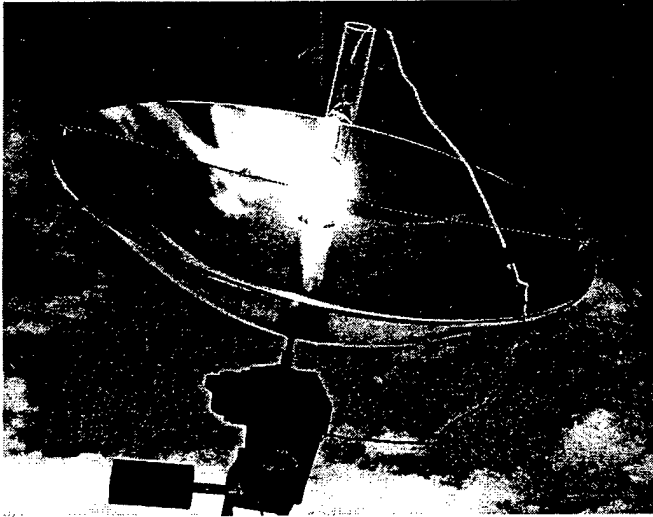
(19)



Building a Quick Thermoacoustic Engine Demo

Reh-Lin Chen and Steven L. Garrett

Graduate Program in Acoustics and Applied Research Laboratory,
Penn State University, P.O. Box 30, State College, PA 16804



Thermoacoustic devices convert thermal energy to acoustic energy (engine) and *vice versa* (refrigerator). Since the invention of the Hofler Tube, used by Tom Hofler as a demonstration for his thesis committee, thermoacoustic engine demonstrations have been useful for introducing thermoacoustic phenomena and motivating further detailed research in this area. Construction of the Hofler tube is complicated [J. A. Adeff, "The Hofler Tube from Hell," Appendix C, Master of Science Thesis, Naval Postgraduate School, Monterey, CA; Sept. 1990, DTIC Report No. AD A 241 320] and requires liquid nitrogen for operation. A similarly impressive thermoacoustic prime mover demonstration constructed by Greg Swift required flowing water to maintain cold-side temperature and a propane torch for operation. We present here a simple, but equally loud, demonstration device, based on our earlier solar-powered design (see suggested reading), that can be constructed from a PyrexTM test tube, commercially available CelcorTM porous ceramic material and Ni-Cr heater wire. No cold-side heat exchanger is required!

As shown in the picture at the right, the one-inch thick CelcorTM material is cut and sanded into a cylindrical shape that can slide easily inside the test tube. Grooves of about 3 mm in

depth are cut in one end of the ceramic using a hacksaw blade to facilitate the serpentine winding of the 26 gauge Ni-Cr heater wire. The heater wire is joined by twisting on to stiff copper (magnet) wires to provide the electrical current and facilitate positioning of the ceramic "stack" within the test tube. Solar heating, as shown with the parabolic dish reflector in the left photo, is also possible.

The test tube acts as a quarter-wave (closed-open) resonator. The heater element has an electrical resistance of about $2\ \Omega$ and will generate loud sound at about 440 Hz for several minutes with 6 Volts applied with a lantern battery, filament transformer or VariacTM. Once all parts are procured, the device can be operational with only one hour of fabrication time.

Parts List

- 8" PyrexTM glass test tube, 1.0" O.D.
- CorningTM catalytic converter, 400 cell/in²; Corning Incorporated, HP-CB-03-1, Corning, New York 14831; Tel: (607) 974-7462.
- OmegaTM gauge 26 Ni-Cr wire heater, \$10.00 (50 ft.); 2.7 Ohm/ft.
- Power source options :

Filament transformer (Digi-Key HM508-ND, \$17.04), Energizer 6V lantern battery, No. 529 (Walmart, \$6.95), 18-in parabolic dish (Edmund Scientific H80254, \$41.95), or large magnifier, Fresnel lens, etc?

Cautions

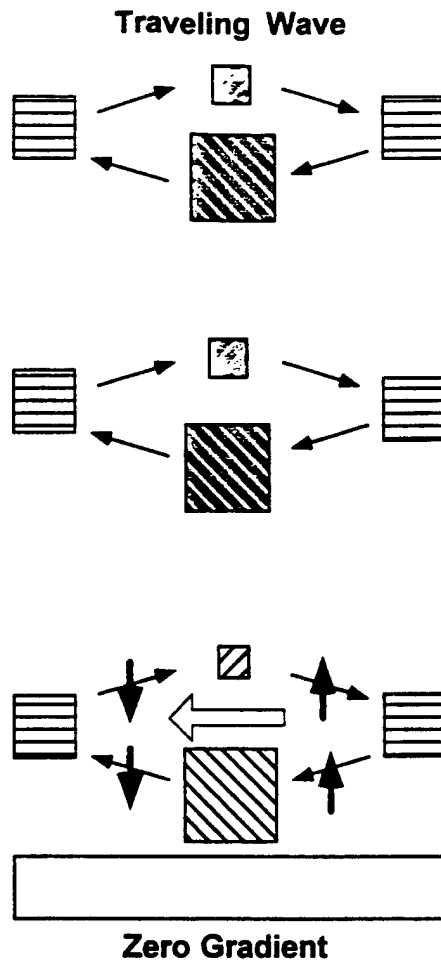
- The glass tube near the heater will be hot when powered.
- The stack will be too bright to stare at when using a parabolic dish concentrator.
- Do not try closing test tube end to drive the $\frac{\lambda}{2}$ mode. The heat causes the air to expand and could possibly explode the glass.

Suggested readings

- R.L. Chen and S.L. Garrett, "Solar/Heat Driven Thermoacoustic Engine", Proceedings of 135th Seattle ASA meeting, Vol. II pp. 813-814 (1998).
- G.W. Swift, "Thermoacoustic Engines and Refrigerators", Physics Today pp.22-28, July (1995).
- The Penn State Thermoacoustics Website :
<http://www.acs.psu.edu/thermoacoustics.html/>; Email: rxc132@psu.edu (Reh-Lin Chen)

Work supported by the Office of Naval Research

22



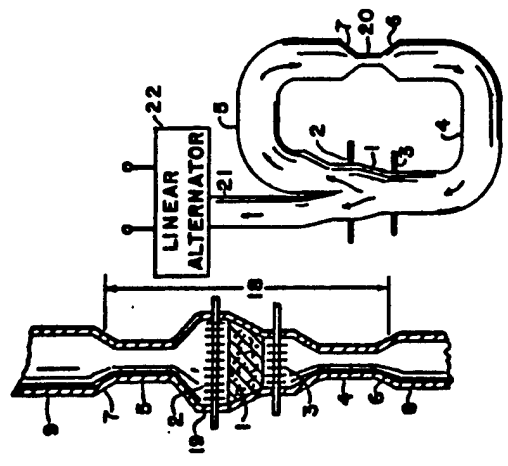
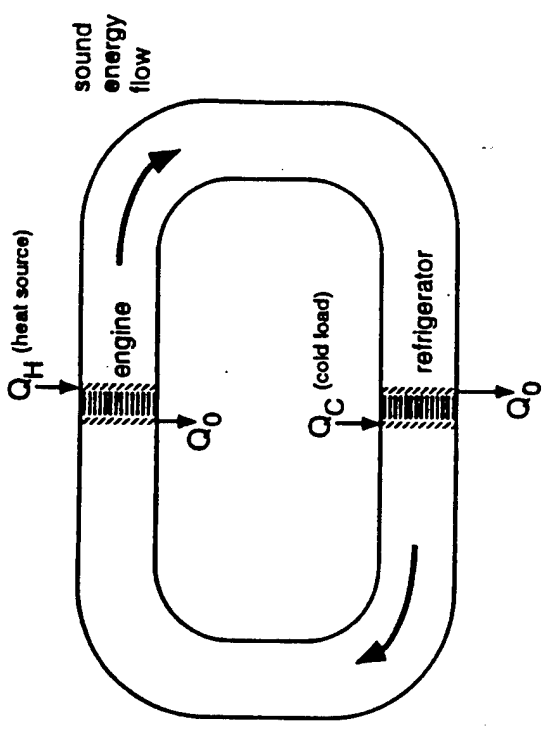
27

Part III

Thermoacoustic Stirling (Traveling Wave Like)

Devices

Traveling wave heat-driven refrigerator (Ceperley, 1975)



Los Alamos Orifice Pulse Tube Refrigerators

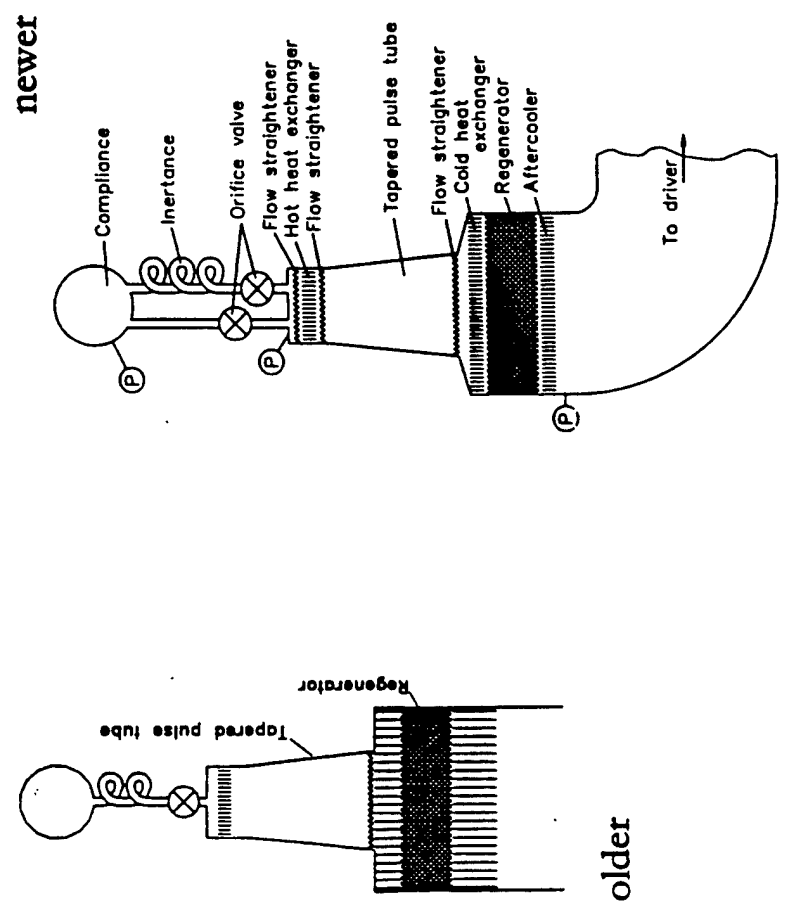


Figure 1.16: Schematic of the Cryenco orifice pulse-tube refrigerator. "p" indicates the location of a pressure sensor. The heat exchanger labeled "hot" and the aftercooler are held at ambient temperature by flowing water.

(27)

(28)

What's essential in Backhaus-Swift TA Stirling?

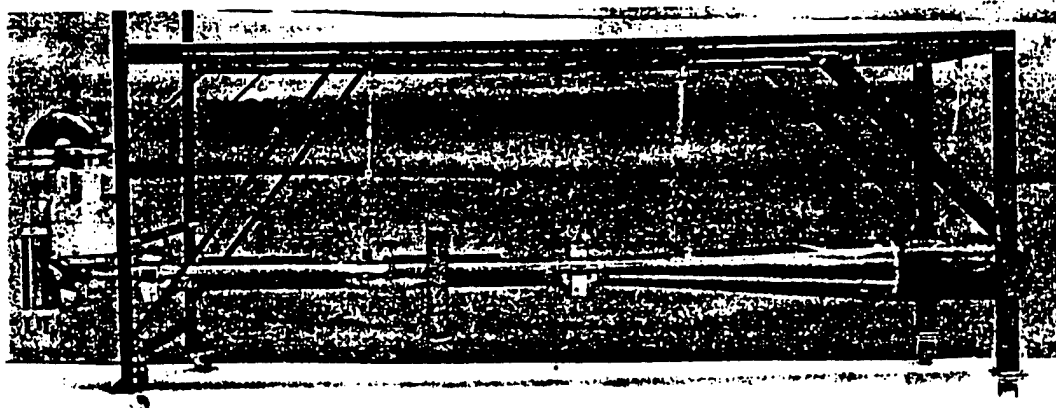
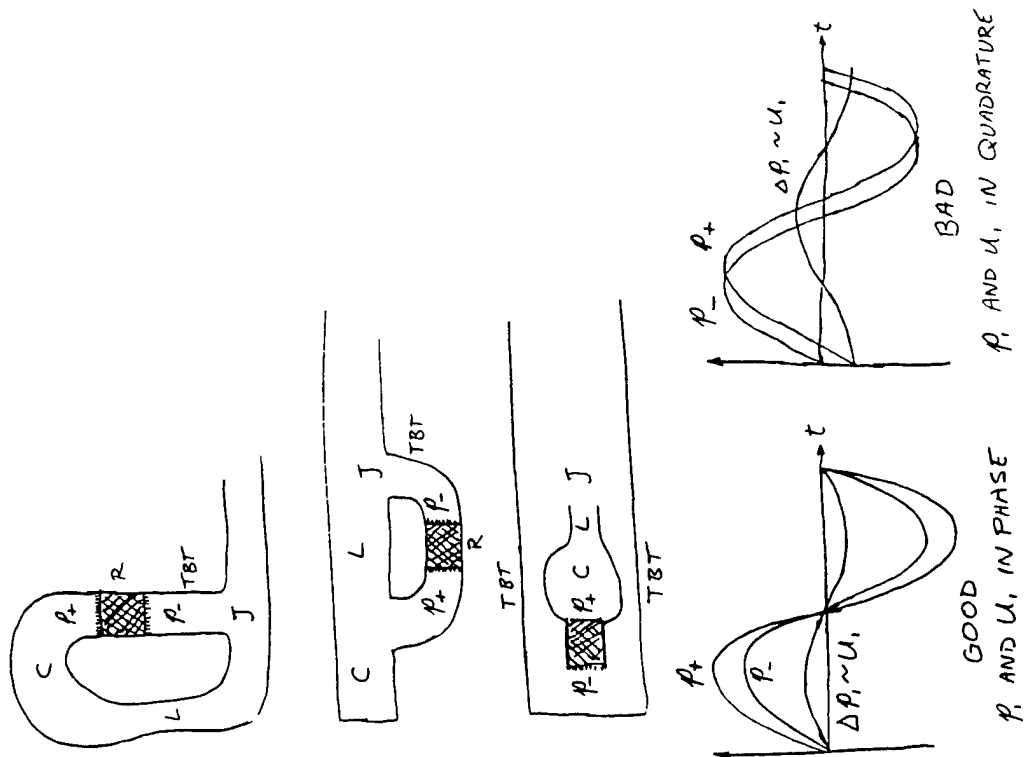
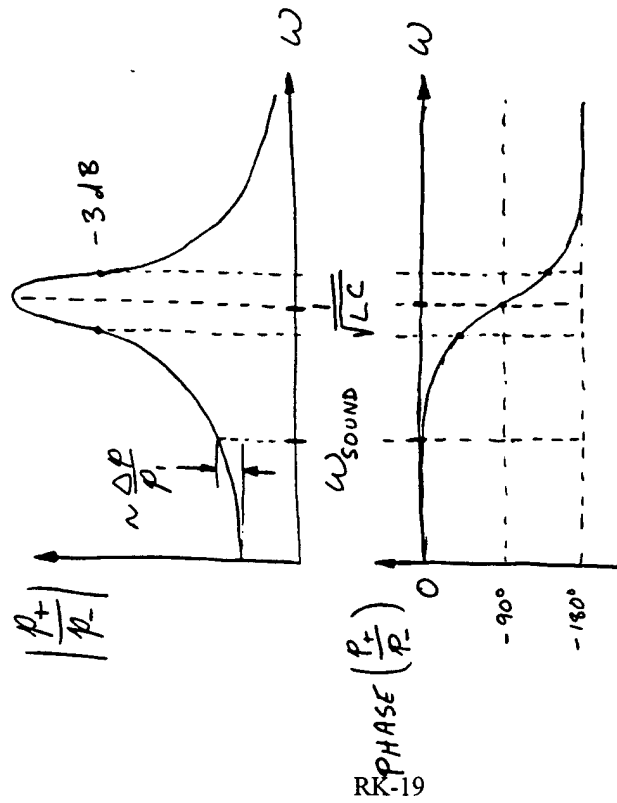


Figure 1.13: Traveling-wave engine example: A research apparatus for initial Los Alamos studies of the performance of a thermoacoustic-Stirling heat engine



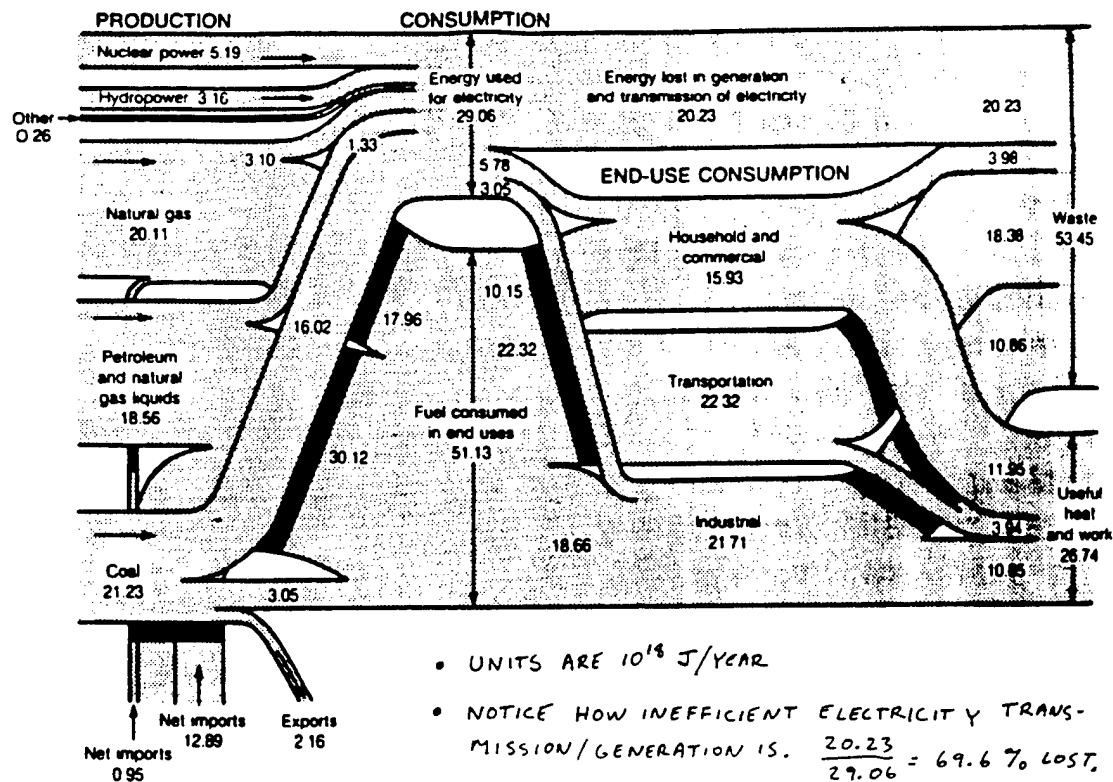


Part IV

Conclusion

$p_+ > p_-$ WITHOUT MUCH PHASE SHIFT

U.S. Annual Energy Usage



• UNITS ARE 10^{18} J/YEAR

• NOTICE HOW INEFFICIENT ELECTRICITY TRANSMISSION/GENERATION IS. $\frac{20.23}{29.06} = 69.6\%$ LOST,

THIS MAKES HEAT DRIVEN TA LOOK GOOD.

• NOTICE HOW MUCH END USE FUEL IS USED IN HOUSEHOLD AND COMMERCIAL, PRESUMABLY FOR HEATING. $\frac{15.93}{80.19} = 19.9\%$. TA HEAT PUMPS LOOK GOOD.

Calculated Performance of a Good Los Alamos Standing Wave Engine:

1000 W work to load, 5380 W heater power

First law efficiency = $1000/5380 = 18\%$

Carnot efficiency = 60%

Percent of Carnot = $18/60 = 30\%$

Why so inefficient?

47% thermal relaxation loss in stack

13% viscous loss in stack

11% visc and therm in heat exchangers

9% heat leak to room

7% viscous and thermal in resonator

5% conduction along stack case

4% conduction along stack

3% dT in heat exchangers

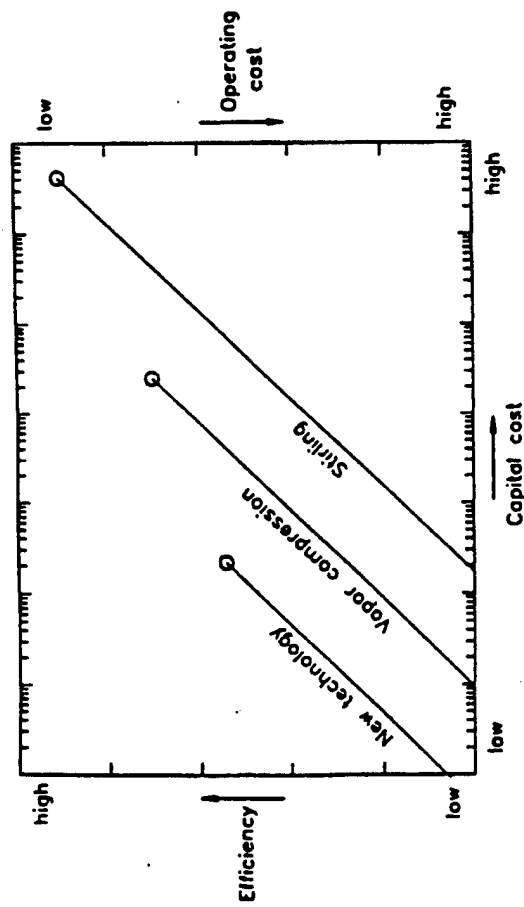
Performance of Los Alamos TA Stirling Engine:

Best efficiency = 30%

Percent of Carnot = 42%

Capital-Operating Cost Tradeoff

The highest ultimate efficiency technology is not necessarily the best at a given capital cost:



POROUS MATERIALS

**JAMES M. SABATIER
NATIONAL CENTER FOR PHYSICAL ACOUSTICS
University of Mississippi**

INTERACTION OF AIRBORNE SOUND WITH THE GROUND

Part I – Acoustic-to-Seismic Coupling

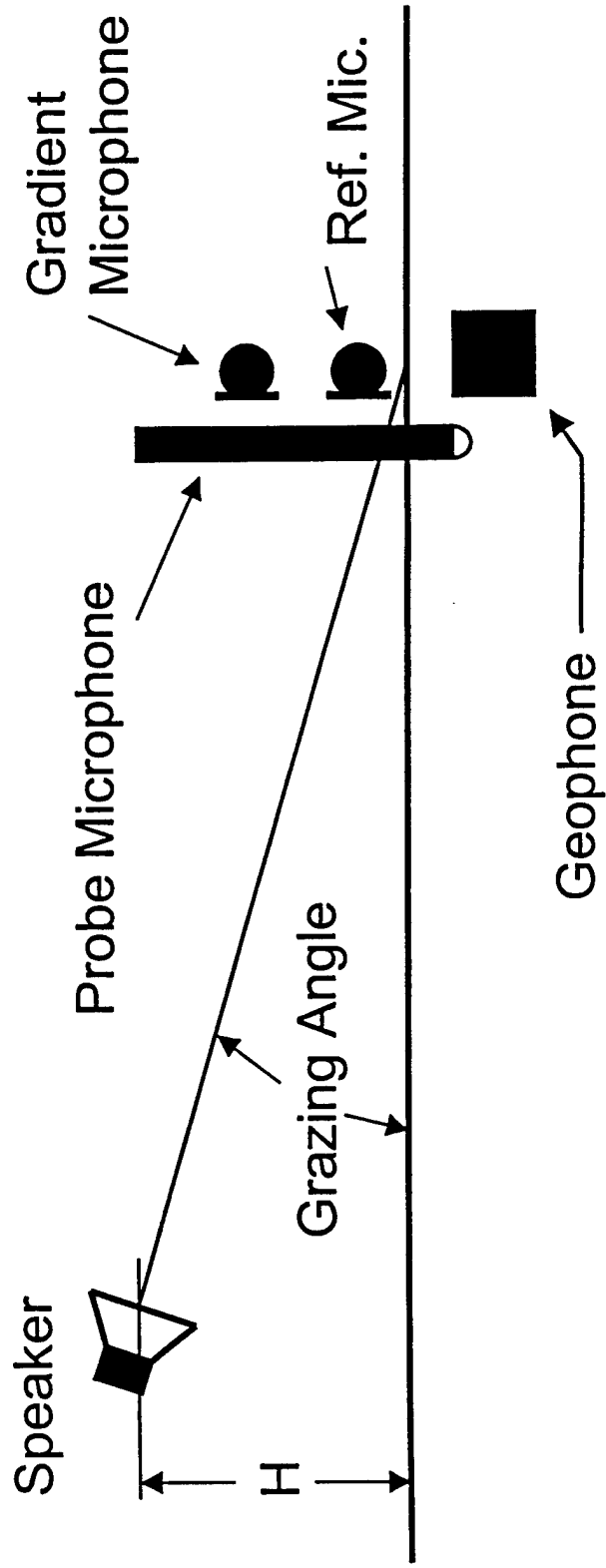
1. EARLY ACOUSTIC MEASUREMENTS ON OUTDOOR GROUNDS
2. POROUS MEDIUM PHYSICAL PROPERTIES
3. SOUND PROPAGATION IN RIGID POROUS MEDIA
4. SOUND PROPAGATION IN PORO-ELASTIC MEDIUM

Part II – Mine Detection

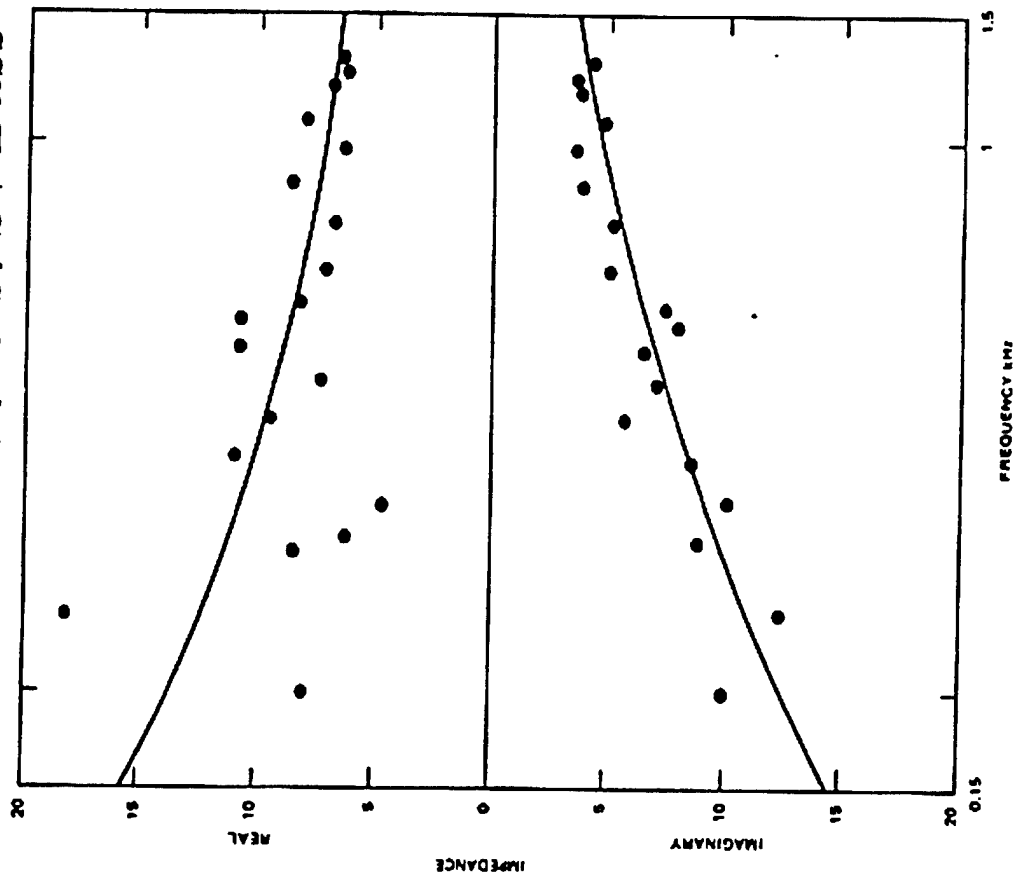
FTP Site:	sweetgum.mcsr.olemiss.edu
Username:	landmine
Password:	sabatier
Change directory:	/ptmp/landmine/

Acoustic/Seismic Coupling Measurements

- Seismic Transfer function
- Acoustic transfer function
- Surface impedance



Normalized complex surface impedance measurements (dots) by Bass



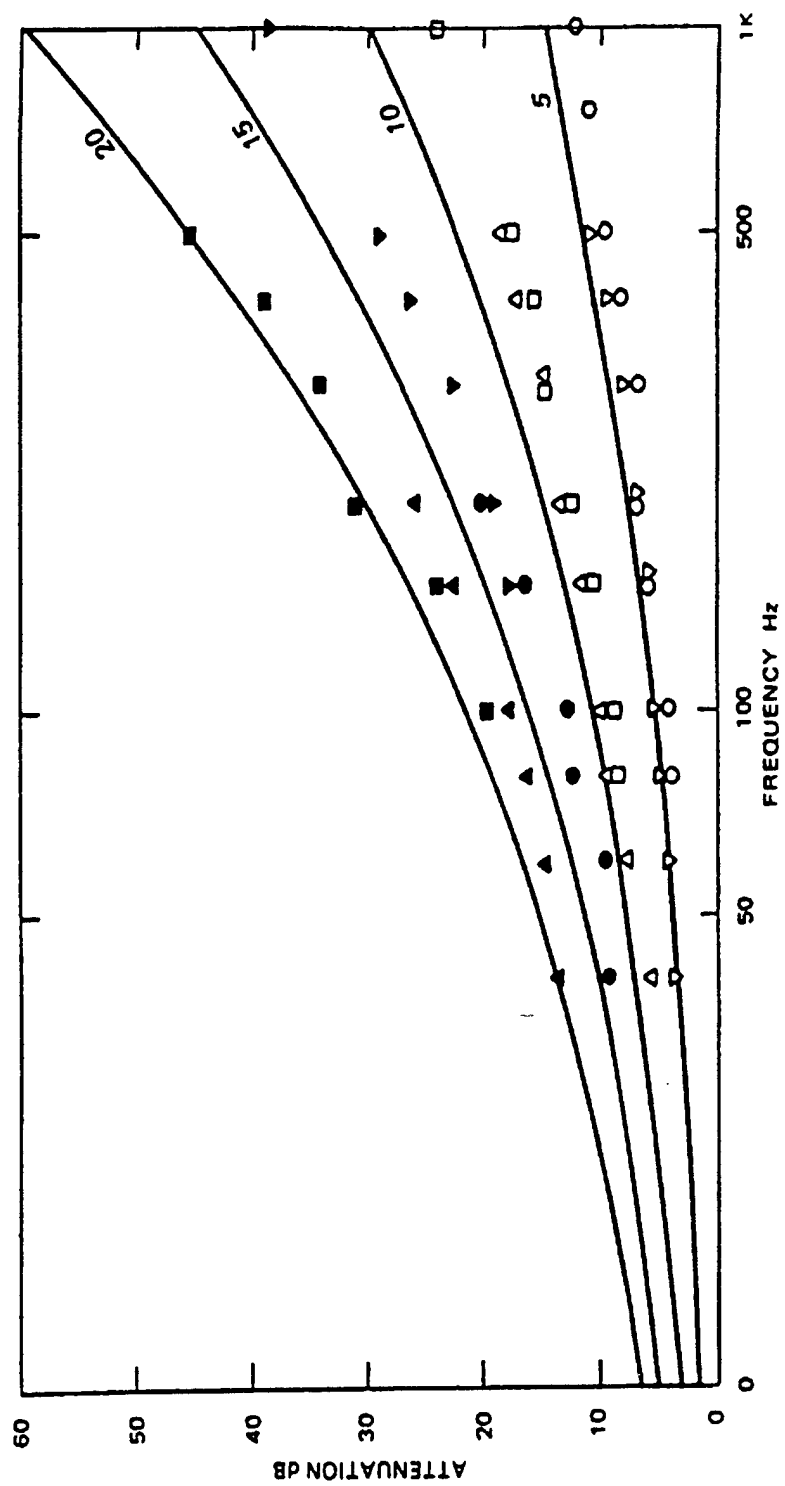


Figure B4. Attenuation versus depth in a sand quarry. Measurements were made with probe at 5 cm (●), 10 cm (○), 15 cm (△), and 20 cm (■).

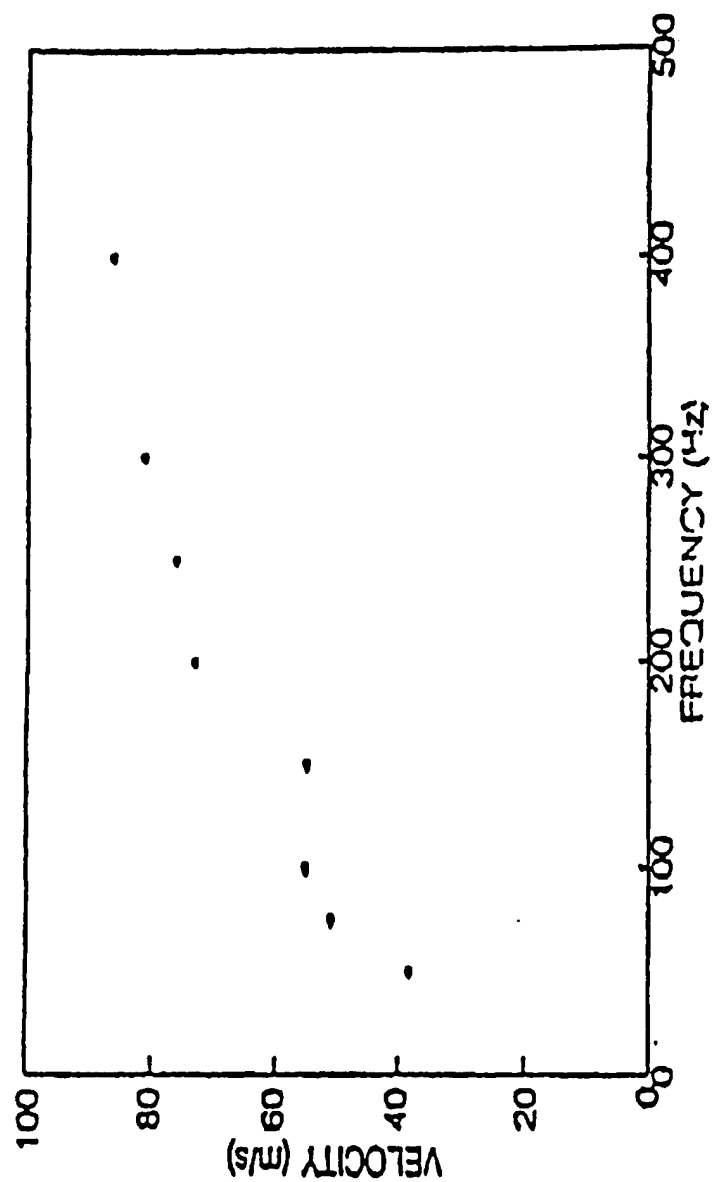


Figure 3.4. Acoustic phase velocity measured with the probe microphone in a sand with a flow resistivity of 85 rayls/cm.

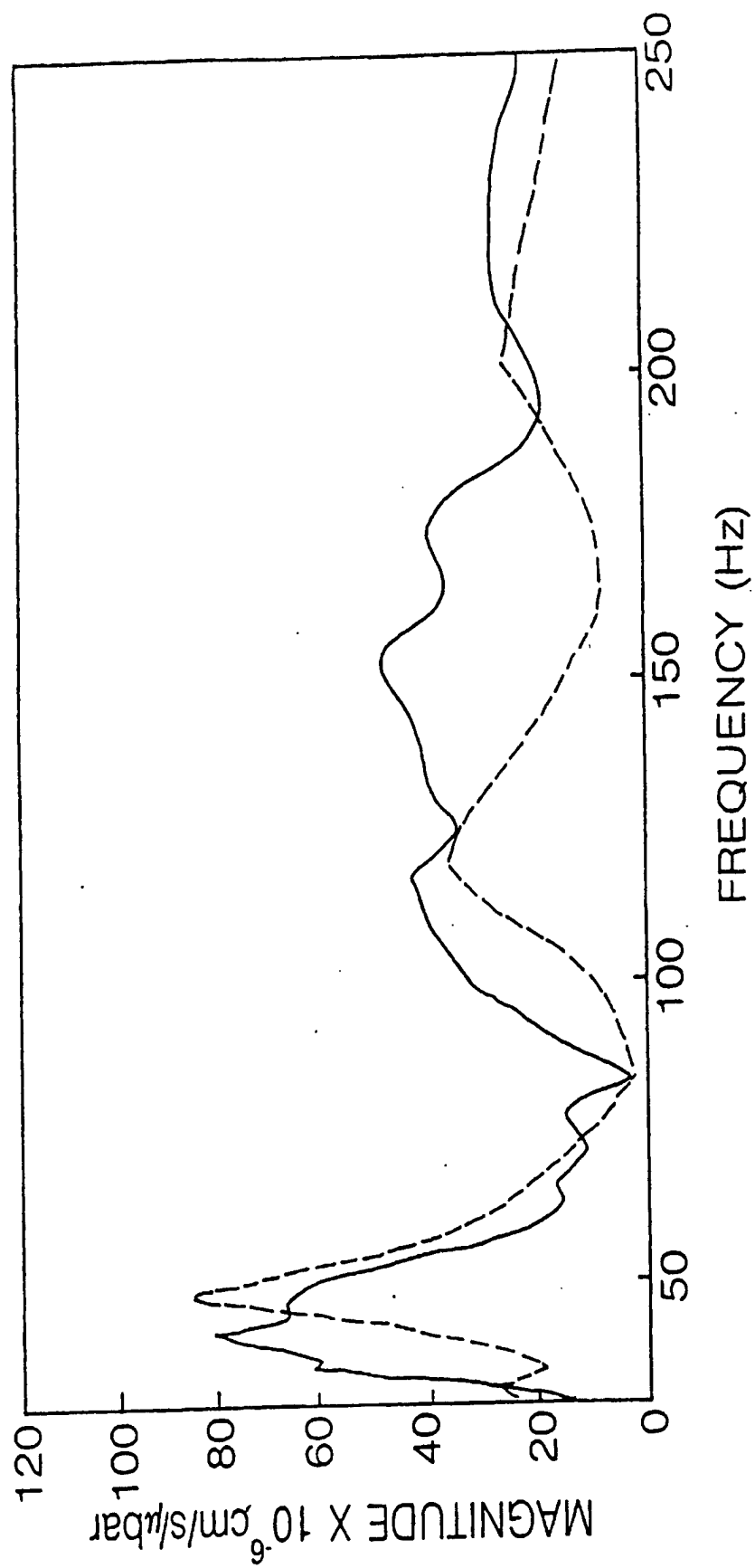


Figure C3. Measured (solid line) and predicted (dashed line) vertical seismic transfer function for Loesh.

PHYSICAL PROPERTIES OF POROUS MATERIALS

The sample material consists of a frame or matrix saturated with a fluid

$\rho_s \equiv$ density of solid component

$\rho_f \equiv$ density of saturating fluid

Porosity (Ω) \equiv $\frac{\text{volume of fluid}}{\text{volume of bulk}}$

$$\Omega = \frac{v_f}{v_b} \quad 1.$$

$$v_b = v_f + v_s \quad 2.$$

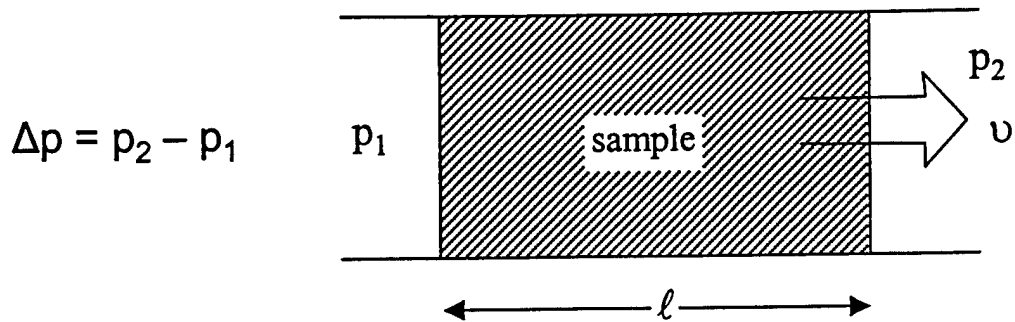
Bulk density of porous material

$$\rho_b = (1 - \Omega)\rho_s + \Omega\rho_f \quad 3.$$

There are no isolated voids

FLOW RESISTIVITY

Porous sample in a pipe of cross-sectional area A . Apply a differential pressure to cause steady flow.



Flow resistance

$$S = \frac{\Delta p}{v} \quad v \equiv \text{average flow velocity/area} \quad 4.$$

Flow resistivity

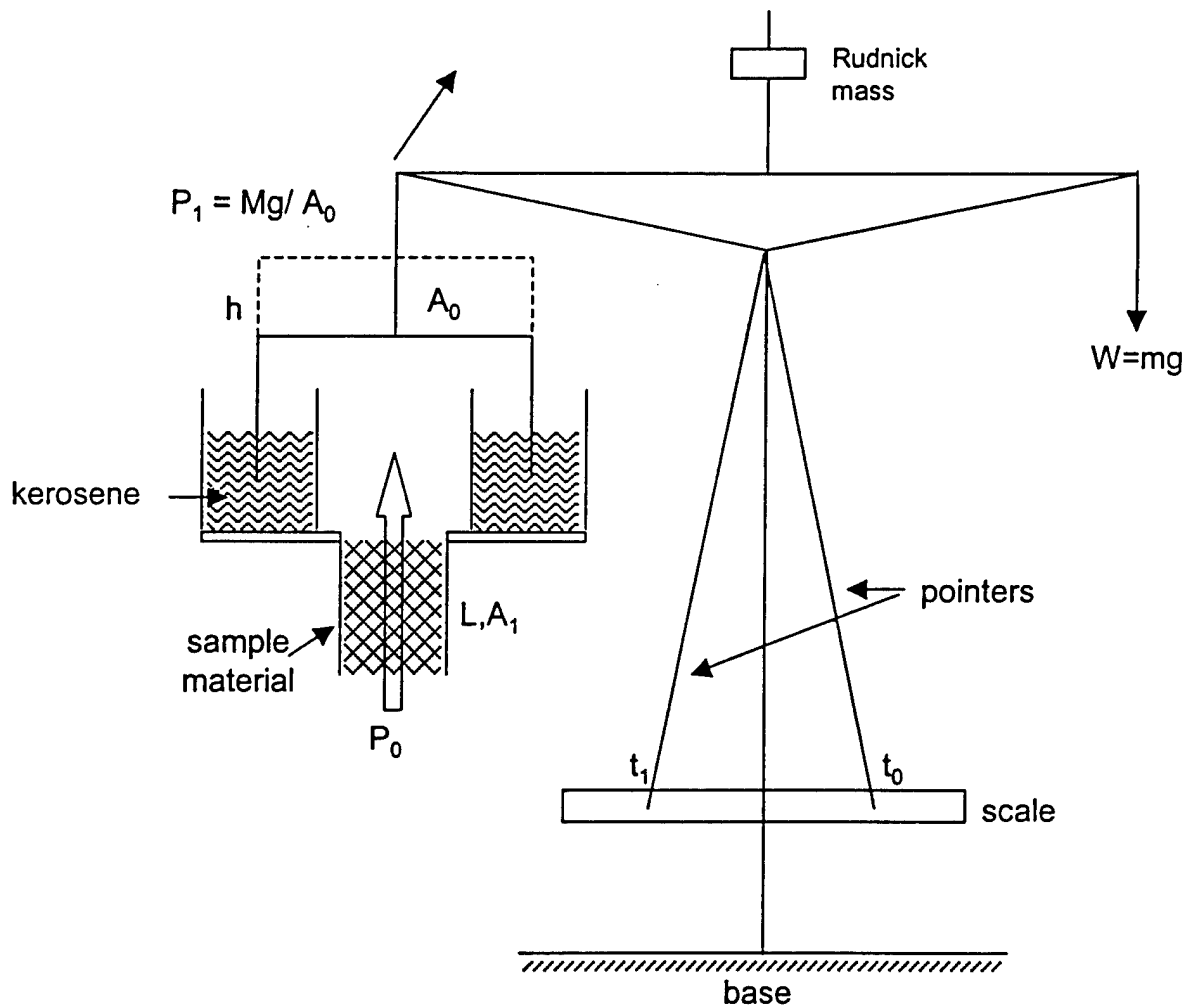
$$\sigma = \frac{S}{l} \quad 5.$$

$$\sigma = \frac{\Delta p}{v \cdot l} \quad (\text{units } \text{Nsm}^{-4}) \quad 6.$$

Measurement Techniques

Leonard's – Simplified Flow Resistance, JASA 17 (1946)
Rudnick – Boundary Modification – JASA

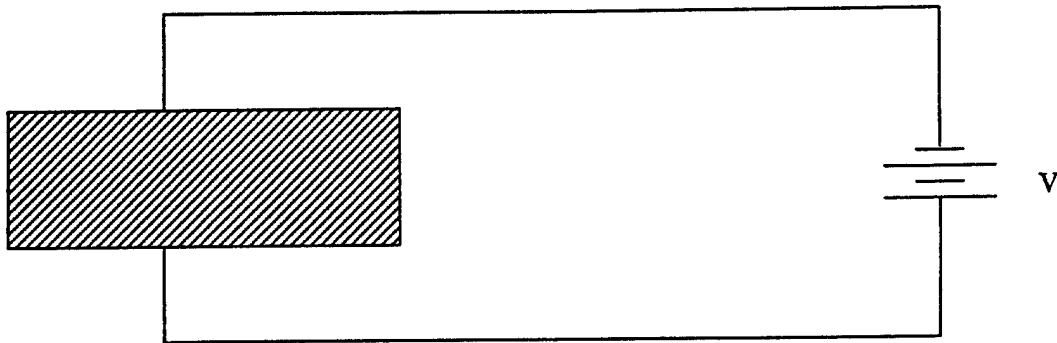
LEONARD'S APPARATUS WITH RUDNICK'S MODIFICATION



$$\sigma = \frac{mg \Delta t A_1}{A^2 h L} \quad 7.$$

TORTUOSITY MEASUREMENT

Dielectric frame or matrix saturated with a conducting fluid



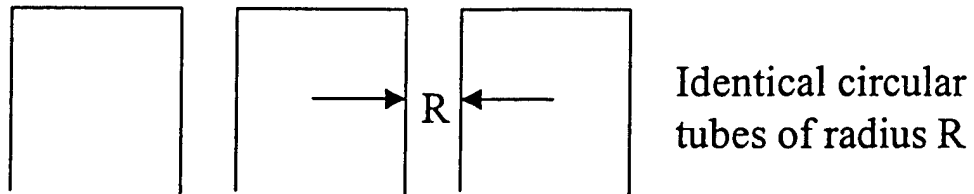
Electrical resistivity of fluid alone = r_f

Electrical resistivity of saturated material = r_c

Tortuosity: $q^2 = \Omega \frac{r_c}{r_f}$ 8.

SIMPLE POROUS MEDIA MODEL

1. "Soda Straw"



$n \equiv$ number of pores of radius R per unit area of cross-section

$$\text{porosity} \equiv \Omega = n\pi R^2$$

2. Geometrical packing of spheres

simple cubic, bcc, etc.

3. More relevant – Random packing of spheres

soils, sediments, sands

A BRIEF REVIEW OF LINEAR IDEAL ACOUSTICS

The linearized equations of state, continuity, and motion are:

$$p(s) = \beta s = \beta \frac{\rho - \rho_0}{\rho_0} \quad \text{"State"} \quad 9.$$

$$\rho_0 \nabla \cdot \bar{u} + \frac{\partial p}{\partial t} = 0 \quad \text{"Continuity"} \quad 10.$$

$$-\nabla p = \rho_0 \frac{\partial \bar{u}}{\partial t} \quad \text{"Motion"} \quad 11.$$

Acoustic variables: p, ρ, u are pressure, density and velocity, respectively

Combine these to yield a wave equation

WAVE EQUATIONS FOR FLUIDS (IDEAL)

$$\nabla^2 p = \frac{1}{c^2} \frac{\partial^2 p}{\partial t^2} \quad 12.$$

$$c^2 = \sqrt{\frac{\beta}{\rho_0}} \quad \beta \equiv \text{adiabatic bulk modulus} \quad 13.$$

$$\beta = \gamma p_0$$

p = acoustic pressure

ρ_0 = air density

GENERAL SOLUTION

$$P = A e^{i(\omega t - kx)} \quad 14.$$

$$k = \frac{\omega}{c} = \omega \sqrt{\frac{\rho_0}{\beta}} \quad 15.$$

FLUIDS WITH ABSORPTION

Write wave number

$$\tilde{k} = (k_r - i\alpha) \quad 16.$$

Solution now is

$$P = e^{-\alpha x} e^{-i(k_r x - \omega t)} \quad 17.$$

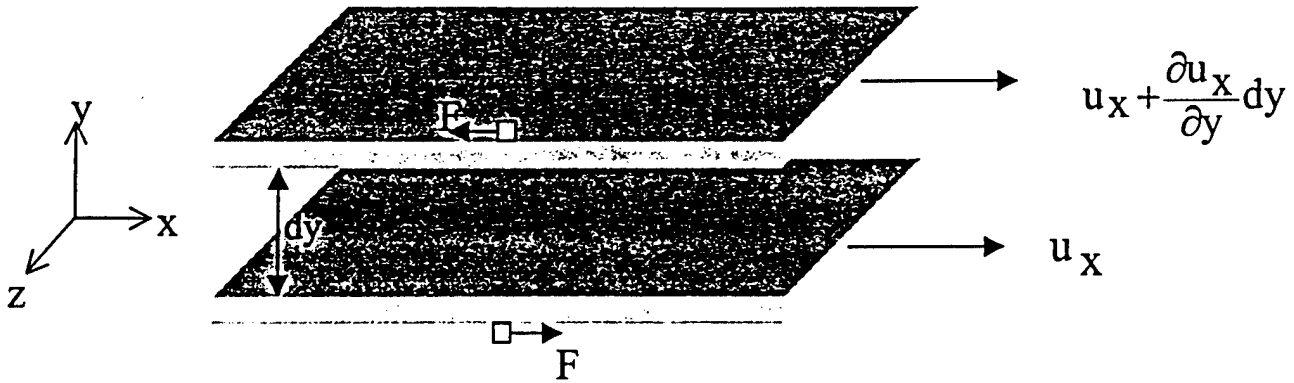
Rewrite Wave Equation as

$$\nabla^2 p = \frac{1}{\tilde{c}^2} \frac{\partial^2 p}{\partial t^2} \quad 18.$$

$$\tilde{k} = \frac{\omega}{\tilde{c}} = \omega \sqrt{\frac{\tilde{\rho}'}{\tilde{\beta}'}} \quad 19.$$

Our goal becomes to determine the effects of viscous friction and thermal conduction $\tilde{\rho}'$ and write these effects down in terms of complex density, $\tilde{\beta}'$, and complex compressibility.

VISCOUS FRICTION FORCE (SHEAR VISCOSITY)



Two fluid layers moving at different speeds

$$F \sim [\Delta u_x, \text{Area}, dy] \quad 20.$$

$$F \propto \left[u_x + \frac{\partial u_x}{\partial y} dy - u_x \right] dx dz \frac{1}{dy} \quad 21.$$

$$\text{Stress} = \frac{F}{A} \approx \frac{\partial u_x}{\partial y} \Rightarrow \text{Strain rate} = \frac{\Delta L}{L} \cdot \frac{1}{t} = \frac{\Delta V}{L} \quad 22.$$

$$P_{xy} = \eta \frac{\partial u_x}{\partial y} \quad 23.$$

For a volume element:

$$P_{xy} = \eta \left(\frac{\partial u_x}{\partial y} + \frac{\partial u_y}{\partial x} \right) \quad \eta \equiv \text{coefficient of viscosity} \quad 24.$$

VISCOUS PENETRATION DEPTH

$\frac{1}{e}$ drop-off of velocity from the wall

$$\delta_{\eta} = \sqrt{\frac{2\eta}{\omega\rho}} \quad \delta_{\eta} \text{ is the viscous penetration depth} \quad 25.$$

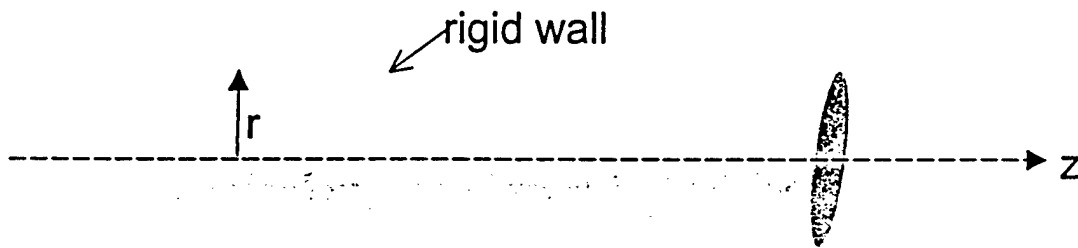
In air at 1.0 kHz, $\rho=1.2\text{ng/m}^3$, $\eta=1.81\times10^{-5}\text{Pa}\cdot\text{s}$

$$\delta_{\eta} = 2.0\times10^{-6}\text{m}$$

SOUND PROPAGATION IN A SINGLE CYLINDRICAL TUBE WITH VISCOUS DRAG AND THERMAL CONDUCTION

Zwicker and Kosten, *Sound Absorbing Materials*

Tube:

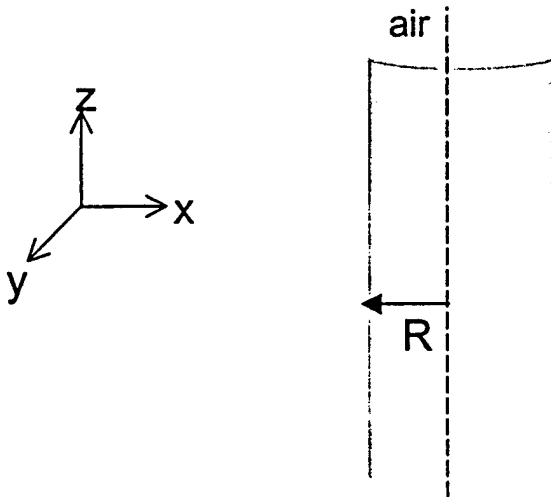


Z. & K. assume: pressure is independent of r ; frequency is below first non-planar mode

Others: Tijdeman, Arnott, Stinson

Show that $p = p(z)$ is valid.

APPLY TO A CYLINDRICAL TUBE



Assume:

$$\begin{aligned} u &= u(z) \\ u_x &= u_y = 0 \\ u_z &= 0 \text{ at } r=R \end{aligned}$$

$$F = ma$$

$$i\omega\rho_0 u_z = \frac{\partial p}{\partial z} + \eta \left(\frac{\partial^2 u_z}{\partial x^2} + \frac{\partial^2 u_z}{\partial y^2} \right) \quad 26.$$

In cylindrical coordinates

$$i\omega\rho_0 u_z = -\frac{\partial p}{\partial z} + \frac{\eta}{r} \frac{\partial}{\partial r} \left(r \frac{\partial u_z}{\partial r} \right) \quad 27.$$

Bessel's equation and solution for velocity

$$u_z = -\frac{1}{i\omega\rho_0} \frac{\partial p}{\partial z} \left(1 - \frac{J_0(\ell r)}{J_0(\ell R)} \right), \quad \ell = \sqrt{\frac{-i\omega\rho_0}{\eta}} \quad 28.$$

AVERAGE VELOCITY ACROSS CYLINDRICAL TUBE

$$\bar{u}_z = \frac{\int_0^R u_z 2\pi r dr}{\pi R^2} \quad 29.$$

$$\bar{u}_z = -\frac{1}{i\omega\rho_0} \frac{\partial p}{\partial z} \left[1 - \frac{2}{s\sqrt{-i}} \frac{J_1(s\sqrt{-i})}{J_0(s\sqrt{-i})} \right] \quad 30.$$

with

$$s = \sqrt{\frac{\omega\rho_0 R^2}{\eta}} = \frac{R\sqrt{2}}{\delta_\eta} \equiv \text{shear wave number} \quad 31.$$

In terms of "effective" or "complex density," $F = ma$ can be written as

$$-\frac{\partial p}{\partial z} = i\omega\rho \bar{u}_z \quad 32.$$

$$\text{where } \rho = \rho_0 \left[1 - \frac{2}{s\sqrt{-i}} \frac{J_1(s\sqrt{-i})}{J_0(s\sqrt{-i})} \right]^{-1} \Rightarrow \text{effective density} \quad 33.$$

Effective density for semi-infinite slit of width $2a$ is

$$\rho = \rho_0 \left[1 - \frac{\tanh(s'\sqrt{i})}{s'\sqrt{i}} \right]^{-1} \quad \text{with} \quad s' = \sqrt{\frac{\omega\rho_0 a^2}{\eta}} \quad 34.$$

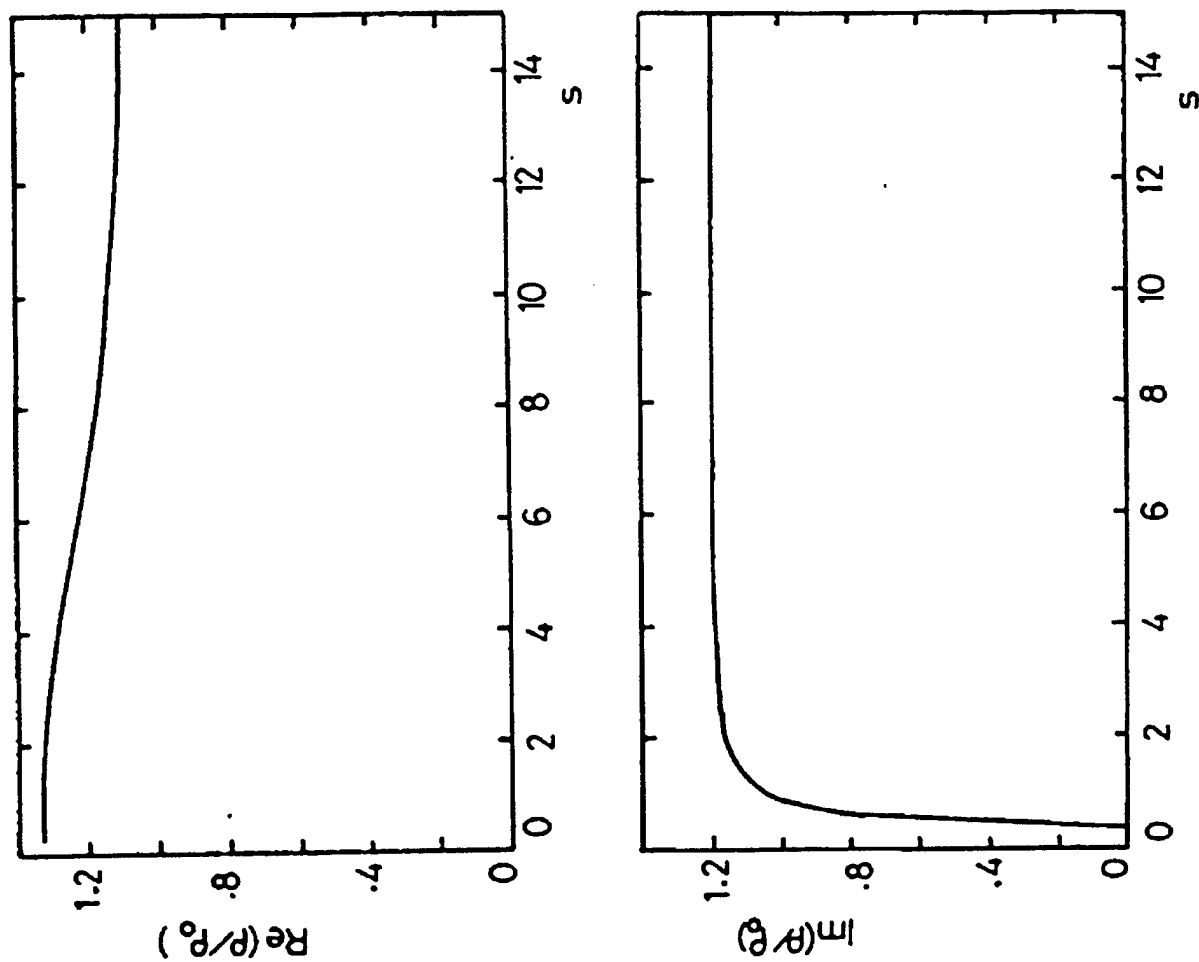


FIG. 4.4. The ratio ρ/ρ_0 , where ρ is the effective density of a fluid of density ρ_0 , in a cylindrical tube having a circular cross-section, as a function of s .

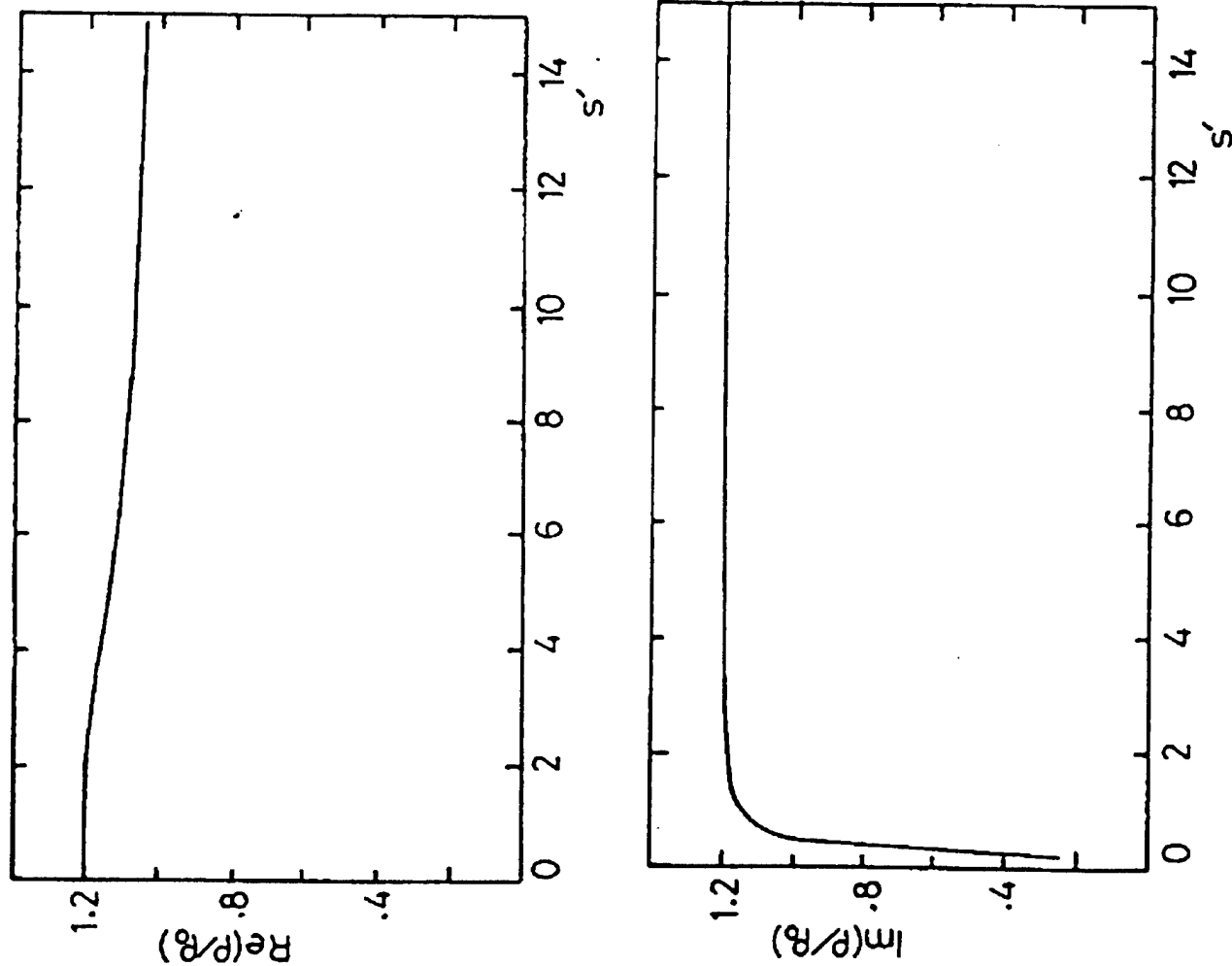


FIG. 4.5. The ratio ρ/ρ_0 , where ρ is the effective density of a fluid of density ρ_0 , in a slit, as a function of s' .

EFFECTIVE BULK MODULUS

(Incorporate Thermal Conductivity)

References:

Attenborough, "Acoustical Characteristics of Porous Materials," Phys. Rep. **82** (3), 1982.

David Craig, "Acoustic Propagation in Fractal Porous Media," Ph.D. Dissertation, University of Mississippi, 1995.

Stinson, JASA **89**, 1991.

Considering heat conduction and compression of the fluid, arrive at effective bulk modulus.

Circular tube:

$$K = \gamma p_0 \left[1 + (\gamma - 1) \frac{2}{N_{Pr} s \sqrt{-i}} \frac{J_1(N_{Pr} s \sqrt{-i})}{J_0(N_{Pr} s \sqrt{-i})} \right]^{-1} \quad 35.$$

$$\gamma = \frac{c_p}{c_v}; N_{pr} \text{ is the Prandtl number} \quad 36.$$

Slit, width $2a$

$$K = \gamma p_0 \left[1 + (\gamma - 1) \frac{\tanh(N_{Pr} s' \sqrt{i})}{N_{Pr} s' \sqrt{i}} \right]^{-1} \quad 37.$$

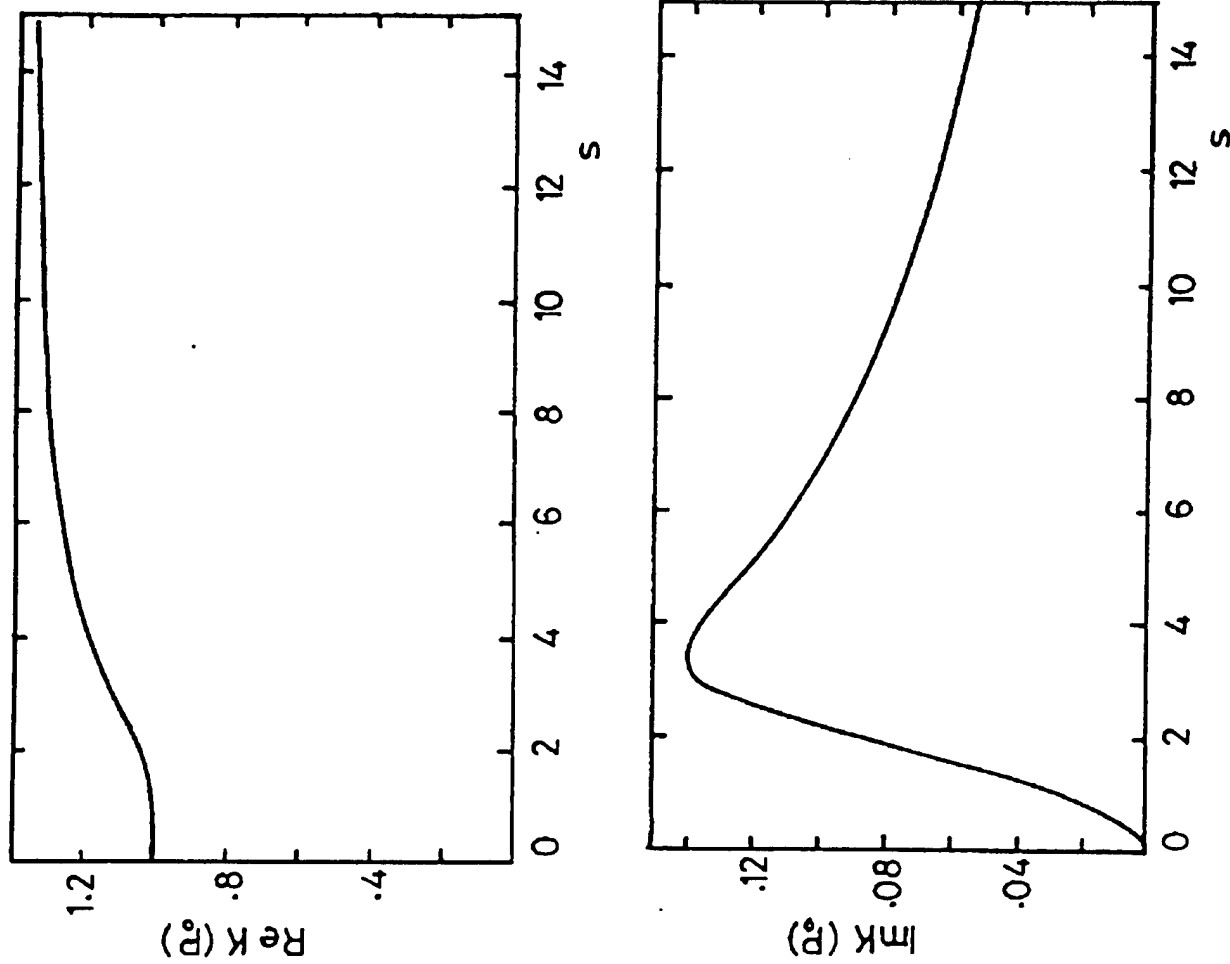


FIG. 4.6. The bulk modulus K of air in a cylindrical tube having a circular cross-section as a function of s . The unit is the atmospheric pressure P_0 .

Propagation of Sound in Porous Media

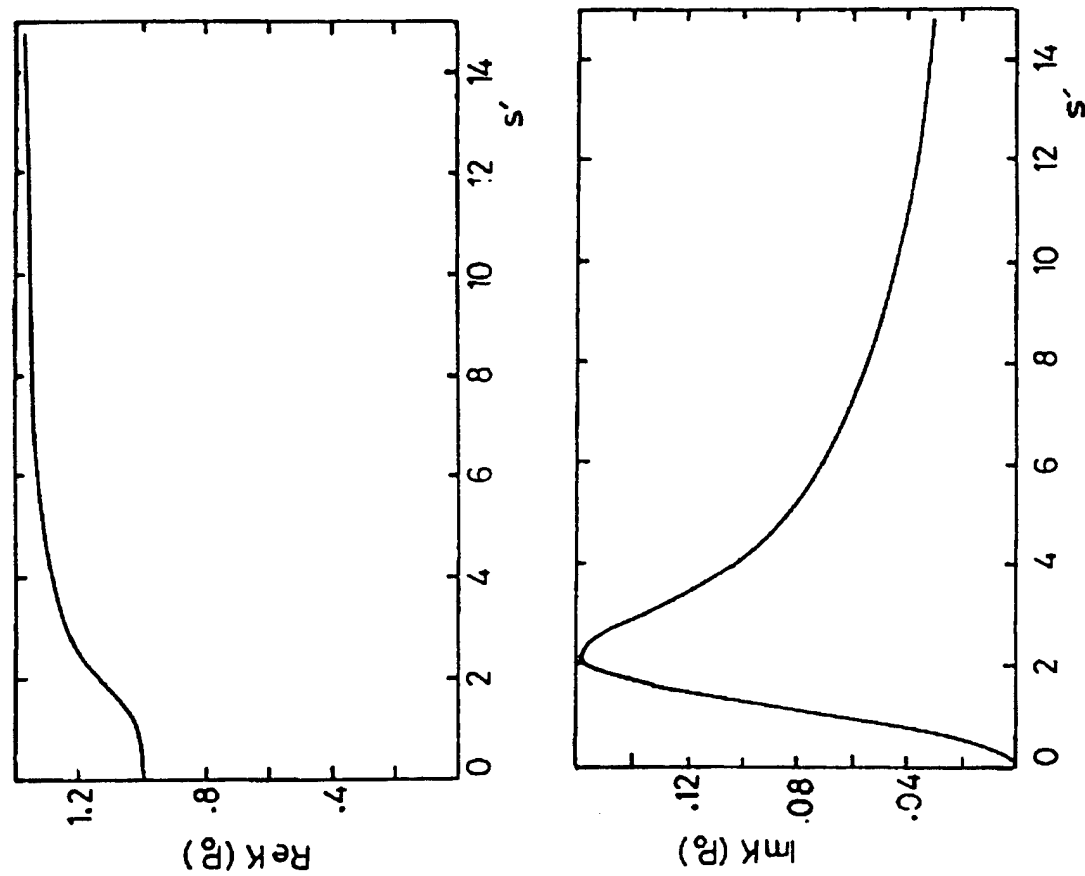
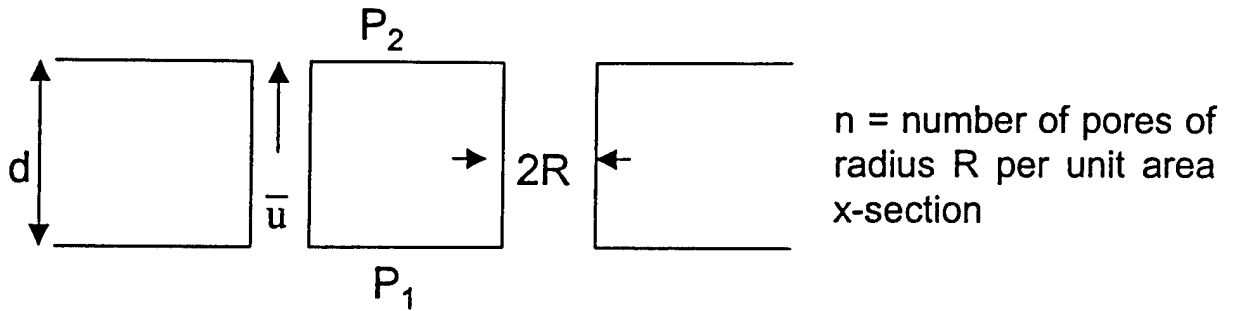


FIG. 4.7. The bulk modulus K of air in a slit as a function of s' . The unit is the atmospheric pressure P_0 .

FLOW RESISTIVITY IN BULK MATERIAL WITH CAPILLARY TUBES



$$\sigma \equiv \frac{\Delta p}{V \cdot d} = \frac{\Delta p}{\bar{u}(n\pi R^2)d} \quad V \equiv \text{volume velocity/unit area} \quad 38.$$

$$\text{For D.C. flow } (\omega=0), \quad \bar{u}_z = \frac{R^2}{8\eta} \left(-\frac{\partial p}{\partial z} \right) \quad 39.$$

$$\text{Substitute for } \frac{\Delta p}{v \cdot d} = \frac{8\eta}{R^2} \quad 40.$$

$$\sigma = \frac{8\eta}{(n\pi R^2)R^2} = \frac{8\eta}{\Omega R^2} \quad 41.$$

$$\text{Recall } s = \sqrt{\frac{\omega \rho_0 R^2}{\eta}}, \text{ and eliminate } \frac{R^2}{\eta} \quad 42.$$

$$s = \sqrt{\frac{8\omega \rho_0}{\sigma \Omega}} \text{ shear wave number with measurables} \quad 43.$$

Rewriting shear wave number for tubes

$$s = \sqrt{\frac{8\omega\rho_o}{\sigma\Omega}} \quad 44.$$

For slits, a similar analysis yields

$$\sigma = \frac{3\eta}{\Omega a^2} \quad 45.$$

$$\text{Recall } s' = \sqrt{\frac{\omega\rho_o a^2}{\eta}} \quad \text{with} \quad \frac{a^2}{\eta} = \frac{3}{\sigma} \quad 46.$$

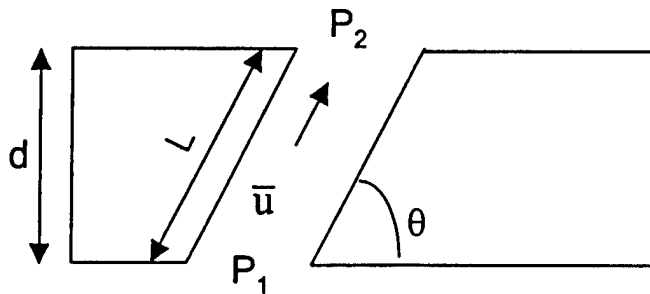
And in terms of σ , Ω

$$s' = \sqrt{\frac{3\omega\rho_o}{\sigma\Omega}} \quad 47.$$

Compare effective density and bulk modulus for bulk material composed of cylinders and slits.

PORE TORTUOSITY

Carman, *Flow of Gases through Porous Materials*



Porosity:

$$\Omega = \frac{n \pi R^2}{\cos \theta}$$

Flow Resistivity: $\frac{\Delta p}{V \cdot d}$, $V \equiv \frac{\text{volume velocity}}{\text{area}}$ 48.

Pressure Gradient in pores: $\frac{P_2 - P_1}{L} = \frac{P_2 - P_1}{d} \cos \theta$ 49.

$$\sigma = \frac{P_2 - P_1}{n (\bar{u} \pi R^2) d}$$
 50.

$$n = \frac{\text{number of pores}}{\text{area}}$$
 51.

For D.C. Flow, $\omega = 0$,

$$\bar{u}_z = \frac{R^2}{8\eta} \left(-\frac{\partial P}{\partial z} \right) \quad \frac{\Delta P}{\bar{u} \Delta z} \rightarrow \frac{8\eta}{R^2} \quad 52.$$

$$\sigma = \frac{8\eta}{R^2 n \pi R^2 \cos \theta} = \frac{8\eta}{n \pi R^4 \cos \theta} \quad 53.$$

Substitute for $\Omega = \frac{n \pi R^2}{\cos \theta}$ 54.

$$\sigma = \frac{8\eta}{\Omega R^2 \cos^2 \theta} \quad 55.$$

Recall $s = \sqrt{\frac{\omega \rho_o R^2}{\eta}}$ 56.

Substitute for $\frac{\eta}{R^2}$

$$\Rightarrow s = \sqrt{\frac{8\omega \rho_o q^2}{\sigma \Omega}} \text{ in terms of measurable quantities} \quad 57.$$

with $q^2 = \frac{1}{\cos^2 \theta}$ 58.

ATTENBOROUGH / BIOT

SCALING BETWEEN CYLINDERS AND SLITS

Attenborough – scaled ρ and k

$$\rho_c(s) \approx \rho_s(5/3s) \quad 59.$$

Biot – scaled “viscous correction function”

Cylinders:

$$G_c(s) = -\frac{s}{4} \sqrt{-i} \frac{T_1}{T_0} \left[1 - \frac{2}{s \sqrt{-i}} \frac{T_1}{T_0} \right]^{-1} \quad 60.$$

$$T_1 = J_1(s \sqrt{-i}); \quad T_0 = J_0(s \sqrt{-i}) \quad 61.$$

$$s = \sqrt{\frac{\omega \rho_0 R^2}{\eta}} \quad 62.$$

Slits:

$$G_s(s') = \frac{1}{3} \sqrt{i} \frac{\tan(s' \sqrt{i})}{\left[1 - \frac{\tan(s' \sqrt{i})}{s' \sqrt{i}} \right]}, \quad s' = \sqrt{\frac{\omega \rho_0 a^2}{\eta}} \quad s = \frac{4}{3} s' \quad 63.$$

$$G_c(s) = G_s(s') \quad 64.$$

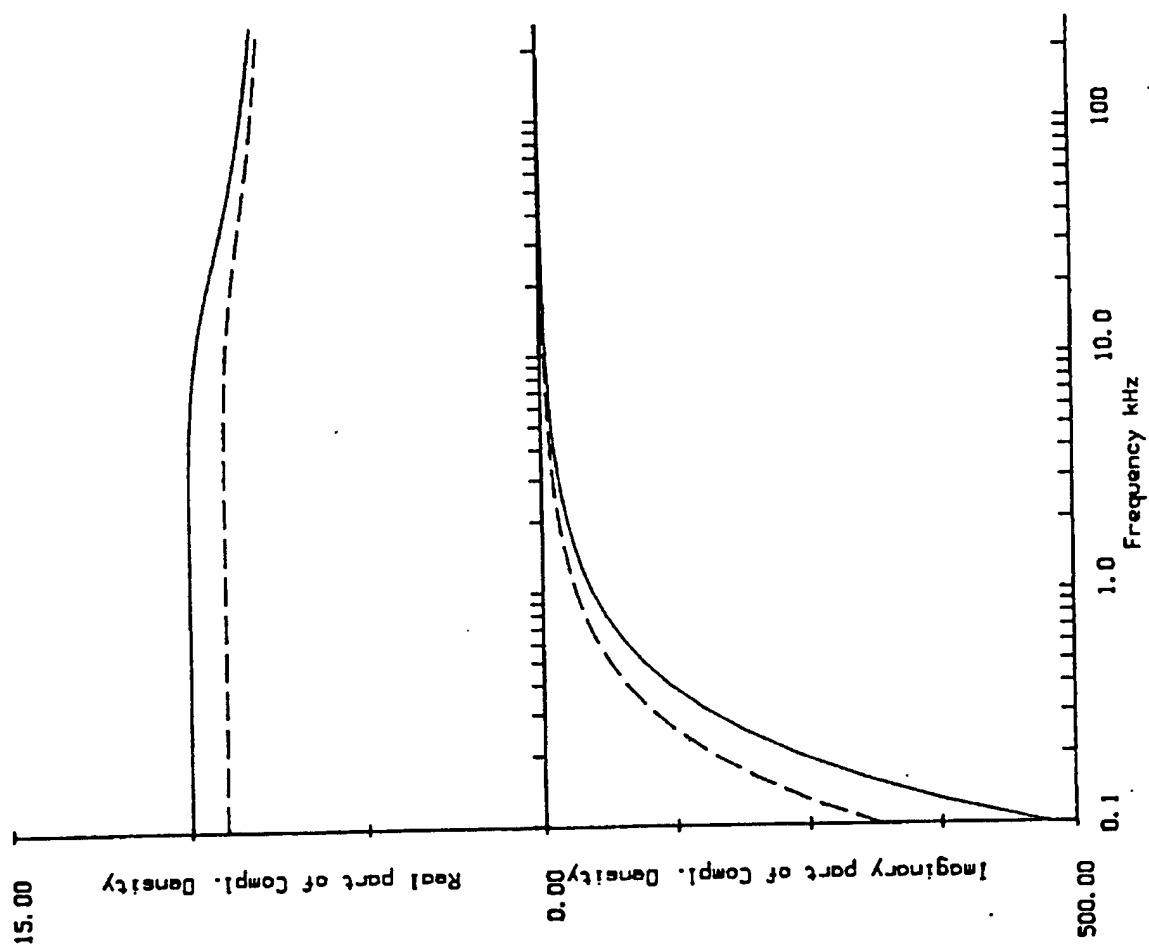


FIG. 3. Plot of real and imaginary parts of $\rho_c(\lambda_c)$ and $\rho_s(\lambda_s)$ against frequency [Eqs. (14) and (15)], where the frequency range $100 < f < 25\,760$ Hz corresponds to $0.119 < \lambda_s < 3.5$.

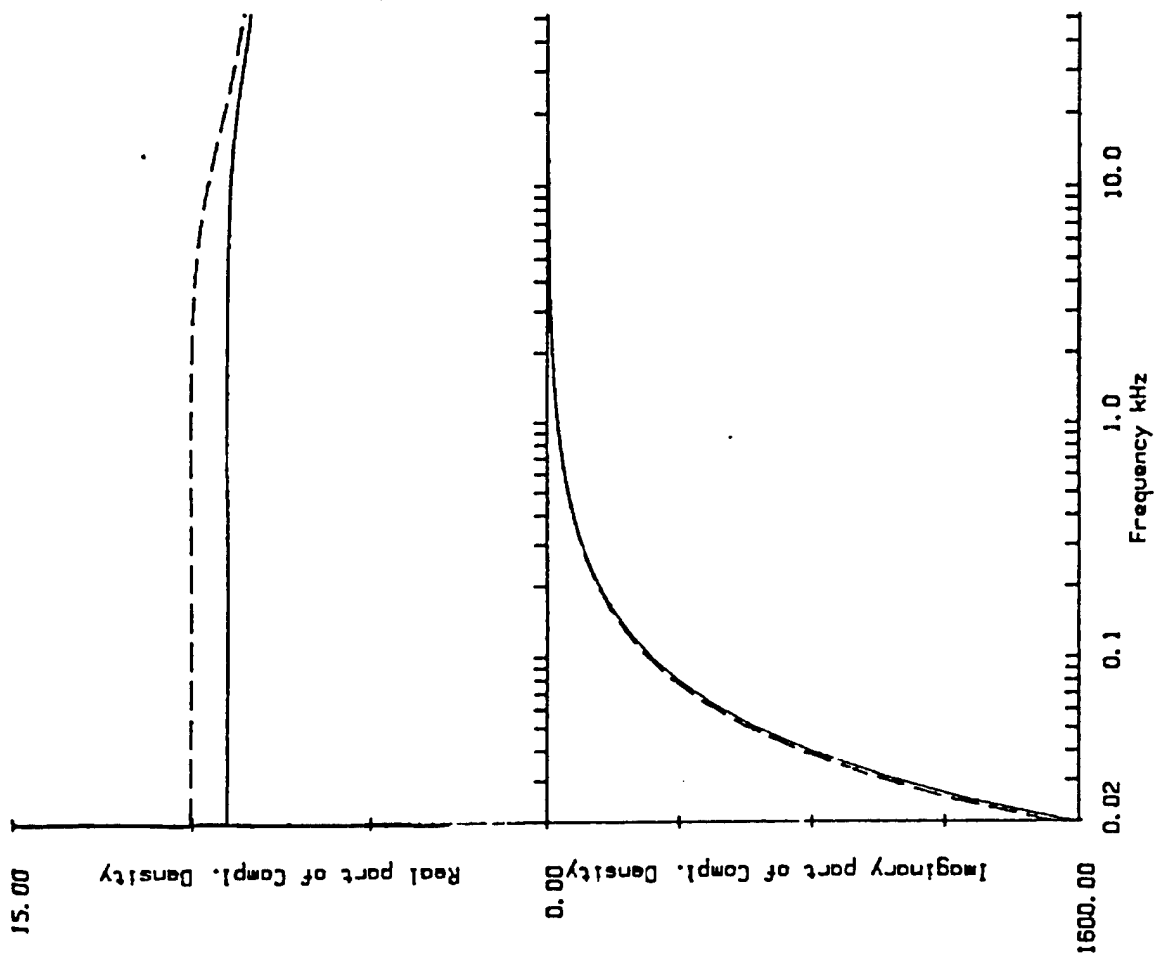


FIG. 4. Test of pore shape scaling for $\rho(\lambda)$. Plot of $\rho_s(\lambda_s)$ (continuous lines) against $\rho_c(5/3 \lambda_s)$ (broken lines) in the range $0.119 < \lambda_s < 6$.

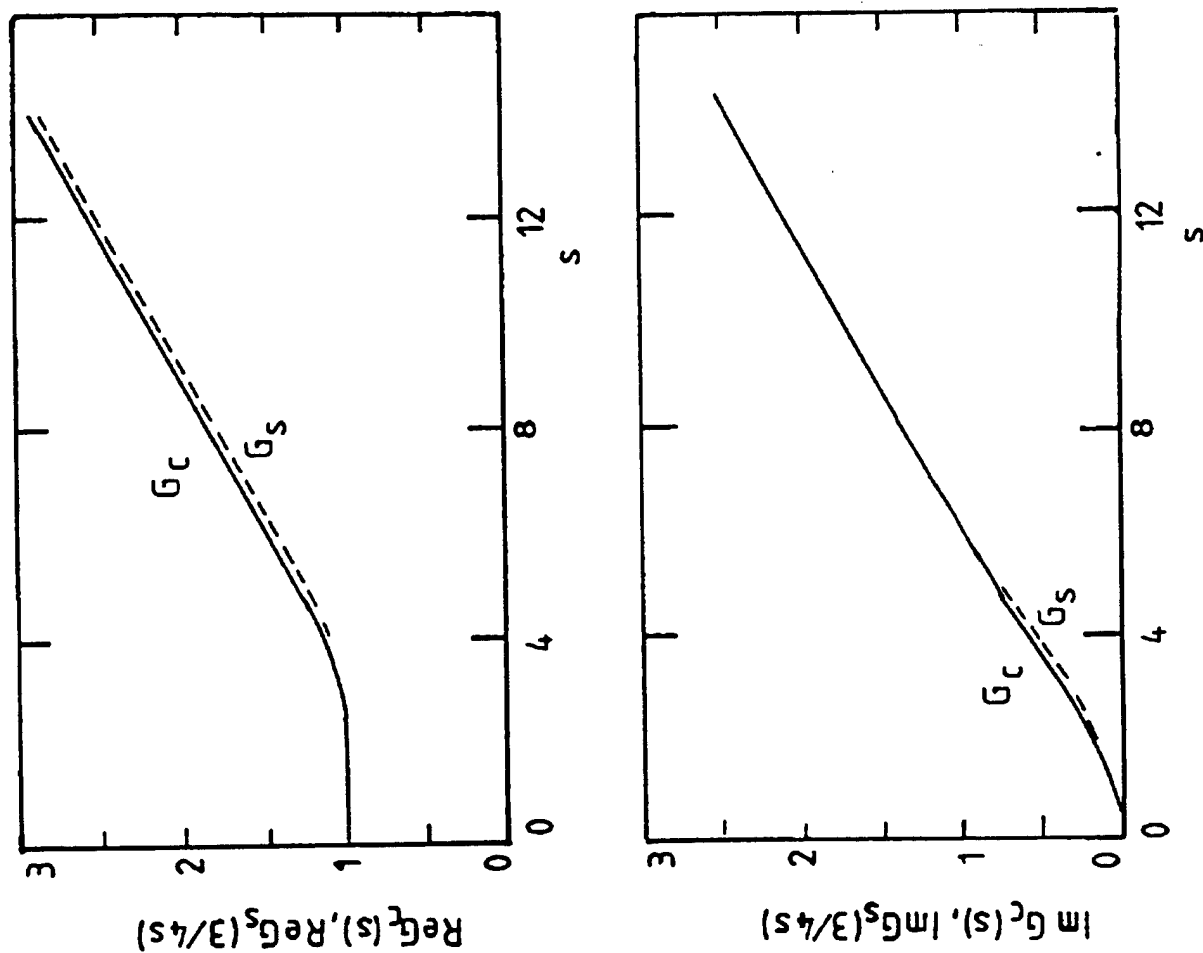


FIG. 4.9. The form factors $G_c(s)$ and $G_s(s')$ for $s' = \frac{3}{4}s$.

RESULTS OF SCALING

Pore Shape: S_p

$$s = \frac{1}{S_p} \sqrt{\frac{8\omega\rho_o q^2}{\sigma\Omega}} \quad 65.$$

Cylinders with $S_p = 1.0$.

Can develop pore shape scaling for other geometries, square or triangular pores, but for outdoor soils not necessary.

SUMMARY – ACOUSTIC WAVE NUMBER

(low frequency approximation)
(Ω , q^2 , σ , S_p)

Bulk wave number

$$k_b = \omega \sqrt{\frac{\rho}{K}} \quad 66.$$

$$k_b = k_o \sqrt{\gamma} \left[a q^2 + \frac{i \sigma \Omega}{S_p \rho_o \omega} \right]^{1/2} \quad 67.$$

$$a = \left(\frac{4}{3} - \frac{\gamma - 1}{\gamma} \right) N_{pr} \quad 68.$$

$$k_o = \frac{\omega}{c_o} \quad 69.$$

For high freq/low flow resistivity

$$k_b \sim k_o \sqrt{\gamma a q^2} \quad 70.$$

$$\Rightarrow \frac{c_o}{c_b} \sim \sqrt{q^2} \quad 71.$$

SUMMARY – ACOUSTIC IMPEDANCE

Low Frequency

$$z = \frac{1}{\rho_0 c_0} \omega \sqrt{\frac{\rho}{k_b}} \quad 72.$$

$$z_{\text{low}} \cong (1+i) \sqrt{\frac{\sigma}{\Omega}}, \quad z_{\text{high}} \cong \sqrt{\frac{q^2}{\Omega^2}} \quad 73.$$

Only ratios of $\frac{\sigma}{\Omega}$ or $\frac{q^2}{\Omega^2}$ can be determined.

Consider low frequency approximation for k_b

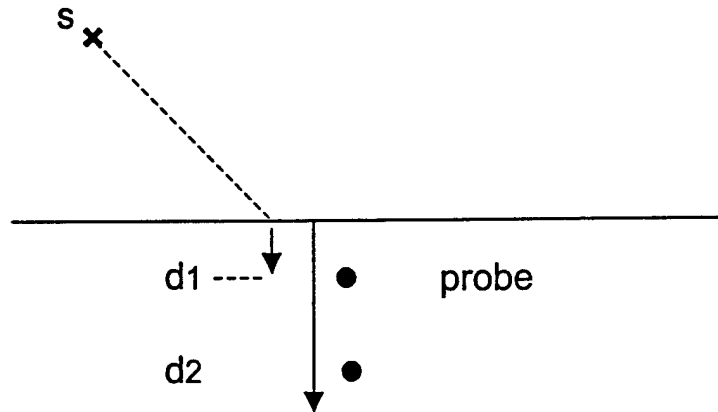
$$k_b \cong k_0 \sqrt{\gamma} \left[a q^2 + i \frac{\sigma \Omega}{\rho_0 \omega} \right]^{1/2} \quad 74.$$

$$a = \left(\frac{4}{3} - \frac{\gamma - 1}{\gamma} \right) N_{Pr} \quad 75.$$

$$\text{Real}[k_b^2] = k_r^2 - k_i^2 \approx a q^2 \omega^2 \quad 76.$$

$$\text{Im}[k_b^2] = 2k_r k_i \cong \gamma \left(\frac{\omega}{c_0} \right)^2 \frac{\sigma \Omega}{\rho_0 \omega} \quad 77.$$

ACOUSTIC PROBE



$$\tilde{T}_{d_2 d_1} \approx \frac{e^{ik_b d_2}}{e^{ik_b d_1}} \quad 78.$$

$$\text{Phase: } \phi = \tan^{-1} \left(\frac{T_I}{T_R} \right) = k_r \Delta d \quad 79.$$

$$\text{Magnitude (dB)} = 10.0 \log_{10} |T|^2 \quad 80.$$

$$= 20 \log_{10} e^{-k_i \Delta d} \quad 81.$$

$$= -20 k_i \Delta d \log_{10} e \quad 82.$$

$$\text{or } k_r = \frac{\phi}{\Delta d}, \text{ and } k_i = - \frac{\text{mag (dB)} \ln 10 .0}{20 .0 \Delta d} \quad 83.$$

Probe Microphone (Electret)

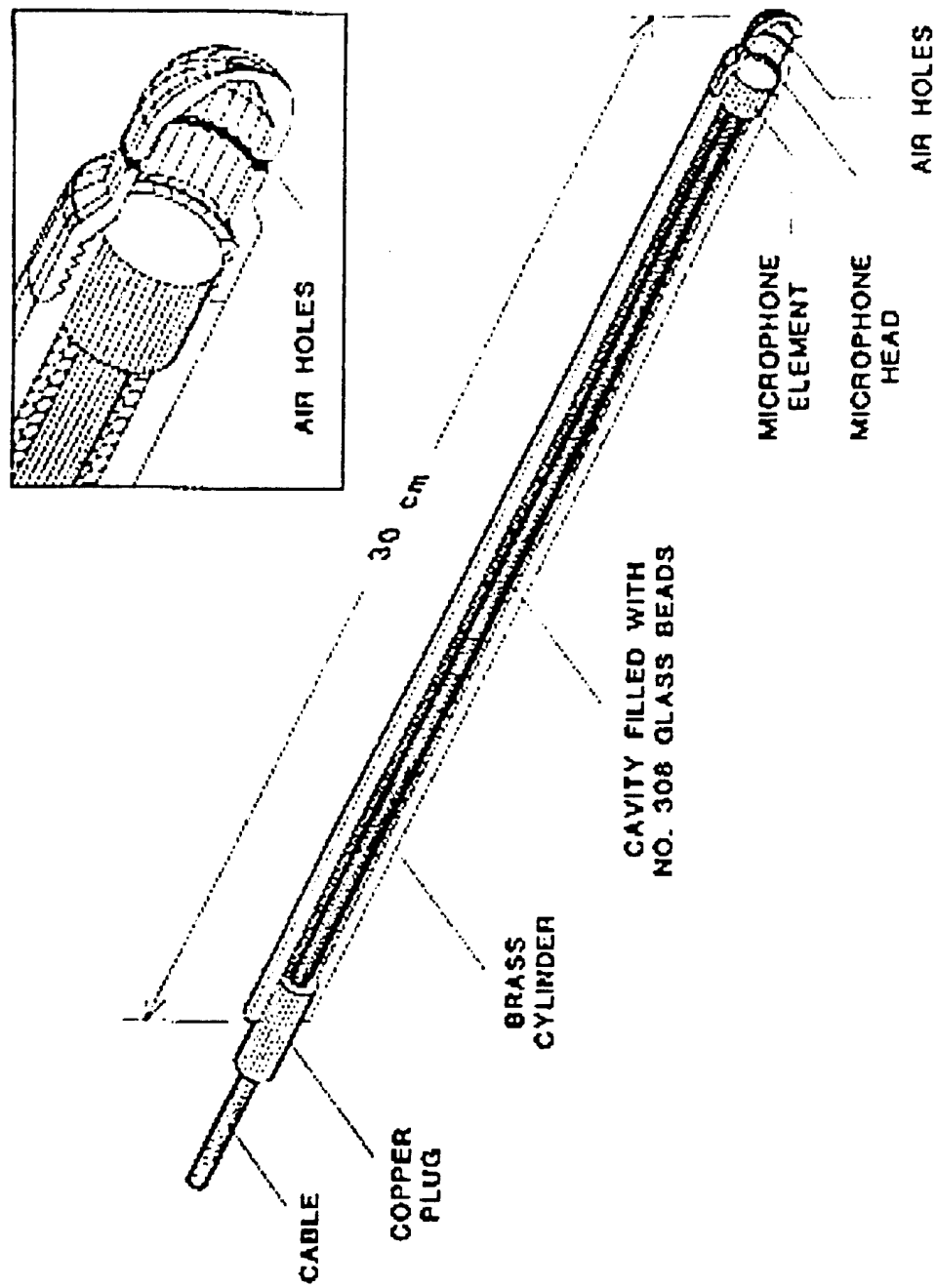
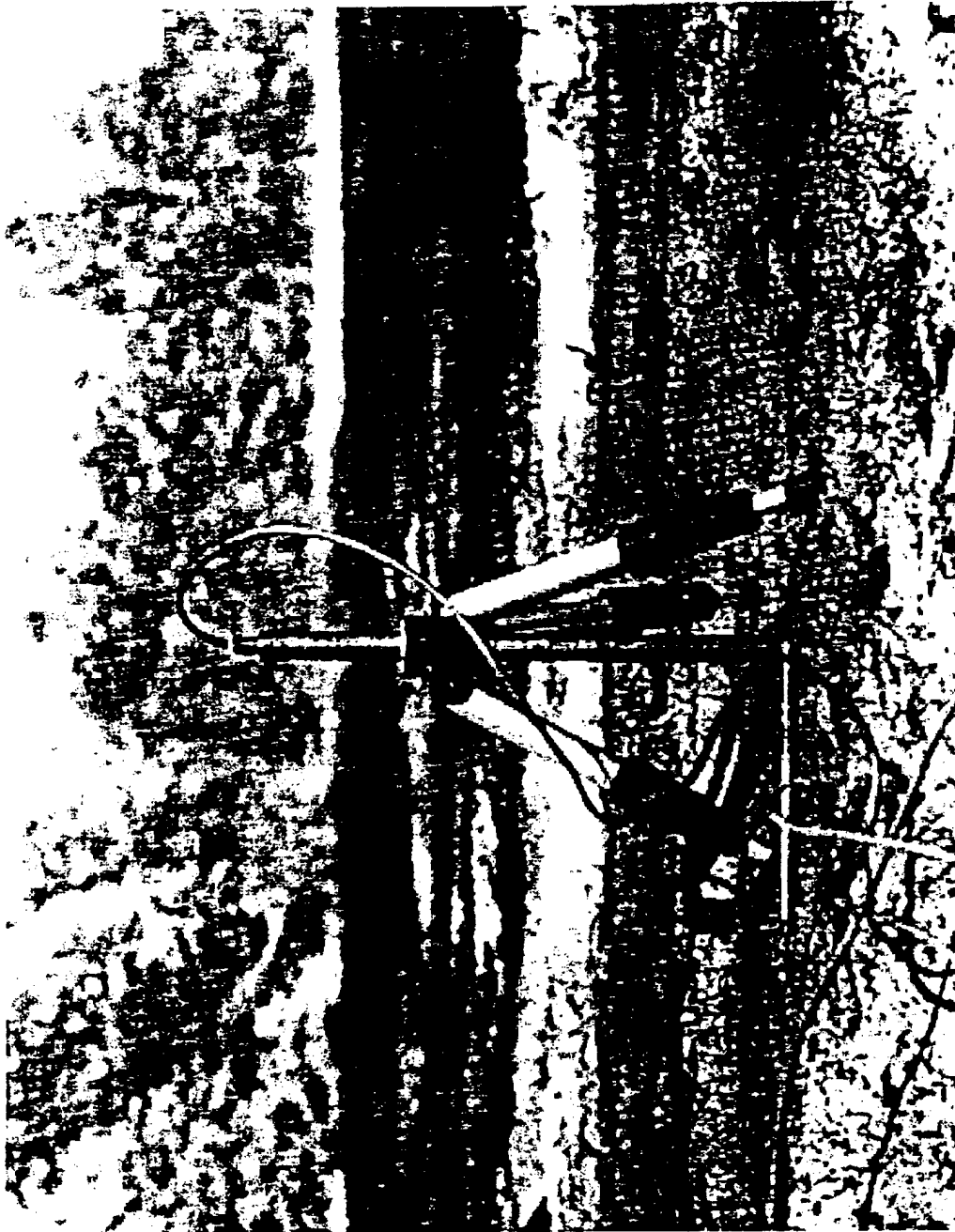


Fig. 1. Diagram of probe microphone. Insert shows enlarged view of the nose cone and microphone element.

Probe Microphone (In-situ)



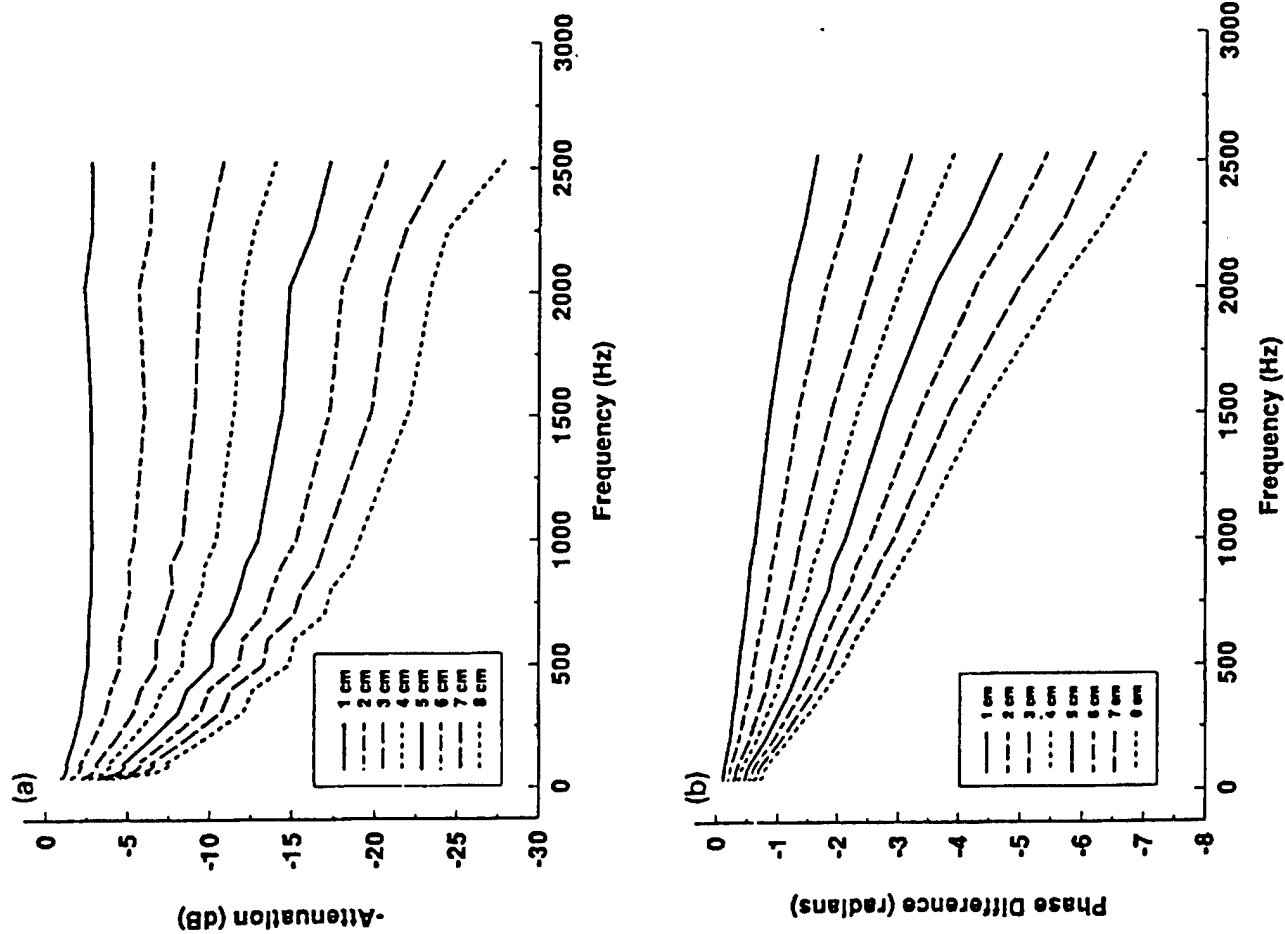


Fig. 4. Magnitude (a) and phase (b) in 500 μm spherical glass beads for depths between 1 and 8 cm.

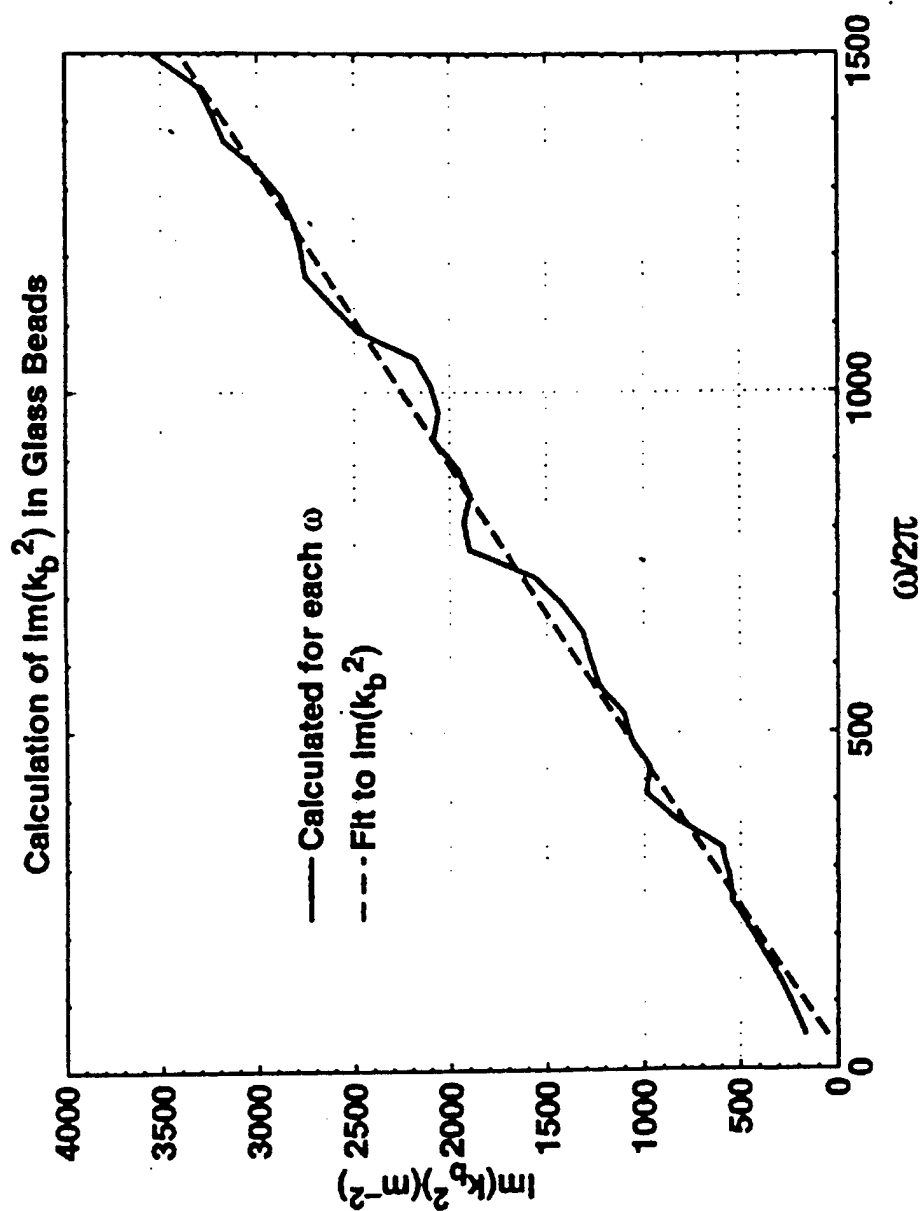


FIG. 6. The imaginary part of k_b^2 from the glass bead probe data is shown (solid line) along with a linear fit $a_1 + b_1 \omega$ (dashed). Using Eq. (9) the coefficient of ω can be used to calculate the product $\sigma_b \Omega$ shown in Table III.

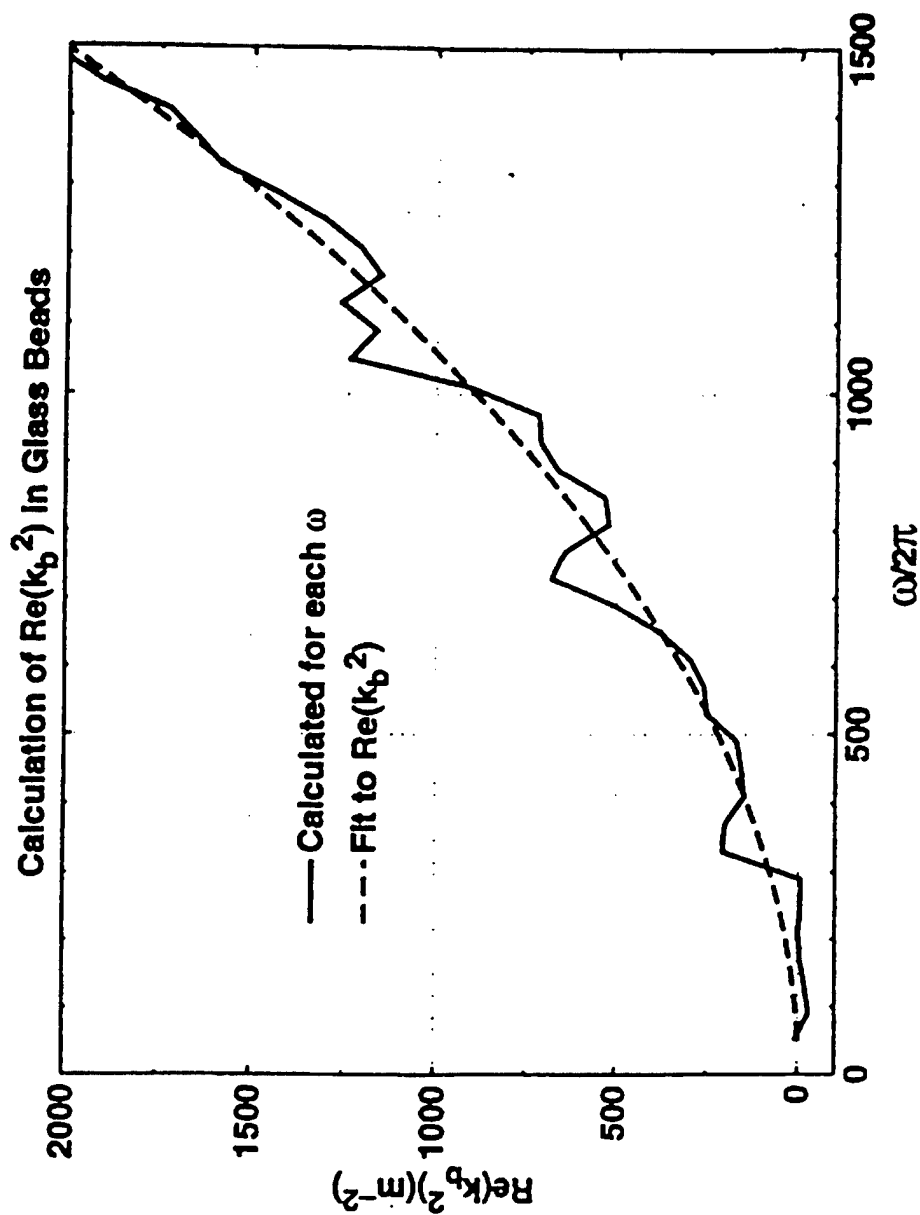
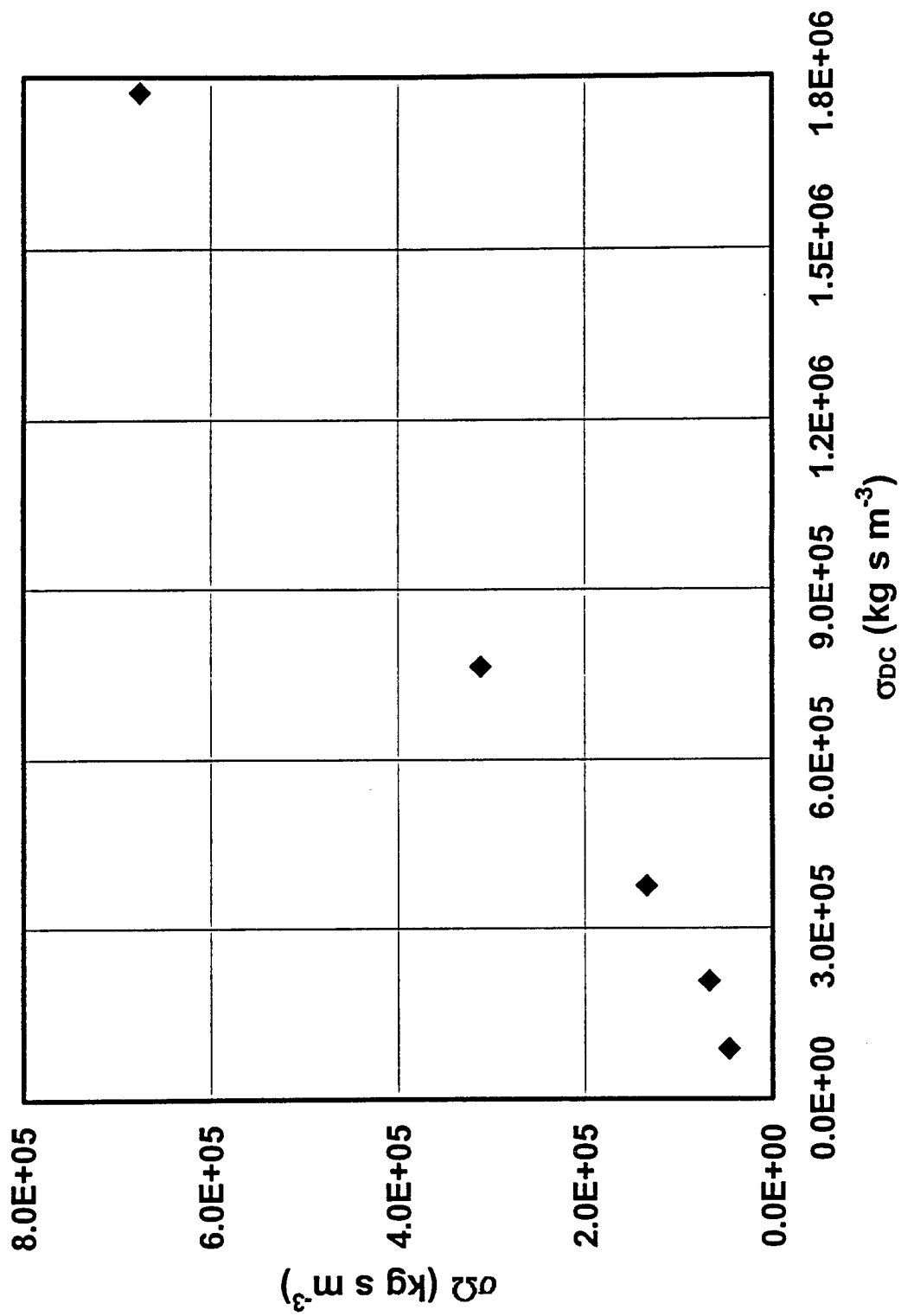


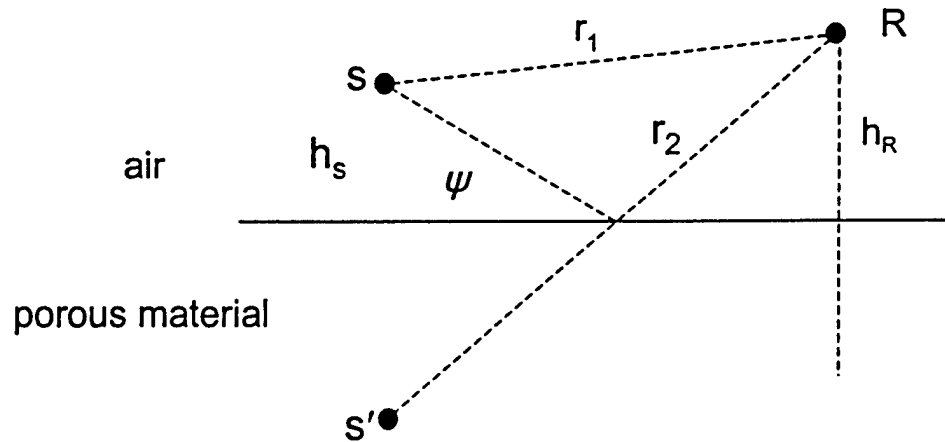
FIG. 5. The value of $\text{Re}(k_b^2)$ calculated from the probe data taken in glass beads is shown (solid line) along with a fit of the form $a_1 + c_1 \omega^2$ (dashed). Equation (8) is used to relate c_1 to q^2 . The value of q^2 calculated from c_1 is the dashed line in Fig. 4 and is given in Table III.

Flow resistivity, Leonard's appar., probe microphone



ACOUSTIC INVERSION FOR PORE PROPERTIES

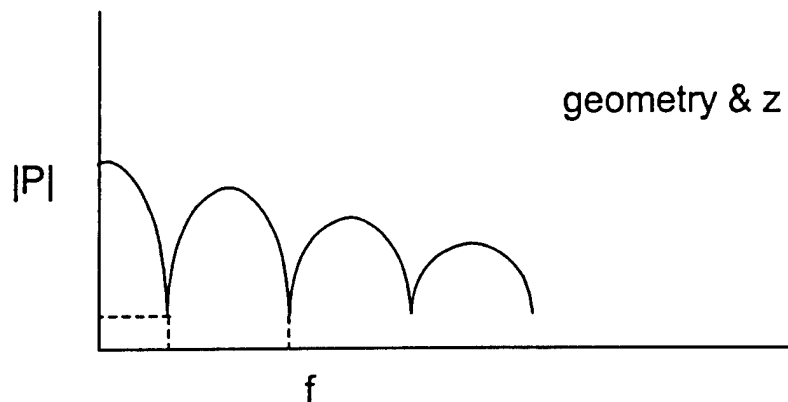
Lloyd's Mirror



$$P_{TOT} = \frac{e^{ik_o r_1}}{r_1} + \frac{Qe^{ik_o r_2}}{r_2} \quad 84.$$

$$Q = R + (1 - R) F(\omega, \psi, z) \quad 85.$$

$$z = z(\Omega, \sigma, q^2) \quad 86.$$



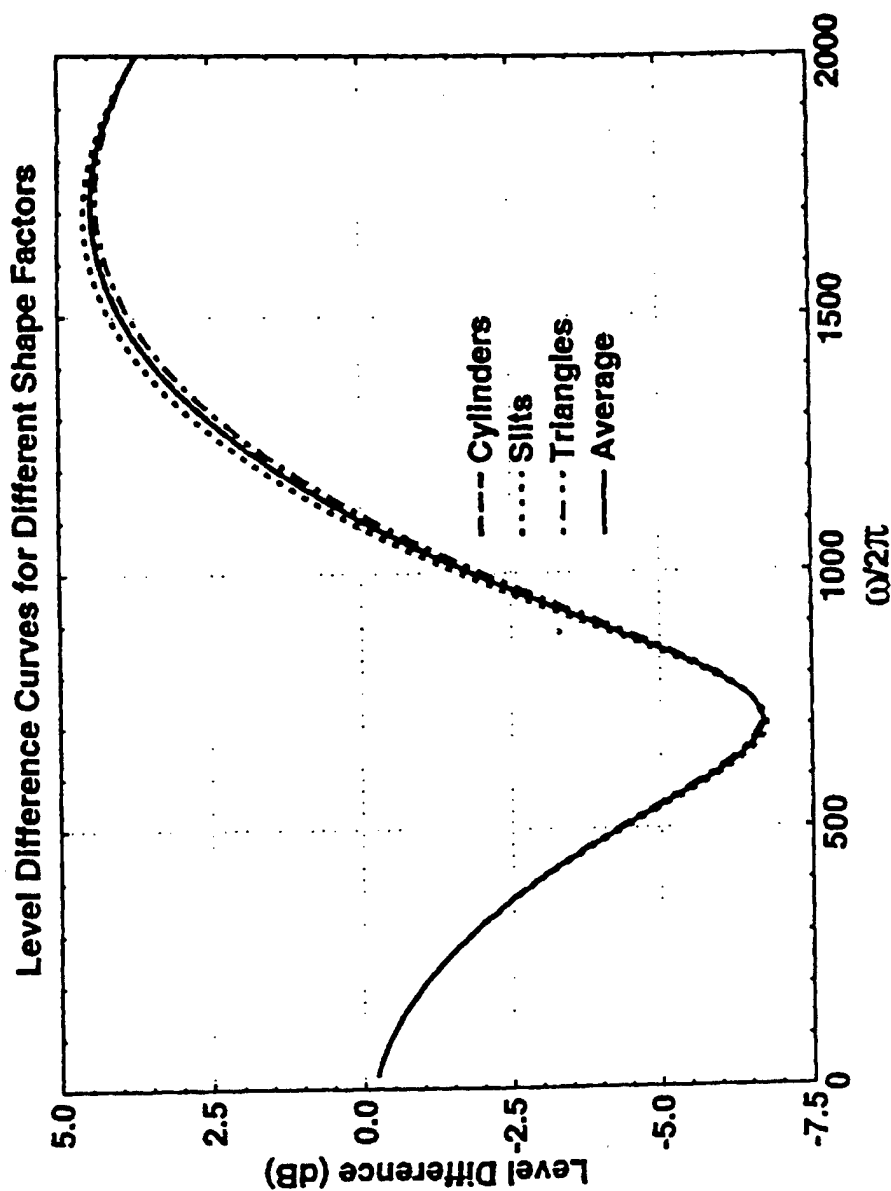


FIG. 2. This figure shows the effect of varying the shape parameter az in calculated level difference spectra. The percent range of variation about the average value is from 92% (for slits) to 107% (for equilateral triangles). There is very little effect on either the location or depth of the primary dip. The geometry used is source height = 40 cm, range = 1.63 m, top microphone at 40 cm, bottom microphone at 10 cm. The rigid-frame porous parameters are $\sigma_b = 75\,000$ (N s/m⁴), $q^2 = 1.90$, and $\Omega = 0.37$.

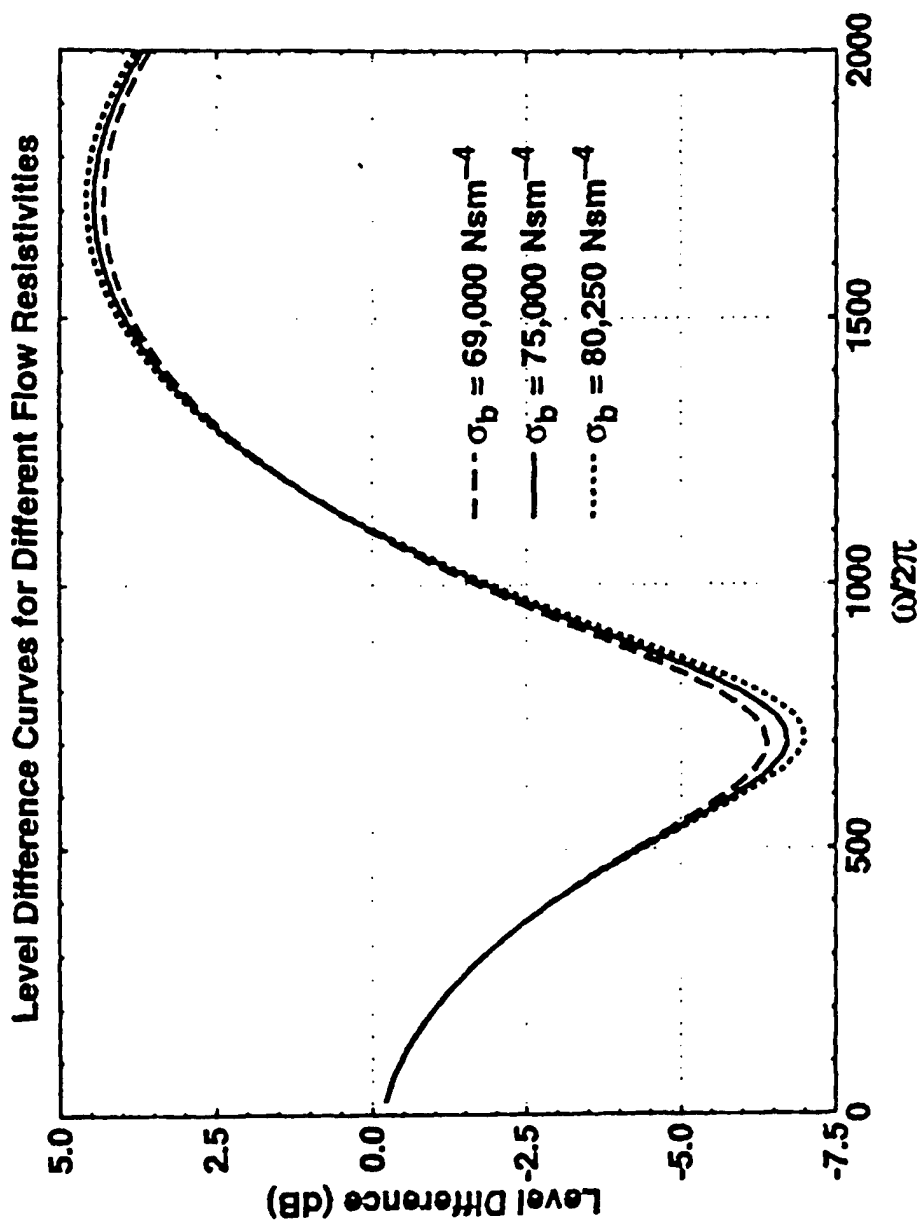


FIG. 3. This figure shows the variation in calculated level difference spectra due to changes in the flow resistivity. The percent variation in σ_b used is the same as that for a_z in Fig. 2. Note that the depth of the dip is much more sensitive to σ_b than to a_z . For the frequency range of interest (up to 1500 Hz) the choice of a_z will not greatly affect the analysis of level difference data. The same geometry was used in this figure as in Fig. 2. Except for σ_b , the same porous parameters were used with $a_z = 1.535$.

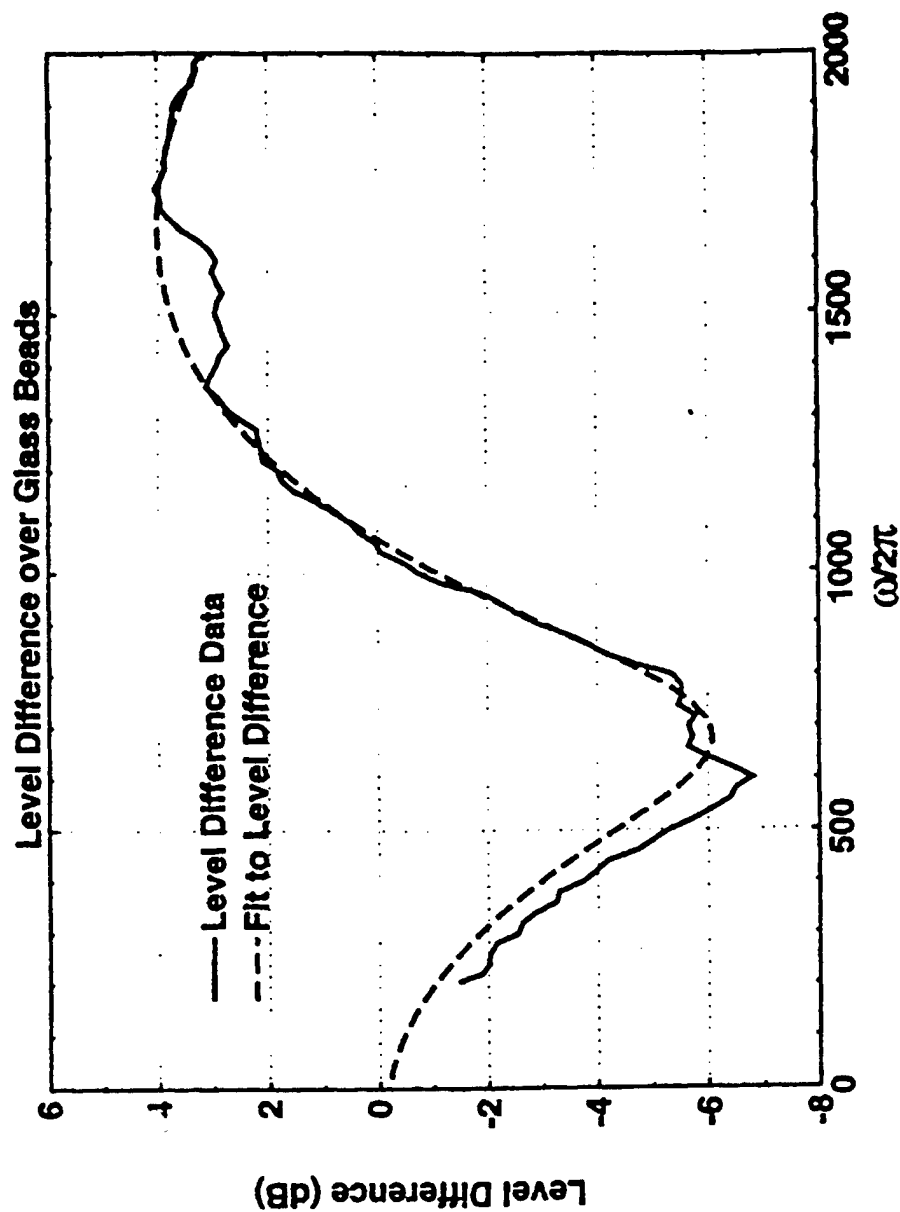


FIG. 7. A level difference spectrum measured over a bed of 500- μm glass beads. The dashed line is a fit over the frequency range of 500 Hz $< \omega/2\pi$ < 1500 Hz. The value of q^2 calculated from the fit $a_1 + c_1 \omega^2$ shown in Fig. 5 was used to allow a calculation of σ_b and Ω from the fit. For the low flow resistivity of the beads used, Eqs. (8) and (9) are not valid above 1500 Hz.

COUPLING OF SOUND INTO PORO-ELASTIC SOIL

- Airborne Source
- Pore Pressure Sensor – Probe Microphone
- Frame Velocity Sensor – Geophone

Rigid frame no longer appropriate

Consider Biot Model for poro-elasticity used in rock physics community

BIOT WAVE EQUATIONS

$$\nabla^2 (He - C\xi) = \frac{\partial^2}{\partial t^2} (\rho_e - \rho_f \xi) \quad 87.$$

$$\nabla^2 (Ce - M\xi) = \frac{\partial^2}{\partial t^2} (\rho_f e - m\xi) - \sigma F(s) \frac{\partial \xi}{\partial t} \quad 88.$$

H, C, M : elastic constants

ρ, ρ_f : frame and fluid density

$m = \frac{q^2 \rho_f}{\Omega}$, inertial coupling

σ : bulk flow resistivity

Dynamic Flow Resistivity

$$F(s) = -\frac{1}{4} \frac{\sqrt{-i} T[\sqrt{-i} s]}{1 - \frac{2}{\sqrt{-i} s T[\sqrt{-i} s]}} \quad 89.$$

where

$$T(\sqrt{-i} s) = \frac{J_1(\sqrt{-i} s)}{J_0(\sqrt{-i} s)} \quad 90.$$

and

$$s = \sqrt{\frac{8\omega\rho_o q^2}{\sigma\Omega}} \quad 91.$$

Idealized volume element attached to the frame; frame and fluid dilatations are:

$$e = \nabla \cdot \bar{u}, \quad 92.$$

$u \equiv$ frame displacement

$e \equiv$ strain of volume element

$$\xi = \Omega(u - U) = \nabla \cdot \bar{w} \quad 93.$$

$U \equiv$ fluid displacement

$w \equiv$ relative fluid displacement

$\xi \equiv$ fluid volume moving in/out of volume element

Rectangular coordinates: $e = e_x + e_y + e_z$; $e_x = \frac{\partial u_x}{\partial x}$, etc.

Elastic constants: H, C, M

k_r : grain bulk modulus

k_f : fluid bulk modulus

k_b : frame bulk modulus

$$H = \frac{(k_r - k_b)^2}{(D - k_b)^2} + k_b + \frac{4}{3}\mu \quad C = k_r \frac{k_r - k_b}{D - k_b} \quad 94.$$

$$D = k_r \left(1 + \Omega \left(\frac{k_r}{k_f} - 1 \right) \right) \quad M = \frac{k_r^2}{D - k_b} \quad 95.$$

STRESS / STRAIN RELATIONS

Components of stress / strain tensor

$$\tau_{xx} = H e - 2\mu(e_x + e_z) - C\xi \quad 96.$$

$$\tau_{xx} = H e - 2\mu(e_z + e_x) - C\xi \quad 97.$$

$$\tau_{xy} = \mu\gamma_z \quad \gamma_z = \frac{1}{2} \left(\frac{\partial u_x}{\partial y} + \frac{\partial u_y}{\partial x} \right) \quad 98.$$

$$\tau_{yz} = \mu\gamma_x \quad \gamma_x = \frac{1}{2} \left(\frac{\partial u_y}{\partial z} + \frac{\partial u_z}{\partial y} \right) \quad 99.$$

$$P_f = M\xi - C e \quad 100.$$

Suppose medium is a fluid

$$\Omega \rightarrow 1$$

$$P_f = M\xi = k_f \times \xi \quad 101.$$

For an elastic solid

$$\Omega \rightarrow 0$$

$$\tau_{zz} = H e - 2\mu(e_x + e_y) \quad 102.$$

$$H = k_r + 4\mu/3 \quad 103.$$

CONSIDER SOLUTIONS FOR WAVE EQUATION

Choose

$$\mathbf{e} = A e^{i(\ell x - \omega t)} \quad 104.$$

$$\xi = B e^{i(\ell x - \omega t)} \quad 105.$$

Substituting into wave equation yields

$$(H\ell^2 - \rho\omega^2)A + (\rho_f\omega^2 - C\ell^2)B = 0 \quad 106.$$

$$(C\ell^2 - \rho_f\omega^2)A + (m\omega^2 - M\ell^2 - i\sigma\omega F(s))B = 0 \quad 107.$$

$$\text{Det}() = 0 \quad 108.$$

Solution is quadratic in $\ell^2 \Rightarrow$ two roots or wave types

Biot Type I, II Waves

Ratio of amplitudes of fluid and frame motion

$$R_i = \frac{B_i}{A_i} = -\frac{(H\ell_i^2 - \rho\omega^2)}{(\rho_f\omega^2 - C\ell_i^2)} \quad 109.$$

Numerical results for “standard input” for soils

Type II Wave
Type I Wave

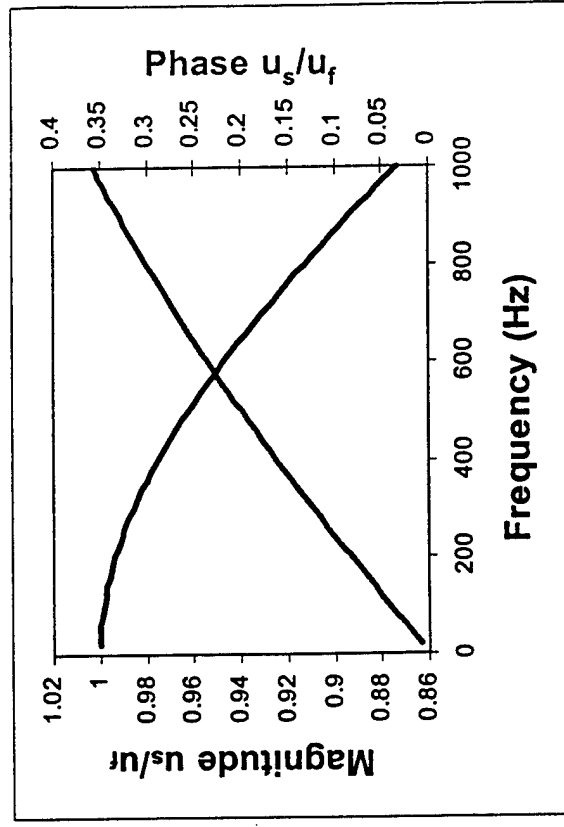
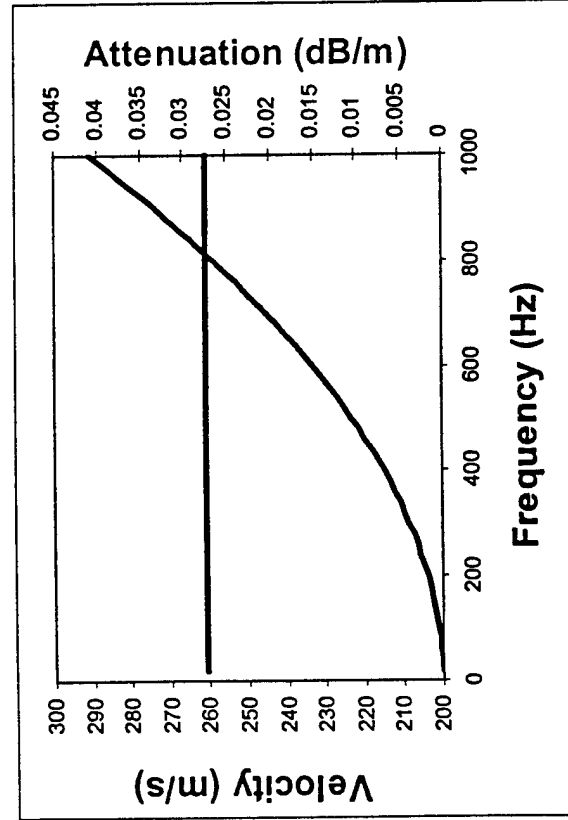
Highly dispersive
Seismic “p-wave”

Plona and Hickey Results

Type I : Compressional Wave ⇓ “Seismic Wave”

- Deforms both solid and fluid components
- Characterized by in phase “bulk” deformation

Air and Sand

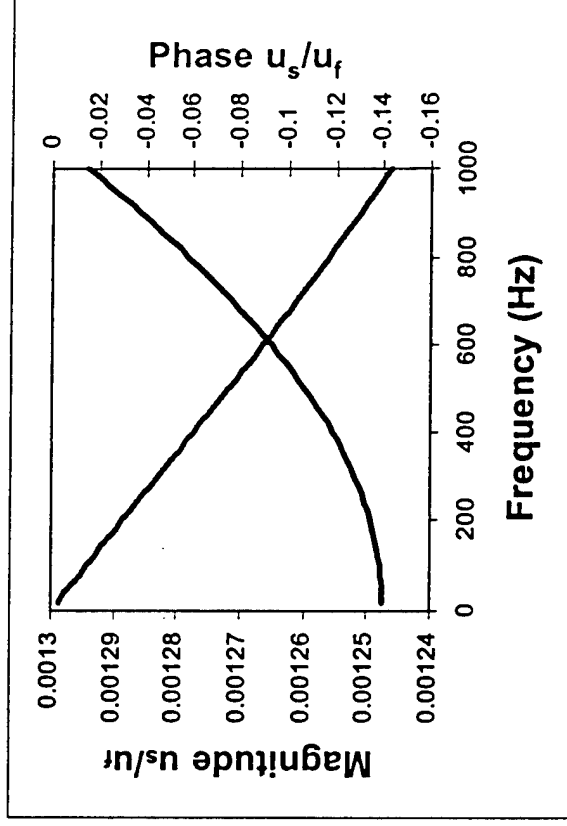
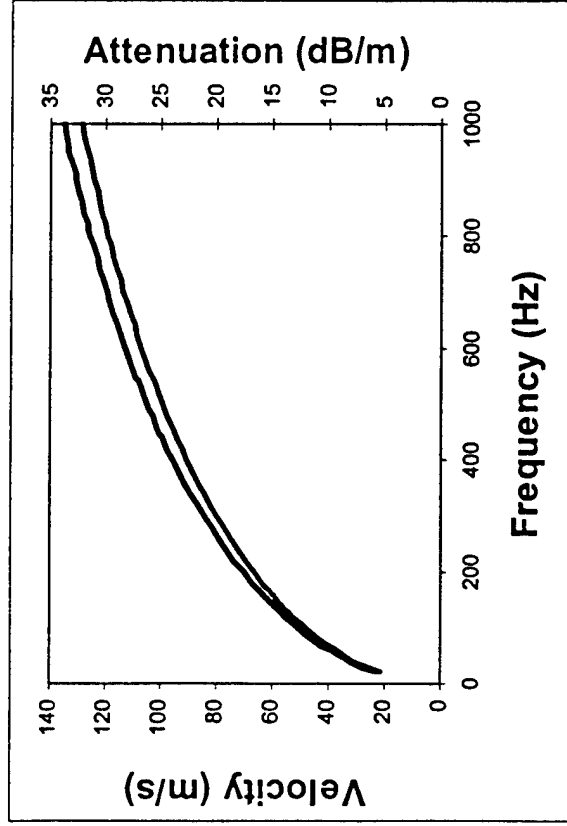


[Return Home](#)

Type II : Compressional Wave \Downarrow “Acoustic Wave”

- Deforms both solid and fluid components
- Characterized by large relative motion

Air and Sand



[Return Home](#)

GENERAL BOUNDARY CONDITIONS For POROUS MATERIALS INTERFACES

Continuity of:

1. σ_{nn}, u_n \perp component of stress, matrix velocity
2. σ_{ns}, u_s \parallel components of stress, velocity
3. s, u_n \perp component of pressure and fluid velocity,
 $s = -\Omega p$

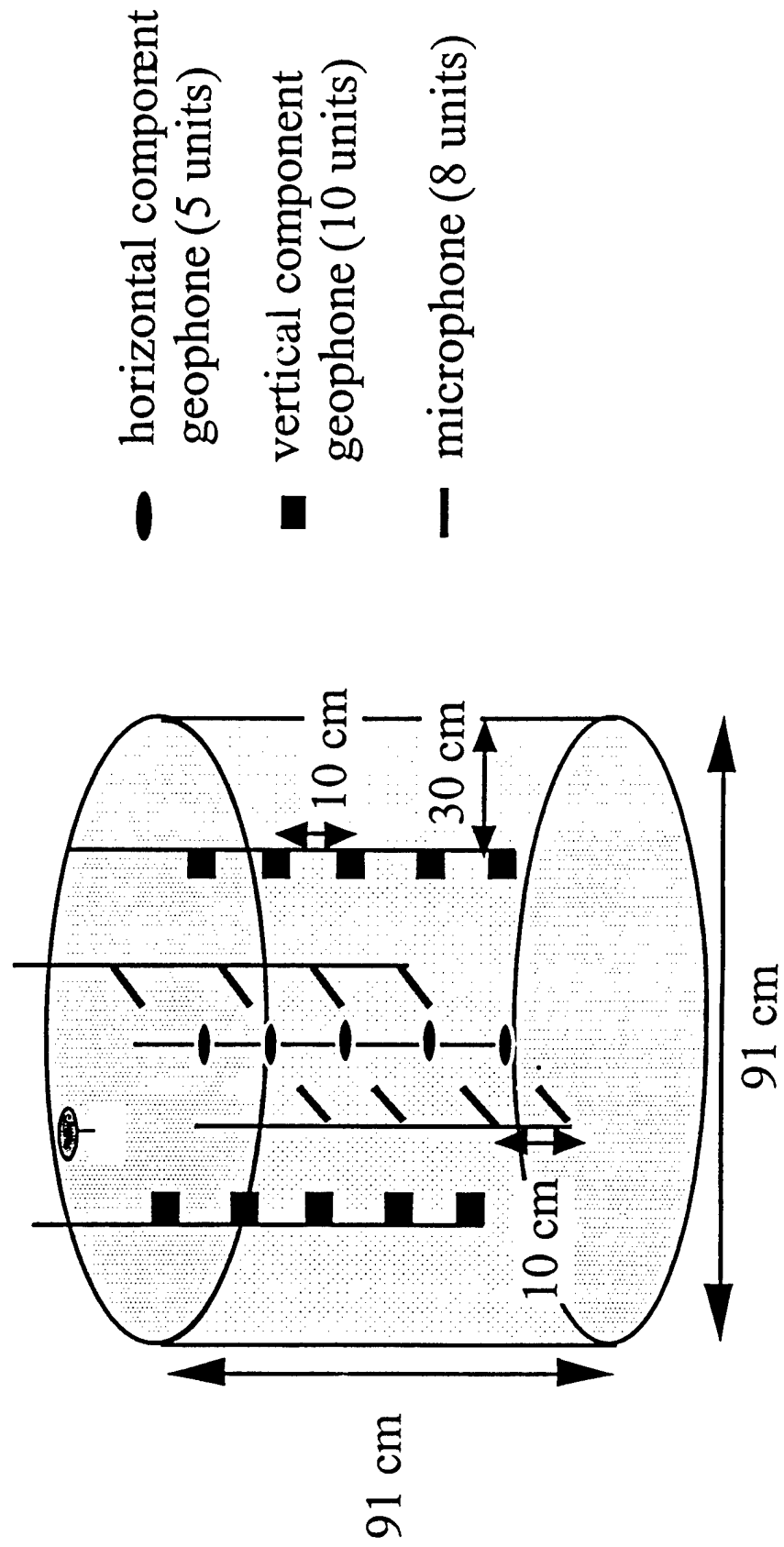
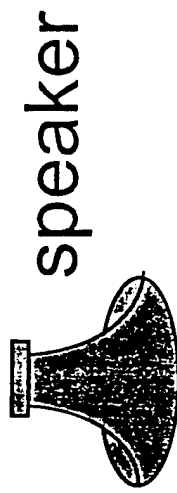
Porous-Solid over solid interface

- | | | |
|--|----------------------|------|
| 1. $\sigma_{nn} + s = \bar{\sigma}_{nn}$ | 2. $u_n = \bar{u}_n$ | 110. |
| 3. $\sigma_{ns} = \bar{\sigma}_{ns}$ | 4. $u_s = \bar{u}_s$ | 111. |
| 5. $U_n - u_n = 0$ | | |

Fluid over porous surface

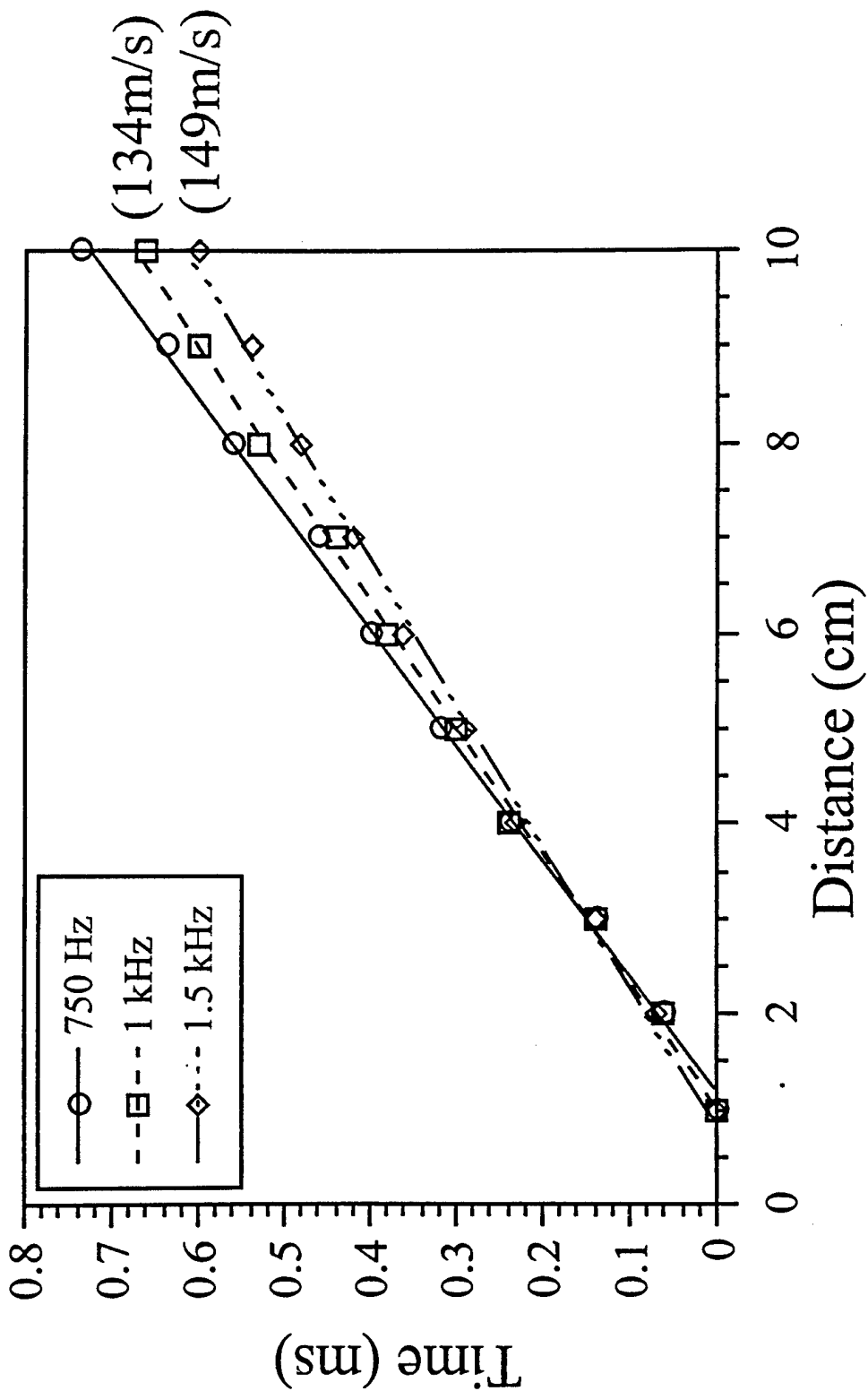
- | | | |
|---------------------------------|---|------|
| 1. $\sigma_{nn} + s = -\bar{p}$ | 2. $(1-\beta)u_n + \beta u_n = \bar{U}_n$ | 112. |
| 3. $\sigma_{ns} = 0$ | 4. $p = \bar{p}$ | 113. |

Lab experiment

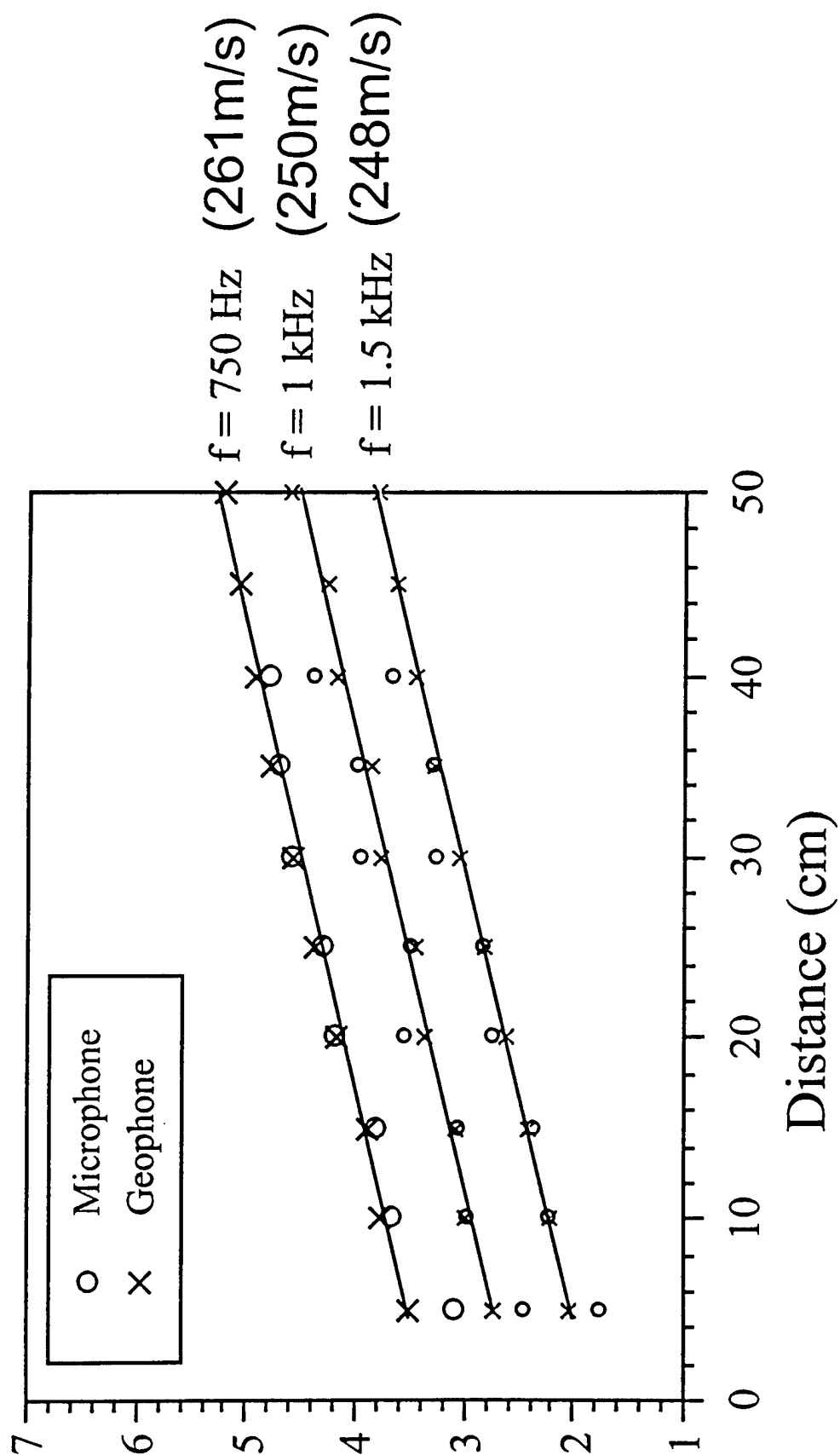


Loudspeaker source

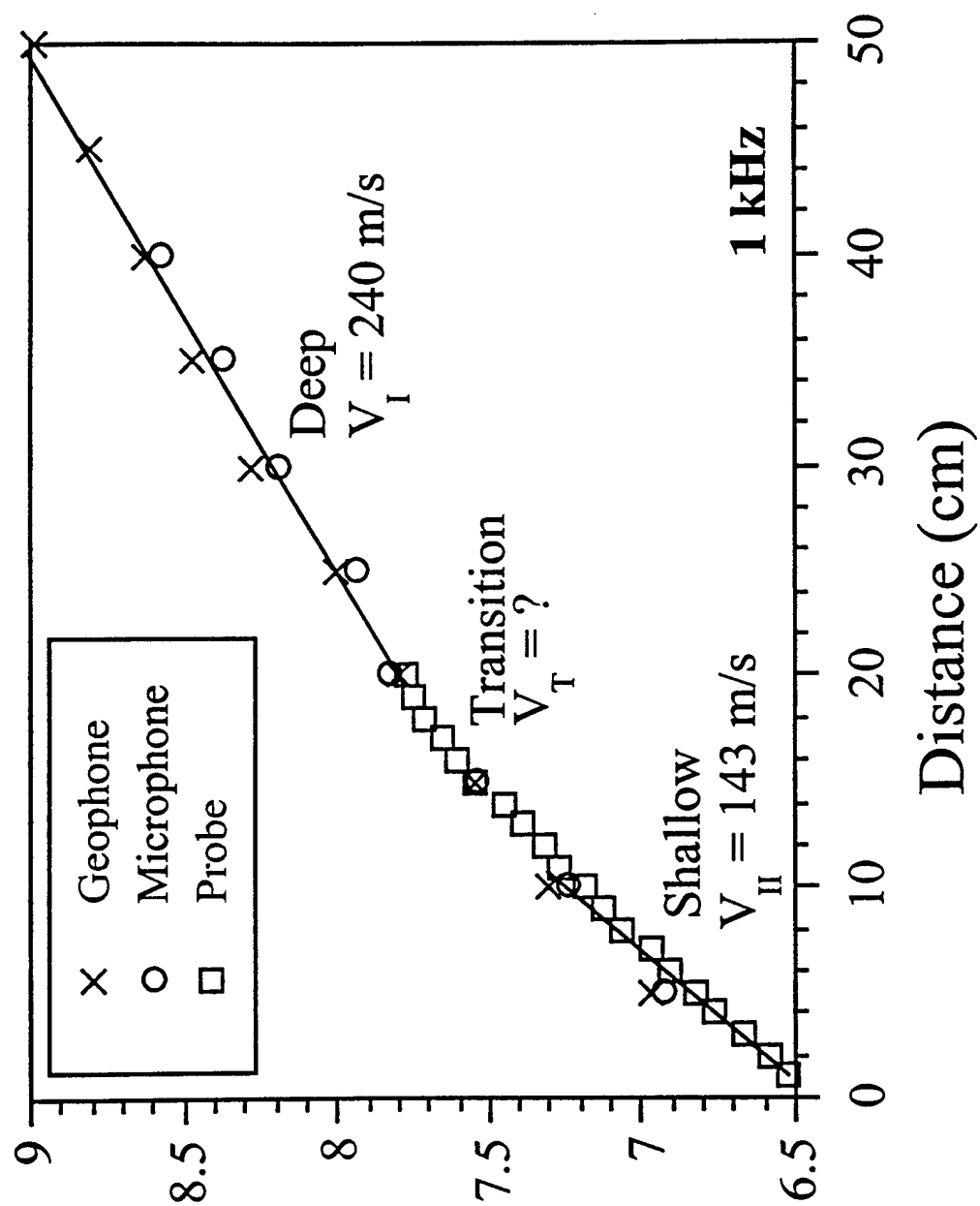
Shallow depth



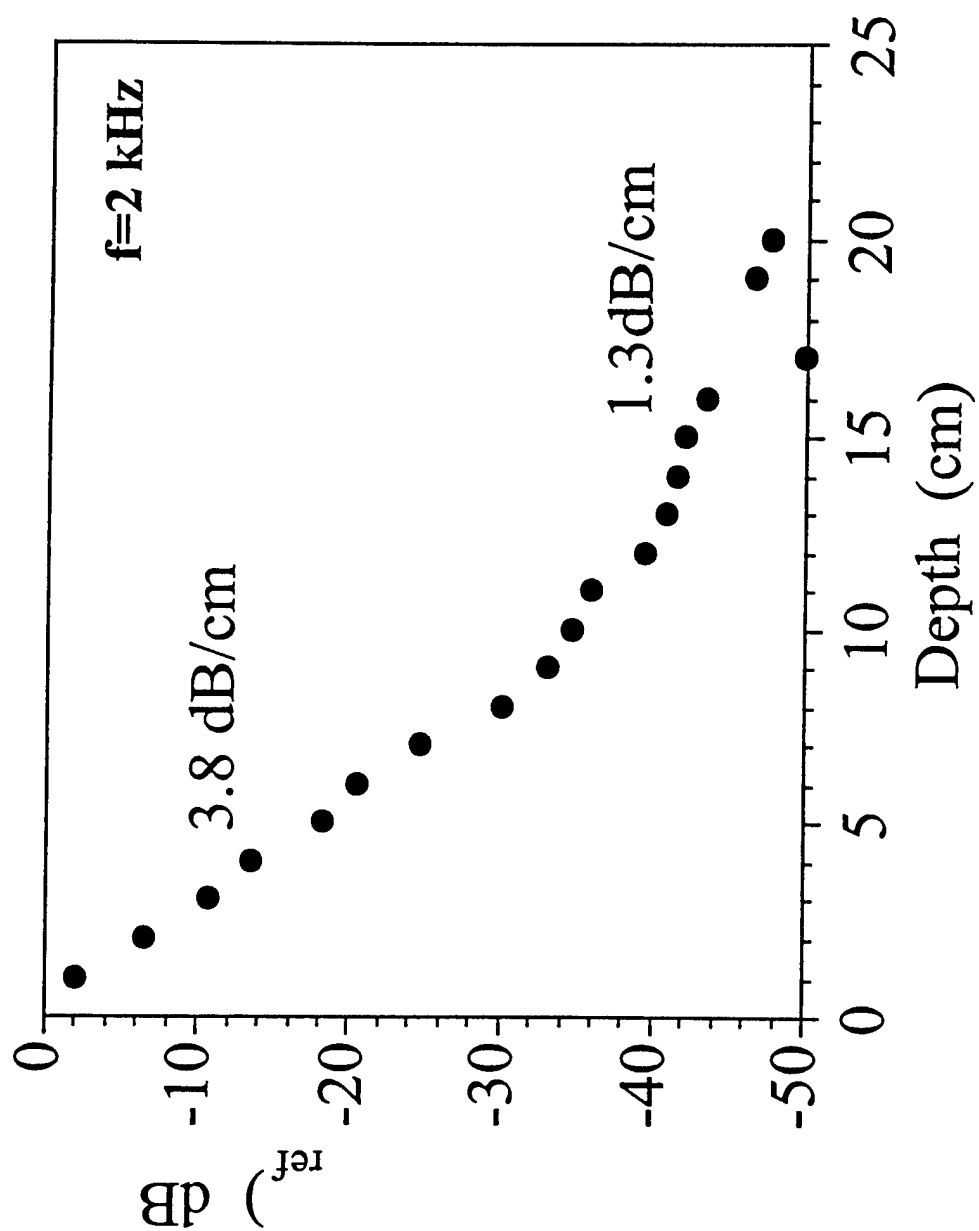
Shaker source



Loudspeaker source



Loudspeaker source



DEFINE QUANTITIES THAT ARE MEASURABLE

Acoustic Surface Impedance

$$P_{\text{surface}} = -ik_f \ell_i (B_I + B_R), \quad i = 1, 2 \quad 114.$$

$$\text{Vel}_{\text{surface}} = -i\omega \cos \theta_i (B_I - B_R), \quad i = 1, 2 \quad 115.$$

Impedance

$$Z = \frac{P}{V} = \frac{k_f \ell_i}{\omega \cos \theta_i} \frac{B_R + B_I}{B_R - B_I} \quad 116.$$

Pressure below surface in porous material

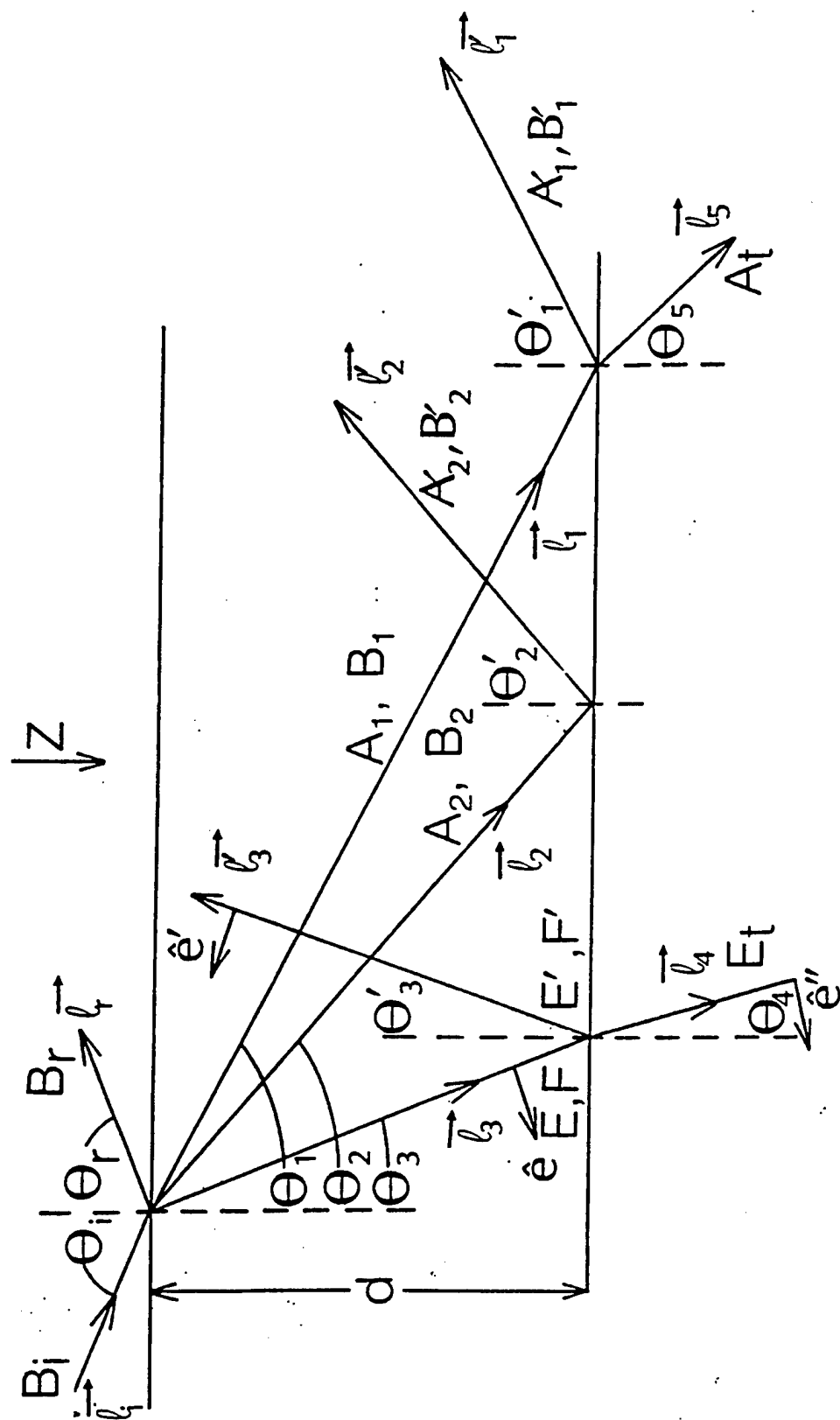
$$P_{\text{below}} = P_i + P_i', \quad i = 1, 2 \quad 117.$$

For down- and up-going waves

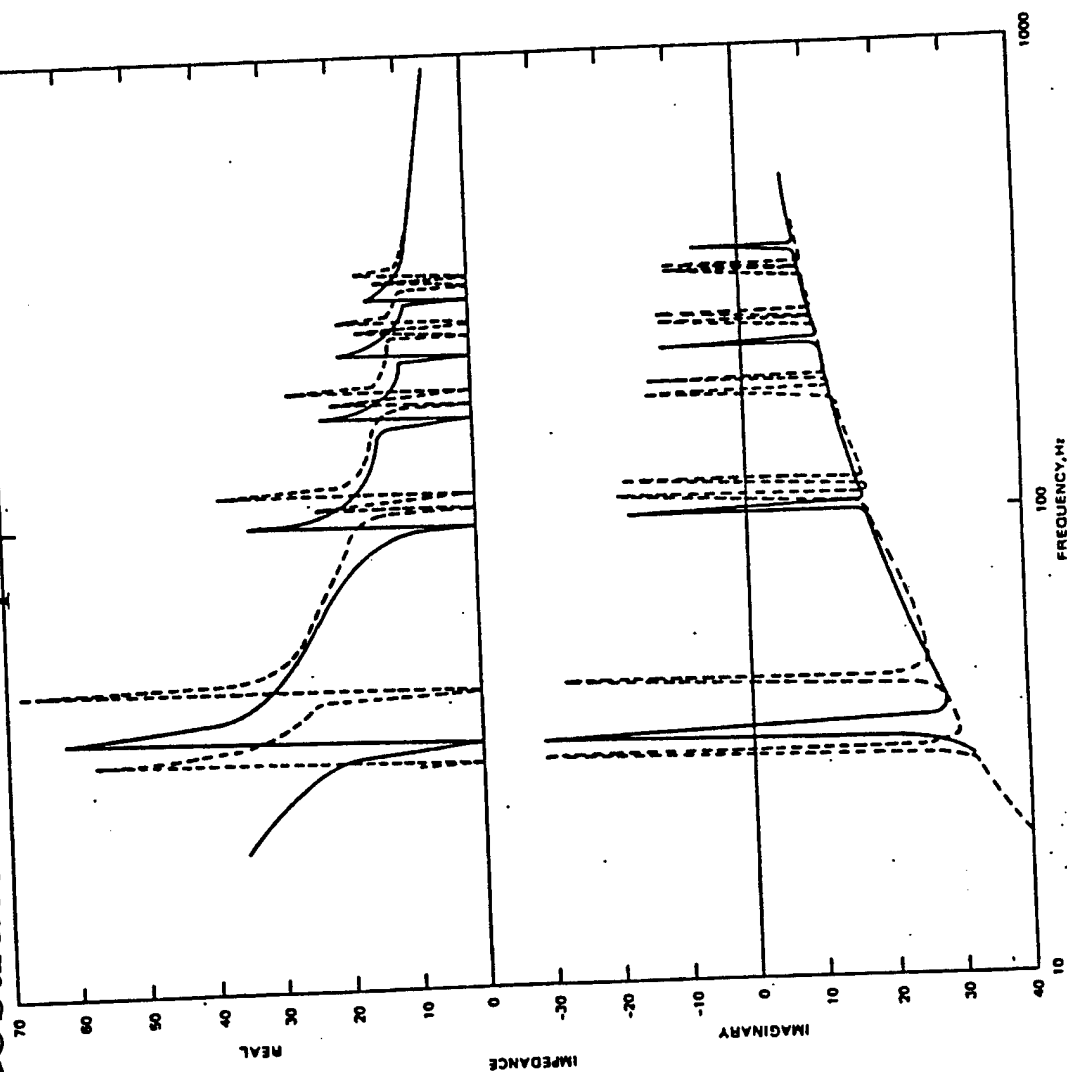
Velocity

V_n is the sum of \perp components of type 1 and 2 going up and down + shear

Plane Wave Layered Poro-Elastic Boundary Value Problem showing assumed wave types. A and B are Biot type I and II wave, E and F are shear wave amplitudesve.

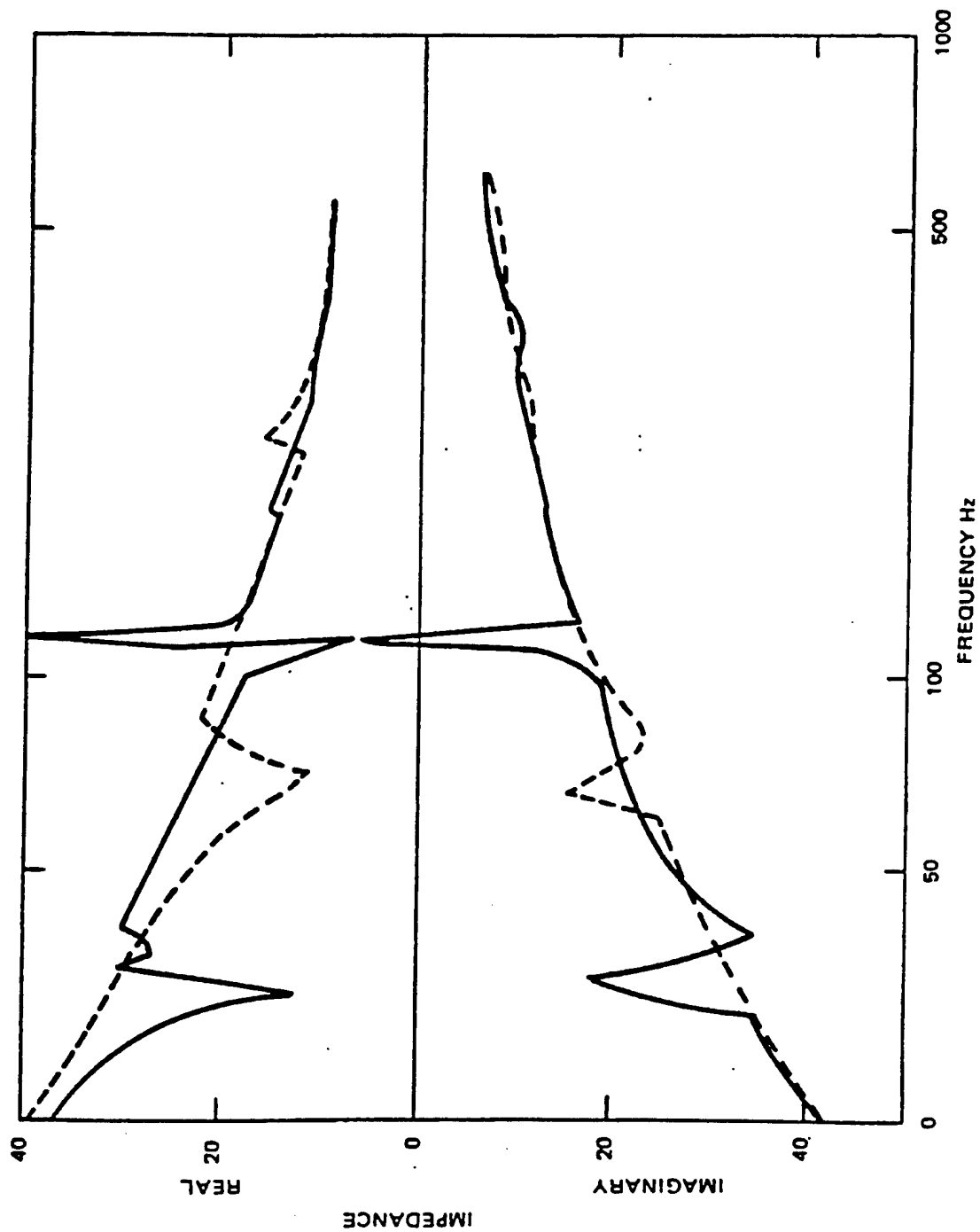


Biot poro-elastic layer impedance, with
substrate waves speeds increased 10 times.



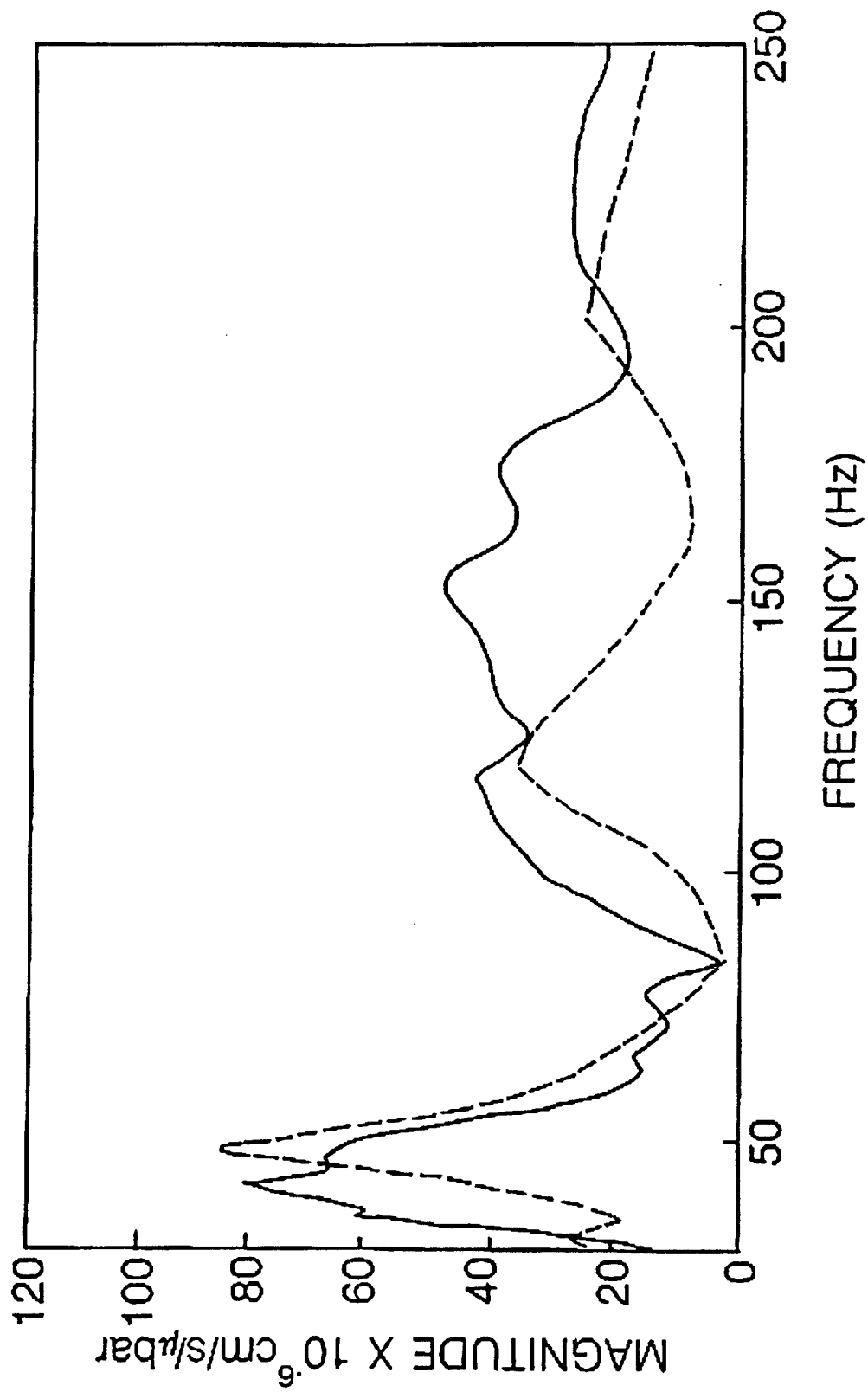
Angle of incidence: 0, 80 degree

Biot, poro-elastic layered impedance

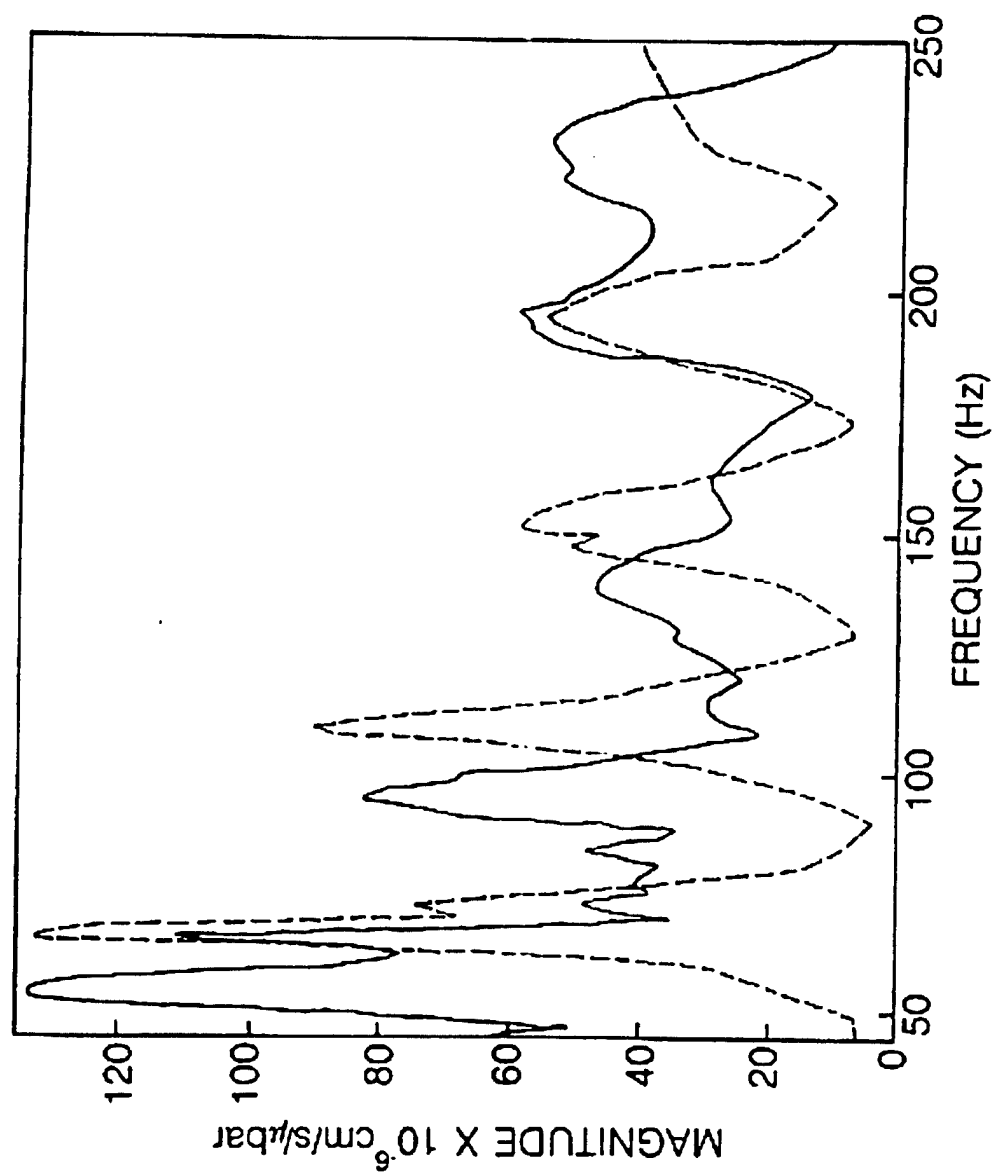


Angle of incidence: 68, 80 degree

Measured and predicted vertical seismic transfer function for a layered poro-elastic ground, loess soil



Measured and predicted vertical seismic transfer function
for a layered poro-elastic ground, dredges sand



Right Renal Artery
Right Renal Vein

Inferior Vena Cava

Aorta

Right Ureter

Bladder

Bladder Stone

Calculi
in
Ureter



Surgical Removal of Stones
From Renal Pelvis and Kidney

Staghorn Calculus

Forceps Basket Electro-
hydraulic Laser



Extracorporeal Shock Wave Lithotripsy

MAG-OX 400
(Form of Magnesium Oxide)
U.S.P. (Heavy)
400 mg.
215 mg. Elemental Magnesium
DOSAGE: 1 TABLET qd
With Meals

complements
of



BLAINE CO. INC. PHARMACEUTICALS

1405 JAMIE LANE
ERLANGER, KENTUCKY 40116

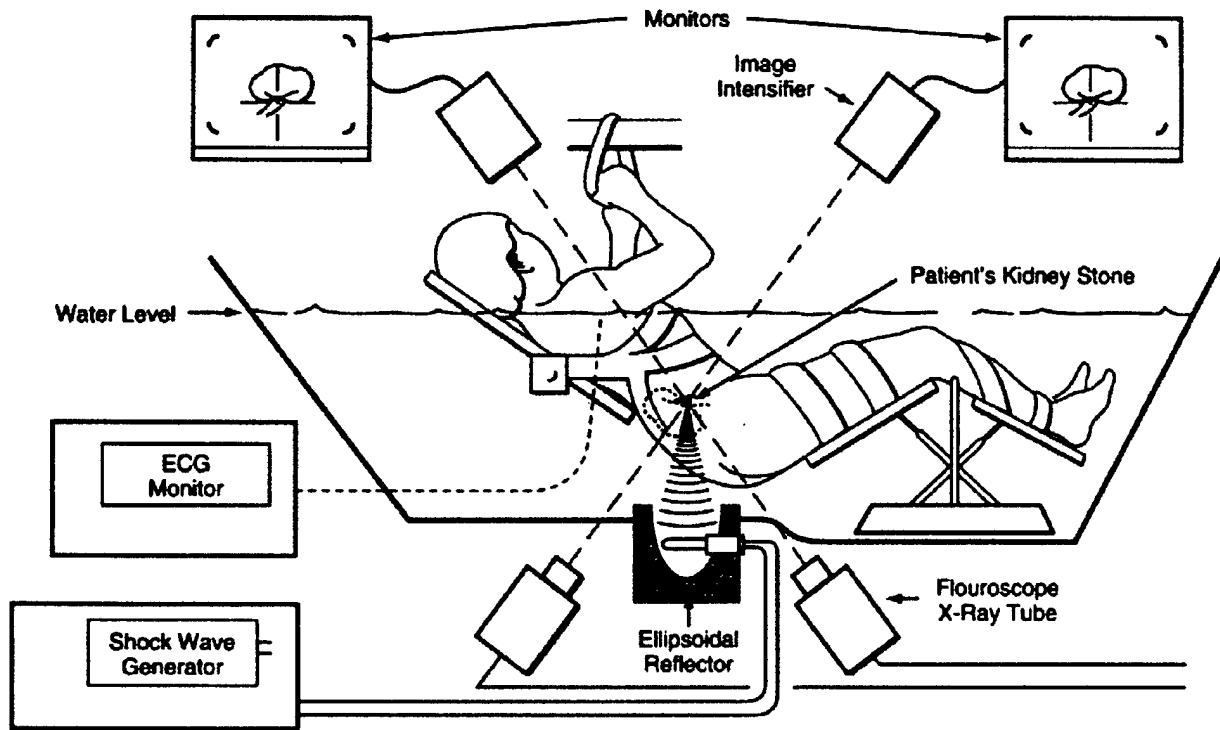
Phone: (606) 263-9437
Fax: (606) 263-9450

URO-MAG
(Form of Magnesium Oxide)
U.S.P. (Heavy)
140 mg.
64.5 mg. Elemental Magnesium
DOSAGE: 1 CAPSULE tid
With Meals

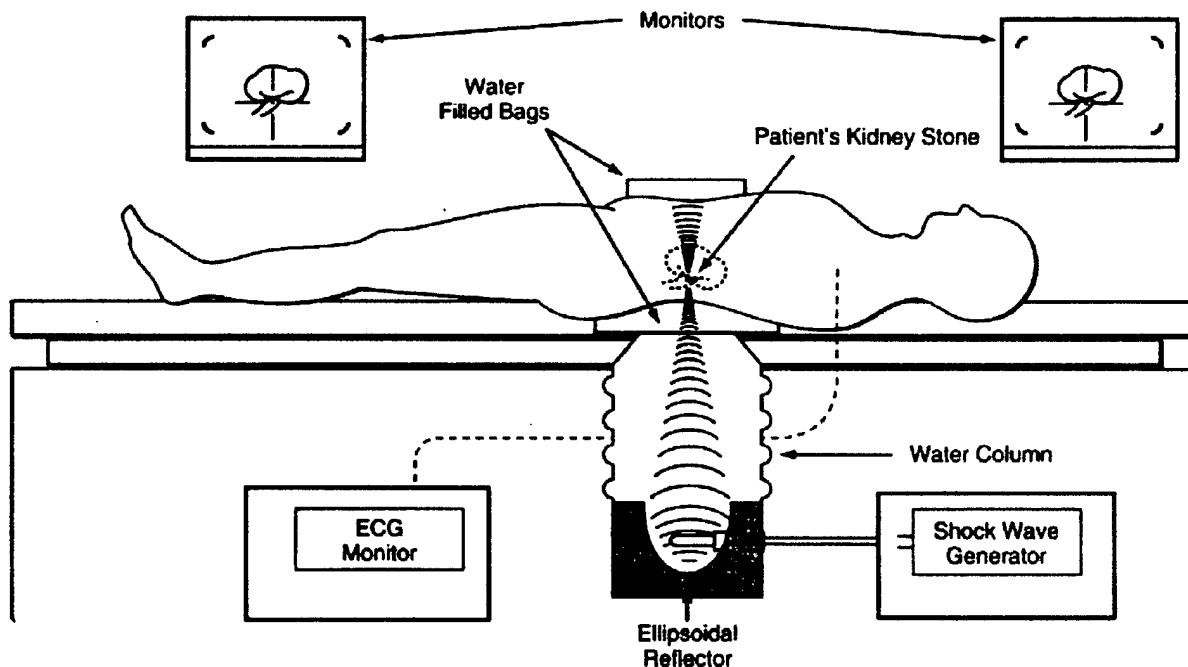
See reverse side for

MAGNESIUM BIBLIOGRAPHY AND ILLUSTRATION OF EXTRACORPOREAL SHOCK WAVE LITHOTRIPSY

First-Generation Extracorporeal Shock Wave Lithotripter



Second-Generation Extracorporeal Shock Wave Lithotripter



Oral Magnesium Oxide Supplements

MAG-OX 400

(Brand of Magnesium Oxide)
U.S.P. (Heavy)
400 mg.
241.3 mg. Elemental Magnesium
DOSAGE: 1 TABLET qd
With Meals

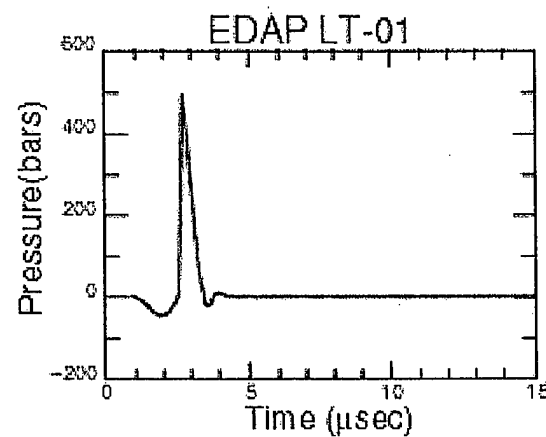
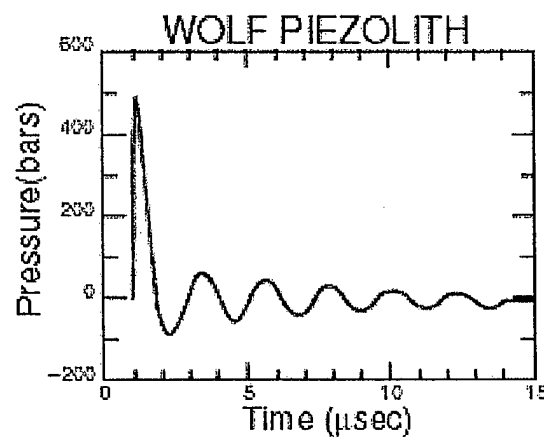
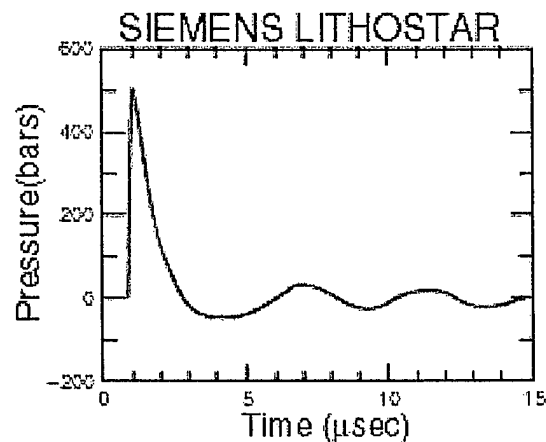
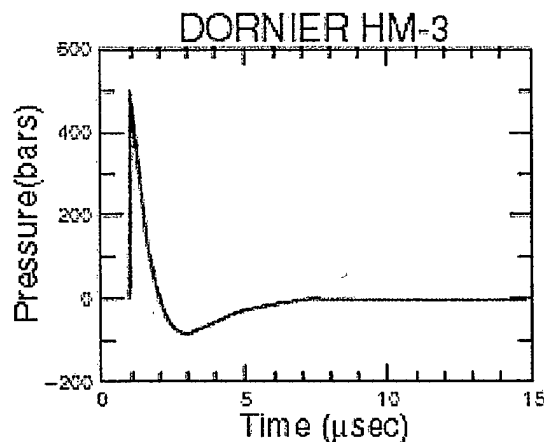
URO-MAG

(Brand of Magnesium Oxide)
U.S.P. (Heavy)
140 mg.
84.5 mg. Elemental Magnesium
DOSAGE: 1 CAPSULE t.i.d.
With Meals

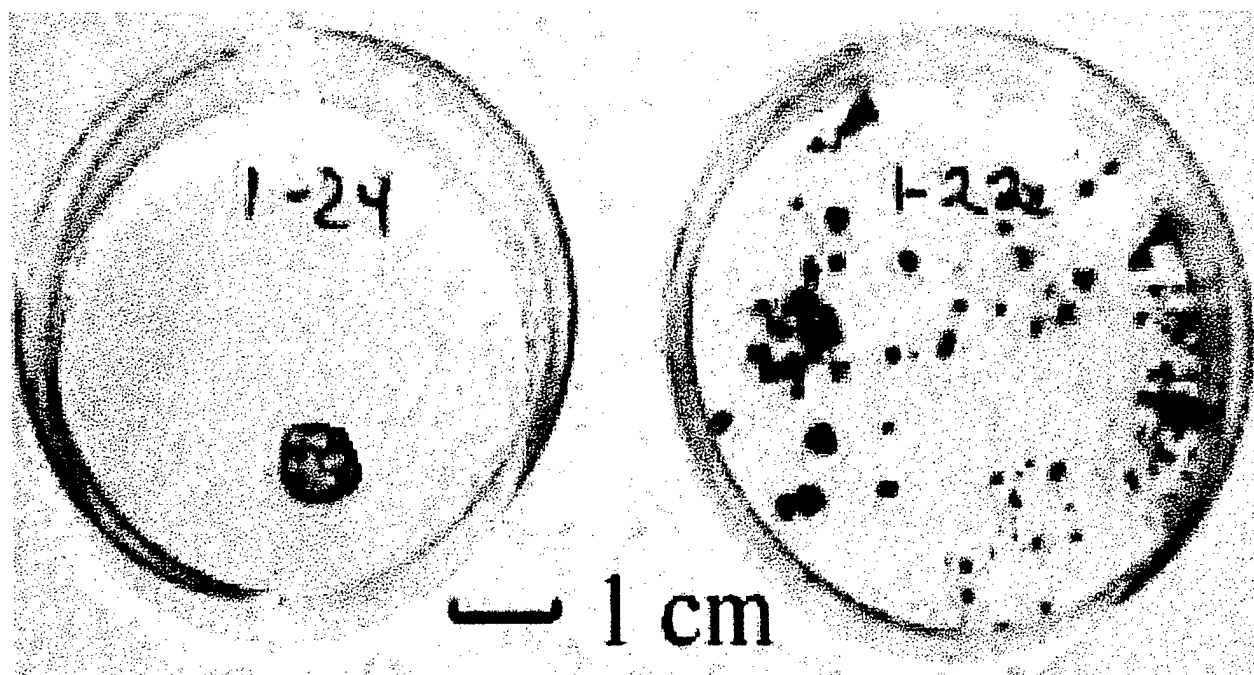
compliments
of

BLAINE
CO INC

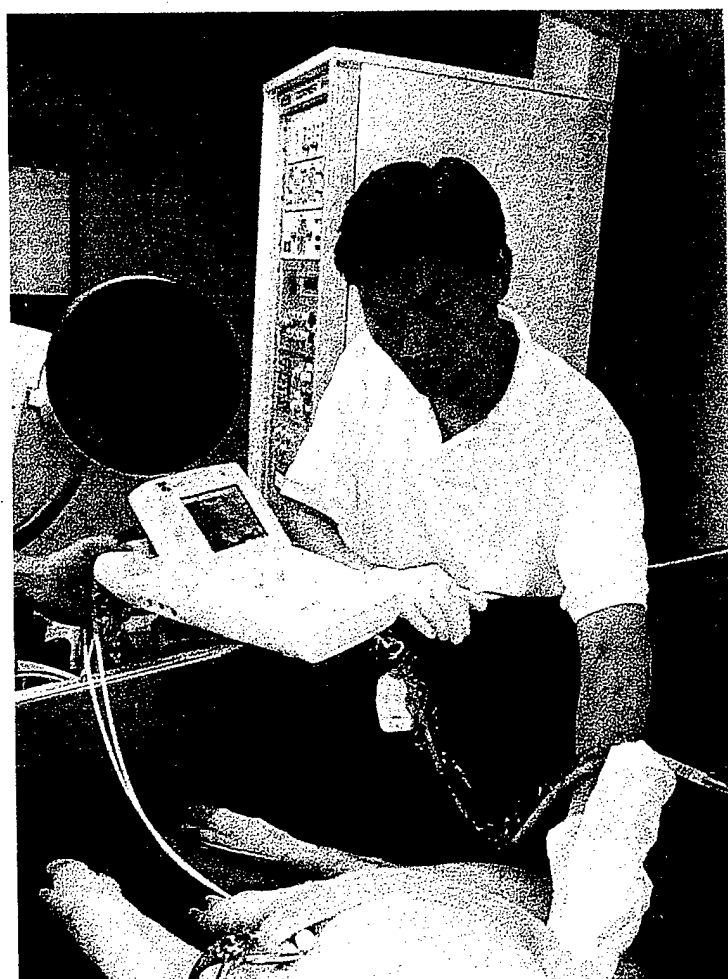
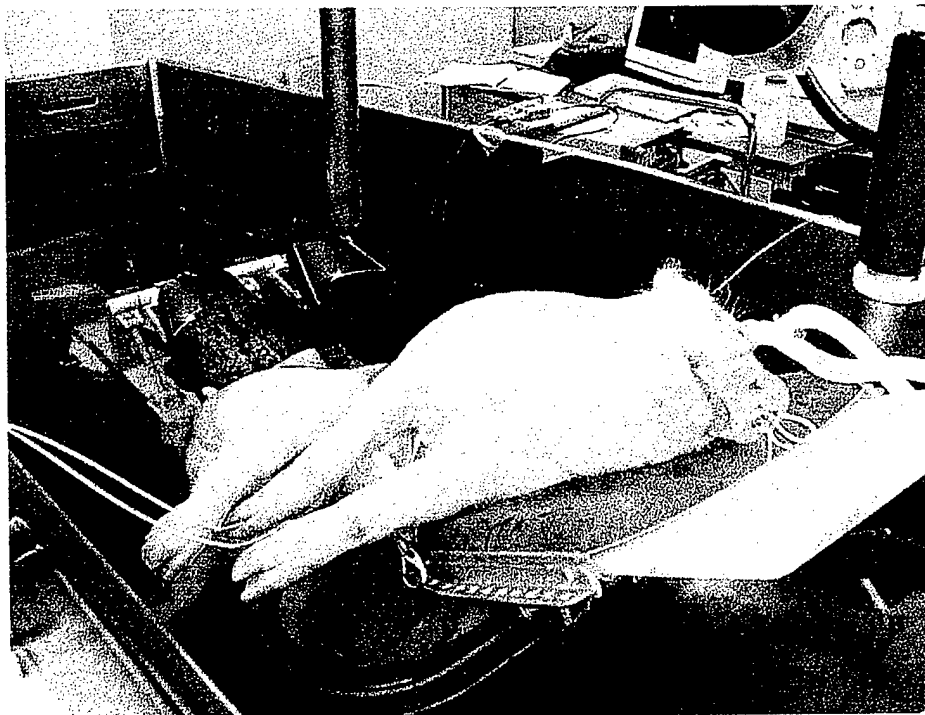
Idealized Pressure Waveforms Produced by Commercially Available Lithotripters



Lithotripsy is successful

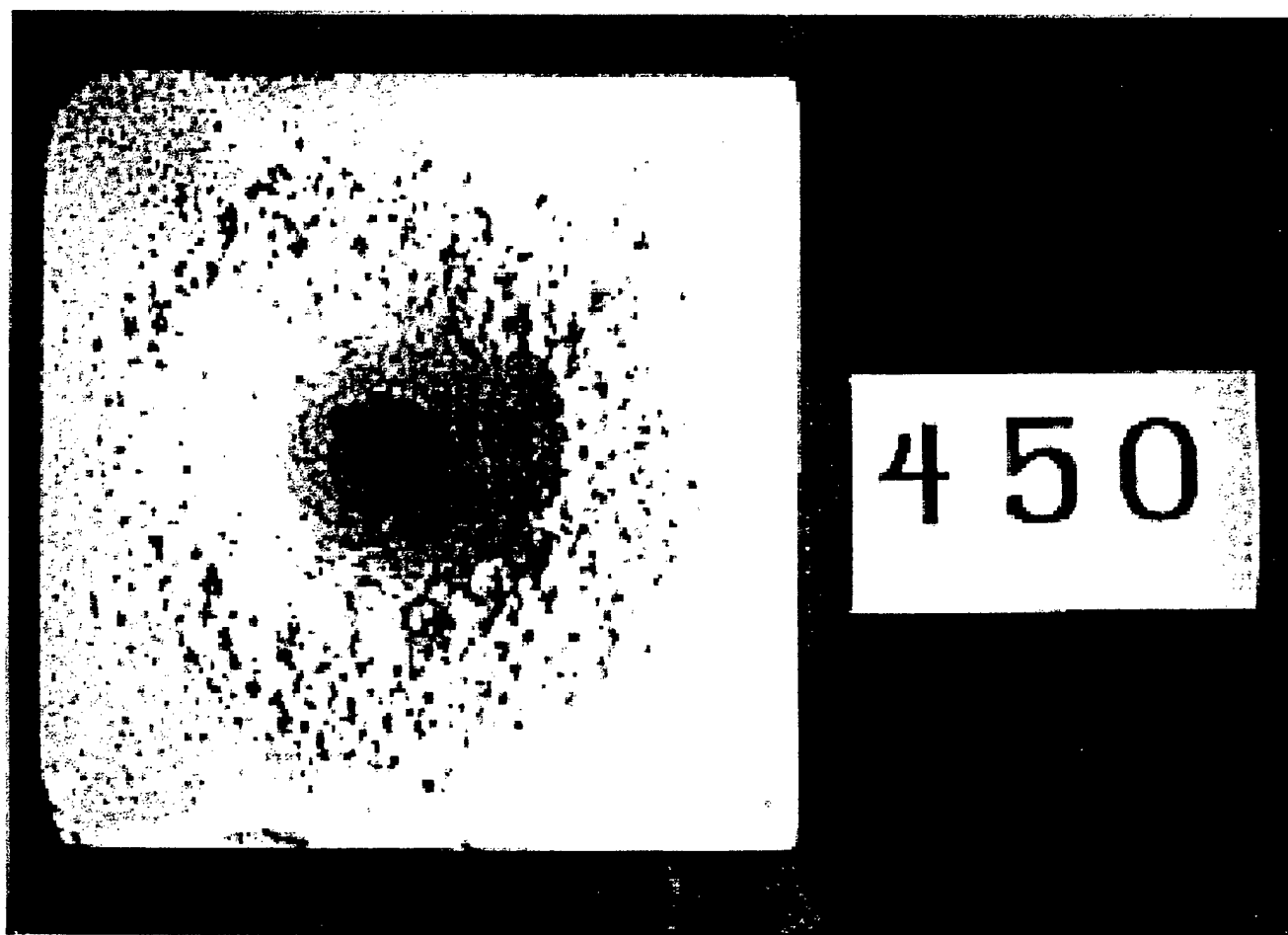
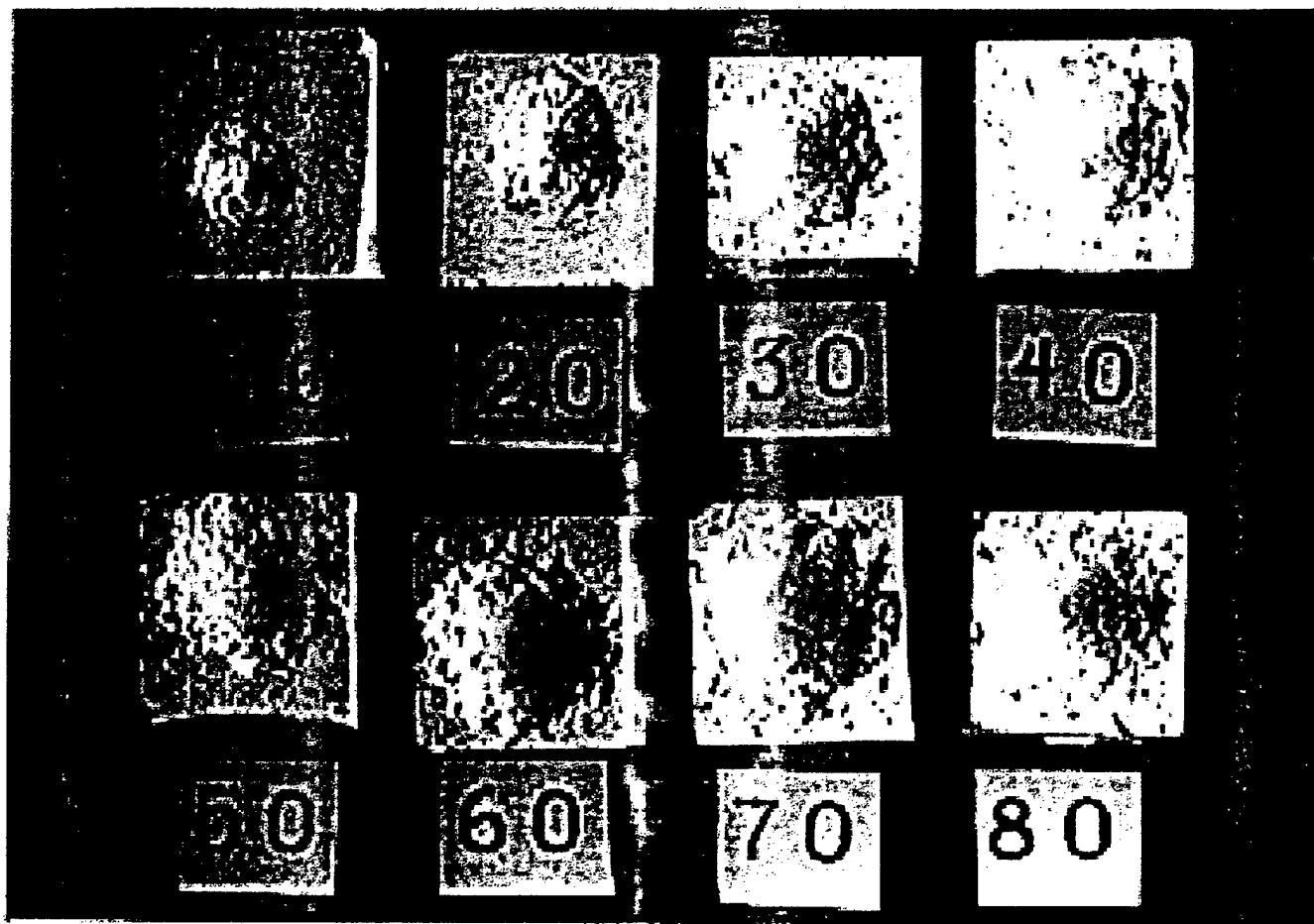


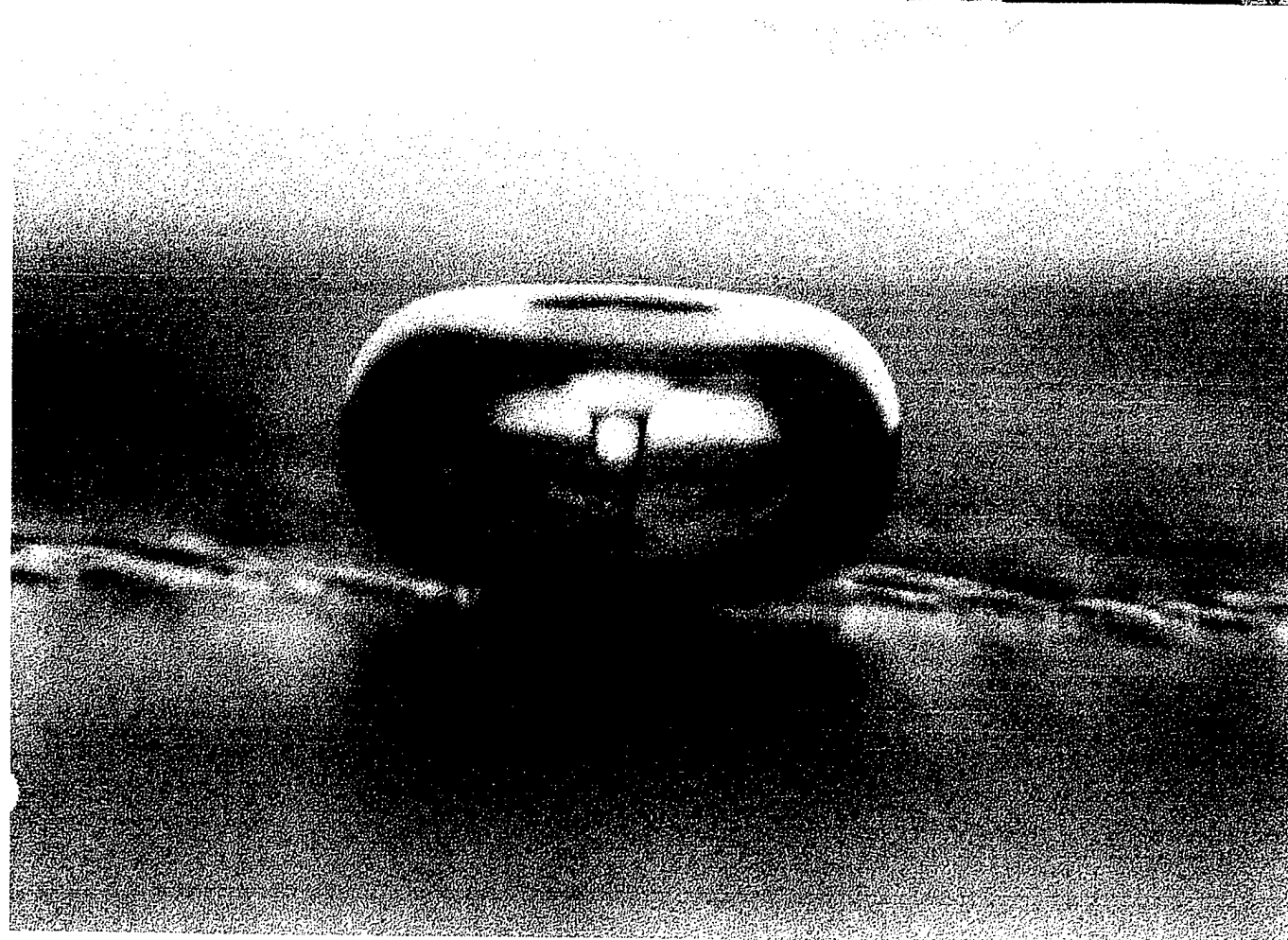
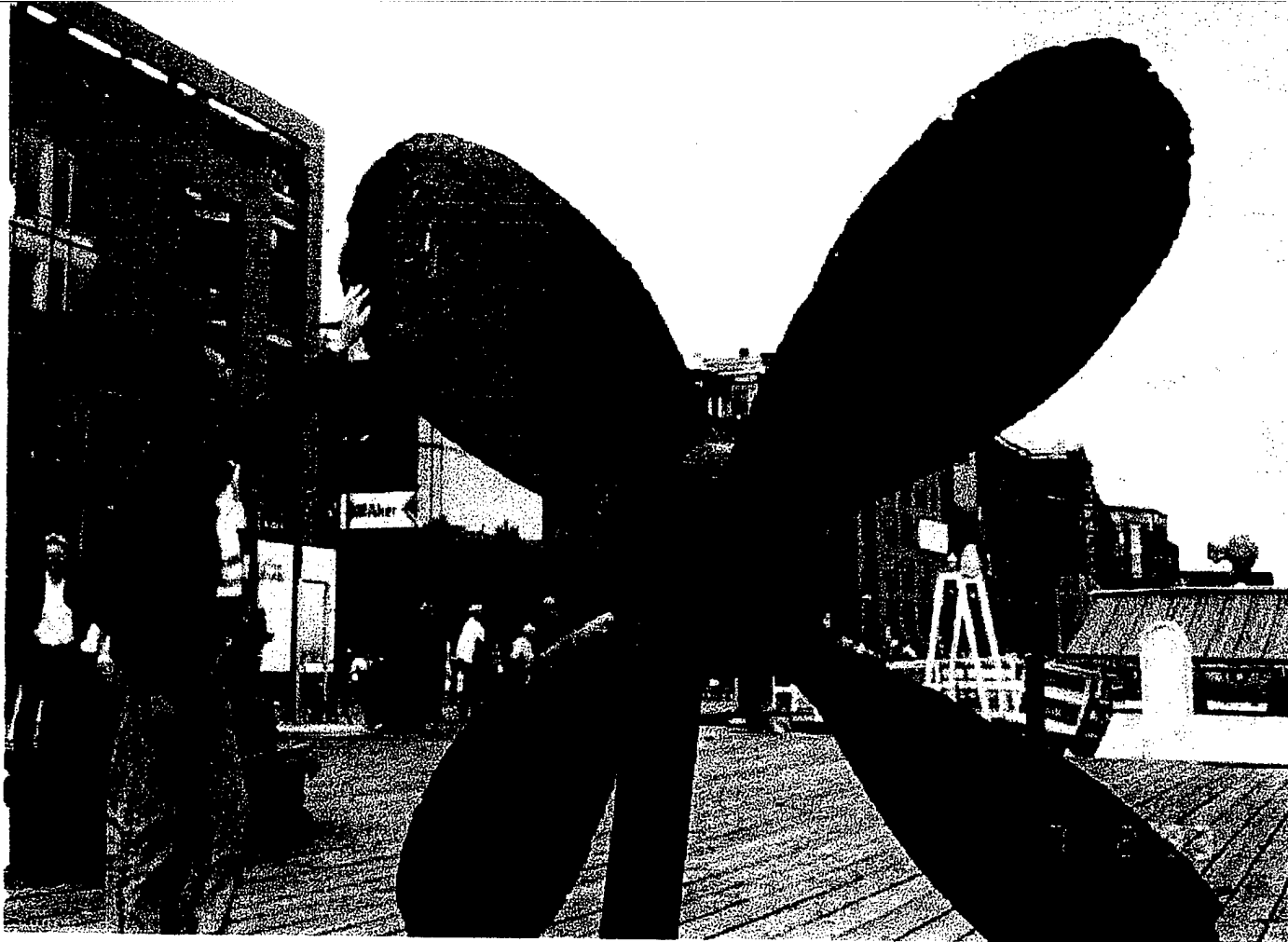
Animal experiments are necessary





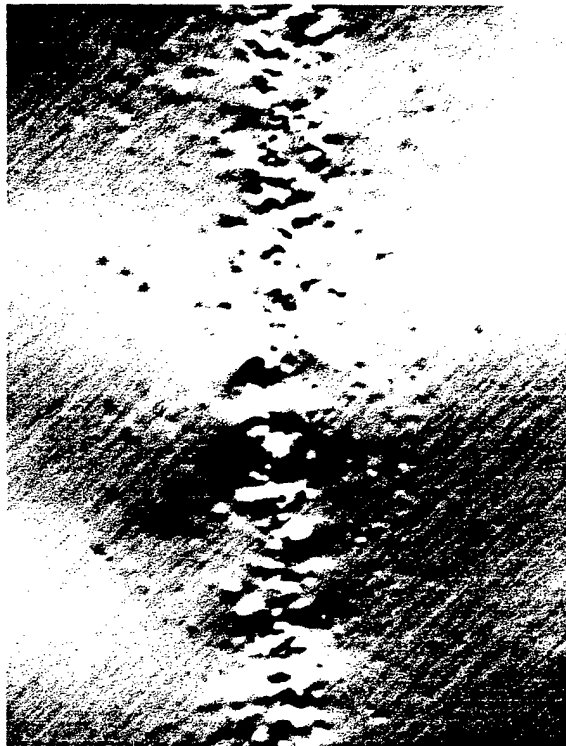
K283-001





Cavitation in a violent mechanical phenomenon

Pits in foil



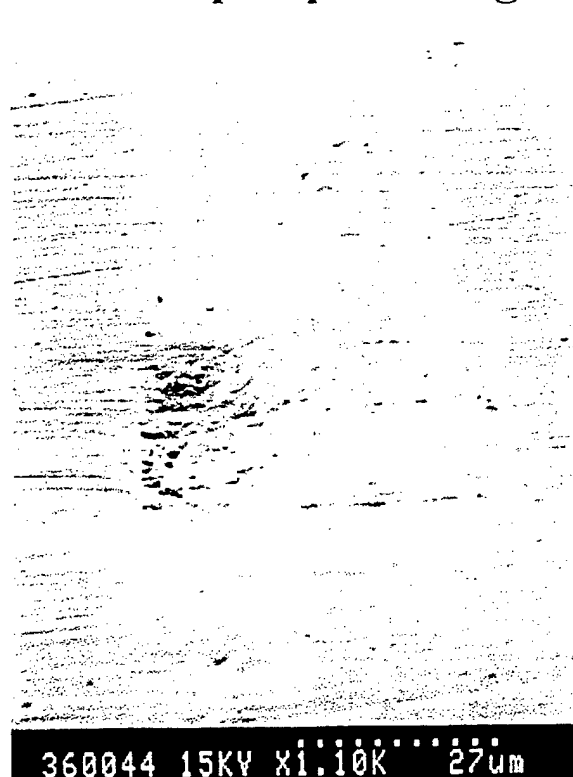
Close up of pit damage



Pits in metal plate



Close up of pit damage



Analytical Results

I. METHOD

The bubble radius versus time curves presented here are calculated by numerical integration (fourth-order Runge-Kutta) of the Gilmore-Akulichev formulation for bubble dynamics⁹:

$$\boxed{R \left(1 - \frac{U}{C}\right) \frac{dU}{dt} + \frac{3}{2} \left(1 - \frac{U}{3C}\right) U^2 = \left(1 + \frac{U}{C}\right) H + \frac{U}{C} \left(1 - \frac{U}{C}\right) R \frac{dH}{dR},} \quad \text{Bubble Eq.} \quad (1)$$

where

$$P = A(\rho/\rho_0)^m - B, \quad (2)$$

$$H = \int_{r_0}^{r(R)} \frac{dP}{\rho}, \quad (3)$$

$$C = [C_l^2 + (m-1)H]^{1/2}, \quad (4)$$

$$P(R) = P_g - 2\sigma/R - (4\mu/R)U, \quad (5)$$

and $U = dR/dt$, C is the speed of sound at the bubble wall, H is the enthalpy of the liquid, P and ρ are the time-varying pressure and density of the liquid, respectively. C_l is the infinitesimal speed of sound in the liquid, ρ_0 is the equilibrium liquid density, P_∞ is the pressure at infinity, $P(R)$ is the pressure at the bubble wall, P_g is the pressure of the gas within the bubble, defined below, P_0 is the ambient pressure of the surrounding liquid, σ is the surface tension, and μ is the coefficient of shear viscosity. Following Lastman and Wentzell,¹⁰ we choose $A = C_l^2 \rho_0 / m$ with $m = 7$ and $B = A - 1$.

The use of Gilmore's equation has two motivations. First, as shown by Vokurka,¹¹ Gilmore's equation is particularly well suited to conditions of high pressure in which the compressibility of the liquid plays an important role. Second, it was desirable to obtain a relatively large quantity of results in a reasonable time. In the formulation used in this study, a polytropic law is used to obtain the pressure inside a bubble; see Eq. (10). A more accurate formalism is available in which heat flow is calculated explicitly,¹² but unfortunately considerable time is involved in obtaining solutions.

The major difference between the present formulation for bubble dynamics and that of Prosperetti *et al.*¹³ lies in the inclusion of thermal damping in the latter. Because thermal damping is not an important process in the case of shock wave induced cavitation, Gilmore's equation provides results with reasonable accuracy. Both viscous and acoustic radiation damping are considered here and, as will be seen, the latter is the primary damping mechanism.

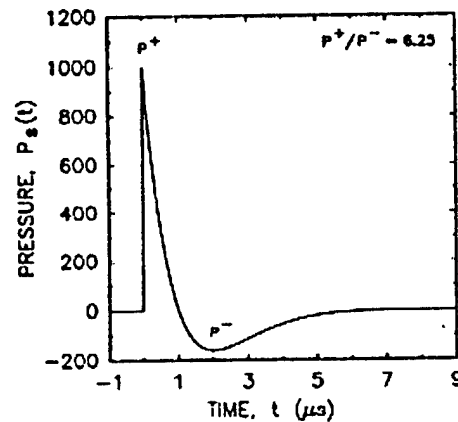


FIG. 1. Modeled form of ESWL pressure waveform as generated by Eq. (6).

The instantaneous number of moles of gas n in a bubble may be calculated from the zero-order solution to the diffusion equation given by Eller and Flynn,¹⁴ their Eq. (24):

$$\boxed{n = n_0 - 4(\pi D)^{1/2} \int_0^t F(\tau') (\tau - \tau')^{-1/2} d\tau'.} \quad (7)$$

The arguments of the integral, a convolution obtained from solution by Laplace transforms, have been interchanged to facilitate the necessary numerical solution. In Eq. (7), D is the diffusion constant of the gas in the liquid, n_0 is the number of moles of gas initially present in the bubble, and

$$\tau = \int_0^t R^2(t') dt', \quad (8)$$

$$F(\tau) = C_0(P_g/P_0) - C_l, \quad (9)$$

where

$$P_g = \left(P_0 + \frac{2\sigma}{R_0}\right) \frac{n}{n_0} \left(\frac{R_0}{R}\right)^{3\eta} \left(\frac{R_{0m}}{R_0}\right)^{3(\eta-1)}, \quad (10)$$

R_0 is the initial equilibrium radius of the bubble, R_{0m} is the time-varying equilibrium bubble radius, η is the polytropic exponent of the gas, C_0 is the saturation concentration of the gas in the liquid, and C_l is the initial concentration of gas in the liquid far from the bubble.

after Eller, JASA 86, 215 (80)

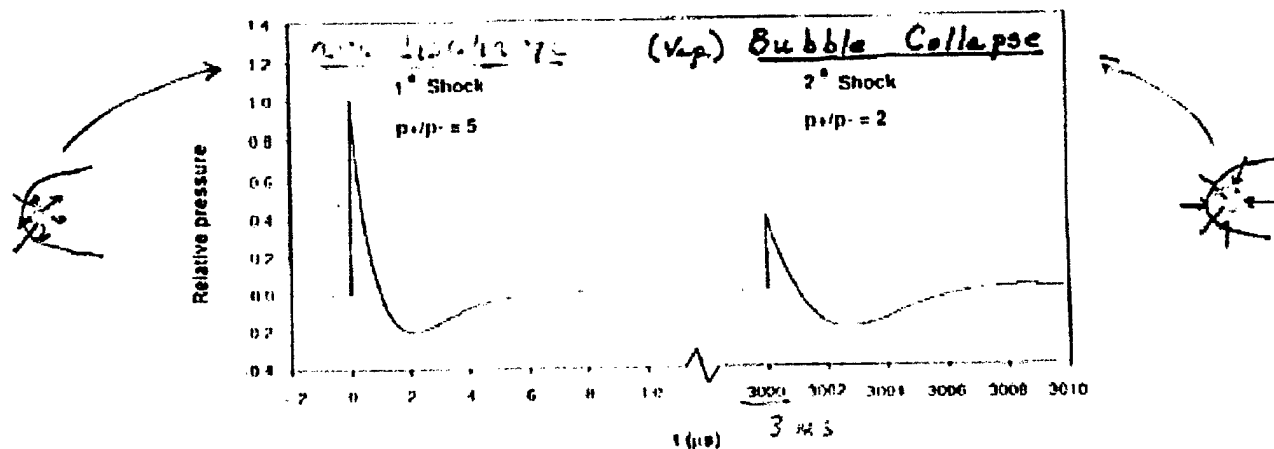


Fig. 1. The normalized pressure waveforms of the first two shocks emitted by an electrohydraulic lithotripter assumed in the theoretical model. Following a single discharge of the lithotripter, a primary shock (1°) of large amplitude (typically, $p_1 = 50$ MPa) is followed some 3 ms later by a secondary shock (2°) of about 40% amplitude with a reduced asymmetry ratio. A third shock of considerably reduced amplitude is also occasionally observed but not considered here.

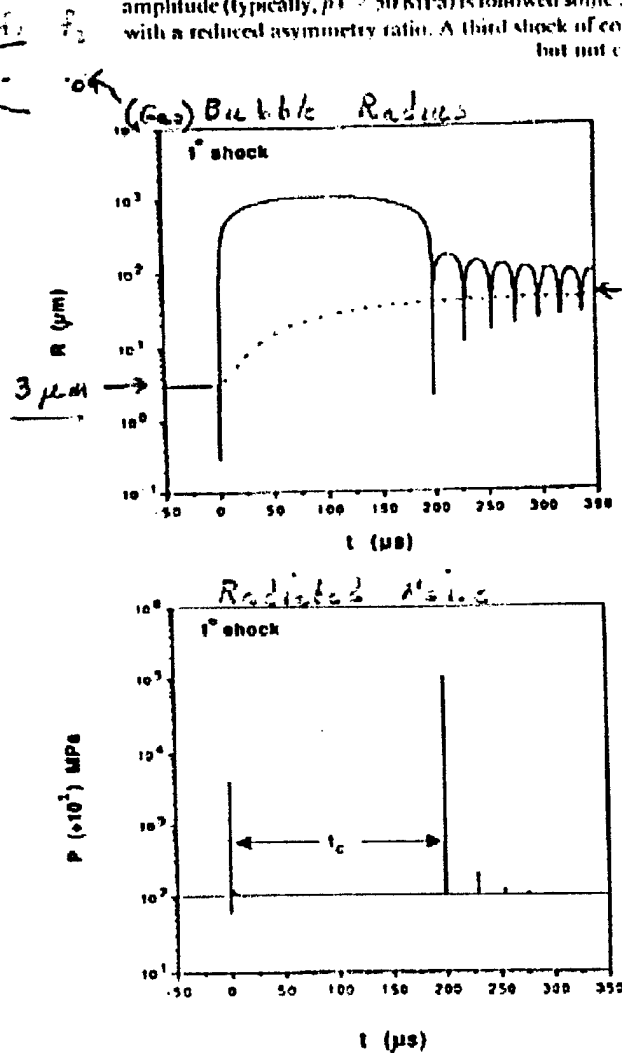


Fig. 2. The predicted bubble response to the primary (1°) shock. The bubble radius variation, $R(t)$, and pressure variation, $P(t)$, at the position of the bubble wall are plotted against time after the primary shock. The calculation assumes the waveform in Fig. 1 with $p_1 = 50$ MPa and an initial bubble radius, $R_0 = 3 \mu\text{m}$.

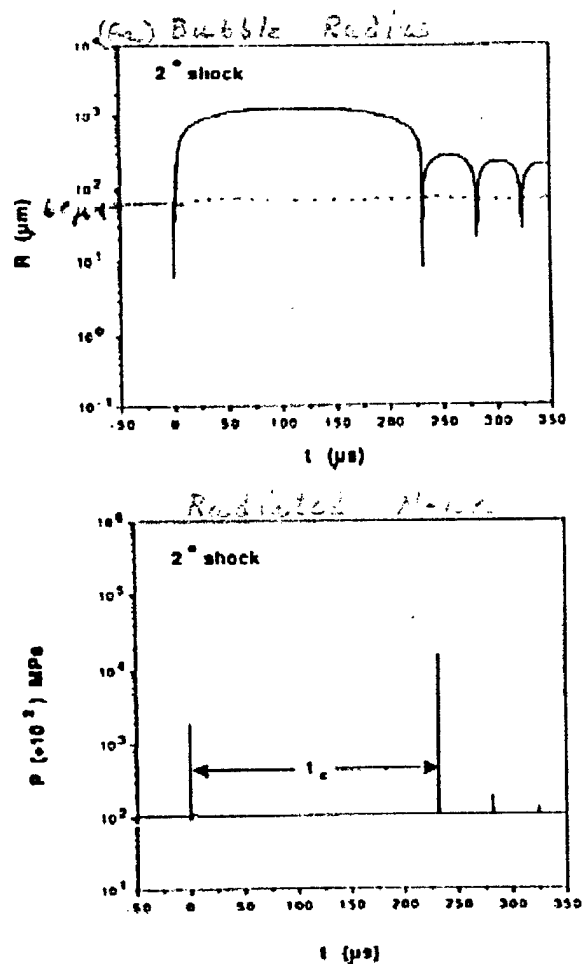
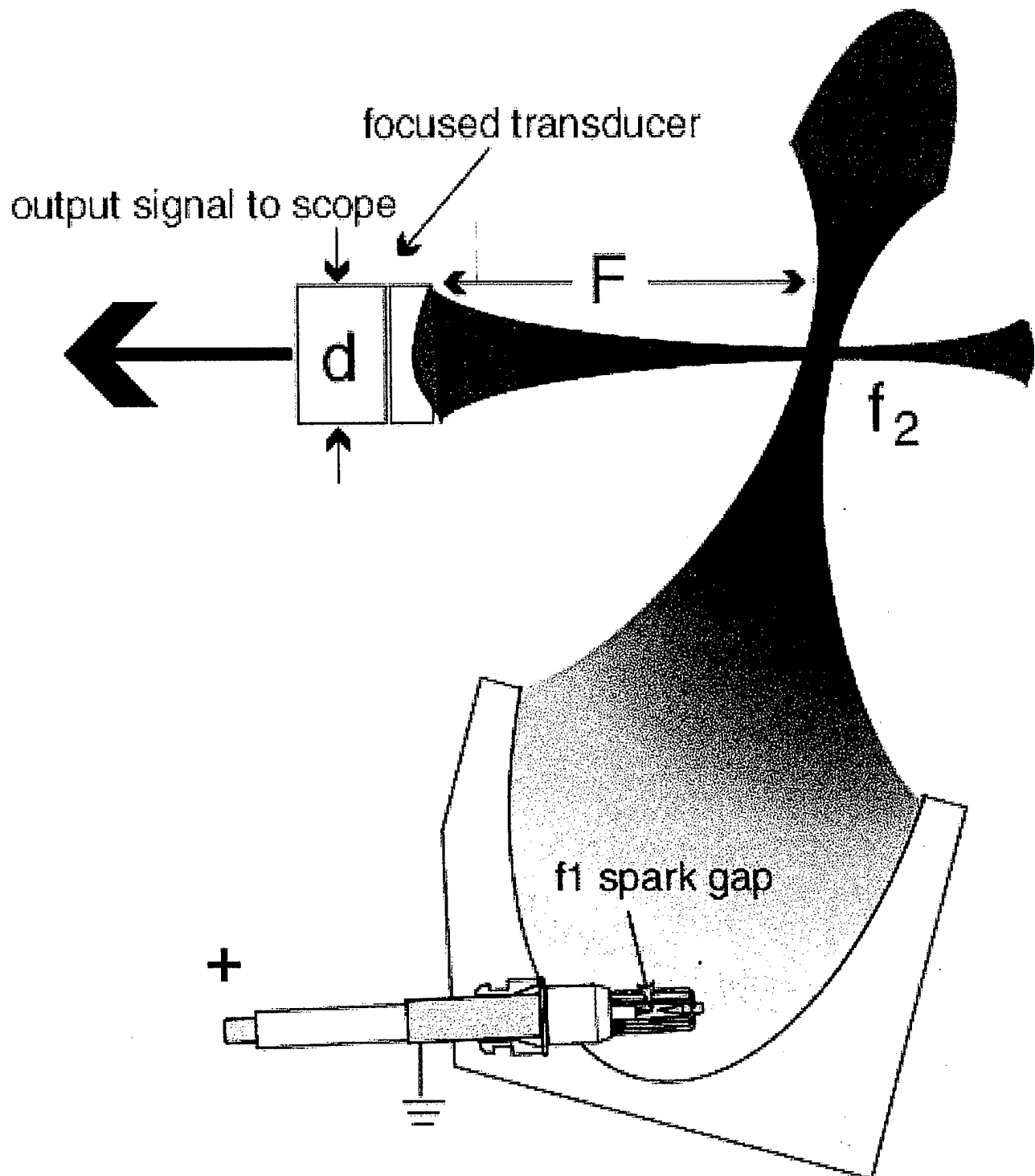


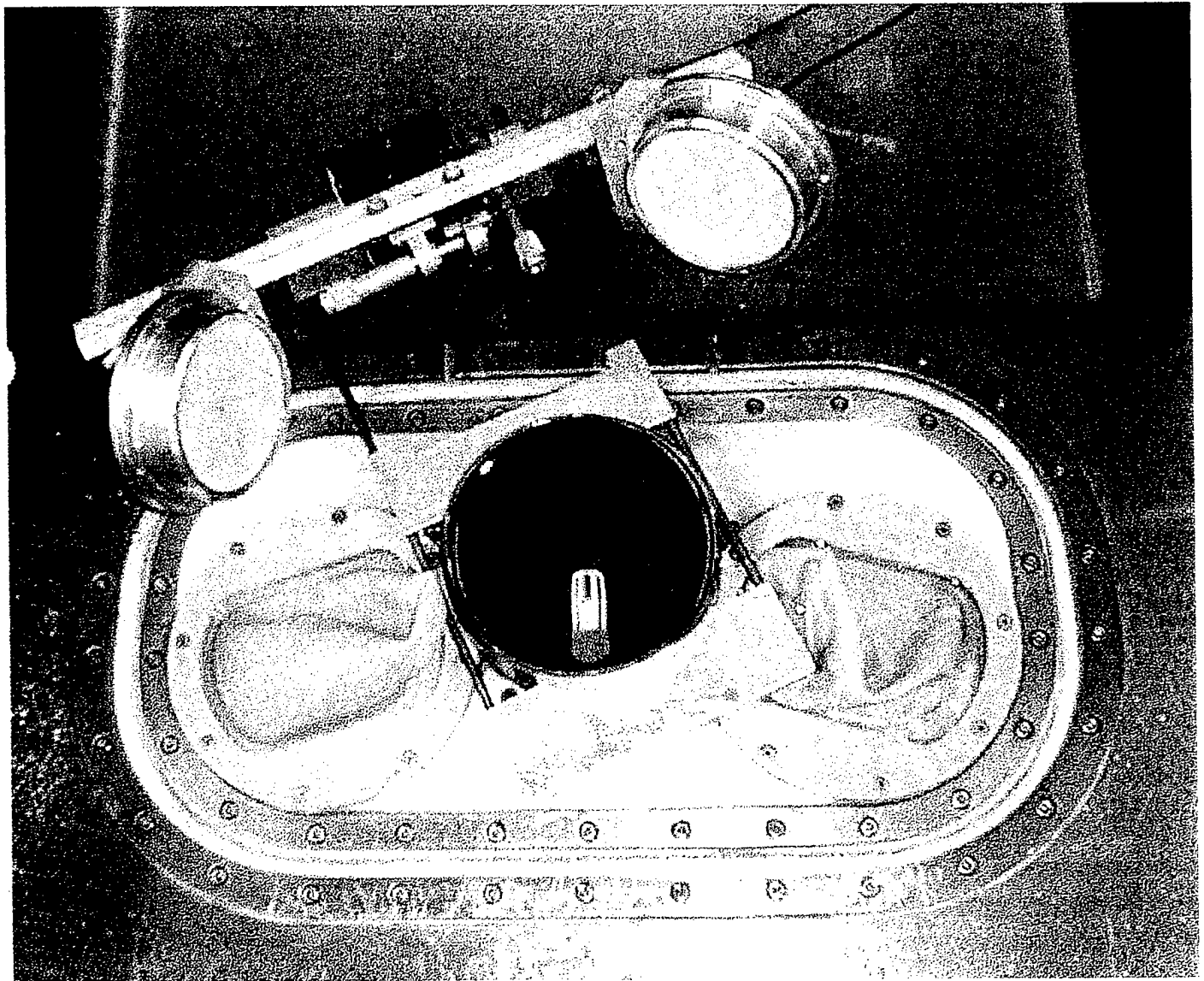
Fig. 3. The predicted bubble response to the secondary (2°) shock. The bubble radius, $R(t)$, and pressure variation, $P(t)$, at the bubble wall are plotted against time after the secondary shock. The calculation assumes, $p_1 = 20$ MPa and an initial bubble size, $R_0 = 60 \mu\text{m}$, this representing the bubble radius following the primary shock.

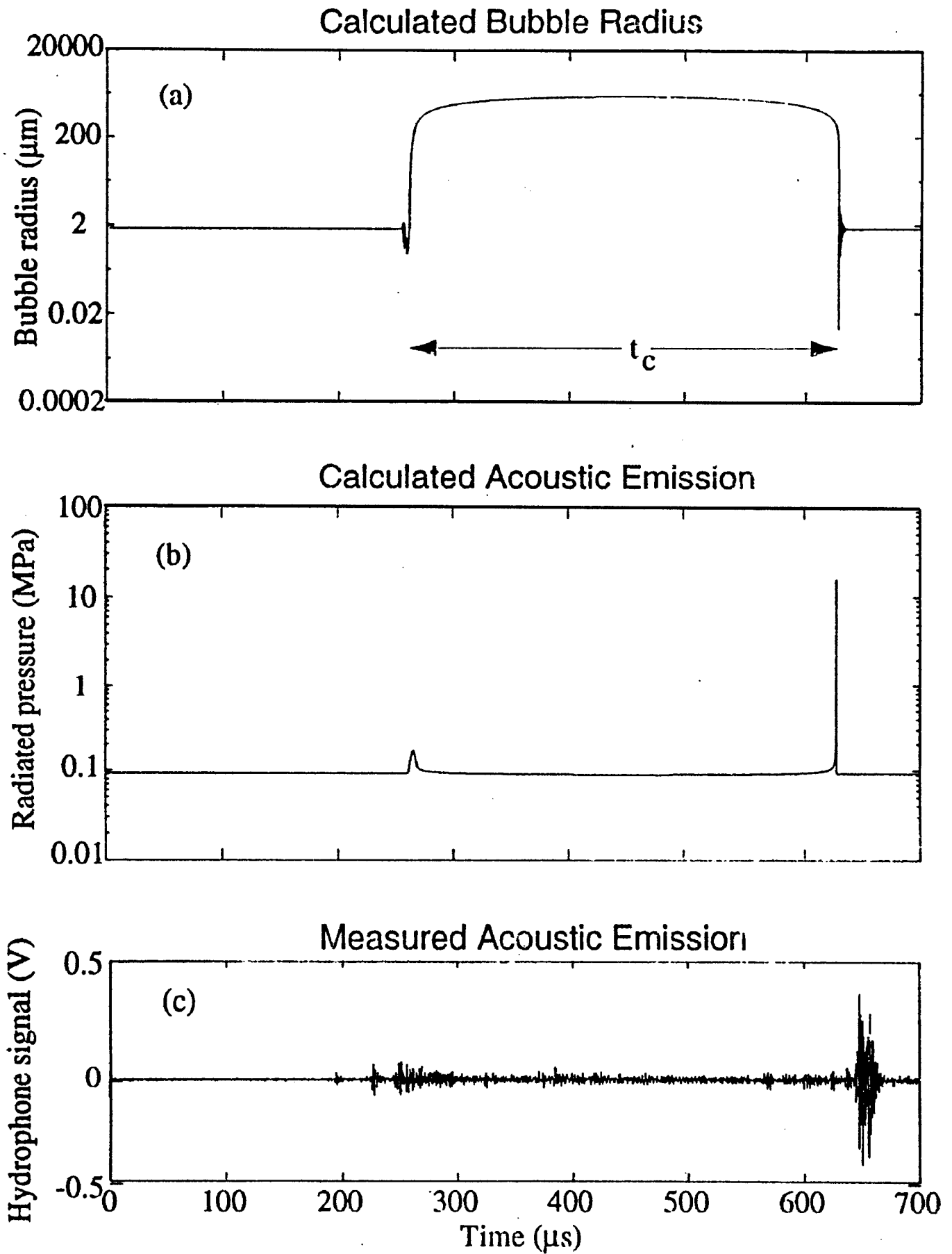
from Coleman et al. UMB 18, 267 (1992)

Passive Cavitation Detection Apparatus

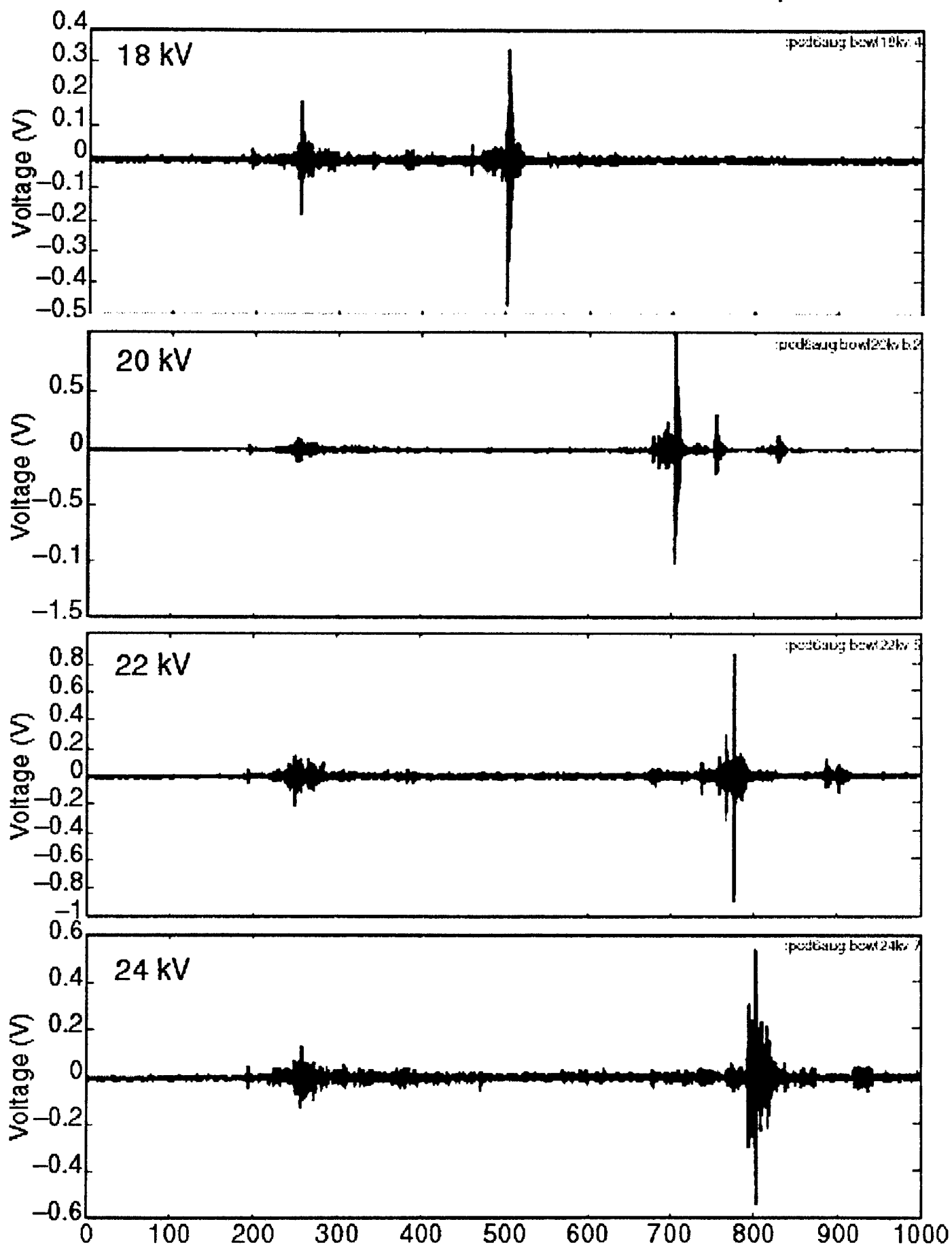


Three Confocal Transducers for Active or Passive Detection of Cavitation Bubbles Produced by the Lithotripter Pulse

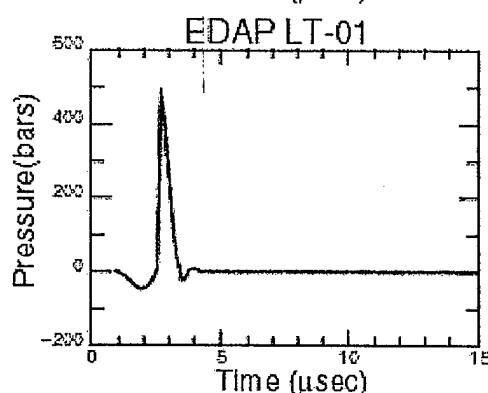
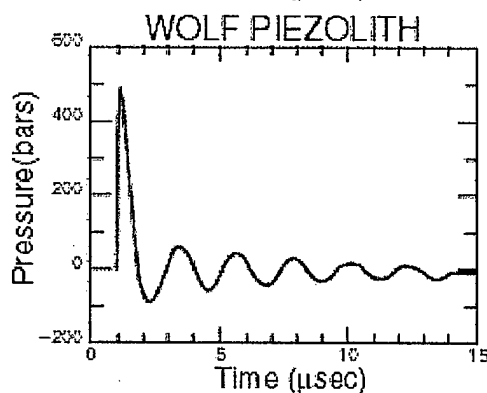
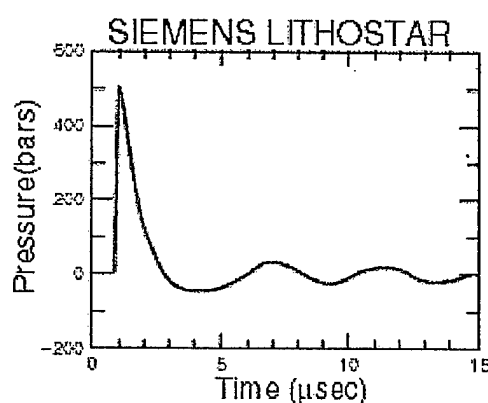
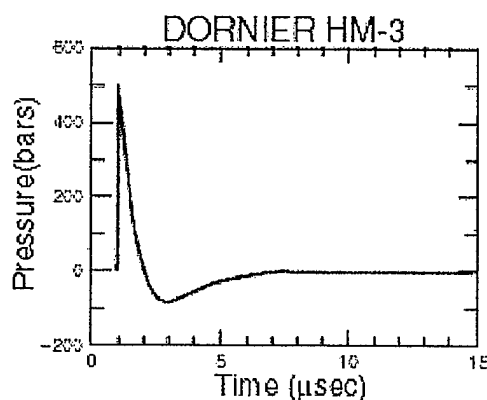




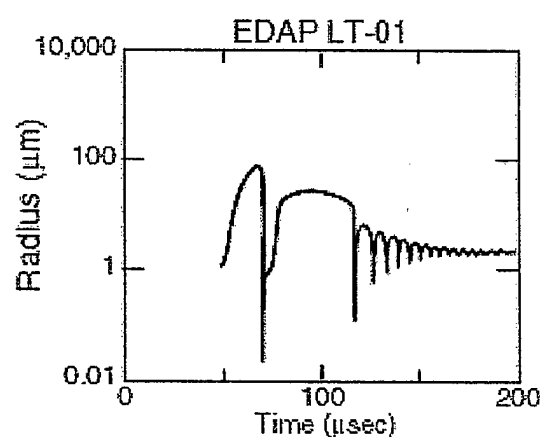
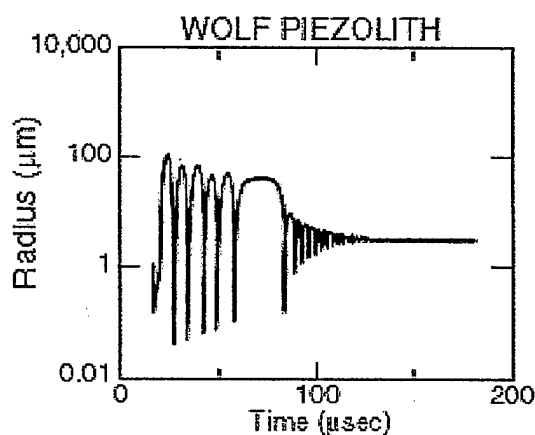
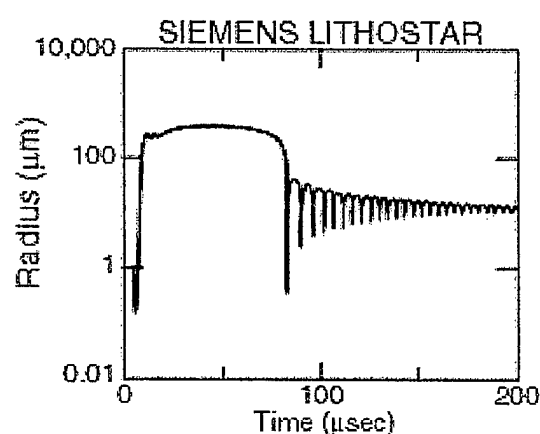
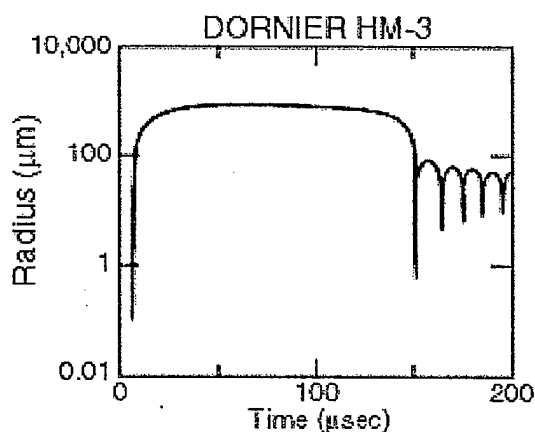
Lithotripsy Passive Cavitation Detection
confocal PZT bowl: 1 MHz, 10 cm radius, 10 cm aperture



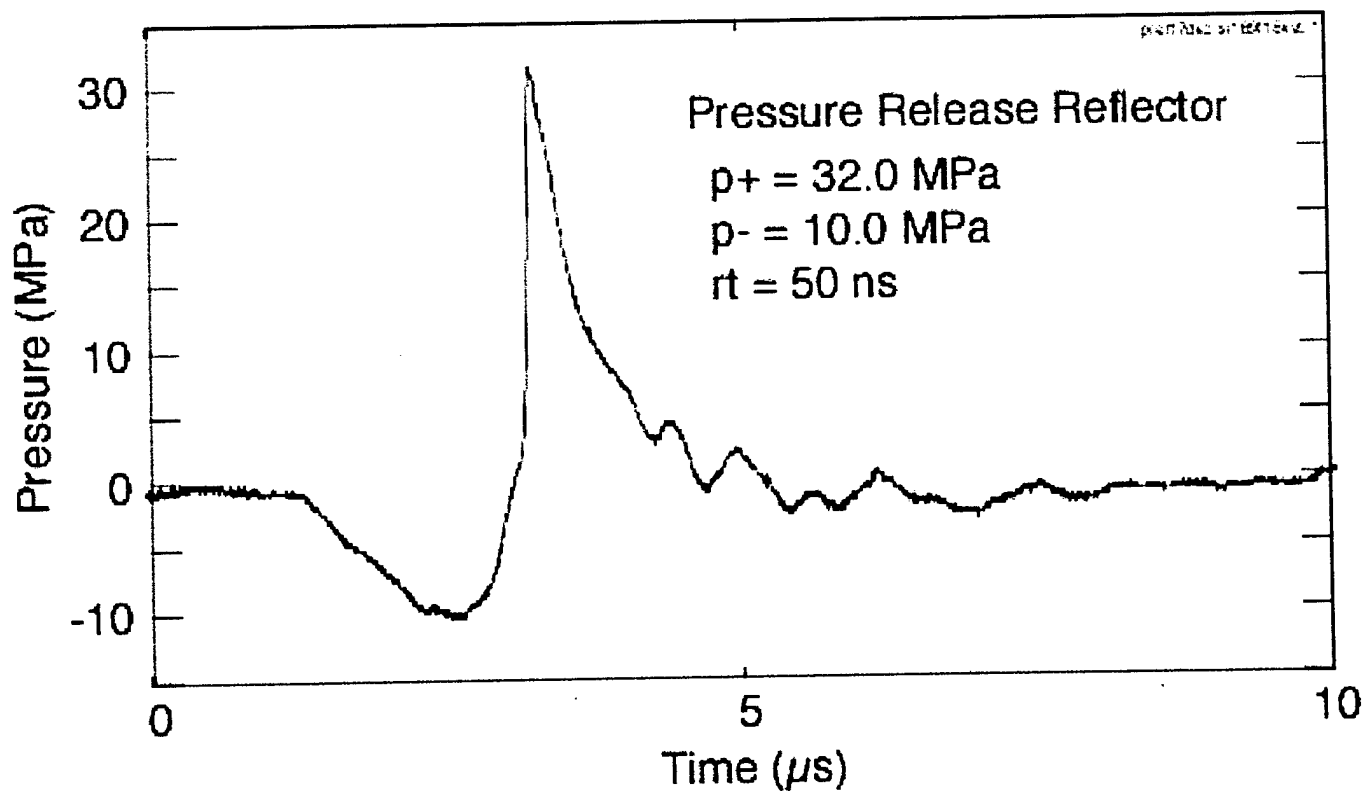
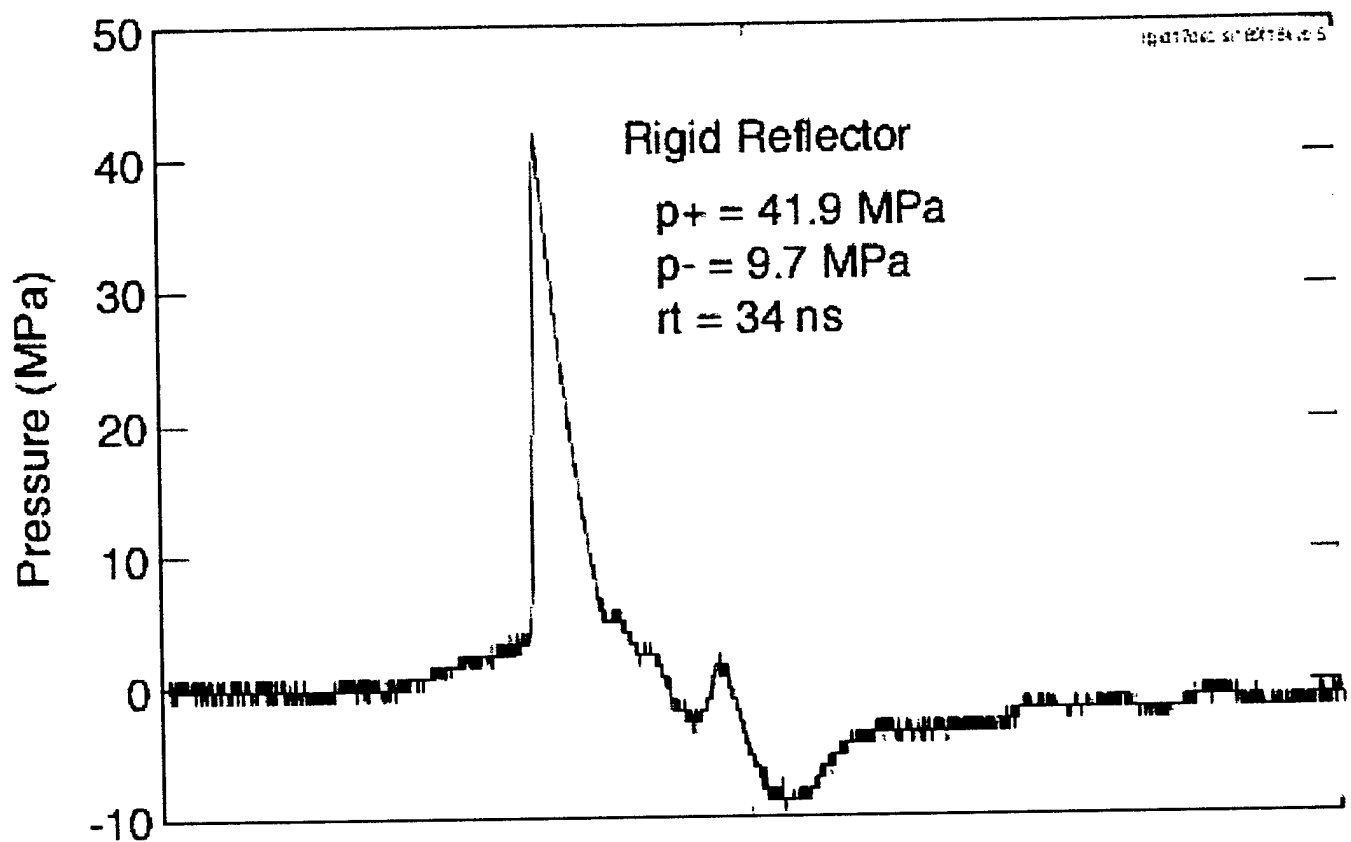
Idealized Pressure Waveforms Produced by Commercially Available Lithotripters



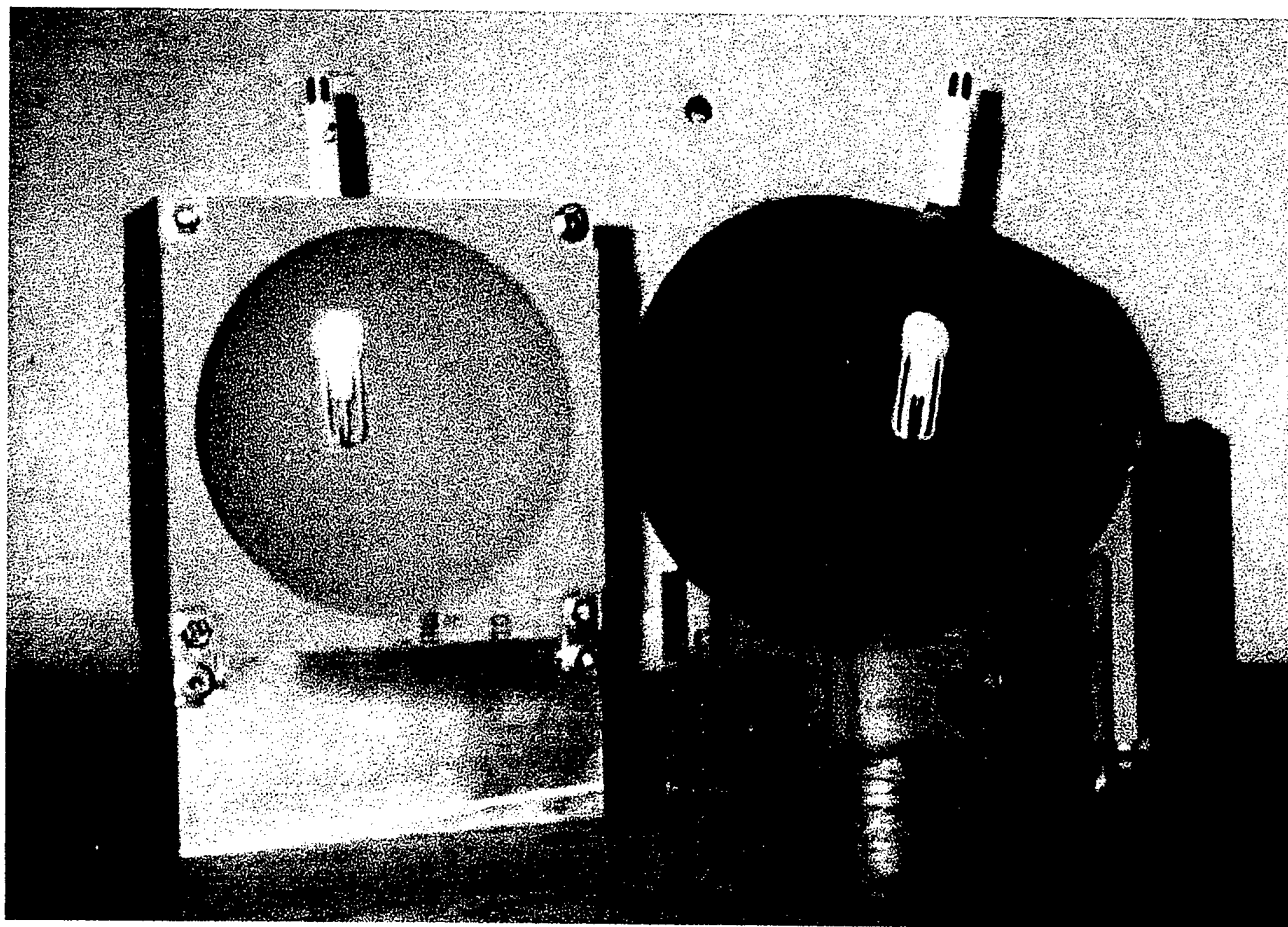
Calculated Responses of $1\ \mu\text{m}$ Bubbles to Pressure Waveforms Shown Above



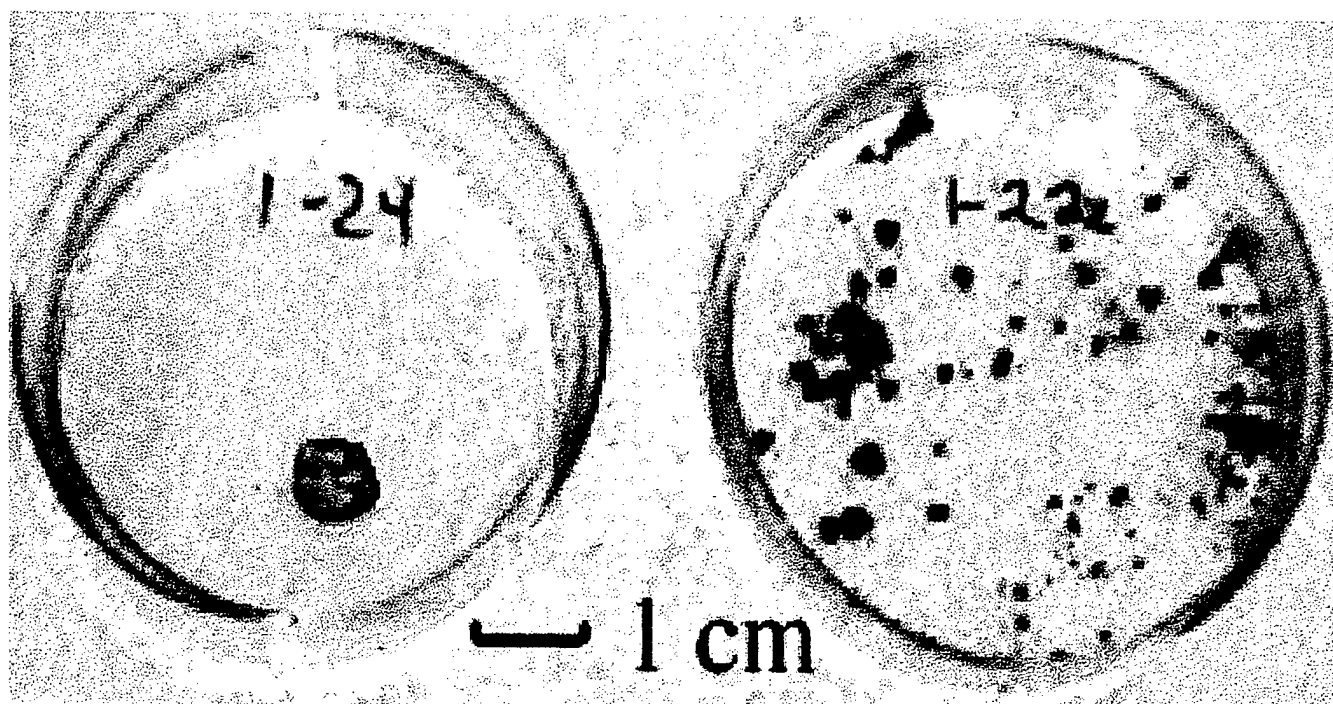
Rigid Reflector vs Pressure Release Reflector



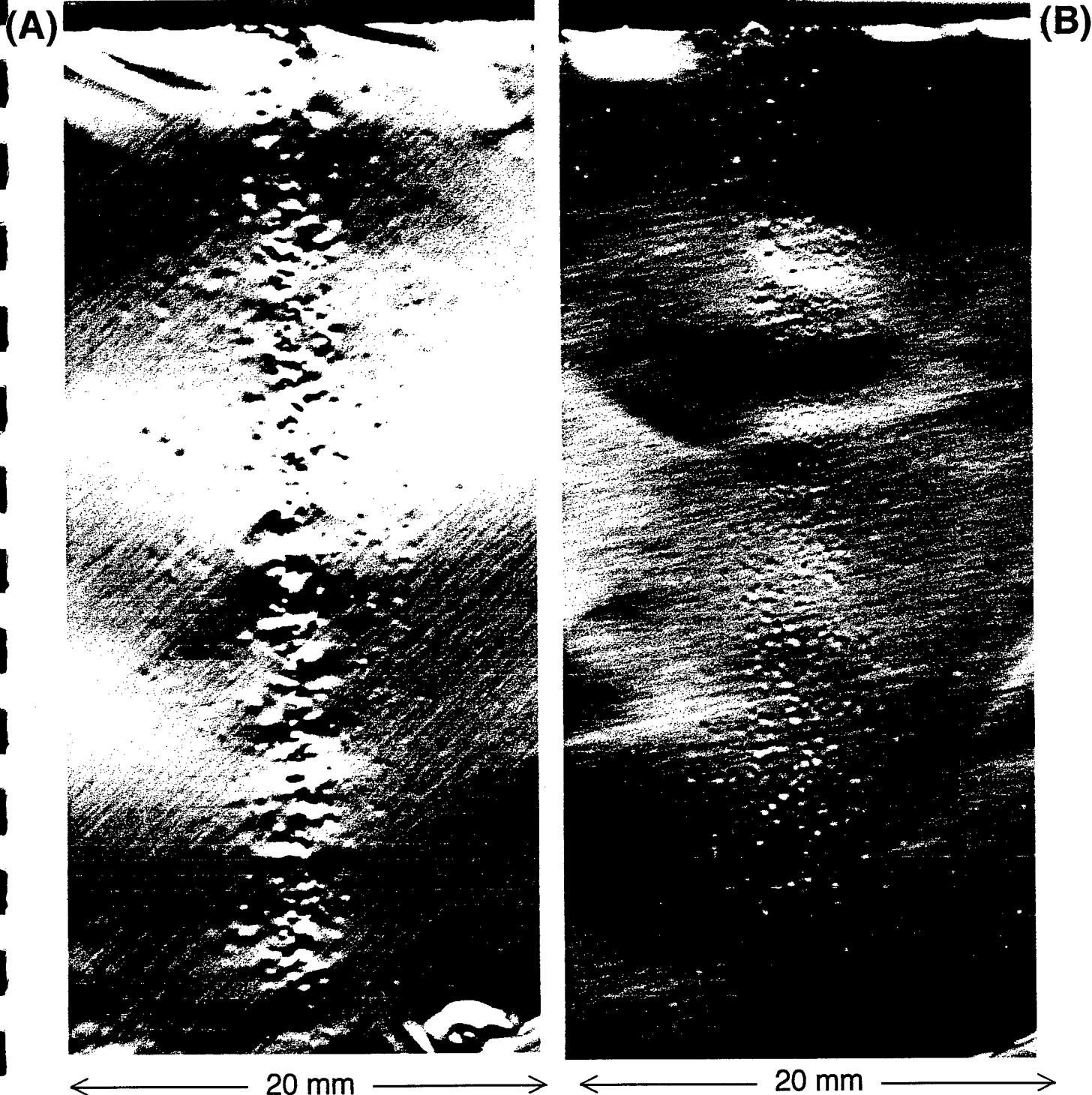
Pressure-release reflector (left) and rigid-reflector (right)



Stones treated with PR (right) and Rigid reflectors (left)

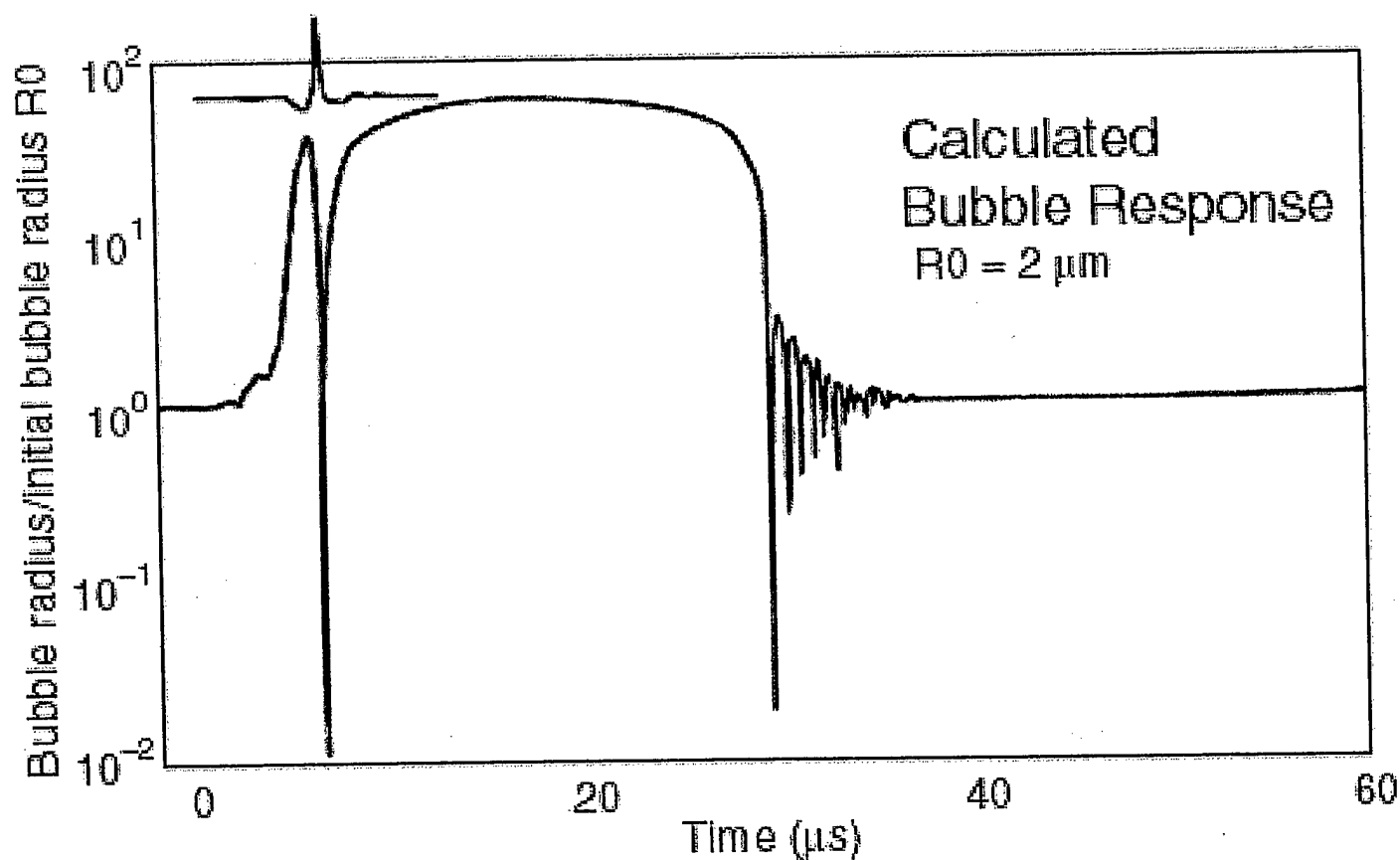
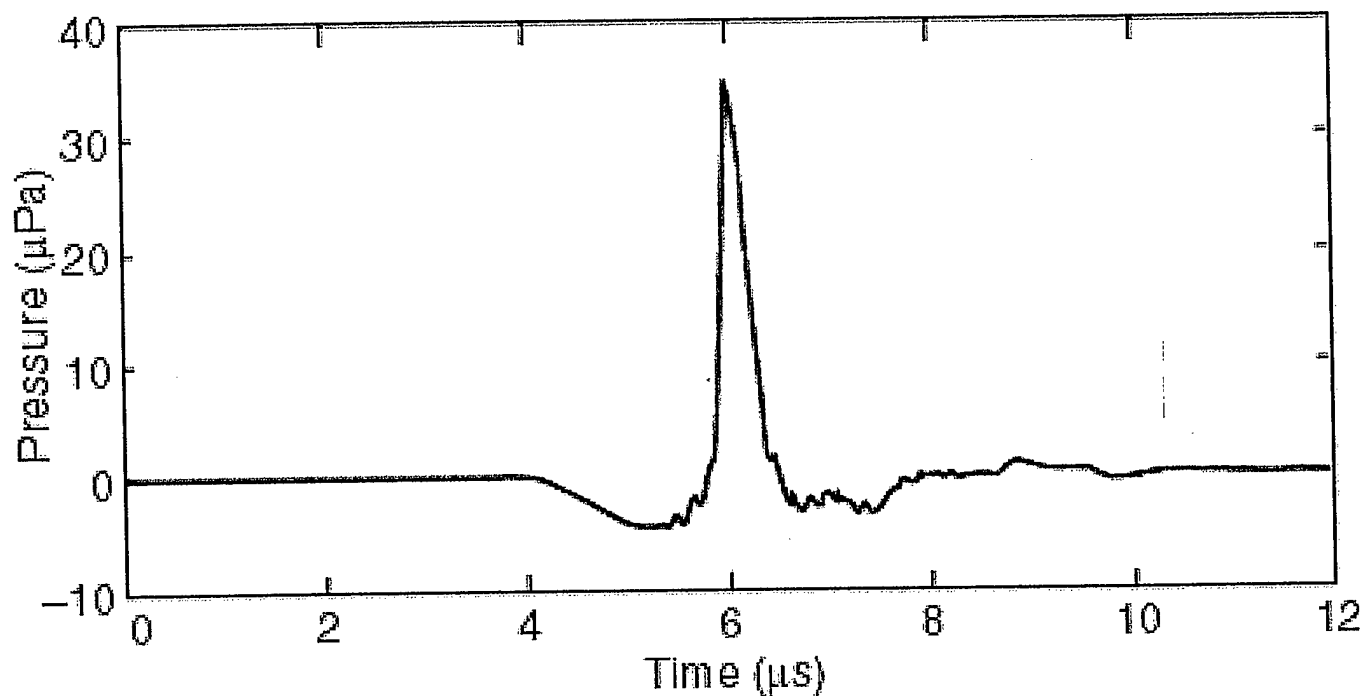


Comparison of Pitting by Ten Pulses Produced by a Rigid Reflector (A) and a Pressure-Release Reflector (B)



Deep gash of pits in (A) dwarfs the tiny weak pits in (B)

Pressure Release Reflector: Bubble Dynamics



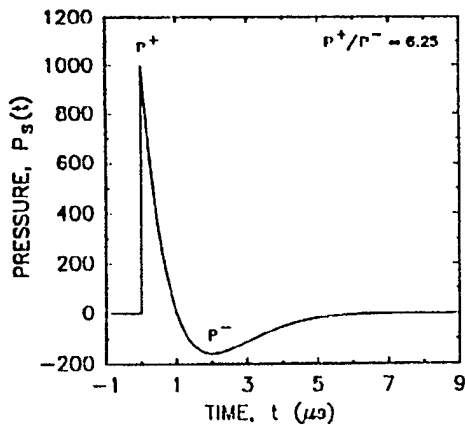


FIG. 1. Modeled form of ESWL pressure waveform as generated by Eq (6).

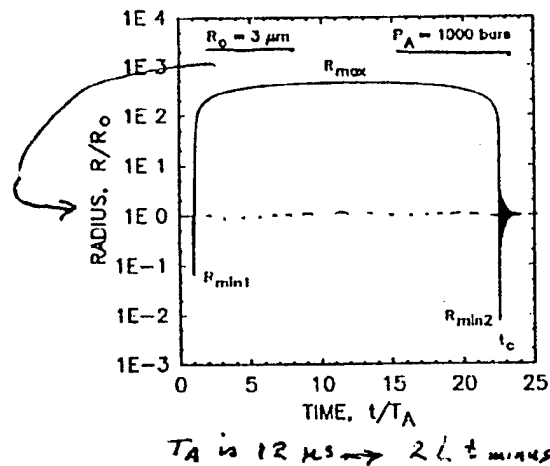


FIG. 2. Bubble response to a 1000-bar ESWL shock calculated without considering gas diffusion, used to define various symbols.

this is wave-form generated by lithotripter

this is response of 3 μm bubble to above waveform. It is not an discharge bubble response

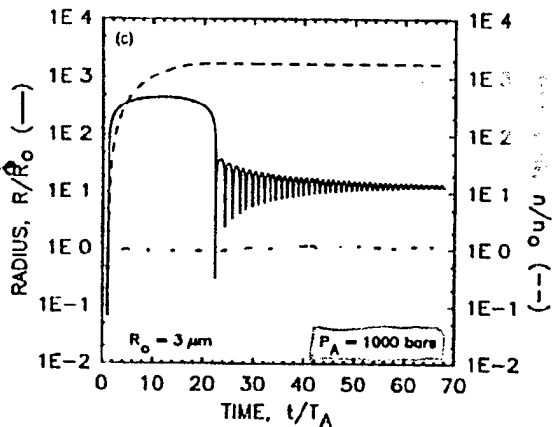
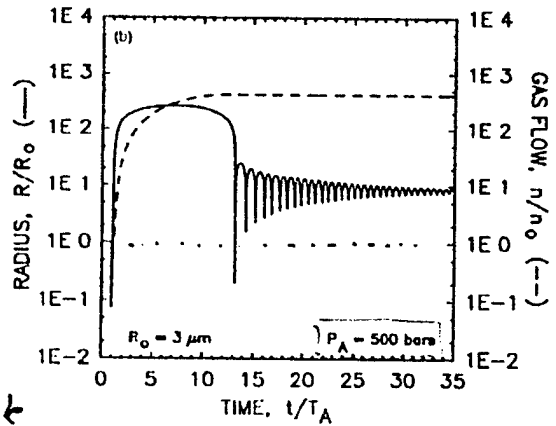
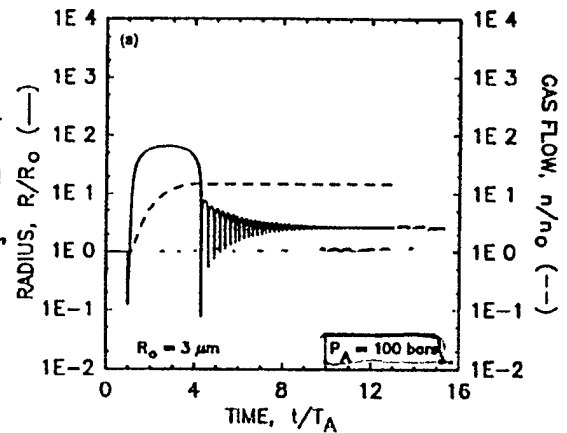
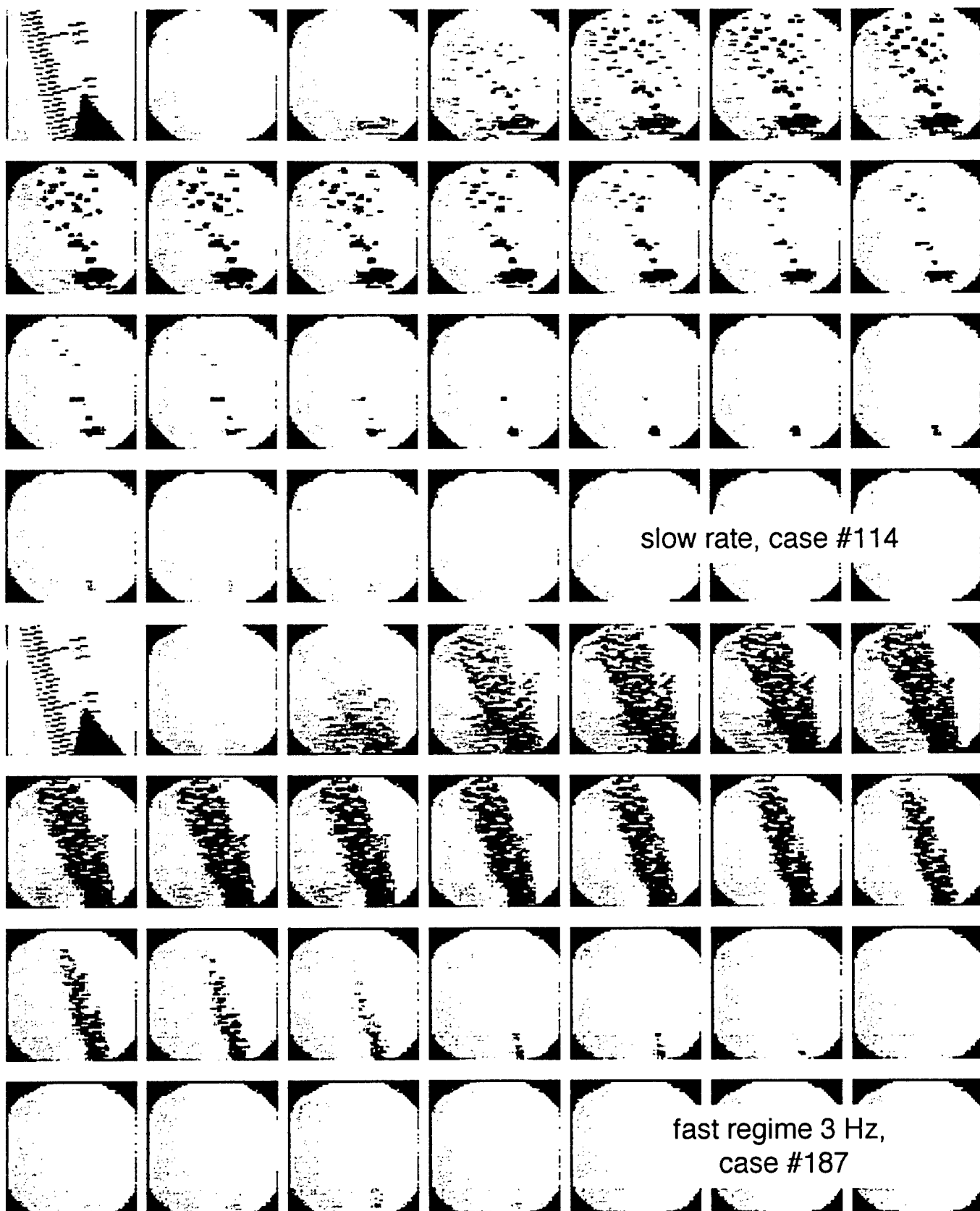


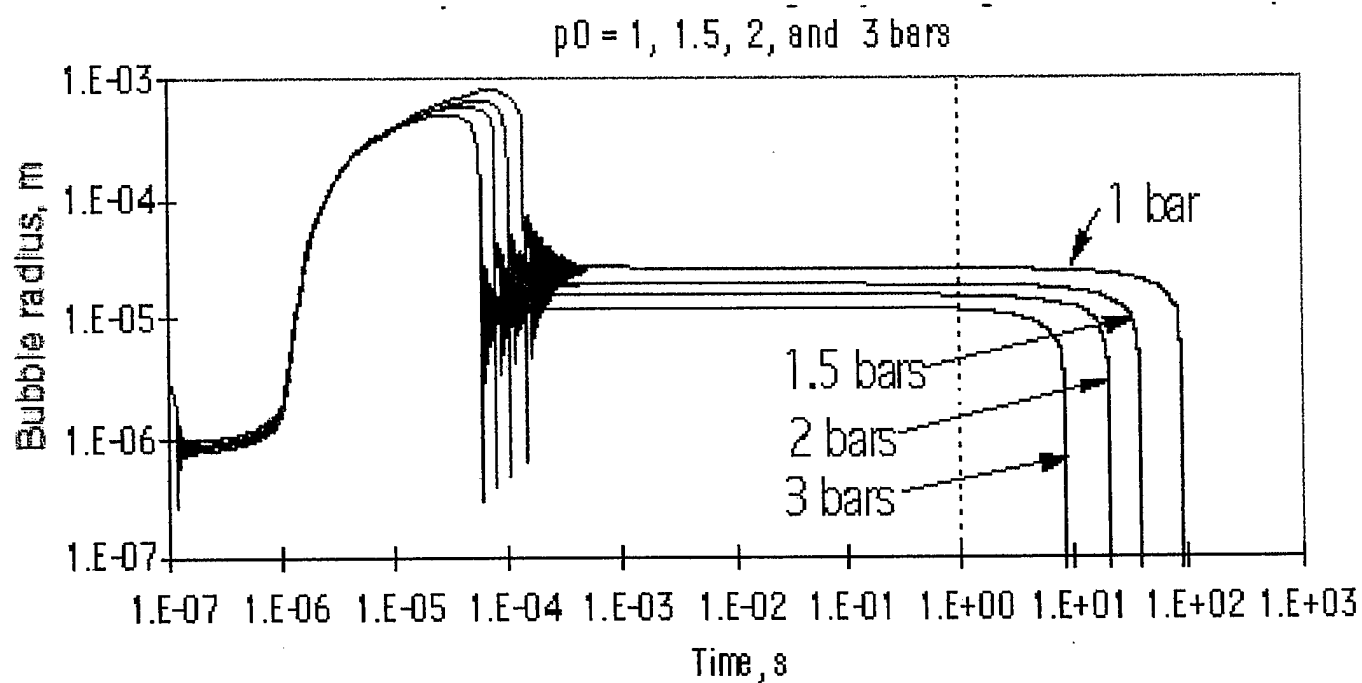
FIG. 3. Responses of a 3-μm bubble, calculated with gas diffusion, to ESWL shocks with amplitudes of (a) 100 bars, (b) 500 bars, and (c) 1000 bars

ESWL and PULSE REPETITION FREQUENCY (PRF)

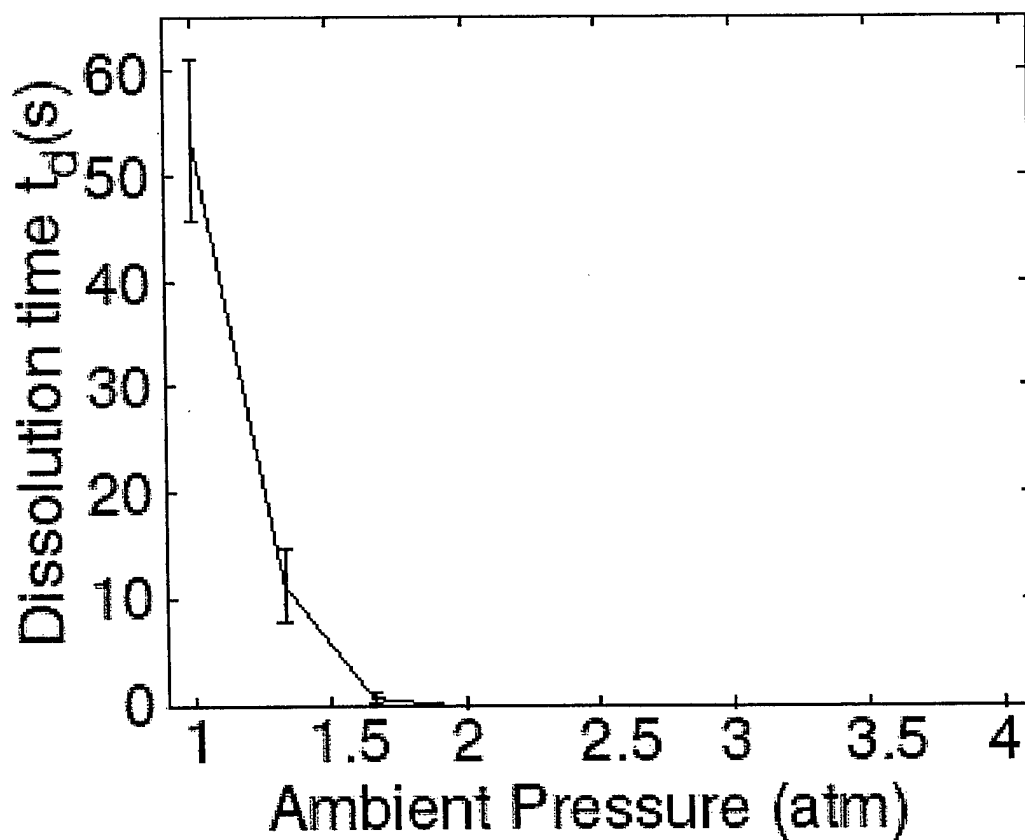


Images of bubble cluster in slow rate regime, $f=0.5$ Hz, and in high repetition rate regime $f=3$ Hz. In both cases overpressure $P=0$ bars and $U=18$ kV. It is seen that in “slow” regime bubble concentration is smaller and the bubbles are bigger. In “fast” regime the bubble concentration is very high and they are fairly small.

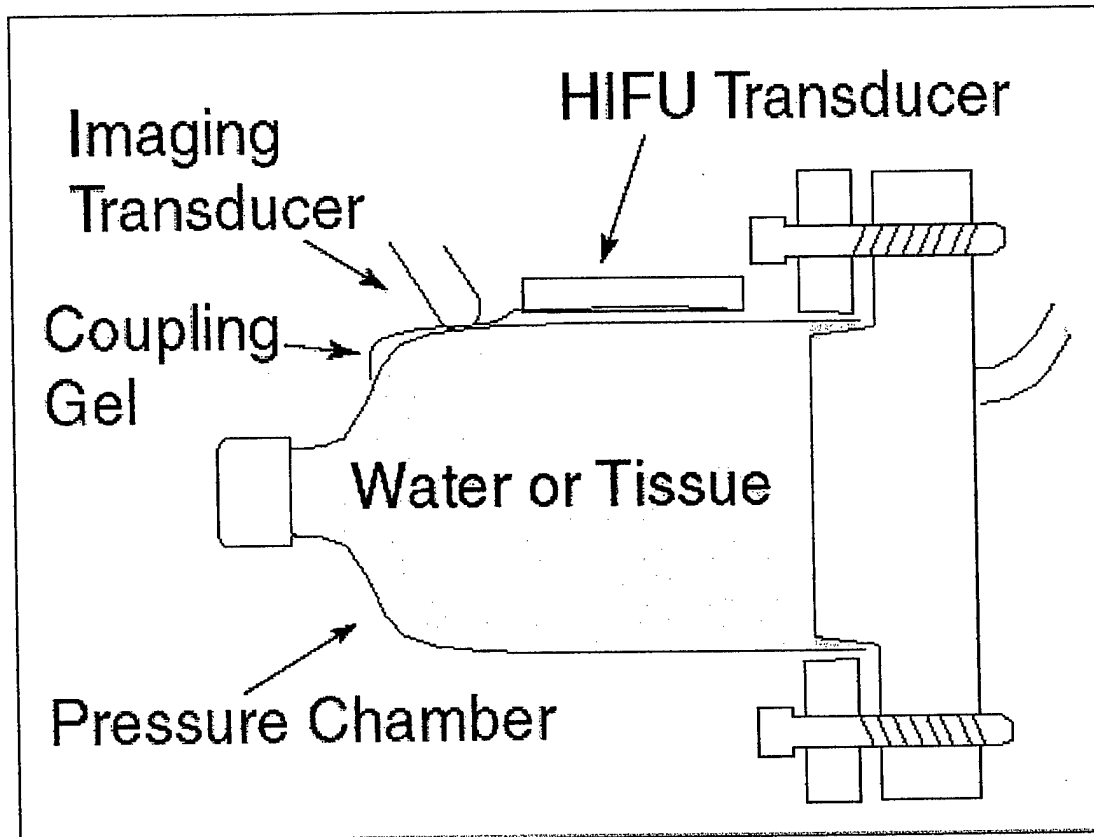
Effect of overpressure on R-t curves of bubbles



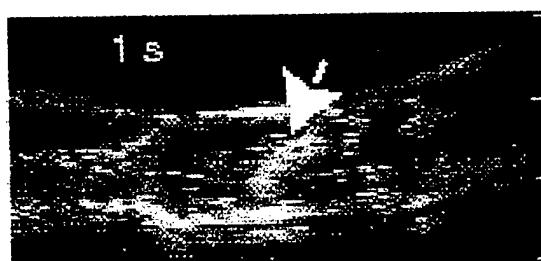
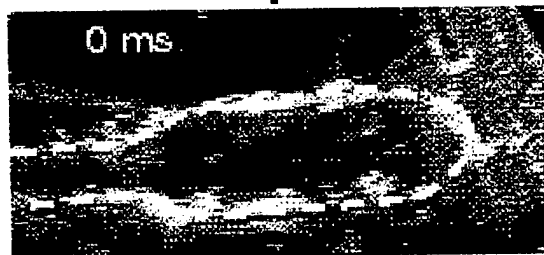
Overpressure rapidly dissolves daughter bubbles



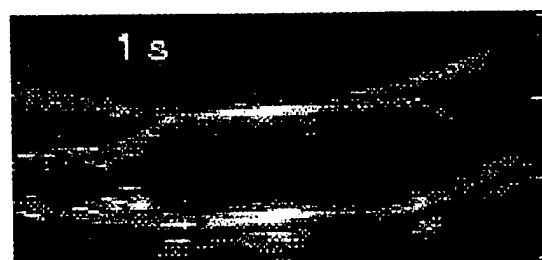
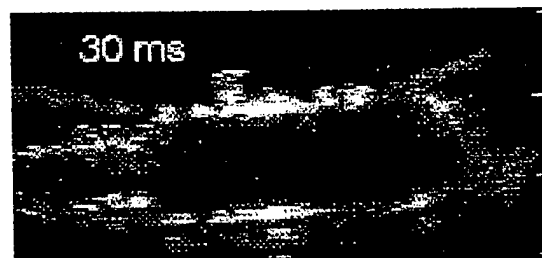
Overpressure Increases Rate of Dissolution of Residual Cavitation Bubbles



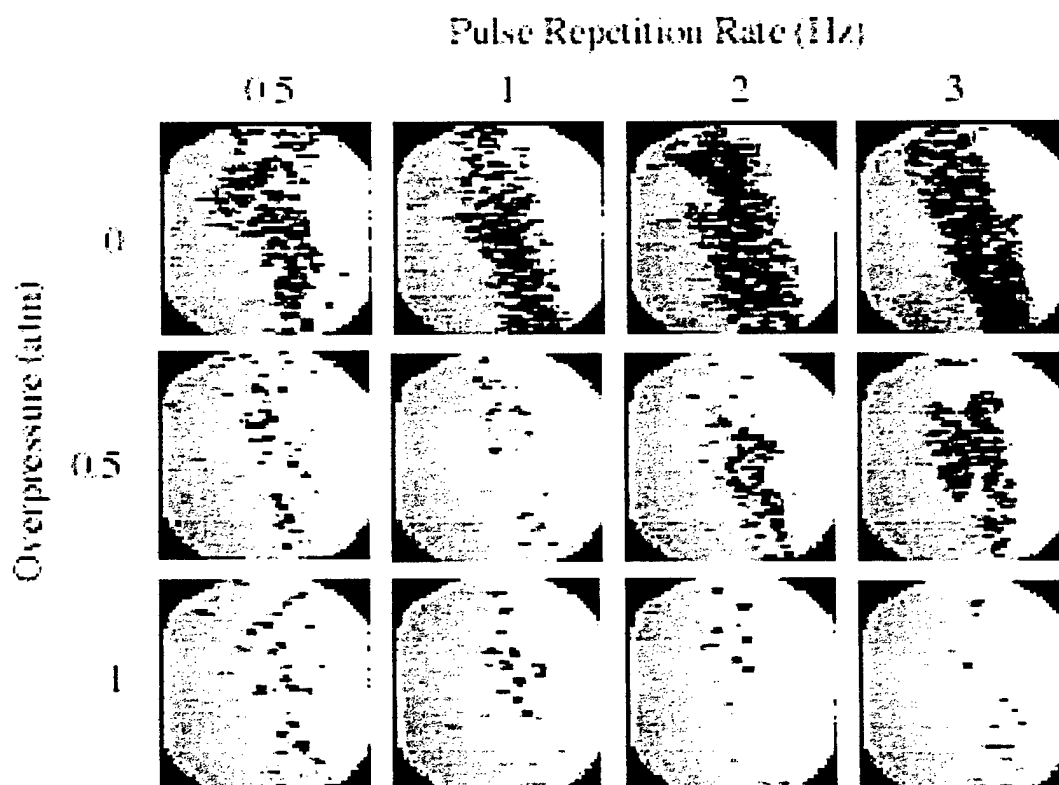
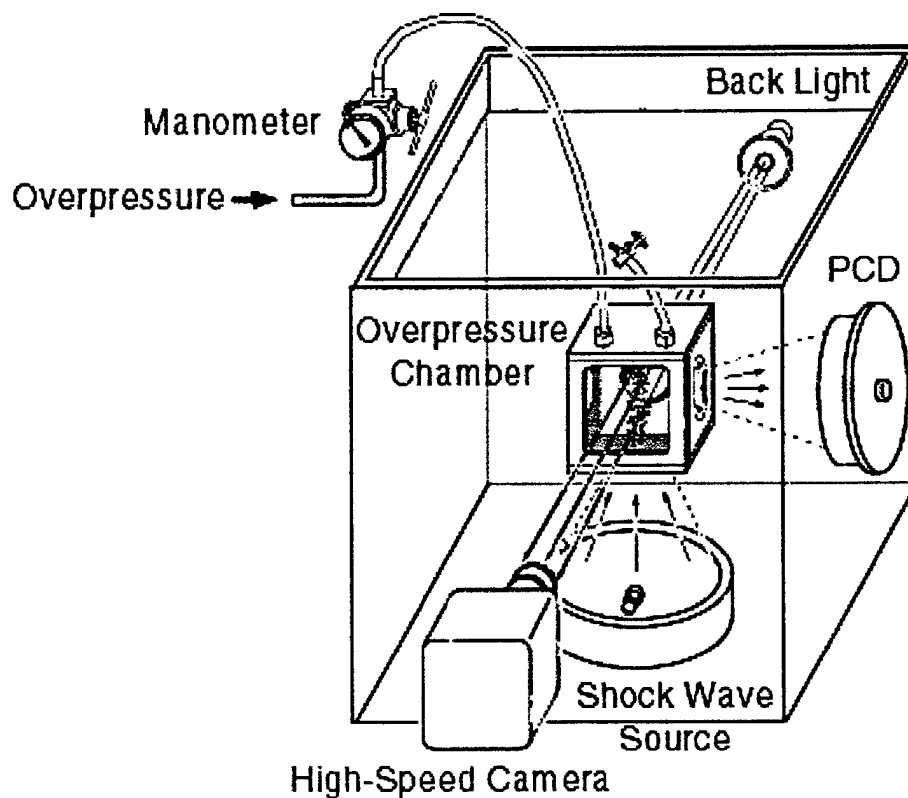
No Overpressure



1 atm Overpressure

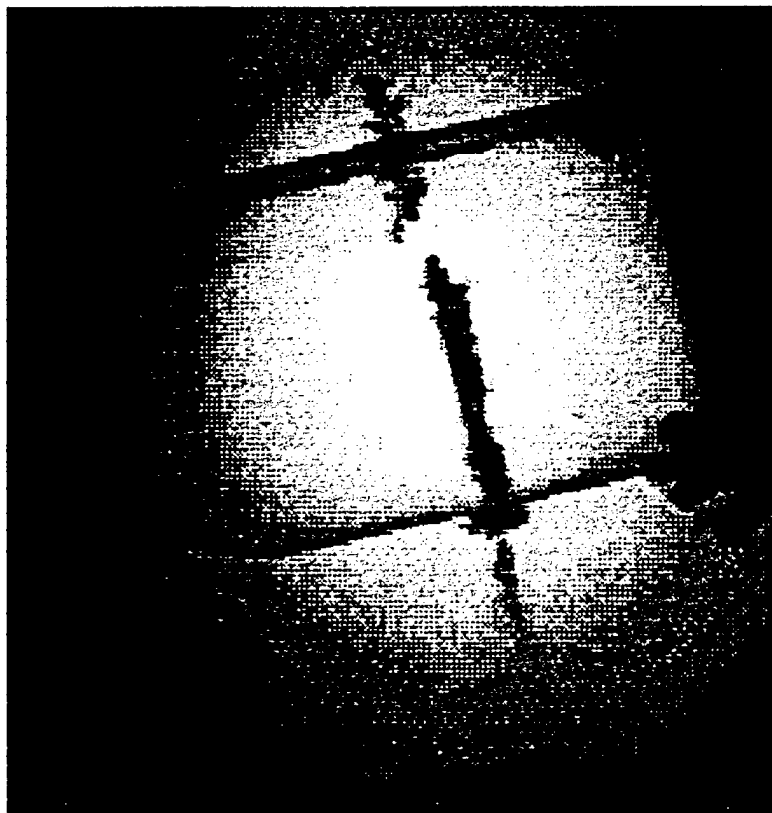


Lithotripter Pressure Chamber

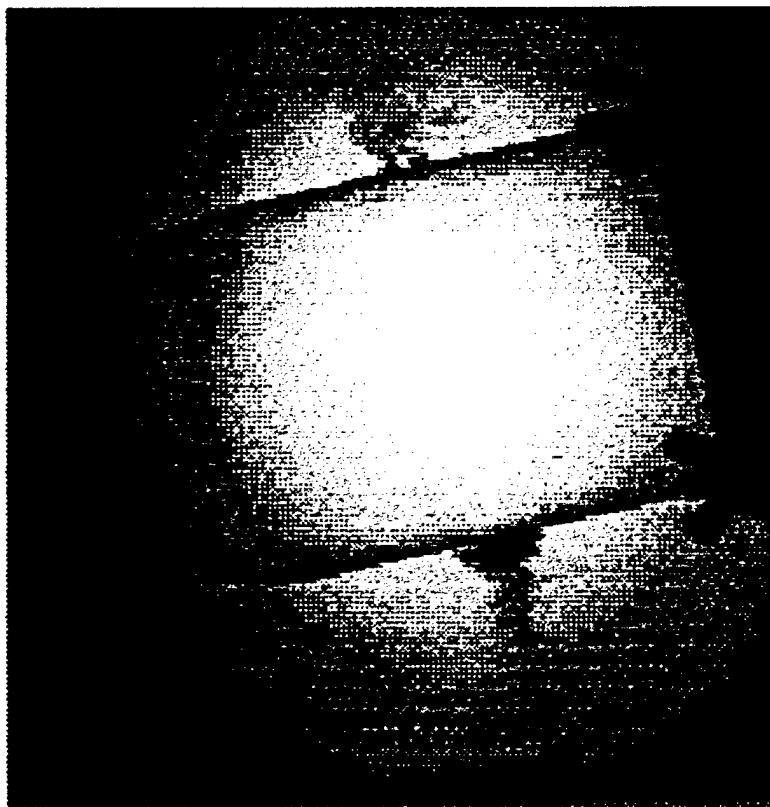


Effect of Overpressure on bubble persistence

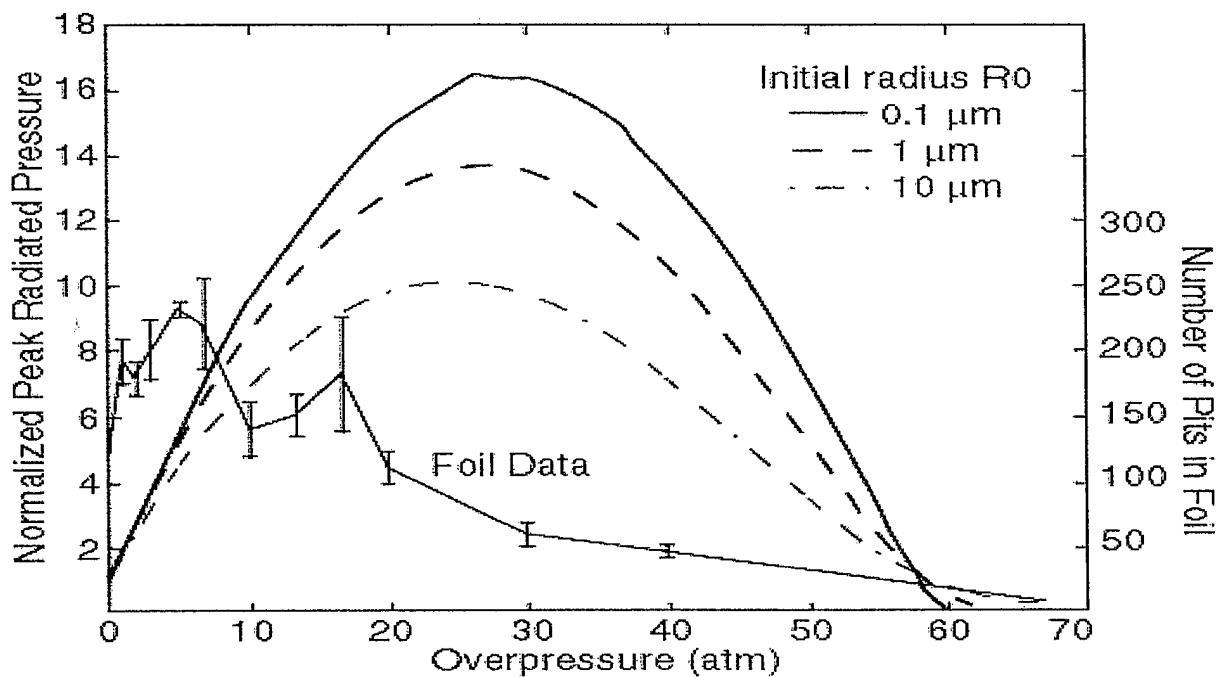
OP = 0 Atm



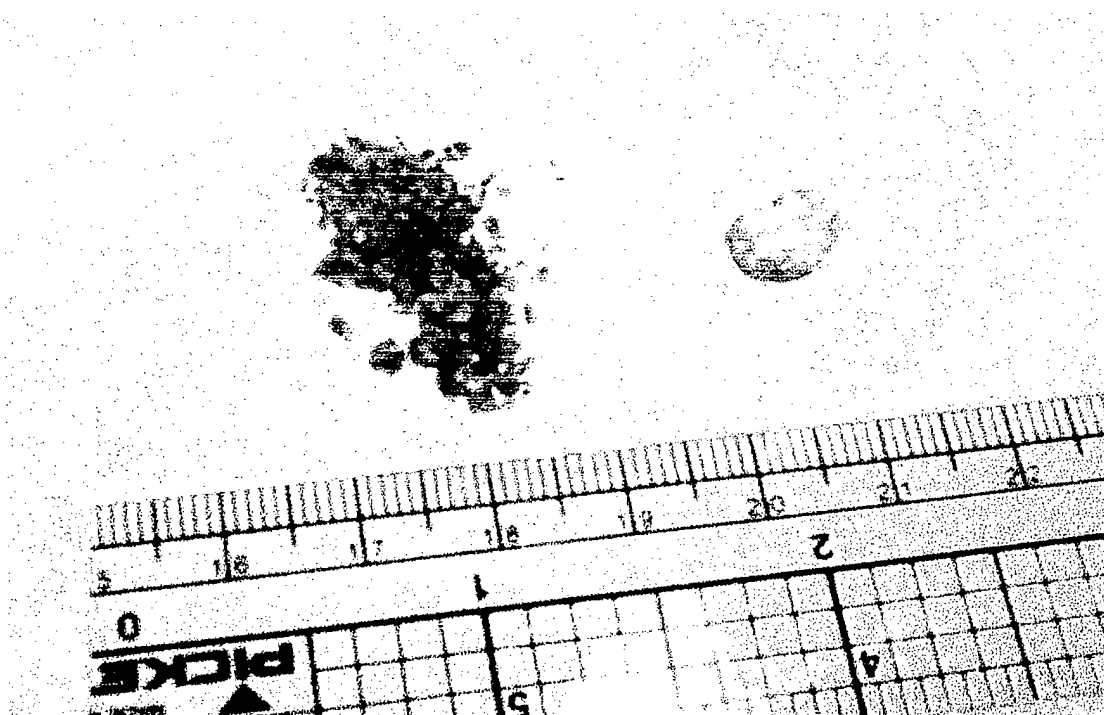
OP = 3 Atm



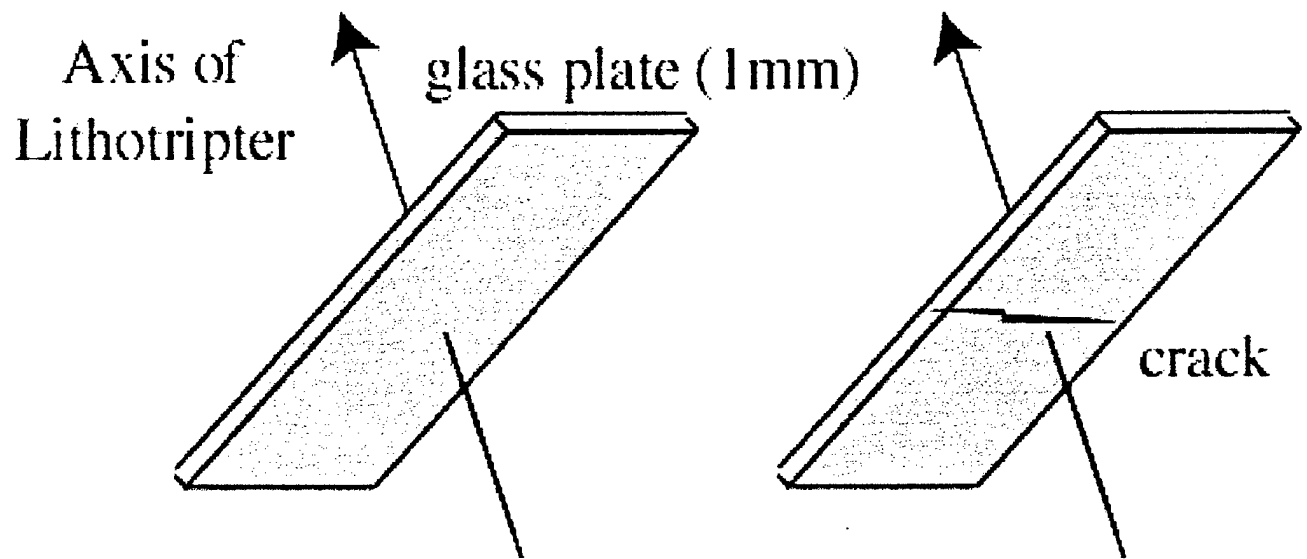
Cavitation Intensity vs Overpressure



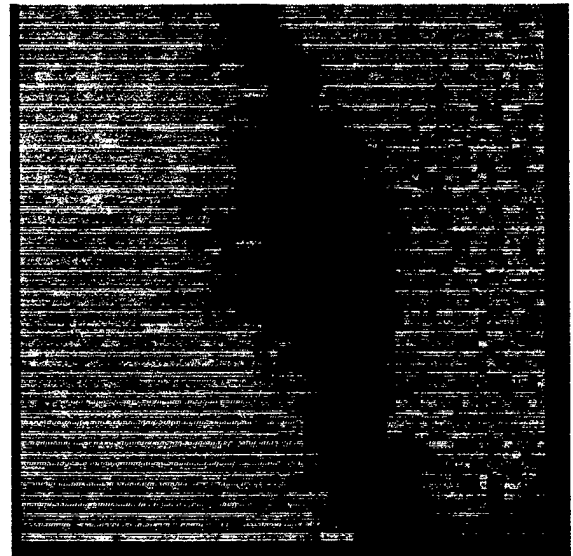
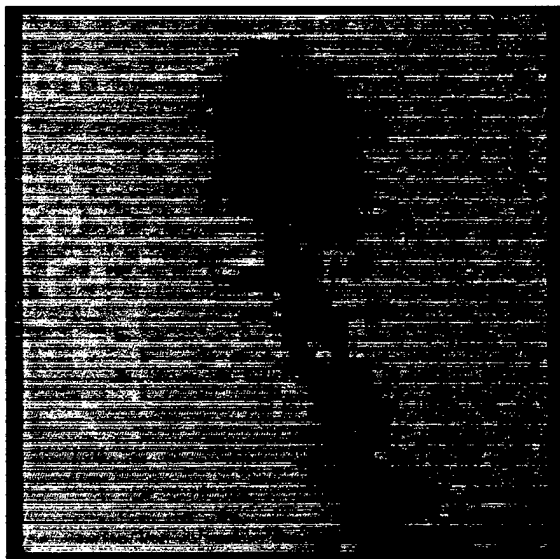
Stone treated at atm pressure (left) and at elevated pressure (right)



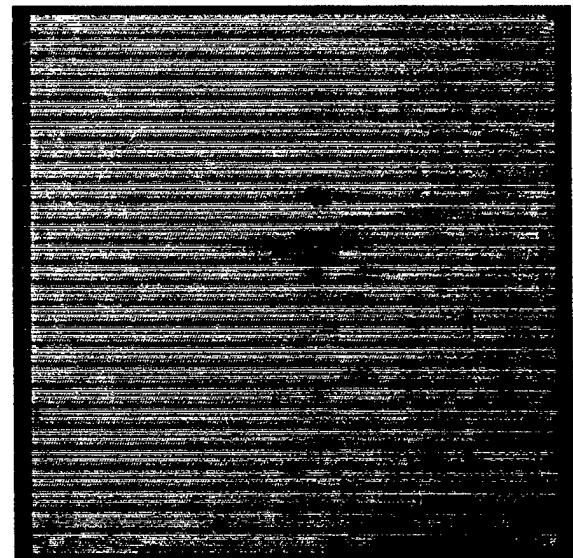
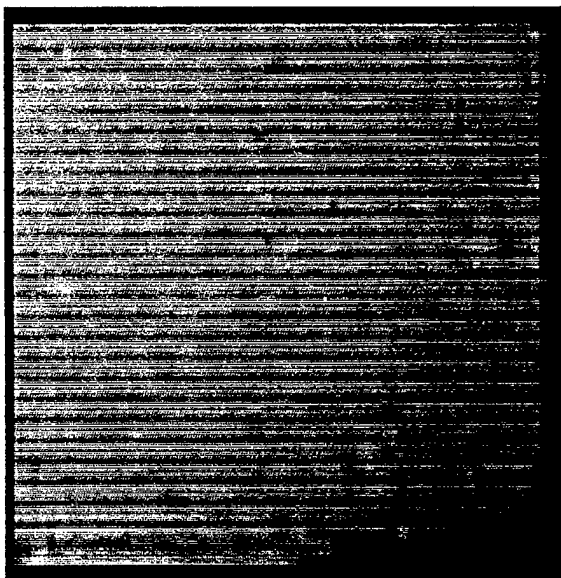
Crack Model



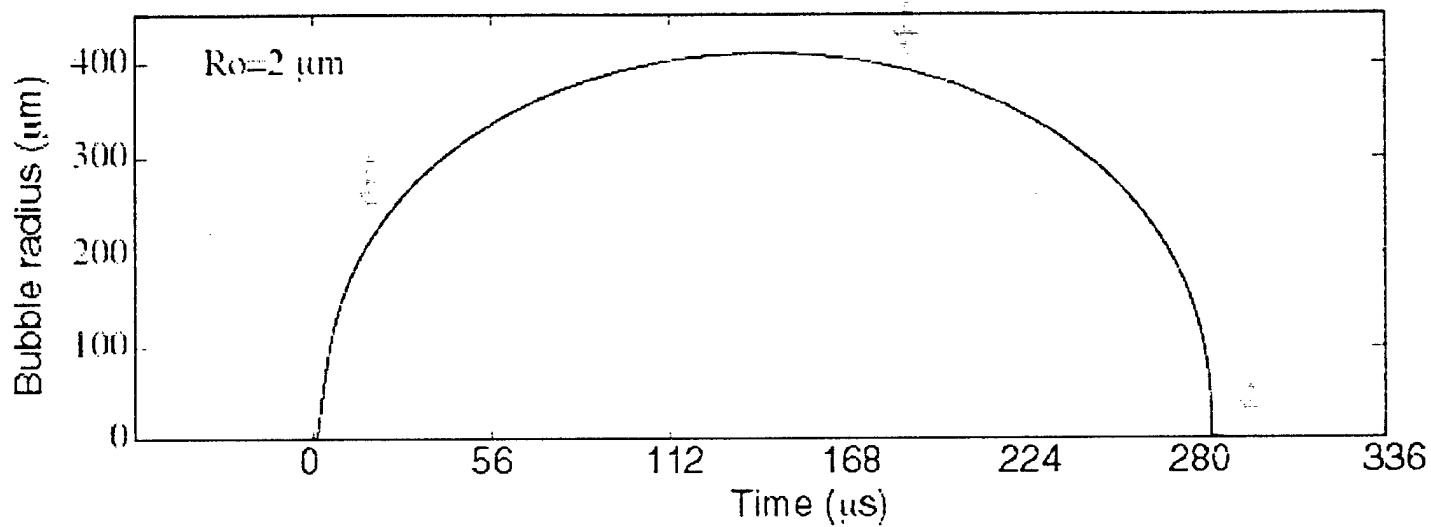
OP=
0 atm



OP=
3 atm



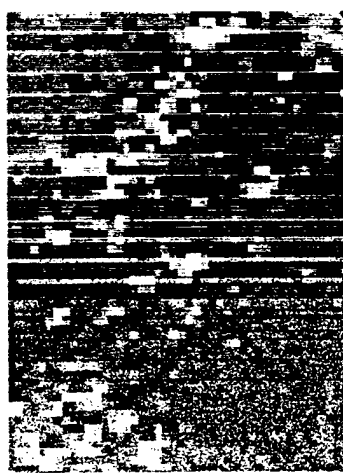
Mitigated and Intensified Cavitation with 2 Pulses



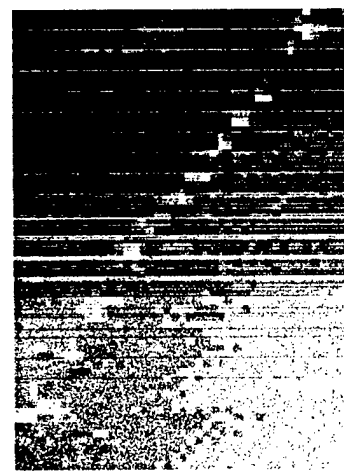
10 mm



$\tau = 25 \mu\text{s}$



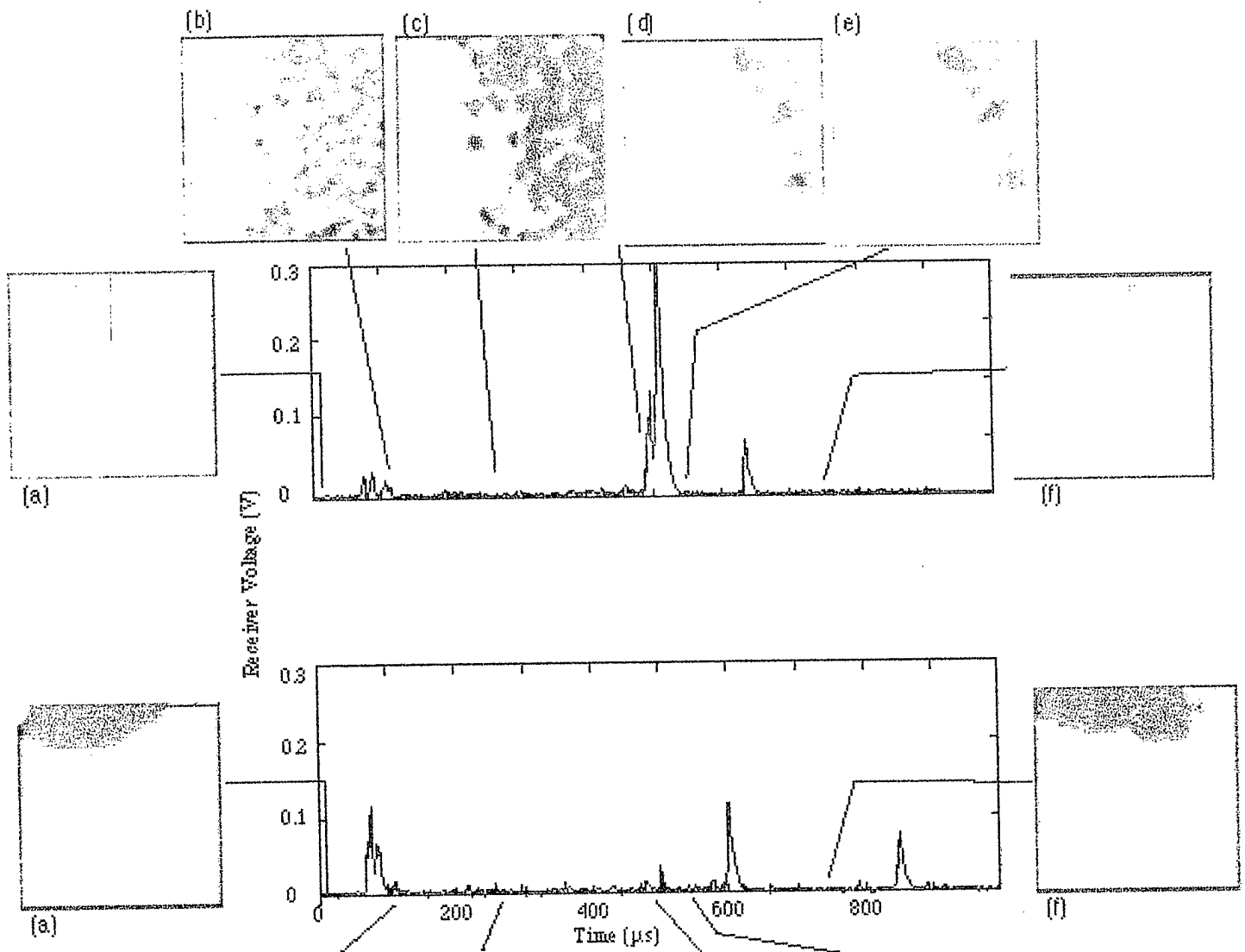
$\tau = 190 \mu\text{s}$



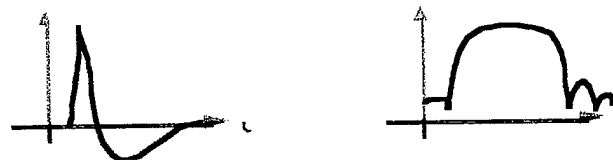
$\tau = 300 \mu\text{s}$

Bubble Cloud Dynamics: Freefield vs Stone

Stone

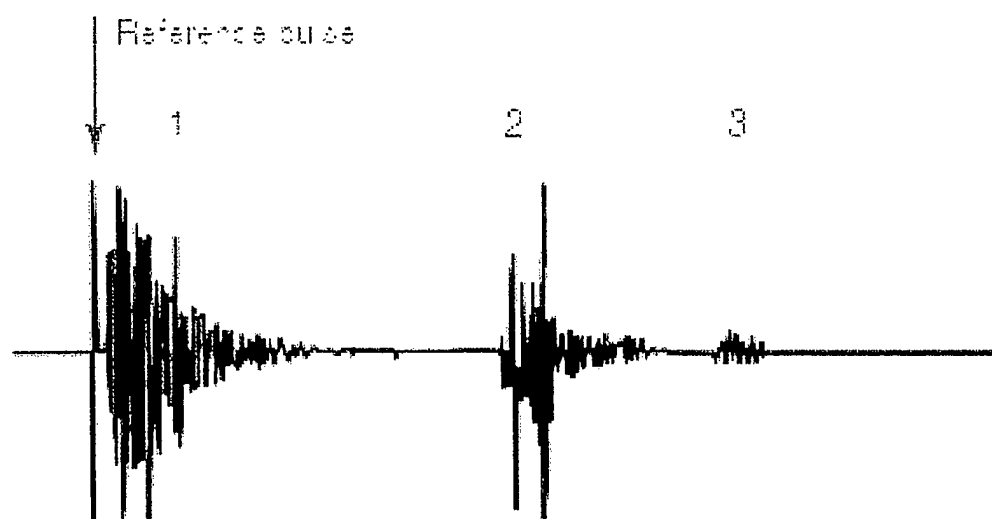


No Stone

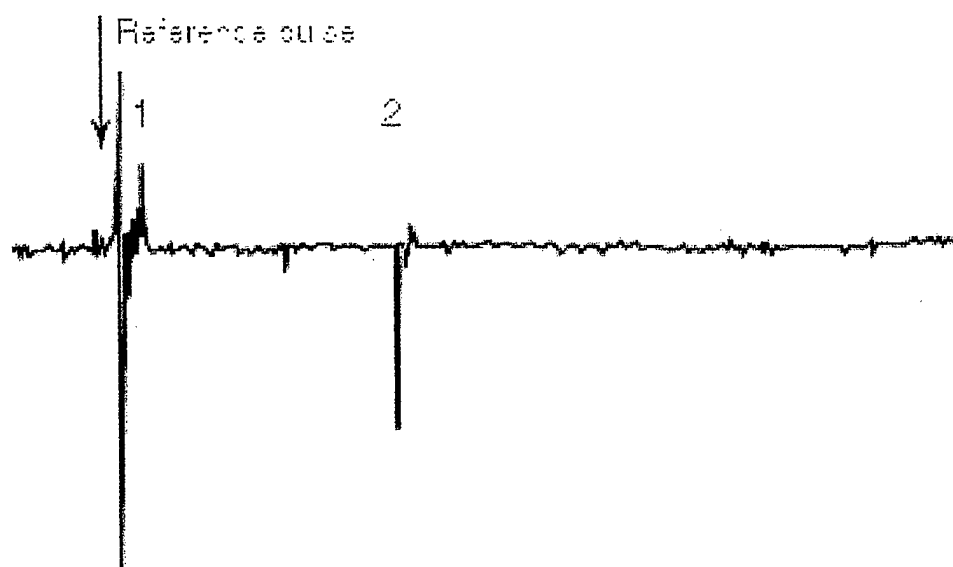


Sonoluminescence and shock wave emissions from ESWL bubbles

Light Emission

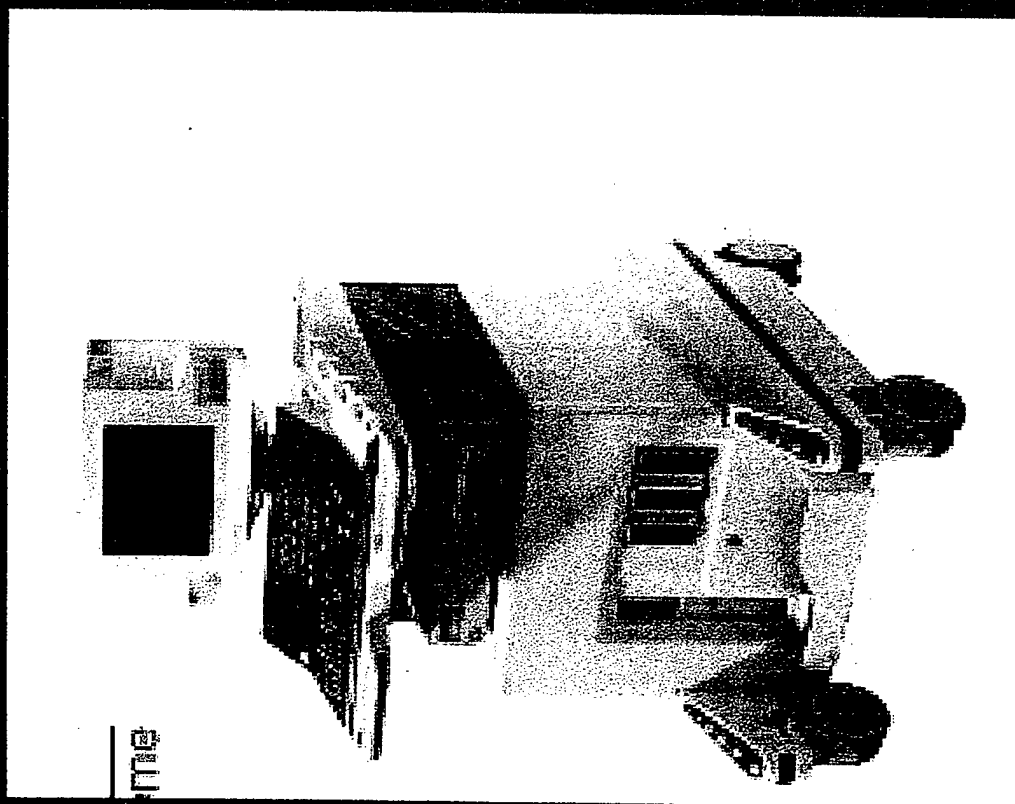


1 Mhz Sound Emission



The remarkable capabilities of diagnostic ultrasound

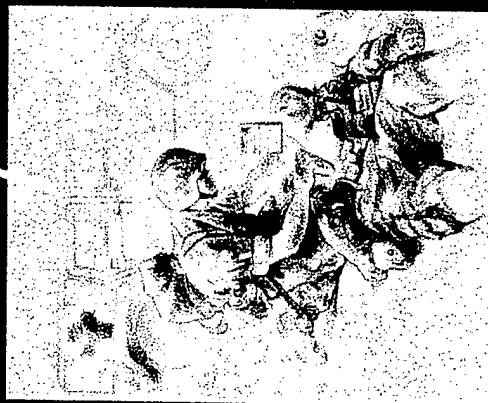
■



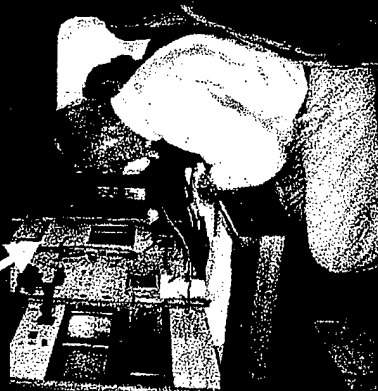
ATL HDI 5000

CIMU • Applied Physics Laboratory • University of Washington

Telemedicine and Medical Ultrasound



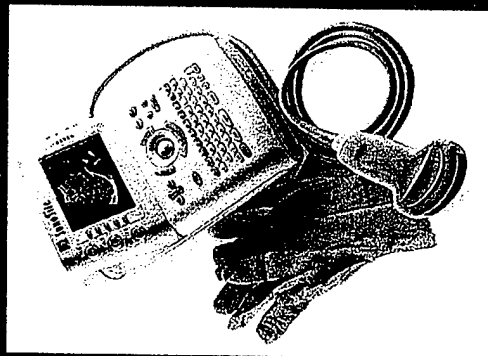
Telemedicine provides the opportunity for remote emergency medicine



ASIC Technology Advantage

Many Boards To One Chip

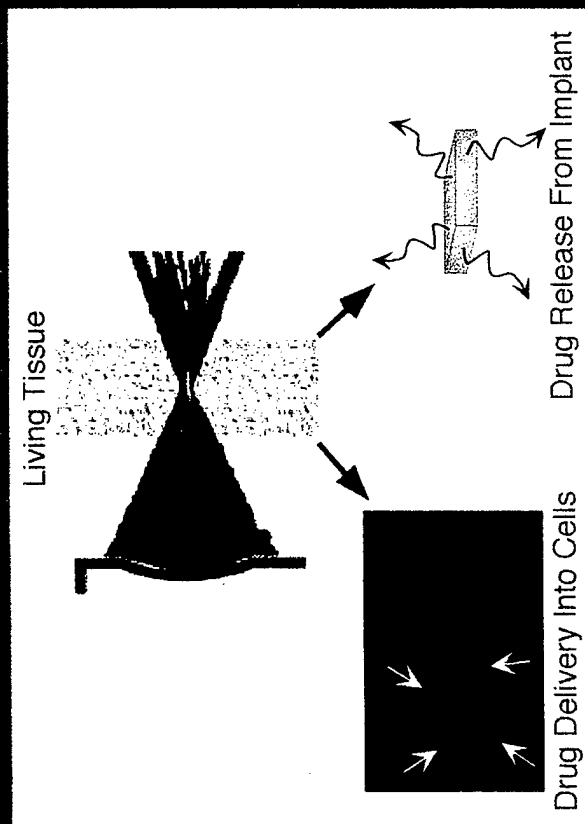
SonoSite



Miniaturization of diagnostic scanners is essential to success

Ultrasonic Drug Delivery and Release

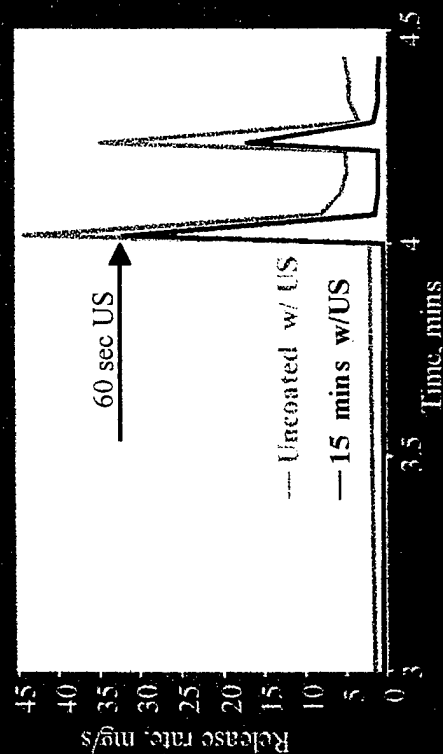
Sonoporation of Dextran (also GFP) into Glioblastoma by HIFU, *in vitro*



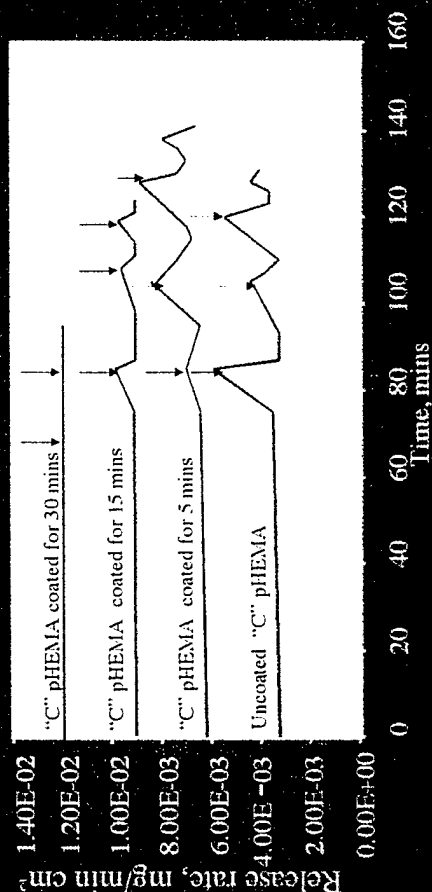
Cell

Cell Fragment

Ultrasonic Drug Release from SAM-Coated Polymer: Antibiotic



Ultrasonic Drug Release from SAM-Coated Polymer: Insulin



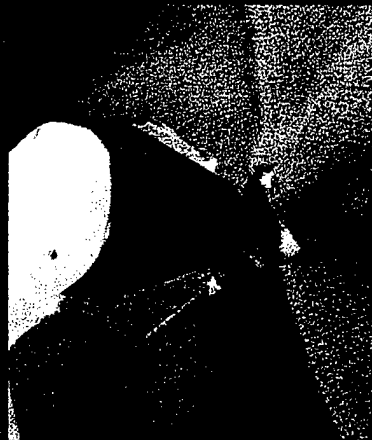
High-Intensity Focused Ultrasound Selectively Disrupts Blood-Brain Barrier, *in vivo*

- Selectively target volumes as small as 1 mm³
- Transient flux of Evans blue-albumin complex (69,500 Daltons), lasting < 96 hours
- No apparent damage as seen by light and electron microscopy

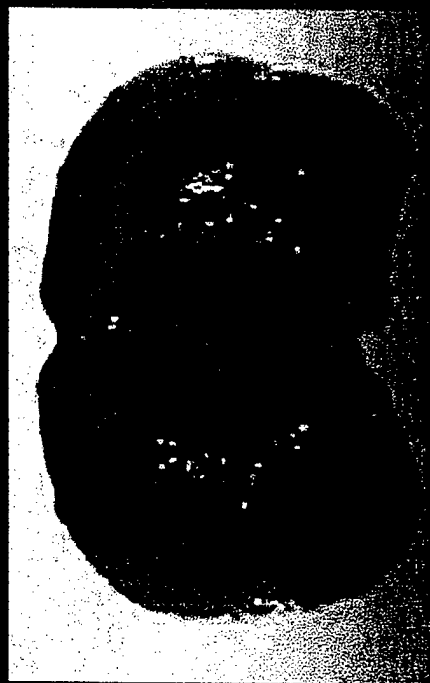
Exposed Dura



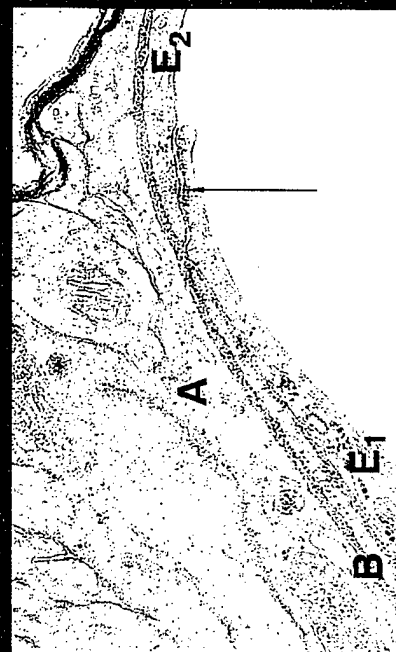
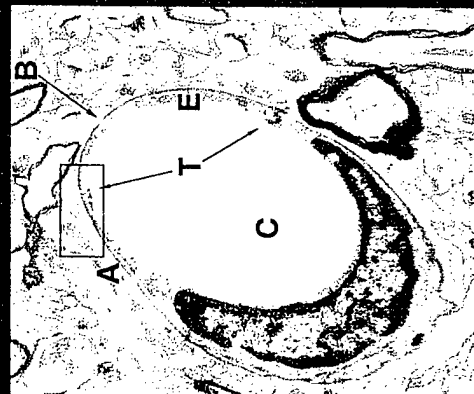
Laser-guided HIFU

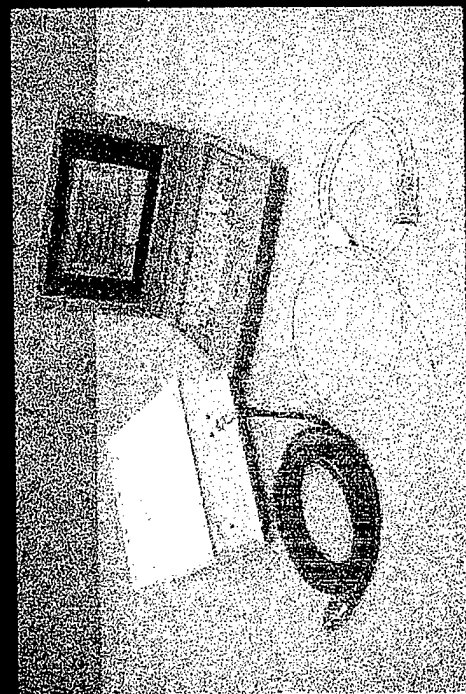


Coronal Slice Showing Evans Blue Flux

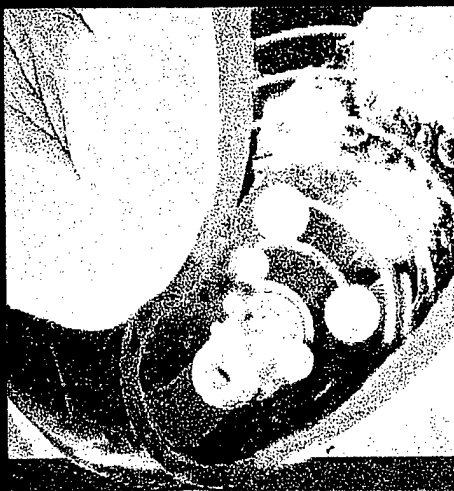


Electron Microscopy Showing Open Tight Junctions

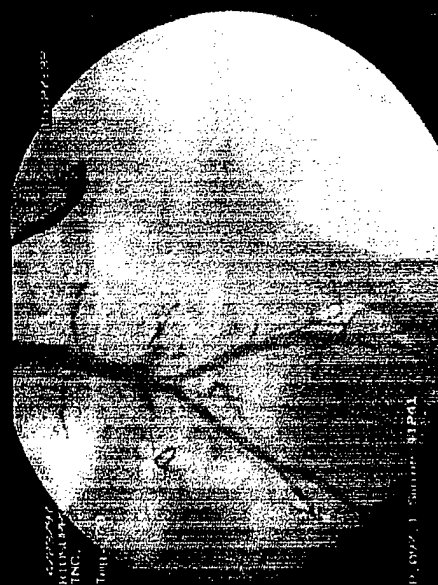




Catheter and Control System



Thrombolytic drug plus ultrasound is delivered at site of clot



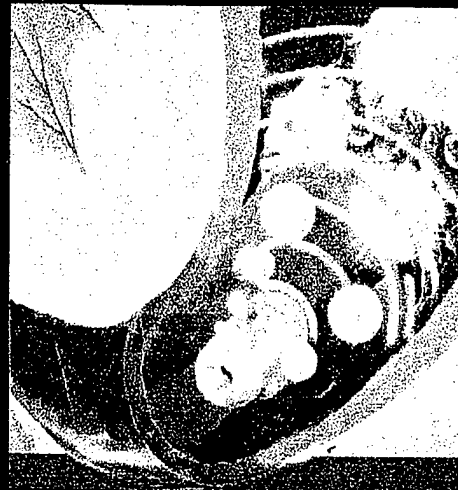
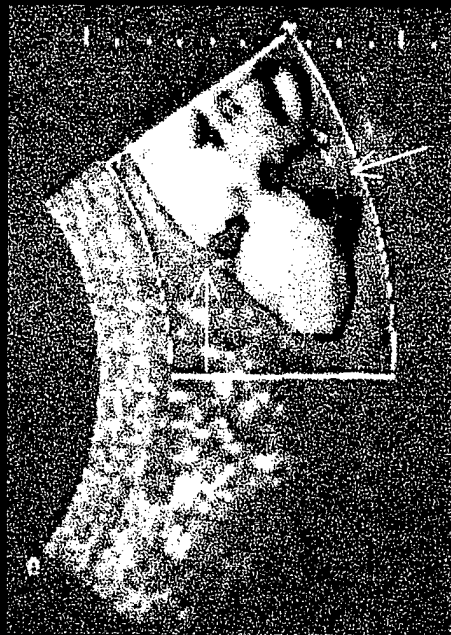
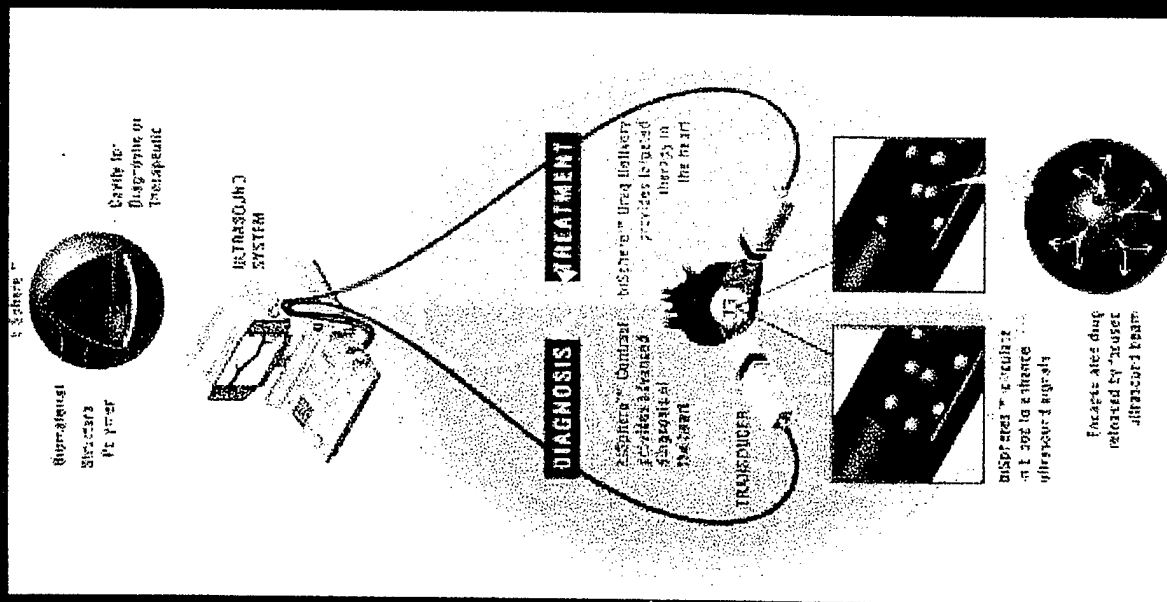
Both branches of a porcine vein are blocked

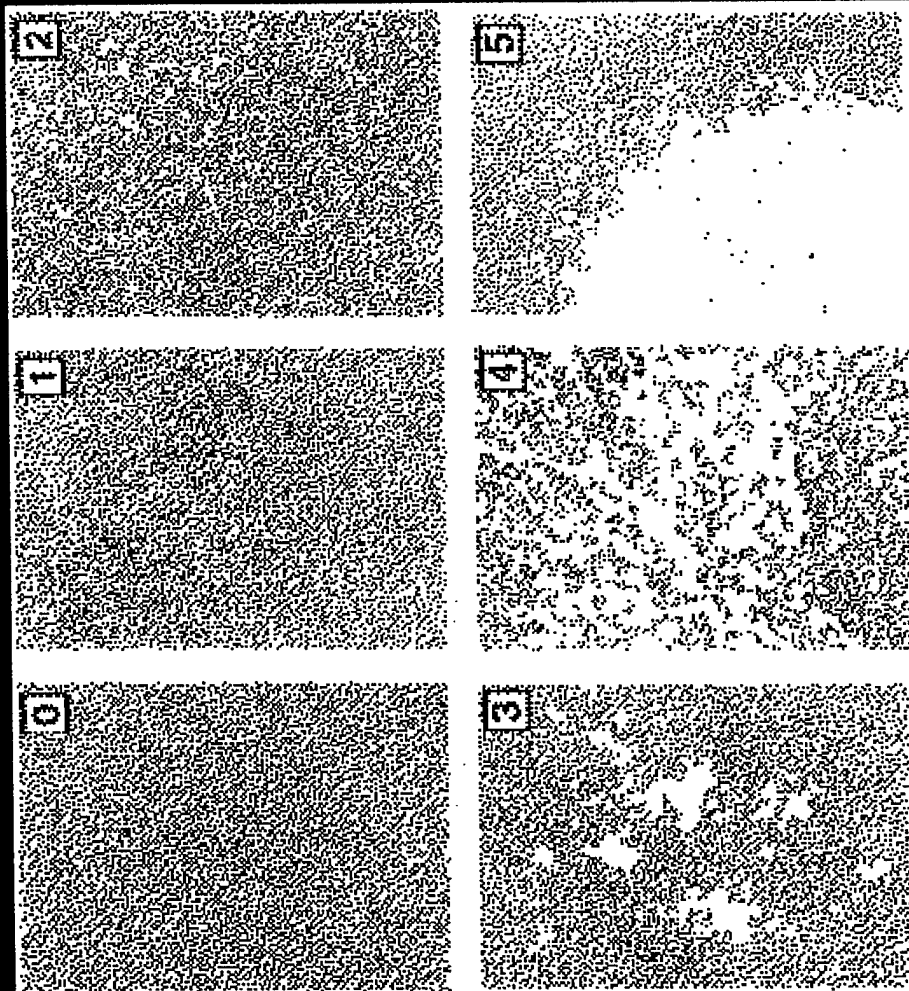


**Branch with drug only remains blocked;
Branch with drug plus US is opened**

CIMU • Applied Physics Laboratory • University of Washington

Ultrasound contrast agents (stabilized microbubbles) can improve both imaging and therapy





Score = 0; uniform cell distribution.

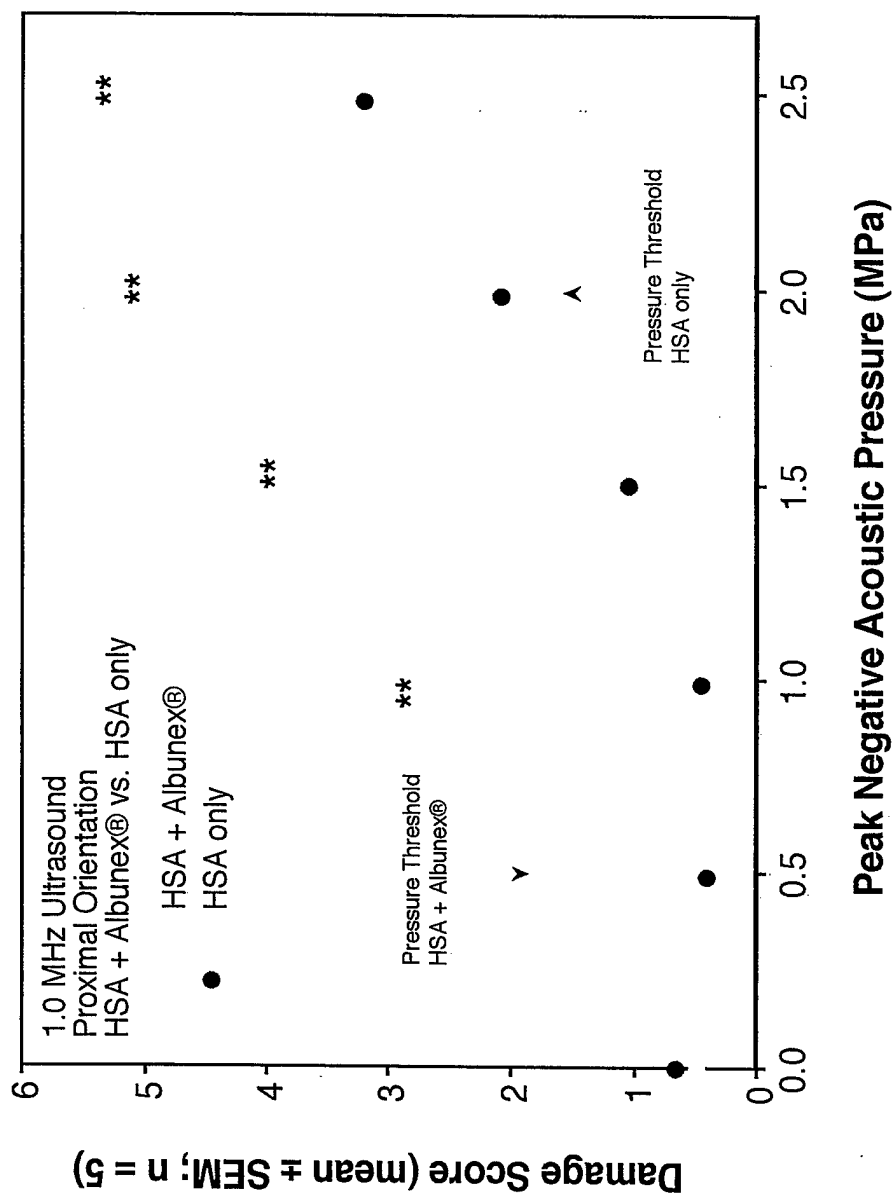
Score = 1; subtle departure from normal appearance.

Score = 2; slight but discernible damage characterized by discrete pock-marks (~100 μm diameter), suggesting their creation by individual bubble-collapse events.

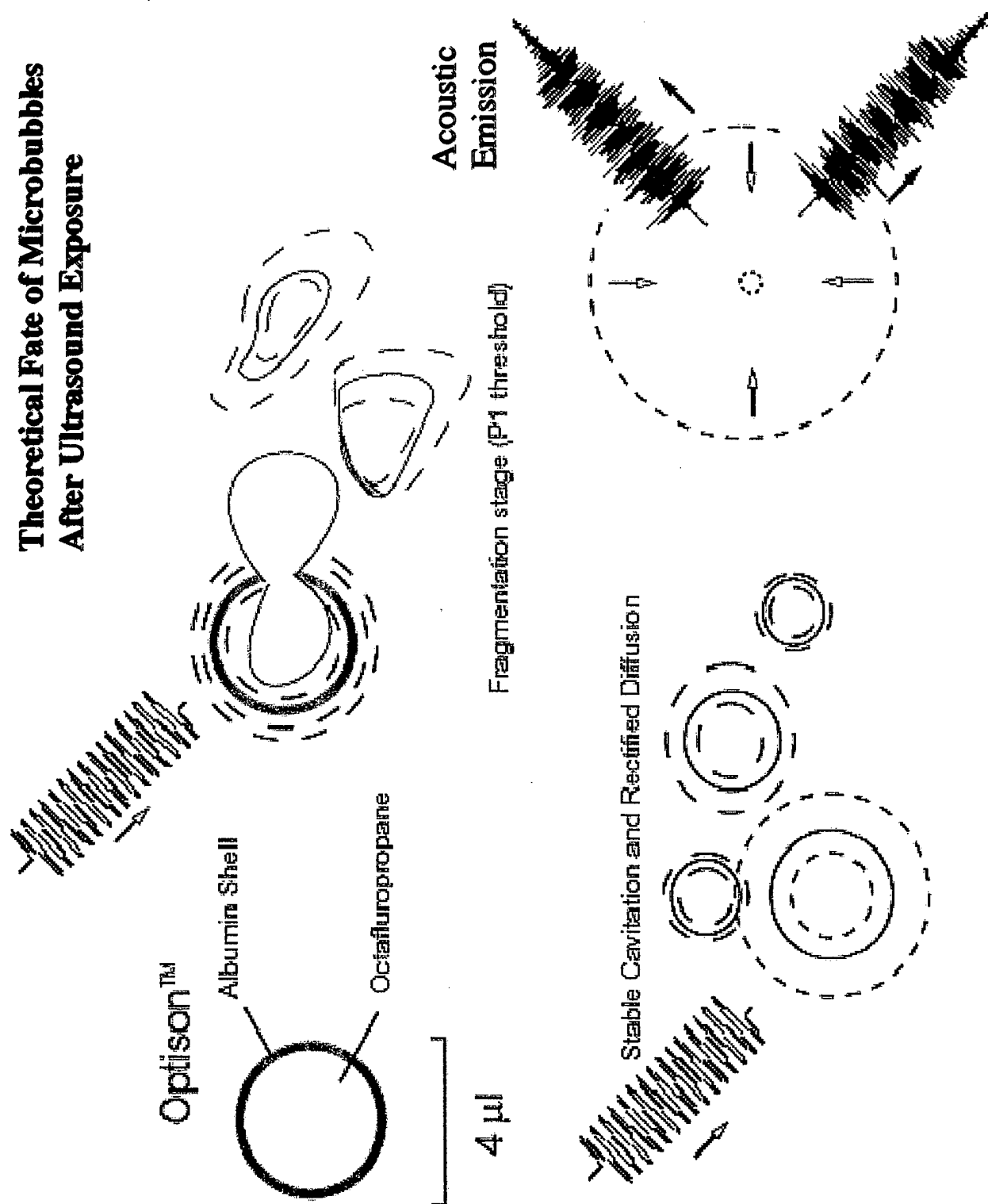
Score = 3; moderate damage, pock-marks widely distributed and on the order of a few hundreds of μm in diameter. Their lobed structure suggests that they are composites of overlapping, smaller pock-marks.

Score = 4; severe damage. Extensive, but incomplete, removal of cells from the central area of the image. At lower magnification, such partially-denuded areas often appeared to radiate from the center toward the periphery of the ML.

Score = 5; complete removal of cells from a circular area (only a portion is illustrated). With increasing distance from the periphery of this 'hole', the severity of damage to the remaining ML decreases in a pattern analogous to descending damage scores of 4 \rightarrow 3 \rightarrow 2.

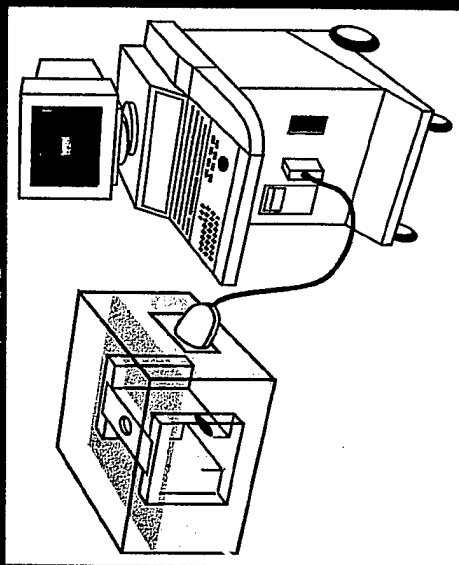


Theoretical Fate of Microbubbles After Ultrasound Exposure

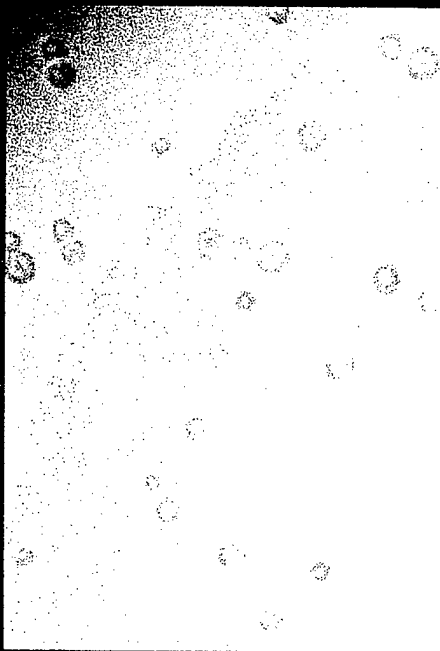


Gas-filled ultrasound contrast agents

Experimental apparatus

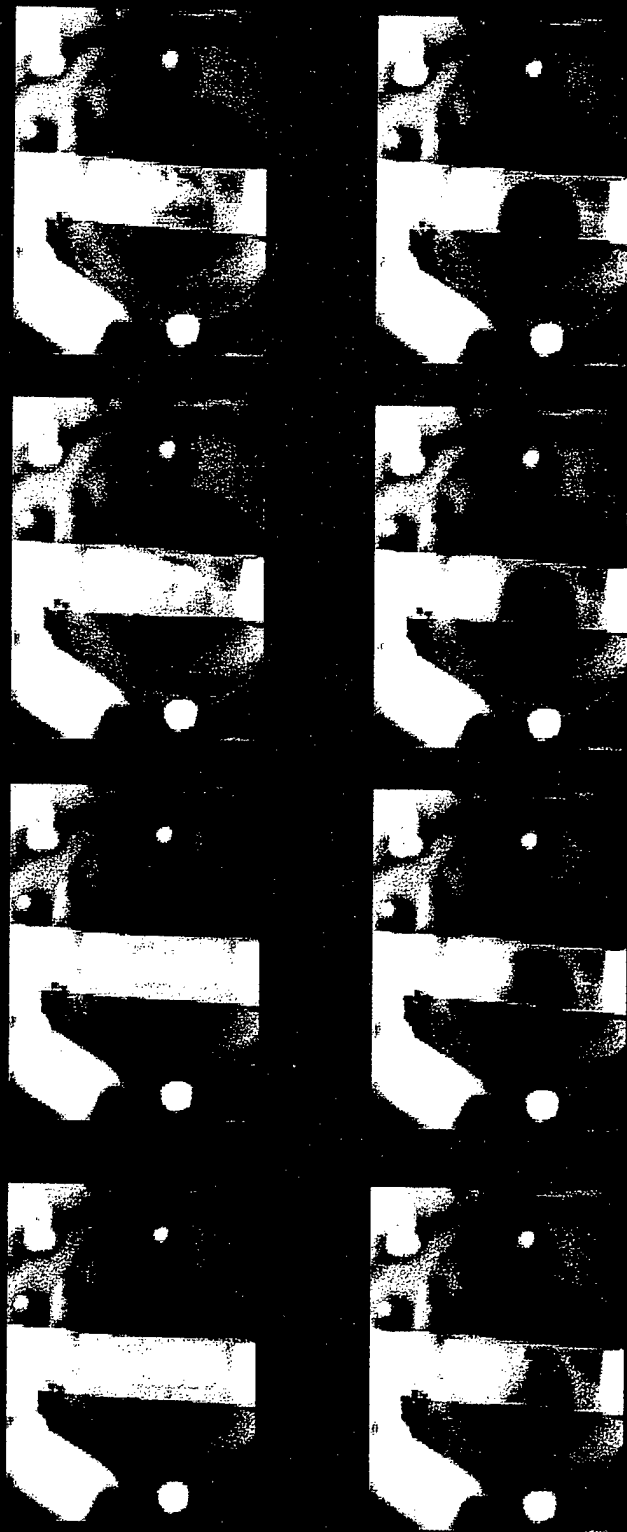


Contrast agents with elastic shells



Scattering properties of contrast agents as a function of concentration

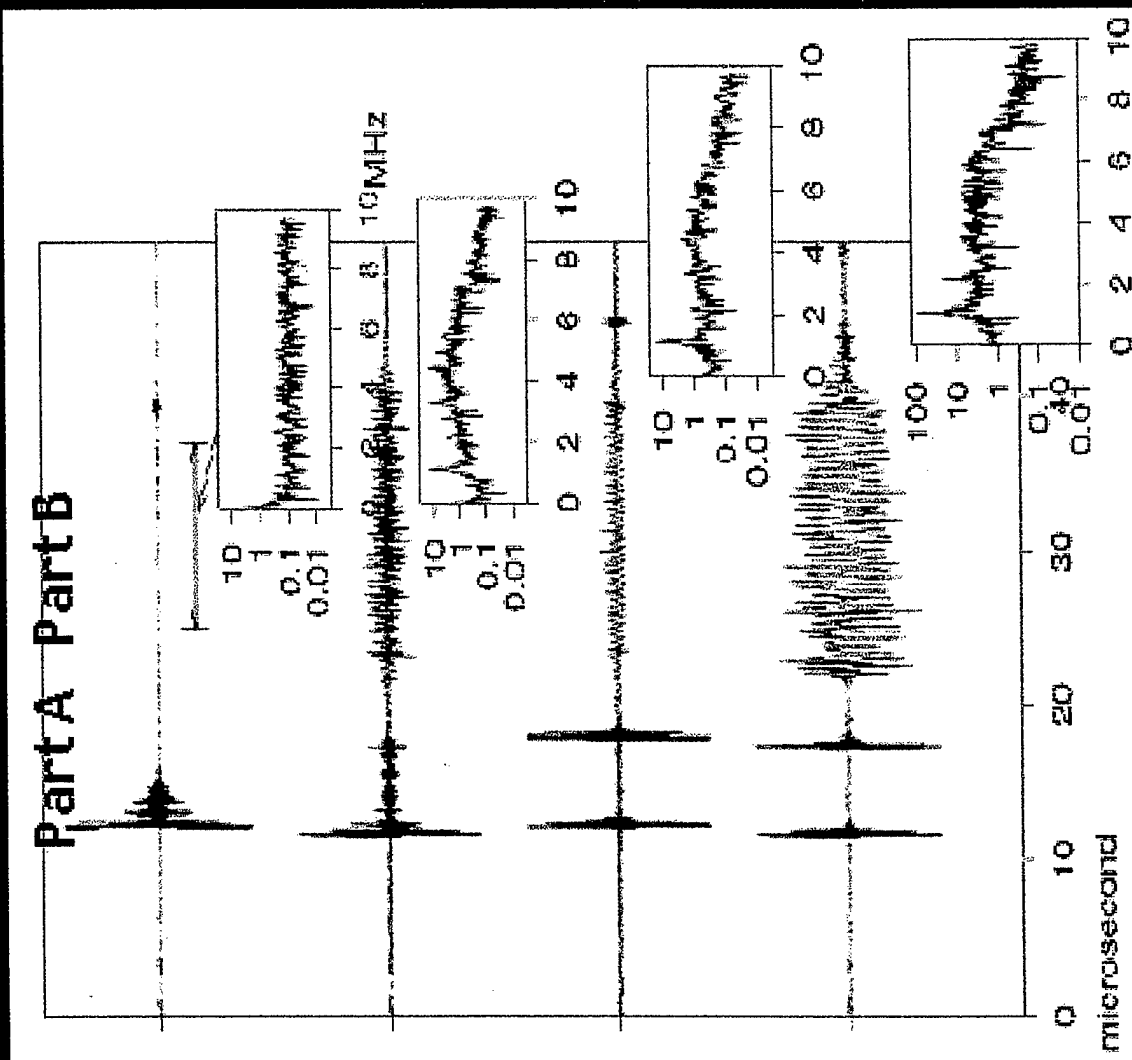




Fragmentation stage:

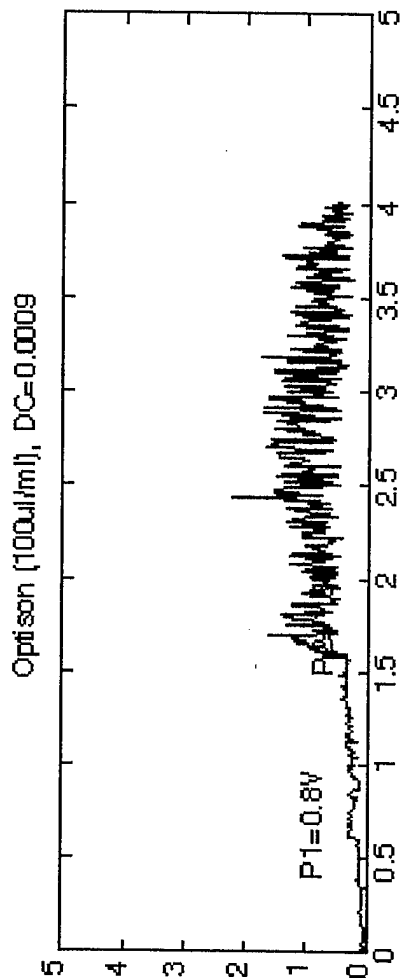
1. bursts of streaming flow
2. Loss of albumin shell
3. Onset of the first inertial cavitation (IC) activity

Part A: Scattering
signals (5 MHz)
Part B: Inertial
Cavitation Signal
(FFT: broadband noise)



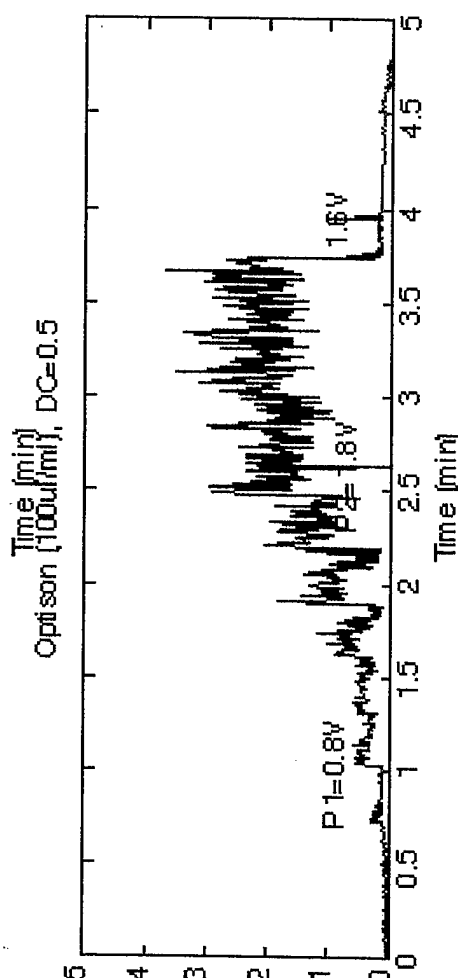
Inertial cavitation of Optison™ at short and long DC

Peak to Peak
Amplitude of
Inertial Cavitation
Signals (V)

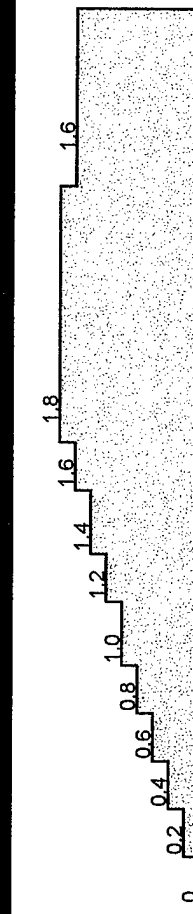


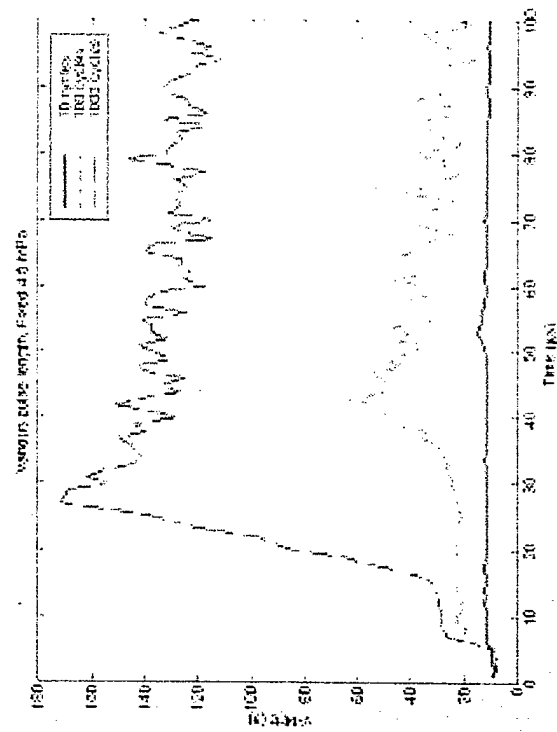
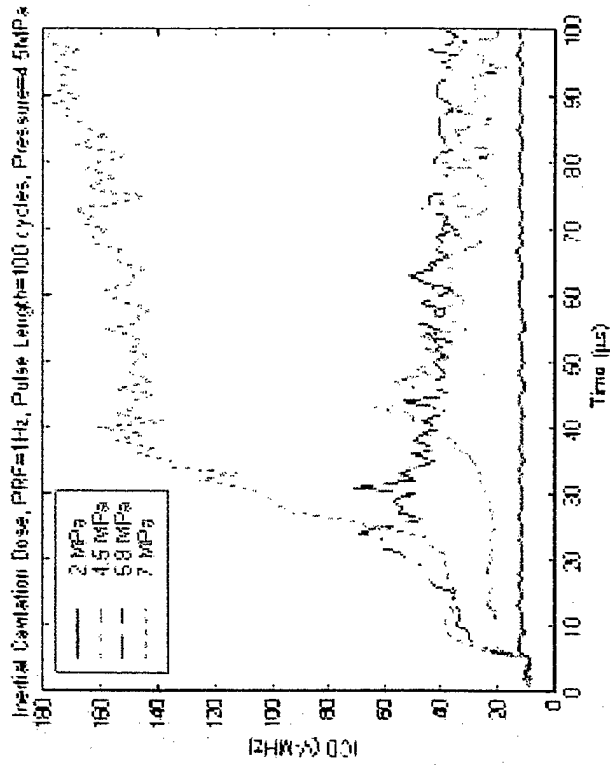
P1=0.8V=0.95 MPa (pp)
P2=-.18V=4.79 MPa (pp)

Peak to Peak
Amplitude of
Inertial Cavitation
Signals (V)

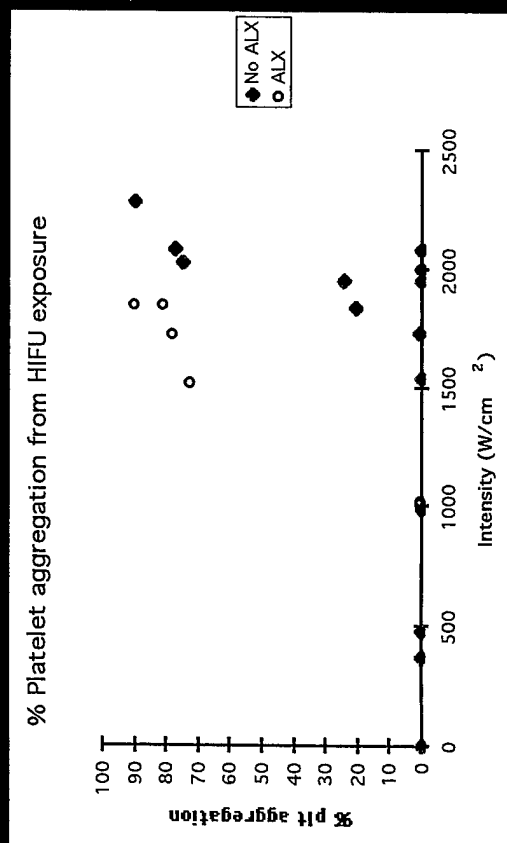
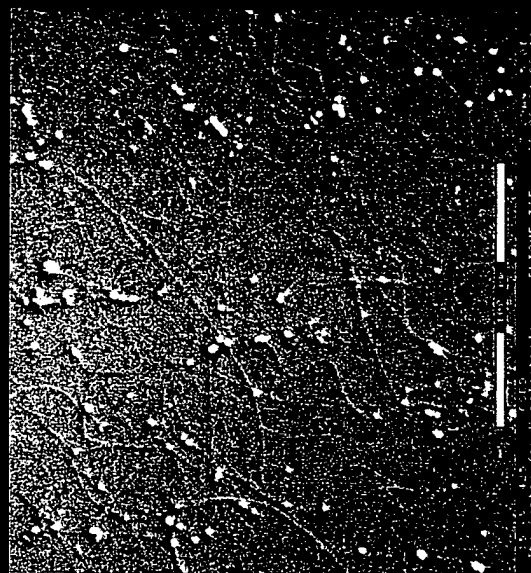
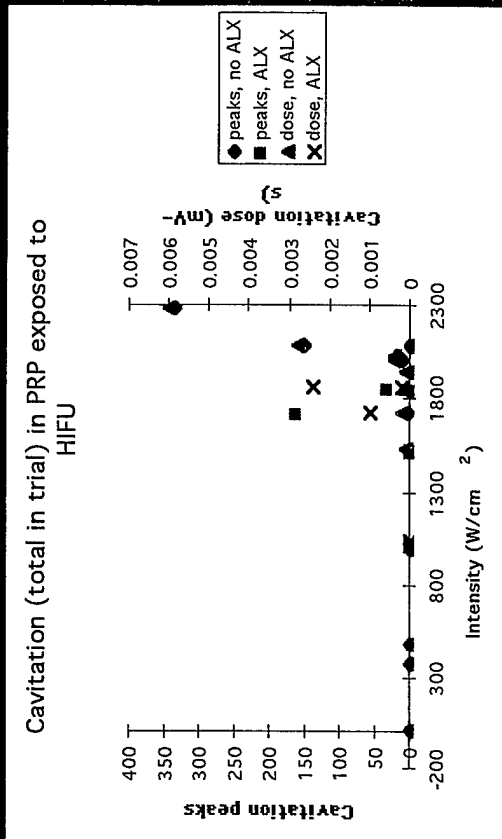
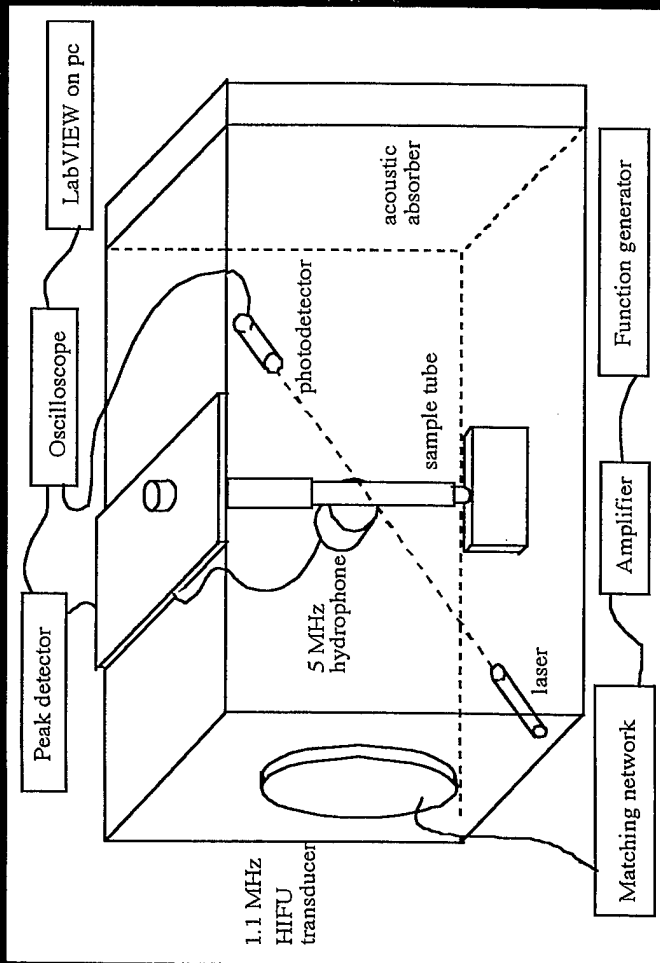


Voltage output
from FG (V)

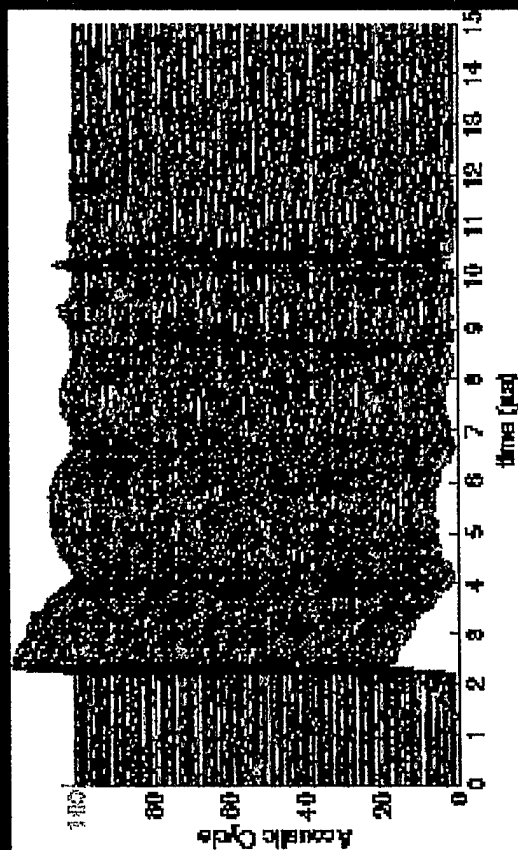
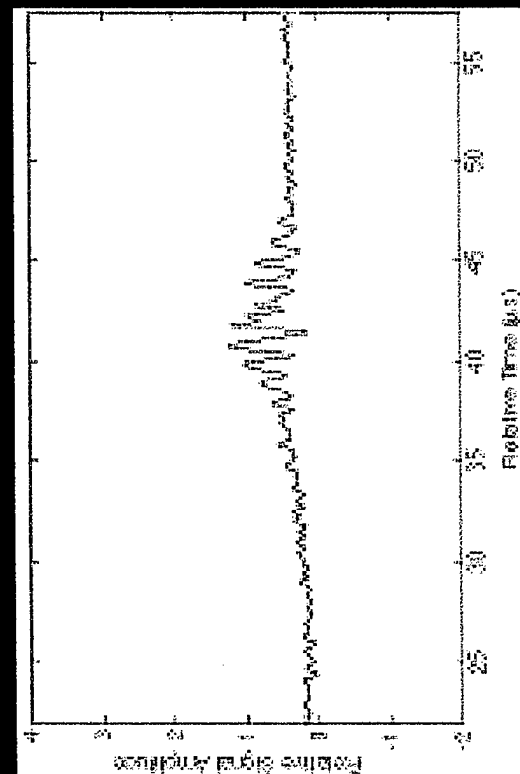
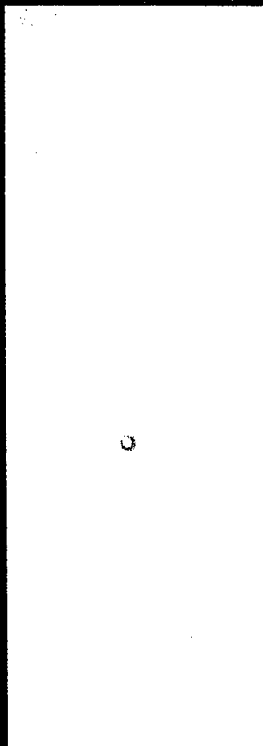
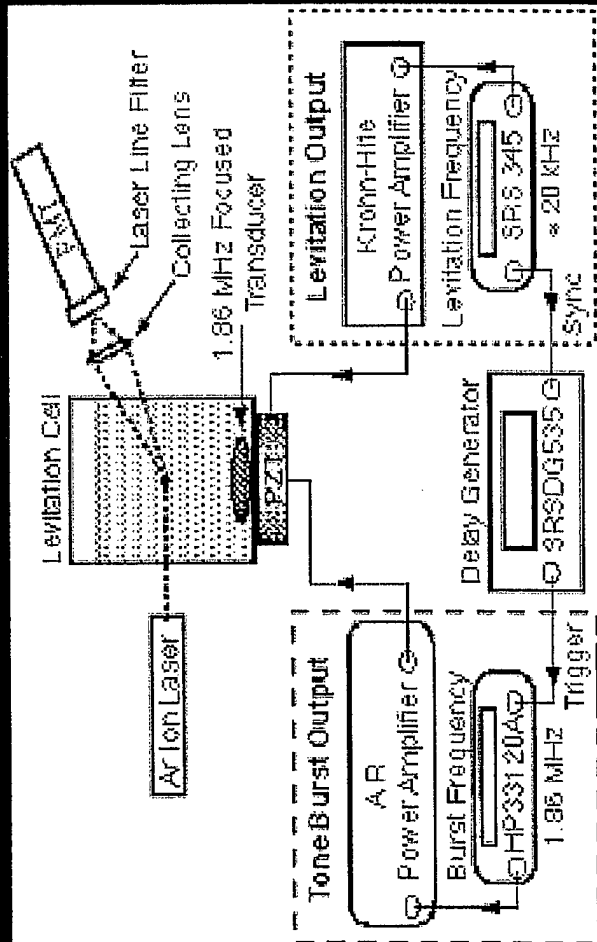




Acoustic Coagulation



With physical acoustics techniques, we can study a single contrast agent microbubble

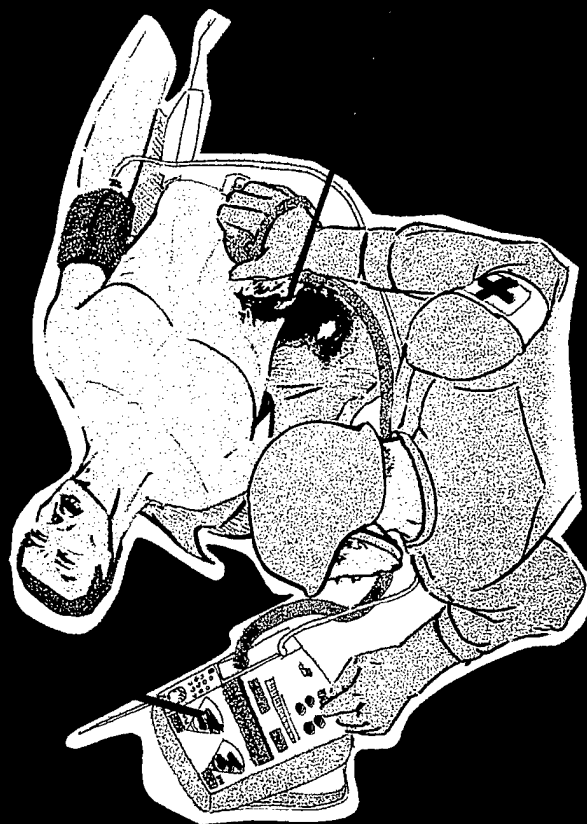


Remote Emergency Medicine

Ultrasound scanners can detect blood flow in organs such as the kidney

On the battlefield, 40% of combat casualty mortality results from exsanguination

High Intensity Focused Ultrasound can stop bleeding



CIMU • Applied Physics Laboratory • University of Washington

Bloodless Ultrasound Surgery

High Intensity Focused Ultrasound (HIFU) can be used for surgery and to stop bleeding

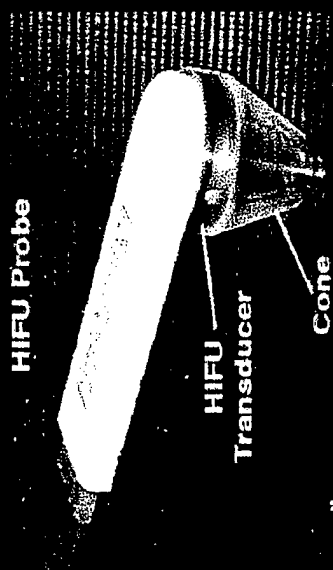
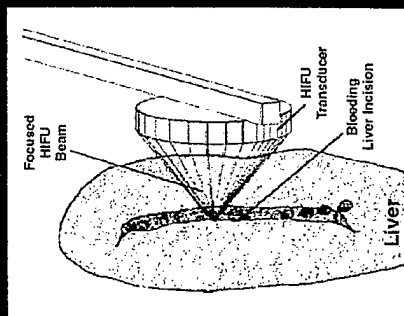
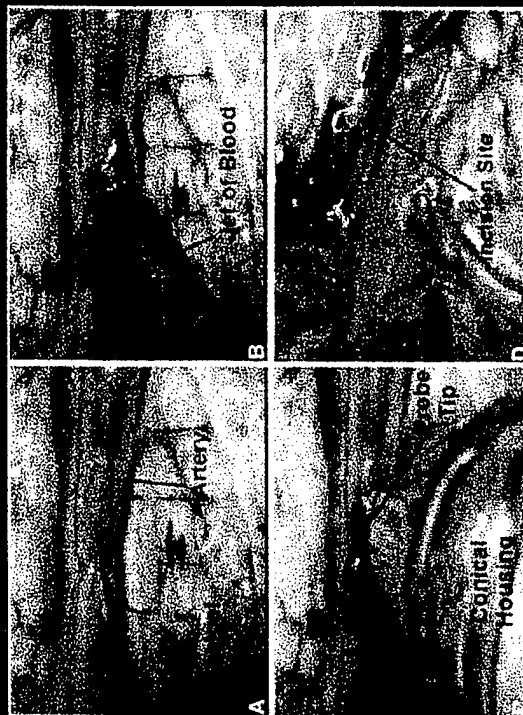
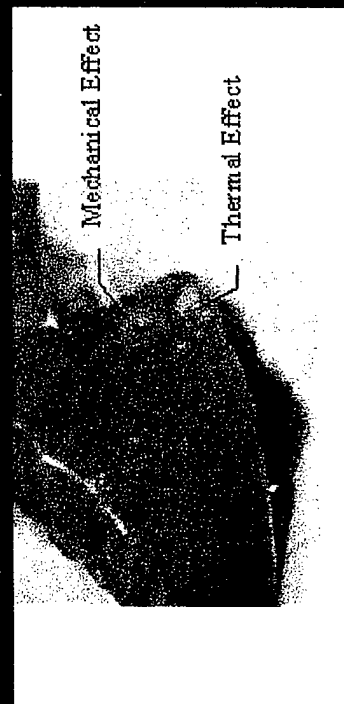


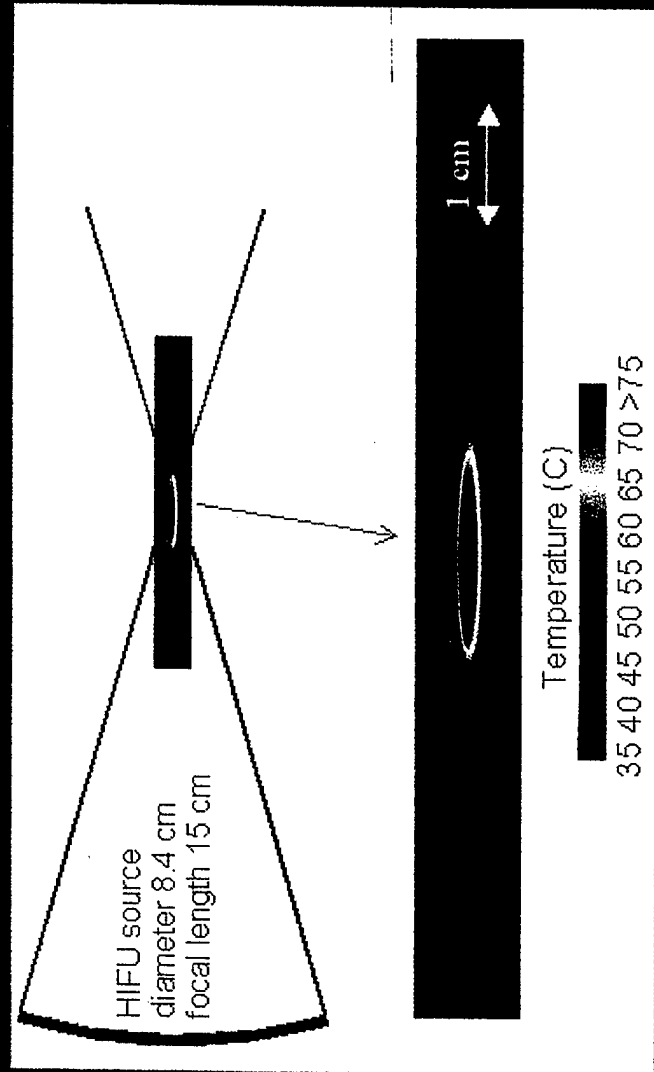
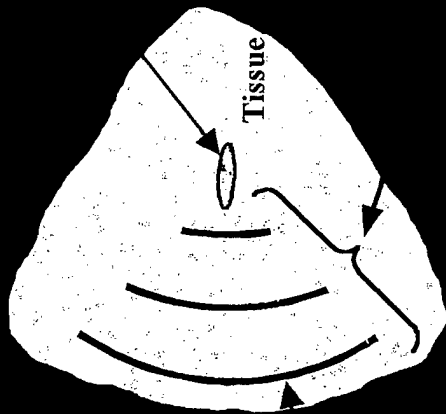
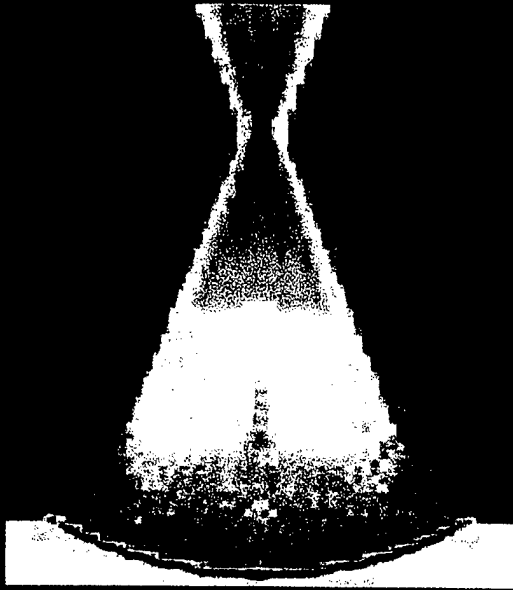
Figure 2

HIFU probes like this can stop bleeding in large veins and arteries within a few seconds



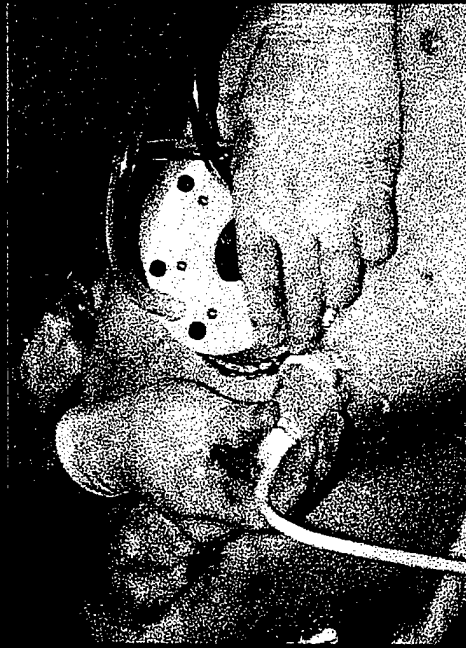
HIFU can ablate tissue and simultaneously prevent the treated area from bleeding





Non-Invasive Cancer Therapy

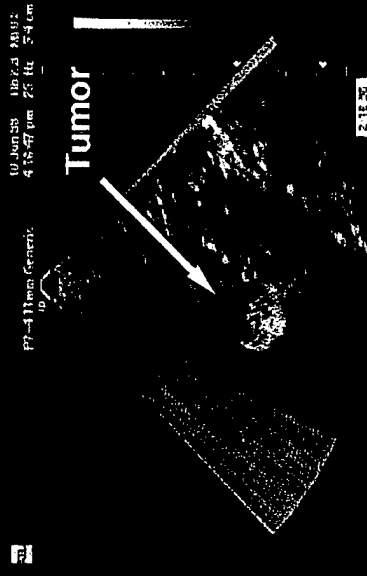
Free-Hand HIFU



Treated Liver



Cancer Tumor Can be Seen with Diagnostic Ultrasound

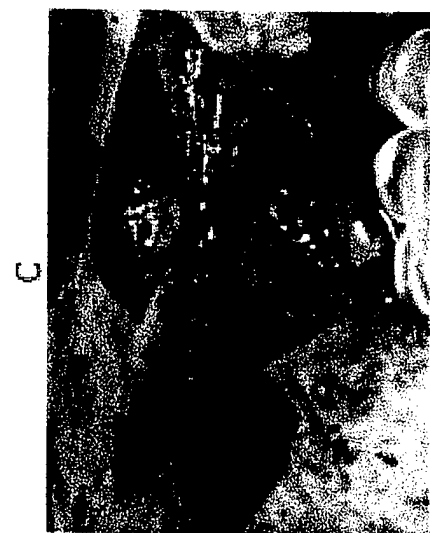
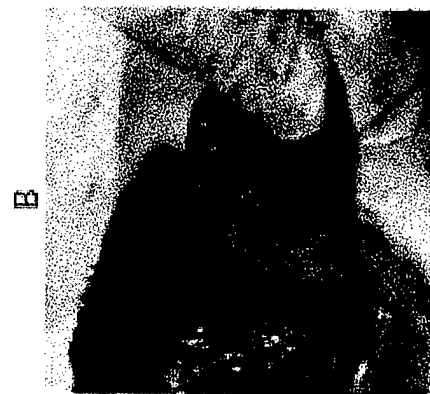
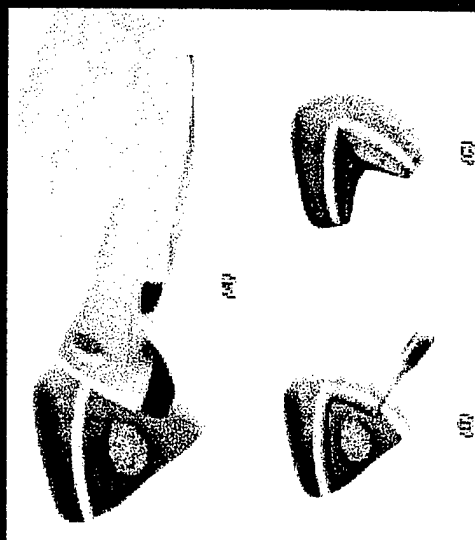
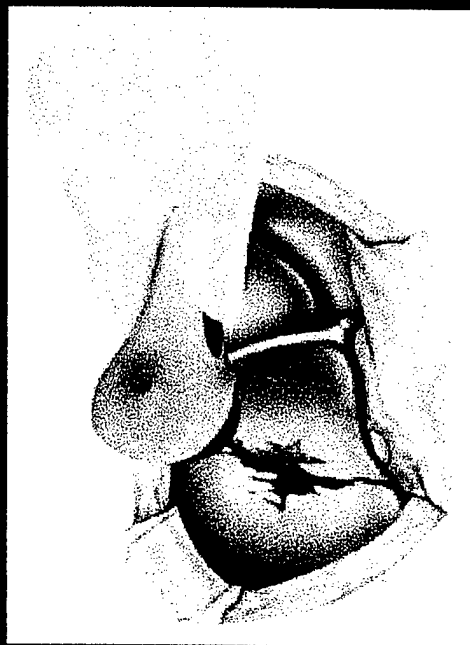


Cancer Tumor Could be Treated with HIFU

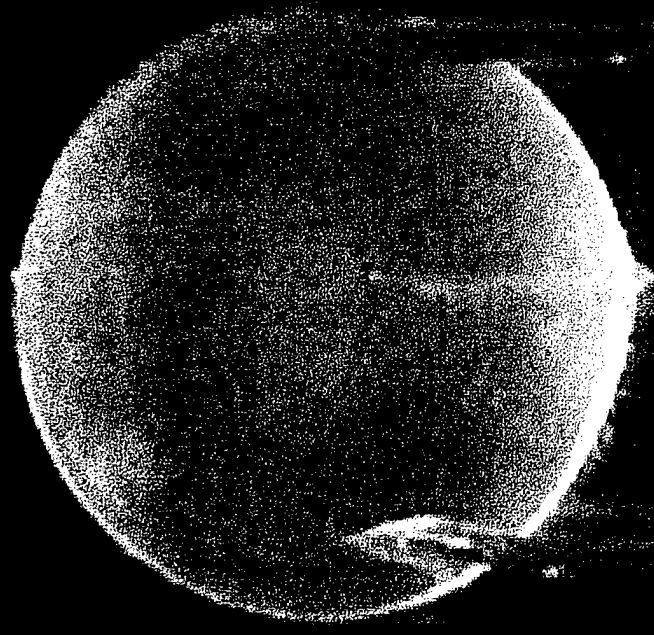


cs Laboratory • Un

HIFU techniques for preauterization



CIMU • Applied Physics Laboratory • University of Washington



CIMU • Applied Physics Laboratory • University of Washington

HIFU-Lesion imaging techniques

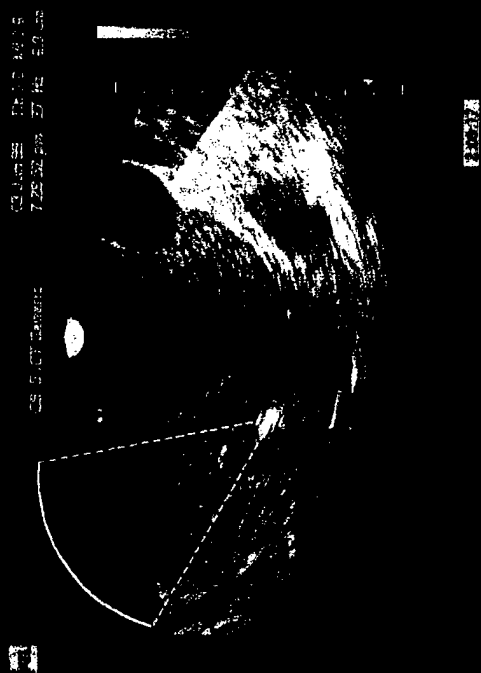
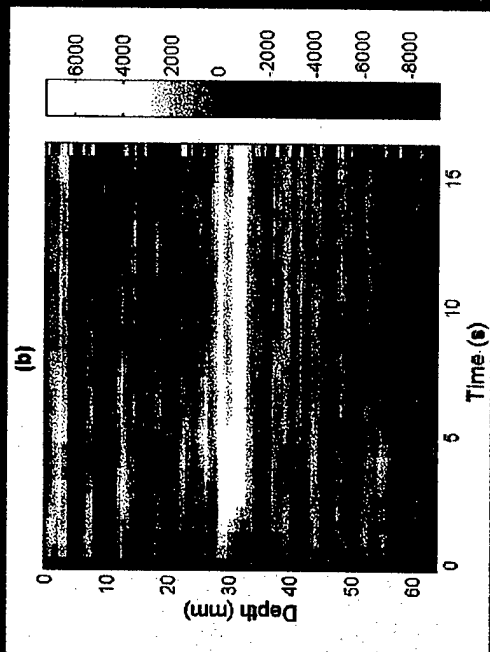
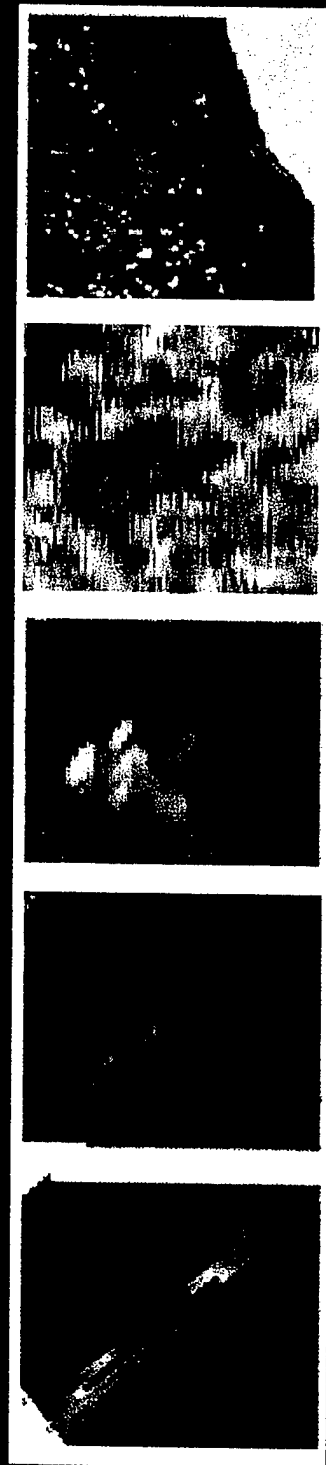


FIGURE 1
HIFU-Focus outgasing



Sound Attenuation

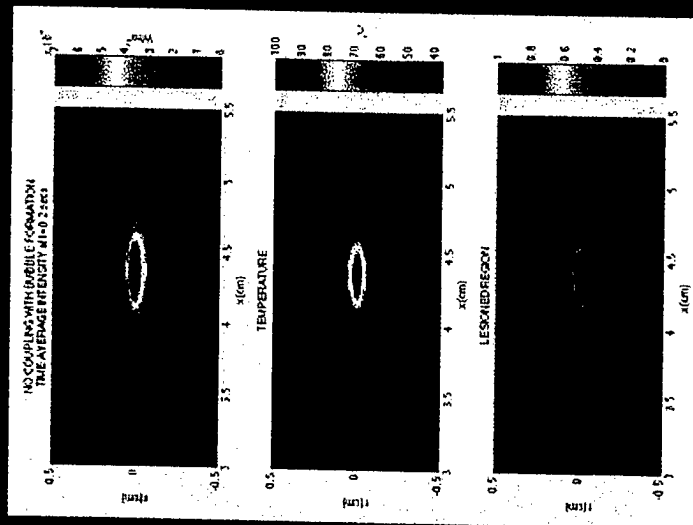


Various Doppler techniques

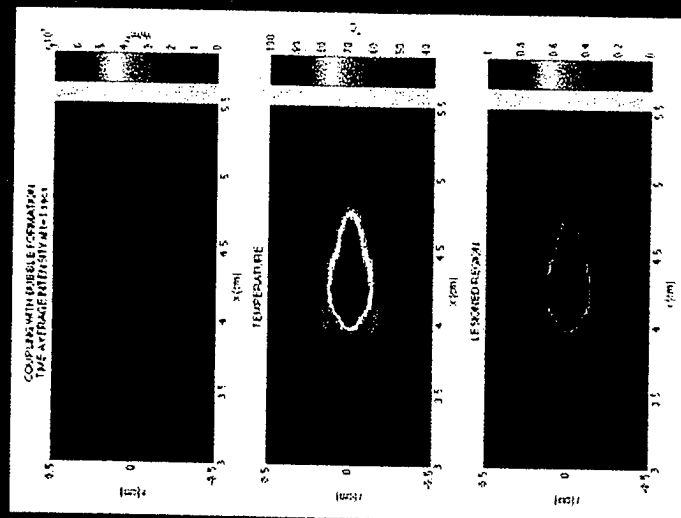
Effect of cavitation during lesion formation



Short fat lesions imply bubbles at focus

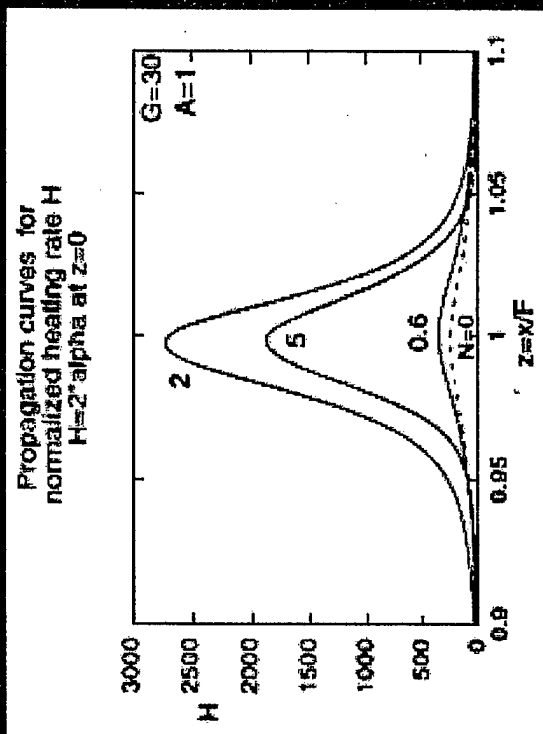
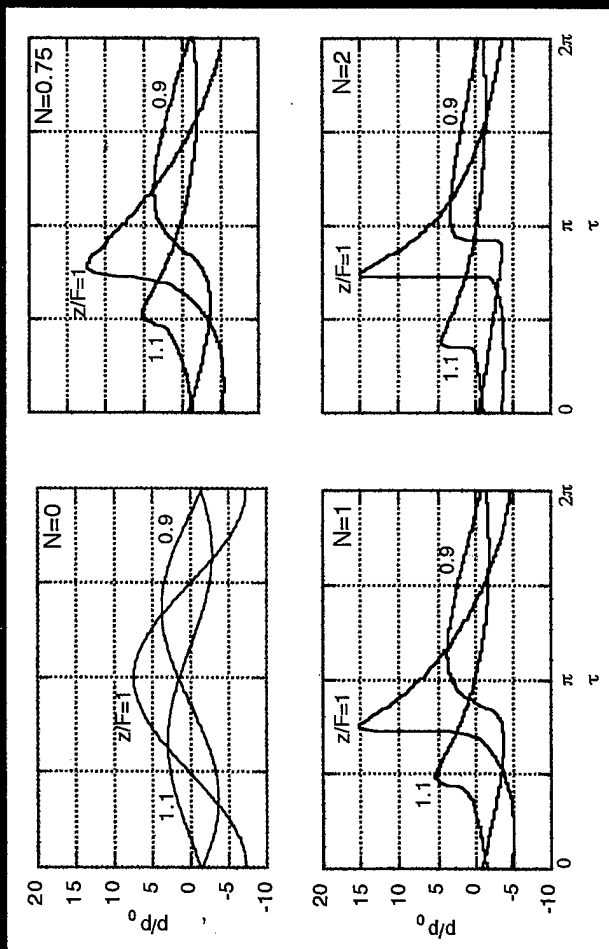


No Cavitation



Cavitation at focus

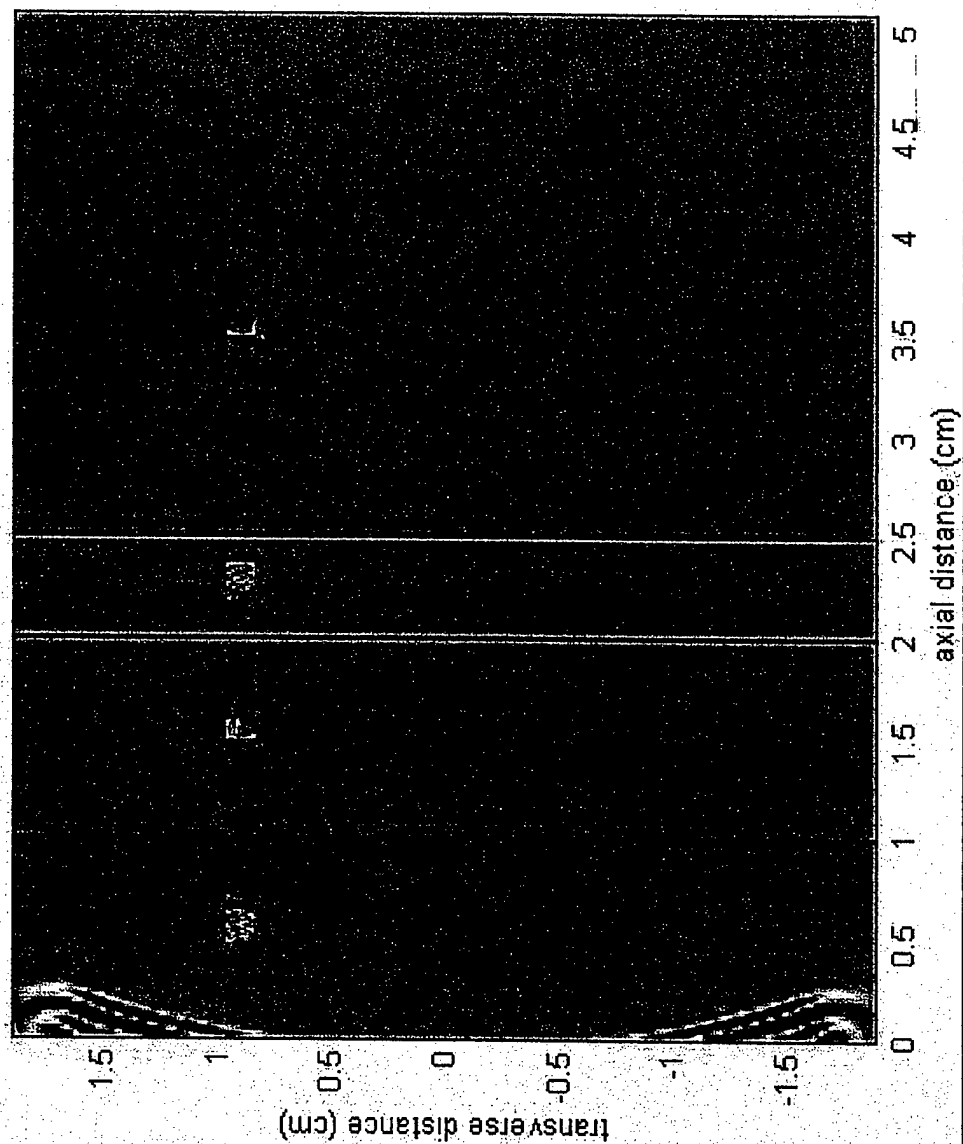
Nonlinear effects of HIFU

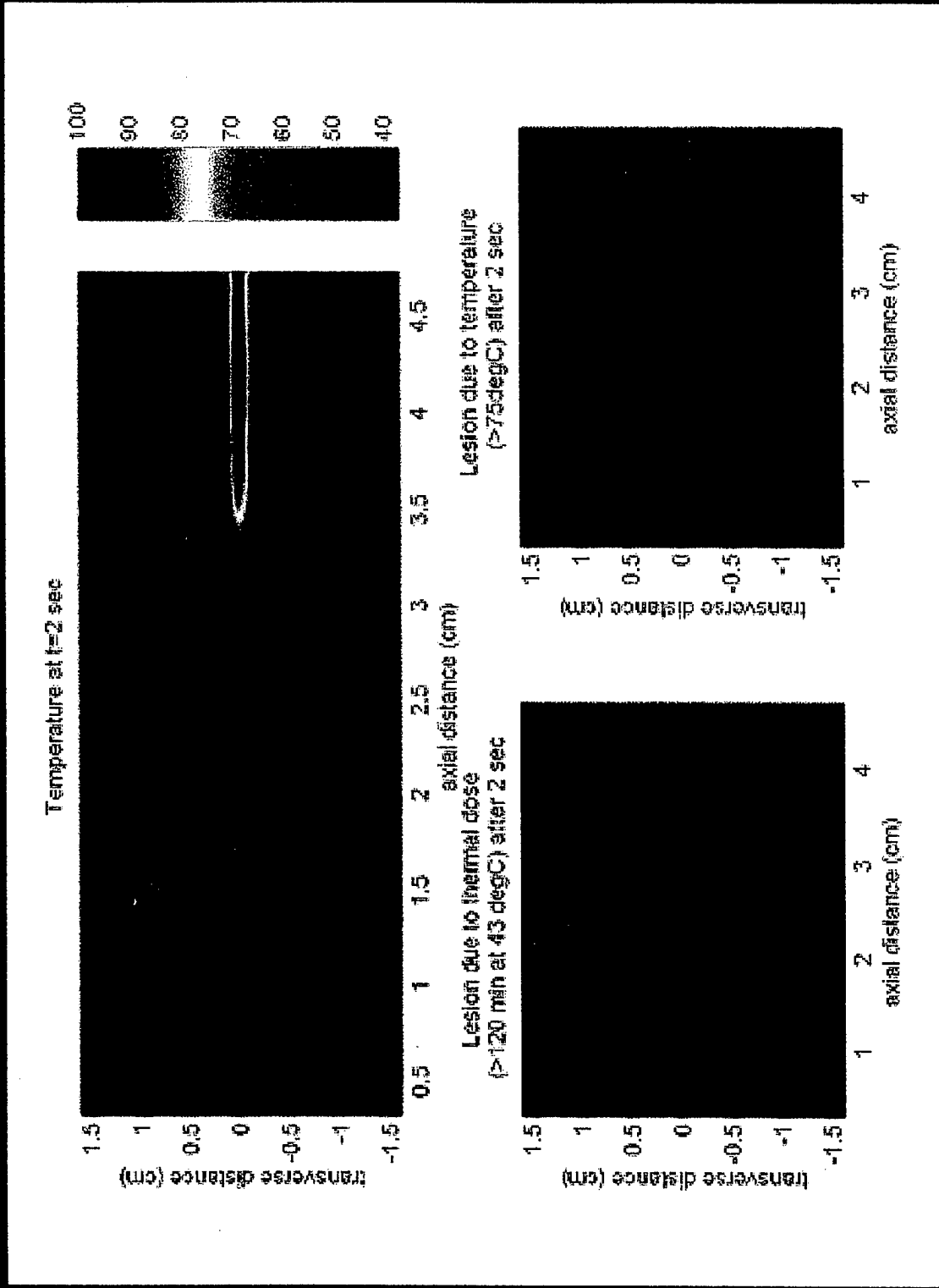


Modeling of HIFU pressure pulse in layered medium

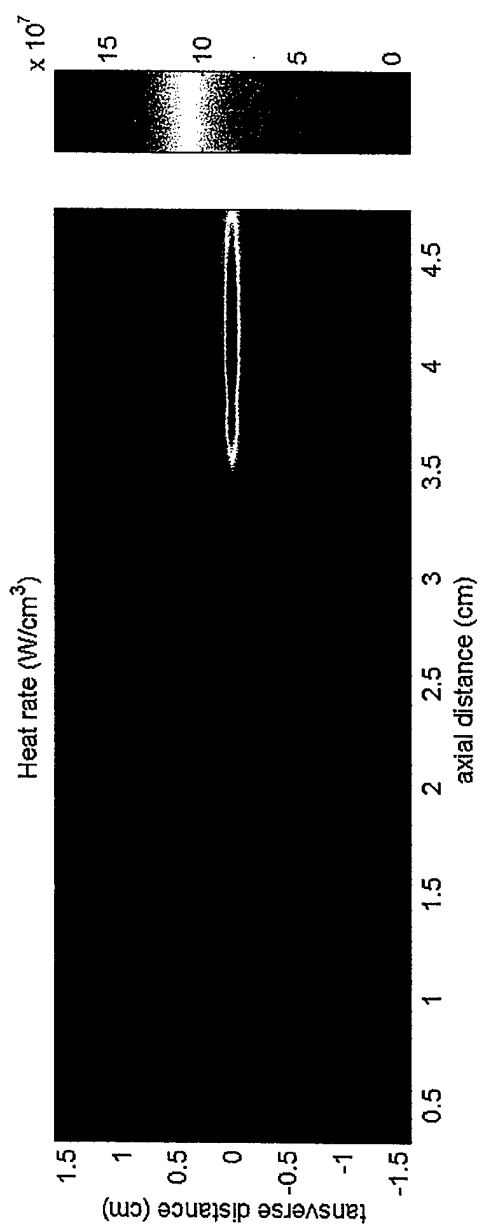
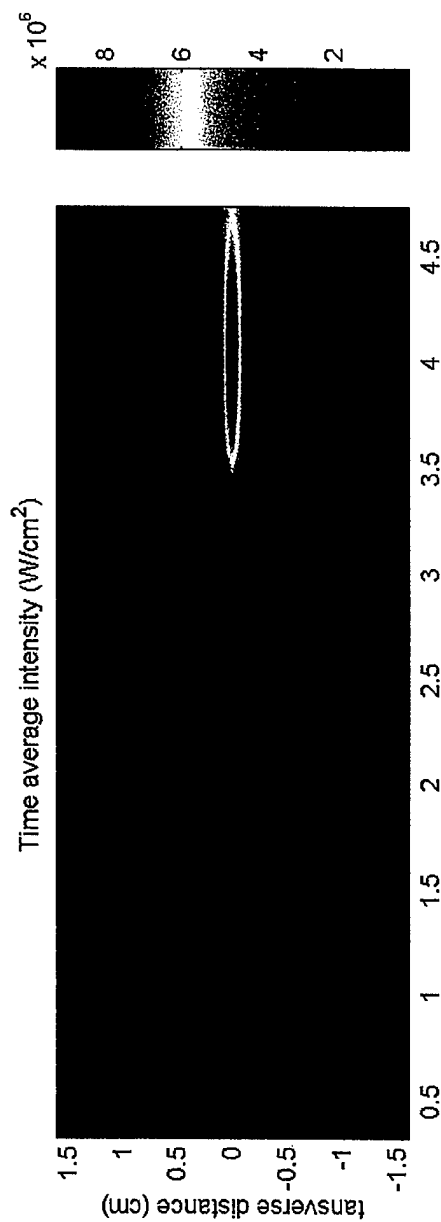
Pressure pulse through layered media

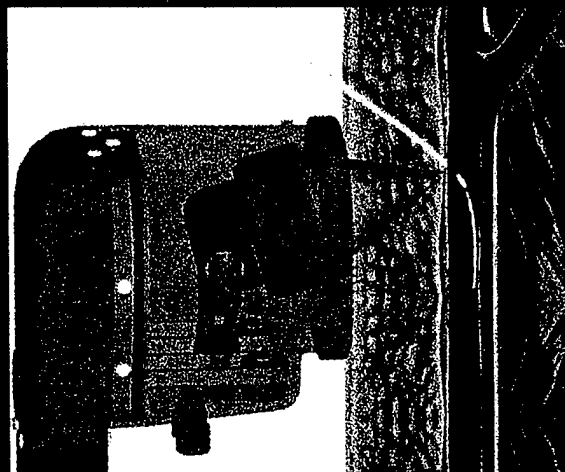
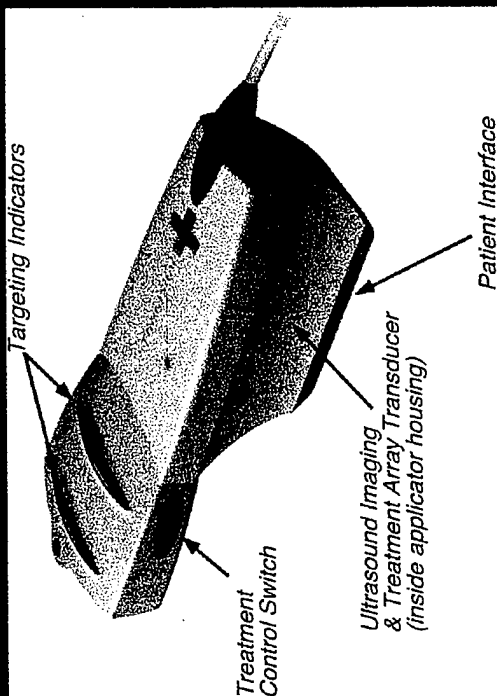
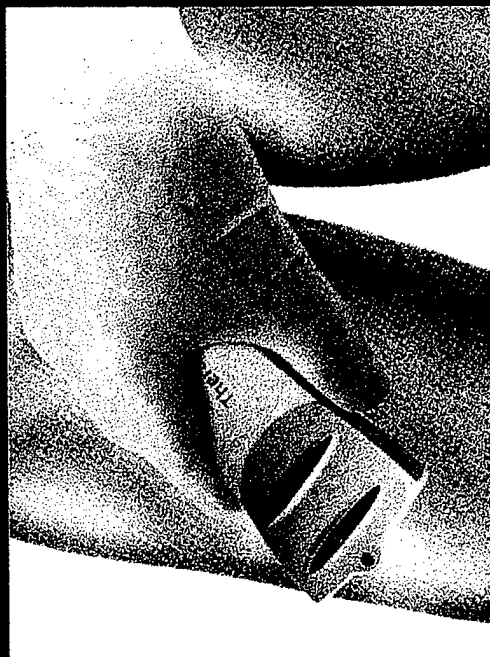
W=water F=fat M=muscle L=liver



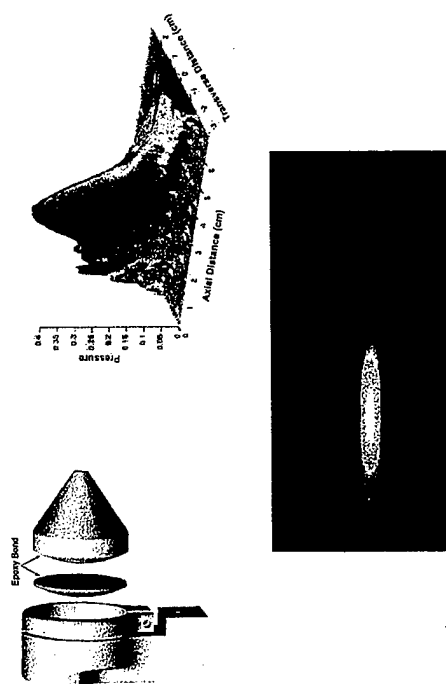


Computational modeling of HIFU field and thermal lesion





Solid Cone HIFU Transducer



**Time in the "Golden Hour" to Onset of Shock
Versus Bleeding Rate After Being Wounded**

Minutes

Death

Shock

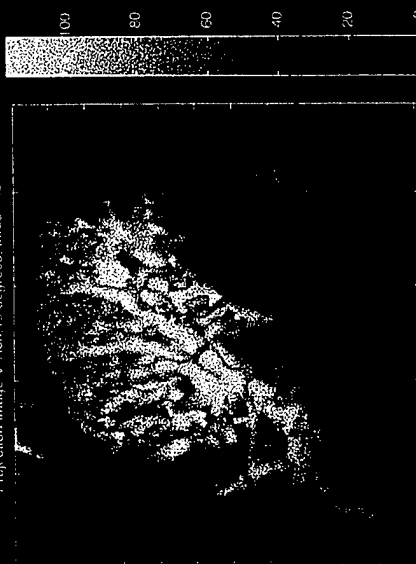
CIMU • Applied Physics Laboratory • University of Washington

Diagnostic Ultrasound Can Image Blood Flow



RENAL VASCULATURE
2D CPA Image of Kidney

Projection Image V Hen 19 degrees, three- 30



3D CPA Image of Liver

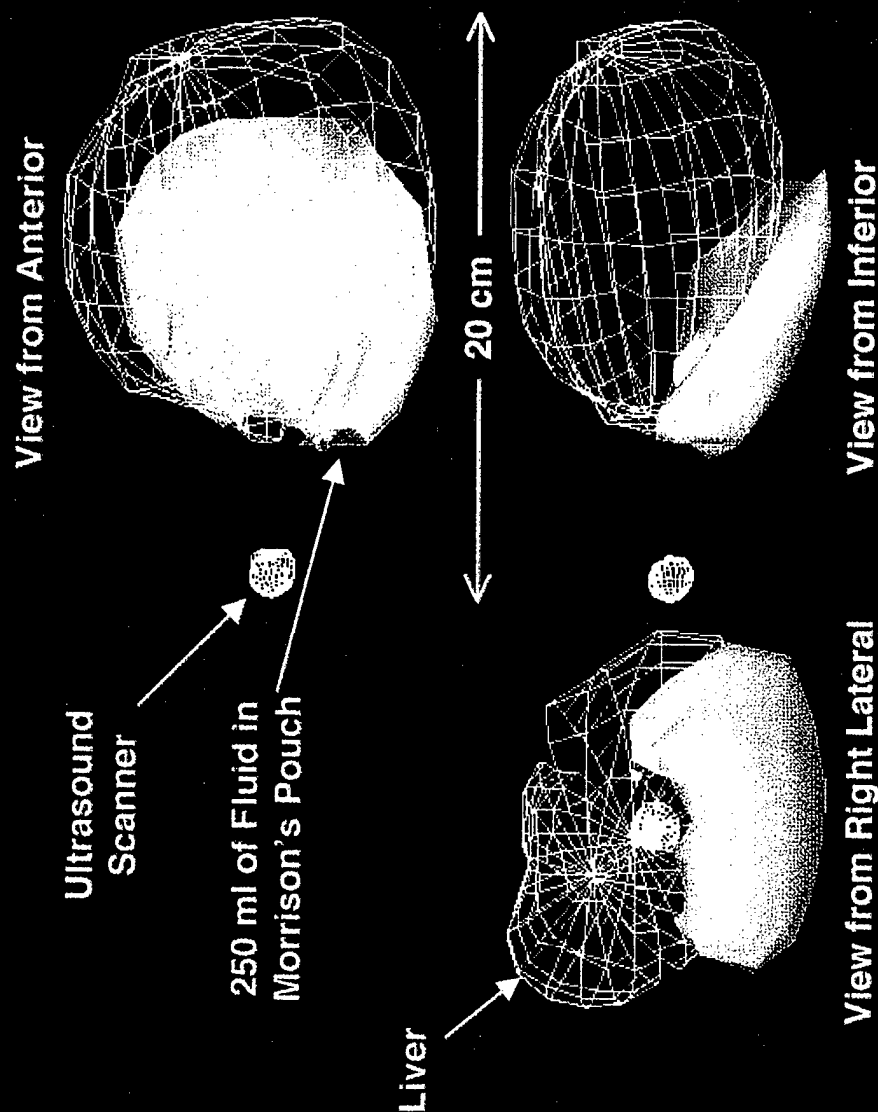
Projection Image Renal 1 degrees, three- 21



3D CPA Image of Kidney

CIMU • Applied Physics Laboratory • University of Washington

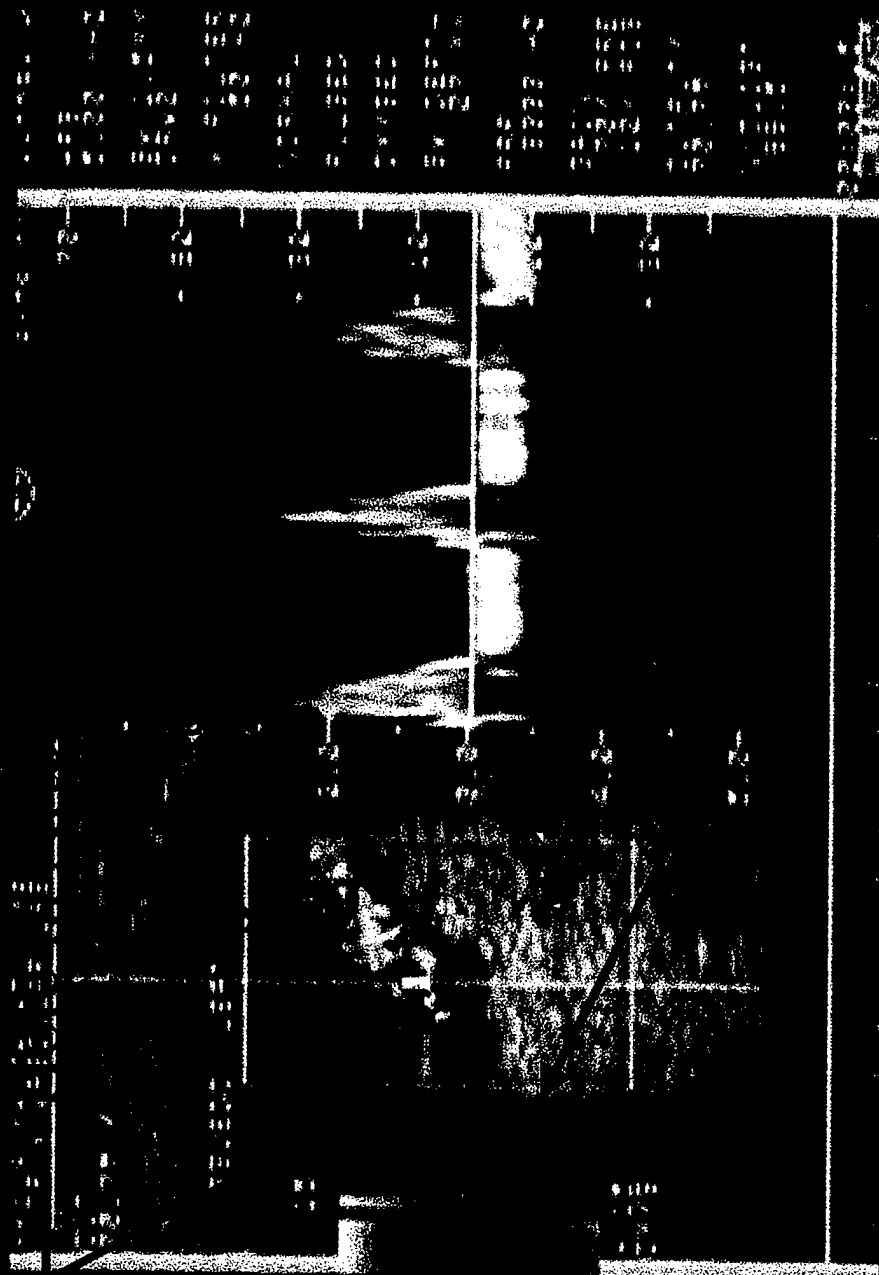
Internal Bleeding Can Be Detected with Portable Diagnostic Ultrasound Scanners



Peritoneal fluid (surface rendered) and liver (wire frame)
taken with a prototype palm-size 3-D ultrasound imager

CIMU • Applied Physics Laboratory • University of Washington

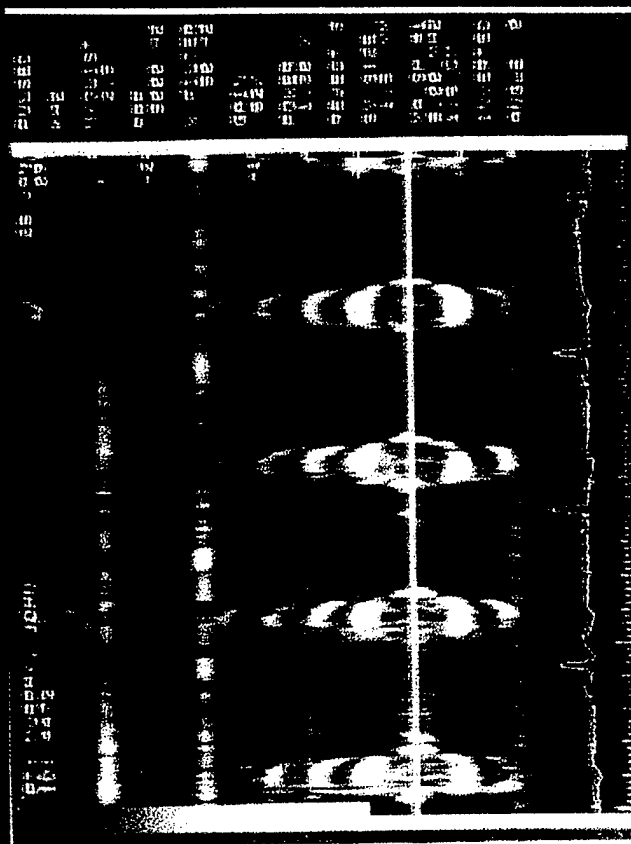
Arterial Bleed into a Human Femoral Artery Pseudoaneurysm



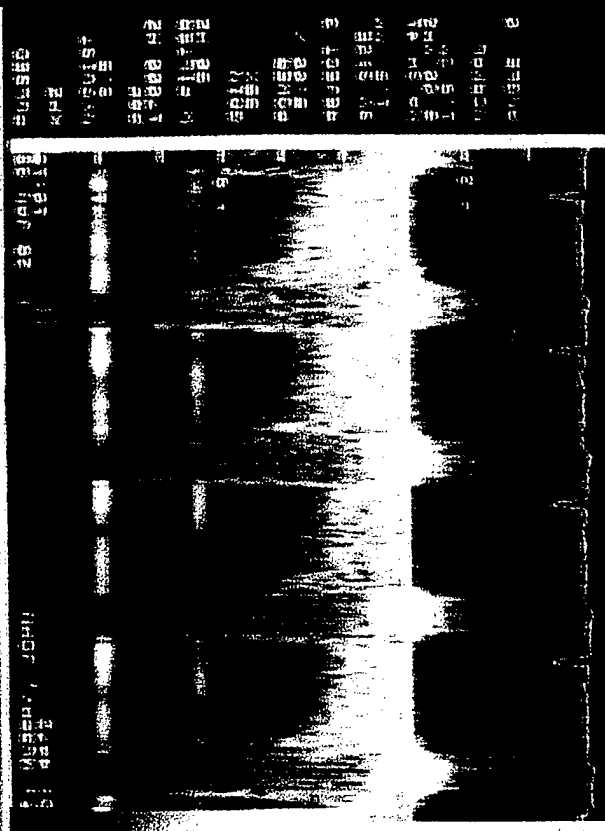
0.5 cc/s

CHU - Applied Physics Laboratory • University of Washington

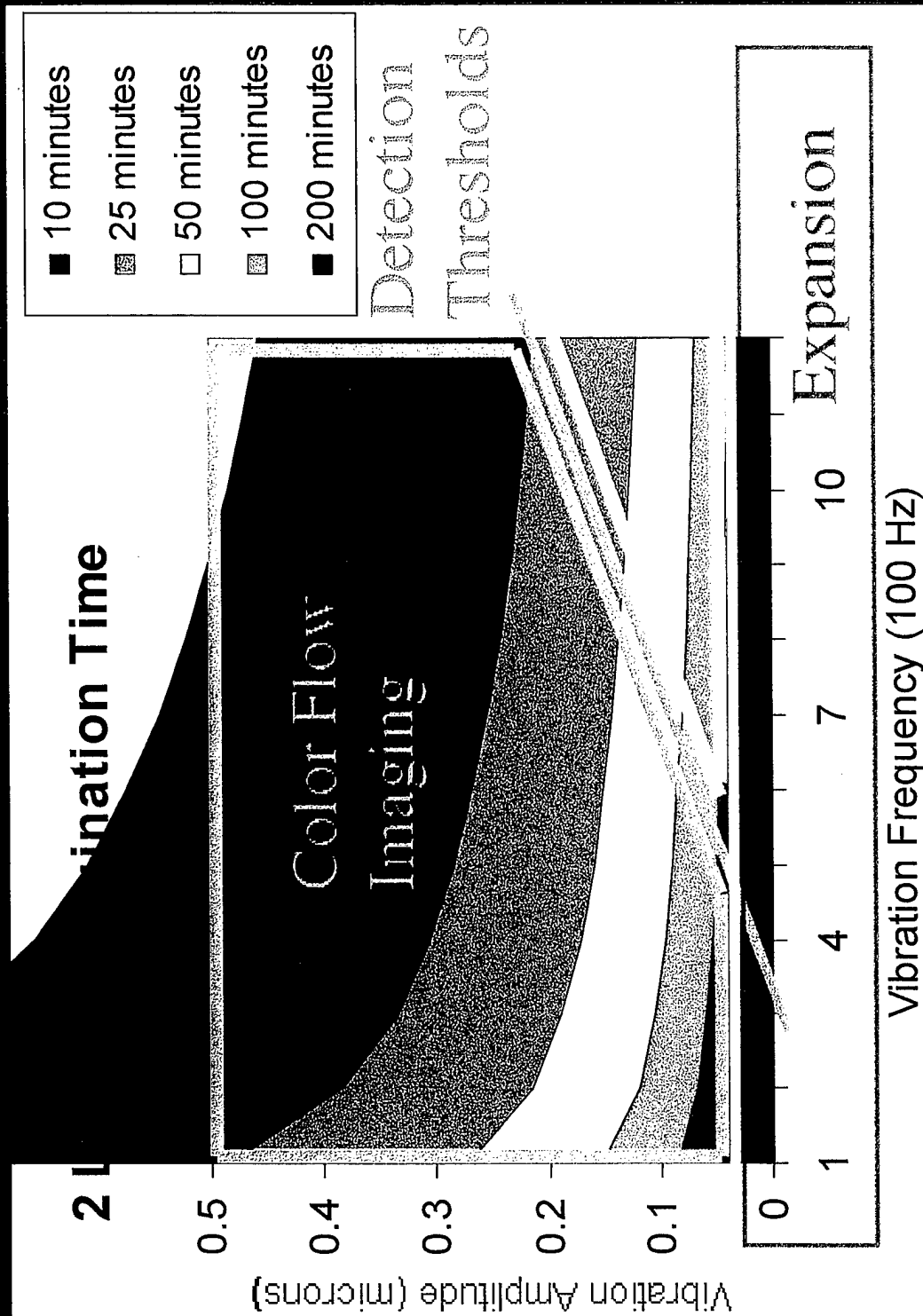
Low Frequency Vibrations "Bruit" caused by the Jet



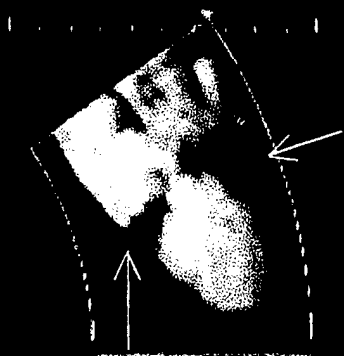
High Velocity Jet Flow in Artery



Vibration from Arterial Bleeding



Diagnostic Ultrasound Can be Used to Localize Bleed Site



CIMU • Applied Physics Laboratory • University of Washington

Bloodless Ultrasound Surgery

High Intensity Focused Ultrasound (HIFU) can be used for surgery and to stop bleeding

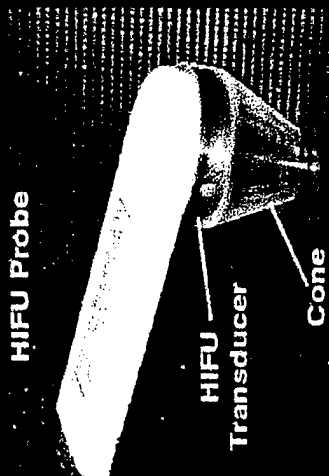
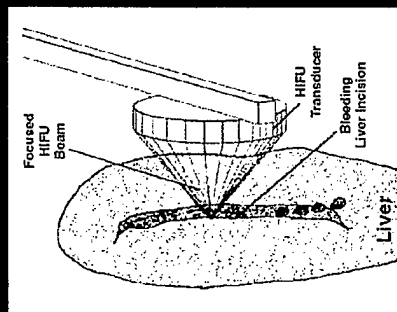
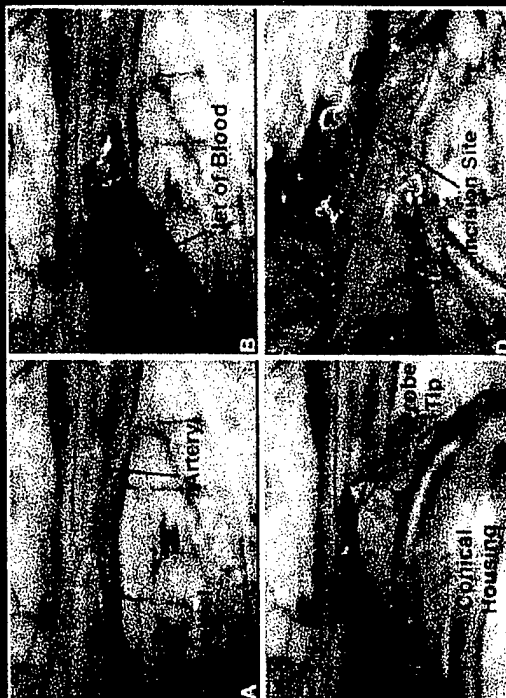
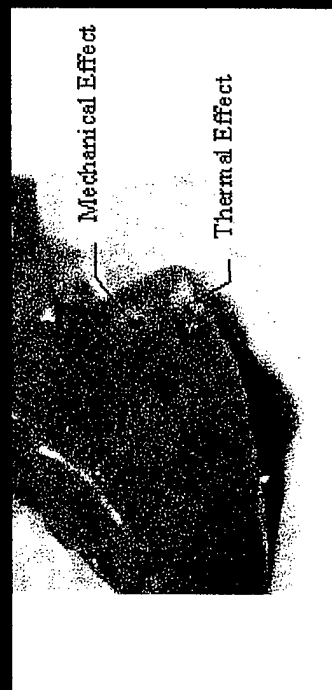


Figure 2

HIFU probes like this can stop bleeding in large veins and arteries within a few seconds



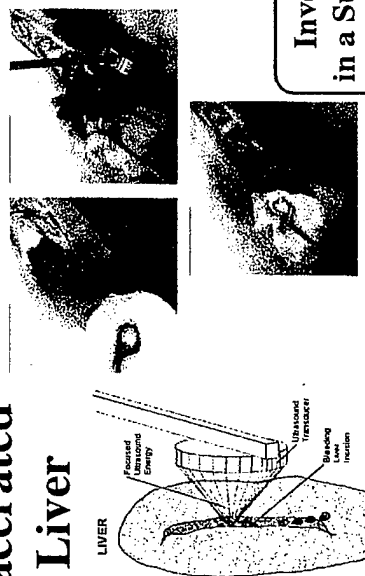
HIFU can ablate tissue and simultaneously prevent the treated area from bleeding



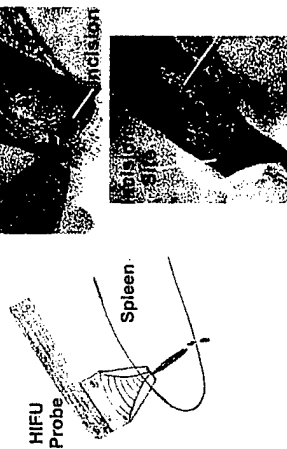
Acoustic Hemostasis: Experimental Studies

Can High Intensity Focused Ultrasound
be Used to Stop Hemorrhage?

Lacerated Liver

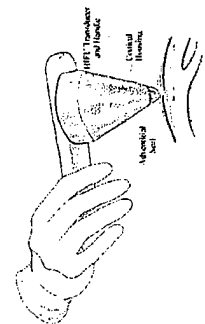


Lacerated Spleen

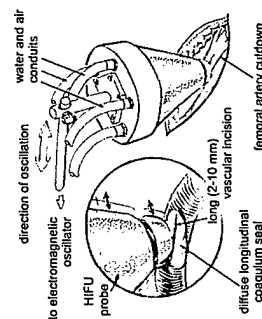


Investigations to Date
in a Surgical Environment

Punctured Blood Vessel

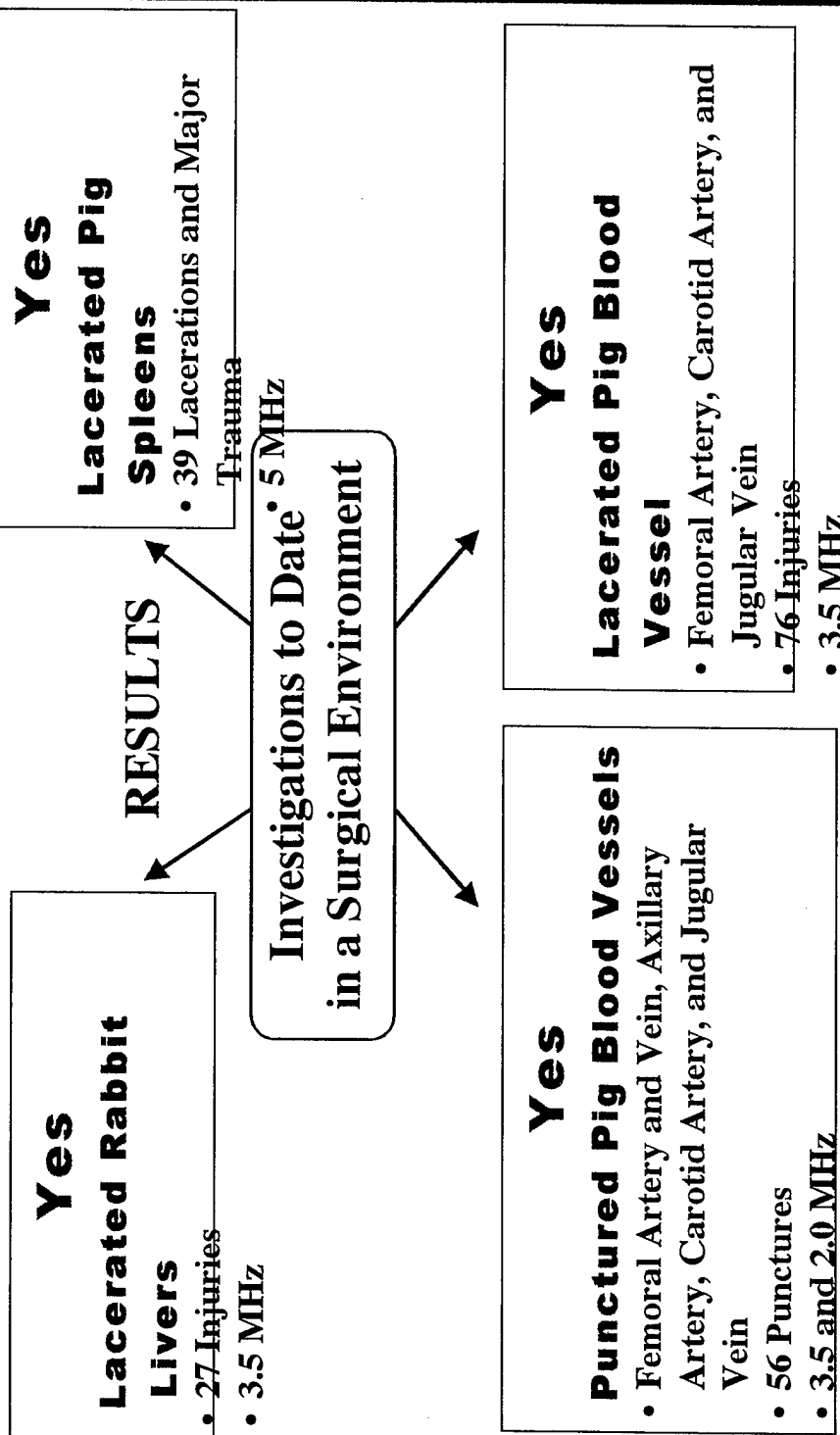


Lacerated Blood Vessel

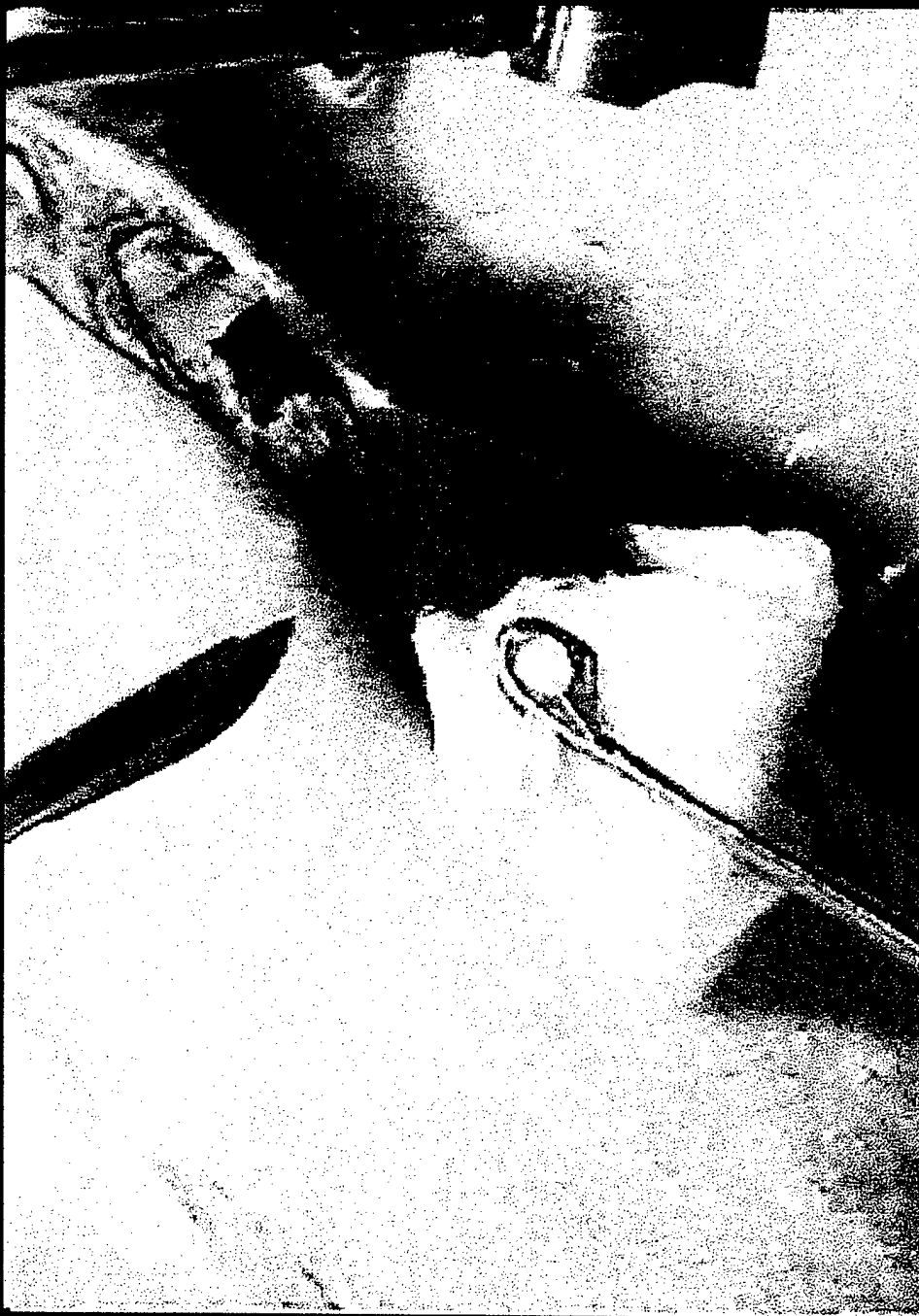


Our success at acoustic hemostasis

Can High Intensity Focused Ultrasound be Used to Stop Hemorrhage?



HIFU Stops Bleeding

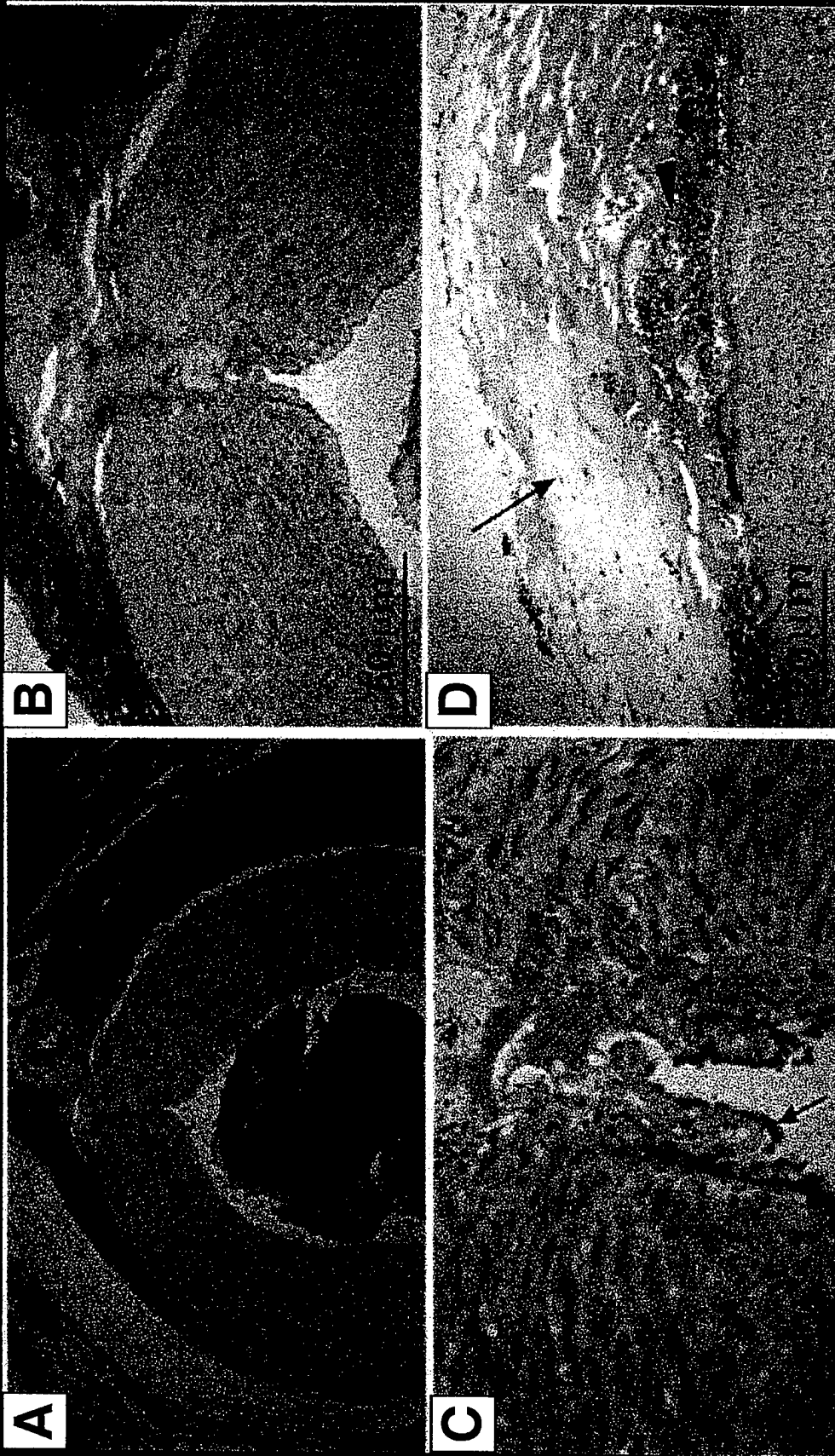


This video shows how HIFU can stop different kinds of bleeds

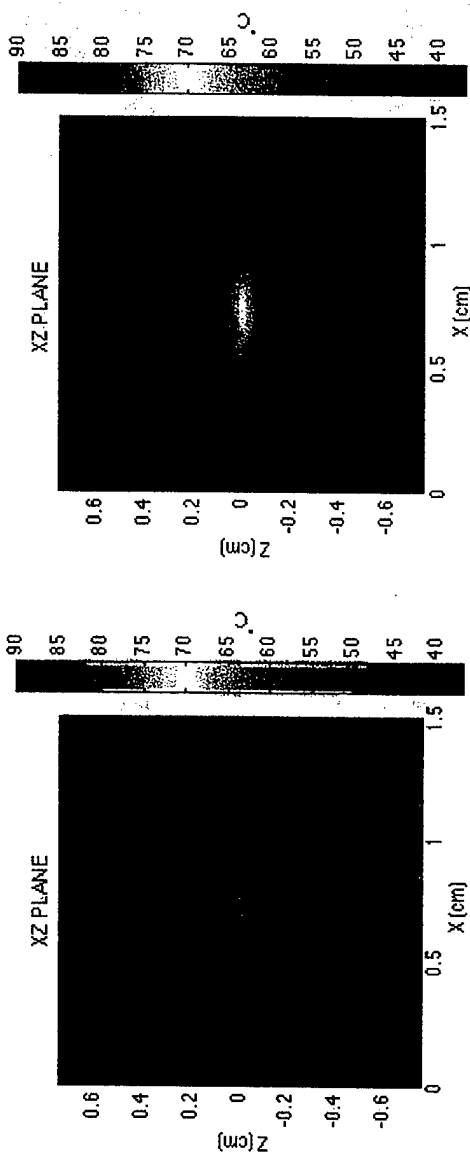
CIMU • Applied Physics Laboratory • University of Washington

Histology of Punctured Artery

(Note no evidence of damage to the lumen.)

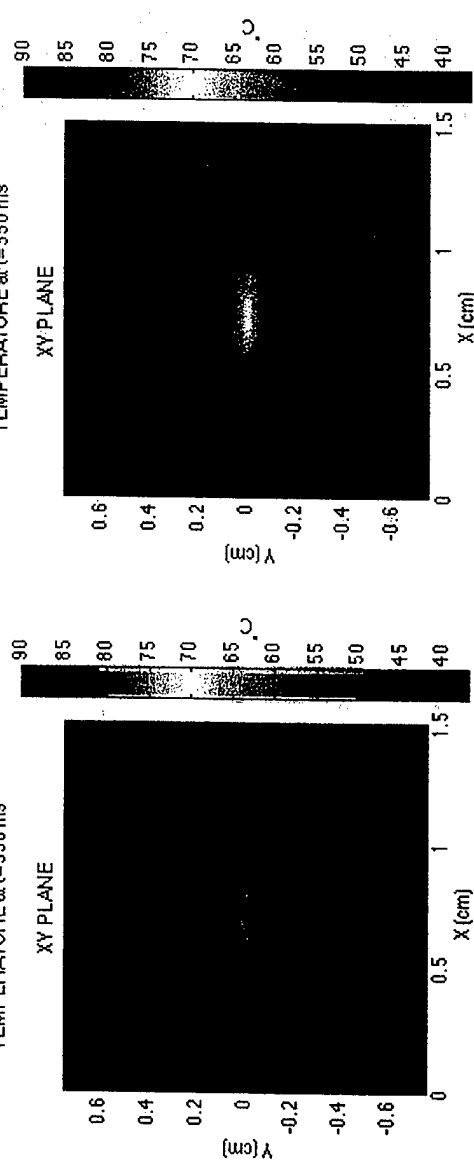


HIFU Generates High Temperatures Only on Surface of Blood Vessels and Not in Interior

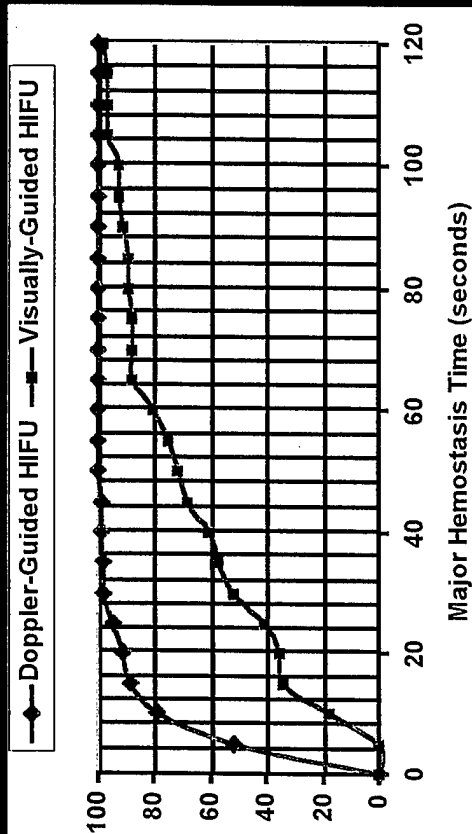
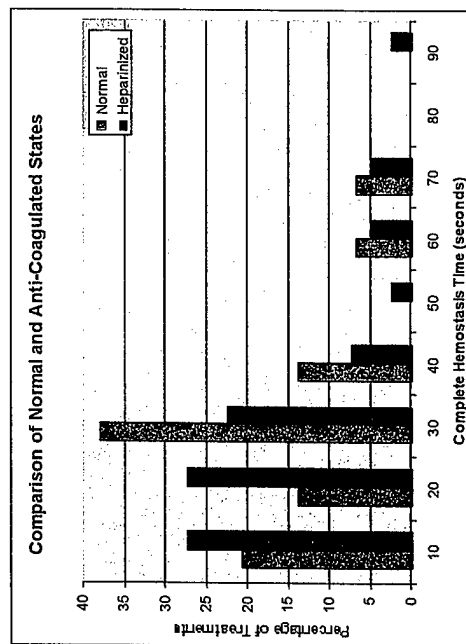
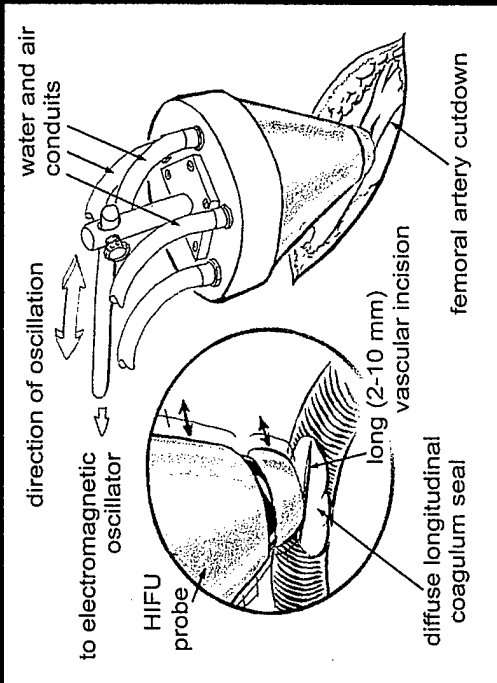
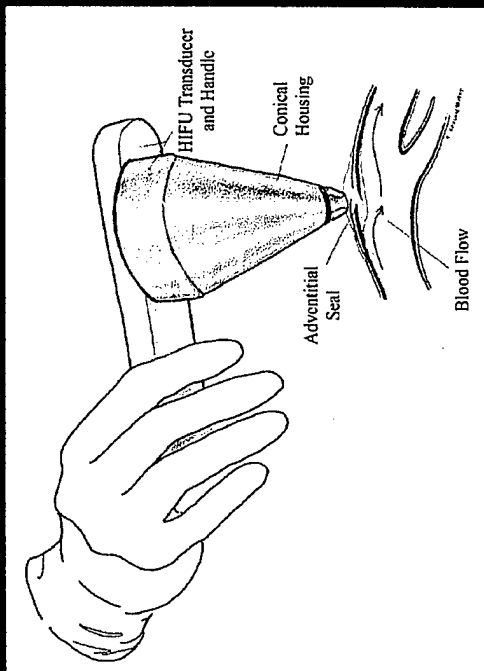


VESSEL PRESENT
Diameter=3 mm
Blood flow velocity=3 cm/s
TEMPERATURE at t=350 ms

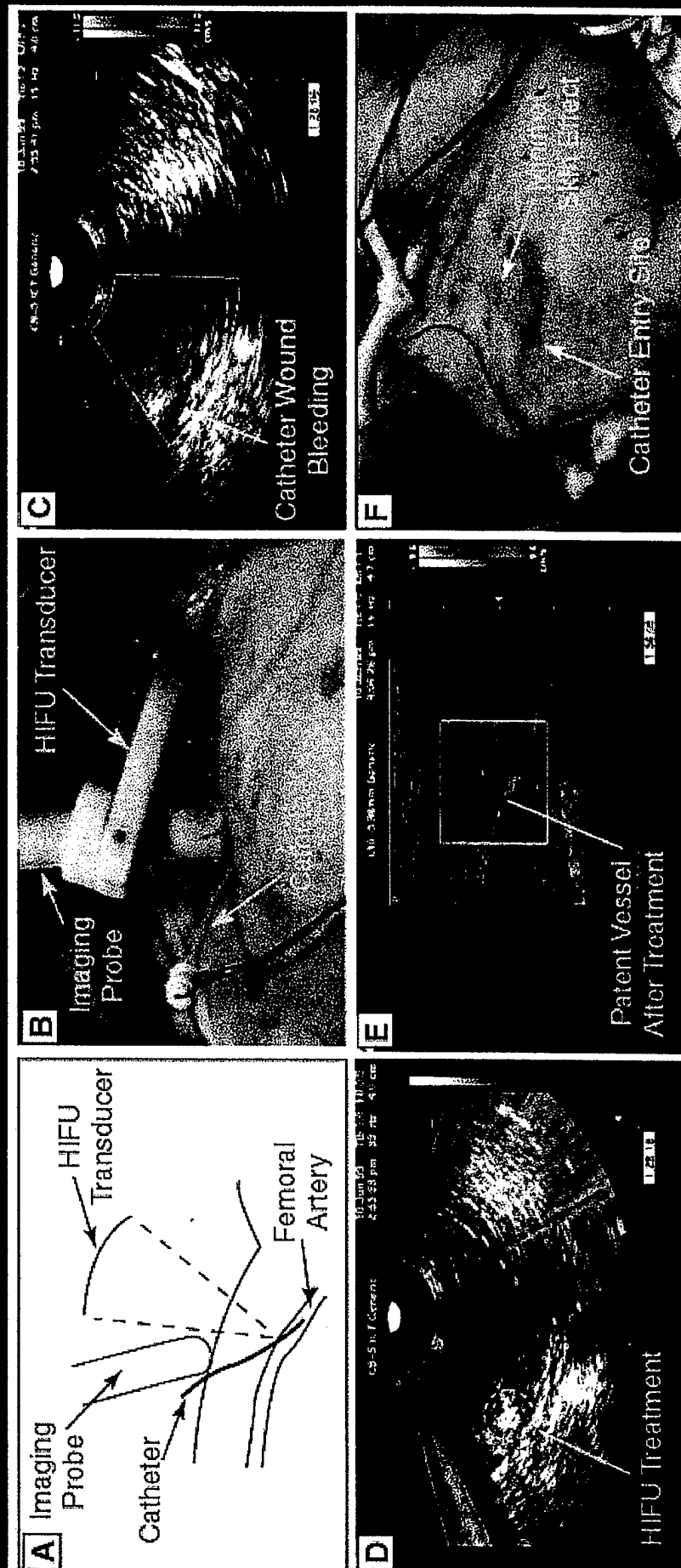
TEMPERATURE at t=350 ms



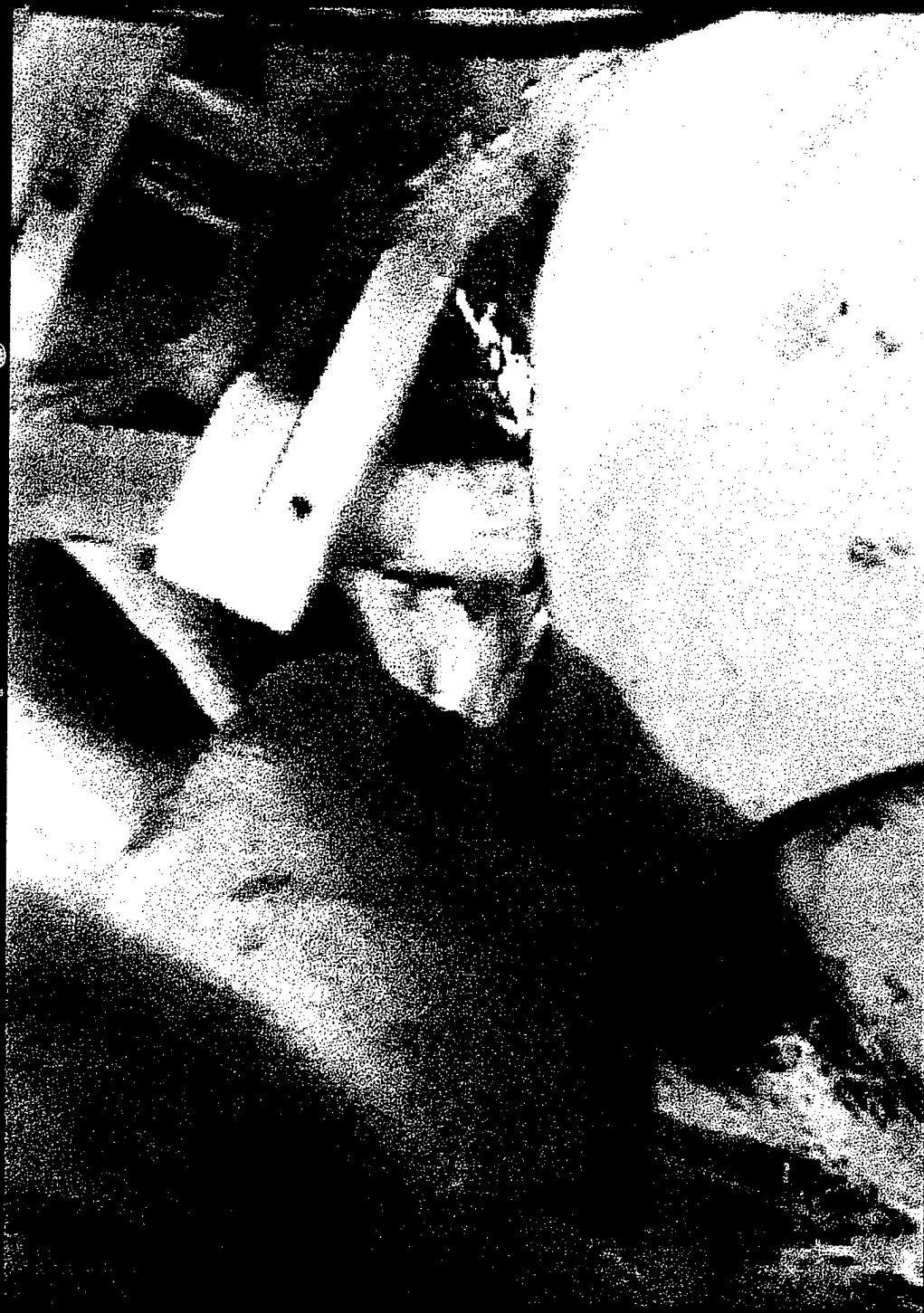
Acoustic hemostasis techniques and some results



Demonstration of Image-guided Transcutaneous Acoustic Hemostasis

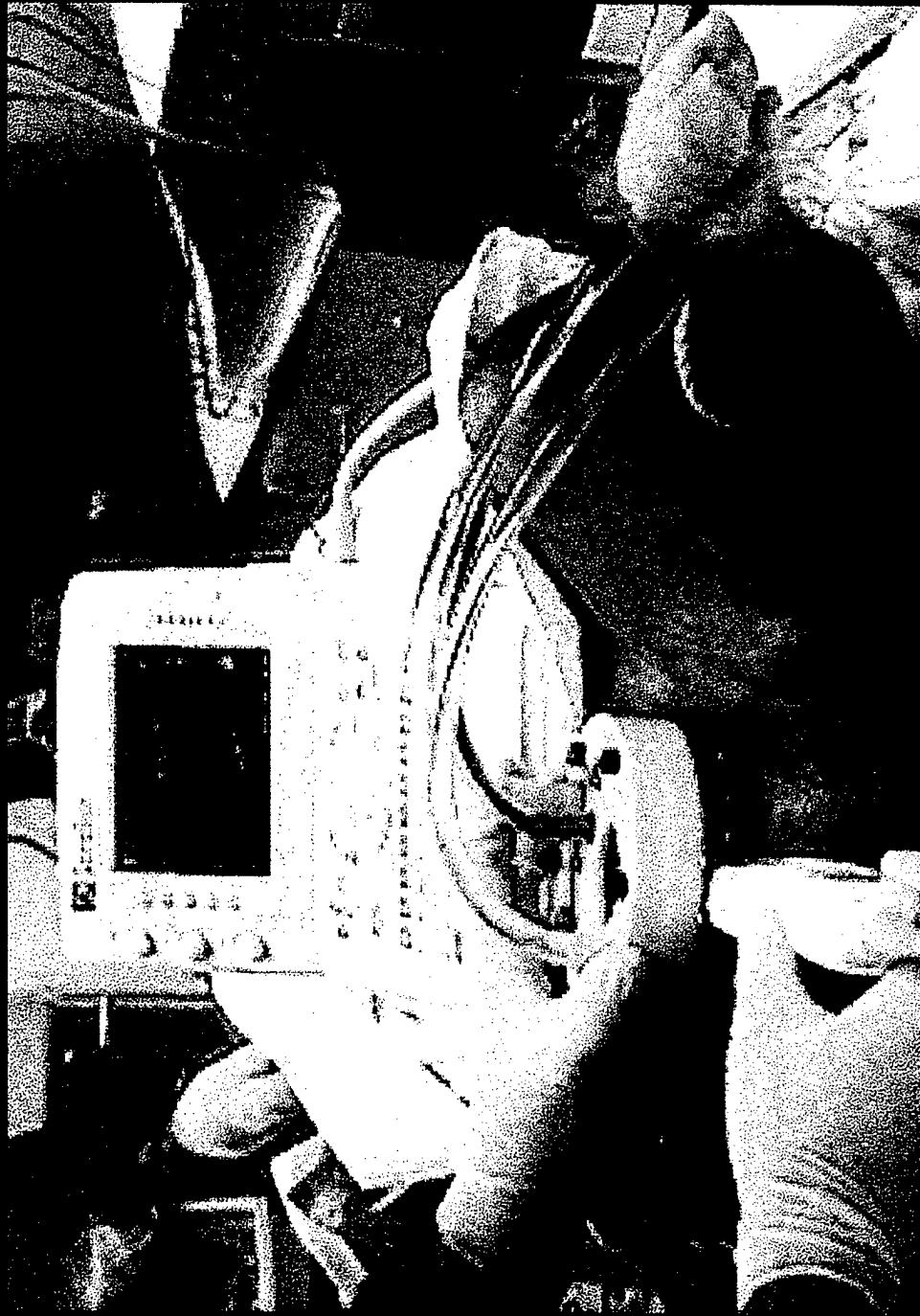


Ultrasound Helps Locate
as Well as Stop the Bleeding



Catheter wound closure using HIFU with Doppler guidance
CIMU • Applied Physics Laboratory • University of Washington

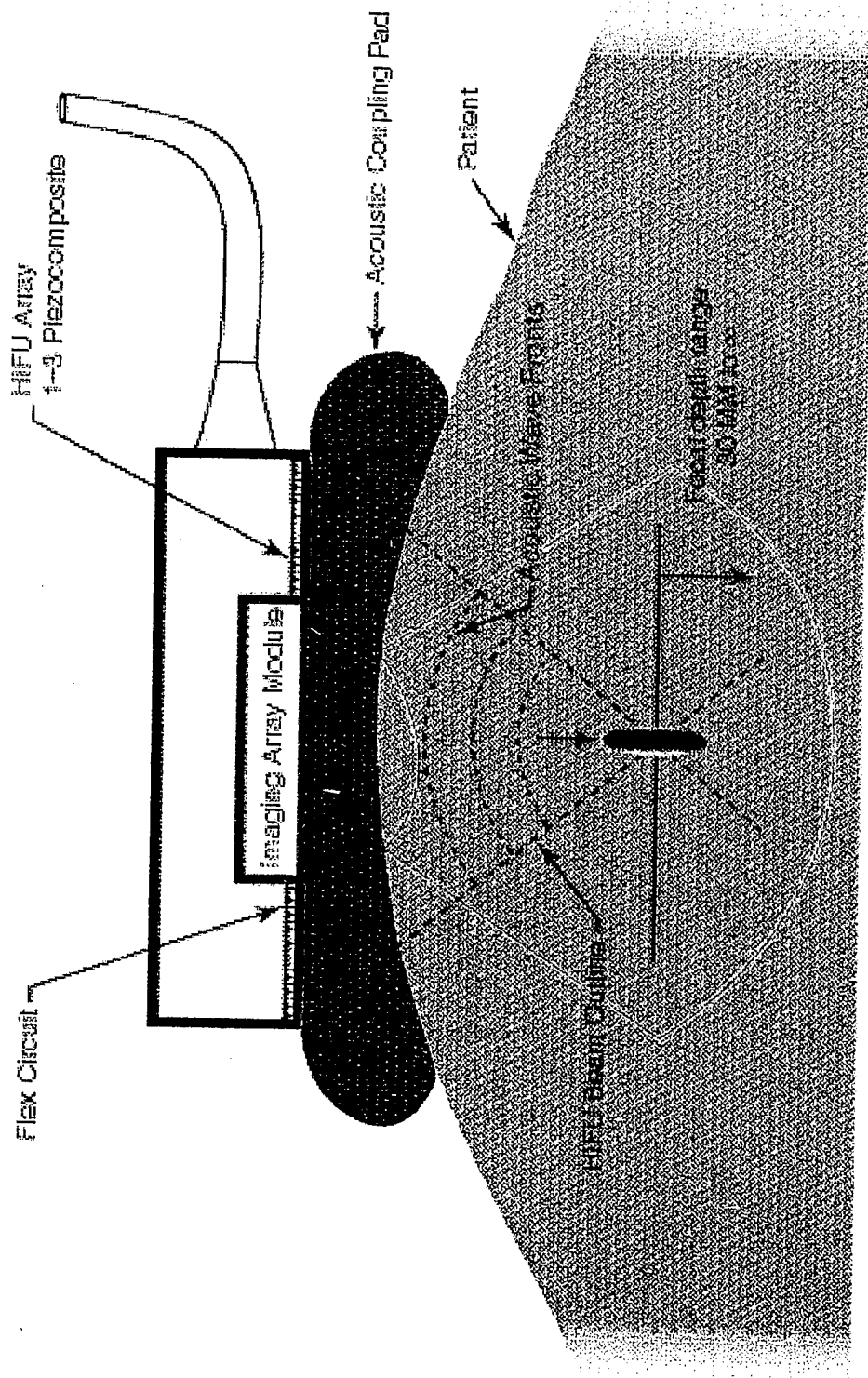
We Can Deliver HIFU Therapy
Through the Skin



Sonosite portable imaging instrument used with a transcutaneous HIFU probe

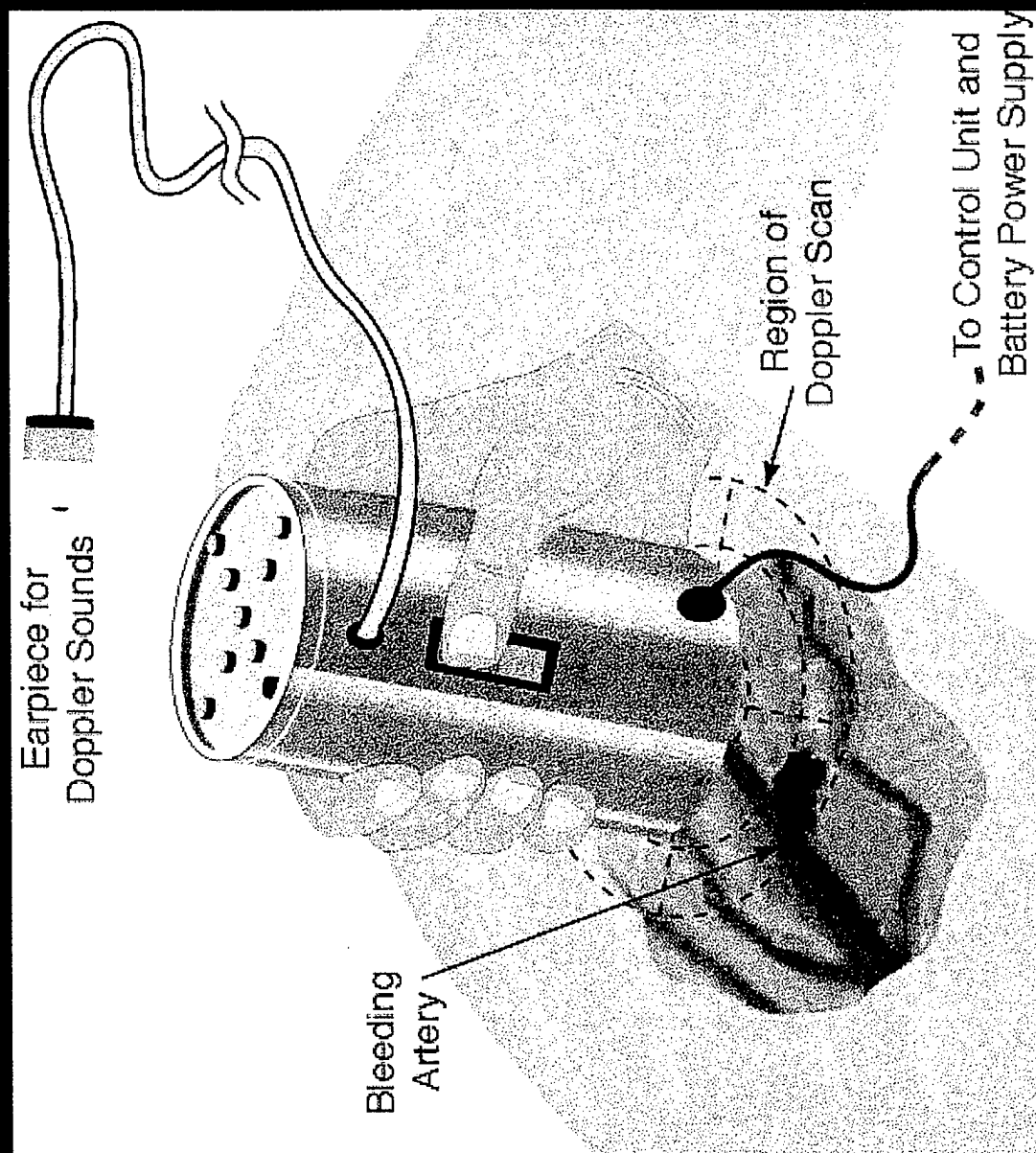
CIMU • Applied Physics Laboratory • University of Washington

Integrated HIFU and Imaging Applicator

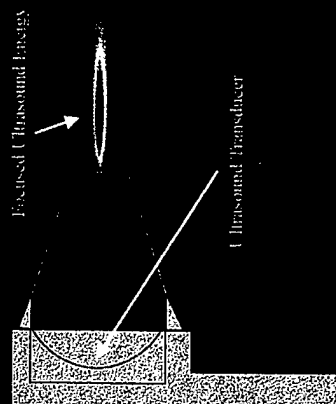


CIMU • Applied Physics Laboratory • University of Washington

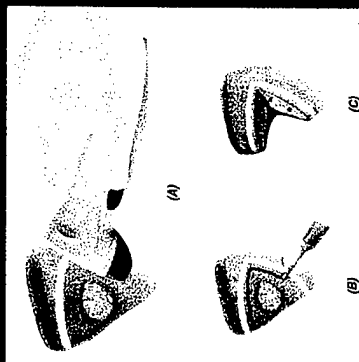
Our conception of a hand-held acoustic hemostasis device for acute arterial bleeding



CIMU • Applied Physics Laboratory • University of Washington



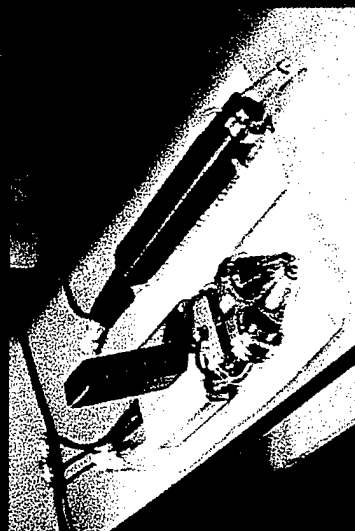
HIFU probes can produce a localized region of high temperature



Precauterization of specific volumes of tissue can be accomplished



These volumes can then be sectioned without bleeding



Examples of HIFU probes developed by Therus

Demonstration of Image-Guided Transcutaneous Liver Treatment

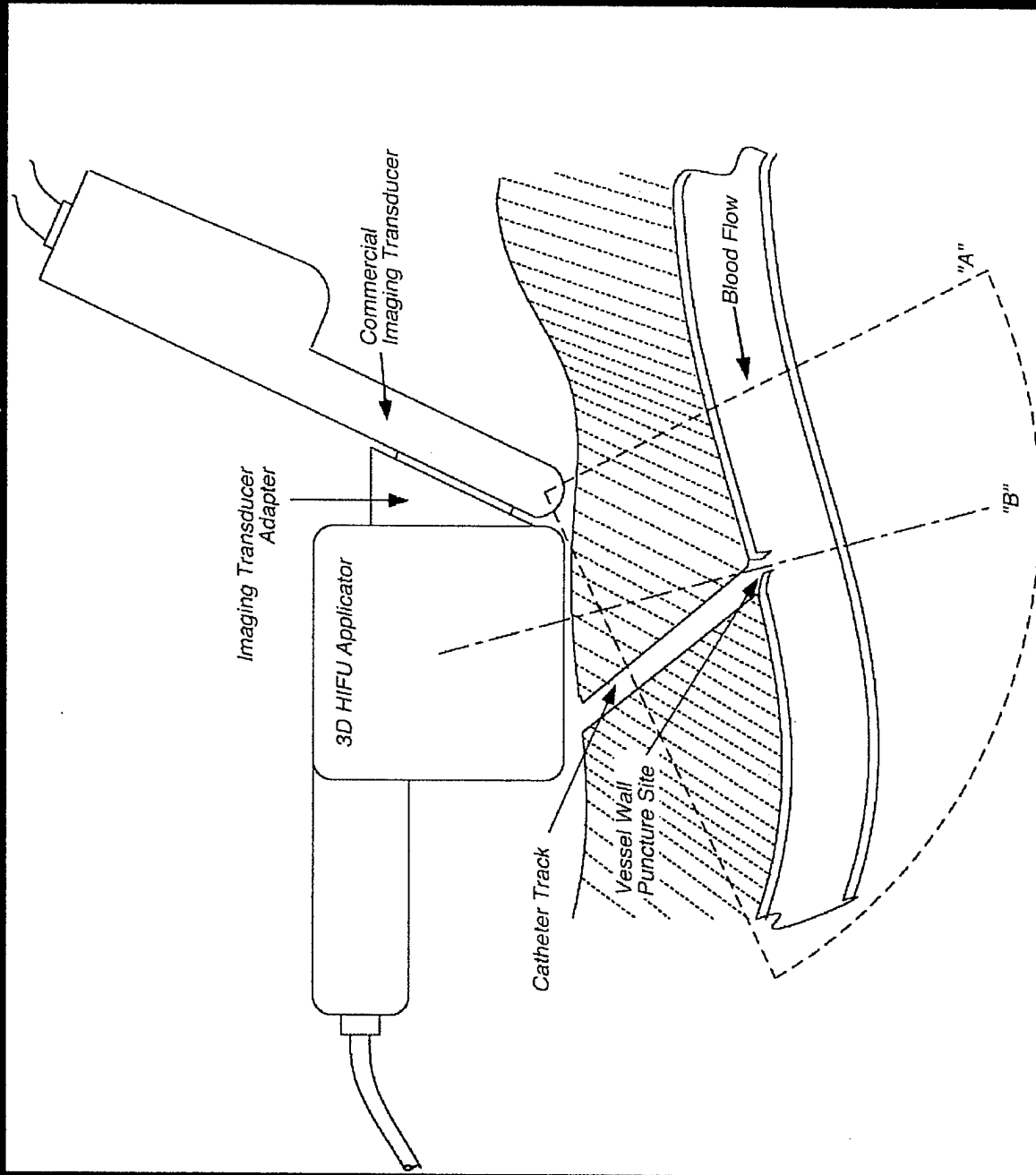
Free-Hand HIFU



Treated Liver

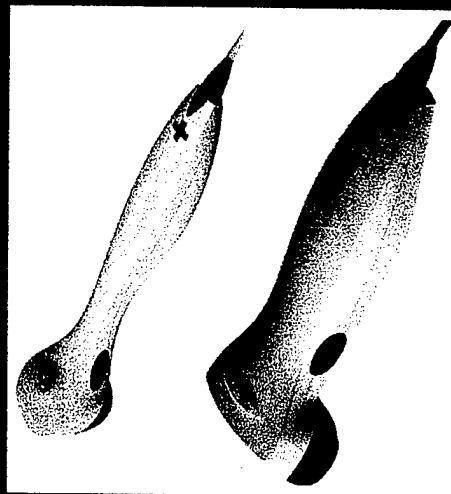
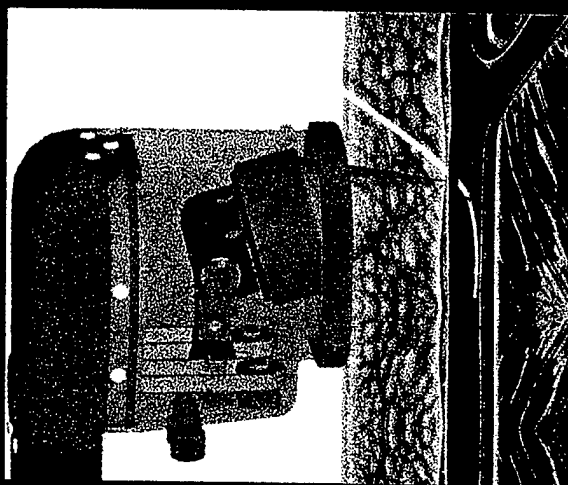
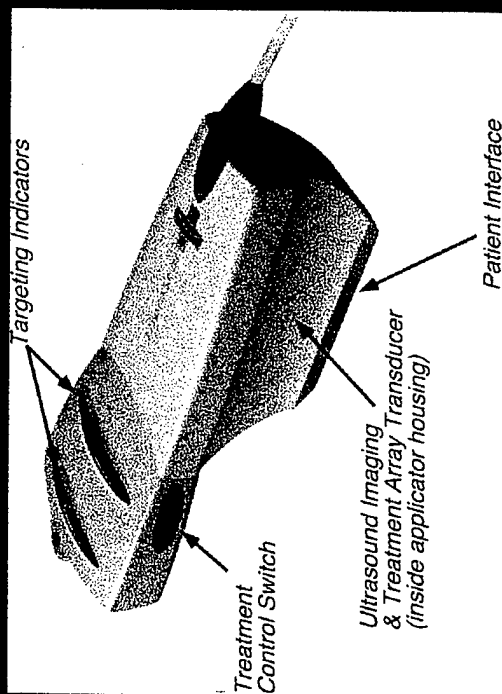


Approach to Catheter Wound Sealing using HIFU



CIMU • Applied Physics Laboratory • University of Washington

Types of transducers to be used for catheter wound sealing



Physical Acoustics Summer School
Asilomar Conference Center
Pacific Grove, CA
June 2000

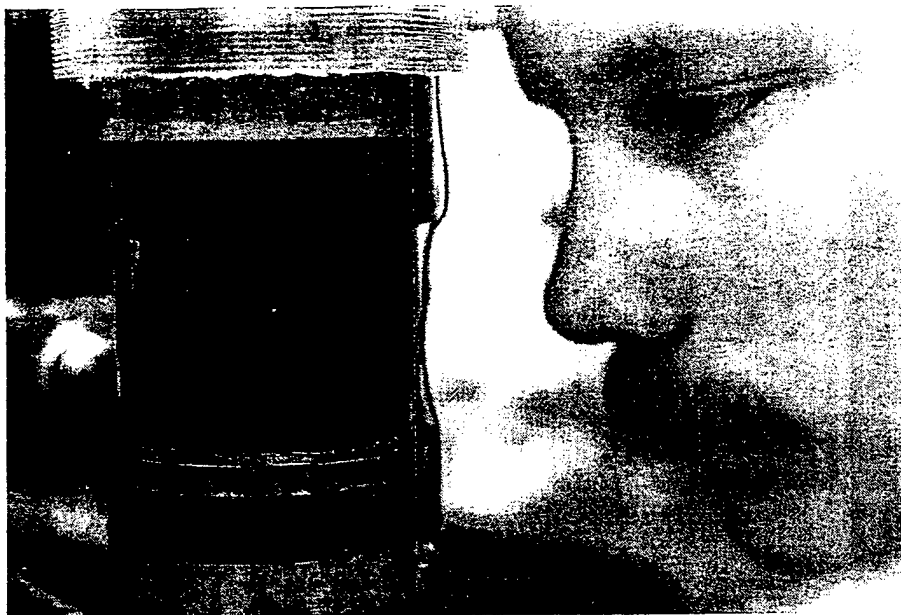
SONOLUMINESCENCE

Thomas J. Matula

Applied Physics laboratory
University of Washington, Seattle WA



Applied Physics Laboratory — University of Washington



Secretary of the Navy Presentation 24 & 25 January 1997

Remarks and slides as parts of a multimedia presentation prepared for delivery by D.R. Russ George, President E-Quest Sciences to The Honorable John H. Dalton Secretary of the Navy, his staff, and top admirals Off Site at Quantico Marine Base

Sonofusion A New Source of Nuclear Energy

(Energy Too Cheap To Meter? An old story or a new paradigm?)

Secretary Dalton, Under Secretary Danzig, Admiral Johnson, Admiral German, General Krulak, General Neal I thank you and your colleagues for inviting me to come to speak and work with you today and tomorrow.

It's a great honor and a privilege to be here to share with the top leadership of the Navy and Marines my view of the future of energy technology. I am very much encouraged by the keen interest and effort put forth to gather this forum together. As you listen to my presentation I am sure you will find I am optimistic about the future and welcome the opportunity to share and consider with you and the rest of the assembled experts here, views which may help you lead the Navy and Marine Corp. into the 21st Century.

Today I head a small high technology start up company in the Silicon Valley in California where we produce devices to control a new form of nuclear energy we call Sonofusion. We have recently completed successful demonstrations of the technology for the Electric Utility Industry through the Electric Power Research Institute. We are now engineering scaled up versions of the experimental devices for a variety of utility, consumer, and aerospace applications.

To give you just a quick overview of the background of this new technology I'll focus on two closely related phenomenon sonoluminescence and sonofusion. Perhaps the better known of these exotic topic areas is Sonoluminescence which is a brief flash of brilliant light produced by cavitation, collapsing bubbles. The origin of the flash is still unknown though many leading scientists speculate that it may have a nuclear origin. It was first reported in science 1920's.



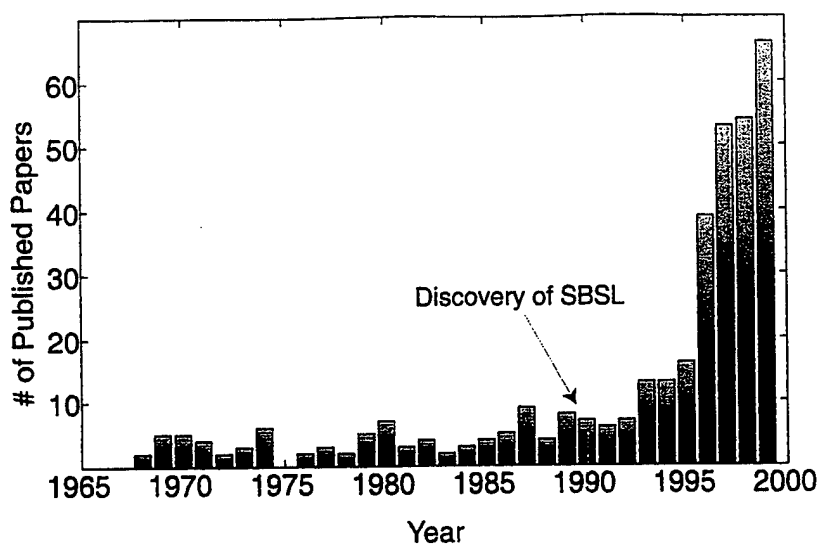
SONOLUMINAL May Day 7:30pm Monday May 1, 1995
Community Christian Church, 4601 Main
Kansas City, Missouri 64112 (816) 561-6531

No Admission Charge

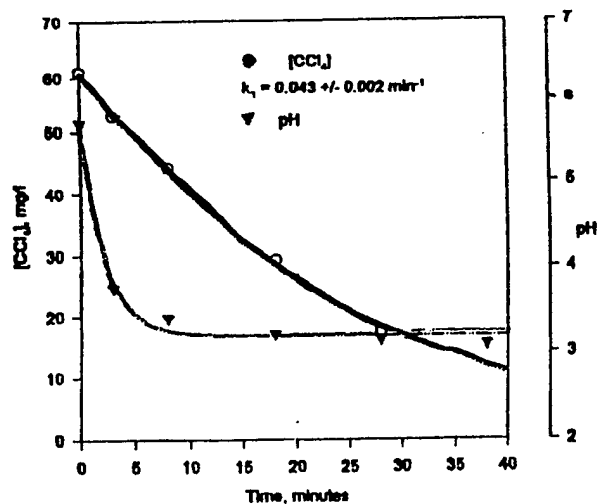
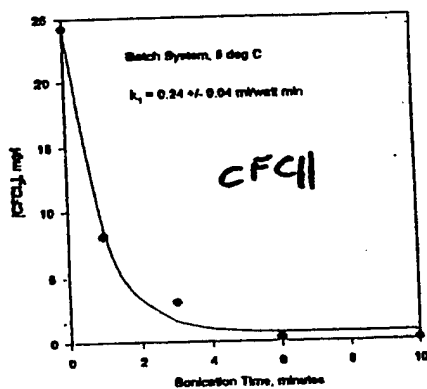
© SONOLUMINAL CIRCLE
& NEW CIRCLE PUBLICATIONS, 1995
T.M. Crutcher, Designer

Sonoluminescence Publications, 1968-1999

6



7



TJM-4



Figure 5. Scanning electron micrograph of 5 μm diameter Zn powder. Neck formation from localized melting is caused by high-velocity interparticle collisions. Similar micrographs and elemental composition maps (by Auger electron spectroscopy) of mixed metal collisions have also been made. Reproduced with permission (14).

(from Doktyca and Suslick, *Science*, 27, 1990)

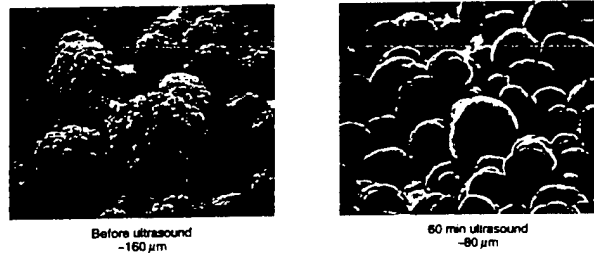
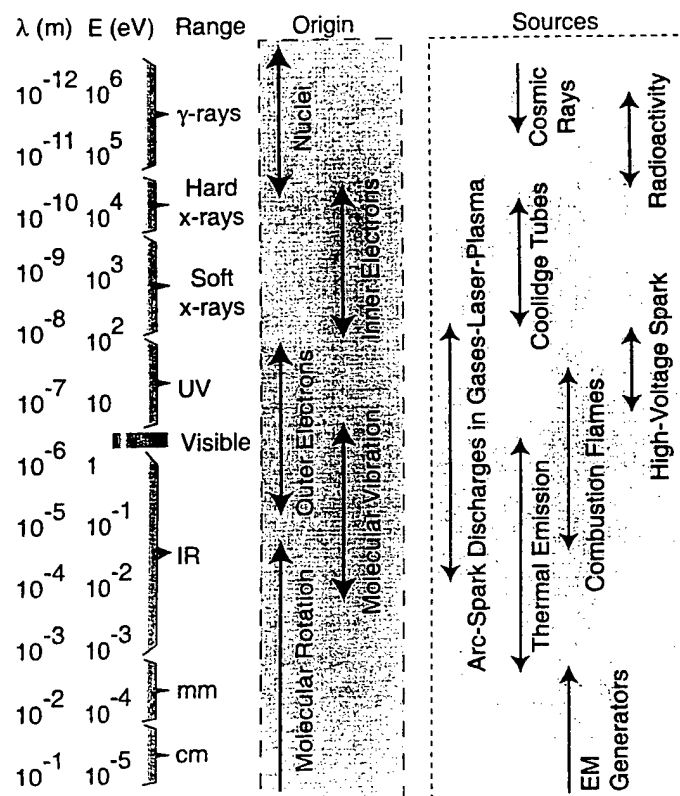


Figure 6. The effect of ultrasonic irradiation on the surface morphology and particle size of Ni powder. Initial particle diameters before ultrasound were $\approx 160 \mu\text{m}$; after ultrasound, $\approx 80 \mu\text{m}$. High-velocity interparticle collisions caused by ultrasonic irradiation of slurries are responsible for the smoothing and removal of passivating oxide coating. Reproduced with permission (15).

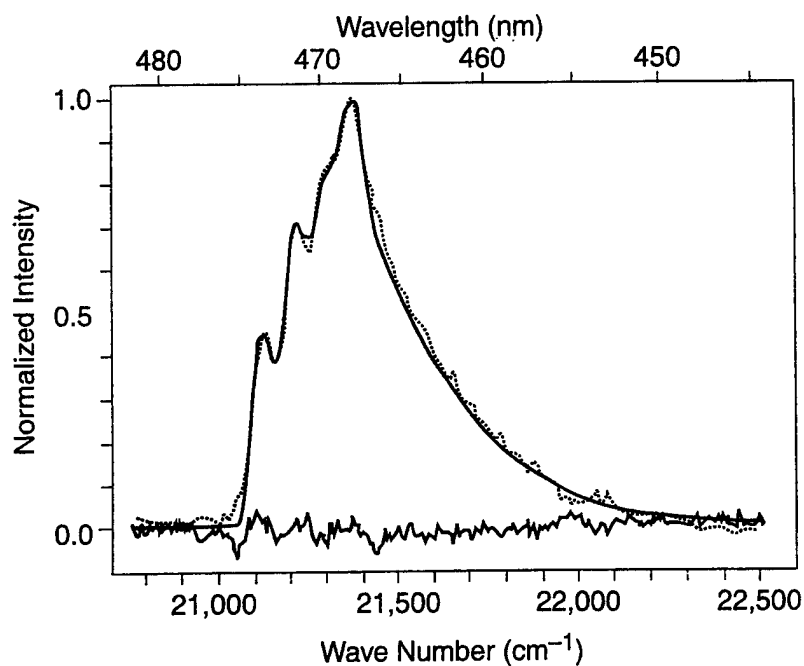
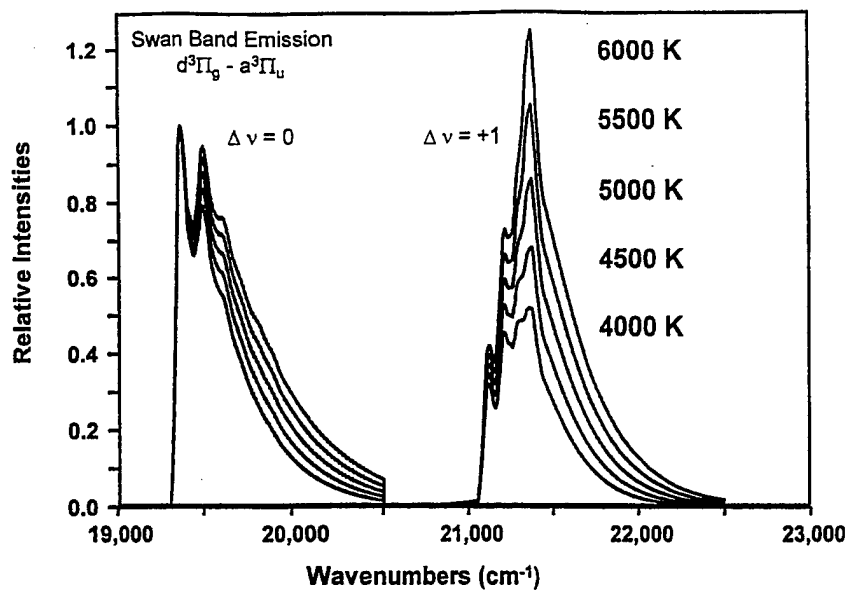
(from Suslick and Doktyca, *Adv. Sonochem.*, 1, 1990)

9

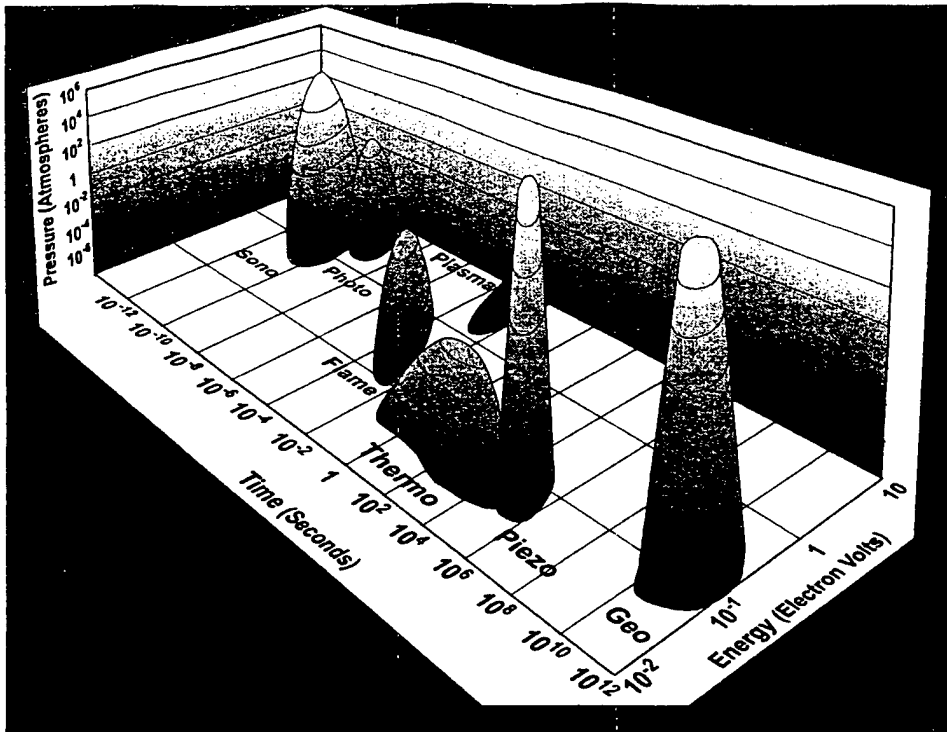
EM Spectrum



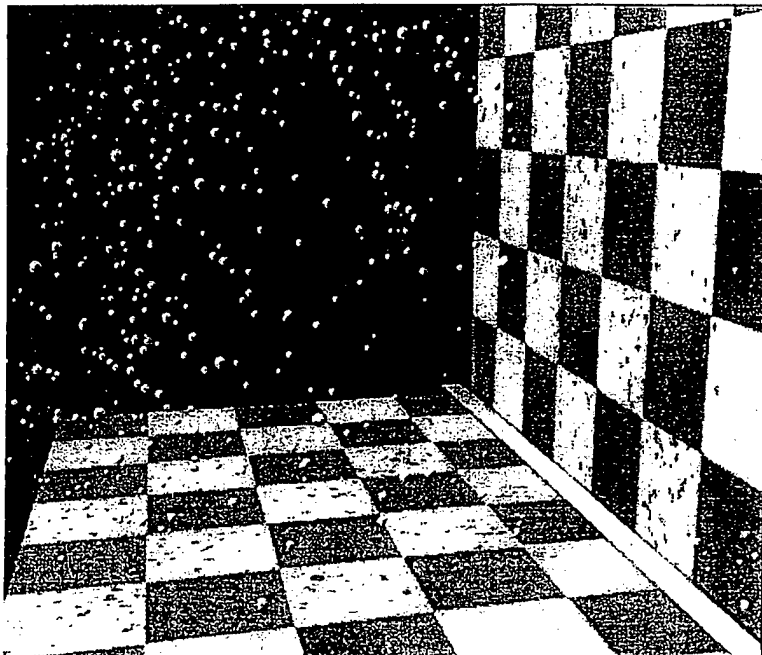
Calculated Spectra of C_2^* vs. Temperature

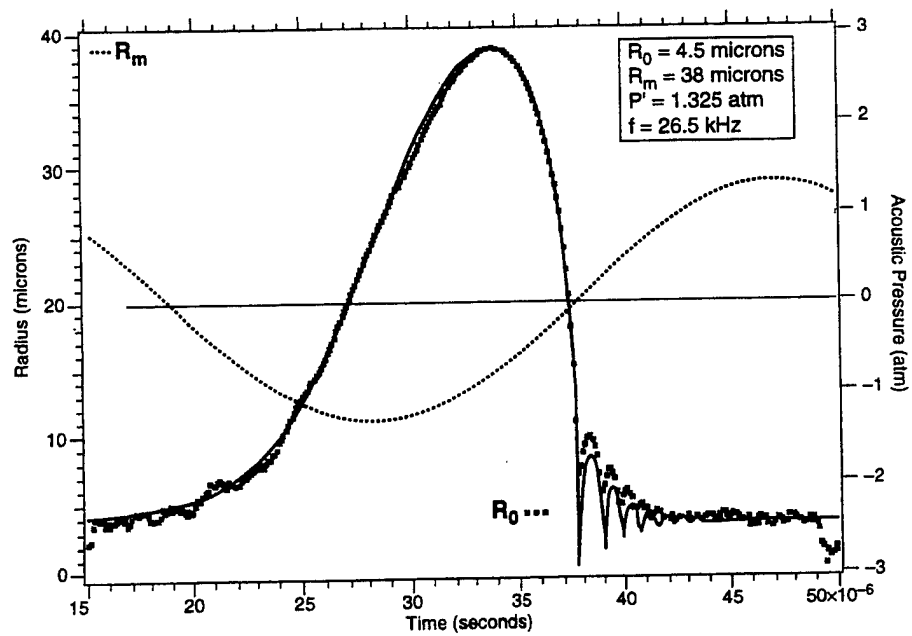


(from Flint and Suslick, *Science*, 20 Sept. 91)



W. Lauterborn et al.





The Rayleigh-Plesset Equation:

$$\rho \left(R \ddot{R} + \frac{3}{2} \dot{R}^2 \right) = \left\{ \left(P_0 + \frac{2\sigma}{R_0} \right) \left(\frac{R_0}{R} \right)^{3\gamma} \right\} - \{ P_0 + P(t) \}$$

Inertial Terms

Total Internal Pressure - Total External Pressure

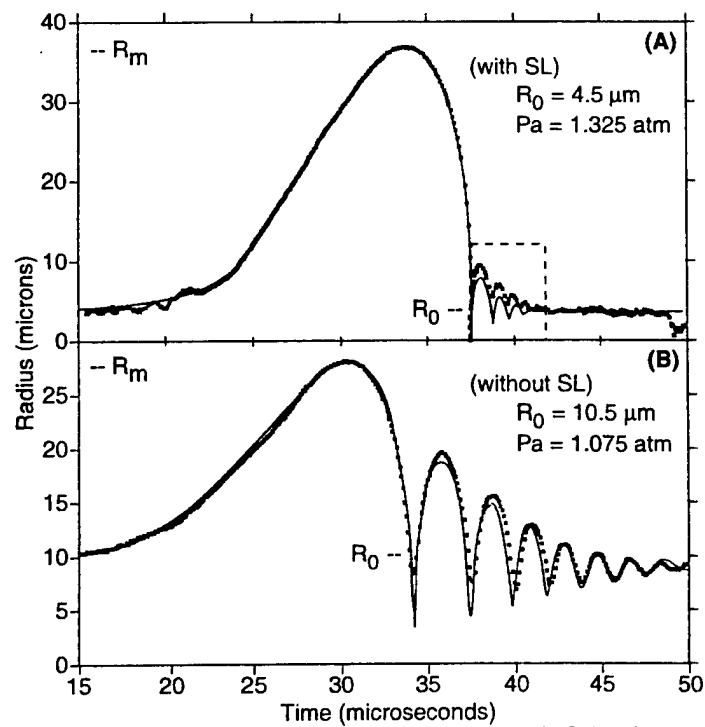
R_0 = Equilibrium (starting) bubble radius

P_0 = Ambient Pressure

σ = Surface tension

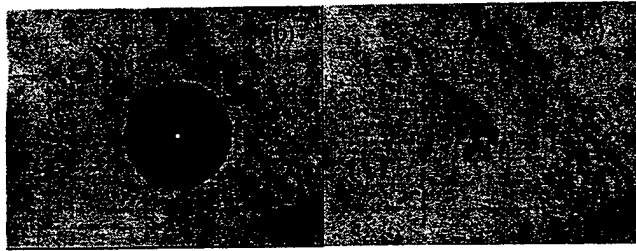
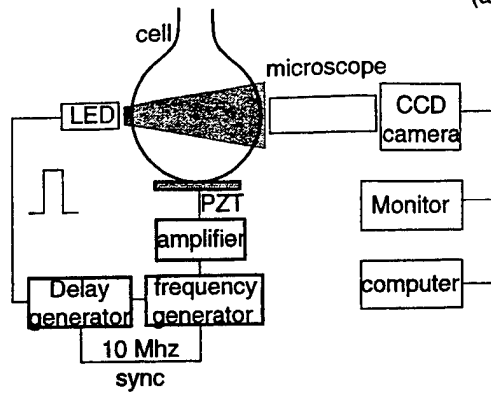
γ = Ratio of specific heats

$P(t)$ = Forcing pressure

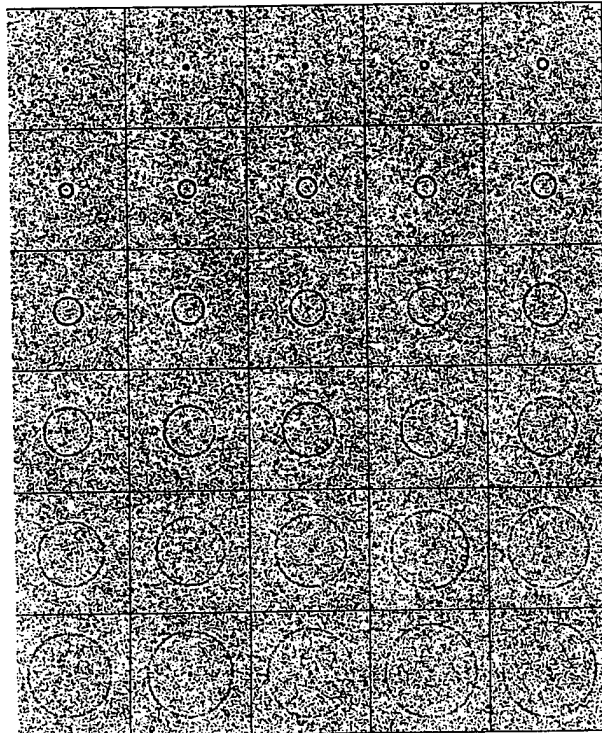


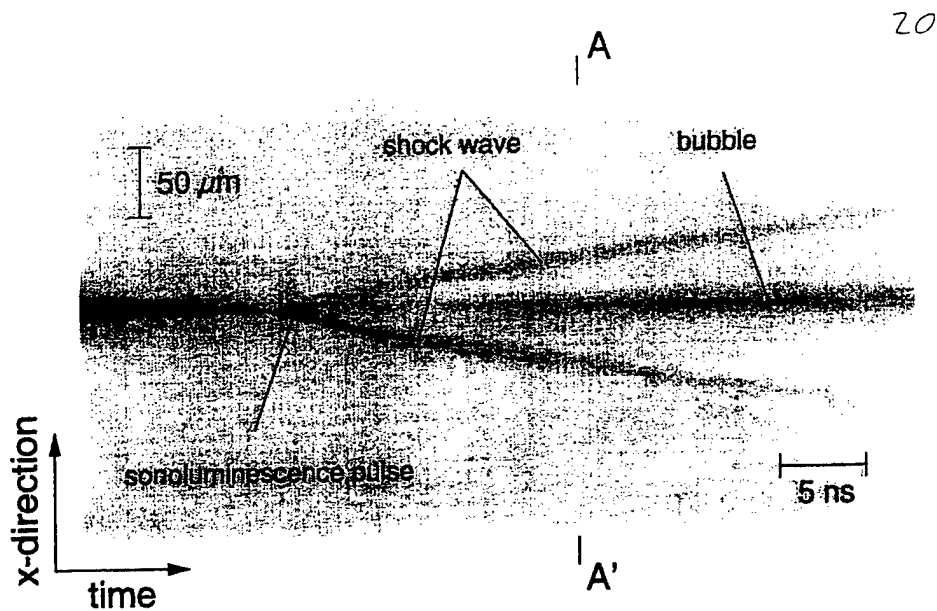
18

(a)



19





(from Pecha and Gompf, Phys. Rev. Lett., 7 Feb 2000)

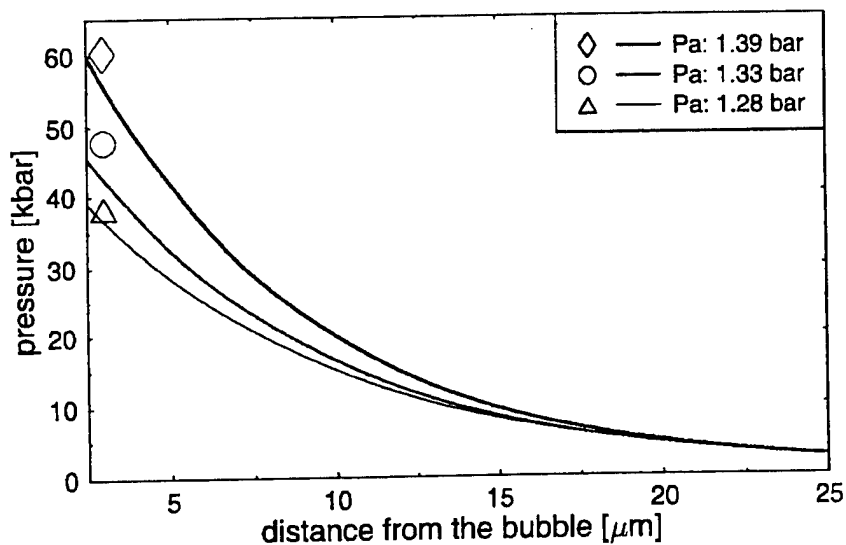
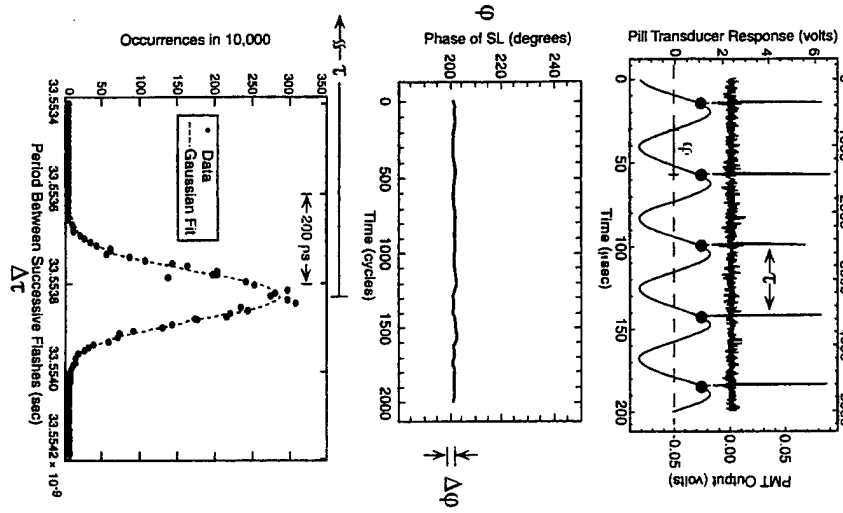


FIG. 4. Shock wave amplitudes vs distance from the bubble and calculated maximum pressures inside the bubble (open symbols) for three different driving pressures of the resonator. Pressure values up to 60 kbar can be reached.

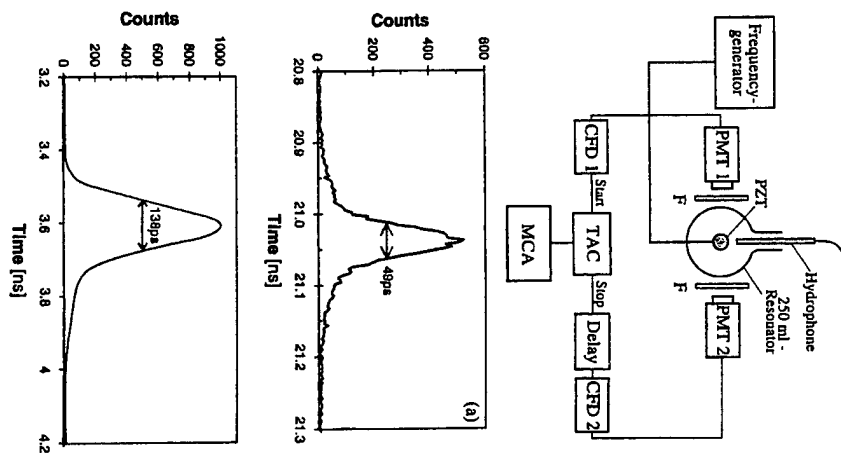
(from Pecha and Gompf, Phys. Rev. Lett., 7 Feb 2000)

22

Sonoluminescence vs Sound Field

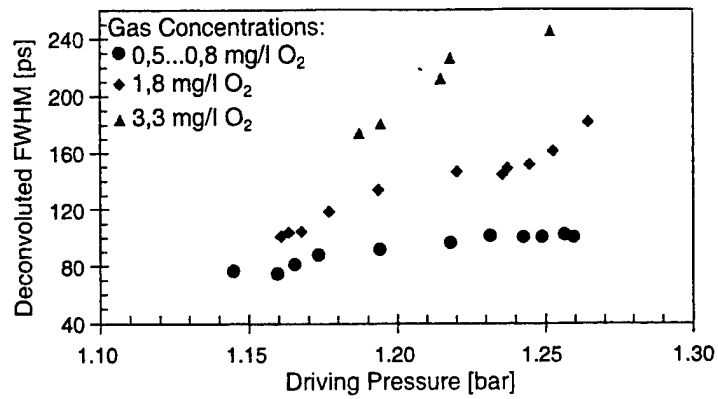


23

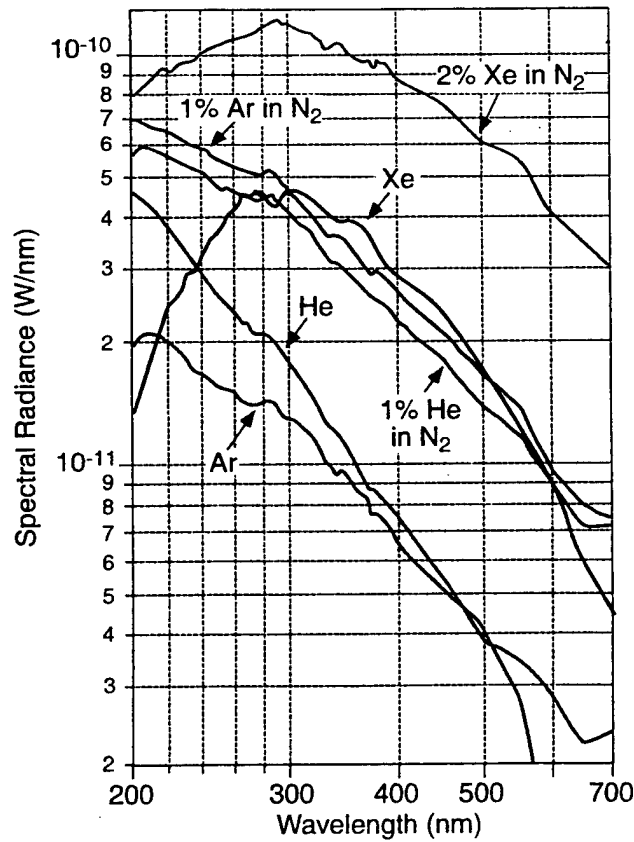


(from Gompi et al., *Phys Rev Lett*, 18 Aug 1997)

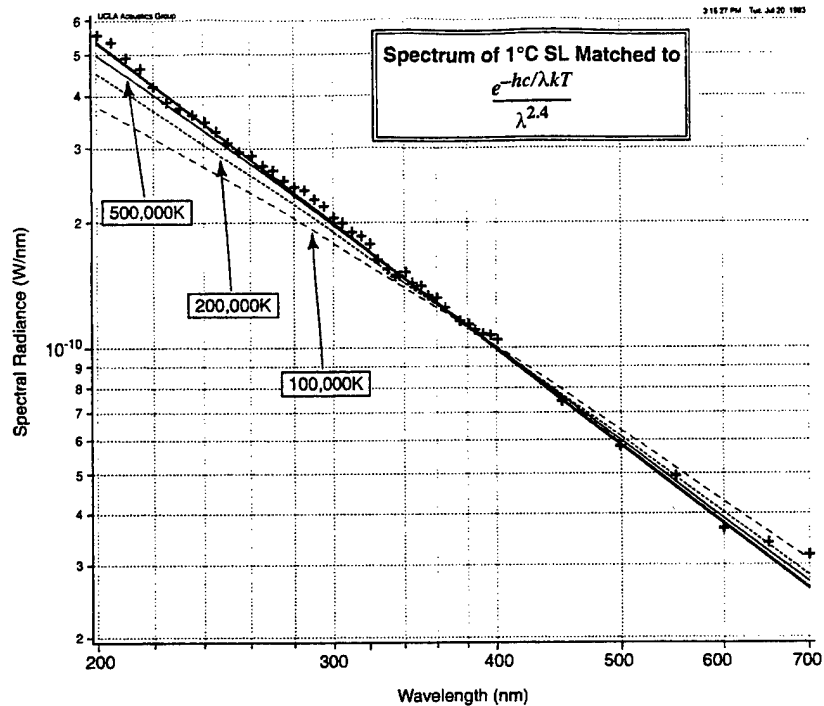
FIG. 4. Dependence of the FWHM of the SL pulse width on driving pressure and gas concentration at room temperature.



(from B. Gompf, R. Günther, G. Nick, R. Pecha, and W. Eisenmenger, *Phys. Rev. Lett.*, 18 Aug 1997)



after Hiller, et al. (*Science*)



27

Questions that were asked:

- SBSL is remarkably stable. Why?
- What is the mechanism for light emission?
- Are the mechanisms for MBSL and SBSL different?
- Can Iraq foil the nuclear test ban treaty???

28

[illegible]

Jack Pank: well, probably to do so. For developed countries with sophisticated economies, it is already possible to produce the full set of instruments of a welfare state without actually taxing the wealthy. But that may not be the best way to achieve the same result, which will then depend on the extent of the tax cut.

own such as Iraq, Iran, Palestine and South Africa - is developing powerful methods, and making their performance increasingly difficult. Although long opposed by the International Atomic Energy Authority.

On 27, September 10, called **THE NEW YORK TIMES** and announced that agreement. If the matter is resolved, it is a multi-composition of 20 million C. of the entire, containing a nuclear fusion reaction.

France and France have been confirmed that can be used to help elsewhere. This week's agreement on France-English nuclear cooperation has been made.

to continue using Power's law as evidence.

However, Dr. Arthur Koestler, Chairman, Defense Committee, and the International Science Bureau, "found other indications are too easily refutable, and all are vulnerable to the effects of natural forces. All are cheap to operate and all are equally demonstrably inaccurate. Except for human tests done by hand, all require such levels of expenditure and time as would be hard to justify by means of automatic means. The entire class of proposed prohibitions of the leader is poor."





Why is the Bubble Stable, Cycle-to-Cycle?

Look at Gas Diffusion across bubble wall!

$$\frac{\partial C}{\partial t} + \bar{v} \cdot \bar{\nabla} C = D \nabla^2 C \quad \text{Fick's Law}$$

C = Gas Concentration in Liquid [mol/m³]

D = Diffusion Constant of Gas [m²/s]

V = liquid velocity

Coupled with Equation of Motion for Bubble

$$\rho \left(R \ddot{R} + \frac{3}{2} \dot{R}^2 \right) = \left\{ \left(P_0 + \frac{2\sigma}{R_0} \right) \left(\frac{R_0}{R} \right)^{3\gamma} \right\} - \{ P_0 + P(t) \}$$

$$C = \frac{P_g}{H} \quad \text{Henry's Law}$$

32

Approximation: Assume $R(t)$ is periodic, and that gas diffusion occurs over longer period than acoustic cycle.

Result:

$$\frac{dN}{dt} \propto \frac{C_{\infty}}{C_R} - \frac{\langle R/R_0 \rangle}{\langle (R/R_0)^4 \rangle}$$

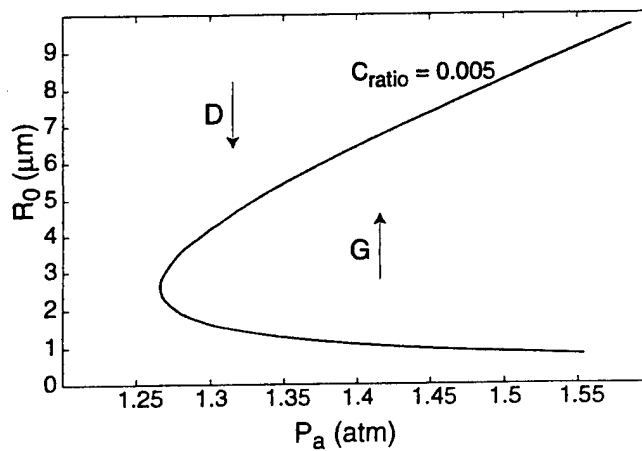
N = Number of Moles

C_{∞} = Dissolved Gas Concentration

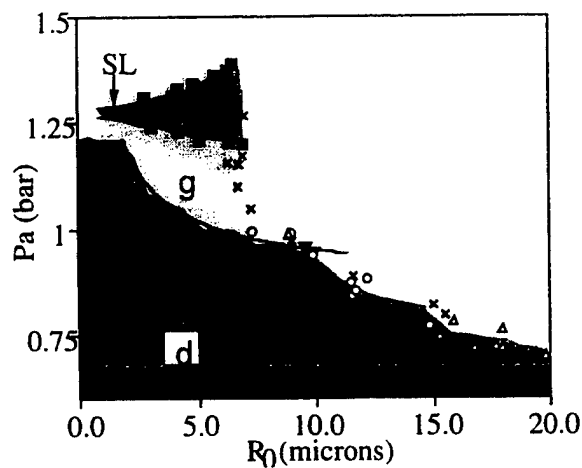
C_R = Saturated Gas Concentration

33

Gas Diffusion Stability Curve

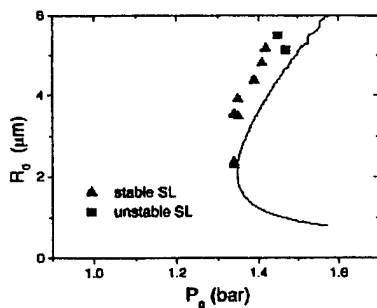


34

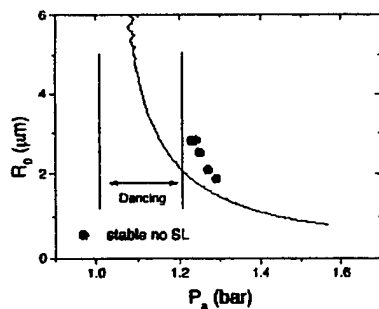


R. G. Holt and D. F. Gaitan, PRL 77, 1996

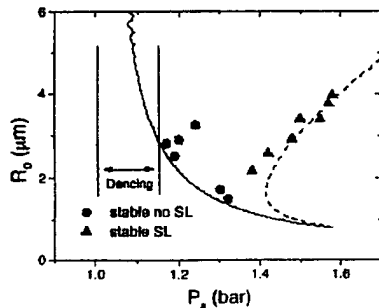
35



Phase diagram for pure argon saturated to 0.26%. The diffusive equilibrium curve is for $C = 0.26\%$ (solid line).



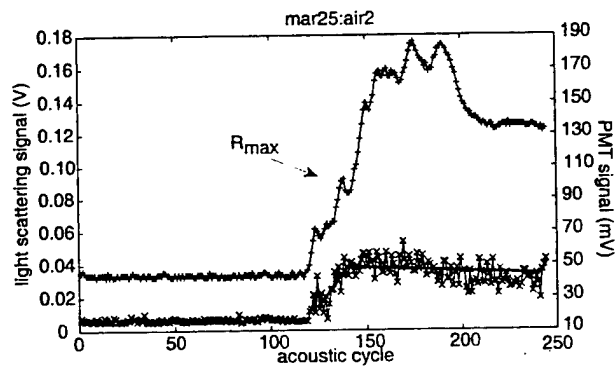
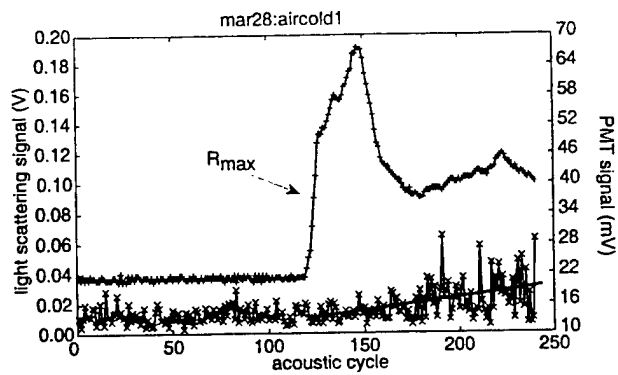
Pure nitrogen saturated to 10%. Equilibrium curve is for $C = 10\%$ (solid line).



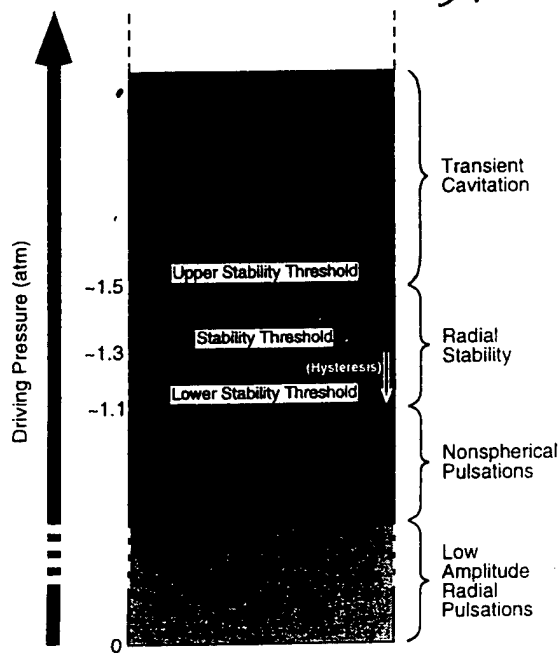
1% argon and 99% nitrogen saturated to 10%, yielding a final argon concentration of 0.1%. The diffusive equilibrium curves are for $C = 10\%$ (solid line) and $C = 0.1\%$ (dashed line).

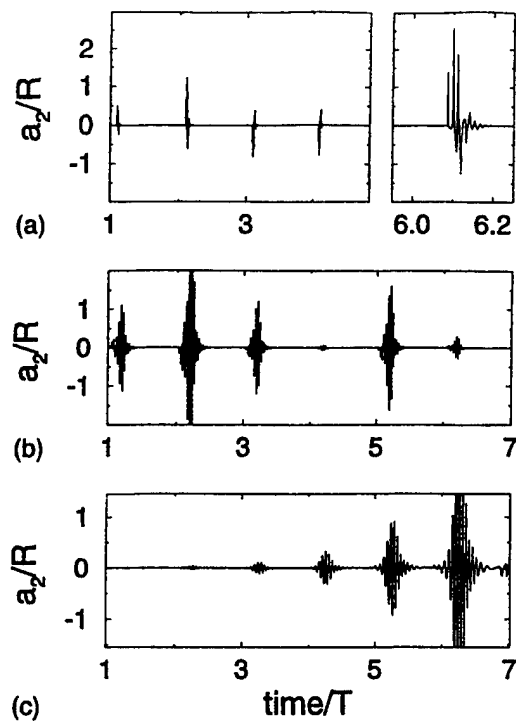
Ketterling and Apfel, PRL, vol 81, 4991-4995 (1998)

36



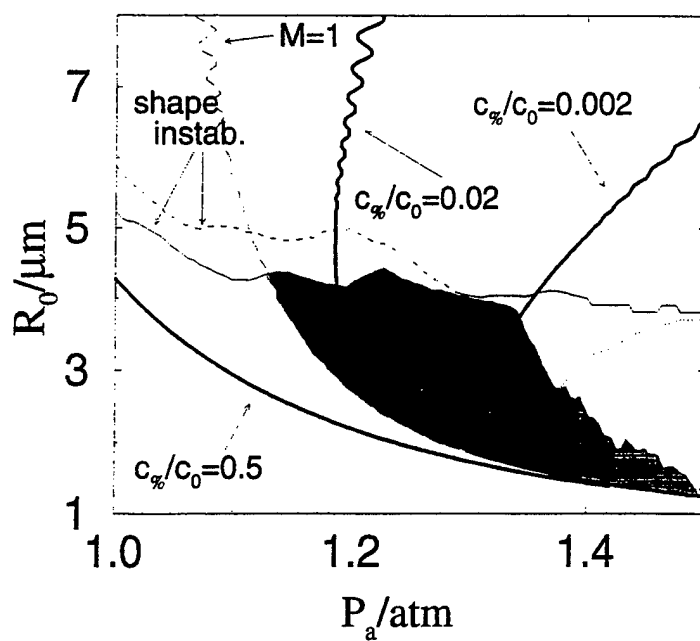
37





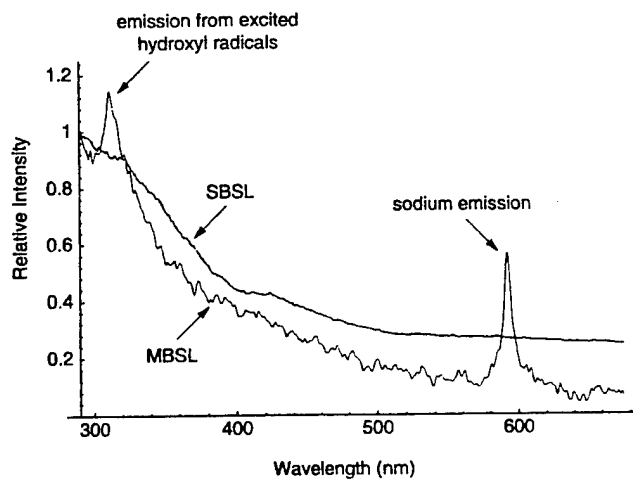
November 1996

Hilgenfeldt, Lohse, and Brenner

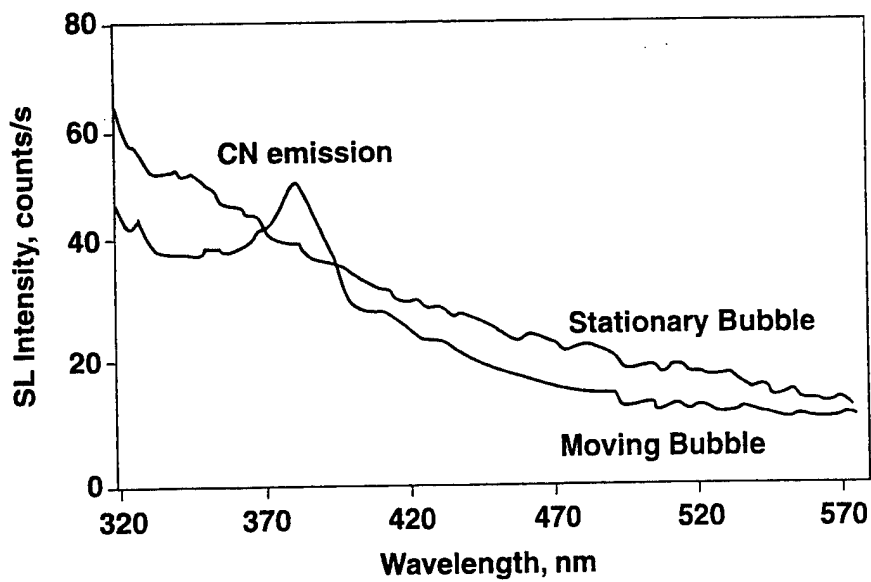


40

SL of air bubble in 0.1 molar
Sodium Chloride / Water Solution

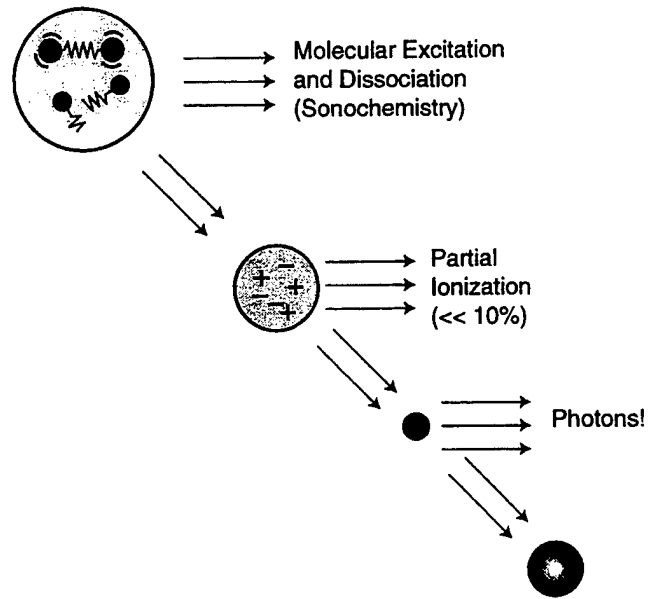


41



Mcnamara, Didenko, & Suslick, *Science*, 11/5/99

Assumptions: Compression Heats Bubble and
Hot Matter Emits Light



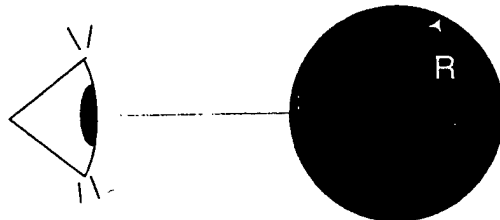
Radiated Power:

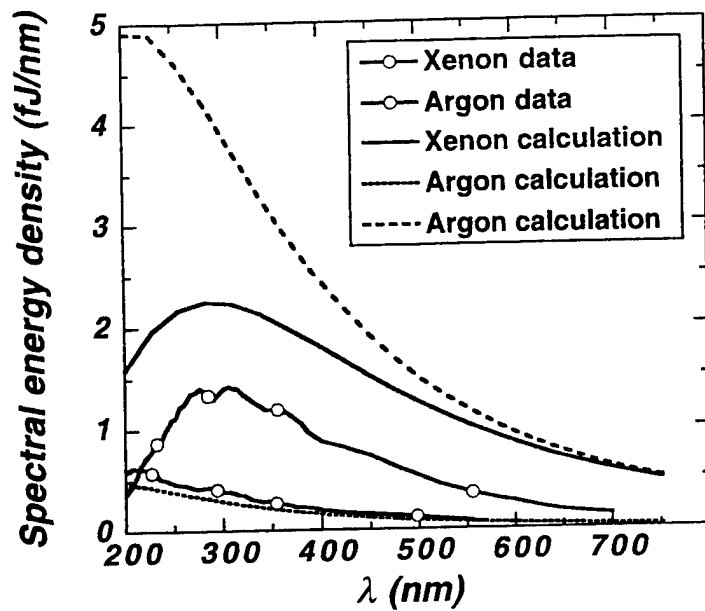
$$\int \sigma T^4(r_{ih}, t) dA + \int_{r_*}^R 4\rho\kappa(\rho, T)\sigma T^4(r, t) dV$$

Optically Thick

Optically Thin

κ = Opacity of radiating matter





W. Moss

45

SONOLUMINESCENCE MECHANISM

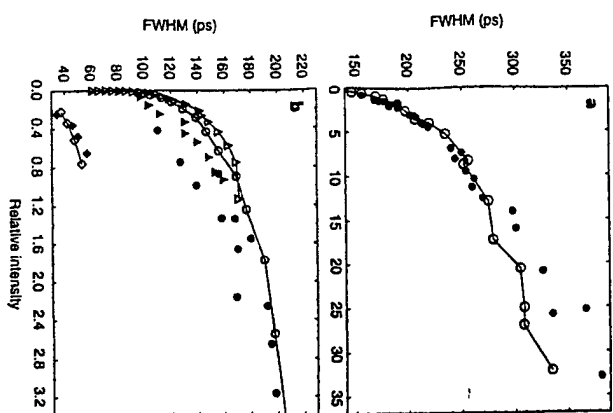
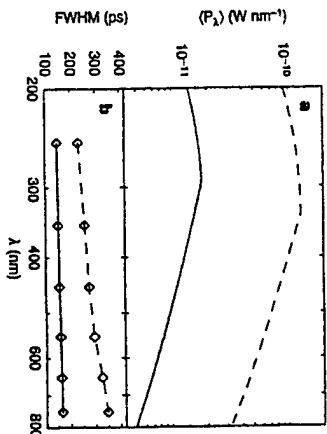
- Thermal Bremsstrahlung (e^- near ions and neutrals)
- Radiative Recombination

$$P_{\lambda}(t) = 4\pi R^2 I^{Pl} \left[1 + \frac{e^{-2\kappa R(t)}}{\kappa R(t)} + \frac{e^{-2\kappa R(t)} - 1}{2\kappa^2 R(t)^2} \right]$$

I^{Pl} = Plank Intensity for a blackbody

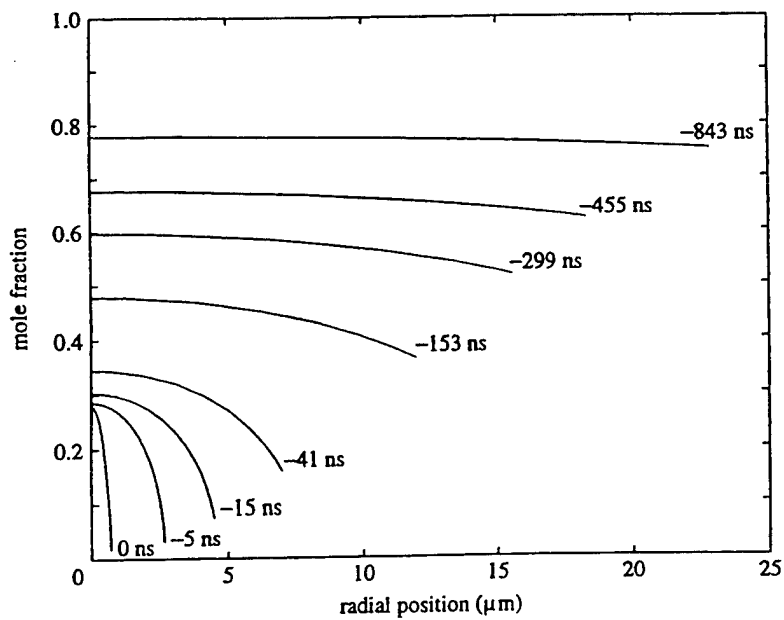
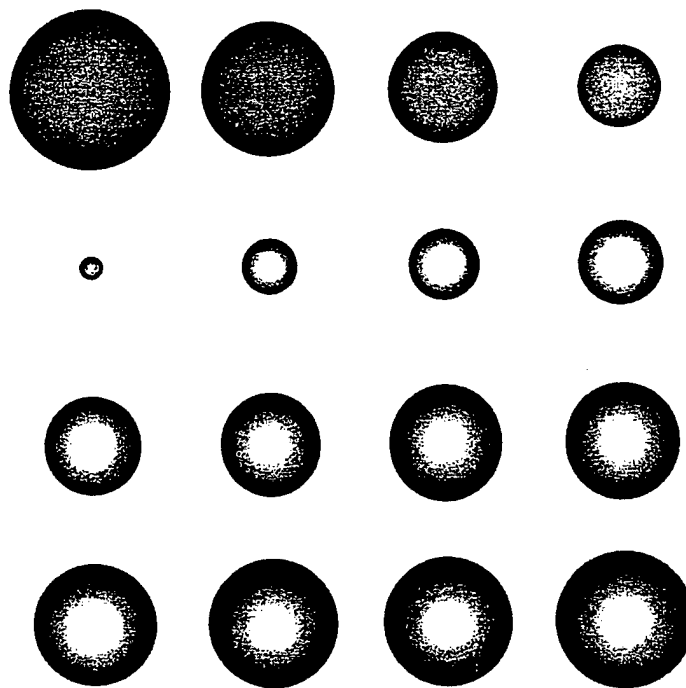
κ = Absorption coefficient (opacity)

46



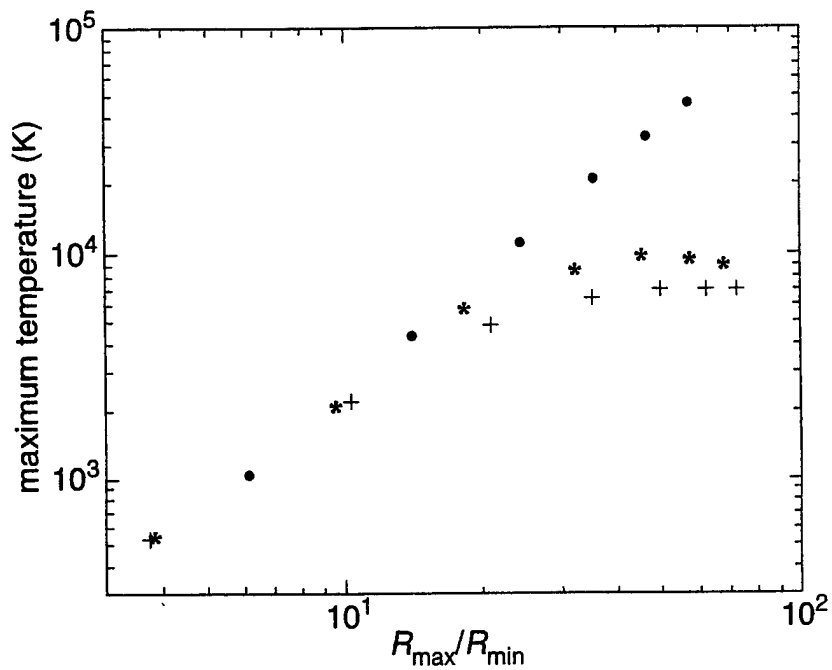
47

No.	Reaction	A_f	B_a
1	$H+O_2=O+OH$	1.92D14	0.0
2	$O+H_2=H+OH$	5.08D4	2.67
3	$OH+H_2=H+H_2O$	2.18D8	1.51
4	$OH+OH=H_2O+O$	2.1D8	1.4
5	$H_2+M=H+H+M$	4.58D19	-1.4
6	Coef. $H_2/2.5/H_2O/16.0/$ $O+O+M=O_2+M$	6.17D15	-0.5
7	Coef. $H_2/2.5/H_2O/16.0/$ $O+H+M=OH+M$	4.72D18	-1.0
8	Coef. $H_2O/5.0/$ $H+OH+M=H_2O+M$	2.25D22	-2.0
9	Coef. $H_2/2.5/H_2O/16.0/$ $H+O_2+M=HO_2+M$	2.00D15	0
10	Coef. $H_2/2.5/H_2O/16.0/$ $HO_2+H=H_2+O_2$	6.63D13	0
11	$HO_2+H=OH+OH$	1.69D14	0
12	$HO_2+O=OH+O_2$	1.81D13	0
13	$HO_2+OH=H_2O+O_2$	1.45D16	-1.0
14	$HO_2+HO_2=H_2O_2+O_2$	3.0D12	0
15	$H_2O_2+M=OH+OH+M$	1.2D17	0
16	Coef. $H_2/2.5/H_2O/16.0/$ $H_2O_2+H=H_2O+OH$	3.2D14	0
17	$H_2O_2+H=H_2+HO_2$	4.82D13	0
18	$H_2O_2+O=OH+HO_2$	9.55D6	2
19	$H_2O_2+OH=H_2O+HO_2$	1.00D13	0



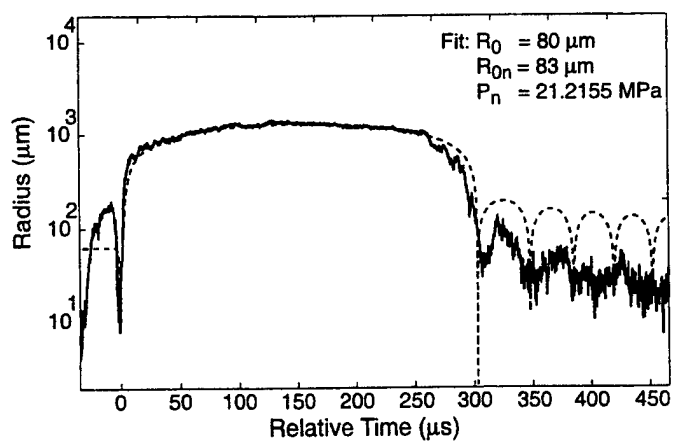
from B.D. Storey and A.J. Szeri

50



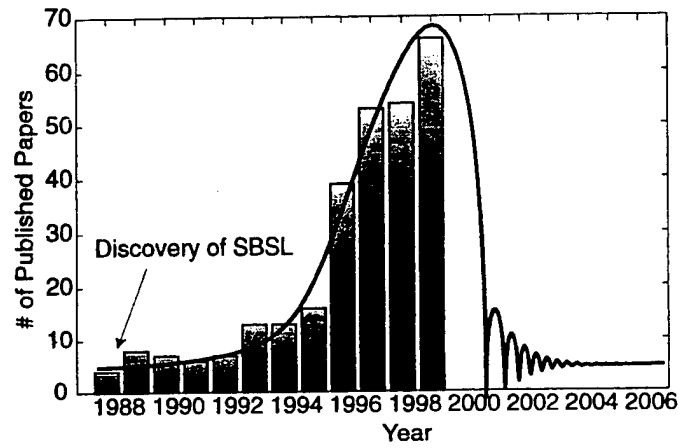
51

R(t) Signal from a Bubble in a Lithotripsy Field

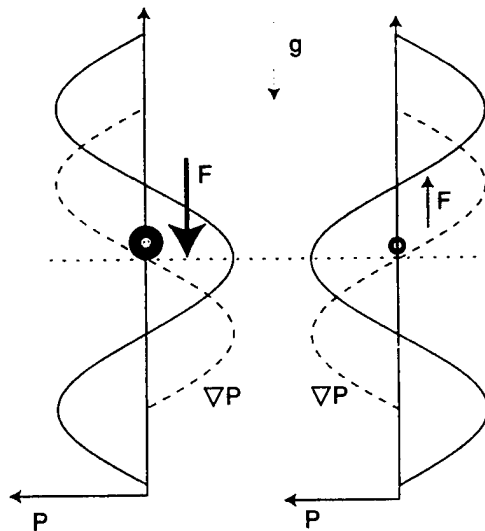


52

Future Publication Prediction



53



Acoustic Radiation Force =

$$F_a = -V(t) \nabla P$$

Buoyancy Force =

$$F_b = \rho g V(t)$$

Equilibrium Requires

$$\langle \rho g V(t) \rangle = -\langle V(t) \nabla P \rangle$$

Acoustic Radiation Force:

$$d\vec{F} = -P(r,t)d\vec{A}$$

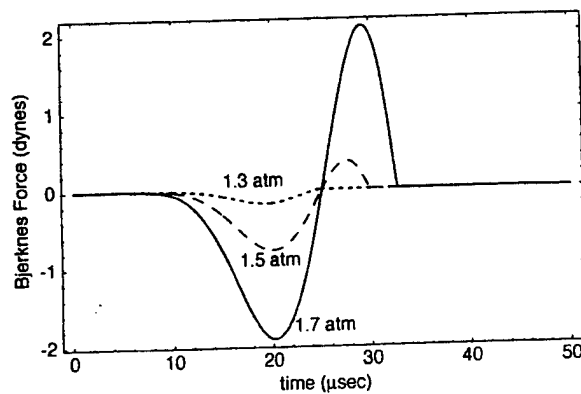
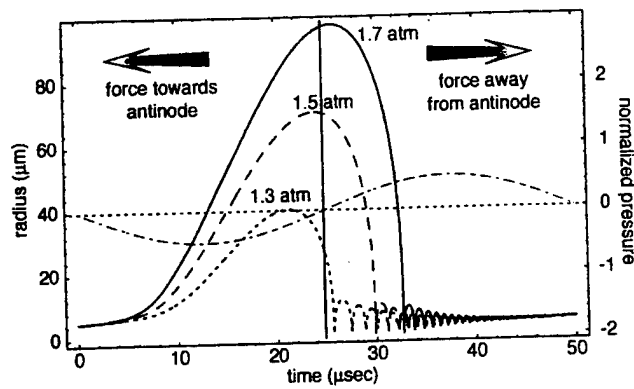
$$\vec{F} = - \int_{Surf} P(r,t)d\vec{A} = \int_{Vol} \nabla P(r,t)dV$$

But, for small bubbles, ∇P is a constant.

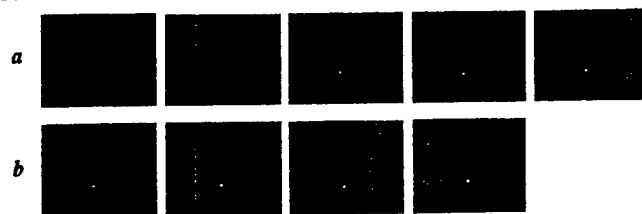
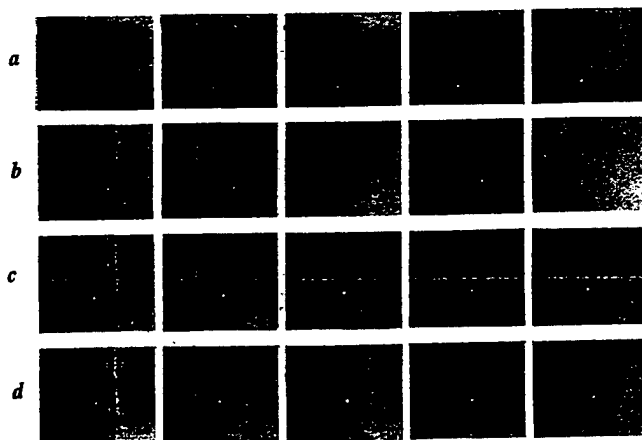
$$\therefore \vec{F} = -\nabla P(r,t)V(t)$$

$$\langle \vec{F} \rangle = -\langle \nabla P(r,t)V(t) \rangle = \text{Bjerknes Force}$$

Bjerknes force on Sonoluminescence bubble



56



(from T. Verraes, et al., 2000)

57

Viscous streaming from an oscillating spherical bubble

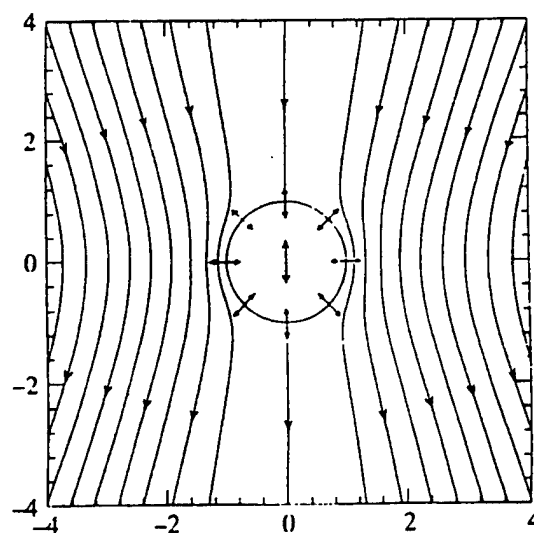
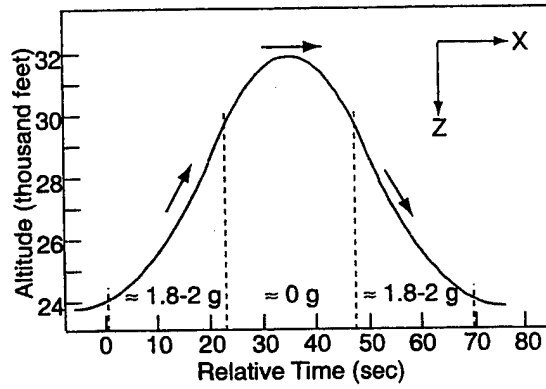


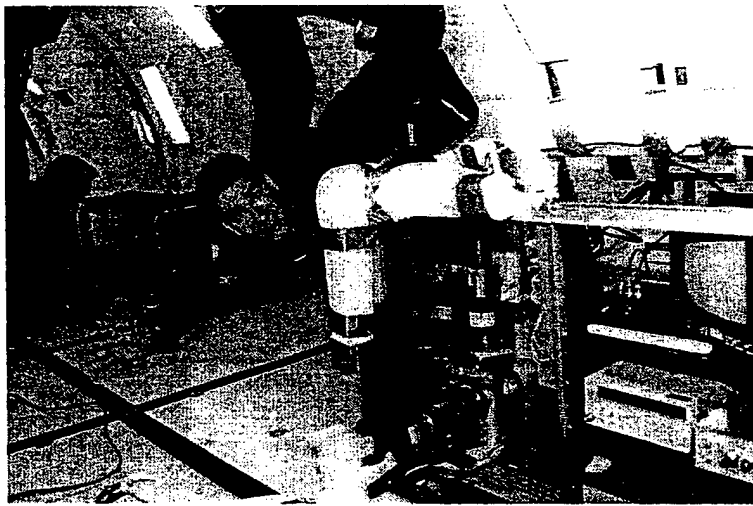
Figure 4. Streamlines for the Lagrangian drift velocity round a spherical bubble executing both lateral and radial oscillations.

M.S. Longuet-Higgins, Proc. R. Soc. Lond. A. (1998)

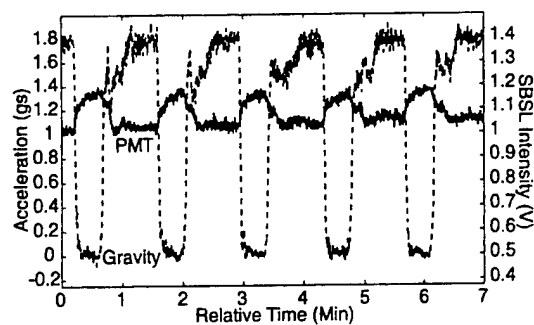
58



59



60



61

Acknowledgements:

Students:

Kirk Hargreaves, Jarred Swalwell
Vassilious Bezzerides, Paul Hilmo
Mike Chittick, Sean Cordry
Ibrahim Hallaj, Bill McNamara
Dave Kuhns, Nicolas Segabarth

PI's

William Moss, Glynn Holt,
Felipe Gaitan, Andrew Szeri,
Franz Grieser, Ken Suslick,
Ronald Roy, Lawrence Crum,

Support: NSF, ONR, ESA, NASA, DOE

REPORT DOCUMENTATION PAGE			Form Approved OMB No. 0704-0188	
Public reporting burden for this collection of information is estimated to average 1 hour per response, including the time for reviewing instructions, searching existing data sources, gathering and maintaining the data needed, and completing and reviewing the collection of information. Send comments regarding this burden estimate or any other aspect of this collection of information, including suggestions for reducing this burden, to Washington Headquarters Services, Directorate for Information Operations and Reports, 1215 Jefferson Davis Highway, Suite 1204, Arlington, VA 22202-4302, and to the Office of Management and Budget, Paperwork Reduction Project (0704-0188), Washington, DC 20503.				
1. AGENCY USE ONLY (Leave Blank)	2. REPORT DATE 30 Sep 01	3. REPORT DYPE AND DATES COVERED Final 22 June 98 - 30 Sep 01		
4. TITLE AND SUBTITLE Proceedings of the 2000 Physical Acoustics Summer School: Volume II. Transparenciess		5. FUNDING NUMBERS PE 61153N G N00014-98-1-0044		
6. AUTHOR(S) Henry E. Bass and Elizabeth A. Furr				
7. PERFORMING ORGANIZATION NAME(S) AND ADDRESS(ES) Jamie L. Whitten National Center for Physical Acoustics The University of Mississippi University, MS 38677		8. PERFORMING ORGANIZATION REPORT NUMBER		
9. SPONSORING / MONITORING AGENCY NAME(S) AND ADDRESS(ES) Office of Naval Research ONR 331 800 North Quincy Street Arlington, VA 22217-5660		10. SPONSORING / MONITORING AGENCY REPORT NUMBER		
11. SUPPLEMENTARY NOTES				
12a. DISTRIBUTION / AVAILABILITY STATEMENT Approved for public release; Distribution unlimited		12b. DISTRIBUTION CODE		
13. ABSTRACT (Maximum 200 words) Volume I of the Proceedings of the 2000 Physical Acoustics Summer School contains verbatim transcriptions of the lectures given at the summer school. Volume II of these proceedings contains copies of the transparencies used by the lecturers and Volume III contains background materials that were sent to student and discussion leader participants prior to the summer school.				
14. SUBJECT TERMS Physical Acoustics, Nonlinear Acoustics, Acoustics Demonstrations, Noise and Sensors, Resonant Ultrasound Spectroscopy, Atmospheric and Meteorological Acoustics, Thermoacoustics, Medical Applications of Acoustics, Sonoluminescence			15. NUMBER OF PAGES 504	
			16. PRICE CODE	
17. SECURITY CLASSIFICATION OF REPORT UNCLASSIFIED	18. SECURITY CLASSIFICATION OF THIS PAGE UNCLASSIFIED	19. SECURITY CLASSIFICATION OF ABSTRACT UNCLASSIFIED	20. LIMITATION OF ABSTRACT	

NSN 7540-01-280-5500

Standard Form 298 (Rev. 2-89)
Prescribed by ANSI Std. Z39-1
298-102